# Indira Gandhi Centre for Atomic Research

2013

ANNUAL REPORT

Government of India
Department of Atomic Energy
Indira Gandhi Centre for
Atomic Research
Kalpakkam 603 102

सत्यमेव जयते

IGCAR

2013

INDIRA GANDHI CENTRE FOR ATOMIC RESEARCH

ANNUAL REPORT

**Government of India
Department of Atomic Energy
Indira Gandhi Centre for
Atomic Research
Kalpakkam 603 102**

"Actions today mould our tomorrows"

- Indira Gandhi

".... The relative role of indigenous science & technology and foreign collaboration

can be highlighted through an analogy.

Indigenous science and technology plays the part of an engine in an aircraft,

while foreign collaboration can play the part of a booster.

A booster in the form of foreign collaboration can give a plane an assisted take-off,

but it will be incapable of independent flight unless it is powered by engines of its own.

If Indian industry is to take-off and be capable of independent flight,

it must be powered by science & technology based in the country ..."

- Homi Jehangir Bhabha

"…..There is a totality about modernisation, and in order to gain confidence,

we must experiment with our resources even at the risk of failure.

There is a need for a constant interplay between basic sciences, technology,

industrial practice and management, if economic progress is to result

from the activity undertaken"

- Vikram Sarabhai

Editorial Committee

Chairman
Dr. P. R. Vasudeva Rao

Convener
Dr. M. Sai Baba

Members
Shri B. Babu
Dr. N. V. Chandra Shekar
Shri K. Ganesan
Shri G. V. Kishore
Dr. C. Mallika
Shri B. K. Nashine
Shri K. Natesan
Shri V. Rajendran
Dr. Saroja Saibaba
Dr. G. Sasikala
Dr. C. V. Srinivas
Ms. S. Usha
Shri K. A. Venkatesan
Dr. Vidya Sundararajan

Address for Correspondence
Dr. P. R. Vasudeva Rao
Chairman, Editorial Committee
Director
Indira Gandhi Centre for Atomic
Research
Kalpakkam - 603 102

Phone : +91-44-2748 0240/234
Fax : +91-44-2748 0060/301
Email : dir@igcar.gov.in
   vasu@igcar.gov.in

Website : www.igcar.gov.in

CONTENTS

FRONT COVER

INDIRA GANDHI CENTRE FOR ATOMIC RESEARCH

2013

IGCAR ANNUAL REPORT 2013

ANNUAL REPORT

Government of India
Department of Atomic Energy
Indira Gandhi Centre for
Atomic Research
Kalpakkam 603 102

1. (a) Chopped U-6Zr fuel pin segments
   (b) U electrodeposit from a typical electrorefining run
   (c) chopped fuel pin after electrorefining

2. Temperature field in storage subassembly

3. Fast Breeder Test Reactor

4. Setup and sodium impingement scenarios
   on the concrete

5. Precision electron diffraction orientation
   imaging microscopy

BACK COVER

Published by Scientific Information Resources Division, IGCAR, Kalpakkam - 603 102
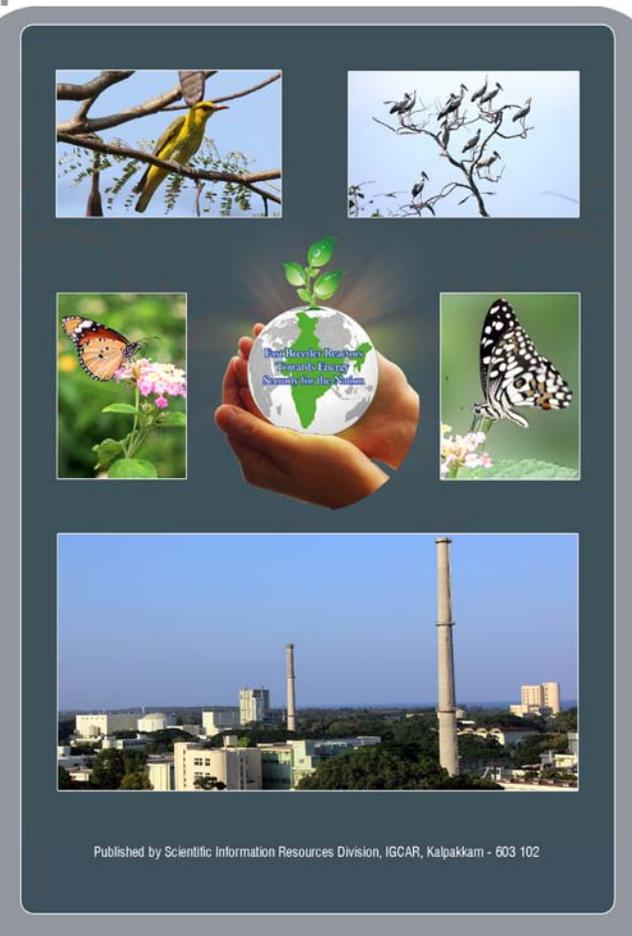
Flora and Fauna at Kalpakkam

Foreword

I have great pleasure in presenting the Annual Report of IGCAR for the year 2013. The year 2013 has seen all round progress in the activities of IGCAR and the report highlights selected achievements of the Centre during the year.

The Fast Breeder Test Reactor, the flagship of our Centre, acquired license to operate until June 2018. FBTR has served as an excellent test facility for various materials including fuels. The introduction of sodium bonded, enriched uranium-zirconium metal fuel pins for test irradiation marks an important step in the development of metal alloy fuels for future fast breeder reactors. The fabrication of sodium bonded test fuel pins with U-19Pu-6Zr alloys slugs has also been completed and the fuel pins will be introduced in FBTR in its next campaign. A capsule containing annual pellets of mixed oxide fuel and two sphere-pac test fuel pins is also currently under irradiation. All these irradiation experiments would provide vital inputs for the fast reactor programme.

Our Centre has broadly met its commitments to the PFBR project. All the major equipment for PFBR have been delivered to BHAVINI, barring a few equipment whose testing is in progress. During the year 2013, the control plug and two primary sodium pumps were delivered to BHAVINI after resolving several technological challenges. The Under Sodium Ultrasonic Scanner has been qualified and is ready for shifting to BHAVINI. The full scope training simulator has been commissioned at BHAVINI. The criticality of PFBR, expected during the coming year will mark an important milestone in our country's fast reactor programme.

With our commitment to PFBR design and construction nearing completion, our focus will now be on the two FBRs to follow. The conceptual design of FBR-1&2 along with detailed design of reactor assembly has been completed through structural mechanics and thermal hydraulics investigations. Our major effort now is to optimize manufacturing sequence and technologies for the permanent components of the reactor assembly towards reducing the cost and time of construction.

CORAL has continued to perform satisfactorily with improved performance. Significant progress has also been made towards completion of construction activities in DFRP and it is possible to start cold commissioning with uranium in the coming year. With the receipt of construction clearance as well as the financial approval for the Fast Reactor Fuel Cycle Facility, the construction work at site is ready to start. Metal fuelled FBRs will be the mainstay of the country's fast reactor programme in the coming decades. The conceptual design of 500 MWe Metallic Demonstration Fast Reactor has been completed. With respect to pyroprocessing of metal fuels, experiments with the Engineering scale Ambient Temperature Electro Refiner facility have provided important inputs to the design of the electrorefiner.

Several generic R&D areas related to FBRs are being addressed by different groups in the Centre. The development of newer clad materials as well as structural materials for fast reactors as well as reprocessing and waste management programmes is a typical example, where we have continued to make sustained progress. During the year, nitrogen enhanced 316LN stainless steel with improved mechanical properties has been developed. In the domain of safety, our efforts have been to understand the sodium concrete interaction and

molten uranium-sodium interaction, adjacent tube wastage phenomenon in Steam Generator, sodium aerosol dispersion in open environment, etc, qualify the leak collection trays at a system level, and obtain accreditation of the Bio-dosimetry Laboratory by AERB till 2016.

Our contributions to other important National programmes include the development of Indian reduced activation ferritic martensitic steel with optimized mechanical properties and the associated fabrication methodologies for the Indian test blanket modules for testing in ITER, in collaboration with IPR, MIDHANI, ARCI, DMRL and DRDL; development of welding procedures for 304HCu SS and alloy 617M boiler tubes produced indigenously as part of the national programme on development of advanced ultra-supercritical technology. In addition, several programmes of societal interest have continued, such as experiments on production of P-32 isotope through irradiation of strontium sulphate in FBTR, development of MCG using SQUID sensors and development of infrared thermography as a screening tool for breast cancer.

During the year, the Centre also had the proud privilege of receiving several eminent visitors including Prof. C. N. R. Rao, who has been conferred the prestigious title of "Bharat Ratna". Such visitors have continued to inspire us in our quest for developing challenging technologies for the country. The technology day celebrations, organized on May 11, also highlighted the high level of passion and excitement among our technical staff, which augurs well for the programme. We are undertaking a Peer Review of the activities in various domains to fine tune the directions of our R&D with inputs from eminent peers. The annual report carries a summary of such activities, besides the technical reports.

On behalf of the editorial team, I thank the authors for providing lucid articles, and their peers who have gone through the content and refined the articulation. I take this opportunity also to thank the editorial team led by Dr. M. Sai Baba, in particular, for their earnest and dedicated efforts in bringing out the annual report with the expected quality. A special word of mention should be made of Shri G. Pentaiah and Shri K. Varathan of SIRD, for their painstaking efforts towards bringing out the report in its present form.

As always, we look forward to the critical comments of the readers, and suggestions for improvement.

(P. R. Vasudeva Rao)
Director, IGCAR

Mission of IGCAR

« *To conduct a broad based multidisciplinary programme of scientific research and advanced engineering development, directed towards the establishment of the technology of Sodium cooled Fast Breeder Reactors (FBR) and associated fuel cycle facilities in the Country*

« *The development and applications of new and improved materials, techniques, equipment and systems for FBRs and*

« *To pursue basic research to achieve breakthroughs in fast reactor technology*

Vision

To be a Global Leader in Sodium cooled Fast Breeder Reactor and associated Fuel Cycle Technologies by 2020
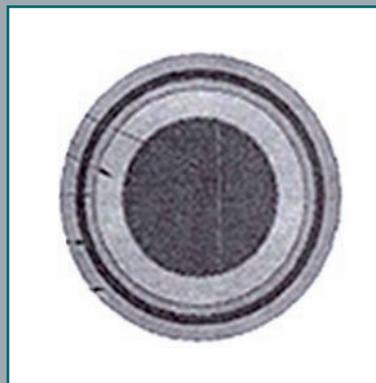
CHAPTER 1

Fast Breeder Test Reactor

I.1   Irradiation of Fuel and Structural Materials

During 2013, FBTR completed 21st irradiation campaign and 22nd irradiation campaign was started. In 21st campaign maximum reactor power was 20.3 MWt. In the 22nd campaign, reactor is being operated at a maximum power of 18 MWt for irradiation of sphere-pac fuel pins. Table 1 shows the irradiation experiments completed/in progress during the year.

All these irradiations are carried out in capsules with three pins (Figure 1). The capsule is loaded in a hexagonal steel carrier.

Metallic fuel irradiation

Irradiation of three pins of enriched U (14.8% ^{235}U) - 6% Zr metal fuel was started in the 21st campaign. Design of the pins and the capsule are same as that of the natural uranium - 6% Zr currently under irradiation in the 4th ring, except that uranium is enriched to 14.8%. The peak linear heat rating is 225 W/cm based on clad hot spot consideration and not fuel melting, which is 655 W/cm. The target burn-up is 25 GWd/t. Since the special subassembly carrying the fuel pin capsule is located in the first ring (01-04), outlet temperature monitoring for plugging detection is required for this subassembly.

Sphere-pac fuel irradiation

A joint proposal has been putup by IGCAR–BARC to irradiate test fuel pins fabricated through sol-gel vibro compaction technology to study the irradiation performance of the fuel pins during the 'beginning of life' phase, in-situ sintering and the column stability. Two such sphere-pac fuel pins and one reference MOX pin in a capsule have been loaded. The sphere-pac pins are required to be irradiated for 200 hours at a linear heat rating
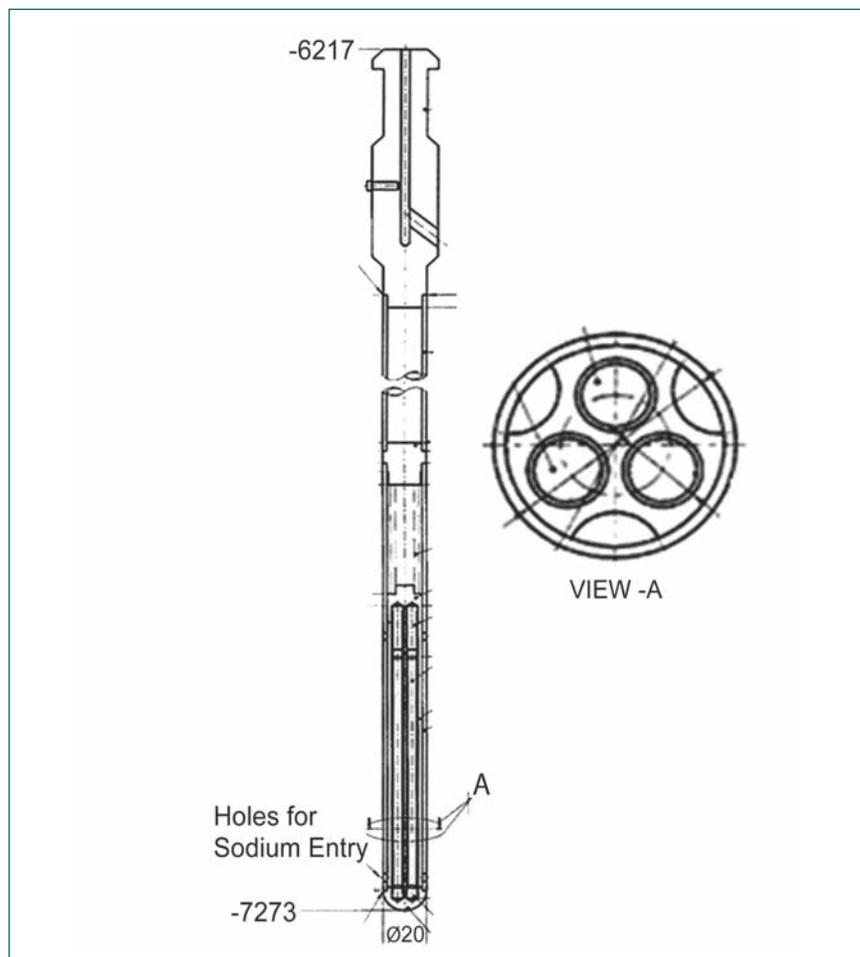

Fig. 1   *Typical irradiation capsule with three pins*

of 205 W/cm at reactor power of 13.9 MWt followed by 100 hours at 260 W/cm at reactor power of 18 MWt. To respect the   linear heat rating limits, the special subassembly is loaded in the second ring core location of 02-08. Since the special subassembly is to be located in the second ring, plugging detection is required for

this subassembly also.

Monitoring of special subassemblies

Two thermocouples are provided for monitoring the outlet temperatures in each core location (except the central location which has three thermocouples). Healthiness of the thermocouples is monitored by comparing their output against

Table 1: The irradiation experiments completed/in progress during the year	
21st campaign	22nd campaign
Irradiation of natural U-Zr sodium bonded metal fuel pins	Irradiation of natural U-Zr sodium bonded metal fuel pins
Irradiation of enriched U-Zr sodium bonded metal fuel pins	Irradiation of enriched U-Zr sodium bonded metal fuel pins
Impact specimens of 304LN & 316LN for low dose irradiation	Impact specimens of 304LN & 316LN for low dose irradiation
Irradiation of TRISO coated particles & Nb-1% Zr-0.1% C for compact high temperature reactor	Irradiation of sphere-pac MOX fuel pins

a threshold of reactor inlet temperature minus 4°C (T_i-4°C). A separate plugging detection supervision program computes the difference between the actual temperature rise of these subassemblies against a fixed threshold which is the expected rise for that subassembly. If the temperature rise exceeds the threshold by 5°C, an alarm 'θi High' appears in control room. If it exceeds 10°C for any one thermocouple, an alarm 'θi excessive' annunciates and SCRAM is initiated if one of the following condition is satisfied.

➢ Both thermocouples are faulty
➢ Both thermocouples exceed 10°C
➢ One thermocouple is faulty and the other exceeds 10°C.

Provision is made for online modification of the fixed threshold for each subassembly. Software modification was carried out in core temperature supervision program and after the completion of internal audit and clearance IV&V (independent verification and validation), the modified software was incorporated in central data processing system (CDPS) of FBTR.

Structural material irradiation

One of the major life limiting factors for FBRs is the loss of ductility of permanent, out-of-core structures which are subjected to low doses of irradiation (typically 2 to 5 dpa). In order to get base-line data on the out-of-core structural materials in PFBR and other future FBRs, tensile, impact and disc specimens of 316LN & 304LN SS from both wrought and full welds and hard coated disc specimens of 304LN & 316LN contained in the capsules (Figure 1) in a carrier subassembly have been loaded in 4th and 5th rings and irradiation was started in the 21st campaign.

IGCAR is developing reduced activation materials for the test
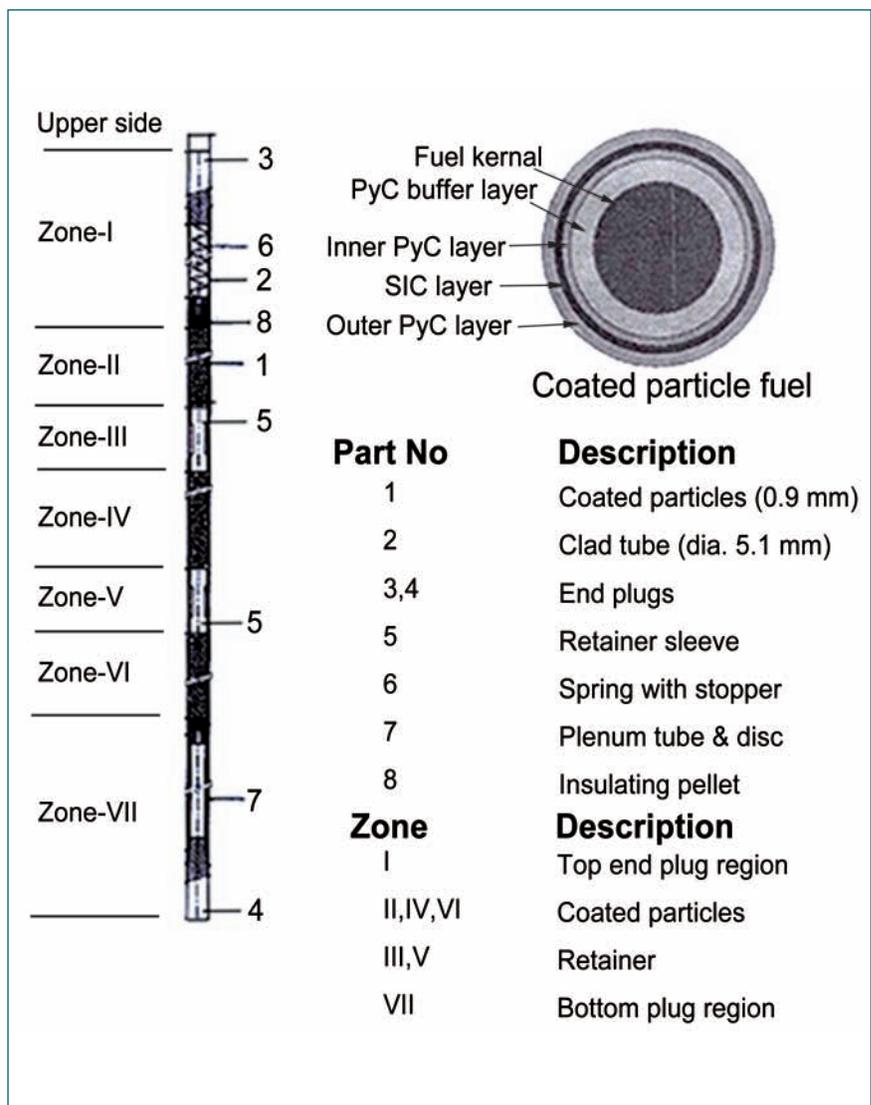
Fig. 2 *Test pin with TRISO coated particle fuel*

blanket modules of the International Thermonuclear Experimental Reactor (ITER). Disc specimens of reduced activation of ferritic & martensitic (RAFM) steels were also included in the capsules. One of the capsules has been discharged at the end of the 21st campaign after it attained a damage of 5.5 dpa and the other will be discharged at the end of the 22nd campaign.

TRISO particles for compact high temperature reactor

Compact high temperature reactor (CHTR) is being designed by BARC with TRISO coated particle type fuel. Based on the proposal from BARC, irradiation of TRISO coated particles being developed for compact high temperature reactor was carried out in the 21st campaign. The TRISO particles are in double containment. Disc specimens of compact high temperature reactor structural materials (Nb-1%Zr-0.1%C) were included in the irradiation capsule. The purpose is to understand the irradiation behavior of the coatings of the TRISO particles and the mechanical properties of the irradiated Nb-1%Zr-0.1%C specimens. In order to use the available irradiation space effectively, cold worked SS316L disc specimens, of relevance to fast reactors, were also included in the capsule. Three pins carrying these materials were irradiated in 5th ring during 21st campaign and discharged for post irradiation examination (Figure 2).

I.2   Relicensing of FBTR

Initial safety review

FBTR was commissioned and made critical well before the creation of the AERB in 1987. SEWG (Safety Evaluation Working Group) had carried out detailed review of the design and safety analysis of FBTR, covered in the preliminary safety analysis report titled 'FBTR hazard evaluation report'. This document was revised addressing the comments of SEWG review and the 'FBTR safety report' was submitted to the DAE-SRC in 1983. The safety analysis chapter was further revised based on core design changes due to use of small carbide core and rated power of 10.6 MWt in 1984. The technical specifications document was prepared based on those of RAPS and MAPS and was reviewed by RRC-CWMF SC and SEWG and approved by DAE-SRC in 1984. DAE-SRC accorded clearance for commissioning and criticality after ensuring availability of important station documents like safety report, technical specifications, system commissioning documents, procedures for physics and engineering experiments, system manuals and trained man power. However, no formal plant operation license was issued and campaign wise clearances were being obtained.

First criticality of FBTR was achieved on October 18, 1985 with a small carbide core and nominal power of 10 MWt. Initially FBTR was operated up to 1 MWt without the steam generator, and later gradually raised to higher power in stages with the commissioning of steam generator, steam water system and the turbo alternator and adding fuel in the core.

Inception of regulation by AERB

With the constitution of AERB in place of DAE-SRC, regulatory procedures were enforced in more formal ways requiring stage wise consent for the new projects, licensing, periodic regulatory inspection and relicensing of operating plants based on periodic safety reviews as per the established safety guidelines and procedures. In addition, periodical review of the safety status of the reactor through committees established at three levels was continued.

Periodic safety review and relicensing

Within the period of operating license of a nuclear power plant AERB grants authorisation for operation for five years normally. Renewal of authorisation after this period is based on a comprehensive safety review considering cumulative effects of plant ageing, irradiation damage, results of in-service inspection, system modifications, operating experience, status and performance of safety systems and safety support systems, revisions to applicable safety standards, environmental impact etc. Preparation of the first periodic safety review document of FBTR was initiated in 2003 based on the periodic safety review document of MAPS. The first draft of periodic safety review document (except a few chapters) was prepared and submitted to Operating Plants Safety Division (OPSD) of AERB for review in 2005. After review of the draft by the OPSD, AERB in 2006, and incorporating the comments updating the plant parameters and other details it was resubmitted. The periodic safety review document was reviewed chapter wise by IGCAR-SC. This was an iterative process and led to 10 drafts till final approval in 2012 by SARCOP.

One of the major exercises required was residual life assessment of the plant equipment as a part of ageing management for components and equipment, which cannot be replaced like block pile components, reactor vessel, grid plate etc. This was done by analysis to estimate the material damage due to neutron dose. Since FBTR has operated below creep range, enough residual life is available for the components whose life is governed by creep-fatigue damage and the life of FBTR is found to be essentially governed by the neutron dose on the grid plate. Stainless steel samples were irradiated to low damage levels and the loss of ductility was assessed. Equipment like obsolete switch gears, protective instrumentation and plant computers were replaced with state of the art systems.

Another major work was the seismic re-evaluation of FBTR to revised seismic level. This was carried out as a joint research project between IGCAR and the AERB-Safety Research Institute by probabilistic seismic hazard analysis method. This involved ten main tasks including preparation of a criteria document, arriving at the review basis ground motion (RBGM) parameter based on analysis of site specific data and existing faults around Kalpakkam, safety analysis for arriving at the seismic structures, systems and components required to be qualified, detailed plant walk-down to identify seismic vulnerabilities due to interactions and easy fixes to overcome the same, analysis of as-built system data to assess adequacy of supports and anchorage, structural analysis for qualifying the various safety related seismic structures, systems and components, testing of components on shake table and finally assessment of seismic

capacity of the structures, systems, components and adequacy of available seismic margin. Entire task was carried out by the team from 2006 to 2010. By December 2009, all the reports were submitted and reviewed by the subcommittees constituted by SARCOP and recommendations for retrofits and easy fixes were identified.

Yet another major work was equipment qualification, qualification of the plant structures, systems and components for ensuring safe shutdown, decay heat removal and containment, to ensure capability of systems for mitigation of the consequences events like extended station black out, loss of coolant accident etc. Qualification of instrumentation from sensor to the final element in the channel for monitoring of temperature, radiation and pressure as part of post accident management in case of beyond design basis accidents, taking into account the harsh ambient condition and high radiation.

Design compliance to present practices was studied and major non compliances like non availability of back up control room, were identified and retrofits were engineered.

The periodic safety document was reviewed by SARCOP in June 2012. The Fukushima accident added a new dimension to the exercise. Analyses of beyond design basis accidents had to be carried out and retrofits for increased design basis flood levels had to be worked out.

Challenges

Periodic safety review was a massive and challenging exercise. There are no parallel reactors from which the methodology for periodic safety review could be adopted. The plant is of vintage design and built at a time when the tools, techniques for analysis, design used were evolving and were more qualitative and manually done as compared to current practice of computer aided tools and codes. As archival methods for data retrieval were not adequate and also since most of the

personnel associated with design/ construction have since retired, data/document retrieval was daunting. Safety analysis had to be carried out afresh for the current core with MK I, MK II and MOX fuels. The same team of FBTR catering to normal operation and maintenance had to carry out periodic safety review. Insistence on formats made the actual document preparation more time consuming. Being a new type of reactor under AERB regulation, the review process also got prolonged.

Though it took a long time of about nine years, it was carried out meaningfully and the final periodic safety review document consisting of 403 pages was completed and was reviewed by SARCOP in June 2013. The strengths and weaknesses of the plant were assessed by a revisit to the safety concerns/issues and operation experience and suitably addressed. Finally FBTR was formally relicensed till June 2018.

I.3   Seismic Retrofits in FBTR

FBTR site is in an area considered free of seismic events (zone number 1 as per IS 875). Nevertheless, considering the importance of the nuclear reactor installation and as a provision for future, seismic coefficients of 0.1 (g) horizontal and 0.05 (g) vertical had been considered in the design of safety related structures and buildings and 0.05 (g) horizontal and 0.025 (g) vertical for auxiliary buildings and structures. However, in view of the higher seismic values used for PFBR, it was required to carry out seismic re-evaluation of FBTR.

Seismic re-evaluation involved identification of the seismic structures, systems & components

for fulfilling the three safety functions-viz. safe shut down, decay heat removal and containment of radioactivity. Structural analysis was carried out for the buildings namely, reactor containment building, control building, service building, steam generator building and structures like cooling tower, diesel day tank and systems like primary and secondary sodium. 'Experience based method' was followed for battery stands, electrical distribution and instrumentation panels. 'Rule of the box method' was applied for components within the I&C panels. Components like electronic timer circuits, functional circuits of the safety critical computer system which are in the form of PCBs, cable

penetration assembly etc. were qualified by testing using the shake table. In order that the functioning of the seismic structures, systems and components located in the neighborhood of non safety related equipment is not hampered due to interferences or interactions during a seismic event from improperly supported equipment, such interfering equipment were identified by detailed plant walk down. A team of seismic experts knowledgeable and experienced in carrying out plant walk down visited various areas of FBTR and checked for interference to SSC, adequacy of anchorage of SSC, supports to various pipelines, tanks and other equipment. The team also

identified URM walls (brick walls or unreinforced masonry walls) close to SSC. After evaluation of the existing anchorage/supports or based on the available documented experience data, the easy fixes and minor retrofits were identified. The team also identified areas housing redundant safety equipment and systems, prone to common cause failures during seismic event due to lack of segregation and also ease of access to critical equipment required for egress and also for safety related manual actions.

The major retrofits required to ensure seismic qualification of FBTR are

i. Replacement of the original unanchored wooden battery stands by seismically qualified metallic stands anchored to the floor (Figure 1)

ii. Seismic anchoring of gas cylinder banks in the plant (Figure 2)

iii. Structural reinforcement of unreinforced masonry walls in service building (ground and first floor) and steam generator building

iv. Reinforcement of steel structure supporting equipment at -2.81 m elevation in reactor containment building

v. Complete segregation of the redundant battery banks of control power supply systems by extending the partition wall and provision of fire proof seismic doors and

vi. Improvement of access to the steam generator trap doors and manually operated valves of pre-heating and emergency cooling (PHEC) system.

The plant walk down also identified panels, structures and equipment which need improvement by means of easy fixes. This involves about 400 such modifications in the plant. Important ones are

i. Support arrangement for field

Fig. 1 *Metallic battery stands*

and armature battery banks of primary and secondary Ward Leonard mounted within the panels

ii. Provision of adequately sized anchors for all safety related I&C panels, electrical distribution cabinets and MCCs and also the equipment and panels which are in their vicinity

iii. Bolting of adjacent panels in RCB, SB, SGB, TB, Electronics & CDPS rooms and relay room to avoid seismic interactions (Figure 3)

iv. Seismic locking of fuel handling flasks and cranes

v. Anchoring of furniture, lead brick partitions between redundant exhaust filter banks, lead bricks used for complementary shielding in reactor containment building

vi. Additional supports for the cable trays located near the SSC

vii. Decongestion of cable trays in RCB -2.81 m elevation

viii. Provision of clamps for relays, improving the supports of the panel mounted recorders and meters

Fig. 2 *Seismic anchoring of gas cylinder banks in the plant*

ix. Clamping of WL system batteries located in the panels

x. Clamping of isolation transformers of control power supply system (Figure 4).

Among the major modifications battery stands have been replaced and all the cylinder banks have been secured with adequate anchorage. Pneumatic mechanism has been provided for operation of the trap door. Battery banks of Ward Leonard drives have been provided with clamps to avoid dislocation during seismic event. Anchoring of MCC panels and bolting of adjacent panels have been completed for RCB, SB, relay room and SGB. Manually operated PHEC valves are being replaced by pneumatic valves operable from control room. URM wall reinforcement is major work which will be taken up during 2014.

In its existing condition during the seismic reevaluation, FBTR was qualifying for a peak ground acceleration (PGA) of 0.09 (g) and with the retrofits and minor fixes it will qualify for a PGA of 0.22 as per the review basis ground motion.

Fig. 3 *Bolting of adjacent panels to avoid seismic interactions*
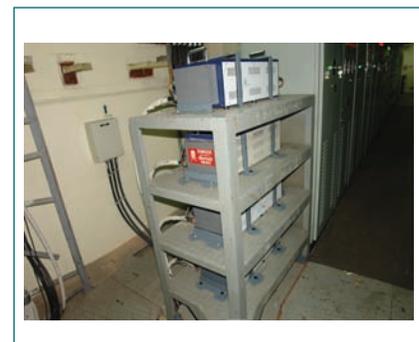
Fig. 4 *Clamping of isolation transformers*

I.4 Service Life Extension Program by Condition Assessment of FBTR Civil Structures

Construction of sodium cooled Fast Breeder Test Reactor (FBTR) was started in 1973 and civil works were completed around 1980. FBTR was designed and constructed using standards, materials and construction practices that existed in the country at the time of construction. However, due to coastal environment exposure as well as reactor operation conditions there may be degradation in concrete and in the embedded steel of civil structures. Hence, condition survey, assessment and mitigation measures are essential for reactor safety, integrity and its operational extension. As a part of license renewal program, it was proposed to carryout ageing studies for reactor containment and various other safety related reinforced concrete buildings such as reactor containment building, steam generator building, control building, turbine building, service building, technical galleries, ventilation stack and cooling tower. Periodical containment leak tight test was carried out at every two year interval since the commissioning of FBTR in 1983. To assess the integrity of reinforced concrete structures, field based non-destructive, semi-destructive and laboratory destructive tests are conducted.

First, non destructive test was planned for measuring concrete cover thickness (which is measured from embedded reinforcement steel surface as shown in Figure 1a), concrete resistivity, ultrasonic pulse velocity (Figure 1b) and rebound hammer properties. Results obtained from the above tests are compared with limits specified in national and international standards. Then corrosion state of reinforcement steel was measured by the potential difference between reinforcement

Fig. 1 *(a) Concrete cover thickness evaluation, (b) ultrasonic pulse velocity measurement on core sample, (c) carbonation test for core samples and (d) core sample test*

steel and concrete. Depth of carbonation of concrete surface was evaluated using phenolphthalein indicator as shown in Figure 1c. Powder sample of cover concrete was collected from various locations and then pH and chloride content of the solutions were evaluated at laboratory.

Compressive strength of concrete was evaluated in-situ using semi-destructive test as shown in Figure 1d. Concrete cores collected from the floor slab were tested for their compressive strength at laboratory. Destructive tests were carried out on standard concrete cube specimens cast using the mix proportion followed at the time of FBTR construction and then compressive strength is obtained. The tests indicated that the intended concrete compressive strength and its alkalinity are well maintained.

During condition assessment study, cover concrete degradation was observed in two locations. One is at staircase region of cooling water structure and the other is reactor containment building isolation wall (technical gallery and outer wall junction at -3.00 Lvl). The reason for the degradation of the above mentioned region is inadequate cover provided at the time of construction. It is to be retrofitted using polymer based impermeable surface coating where steel reinforcement is susceptible for corrosion.

Reactor containment integrity is being examined biennially to verify the leak rate at an internal pressure of 150 mbar for 24 hours. After every test, pin-hole areas, where negligible leaks were observed, are applied with two coats of plain epoxy araldite. Soap solution was sprayed over dome and outer surface of reactor containment building wall areas between -14.5 to +19.75 m level and froth formation was inspected. Since the leak points are plugged by epoxy araldite, after every test, leak locations are getting shifted and hence, there is no significant change in the overall leak rate of reactor containment building. The permissible leak rate is 0.1% of the volume/hour for an internal test pressure of 235 mbar. However, the observed leak rate during all periodical tests was much less than the permissible leak rate limit as illustrated in Figure 2.

After careful evaluation of the conditions of structural concrete and embedded reinforcement steel, it is recommended for regulatory clearance for the continuous intended operation of FBTR.
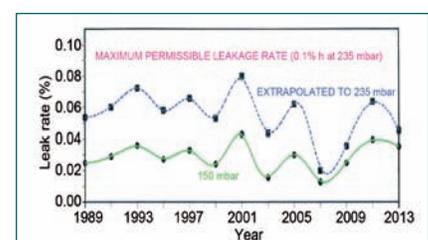
Fig. 2 *Periodical leak rate test of RCB-FBTR (by ROMG & CEG)*

I.5   Identification of Failed Fuel Pin and Verification of Integrity of other Pins from the Failed FBTR Fuel Subassembly through NDE

Fig. 1 *Profile of flat-to-flat distance along the length of the FBTR failed FSA*

In February 2011, when FBTR was operating at 18 MWt, SCRAM occurred due to delayed neutron detector signals. Clad rupture detection monitors in cover gas circuit also gave alarm due to increased activity indicating fuel pin failure. The failed fuel subassembly (FFSA) was subsequently identified and discharged from the reactor. The FFSA was received in the hot cells of Radio-metallurgy Laboratory (RML) for post irradiation examination (PIE) in January 2013, after adequate cooling.

To handle and examine the FFSA, unique custom built equipment and gadgets were designed and commissioned in the hot cells. Prior to receipt of FFSA, hot cells were cleared of radioactive waste to minimise the alpha waste volume and prevent the possibility of spread of alpha contamination. Visual examination of FFSA using nuclear periscope did not indicate any significant abnormalities on the external surfaces. Subsequently, the FFSA was subjected to ultrasonic ethanol cleaning to remove the residual sodium.

Dimensional changes in the FFSA were measured using a profilometer fitted with an inductive touch probe to determine hexcan dilation and head-to-foot misalignment. The corner-to-corner distances (CCD) (Figure 1) and widths-across-flats (WAF) were evaluated from the reconstructed cross sections obtained during metrology. Maximum increase in WAF and CCD are 0.9 and 1.2 mm respectively. This corresponds to a peak dilation strain of about 1.2-1.8% across the faces.

The FFSA was sectioned transversely using laser and the bundle of 61 fuel pins was safely pulled out from the subassembly. During extraction, load on the fuel pin bundle was closely monitored using a load cell connected to the pulling device. A special protective sleeve prevented bending stresses on the bundle. Sixty-one fuel pins in the bundle were then subjected to visual examination. One of the fuel pins indicated failure and was inspected using a colour CCD camera. A rupture with a linear opening of around 60 mm length and 3 mm width was observed in this pin (Figure 2a).

Eddy current testing (ECT) was carried out on the remaining sixty fuel pins using a differential encircling probe specially designed for testing the fuel pins with spacer wire. The ECT system was calibrated using a calibration pin having a hole of 0.5 mm diameter. Though a few fuel pins showed defect like indications, no gross failure of fuel pins was indicated.

The sixty fuel pins were then subjected to leak testing to verify their integrity and to ensure that only a single pin in the FFSA had failed. A thermal conductivity based leak detector (sensitivity: 1×10^{-5} std. cc/s) was used for leak testing. Helium (He) bombing and sniffing method was adopted. Each time, two fuel pins and a calibration pin with a leak rate of 2×10^{-3} std. cc/s were pressurised together with 'He' at a pressure of 0.5 MPa/h. After bombing, one pin at a time was put in a sniffing chamber provided with a 2.5 m long, 1.6 mm diameter stainless steel tubing which terminates in the special glove box (Figure 2b) installed outside the hot cell. A sniffer leak detector located in the glove box was used to detect any 'He' signal from the stainless steel tubing. Fuel pins were certified leak tight if no 'He' was detected from the pin. 'He' signal from the calibration pin, which was tested after the two fuel pins, was used to validate the procedure for each lot. Sensitivity under test condition was 1×10^{-4} std. cc/s. All sixty pins passed this test, confirming that only one pin had failed in the FFSA.

Further analysis is in progress for finding the root cause of the fuel pin failure.
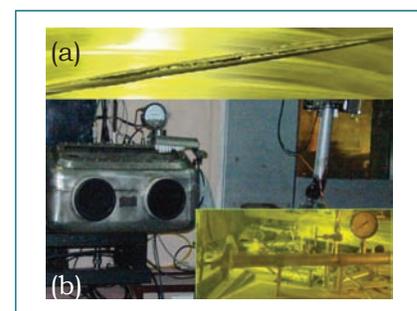
Fig. 2 *(a) Photograph of the failed fuel pin and (b) special glove box installed for leak testing of fuel pins. Inset shows bombing chamber for 'He' pressurization*

I.6 Synthesis of Thermal Performance of FBTR Core through CFD Simulations

In FBTR, there are six control rods wherein ^{10}B enriched B_4C is used as the control material. Heat is generated in the control rod because of irradiation and needs to be removed to maintain it within acceptable temperature. During normal operation, the control rods are partially inserted in the core and sodium continuously flows through it for the purpose of cooling. The sodium outlet temperature from control subassembly is not monitored, unlike what is done in the case of fuel subassemblies. Due to the absence of flow monitoring, it is essential that the sodium temperature in the control subassembly be below the boiling point and also the centre line temperature of absorber pins be less than the melting point of B_4C in the hypothetical event of complete flow blockage in control subassembly. Towards this, a detailed 3-D computational fluid dynamics investigation of temperature distribution in the control subassembly has been carried out, considering actual sodium temperature distribution in the neighbouring subassembly. The computational domain consisted of B_4C pellets, stagnant sodium within the control subassembly, hexcan of the control subassembly and inter-wrapper sodium.

It is found that the maximum temperature in the centre line of the B_4C pin is 1113 K which is much less than the melting point of B_4C, viz. 2648 K (Figure 1). The maximum value of sodium temperature in the control subassembly is 882 K, which is also less than the boiling point of sodium, viz., 1153 K. Thus, it is established that there is no risk of sodium boiling or B_4C pellet melting even when the control subassembly

is completely blocked.

Fuel subassembly after attaining required burn-up are shifted to storage locations and cooled till decay power reduces to the level of handling. During internal storage decay heat is generated in the spent fuel subassembly and the same is removed by continuous sodium flow through it. Heat generated in the storage subassembly is 4.2 kW, one day after shutdown (corresponding to 150 GWd/t burn-up). The sodium outlet temperature from storage subassembly is not monitored. Hence, it is essential to ensure that the sodium temperature in the storage subassembly be below its boiling point and also the peak clad temperature should be less than 823 K, in the hypothetical event of complete flow blockage in storage subassembly. This necessitates the need to find out the temperature distribution in the storage subassembly during the event of complete flow blockage. Towards this, a detailed 3-D computational fluid dynamics investigation of temperature distribution in the storage subassembly has been carried out. The computational domain consists of fuel pellets, clad, stagnant sodium within the storage subassembly, hexcan of the storage subassembly and inter-wrapper sodium, and hexcans
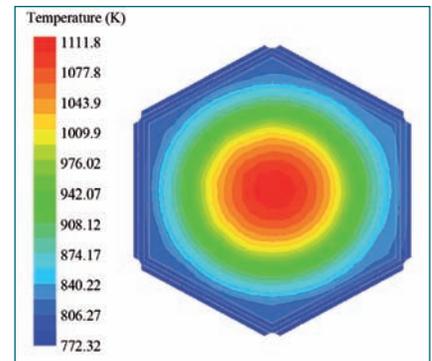

Fig. 1 Temperature (K) at midsection of active zone of control rod

of neighbouring fuel. A sectional view of computational mesh and temperature field in the storage subassembly are depicted in Figures 2a and 2b. A maximum temperature of 776 K is observed in the clad which is less than the limiting peak clad temperature of 823 K. The maximum value of sodium temperature observed in storage subassembly is 776 K, which is also less than the boiling point of sodium. Thus, it is established that there is no risk of sodium boiling or clad temperature exceeding the permissible limit even when the storage subassembly is completely blocked.

As a part of metal fuel development, it is planned to irradiate a capsule containing three metal fuel pins of composition U-19wt%Pu-6wt%Zr with sodium bonding locked into a special subassembly (ISZ100). The
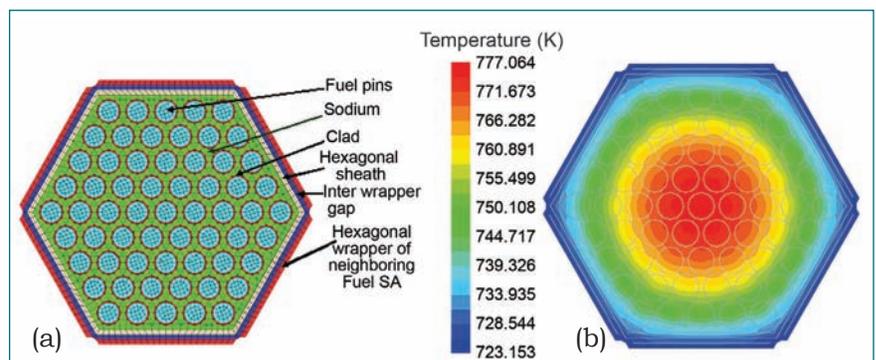

Fig. 2 (a) Computational mesh and (b) temperature field in storage subassembly

special subassembly will be loaded in (01-01) position for irradiation. This position is chosen to have the required neutron flux. Coolant flow through the special subassembly to remove the heat generated in the fuel pins is 1.09 kg/s, which is much less than that of the neighboring fuel subassembly. Detailed parametric studies indicated that positive flow through the subassembly is essential to avoid sodium boiling. Hence, it became imperative to demonstrate that the core temperature monitoring system, with its present stuck 80 mm position is able to detect any growing flow blockage at its infancy.

Towards understanding the temperature dilution characteristics of the sodium streams emanating from the special subassembly 3-dimensional thermal hydraulic analysis of coolant mixing below the core cover plate has been carried out. It is seen that there is a large dilution of 36 degree
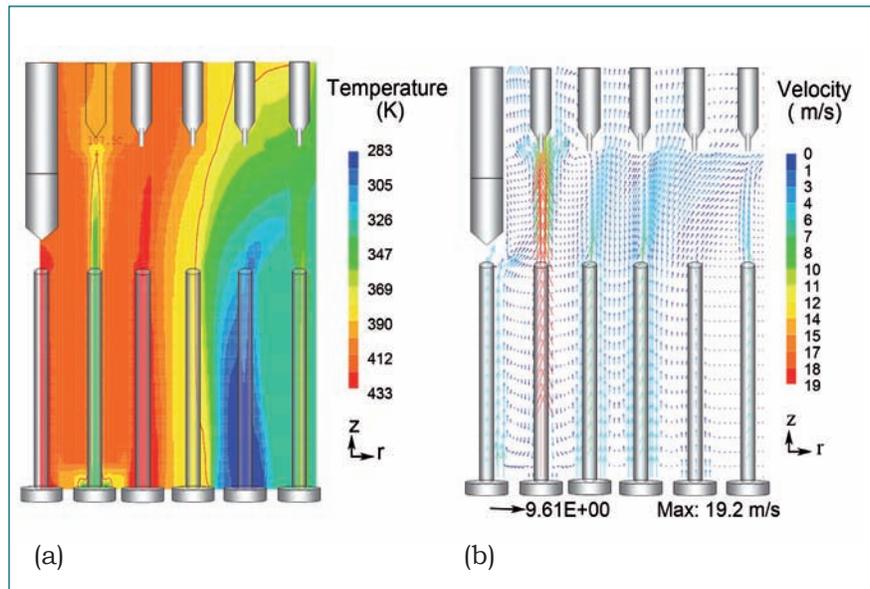
Fig. 3 *(a) Temperature and (b) velocity distributions in a vertical section through 01-04 subassemblies with 30% flow blockage in metallic pin subassembly*

in the thermocouple reading of the subassembly during normal operation of the reactor. However, during a partial flow blockage scenario in the subassembly, a rise of 10 degree in its thermocouple reading is seen when the flow reduction in the subassembly is 30%. To respect a clad hotspot temperature of 963 K, the permissible flow reduction is determined to be 72.5%. Hence, a safe plugging detection of enriched uranium metal fuel subassembly is assured within 30% of flow blockage in the subassembly (Figure 3).

I.7   Conceptual Design of Back-up Control Station for FBTR

During the periodic safety review (PSR) of FBTR by SARCOP, one of the stipulations was to submit a report on the compliance of FBTR to the current practices. This led to identification of a few non compliances, one of which was non availability of a backup control room in FBTR. Post-Fukushima safety review of FBTR by an internal task force also indicated the need to have a facility for controlling and monitoring critical parameters during situations like major fire or DBA/BDBAs which may render the FBTR main control room (MCR) inaccessible or uninhabitable. Though adequate measures have been provided in the design of FBTR control room to ensure availability at all foreseeable situations including DBA, as per the present practices, provision should exist to address extremely low probability events also. This led to the need for a back-up control and monitoring station (BCMS) for FBTR in a seismically qualified flood-safe building (SFSB).

A seismically qualified; flood safe building (SFSB) with FFL of 13.1 m based on the revised design basis flood level (considering inundation due to Tsunami), is proposed to be constructed on the northern side of FBTR Service Building and connected to FBTR main building by a corridor at the first floor of Service Building. This being close to the main control room, provides quick access in case of emergency. This building consists of ground floor and first floor. It is proposed to locate BCMS in the first floor.

The BCMS will have facility to carry out the following important safety functions and monitoring generally as per AERB safety guide AERB/SG/D-20.

- A SCRAM push-button to shutdown the reactor
- 'Effective SCRAM' display window to indicate that the reactor is in safe shutdown

state, and a display window for "0" mm position indication of the control rod drive mechanisms (CRDMs) to indicate whether all the control rods have reached the bottom are provided

- Important heat transport system parameters like sodium flow and temperature are provided to monitor the decay heat removal for an extended period of time
- OPEN/CLOSE status lamps for the RCB supply, exhaust and effluent system isolation dampers which are provided to ensure RCB isolation to facilitate containment of radioactivity if required
- RCB temperature, pressure and radiation level, wind speed meter, water logging and fire alarms for monitoring other off normal conditions.

The BCMS consists of a vertical floor mounted panel with controls, indication lamps, display windows and a 24 pen recorder. A dedicated 220 V single phase, AC UPS unit with adequate battery backup is provided. All other power supplies required for instruments, indication lamps and display windows will be derived from this UPS unit. Power supply from the flood safe DGs proposed to be located in the same building will also be available.

Even though BCMS is a retrofitting work, it is decided to provide dedicated sensors wherever possible to measure and indicate all critical signals. However, where it is not feasible to provide dedicated sensors/channels, the signal will be tapped from the existing sensors through buffer amplifier to provide exclusive indication in BCMS. Separate cables will be run between sensors and BCMS in a diversified route to the maximum extent possible. Fire Retardant Low Smoke (FRLS) cables will be used.

At present, plant data from many computer-based systems are available to the operators in the MCR. It is proposed to extend the plant information available in MCR to BCMS through a dedicated LAN, which will help in monitoring the plant parameters when control is taken over from BCMS. Some information related to BCMS namely, fire in BCMS, off normal temperature and power supply failure alarm and displays will be provided in the MCR.

BCMS is reachable quickly (within 5 minutes) easily and by two different routes, namely, through the first floor corridor between Control Building and Service Building and the other route is through FBTR ground floor and through the ground floor of SFSB. The routes within the control building/service building will be provided with self-illuminated guide marks visible in perfect darkness in addition to the lamps with self contained battery/solar powered lamps. Entry to BCMS will be restricted and through RFID enabled access control system for authorized personnel. It will also be provided with a physical lock with the key kept available in the MCR. A spare key for the same will be kept in a box with glass cover, which may be accessed by breaking the glass for use during emergency. The BCMS control panel will be seismically qualified as per relevant standards. The BCMS in the flood safe service building will be installed and commissioned by December 2015 as a part of 12th plan project "Safety upgradation of FBTR".

I.8   Irradiation of Metallic and Sphere Pac Fuel Pins and Compact High Temperature Reactor Materials in FBTR

It is planned to achieve increased nuclear electricity generation through addition of Fast Breeder Reactors (FBRs) with metallic fuelled core. Metallic fuel has the advantage of higher breeding ratio and lower doubling time, thus increasing the possibility of adding FBRs in quick succession.

Towards development of metallic fuel, irradiation experiments are carried out in FBTR. Six numbers of sodium-bonded U-6%Zr metallic fuel pins and three numbers of 14% enriched U-6%Zr metallic fuel pins were fabricated by Chemistry Group of IGCAR. To irradiate these fuel pins in FBTR, an irradiation capsule was designed, and three such capsules were fabricated with each capsule containing three metallic fuel pins. Inside the capsule, the fuel pins are arranged in three positioning holes, located 120° apart, on top and bottom. To remove the heat generated in the metallic fuel pins and keep the temperature of the fuel within the allowable safe limit, the sodium flow through the capsule was enhanced by adding sodium entry holes in the end plug of the irradiation capsule. In addition, the orifice of diameter 4 mm fitted at the foot of the carrier subassembly, in which the capsule is inserted for loading in FBTR, has been removed to increase the sodium flow rate through the carrier subassembly by about

10 times. These metallic fuel pins are undergoing irradiation in FBTR presently to different burn-up levels. Post-irradiation examination (PIE) will be carried out on the irradiated metallic fuel pins to determine the behaviour of the fuel pins at progressively higher burn-up values. The irradiation capsule and endplug for sodium flow are shown in Figures 1 and 2.

In view of the advantages offered by sol-gel based fuel fabrication methods such as elimination of handling radiotoxic dust, high amenability for remote handling and high homogeneity of the fuel, development of sol-gel vibro-compaction technology is being pursued in BARC and IGCAR. Two sphere-pac fuel pins containing a mixture of UO_2-PuO_2 & UO_2 micro-spheres, with one for PIE and the other for dissolution studies, have been fabricated by CG, IGCAR. Irradiation of these fuel pins along with a reference fuel pin made of mixed oxide fuel pellets is in progress in FBTR, using an irradiation capsule similar to that used for irradiation of metallic fuel pins. Duration of irradiation envisaged is 200 h at 205 W/cm and 100 h at 260 W/cm
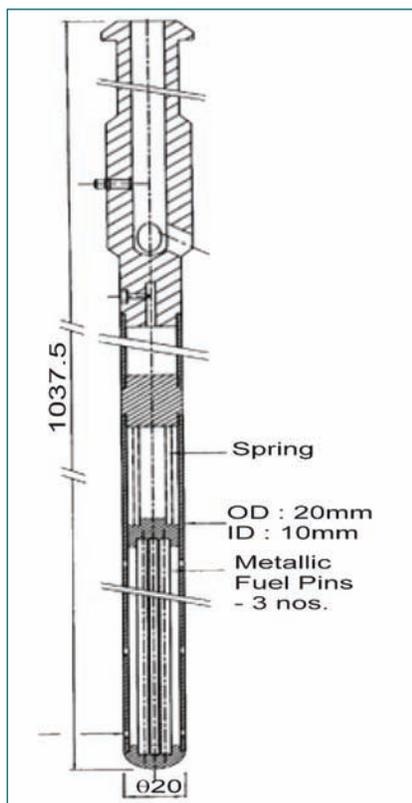

Fig. 1 Irradiation capsule

with a total burn-up of about 1300 MWd/t.

An irradiation experiment has also been carried out in FBTR, as a joint BARC-IGCAR programme, on materials to be used in Compact High Temperature Reactor (CHTR), being developed by BARC. Experimental pins containing CHTR TRISO (Tri-structural Isotropic)

Fig. 2 End plug with slots for sodium flow

coated surrogate fuel particles of 0.9 mm diameter, and disc specimens of CHTR structural material (Nb-1%Zr-0.1%C), fabricated by BARC, have been encapsulated in two separate leak tight tubes to avoid the possible release of any fine particles to reactor sodium in the unlikely event of breach in the experimental pins during irradiation. Helium was filled in between the experimental pin and the encasing tube using a specially designed experimental set-up. These two pins along with an experimental pin containing cold worked 316LN stainless steel specimens have recently been irradiated in FBTR to a neutron fluence of 10^{21} n/cm^2. The experimental pins containing CHTR materials will be retrieved from the irradiation capsule at Radiometallurgy Laboratory and transported to BARC for PIE.

# I.9 Experimental Determination of the Solidus Temperature of Mark I Mixed Carbide FBTR Fuel

The temperature at which the melting sets-in in a multiphasic alloy is called as its "solidus" temperature, while the temperature at which the entire alloy turns into a liquid corresponds to its "liquidus" temperature. Among the physicochemical properties of nuclear fuels, their "melting point" is an important fundamental property.

When these fuels are multiphasic materials the term "melting point" is rather inappropriate. The lowest temperature at which liquid appears first when the fuel is heated, is more relevant. This could be the solidus temperature or the temperature pertaining to a phase equilibria in which liquid is formed. A reasonably accurate knowledge

of this temperature is necessary in order to estimate the linear heat rating of the fuel.

The onset of melting in a substance could be determined by a variety of techniques. These techniques use the change in a physical property which accompanies melting. The physical property in question could include but is not limited to the

variation in the following; specimen temperature, resistivity, reflectivity, emissivity, thermomechanical property (volume or linear expansion), thermophysical property viz., enthalpy, vapour pressure, chemical potential etc. The most popular technique among these is the differential thermal analysis (DTA) in which the relative change in the specimen temperature is monitored with respect to an inert reference. Commercial equipment are available which could accurately determine the melting transitions up to at least 2273 K. However, difficulties are often encountered in using these equipment in the determination of melting points of radioactive and chemically reactive alloys. These are mainly caused by the reactivity of the molten alloy with the container and in the customization of these equipment to suit measurements in a controlled ambience, like in a dry box, the latter being is necessary for handling air-sensitive substances. In order to circumvent these experimental difficulties, a new experimental facility was established in our Centre for the determination of melting point of fuel materials. This set-up is based on the "spot" technique, a thermo-optometric technique developed at the Argonne National Laboratory, USA and pursued later at BARC. In this technique, the change in the reflectivity of the sample is monitored during melting. This technique is amenable for remotization, simple and quick. In a typical measurement the sample held in a container with lid having a small orifice (a Knudsen cell) typically about 0.5 mm diameter is heated under vacuum ($\sim 10^{-6}$ mbar) remotely with the help of electromagnetic induction (radiofrequency). The orifice of the cup is viewed remotely with the help of a magnifying device. Upon melting the image of the orifice
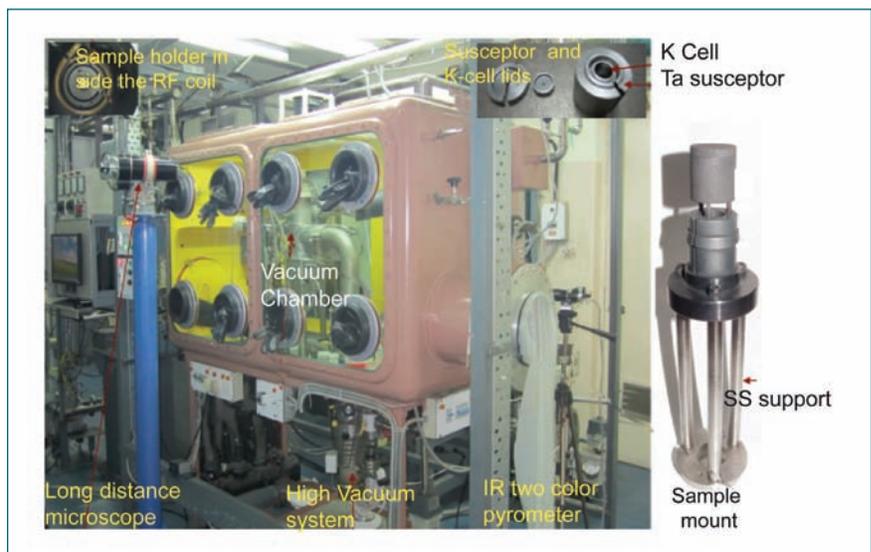
Fig. 1 *Experimental set-up used for measuring the solidus temperature of Mark-I FBTR fuel*

appears on the molten surface as a black spot. If the melting is partial (like in the case of a solidus temperature) then many tiny black spots appear which coalesce to form a single large spot at the liquidus temperature. Many experimental improvisations were made to the experimental set up used by the inventors of this technique. With the help of these refinements, (i.e. by replacing the low magnification pyrometer telescope with a long distance microscope fitted with a video camera), the melting could be videographed and a high temperature remote low magnification microscopy of the sample could be carried out.

The accuracy of this experimental technique was established to be ± 2 K by measuring the melting points of pure metals as well as by investigating the solidus and liquidus temperatures in well known binary alloy systems.

With this experimental system (Figure 1), the solidus temperature of Mark-I FBTR fuel (*a biphasic mixture of the mono and sesqui carbides of U and Pu with Pu/(U+Pu) = 0.7*) was measured by using the spot-technique. About 700 mg of the pellet was taken in a "carburized tantalum" cup that was held in a molybdenum Knudsen cell. This assembly was heated

under vacuum at a heating rate of 1 K/min from 2130 K and at 20 K/min below 2130 K. At 2161 K, a few "broken spots" were formed that corresponded to the solidus temperature 2161±5 K of the Mark-I FBTR fuel (Figure 2a). This is the first direct measurement of the solidus temperature of Mark-I FBTR fuel. Earlier measurements employed rather an indirect technique, viz., incipient melting (2148±25 K). Our data is within the error limits of the earlier measurements and is more accurate than the previous measurements.

The melting of the fuel was confirmed by removing the sample after the experiment and photographing the frozen alloy which indicated slumping (Figure 2b). Further efforts are underway in order to measure the solidus temperature of Mark-II fuel as well as U Pu-Zr alloy fuel.
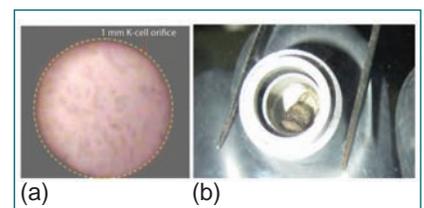
Fig. 2 *Photographs showing (a) the spots appearing at the solidus temperature of Mark-I mixed carbide FBTR fuel and (b) slumping of the fuel after melting and solidification*

I.10 Development of a Flow Sheet for the Production of ^{32}P by ^{32}S (n, p) ^{32}P

^{32}P labelled compounds such as ^{32}P - orthophosphate and sodium [^{32}P] phosphate are useful in treating bone pain palliation as well as polycythemia vera and thrombocythaemia. ^{32}P is a pure beta emitter with half life of 14.28 d and can be produced using either thermal capture by ^{31}P through ^{31}P (n, γ) ^{32}P or nuclear reaction using fast neutrons, ^{32}S (n, p) ^{32}P. The former reaction gives a higher yield but results in ^{32}P of lower specific activity while the latter results in ^{32}P of higher specific activity. Since the elemental sulphur has low melting (393 K) and boiling points (717 K), sulphur was preferred as one of its compound forms for preliminary trials. Among the various sulphur bearing targets, strontium sulphate has been identified as the most favourable target material.

The present work describes the studies on the development of a flow sheet for the production of ^{32}P using strontium sulphate as the target material. The irradiation of the target material was carried out using the fast flux available in KAlpakkam MINI Reactor (KAMINI).

1g of $SrSO_4$ was irradiated in KAMINI reactor at pneumatic fast transfer system (PFTS) for 6 hours. A portion of the irradiated $SrSO_4$ target was dissolved in water by converting it into its carbonate precipitate by adding sodium carbonate under appropriate experimental conditions.

$$SrSO_4 + Na_2CO_3 \xrightarrow{\Delta, Stirring} SrCO_3 \downarrow + Na_2SO_4$$

The filtered strontium carbonate precipitate was taken in HCl medium. Ferric chloride and ammonium hydroxide were added into the solution to get the ferric hydroxide precipitate. ^{32}P present in the solution was also precipitated as ferric phosphate. Low amounts of ferric phosphate was collected along with the large amount of ferric hydroxide precipitate.

$$FeCl_3 + PO_4^{3-} \longrightarrow FePO_4 \downarrow + 3Cl^-$$

$$FeCl_3 + 3NH_4OH \longrightarrow Fe(OH)_3 \downarrow + 3NH_4Cl$$
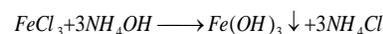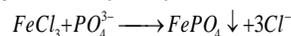
This precipitate was dissolved in HCl medium and the same was passed through cationic exchange chromatography column containing DOWEX 50WX8 resin. The anionic phosphate fraction was just washed off the column, while the cationic impurities such as Sr and Fe were held in the column (Figure 1) itself. Thus, the labelled phosphate was obtained in its purified form. Similarly, ^{32}P from the filtrate of the strontium carbonate precipitate was also collected by the same ferric phosphate precipitation method. The total amount of ^{32}P obtained by this method was quantified using Cerenkov counting and the same was found to be 7.57 µCi/g of strontium sulphate target. This corresponded to 99.8% of the calculated yield of ^{32}P from strontium sulphate target.

The absence of gamma emitting radionuclidic impurities in the ^{32}P fraction was confirmed by gamma spectrometry using HPGe detector. The absence of any other beta emitting nuclides in the ^{32}P fraction was also confirmed by establishing the half-life from the decay profile of the dissolver solution using Cerenkov detector which corresponded to pure ^{32}P (Figure 2) i.e. the half-life for the source obtained experimentally was found to be 14.1 d as compared to the reported value of 14.28 d.

The flow sheet for the radiochemical processing of ^{32}P for the KAMINI irradiated $SrSO_4$ target material has thus been established. The production of ^{32}P using the large flux of fast neutrons available in FBTR will be taken up in future based on this flow-sheet.
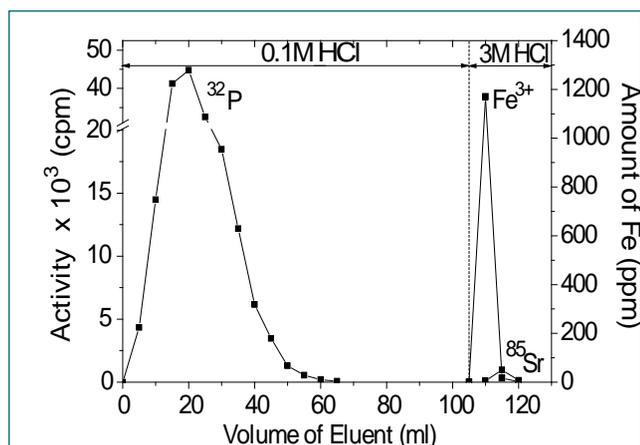

Fig. 1 *Ion-exchange profile of ^{32}P*
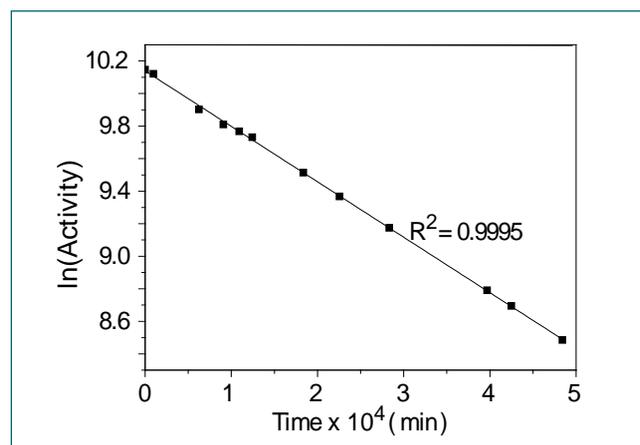
Fig. 2 *Decay profile of ^{32}P in the purified fraction from the dissolver solution of the irradiated target (slope = 5.68*E-07 s^{-1}; decay constant of ^{32}P= 5.62*E-07 s^{-1})*
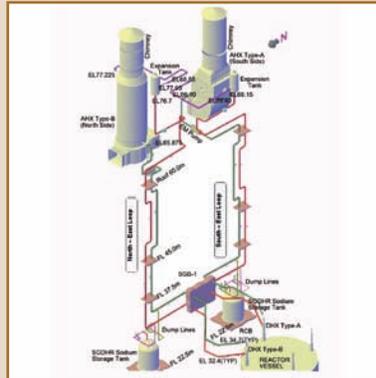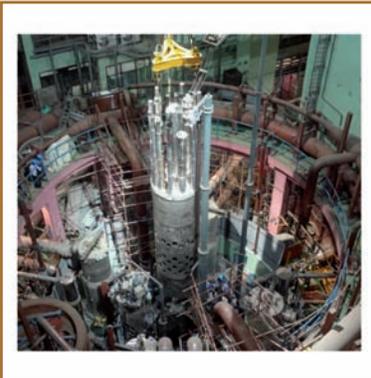
CHAPTER 2

Prototype Fast Breeder Reactor

II.1 Construction Status of Prototype Fast Breeder Reactor

The civil construction of nuclear island buildings has been completed (Figure 1). The nuclear island houses seventeen buildings, out of which eight buildings namely Reactor Containment Building (RCB), Steam Generator Buildings (SGB) - (two numbers), Electrical Buildings (EB) - (two numbers), Control Building (CB), Radioactive Waste Building (RWB) and Fuel Building(FB) are connected together as a single structure on a common raft and is called Nuclear Island Connected Buildings (NICB).

The reactor vault of PFBR is nearing completion with all major reactor equipments in place. Critical in-situ heavy density concreting has been done for large and small rotating plugs without affecting the nuclear clean environment by maintaining foreign material exclusion procedure.

Heat transport sodium piping for secondary system erection is in an advanced stage and major sodium system components including four numbers of intermediate heat exchangers, two numbers of secondary sodium pumps, two numbers of sodium to air heat

Fig. 1 Overall view of PFBR site

exchangers and two numbers of primary sodium pumps have been erected.

Control plug (Figures 2 and 3) which houses the control and safety rod drive mechanism (CSRDM) and diverse safety rod drive mechanism (DSRDM) have been erected over roof slab. The secondary ramp and secondary tilting mechanism which forms a part of inclined fuel transfer machine used for fuel transfer has been fixed to grid plate.

The construction of fuel building has been completed and erection of major fuel handling components has been completed. Commissioning of

fuel handling equipment is nearing completion.

The entire civil structural works of electrical building 1&2 has been completed the electrical and instrumentation system are in advance stage of commissioning. Main control room, back-up control room and handling control room panels have been erected in the control building. Commissioning of all the four numbers of emergency diesel generators from control room has been completed. 230 kV gas insulated switchyard and 6.6 kV switchyard boards have been commissioned. All the three
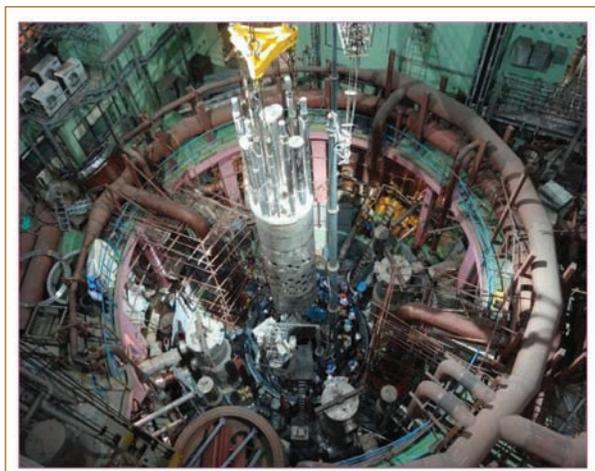

*Fig. 2* Erection of control plug
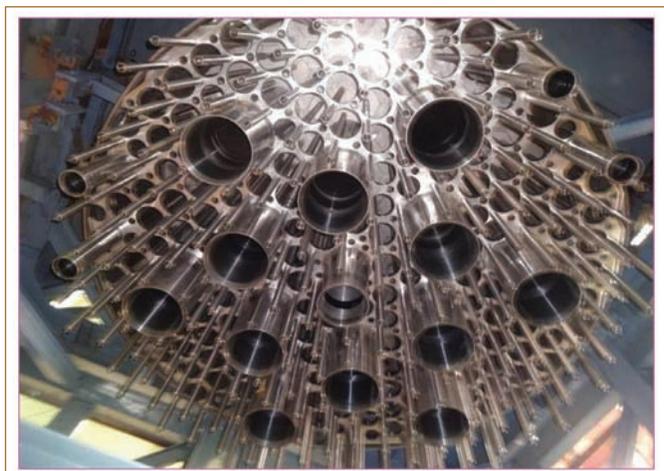
Fig. 3 Bottom side view of control plug

outgoing transmission lines from switchyard have been charged and connected to southern India grid.

Commissioning of the conventional and auxiliary supporting systems such as raw water, emergency service water, demineralized water and compressed air have been completed. Commissioning works for the plant ventilation system has advanced substantially. The commissioning of critical equipment from control room is being pursued now.

The balance of plant houses the turbine building, raw-water & fire-water pump house, de-mineralization plant (DM plant), auxiliary boiler plant, effluent treatment plant and open reservoir.

The civil construction work of turbine building has been completed and erection of turbine equipments

Fig. 4 Overall view of turbine floor

and all auxiliary equipments have been completed. Turbine box-up, main steam piping and the major milestone of turbine rolling on barring gear have been completed. Auxiliary boiler light up, safety valve floating and steam blowing activities have been completed (Figure 4).

The construction of forebay is nearing completion. The civil construction works of sea water pump house has been completed and erection of condenser cooling water pumps, auxiliary sea water
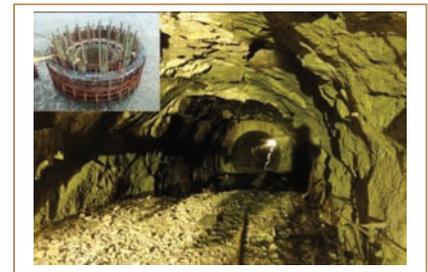
Fig. 5 Sea water intake tunnel

pumps have been completed.

In the sea water intake structure, the caisson has been reached upto hard rock level. Excavation of hard rock has been completed. The horizontal sea water intake tunnel and vertical shaft of the tunnel has been connected and made through (Figure 5). Erection of stop log gates and trash racks are under progress.

The project has achieved an overall physical progress of 96.5% at the end of 2013.

II.2 Manufacture of Control Plug : A Challenging Milestone in PFBR Construction

Control plug is a part of top shield of reactor assembly (Figure 1). It is inline with the reactor core and is supported eccentrically on the Small Rotatable Plug. It houses the absorber rod drive mechanisms, core monitoring thermocouples, neutron detectors, central canal plug, failed fuel location module etc. It helps in the mixing of sodium exiting from the core, minimises free level sodium perturbations and also acts as biological and thermal shield.

Diameter of control plug has to be as small as possible as it will decide the size of roof slab and hence main vessel. At the same time it has to cover all fuel subassemblies for temperature monitoring and house all the above mentioned items

enabling access for operation and minor maintenance. Height and diameter of control plug are fixed as 12375 mm & 2250 mm respectively. For manufacturability and based on functionality, control plug is divided into three subassemblies, viz., skirt assembly, middle assembly and mechanism box. Skirt assembly and components present in sodium environment are made of SS 316 LN and remaining items are made of carbon steel. Major modes of failure considered in the design of skirt assembly components are based on thermal loading such as creep-fatigue interactions, thermal stripping and thermal shock. These are taken care by positioning welds away from the plate shell joints and providing thermal shields. Shroud

Fig. 1 Control plug

tubes/guides are provided for protecting the internals from flow induced vibration. Thermal design of middle assembly was challenging due to the contradicting temperature requirements above the top plate of the assembly. Temperature at this region should be above 90°C considering the sodium aerosol deposition, at the same time it shall not exceed 120°C which is the flash point of dash pot oil of control and safety rod drive mechanism. Steel plates are stacked in argon filled boxed structure with variable gaps to reduce the temperature from ~420°C to 110°C linearly (Figure 2). Since absorber rod drive mechanisms are supported on top plate, ΔT across the top plate is to be kept below 2°C to limit its slope, which is achieved by providing insulation above the top plate. Mechanism box was designed to provide protection to the items supported on top plate. Internal space of mechanism box is partitioned to maintain 110°C in its bottom region and ~60°C at the top region for instrumentation. Thickness of shell was kept as 30 mm considering shielding requirements.

Routing of tubes (φ10x1thk), housing core monitoring thermocouple probes (210 numbers), sodium sampling tubes of failed fuel location module (198 numbers), argon purging tubes (66 numbers) without interference with the internals of control plug were challenging during design and manufacturing stage. Thermocouple tubes were bunched into six groups and routed to their respective locations above each subassembly from 11 m height avoiding interference with shroud tubes (Figure 3). Tube routing was finalized based on solid modeling and each tube was bent accordingly before assembly. Thermocouple tubes were welded to sampling sleeves at one end and rolled and welded at other end. Thus there are only two discontinuities in the entire profile.

Hard facing by colmonoy deposition was carried out on surface of 78 numbers of stainless steel components, which are in contact in high temperature and with relative movements in sodium. Based on the thickness of tubes and complexity of geometry of item to be hard faced, procedure was developed for each item. Defects in colmonoy deposits and distortions in the hard faced items were rectified by suitable methods without affecting the functionality of the items.

Primary leak-tightness of the thermocouple probe housing tubes with top plate was to be achieved by silver brazing as per original design. To facilitate assembly, clearance between the above mentioned items was increased, due to which silver brazing was not possible. Hence rolled and welded joints were adapted instead of brazing. The design of tube sheaths and the adaptor to which the tubes were to be welded were modified to suit the modified method. Mock-ups were done in-house and at manufacturer's site to establish the procedure. After successfully qualifying the procedure, the same was successfully implemented.

Sixty numbers of thermocouples are fixed on various parts in middle and skirt assembly of control plug for surface temperature monitoring. Thermocouples with lemo-connectors are bunched and taken out through three outlets in top plate of control plug, which is a leak tight boundary. Considering the larger lemo-connector diameter and smaller thermocouple diameter, a special set-up was designed for achieving leak-tightness. Silver brazing of the thermocouples with top plate was chosen for the same. Technology development for the procedure was carried out at IGCAR. After qualifying the procedure, brazing was carried out by IGCAR at manufacturers shop (Figure 4).

Welding was the one of the most critical activity in control plug manufacture. There were ~3000 welding operations including dissimilar welds involving carbon steel and stainless steel. Majority of the welds were autogeneous welds carried out using the Polysoude orbital welding machine. Diameter of the tubes/ pipes to be welded ranged from 12 mm to 360 mm. The minimum thickness of the thermocouple tube sheath to be welded was 0.8 mm. Since thermocouple probes had to pass through these

Fig. 2 *Stacking shielding plates in middle assembly*

Fig. 3 *View of skirt assembly before shell welding*

Fig. 4 *Brazing of thermocouples*

tubes, extra penetration should be kept within 0.2 mm. Welding of 210 thermocouple tube sheaths on core cover plate and 198 sampling tubes to base plate of failed fuel location module with very stringent space constraints were very challenging tasks (Figure 5). Long slender tubes of ~11 m were welded and machined with precise tolerances. Various defects observed such as suck back, porosities etc were rectified by improving the process parameters, joint design, purge gas supply configuration etc.

Control plug being a Class-I component, non-destructive examination requirements of all welds and other leak-tight joints were very stringent. Radiography was carried out for ~3000 joints.

Fig. 5 *Welding of thermocouple tubes*

Main challenge faced was accessibility of joints due to limited space especially in case of tube welding. Portable X-ray machine (Baltograph) of ~100 mm diameter was used for radiography of these joints. With mock-ups, sequencing of radiography was established and this was successfully carried out for all the specified joints. Helium Leak test was required for all joints in cover gas boundary. Carrying out

Fig. 6 *Making control plug from vertical to horizontal with handling structure*

helium leak test for assembly joints called for design and manufacture of special fixtures.

The design of the structure suitable for building up the control plug over it, tilting (~60 tons) and transportation was very challenging (Figure 6). The control plug with very stringent specifications for both assembly and erection tolerances was successfully manufactured, handled, transported and erected at site.

II.3 Modifications and Sodium Testing of Transfer Arm

In-sodium performance testing of transfer arm was carried out in test vessel-5 of LCTR (Figure 1). Testing was carried out in two campaigns. In first campaign, series of tests were done in ambient condition, in hot air and in hot argon at different temperatures ranging from 30 to 160 °C. Subsequently, 61 cycles of sodium testing at 200 °C was carried out followed by the high temperature hold test at 400 °C for 100 hours. Then sodium testing at 200 °C was resumed and one cycle of testing was done without any problem. During 63rd cycle of sodium testing, inner tube got jammed with the outer tube. Transfer arm was therefore dismantled from the test vessel-5 after sodium cleaning by water vapour–CO$_2$ process. Investigations revealed that connecting rod of inner tube was jammed with the offset arm of the outer tube.

Modification to the gripper assembly was made by providing two numbers of guide bushes in offset arm with colomnoy-5 hardfacing to minimize wear. Offset arm with new guide bushes was assembled in outer tube and finger actuation was carried out with the help of linear actuator. Scoring marks were observed in the connecting rod due to rubbing with colomnoy coated surfaces of the guide bushes and finger actuation was not smooth. Hence guide bushes were removed, new rails and guide arrangement was provided in the gap between offset arm of the outer tube to connecting piece of the inner tube (Figures 2 and 3). To minimise friction and wear, rubbing surface of the rails and guide were hard chrome plated.

During first campaign of sodium testing full travel of the guide tube from loaded transfer position to parking position could not be carried

out in a single stretch at 200 °C due to insufficient clearance. Hence bore of the guiding surface of length 150 mm in oval shield plug was increased by 200 microns using
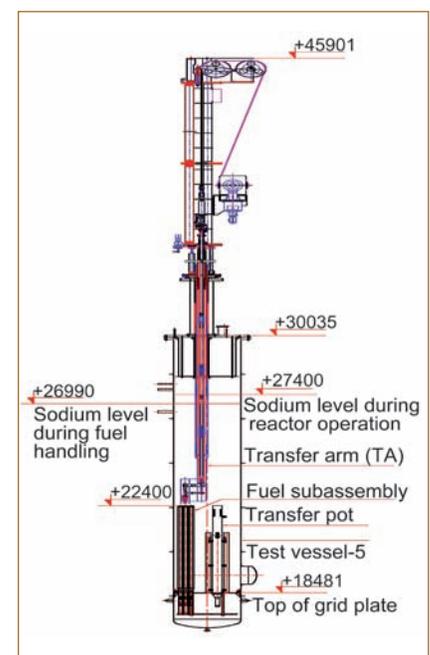
Fig. 1 *Schematic of transfer arm in test vessel-5*

special honing machine.

All the static and dynamic seals of the transfer arm were replaced by new seals. Required design modifications in the oil seals provided between oval shield plug and guide tube were made as per IS-5129. Leak testing of dynamic seals viz. oil seals and V-seals (which is provided between shielding sleeve and outer tube) was done separately by inter seal pressurization and leak rates were within acceptable limits.

Prior to hot air testing, load cell of the tension sensing mechanism was calibrated by applying known loads.

During second campaign of testing, transfer arm was tested for 5 cycles in air at room temperature, 13 cycles in hot air at different temperature viz. 60, 80, 100, 120, 140 and 160 °C without any problem. Then vessel was cooled back to room temperature. Mating surface of the new guide and rails arrangement were inspected and no rubbing or scoring marks were observed which gave enough confidence to proceed with sodium testing.

Fig. 2   Machined guide and rails

Fig. 3   Guide and rails assembled in transfer arm

Bellows were welded between inner tube to outer tube and all leak paths of outer tube were seal welded. Then leak testing was done by applying 600 mbar pressure using argon in the space between inner and outer tubes and leak tightness confirmed.

Bottom dished end of the test vessels was welded and prior to sodium filling, twelve cycles of testing with hot argon was carried out at different temperatures viz. 60, 80, 100, 120, 140 and 160°C. Travel of the guide tube was checked at 160°C and movement was found

to be satisfactory. Then sodium was filled at 200°C and 600 cycles of sodium testing carried out. To study the performance of the machine after sodium deposition in the clearances between outer tube to shielding sleeve, shielding sleeve to guide tube and guide tube to oval shield plug, 100 hours of dwell period at 547 °C (reactor operating condition) was carried out midway through the cyclic testing. During testing overall performance of the machine was satisfactory and all performance parameters were normal.

II.4   Analysis carried out Towards Safety Clearance for PFBR Commissioning

Before initial sodium filling in the primary sodium circuit, the reactor assembly internals of PFBR are to be preheated to a minimum temperature of 150°C to avoid solidification of sodium and hot shocks to components during sodium filling. Preheating of reactor assembly is an important stage during commissioning of the reactor. It is envisaged to carry out preheating with all reactor assembly components including primary sodium pumps in position. Preheating has to be gradual and also the temperature difference

between various parts of the reactor assembly during preheating should be minimum. Towards these, detailed thermal hydraulic and structural mechanical studies have been carried out and the scheme for preheating has been finalized.

Preheating is carried out by circulating hot nitrogen gas through the reactor assembly. Hot gas would be led into the pool through pipe spools inserted through the penetrations in the top shield. Inlet of nitrogen to the reactor assembly is made at five locations viz. (a) through an opening in

large rotating plug, (b) through an opening in small rotating plug and (c) through three in-service inspection openings in the annular space between main vessel and safety vessel. The return of nitrogen is taken through four locations, viz. (i) through an opening in the roof slab and (ii) through three in-service inspection openings in the annular space between main vessel and safety vessel.

Initially, the reactor assembly, annulus of main vessel and safety vessel and circuit will be purged with nitrogen to eliminate all air in
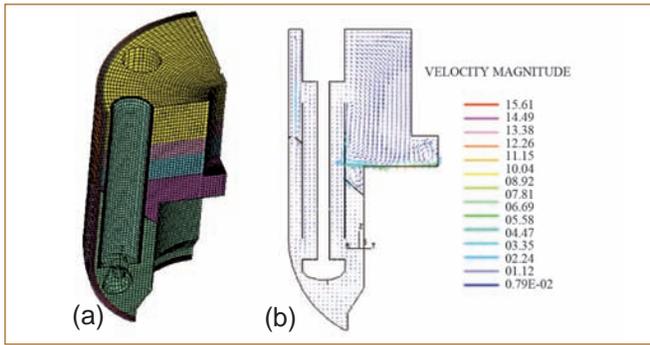
Fig. 1 (a) Computational fluid dynamics mesh and (b) nitrogen flow distribution in reactor assembly at a vertical plane through intermediate heat exchanger during preheating
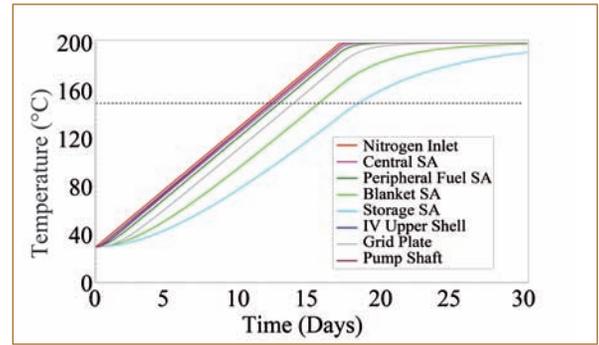
Fig. 2 Temperature evolution in various components of reactor assembly

the system. The purging operation is continued till required nitrogen purity level is achieved. The preheating of primary sodium circuit is initiated by starting the nitrogen blowers and electrical heaters. The nominal nitrogen flow rate will be ~ 10 kg/s and the temperature rise across the electrical heater bank is ~10°C. The nitrogen outlet temperature from the heater bank is set to rise by 10°C per day. This ensures the uniform temperature rise in the reactor assembly structures. Hence, the temperature difference between reactor assembly structures is limited and induced thermal stresses are within limits.

The hot nitrogen supply to the reactor assembly is by (i) opening for observation facility in small rotating plug (300 NB) and (ii) access opening to in-vessel transfer position in large rotating plug (450 NB). The nitrogen return from the reactor assembly is from the cold pool through the opening for cold pool level detector in roof slab (450 NB). The purpose of the thermal analysis is to determine

(i) Nitrogen flow through various paths in reactor assembly

(ii) Temperature evolution in various structures to ensure uniform heating and to determine the duration of preheating

(iii) Estimation of heat transfer coefficient to determine

differential heating rate in critical junctions and

(iv) Possible induced thermal stresses possible.

Thermal hydraulic analysis was carried out in two stages. In the first stage, 3-dimensional flow distribution of nitrogen in the reactor assembly was determined by a computational fluid dynamic study. The computational fluid dynamics mesh and nitrogen flow patterns in a vertical plane through intermediate heat exchanger are depicted in Figures 1a and 1b. From this stage, the flow fractions through various paths, viz., (i) core, (ii) intermediate heat exchanger, (iii) primary sodium pumps standpipe, (iv) cold pool annulus (between inner vessel and inner thermal baffle), (v) thermal baffle annulus (restitution plenum) and (vi) outer annulus of main vessel cooling system (feeding plenum), that connect hot and cold pools are found to be 6.7, 27.4, 12.8, 41.3, 11.5 and 0.4% respectively.

Taking these flow fractions, the temperature evolutions in various structures have been determined in the second stage. Evolutions of central fuel subassembly, peripheral fuel subassembly, blanket subassembly, storage subassembly, grid plate, inner vessel and pump shaft are depicted in Figure 2. In these calculations the nitrogen inlet temperature is taken to vary as a ramp at the rate of 10 K/day. It is seen that temperatures of inner vessel, primary sodium pumps shaft

and central subassembly closely follow that of the inlet nitrogen temperature. The temperature rise in grid plate is slower than that of the core subassembly since it receives the spent nitrogen from the subassembly. The maximum temperature difference between grid plate and inner vessel is <16 K. The temperature rise in storage subassembly is the slowest as it receives less nitrogen flow rate. Based on the thermal analysis, it is seen that preheating time is controlled by the storage subassembly. Considering possible uncertainties in the calculations and heat losses, the preheating time is ~20 days.

The concern in structural analysis is the structural integrity of the following junctions involving thick and thin parts.

- Intermediate heat exchanger thick tube sheet with thin tube

- Fuel pins with thick subassembly parts

- Grid plate sleeve with top & bottom plate

- Main vessel cooling pipe with core support structure support plate.

With the heat transfer coefficient values varying from 1-50 W/m²K, the temperature differences of all the above junctions are determined and subsequently stresses are found to be insignificant. Hence, the preheating of reactor assembly at 10K per day for 20 days is acceptable.

II.5 Auxiliary Systems for High Temperature Testing of Inclined Fuel Transfer Machine

Inclined fuel transfer machine is the ex-vessel transfer machine of PFBR meant for transferring of spent subassemblies from inside the reactor to fuel building and fresh subassemblies from fuel building to inside the reactor. Primary ramp and primary tilting mechanism are the primary side components of the inclined fuel transfer machine, located inside the reactor. These primary side components were manufactured ahead of other components of inclined fuel transfer machine and tested in sodium at large component test rig at FRTG and later assembled in the reactor. Integral testing of the inclined fuel transfer machine was carried out along with non reactor grade full scale primary ramp and primary tilting mechanism in hot air at supplier's (M/s. MTAR, Hyderabad) shop floor. After manufacture, the machine was assembled at shop floor (Figure 1) and 65 cycles of testing at ambient condition completed successfully.

In reactor, during fuel handling, primary ramp and primary tilting mechanism are at 200 °C and primary ramp liner, shield plug and primary ramp cell liner are maintained at 120 °C. During hot air testing, pre-heating of various parts of the inclined fuel transfer machine and cooling at seal locations simulating reactor fuel handling condition was done by air using heating and cooling systems. Actuation of the pneumatic actuator pins and gate valve was done by a 6 bar air system. Pressurization of inflatable seals to 400/700 mbar corresponding to fuel handling/reactor operating conditions was done using an argon supply

system. To simulate the deflections of the primary ramp and primary tilting mechanism due to increase in temperature between installation and fuel handling condition, primary tilting mechanism was moved downward by 30 mm and radially by 10 mm. Primary ramp was moved in radial direction by 5 mm.

Fabrication of the piping system connecting the heating and cooling systems to fixed end of the hoses in cable drag chain was completed. Piping system connecting the moving end of the hoses to supply nozzles in rotating components of inclined fuel transfer machine was also completed.

Commissioning checks of the air heating system were done by operating the system in bypass mode and the process parameters such as flow (280 m³/h at 45 °C), temperature of air at outlet of heater vessel (200 °C) and inlet of the blower (45 °C) measured and confirmed to be within specified limits.

The air cooling system was commissioned and the flow achieved was 60 m³/h. All the instruments such as pressure gauges, pressure transmitters and air pressure regulators were calibrated in the required range and the safety relief valve calibrated and set at specified value (6.2 bar). Electrical (48 V DC) supply and (6 bar) air supply for pneumatic actuation was given and the operation of actuation of the gate valve and locking pins was done through inclined fuel transfer machine control panel.

The argon supply system for actuation of the inflatable seals was commissioned. All the instruments were calibrated. The safety relief

Fig. 1 *Inclined fuel transfer machine*

valves in 400/700 mbar lines were set to 450/750 mbar. Smooth operation of all the solenoid operated pneumatic valves was checked and inflatable seals were pressurized to 700 mbar for leak testing of the inclined fuel transfer machine.

Heating of the primary ramp and primary tilting mechanism, primary cell liner, secondary cell liner, primary gate valve, secondary gate valve and shield plug was done by electrical heaters. Electrical heaters were fixed and connected to SSR based heater control panel. A control panel with 15 PID controllers and a data acquisition system was provided for controlling the temperature. Installation of heaters, thermocouples and insulations on the parts was completed. By setting in the PID controllers at 40 °C, temperature of the parts of inclined fuel transfer machine was raised and the performance of the electrical heating system for heating of the inclined fuel transfer machine parts were found to be satisfactory.

II.6 Performance Testing of Under Sodium Ultrasonic Scanner for PFBR

An under sodium ultrasonic scanner (USUSS) has been developed for PFBR to detect protrusion, growth and bowing of the fuel subassemblies before every fuel handling operation. For qualifying the scanner to use in the reactor, the scanner along with the ultrasonic transducers, control and drive system of automation and ultrasonic imaging system were tested in water and sodium facilities at FRTG.

Assembly of scanner

USUSS consists of upper and lower parts. The upper part consists of two AC servo motors for translational movement and rotational movement of the spinner tube. The lower part consists of 7.5 metres long spinner tube with transducer housing at the bottom with ultrasonic transducers. The top end is coupled to the automation to facilitate translation and rotational movement of the spinner tube. Scanner assembly is shown in Figure 1.

In order to test the functionality of the scanner in water and sodium, a target assembly consisting of dummy subassemblies are positioned to the bottom of the transducer holder using tie rods as shown in Figure 2. The target assembly for the scanner consists of nineteen subassemblies simulating the central subassembly, first and second rings of PFBR core configuration and five subassemblies simulating the protrusion of various heights and orientation.

Alignment of transducers in water

Before conducting imaging experiments ultrasonic transducers were aligned in water. Side viewing transducers were aligned using retro reflectors to an inclination accuracy of 0.6° and downward viewing transducers were aligned using stainless steel plate placed beneath the downward viewing transducers.

Imaging of subassembly top surface using downward viewing transducers

Imaging of subassembly top surface was carried out in water and sodium using ultrasonic imaging system. Transducer holder was rotated by 360° in steps of 1° and echo signals were acquired from top surface of the subassemblies using downward viewing transducers. C-Scan image for echo signals received in water and sodium are comparable.

Imaging of protruded subassembly using side viewing transducers

Imaging of protruded subassembly was carried out in water and sodium using ultrasonic imaging system. Transducer holder was moved up by 60 mm in steps of 2 mm. After each 2 mm step of upward translation movement, transducer holder was rotated by 360°, in steps of 0.5°. The echo signals received from the protruded subassemblies in water and sodium were plotted in 3D format as shown in Figures 3a and 3b.

The USUSS has been confirmed for use in PFBR based on satisfactory performance during testing in water and in sodium.

Fig. 1 *Scanner assembly*

Fig. 2 *Target subassemblies and transducer holder with transducers*


(a) (b)
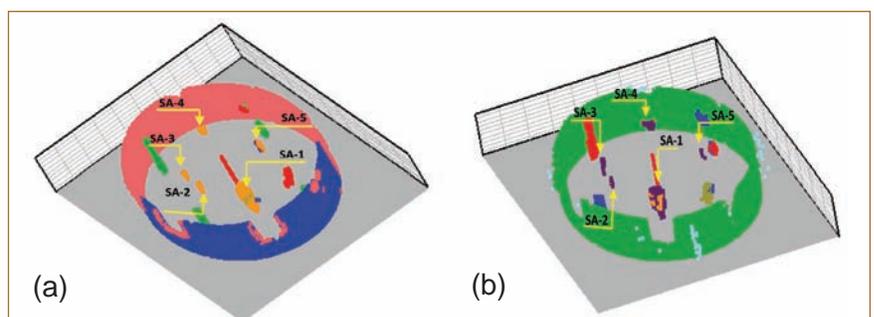
Fig. 3 *3D image showing protruded subassemblies in (a) water and (b) sodium*

II.7 Development of Extended Spark Plug Type Leak Detector (ESPLD) for PFBR

Fig. 1 Sensor portion and inset showing sensor end (without protection cap)

The main vessel of PFBR contains reactor components, which are immersed in sodium pool. In case of sodium leak from the main vessel, it will be collected in the safety vessel. For detecting the leak from main vessel, two diverse methods are used. One of which is based on electrical conductivity and the other is based on mutual inductance principle. Two numbers of ESPLDs are used which work on electrical conductivity principles. Sensing end of the leak detector is located in Nitrogen atmosphere at the bottom most point inside the safety vessel where sodium gets collected in case of leak. The temperature near the sensor will be around 400 °C. As per ASME code, a leak rate of 100 g/h of sodium should be detected in 250 h in the inert atmosphere. This sensor will detect the leak as soon as the leaked sodium touches the tip of the sensor.

The schematic and photographic active sensor portion is as shown in Figure 1. It consists of a centre needle stainless steel tube insulated from the outer stainless steel tube by alumina, using vacuum brazing technique at BARC.

The overall dimension of the sensor is 5 mm dia. and 49.5 mm length which is limited by the complex guide tube (O.D-10 mm/I.D 8 mm) profile which is welded in the safety vessel. The guide tube diameter was restricted to 10 mm to avoid interference of ISI vehicle movement and hence the size of the sensor dia. is also restricted. 25 meter long mineral insulated(MI) cable of dia. 1.5 mm was brought through a thin walled stainless steel capillary tube of 4 mm dia., to protect the cable and also for ease of insertion/withdrawal

in the guide tube. The active sensor tip portion was protected to avoid damage during insertion by stainless steel protection cap.

The sensor active portion was initially assembled using 1 mm dia. MI cable with copper conductor and the SS sleeves are brazed, but after fabrication, the copper conductor got broken due to unequal thermal expansion between stainless steel and copper. Hence 1.5 mm dia MI cable with SS conductor was selected considering the thermal expansion effect and strength. The assembly of this sensor consists of five laser welding joints with close tolerance. The stainless steel sleeve and 25 meter long MI cable is to be joined using laser welding. Each joint has different sizes and has different welding parameters. One of the challenging jobs is to laser weld the mineral insulated cable center conductor (0.59 mm dia.) to the SS needle. For this weld joint, 30 mm long mineral insulated cable's conductor portion has to be machined from 0.9 mm dia. to 0.59 mm dia. Specially designed jigs and fixtures were used to machine the conductor successfully at IDEAS. To set the welding parameters, and for welding procedure qualification, three sets of mock up pieces are machined and welding parameters are set. The welding procedure has to be

qualified by liquid penetrant test and metallographic examination. After improving the insulation resistance value of MI cable using tape heater, the laser welding was carried out on the actual job. After insertion of sensor in the guide tube of PFBR, the leak tightness of the sensor should be ensured (Nitrogen). Hence a leak tight arrangement was also designed, for (1) guide tube, (2) capillary tube and (3) MI cable which are shown in Figure 2. The leak tight arrangement will be welded after insertion of the sensor in the guide tube at PFBR site.

The ESPLD has been developed with required quality assurance requirements for use in PFBR.
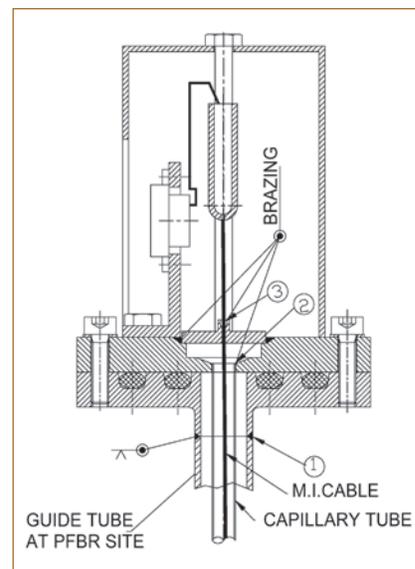
Fig. 2 Leak tight arrangement

II.8 Manufacture of Nickel Coil Assemblies for Detection of Hydrogen in PFBR Secondary Cover Gas Circuit

The cover gas hydrogen meter is used to measure the concentration of hydrogen in the cover gas of the secondary sodium circuits in Prototype Fast Breeder Reactor. It is housed in the buffer or expansion tank of secondary sodium circuit where the sodium temperature is limited to 250°C and argon carrier gas flows through the nickel coil assembly. Cover gas is circulating around the nickel coils by natural convection. In case of sodium-water reaction in secondary sodium circuits, part of the hydrogen produced reaches the cover gas. Hydrogen present in the cover gas diffuses into the nickel coil. The cover gas at operating temperature is carried by argon to the thermal conductivity detector (TCD). The TCD makes use of the difference in thermal conductivity of argon and argon-hydrogen mixture to detect the hydrogen and the output of the TCD is proportional to the hydrogen in cover gas.

The nickel coil assembly as seen in Figure 1 consists of a central pipe on which seven numbers of thin walled nickel tubes (each of 1 meter long, 2.5 mm outer dia and 0.25 mm thick) are fastened. The ends of nickel tube are connected serially by means of specially designed groove weld joints made in a stainless steel flange. The two ends of the seven metre long nickel coil are connected to ¼" stainless steel tubes which are welded above the top of the flange. These stainless steel tubes serve as the gas inlet and outlet for the nickel coil. The central pipe is closed at the bottom with a 10 mm thick stainless steel plate.

The top flange can be welded to an adaptor on the expansion tank of secondary sodium circuit and thus gets fixed in vertical position in the cover gas space. Through the opening of the central pipe, a compact and replaceable 1.5 kW heater is introduced and is used to heat the nickel coil to the operating temperature (500°C). Three thermo-wells are provided in the top flange to accommodate thermocouples for measuring the temperature of the nickel coil at different elevations. The thermocouple in the thermo-well that is located at the center of the central pipe is used for controlling the temperature of the nickel coil assembly.

Thin walled nickel tubes were bent to 'U' shape using a specially designed and fabricated fixture. Since nickel tubes are very soft after annealing heat treatment, it requires careful handling during manufacture. Hence, 1.5 mm diameter nickel wire is inserted into the nickel tube for safe handling and ease to work with it during bend forming. The internal volume of the nickel coil is optimised for a given tube dimension, which in turn reduces the travel time of carrier gas from one end of the nickel coil to other end.

Bi-metal lip seal welding of nickel tubes with austenitic stainless steel end sleeves was a challenging work. Successful welding of nickel material requires suitable weld joint design and proper maintenance of the cleanliness. It is also to be ensured that the surface is free from contaminants like organic compounds, dirt, foreign material and purity of argon gas for shielding

and purging. Mock-up welding was carried to qualify the bi-metal weld joints. The wall thickness of the nickel tube is 0.25 mm, proper care in handling the tubes during manufacture and good skill of the welder is important to carry out the lip seal welding successfully to achieve leak tightness.

Surface contact of nickel tubes with central pipe is the one of the functional requirement for uniform heating of the nickel tubes. Maintaining straightness of the nickel tubes, assembling the tubes with central pipe was a tough task. Central pipe and nickel tubes were fixed in position, using stainless steel AISI-316 strips and by spot welding. After final assembly, non destructive inspections like liquid penetrant examination, radiography examination and helium leak test under vacuum were carried out to ensure the quality of weld as per the requirement.

Fig. 1 Nickel coil assembly

II.9 Technological Feedback in Primary Sodium Pump Testing and Design & Development of Large Diameter Stainless Steel Thin Shell Bellows

The primary sodium pumps(PSP) of PFBR are manufactured, successfully assembled and tested in both vertical and inclined conditions at manufacturer's site. Ascertaining of compliance of test results to design values was also completed.

Tilting – a unique feature of primary sodium pumps

The top flange of the pumps are mounted on the reactor roof slab (carbon steel material) (373 K) which extend downward vertically into the cold pool. The lower end of the pump (670 K) is connected to the nozzle of the spherical header of the primary pipe (SS material) through suitable connector called pump to pipe connection (PPC) are also called as receptacle (Figure 1a).There exist differential thermal movements between the two because of different temperatures. Hence, pipe where the pump is received is offset during erection at lower temperature so that it will become straight after the cold pool temperature is raised (due to thermal expansion) to 670 K during reactor operation. This tilting is accommodated by spherical seat in the pump. The tilting of the pump results in a combined parallel and angular misalignment at the coupling location (Figure 1b). A gear type spacer coupling is provided to accommodate the combined misalignments.

Challenges during initial inclined test trials at manufacturer's site

(a) Coupling performance

During the inclined testing of PSP at manufacturer's site, the performance of the coupling was not satisfactory. Few teeth got damaged during
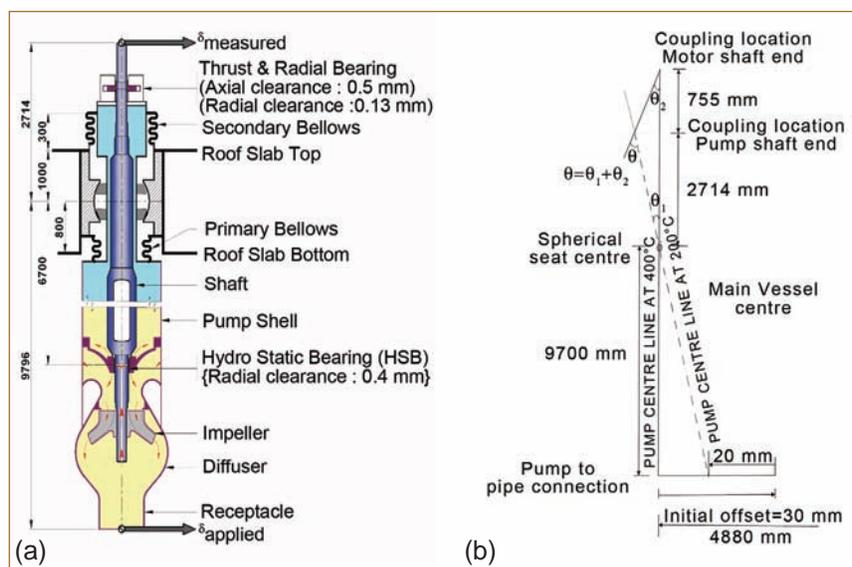

Fig. 1 (a) Primary sodium pump and (b) its tilting

the inclined testing. After detailed review of the damaged teeth, it was suggested to make following changes such as modification in the crowning of the teeth and increasing the hardness of teeth from 250 to 400 BHN. With the above design changes, the coupling performed successfully during subsequent tilting operation.

(b) Effect of secondary bellows

During the testing of PSP in inclined condition, it was observed that the secondary bellows (manufactured with a thickness of 1.6 mm) is not permitting the proportional movement at the top when the pump was pulled at the bottom to achieve the required inclination.

Need for bellows in the pumps

There are two stainless steel (SS 304L) bellows in the Primary Sodium Pump of PFBR. They are called primary and secondary bellows (Figure 1a). The primary bellows is provided to seal the reactor cover gas 'argon' leakage to reactor containment building (RCB) through the pump clearances. The

primary purpose of the secondary bellows is to provide sealing for the inter seal argon (which is purged at 200 mbar (g) 90 mbar above the cover gas argon pressure). As a secondary function, these bellows will also prevent escape of cover gas argon in case of failure of primary bellows. Apart from sealing, these bellows must also have some rigidity to improve natural frequency. However, high stiffness is not preferred from free tilting considerations.

### Criteria for optimization of thickness of bellows

Pump should run smoothly under inclined condition without any bending of the shaft. The major components in the pump that give resistance to tilting are primary bellows (below the spherical seat), secondary bellows (above the spherical seat) and friction force in the spherical seat. Therefore, the stiffness of the bellows should be minimum, which is influenced by the thickness of the bellows. Thickness is varied to derive the desired

stiffness, keeping other parameters such as lateral and axial sizes of the bellows and the mating flanges that have many constraints. Hence, an optimum thickness for bellows is determined considering the design pressure, manufacturability and stiffness requirements. Detailed structural analysis was carried out to optimize the stiffness of bellows.

Criteria for maximum allowable thickness

If there are no bellows, the pump shell and in turn the shaft will tilt freely about the centre of spherical seat and there will not be any bending of the shaft. Also, there will be no force on primary pipes. With the bellows, the shell acts like cantilever beam type structure and undergoes bending upon application of radial displacement at the receptacle at the bottom end. Since, both shaft and shell are attached rigidly to the top flange; the shaft would also bend under force generated at the hydrostatic bearing (HSB). Due to this, the following effects are foreseen.

(1) Force will be developed (Figure 2a) on the shaft at HSB locations which in turn induces additional bending stress at its top support location. The maximum allowable value should be ≤ 10 % of yield stress at operating temperature (14 MPa)

(2) Reduction of radial clearance at the HSB should be ≤ 20 µm to prevent any possibility of metal to metal impacts during operating basis earthquake (OBE) for all
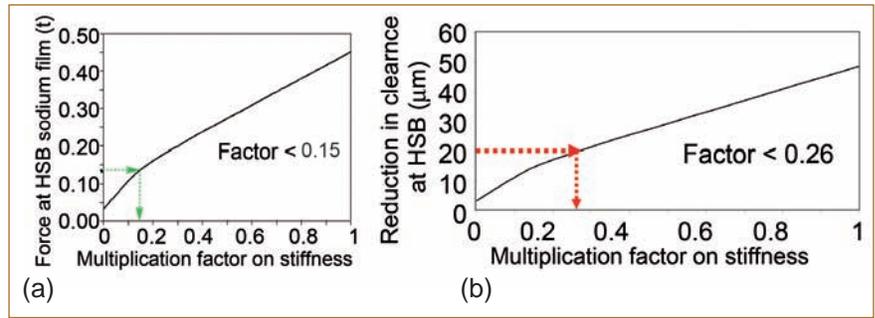
Fig. 2 *(a) Force on shaft and (b) reduction in radial clearance at the hydrostatic bearing*

operating speed (Figure 2b)

(3) Additional force developed on the primary pipes should be limited (Figure 3a) so as to restrict the additional bending stress in the highly stressed location of pipes ≤ 10% of yield stress at operating temperature (12 MPa)

(4) Fundamental natural frequency of the shaft should not be reduced by 10%.

In order to comply the above criteria, detailed finite element analysis has been carried out using beam model including stiffness of all the pump components. The reference stiffness was calculated for the thickness of both the bellows at 1.6 mm, the thickness with which bellows was initially supplied for the pump. It is observed that the effect of stiffness of primary bellows is marginal on bending of shell/shaft combination and hence, the analysis is carried out by changing stiffness of the secondary bellows as a parameter. To meet all the above criteria as well as minimum thickness required from pressure loading and possible

wall thinning during manufacturing, thickness close to 0.6 mm is arrived for the secondary bellows keeping other parameters like depth and height of the bellows unaltered shows the proportional movement (Figure 3b) at the top of pump for tilting at the bottom for various multiplication factor on the reference stiffness (multiplication factor of 1.0 is for thickness of secondary bellows as 1.6 mm).

With a multiplication factor of 0.35 (i.e thickness of bellows close to 0.6 mm) a proportional movement very close to the anticipated value is observed. Small difference on the deviation from the expected movement is attributed to the effect of stiffness of primary bellows.

Manufacturing of secondary bellows with 0.5 mm thickness

The manufacturing of thin bellows with 0.5 mm thickness with mean diameter of around 1470 mm was successfully completed (Figure 4) in house after many trials with a novel and economical process adopted using set of innovatively made adjustable dies.
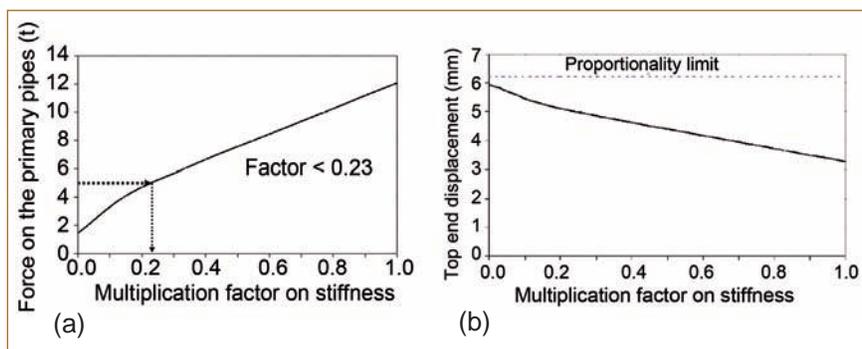
Fig. 3 (a) *Force on primary pipe (tonnes) and (b) proportional movement (mm)*

Fig. 4 *Completed bellows*

II.10   Seismic Qualification of Indigenously Developed Gate Valve and Shield Plug for Inclined Fuel Transfer Machine

Inclined fuel transfer machine for PFBR is used to transfer subassemblies from the In-vessel transfer post located in the periphery of the core to ex-vessel transfer post located in fuel building. A rotatable shield leg connects the primary side and secondary side, both of which are provided with leak tight gate valves. At a time, only one of the valves is open, connecting rotatable shield leg with either primary or secondary side maintaining required leak tightness and also avoiding direct connection of reactor system to outside. A shield plug with lead shielding of 350 mm thick is provided above the primary ramp for attenuating primary sodium gamma rays during the reactor operation. Both the gate valve and shield plug are large sized heavy components designed indigenously and manufactured at M/s MTAR, Hyderabad. The structural integrity and functionality of these large size components are demonstrated for operating basis earthquake and safe shut down earthquake using 10 t shake table at the Structural Mechanics Laboratory (SML) with the respective spectrum compatible earthquake excitations. The test arrangements for the gate valve and shield plug are given in Figures 1 and 2 respectively.

Both these components (gate valve and shield plug) are mounted on a fabricated support structure which simulates the actual mounting arrangement. The floor response spectra corresponding to the reactor vault top location (EL 31.00 in reactor vault location) is taken as the required response spectra for the experiment. The valve and the shield plug have been tested for five operating basis earthquakes and one safe shut down earthquake using the respective spectrum compatible time histories such that the time response spectra envelops required response spectra. Accordingly generated a typical spectrum compatible time history is shown in Figure 3. It is for the X direction operating basis earthquake excitation.

Before starting the experiment, the valve is kept in the closed condition by applying pressure of 6 bar.
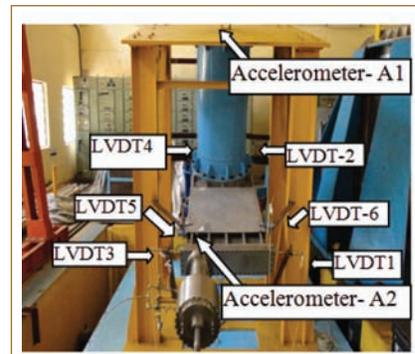

Fig. 1 *Test arrangement for gate valve*

Healthiness of the valve is checked before conducting the experiment.

The pressure retaining capacity of the valve during the vibration is monitored using pressure sensors and found that there is no appreciable variation in the pressure. There is no impact sound between sliding parts during the experiment indicating that the relative displacements between different sliding parts in the valve was within the acceptable limits. After completing the operating basis earthquake tests, the valve operability has been ensured by opening and closing the valve 10 times and ensured the smooth operation of the valve. Subsequent
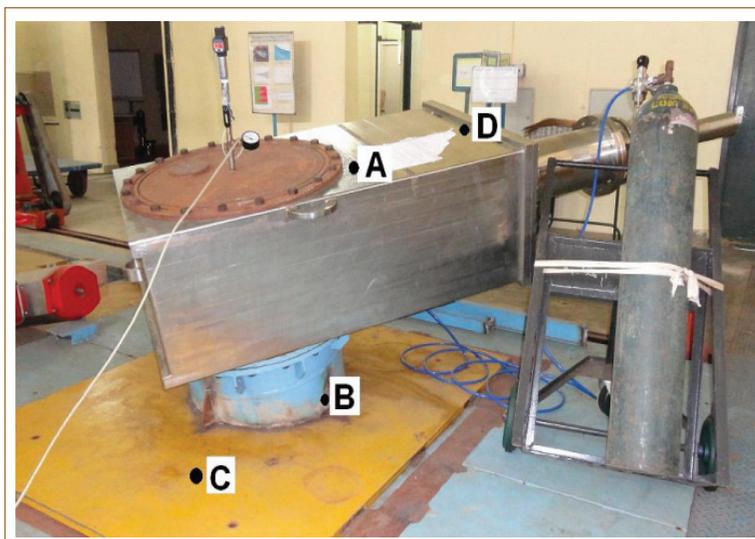

Fig. 2 *Test arrangement for shield plug*
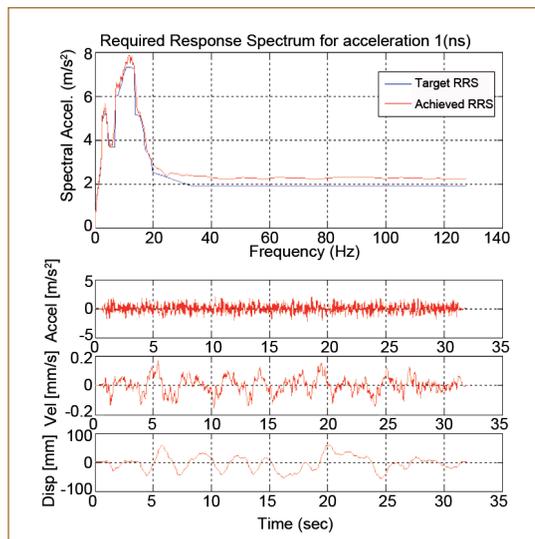
***Fig. 3*** *Typical spectrum compatible time history used for the experiment*

to the functional operability, the leak tightness of valve has been ensured by helium leak test. The helium leak test demonstrated that the leak rate of the valve found less than 10^{-6} Pa m^3/s and thus meeting the specified requirement. After the operating basis earthquake test, the valve has been subjected to safe shut down earthquake loading and the leak tightness of the valve after the test has been ensured by helium leak test, similar to that of operating basis earthquake test and it has been demonstrated that the leak rate was less than the acceptable limit. To determine the duty of the connecting bellows for the valves, the deflection at the flange locations are measured using linear voltage displacement transducers. Figure 4 shows the maximum response observed during SSE loading condition. The bellow has been designed for the above observed displacement.

The shield plug was mounted on the shake table at an angle of 17º to the vertical and 55º in the horizontal plane in a support structure as shown in Figure 2. The top and bottom flanges closed with dummy plates along with additional O-rings for bottom flanges to ensure leak tightness. Before experiment a pressure of 120 mbar was applied between the bottom blind flange and bottom face of the shield plug. Subsequently, it was confirmed that the leak tightness of the shield plug was less than 10^{-6} Pa m^3/s by helium leak test.
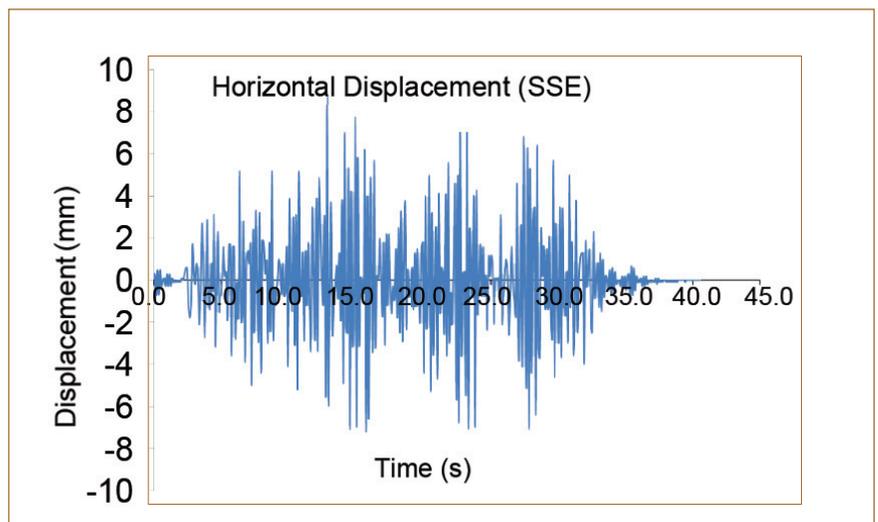
Fig. 4 Maximum horizontal movement of the valve during SSE loading

The shield plug assembly subjected for five operating basis earthquake as per the required floor response spectra. After each operating basis earthquake smooth opening and closing of the shield plug is demonstrated for ten cycles. Subsequently, it is subjected to safe shut down earthquake condition. The leak tightness of the shield plug assembly is confirmed at the end of both operating basis earthquake and safe shut down earthquake by helium leak test.

Strain gauges are pasted at the critical locations towards capturing the structural integrity under operating basis earthquake and safe shut down earthquake. The maximum strain observed during the operating basis earthquake is given in Figure 5 along the hoop direction. It is observed at the location A from

the Figure 2. The maximum range of the observed strain is 187 microns.

The maximum strain observed during the safe shut down earthquake is given in Figure 6 along the hoop direction. It is observed at the location B from the Figure 2. The maximum range of the observed strain is 848 microns. Since both these values are within the elastic regime, there is no concern of structural integrity.

The inspection carried out during and after the operating basis earthquake and safe shut down earthquake tests indicate that the structural integrity and functional requirements are met for both inclined fuel transfer machine gate valve and the shield plug assembly under the specified type test of operating basis earthquake and safe shut down earthquake.
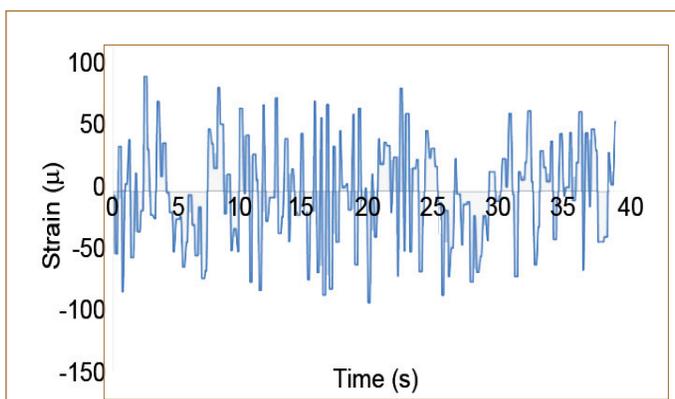
Fig. 5 Maximum strain found during OBE for the shied plug assembly
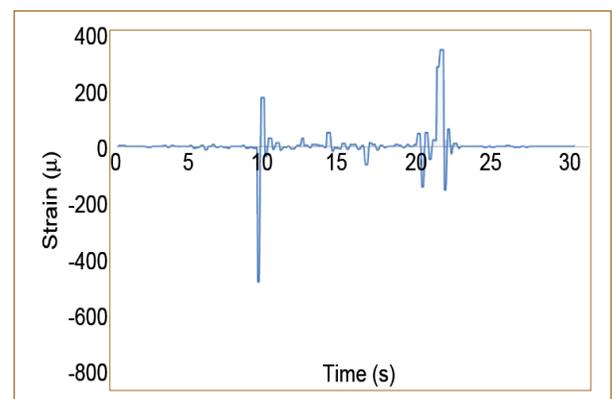
Fig. 6 Maximum strain found during SSE for the shied plug assembly

II.11   Seismic Margin Assessment of SGDHR System by Integrated Seismic Analysis

Safety grade decay heat removal system (SGHDR) of PFBR is a passive decay heat removal system consisting of four independent loops, each capable of removing decay heat of 8 MW. Three out of four loops are sufficient to remove the entire decay heat generated in the reactor. Each loop consists of decay heat exchanger (DHX), expansion tank, air heat exchanger (AHX), storage tank and pipelines connecting these components. Piping system carrying hot sodium from decay heat exchanger to air heat exchanger is called hot leg and the piping system carrying cold sodium from air heat exchanger back to decay heat exchanger is called cold leg. Cold leg and hot leg are connected to the storage tank through fast dump lines. In addition to redundancy, diversity has been built into the system by using two types of DHX (DHX A&B) and two types of AHX (AHX A&B) with four different piping layouts. Out of the four safety grade decay heat removal system circuits, SGDHR south east loop, south west loop are with decay heat exchangers and air heat exchanger of type-A and north east and north west loop are with type-B air heat exchanger and decay heat exchanger. Figure 1 shows the layout of SGDHR north east and south east loop in steam generator building (SGB1).

These dedicated passive decay heat removal systems are designed to operate under all design basis events including extreme seismic loading conditions and beyond design basis events such as hypothetical core disruptive accident. The seismic design of piping systems and components of SGDHR systems are carried out
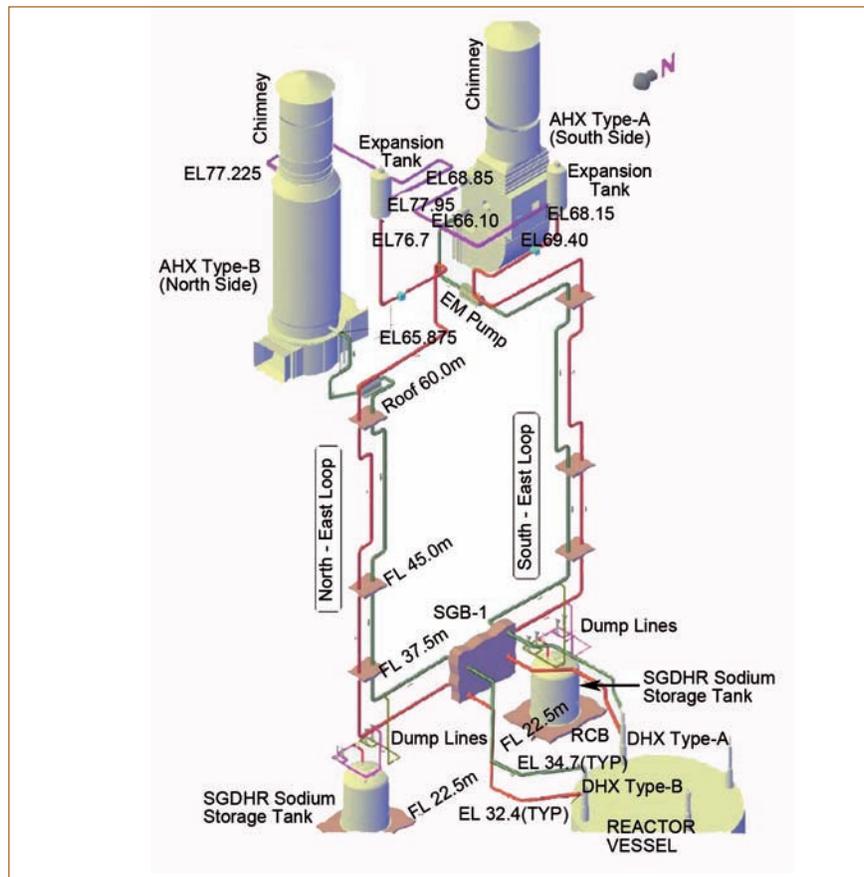

Fig. 1 Layout of safety grade decay heat removal system in SGB-1

by detailed seismic analyses of the system. In order to estimate the seismic margin of the SGDHR system to withstand an earthquake beyond the safe shutdown earthquake level, integrated seismic analyses of SGDHR system has been carried out. The integrated system consists of all the equipments and piping system of SGDHR loop. This model helps in capturing the coupling effect of piping systems and components during seismic excitations. Finite element model of integrated north west loop with type-A heat exchangers are shown in Figure 2. Here, the piping system is modelled by pipe elements and the connecting equipments are modelled by equivalent beam elements. Restrains and anchors are provided at appropriate locations

based on the support layout of the piping system. The snubbers which are suggested based on the
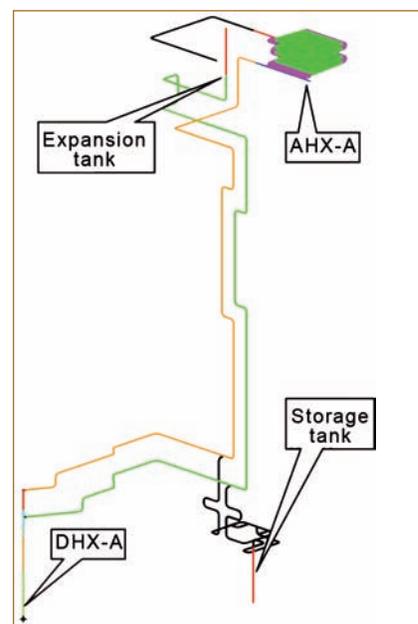
*Fig. 2   Finite element model of SGDHR north west loop*

uncoupled analyses of the system are modelled by linear springs with respective snubber stiffnesses given in the snubber catalogue.

Seismic analysis of the integrated system is carried out for safe shutdown earthquake loading condition by response spectrum method using general purpose finite element code CAST3M. Spectrums for north-south, east-west and vertical directions corresponding to 5% damping are generated by enveloping the response spectrums of all support locations of the components and piping of SGDHR system. Response is computed by modal superposition method. Towards this, first free vibration analysis of the integrated system has been carried out to extract the modes upto 35 Hz. Figure 3 shows predominant modes of safety grade decay heat removal system south east loop. Modal analysis of the system indicates strong coupling between some of the equipments and piping system based on the frequency ratio of piping and major components. The response of the integrated system is estimated by assuming a damping ratio of 5% for the entire system. Complete quadratic combination method is used for the modal combination and the spatial combination of the responses are carried out by square root of sum of squares method.

Forces, moments and stresses at the critical locations such as pipe bends, tees, nozzles and support locations are extracted. Responses obtained from the integrated analysis has been compared with the responses obtained from un coupled analysis of the piping system. Comparison indicates that decay heat exchanger which have a fundamental frequency of 6.7 Hz have strong coupling with the pipe line while the dynamic behavior of the air heat exchanger header have marginal effect on the piping responses. The responses of the dump lines are strongly coupled with dynamics of the storage tank during the seismic excitation.

Stress intensity in the piping systems at critical locations are estimated based on RCC-MR rules for pipe design using the stress indices calculated based on the diameter and thickness of the piping component. The stress indices values for bends and tee connections are given in Table 1. The stress intensity values at various locations are estimated by calculating the resultant bending moments by considering the static and dynamic loading. The nominal stress intensity values estimated from the resultant bending moments are multiplied by the stress indices to estimate the actual stress intensity values at various piping components such as as bends and tee junctions. The analysis indicates that the tee junctions
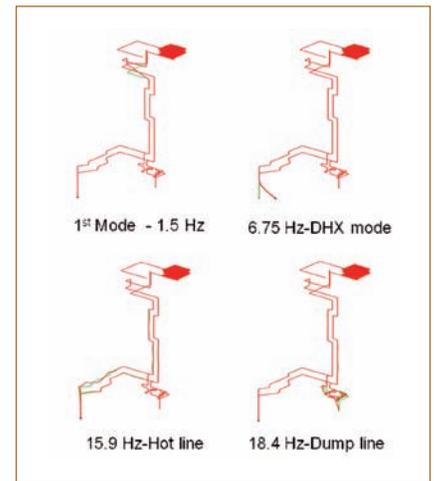
Fig. 3 *Predominant modes*

and bends are most severely stressed components in the piping system. The dynamic response of the safety grade decay heat removal system obtained from the integrated analyses are compared with the responses estimated for the same system by un-coupled analyses. The comparison of the stress intensity values are tabulated in Table 2 for different part of SGDHR piping system. Here it may be noted that the safe shutdown earthquake is considered in Level-D operating condition and the allowable stress for piping for level-D corresponding to an operating temperature of 550°C is 288 MPa while the maximum stress intensity estimated from the coupled analysis is 228 MPa showing a margin of 60 MPa. Hence, the safety grade decay heat removal system can withstand an earthquake 1.26 times more than the present safe shutdown earthquake.

Table 1: Stress indices for piping components		
Location	Stress indices	Value
Straight pipe	B1	0.5
	B2	1.0
Bend	B1	0.5
	B2	5.826
Tee between hot leg and dump line	B1	1.0
	B2 (Runner)	4.487
	B2 (Branch)	3.590
Tee between cold leg and dump line	B1	1.0
	B2 (Runner)	1.932
	B2 (Branch)	1.546

Table 2: Comparison of stress intensity by coupled and uncoupled analyses			
Equipment	Location	Stress intensity (Pm + Pb) MPa Allowable limit = 288 MPa	
		Coupled analysis	Uncoupled analysis
Hot leg	Tee	88.32	114.66
	Bend	238.2	214.4
Cold leg	Tee	57.12	30.53
	Bend	197.6	168.3
Dump line	Tee	229.3	215.1

II.12 Vibration Studies of PFBR Primary Sodium Pump

In PFBR two numbers of sodium pumps are used in the primary circuit to circulate sodium in the primary vessel. Performance testing of primary sodium pump (PSP) was carried out in the water test bed at manufacturer's premises. Figure 1 shows the assembled view of PFBR primary sodium pump at the test bed.

Machinery vibration measurements were carried out on the pump during the testing. Overall vibration amplitude and vibration spectra were measured using machinery vibration analyzer in two axis - horizontal (radial) and vertical (axial) directions at the top mechanical seal location. Apart from this, online condition monitoring system was used to continuously monitor the vibration levels on the pump and on the motor at critical locations.

Figure 2a shows the locations of online sensor mounted on the pump mechanical seal locations and Figure 2b shows the sensors on motor drive end location. Measurements were carried out under various test conditions.

In the first phase, endurance testing of the pump for 50 hours was carried out at 540 rpm. Later, measurements were carried out

**Fig. 1** *Primary sodium pump-1 at test bed*
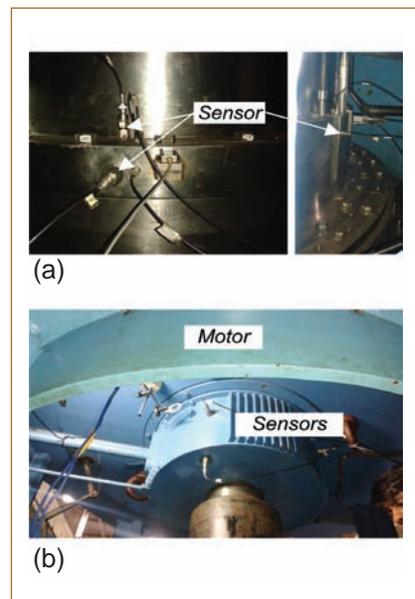
Fig. 2 *(a) Online sensor on top seal and (b) sensor on motor drive end*

with various pump speeds and finally for various net positive suction head conditions.

Figure 3a shows a typical vibration spectra measured at the top mechanical seal during the endurance testing at 540 rpm. After endurance testing, pump was tested for different water flow conditions at three different rpm conditions (540, 520 and 265 rpm). The variation in vibration amplitudes during net positive suction head testing is shown in Figure 3b. A typical plot of vibration data from the online system during the endurance

testing is shown in Figure 3c.

The amplitude of vibration measured during the entire test was found to be well within the limit of 2.5 mm/s specified for PFBR primary sodium pump. After endurance testing, primary sodium pump was tilted in the test bed and inclined testing was also carried out for four hours. Figure 3d shows typical vibration spectra during the inclined testing.

The overall vibration values were well within the permissible limit during all the test campaigns.
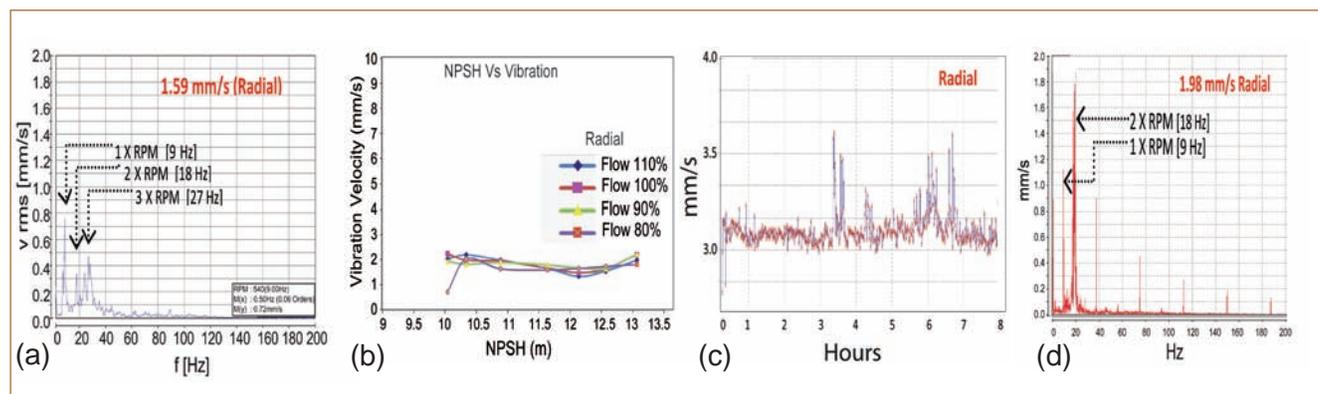

Fig. 3 *(a) Vibration spectra at 540 rpm, (b) net positive suction head test results at 540 rpm, (c) on-line vibration trending and (d) vibration spectra (inclined test)*

II.13 Impact Assessment of Transmission Fault Clearance on PFBR Plant Electrical Systems and Process Systems

Grid electrical disturbances are commonly characterized by variances in the grid voltage and/ or frequency. These significant deviations can disrupt the dynamic state of process systems equilibrium in a Nuclear Power Plant. In order to study dynamic behavior of PFBR electrical system during these transients, PFBR electrical system and associated grid near to PFBR plant is modeled in ETAP software package.

In PFBR, Class-IV 6.6 kV buses (two numbers of unit buses and two numbers of station buses) supply power to all electrical systems in the plant. station buses are connected to the grid through station transformer. Unit buses are connected to grid through unit auxiliary transformers and generator transformer. When PFBR generator is in operation PFBR turbo-generator is connected to unit buses through unit auxiliary transformers. This arrangement is shown in Figure 1. Among the many transients studied, 3-phase faults occurring in transmission system and their impact on PFBR electrical systems and process systems are highlighted.
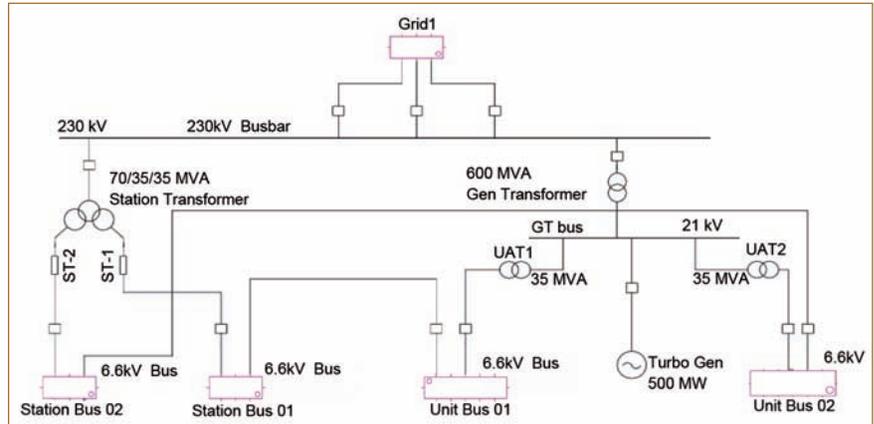

Fig. 1 *PFBR electrical system and associated grid model in ETAP software*

Fault transients impact on plant electrical system

Each of the six transmission lines connecting plant and the grid are provided with two main protections which operate and isolate the fault in 100 ms. Typical backup protection clears the fault within 350 ms. For the purpose of analysis, practical main protection fault clearance of 100 ms and worst case backup protection fault clearance of 500 ms are considered. Key observations made from the simulation are

- Faults occurring in transmission system near to PFBR plant have significant impact on plant systems compared to fault

occurring at the far end of the transmission system

- During fault clearance, major fluctuations in the voltage and frequency profiles are observed in 230 kV switchyard busbar. PFBR generator bus is less susceptible to voltage fluctuations caused by faults because of the presence of automatic voltage regulator system

- When PFBR generator is in operation, it is noted that voltage profiles of unit buses are better than station buses. This is because unit buses are connected to the generator bus through unit auxiliary transformers. During
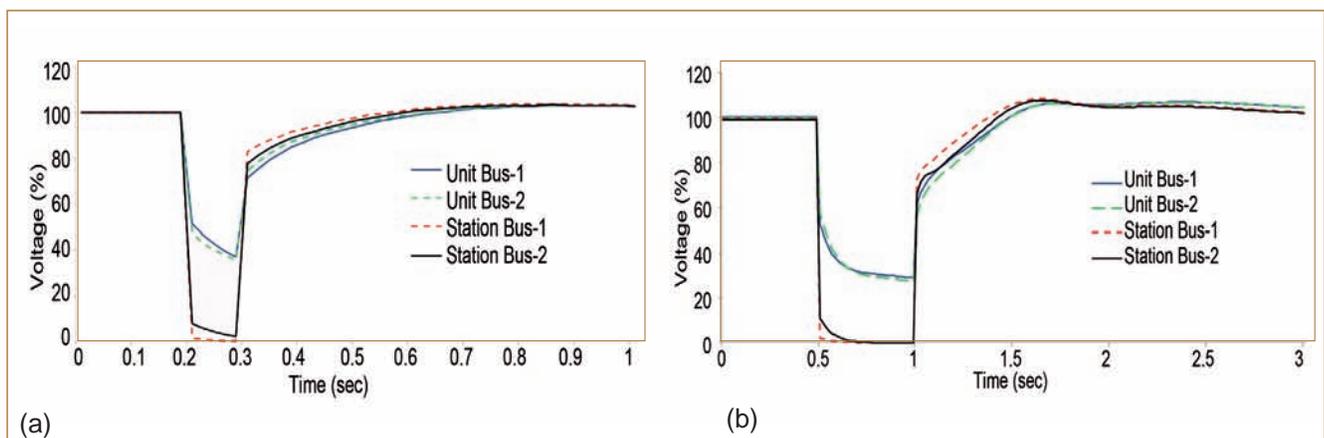

Fig. 2 *Voltage profiles at Class-IV 6.6 kV buses for fault clearance in (a)100 ms and (b) 500 ms*

the fault or other disturbances, automatic voltage regulator of PFBR generator reduces the dip in the voltage levels in unit buses

- Majority of the station electrical loads particularly emergency loads are connected to UB1 and UB2 as the voltage deviations on these buses are comparatively better than station buses for a given electrical fault clearance

- When fault occurs in transmission system near to switchyard bus, it is observed that the voltages of station buses dip close to zero

- When fault clearing time is in 100 ms, voltage levels of the PFBR buses restore back to the normal in 0.2 seconds. In case of the fault clearing in 500 ms, bus voltages restores back within 0.2 to 1 seconds after the fault clearance. Voltage profiles for the unit buses and station buses for fault clearance in 100 ms and 500 msec are shown in Figures 2a and 2b respectively. It is observed that motor feeders do not trip due to under voltage even when fault is cleared within 500 ms

- PFBR turbo-generator rotor angle, output power, stator current profiles undergo more oscillations when the fault clearing time is within 500 ms compared to fault cleared within 100 ms as expected. This profile can be observed from Figure 3. PFBR turbo-generator comes to new steady state after 2.5 sec after fault clearance

- It is noted that subsequent to fault clearance, large 6.6 kV motors connected to station buses draw inrush currents as high as almost five to six times. Higher but large motors connected to unit buses draws relatively lower inrush currents of three times the full load currents on fault clearance

and stabilization.

Fault transients impact on process systems

- State of the art variable speed drives employed in PFBR guards the reactor coolant pump motors from the degraded input power supply to the drive system. Variable speed drives system along with flywheel mechanism is able to override the above transients. Hence, no significant impacts on primary and secondary sodium systems by grid transients are expected for fault cleared even in 500 ms

- In the steam water system, degraded grid conditions can affect the performance of the boiler feed pump, circulating water pumps and condensate extract pumps through their motor performance

  Even for fault cleared in 500 ms by backup protection, it is observed that the voltage at the motor connected bus terminals restores back within trip settings of the motors. Pumps slow down momentarily and then reaccelerate to reach the normal speed after the fault is cleared. Therefore, the fault cleared in 500 ms steam water system does not have any impact on the above defined transients

- Most of the plant auxiliary motor loads and other process related loads are connected to 415 V busbars through electromagnetic contactors.

  Since major 415 V plant loads related to normal, safety and safety related loads are connected to unit buses during normal operation of the plant the potential for tripping during these transients is less compared to auxiliary loads connected to station buses due to better voltage control at unit buses. However contactors are planned to be provided with low voltage ride through facility modules which will increase the voltage sag immunity and helps in over-riding these transients.

- Class-II and Class-I power supply systems are having battery backup with rectifiers/ inverters. The protection trip settings planned will safeguard the rectifiers and inverters from tripping during transient faults.

Many system studies are carried out to verify the adequacy of the system design during grid disturbance. The analysis using ETAP package assures PFBR plant design can tide over worst case fault transients expected in the grid. The continuity of the operation is not affected.
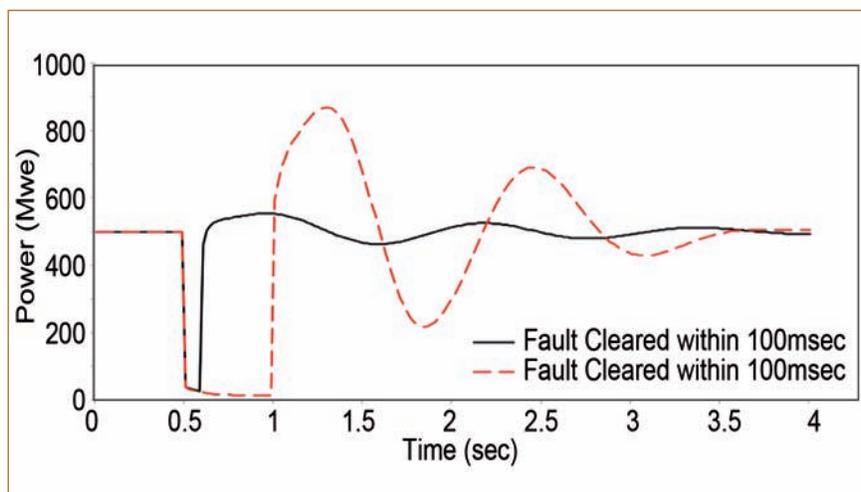

Fig. 3 *PFBR turbo-generator electrical power output for fault transient*

II.14 Radiometry Testing of PFBR Roof Slab Calibration Blocks and Sector Mock-Up Structure

The PFBR roof slab is designed to be poured with high density concrete (heavy density hematite aggregate ore mixture). The thickness is of 1.2 m. The roof slab is made in sectors. There are cooling pipes and the channels running through the roof slab. The concrete will be poured in each sector boxes through openings on the top. The concrete pouring is such that non-uniformity in concrete density should be within 5% tolerance. Also it should be ensured that concrete is properly filled around the internal structures like cooling pipes etc. Hence, prior to the actual pouring of PFBR roof slabs, two calibration blocks of dimension 800 x 600 x 1200 mm, one with $3.63 g/cm^3$ and other with $3.86 g/cm^3$ were poured and subjected to radiometry testing. The radiometry testing (Figure 1a) on calibration blocks helped in qualifying the density of the concrete mixture and pouring technique. Based on this result, a sector model of roof slab (cooling box) was poured with designed heavy density concrete and the same is subjected to radiometry testing.

In radiometry testing ^{60}Co source is used. The source is placed inside the shielding structure using source guides and the transmitted dose rate is measured over the outer surface of the testing structure.

Based on the source strength, shielding thickness, concrete density the expected dose rate on the outer surface of the structure is calculated. The measured dose rate is compared with expected dose rate to infer the uniformity of concrete pouring and the density/thickness reduction. The dose rate measurements were made with NaI(Tl) detector based nSv level survey meter (Target make Identifinder).

Calibration block – I

The dimension of the box type block was 800 x 600 x 1200 mm poured with concrete heavy density $3.65 g/cm^3$. The source guide was provided vertically at the centre along the height (Figure 1b).

The outer surface of the block was grided (5x5 cm) and each grid is identified by column alphabet and row number. The source was placed inside the source guide and moved from bottom to top in 5 cm steps. For each step, the detector is placed on grids (the outer surface of block) in line with source position vertically. Then all grids in a row are scanned for dose rate. The measured dose rates were corrected for background radiation level and compared with expected dose rate. Figure 2 shows the uniformity of the pouring along the height (row no) and the observed density variation
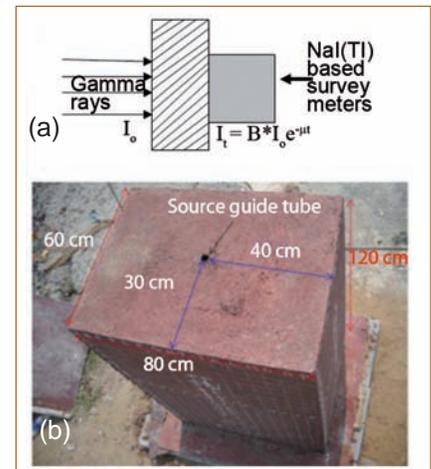

Fig. 1 (a) Schematic of radiometry testing and (b)calibration block with source

from expected density ($3.65 g/cm^3$) in dose rate. The radiometry could bring out the off centering of source guide towards north by showing higher dose rates in northern side grids and correspondingly lesser dose rate in southern side grids (Figure 3). Radiometry testing of calibration block-I showed that the poured density is close to $3.63 g/cm^3$ and the uniformity of pouring is good at all tested locations. Local variation observed is within 3% of design density.

Calibration block – II

This block was having same dimension as block-I. Concrete mix density of $3.93 g/cm^3$ was used. Typical variation of dose rate observed over western side of the
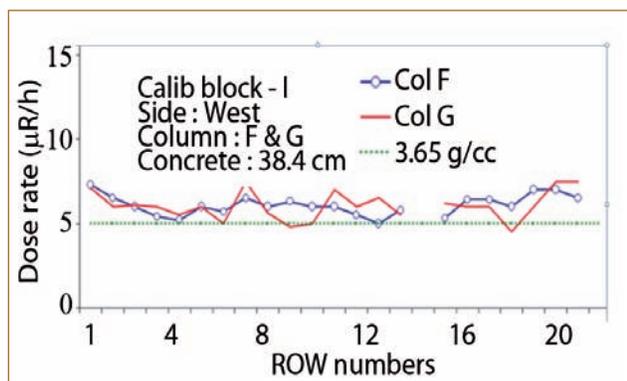

Fig. 2 Observed density variation
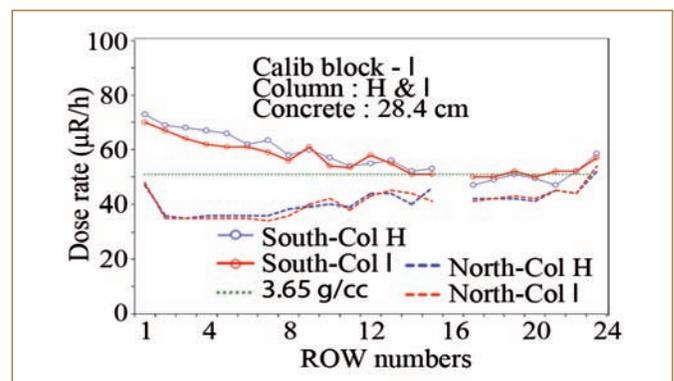

Fig. 3 Off centering of source guide
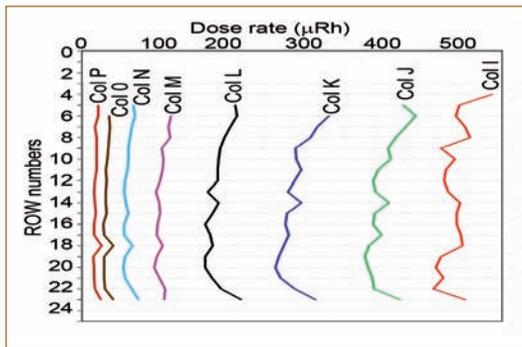
**Fig. 4** *Observed dose variation over grids on western side*
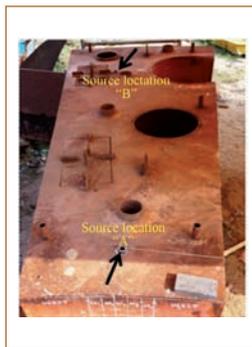

Fig. 5 *PFBR roof slab sector mock-up*
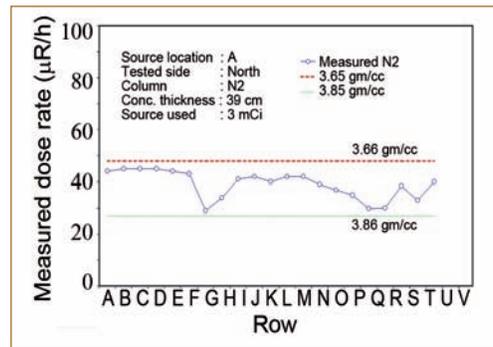
Fig. 6 *Dose rate variation at location "A" with density tolerance limit*

block is shown in Figure 4. The variations observed in the dose rate indicate that the density variation is within 5% of the designed density 3.93 g/cm^3. Even that variation is due to the unevenness of the surface upto 1cm. Also the pouring is observed uniform throughout the block. The calibration block-II measured doserate values were further validated with monte carlo n-particle code simulation.

PFBR roof slab sector mock-up structure

A sector mock-up structure having similar dimensions and interfering structures as in actual roof slab is poured with high density (3.86 g/cm^3) concrete. The top 20cm is grouting concrete with density of 3.16 g/cm^3. For the radiometry testing requirement, source guides tubes were placed at two pre-selected locations in the sector mock-up structure. The locations of guides were chosen such that radiometry testing would cover the areas around

interfering structures and the corners of the sector where the concrete flow could not be uniform or presence of voids possible. The actual mock-up structure is shown Figure 5 along with source locations marked. At location "A" there is no internal structure and the concrete thickness in north & south direction is same with respect to source location. At location "B", in the north side a pipe structure is running through the sector mock-up. The concrete flow over and above this should be tested.

The observed typical doserate variation in the north side surface corresponding to source location "A" is shown in Figure 6. The observed density variation is within 5% (3.66 g/cm^3) of designed density (3.86g/cm^3). The similar variation trend is observed in all other tested locations where concrete only is present.

The doserate variation observed at the north side for source location "B" where internal piping is present is

shown Figure 7. The increased dose rate from row "H" to "M" indicates the presence internal piping. The uniform doserate observed on either side of the piping confirms the presence of uniform concrete density around the piping. The piping dimension inferred from radiometry matched very well with the actual one. The grouting concrete portion of mock-up structure was also evaluated. Figure 8 shows the dose rate variation over the grouting concrete portion corresponding to source location "A". The measured doserate values indicate the uniformity of grouting concrete with density of 3.16 g/cm^3.

Radiometry testing results of sector mock-up structure of PFBR roof slab helped in ensuring the uniform concrete pouring in overall structure as well around the internal piping structures and any observed variation were within 5% of designed density. The radiometry testing played an important role in getting regulatory clearance for PFBR roof slab erection.
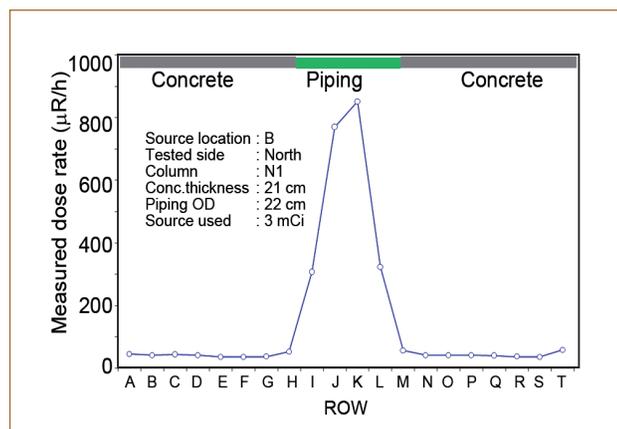

**Fig. 7** *Dose rate variation around the internal piping*
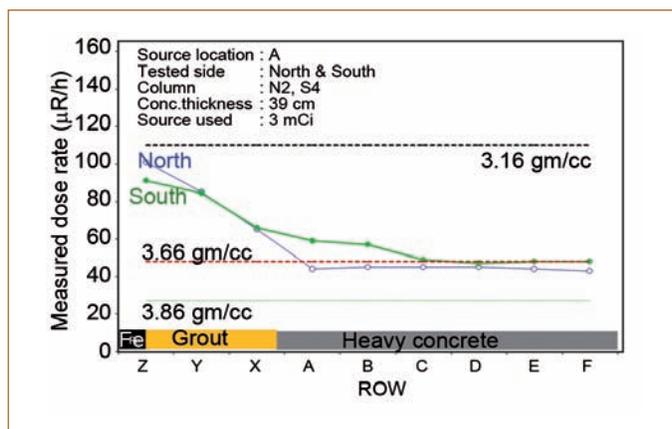
Fig. 8 *Dose rate variation over the grouting portion – location "B"*

II.15   Development of I&C for Spent Subassembly Storage Bay Transfer Machine of PFBR

Spent subassembly storage bay transfer machine (SSTM) handles spent fuel subassemblies, blankets and absorbers to store them in storage racks arranged within the storage bay and further shifting to spent subassembly transport cask. A dedicated embedded system is designed and developed to control SSTM remotely from handling control room. Since the failure of the system affects the safety and availability of the nuclear plant, the control system has to be highly reliable and available. In addition to standard development methodology and life cycle process, a model based environment is also adopted for the development of control logic. Safety critical application development environment (SCADE) is used to develop, simulate, analyse the model coverage, formally verify the control logic and generate 'C' code based on the verified model. System was functionally qualified successfully.

Spent subassembly storage bay transfer machine

SSTM consists of four drives, namely long travel (LT), cross travel (CT), gripper hoist (GH) and gripper finger (GF). LT and CT drives are moved by the control system to position the machine in the target X and Y direction respectively. GH is raised from or lowered to the subassembly location and then GF is made to grip or release the target subassembly. The LT distance over the storage bay is 32 m and CT distance is 4.8 m approx. The GH is taken to different elevations from 0 to 8 m based on the operations being handled by SSTM. SSTM is provided with different types of sensors to measure the position of LT, CT and GH drives and load on
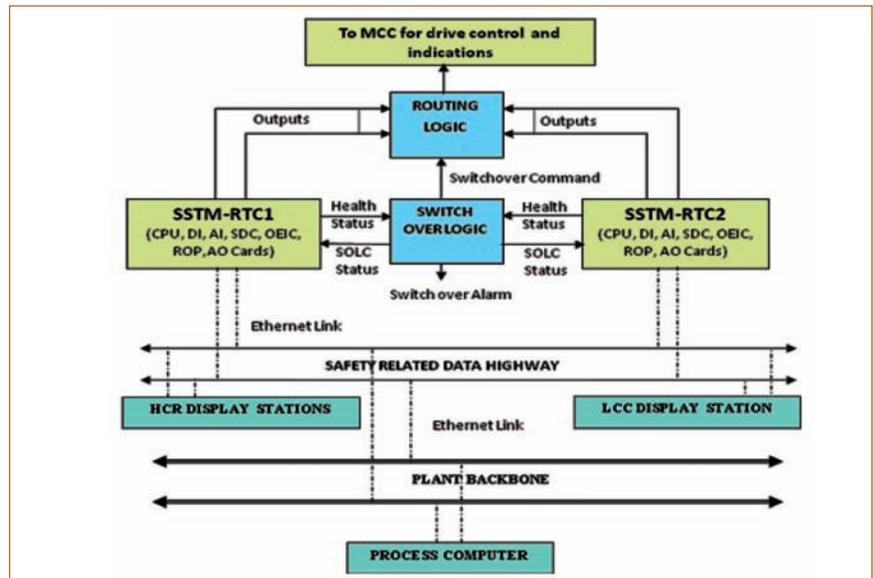

Fig. 1 *Architecture of spent subassembly storage bay transfer machine control system*

the mechanism. Synchro control transmitters and absolute optical encoders are used to measure the positions of LT, CT and GH drives, LVDT for GF position and loadcell is used to measure the load on the mechanism.

Architecture of control system

SSTM control system is classified as safety-related (SC-2) system and is having dual redundant, fault tolerant architecture as shown in Figure 1. The fault tolerant real time computer (RTC) consists of two subsystems RTC1 and RTC2 and a Switch Over Logic System (SOLS). The SOLS comprises of switch over logic circuit (SOLC) and routing logic. SOLS monitors the healthiness of subsystems to take necessary action to switch the healthy subsystem's outputs to the field, to actuate different drives of SSTM. In addition SOLS alerts the operator on failure of the RTCs. When both the subsystems are healthy, RTC1's outputs are routed to the plant. When RTC1 fails, RTC2's outputs are automatically routed to the plant. Even when RTC1

is restored back, RTC2 will continue to be the active system and RTC1 will be a hot standby system. Both the subsystems send the acquired as well as the processed data to the display stations of handling control room (HCR) and local control centre (LCC) and process computer through dedicated SC2 data highway. The process computer logs the data and sends necessary configuration parameters and other data to the subsystems.

System development methodology

The control system for SSTM is classified as SC2 system and hence a standard system development methodology is followed. Each phase of the development methodology is prepared in line with IEEE standards. System requirements specification (SyRS) is the most essential document for designing and developing the control system. SyRS is verified with respect to the control and operation requirements. Software requirements specification (SRS) is developed based on SyRS, software design description (SDD)

is prepared based on SRS and software coding is carried out based on SDD. Software unit testing is carried out to check the functionality of each module independently. Simultaneously, hardware requirements specification (HRS) and hardware design description were also prepared. Then hardware design implementation was done and tested. Then software was integrated with the hardware and tested on the target. Every document was verified by independent verification and validation (IV&V) committee before proceeding to next phase of the development.

Hardware design and development

VME bus based real time computer (RTC) is used with MC68020 processor based CPU and associated input and output boards. CPU card is designed with 32 bit MC68020 processor running at 16MHz, MC68882 - floating point processor, VME controller, EPROM, SRAM with EDAC, EEPROM, programmable watchdog timer, RS-232 and ethernet communications. The power supply to RTC system is also fault tolerant. Each subsystem receives 130 digital inputs, 3 analog inputs, 3 synchro inputs, 3 optical encoder inputs, soft data inputs & configuration parameters from process computer, soft control commands from control console, control panel & LCC, updates 28 relay outputs, 3 analog outputs and soft data outputs of all acquired /processed data. Dual subsystems are kept in a twin cabinet, one containing subsystem-1 and SOLS, relevant power supply modules and another containing the subsystem-2 and its power supplies. Necessary interface modules to interface with the field and signal conditioning modules for analog signals are connected on the rear side of the cabinet.
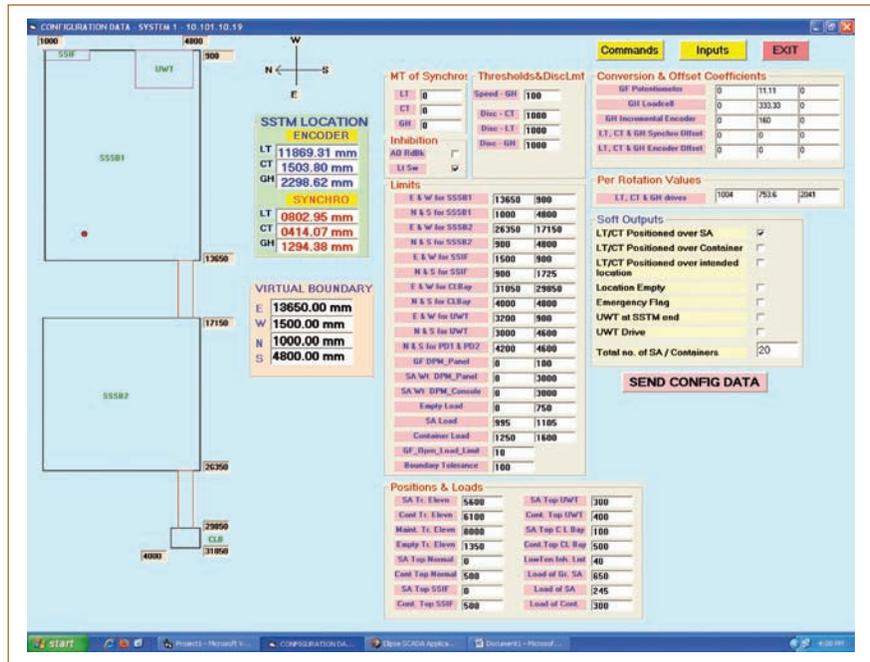

Fig. 2 *HMI for spent subassembly storage bay transfer machine control system*

Software design and development

The development of control logic of application software for the control system is carried out using SCADE suite, as shown in Figure 3, using which the control logic is modeled. The developed model is simulated for its correctness and model coverage analysis is carried out with MC/DC coverage criteria. Once the design is verified through the above, design safety of the system is also confirmed by formal verification, supported by the suite. The safety properties of the system are chosen from the system requirements and they are modeled to observe the control logic behavior to not to violate the safety.

Validation of SSTM control system

Test cases were generated from the system requirements and validation was carried out by IV&V team. All analog and digital inputs were simulated using PLC based dynamic signal simulator. Synchros and Encoders were used to simulate the angular position. Human machine interface (HMI) was developed in VB, which contains, soft control panel to issue control commands for manual and computer guided mode of operation(Figure 2). In manual mode of operation, the drive, mode and handling were first selected by the operator and then command was issued to move the respective drive. In computer guided mode, 13 micro steps were followed, where the operator issues command one by one in a sequential manner. HMI was also developed to simulate process computer functions to send configuration and soft inputs to the SSTM control system and a separate window gives full information about the SSTM status. A mimic was also developed in VB as shown in Figure 2, to show the movement of the SSTM during various operations in all the three storage bays. The system was thus validated successfully and cabinets were shifted to PFBR site.

Fig. 3 *SCADE environment*

II.16 Environmental and EMI/EMC Qualification of Instrumentation for Dashpot Oil level Sensors and Differential Pressure Sensors for PFBR

Indigenously developed dash pot oil level monitoring system (DOLMS) for real time monitoring of oil level in dashpot for CSRDM system of PFBR and differential pressure monitoring system (DPMS) for precise monitoring and control of differential pressure in PFBR have been subjected to Environmental tests using the facility available at EIRSG and EMI/EMC qualification tests in SAMEER, Chennai.

In case of dash pot oil level monitoring system, the trains of rectangular pulses at the outputs of the oil level and thermal sensors are processed by two independent signal processing and data presentation systems. Dash pot oil level monitoring system is a microcontroller based system which has a local 4x16 LCD to display the oil level and temperature along with alarm LEDs to indicate different alarms. The measured parameter is communicated to personnal computers via ethernet port for data logging and graphical presentation. Differential pressure monitoring system is designed to measure the pulse count from differential pressure sensor, converts it to differential pressure in mbar and displays it in 4 digit seven segment display. Differential pressure indicator unit is connected to differential pressure monitoring system via RS485 which mimics the display of differential pressure monitoring system to the user in control room. In PFBR, a total of nine numbers of dash pot oil level monitoring systems and fifteen numbers of differential pressure monitoring system will be deployed.

Before subjecting the dash pot oil level monitoring system to the above qualification tests, the following design considerations have been taken into account.

(i) dash pot oil level monitoring system is powered with dual 5V power supply which is EMI/EMC compatible

(ii) High performance EMI filter is placed at the power entry to reduce the conducted emission from the device and it also increases the immunity to conducted noises

(iii) The chassis of the system is properly earthed to reduce radiated noise and to increase the immunity to radiated susceptibility

(iv) All the PCBs are subjected to conformal coating in order to protect them during environmental tests.

Similarly, in the case of differential pressure monitoring system,

(i) Proper EMI/EMC compatible AC-DC power supply of appropriate rating is selected

(ii) High performance EMI filter is placed at the power entry to reduce the conducted emission from the device as well as increase the immunity to conducted noises

(iii) Additional protective components like TVS diodes are used to protect sensitive IC from transients

(iv) PCB design is carried out as per the EMI/EMC guidelines to reduce emissions

(v) The chassis of the system is properly earthed and proper care is taken in internal wiring to reduce radiated noise and to increase the immunity to radiated susceptibility.

The configuration for test in each case is setup exactly identical to the actual implementation of the system in PFBR as shown in Figures 1a and 1b. The inputs
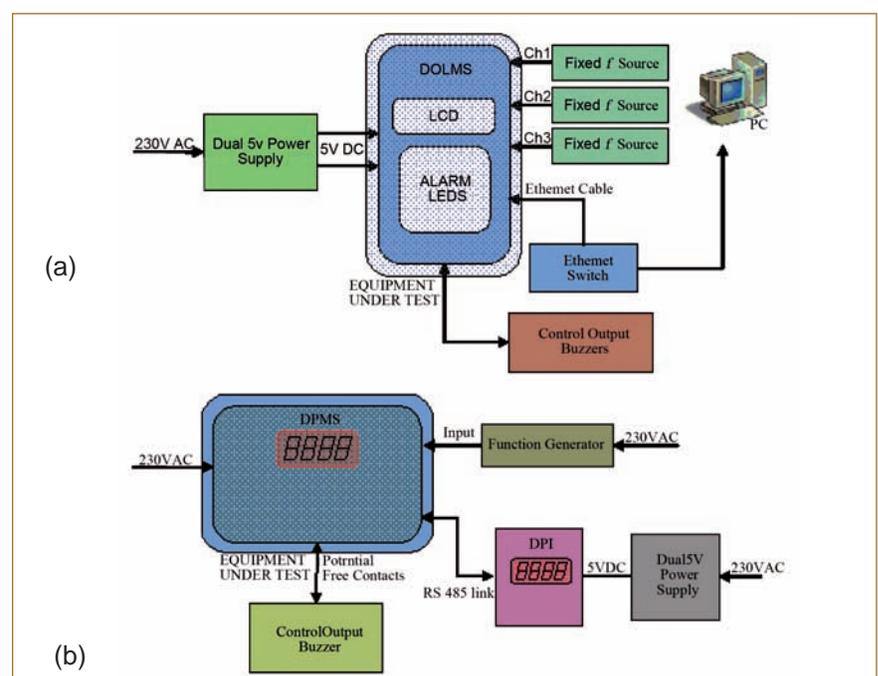

Fig. 1 *Block diagram of test setup (a) dash pot oil level monitoring system and (b) differential pressure monitoring system*

signals are simulated from constant frequency sources whose values are selected so that it falls within range of sensor output. The relay control actuation is indicated using buzzer which is connected to potential free contacts. For environmental qualification tests and EMI/EMC qualification tests of dash pot oil level monitoring system, the instrument was kept inside whereas the power supply unit was placed outside the test chamber. But, in case of differential pressure monitoring system, the instrument cabinet which accommodated power supply unit was placed in the test chamber. The power supply to the indicator unit was kept outside.

Both devices(dash pot oil level monitoring and differential pressure monitoring systems) were subjected to the following environmental tests as per IS 9000 standards (a) dry cold test, (b) dry heat test, (c) temperature cycle test and (d) damp heat test. They passed all the tests successfully. Figure 2 shows the photograph of environmental qualification test chamber.

All the EMI/EMC tests specified for AC input systems were carried out for differential pressure monitoring system while a few tests were conducted for dash pot oil level monitoring system since it is a DC input system. These tests were

Fig. 2 Photograph of environmental chamber

carried out in SAMEER (Figures 3a and 3b) to ensure that the devices perform their functions even in presence of electrical disturbances in the operating environment. The dash pot oil level monitoring system was subjected to following tests viz. radiated emission, conducted emission-single phase power line, radiated susceptibility and conducted radio frequency-single phase as per IEC-61000 standards. In case of radiated emission there was slight deviation from the specified limit of CISPR-11. All other tests passed successfully. In addition to the above tests the differential pressure monitoring system was also subjected to additional EMI/ EMC tests (as recommended in IEC-61000 standards). Those tests are electrostatic discharge, electrical fast transient - power line, surge - single phase, power frequency magnetic field, damped oscillatory (1MHz & 100kHz) - single phase, ring wave, pulse magnetic field, harmonic emission, voltage harmonics & inter-harmonics, variation of frequency in power supply systems. All test results were within the limit except minor deviation of result of radiated emission from the recommended limit of CISPR 11. From the performance tests as described above, both the indigenous devices qualified to be used in PFBR.
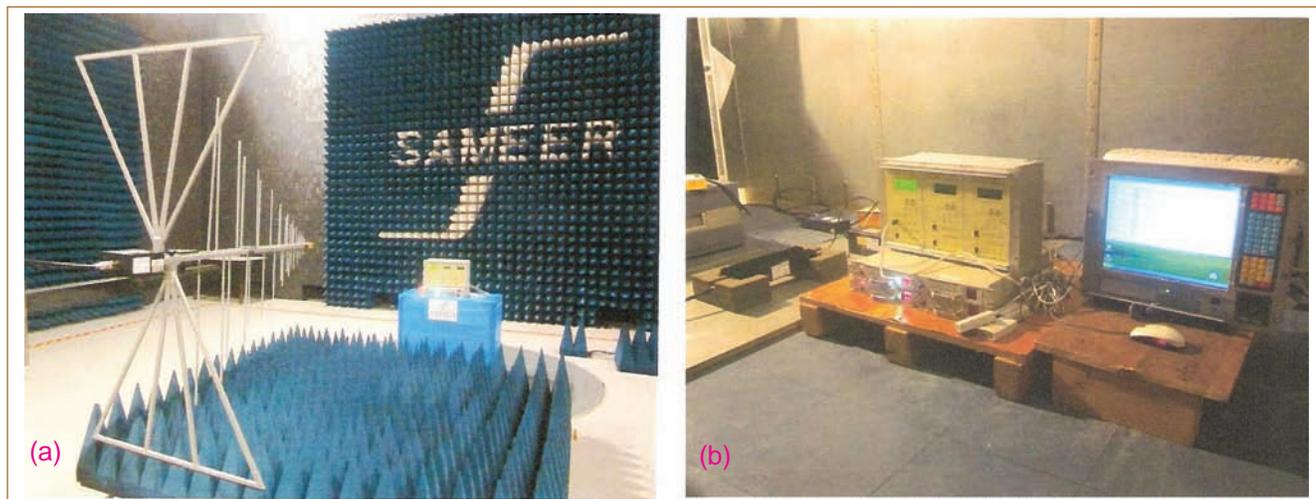

Fig. 3 EMI/EMC test setup (a) radiated susceptibility and (b) conducted radio frequency immunity

II.17 Modeling, Simulation, Testing and Commissioning of Fuel Handling Startup in KALBR-SIM at Training Centre, BHAVINI

A Full Scope Replica Operator Training Simulator named KALBR-SIM is being developed to provide an efficient platform for imparting training for nuclear power plant operators. The scope of PFBR operator training simulator includes the modeling and simulation of all fuel handling equipments and their operations. This consists of fuel handling start-up operation (FSU), transfer arm (TA), large rotatable plug (LRP) and small rotatable plug (SRP), inclined fuel transfer machine (IFTM), cell transfer machine (CTM), under water trolley (UWT), spent subassembly transfer machine (SSTM) etc.

The fuel handling startup system operation takes place when the reactor is in shutdown state. In order to ensure safe and smooth transition from reactor shutdown state (RSD) to reactor fuel handling state (RFH), sixteen fuel handling startup conditions are to be satisfied. These conditions give authorization to start fuel handling. The scope of simulation of fuel handling startup system of PFBR covers simulation and logic modeling of all sixteen main/sub conditions to start the fuel handling activities. PFBR operation states and fuel handling startup operations are shown in Figure 1.
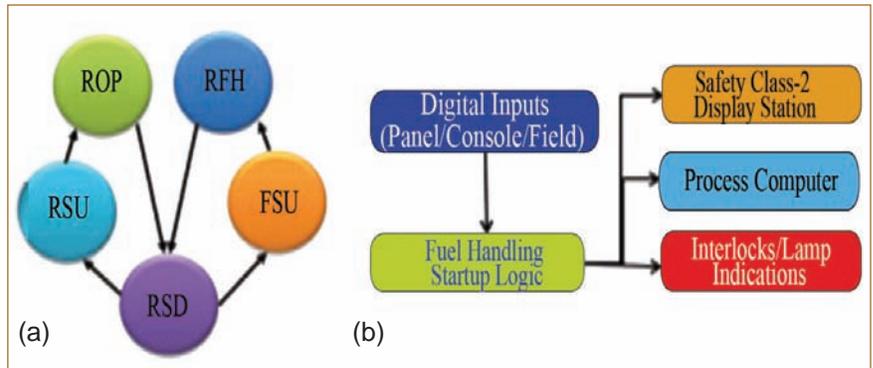

Fig. 1 *PFBR (a) operation states and (b) fuel handling startup operation*

Simulation and modeling of fuel handling startup was taken up and sixteen conditions were coded in simulator. Panel input/output related variables for control switches (gang and key), push buttons, light-emitting diode lamps were added in the signal table of the database. New variables were created in the external code fuel handling system for publishing. Data values were received from logic and other systems by subscribing. Graphical user interface related to startup screen was also modeled using Genlogic which was installed in simulator workstations at BHAVINI and coding in java for front end graphical user interface was done. It has one main screen in which all the sixteen conditions will be displayed either as satisfied, not satisfied or

inhibited by green, red and blue colors respectively (Figure 2). Details for the sub conditions can be accessed through the main menu options provided.

Universal datagram protocol socket based multithreaded framework based on client/server architecture for cross-platform data communication was written in full scope replica PFBR operator training simulator to communicate with front end of fuel handling startup graphical user interface. A WinSock application was written in JAVA in windows platform. A universal datagram protocol socket was created and binded with port address of simulator server which resided in UNIX platform. Send and receive functions were written at either end and successful communication was established and tested (Figure 3).
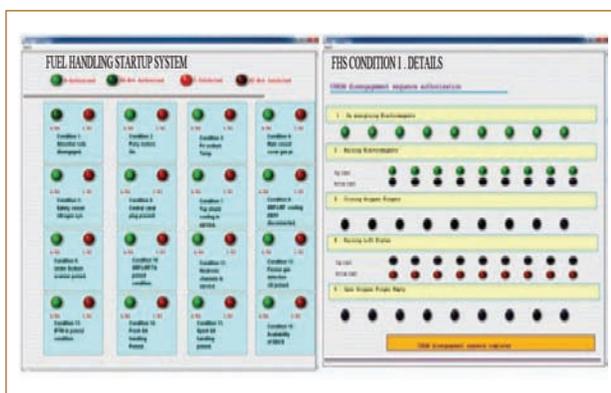

*Fig. 2* *Fuel handling startup front end GUI*
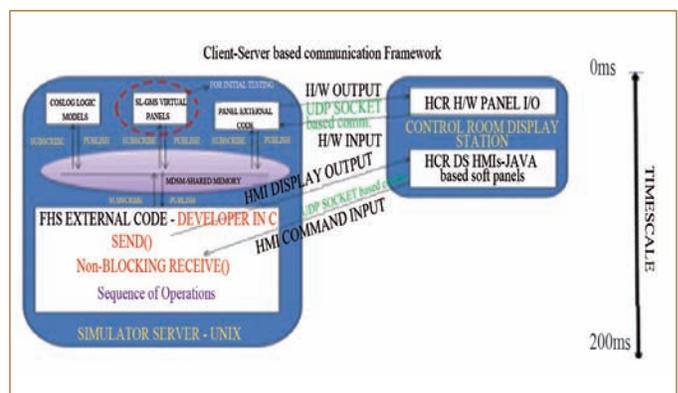
Fig. 3 *Fuel handling startup simulation inter process communication*

II.18   Correlation of NDE & Metallography to Detect FCCI in the Fuel Pins of PFBR MOX Test Subassembly

A 37 pin test sub-assembly with MOX fuel composition proposed to be used in PFBR was irradiated in FBTR at a peak linear heat rating of 450 W/cm to a maximum fuel burn-up of 112 GWd/t and a peak displacement damage of 56 dpa in the D9 structural material. Post irradiation examinations (PIE) results confirming satisfactory performance of the fuel and alloy D9 wrapper and clad material have been reported earlier. Seemingly unrelated observations from diverse techniques viz. neutron radiography (NR), eddy current testing (ECT) and gamma scanning (GS) of the fuel pins have been correlated to predict and establish the emergence of fuel-clad chemical interaction (FCCI) as the life-limiting condition for the fuel pin at higher burn-ups.

A differential encircling eddy current probe operating at 350 kHz was used to scan the fuel pin along its length. Signal processing techniques were employed to improve S/N by 20 dB. A series of localised indications were observed between 150 mm and 220 mm from the bottom of the fuel column. Phase angle analysis revealed that these indications originate from clad inner wall.

Axial distribution of ^{137}Cs was obtained during GS of selected fuel pins. ^{137}Cs being a volatile fission product, tends to migrate to relatively colder regions in the fuel pin, such as inter-fuel pellet gaps and cracks. Hence, peaks in the axial profile of ^{137}Cs correspond to regions that are conducive to fuel- clad chemical interaction and consequent clad wall thinning. Comparison of the axial profile of ^{137}Cs with eddy current signals obtained for the selected pin yielded
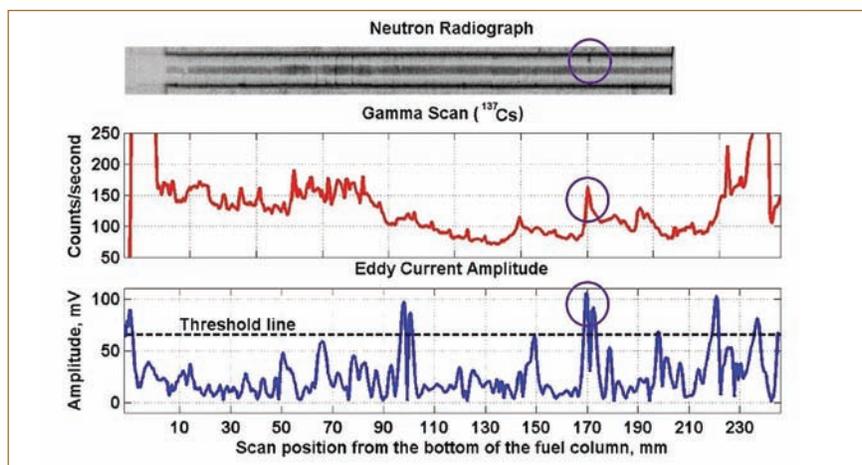
**Fig. 1** *ECT signal superimposed on axial ^{137}Cs profile and neutron radiograph*

locations on the clad inner wall where ^{137}Cs accumulation coincided with a clad inner wall anomalies indicated by ECT.

NR images of this fuel pin revealed inter-pellet gaps, pellet-clad gaps and the condition of pellets. On comparison with ECT and GS results, NR images revealed a crack with significant width at one of the locations of the anomalies observed in ECT and GS, confirming this location as a potential site for clad attack. For this pin, the signatures from the three NDE techniques have been superimposed and shown in Figure 1. The techniques ECT, GS and NR helped to predict the worst affected location in the fuel pin, thus minimizing the man-rem intensive efforts for carrying out metallography on multiple specimens to reveal the worst condition.

In order to confirm the combined inference from the three diverse NDE techniques, a metallographic section was carefully extracted from within 1 to 2 mm of this axial location. Sequential grinding and polishing of the specimen was done in the hot-cell. Utmost care was taken to arrive at the exact

location of the defect indication during specimen preparation. Clad wall thinning was indeed observed at two circumferential locations at this cross section. The maximum clad wall thickness reduction seen is 80 μm (Figure 2), which agrees well with modelling predictions.

Synergistic correlation among diverse NDE techniques indicated the emergence of FCCI as the precursor that determines the limit of burn-up of the fuel pin. This was confirmed through destructive metallographic examination, demonstrating how various PIE techniques have been employed judiciously to reveal FCCI as the life limiting condition of the PFBR MOX fuel.
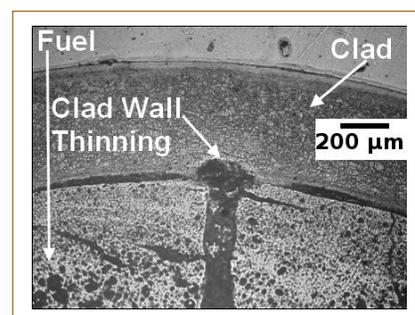

Fig. 2 *Fuel pin cross-section at location marked in Figure 1*
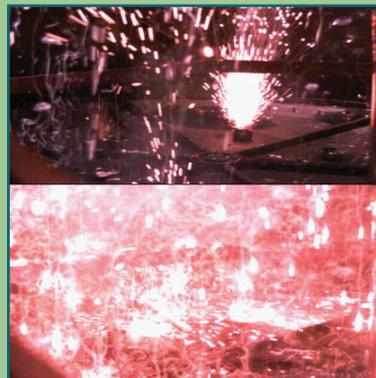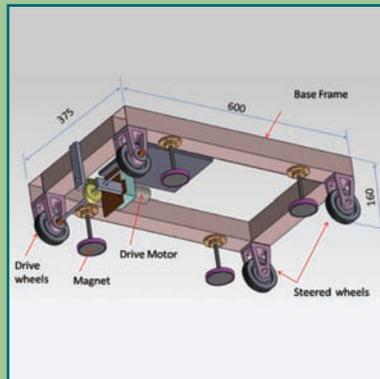
CHAPTER 3

Research & Development for FBRs

III.1　Status on Design of FBR 1 & 2

With the objective of achieving improved economy and enhanced safety towards commercial exploitation, the design of PFBR has been reviewed critically and updated for the future fast reactors including FBR 1&2 (Figure 1).

Reactor assembly

Construction experience of PFBR indicates that manufacturing and erection of reactor assembly, particularly long delivery components control the overall schedule of the project. The manufacturing and integration of roof slab, which is a large dimensioned box type structure, was very challenging in view of technological problems such as lamellar tearing along with heavy mass. So, the configuration has been modified to dome shaped structure for FBR 1 & 2 (Figure 2). Secondly, machining and assembly of the large diameter grid plate with about 14,000 individual items including 1758 sleeves and complex technology for hard facing of large diameter tracks with colmonoy deposit, involved huge time and cost. This too has been modified with welded concept (Figure 3) having reduced diameter plenum, number of sleeves and parts together with elimination of large diameter hard face tracks.

Towards achieving enhanced safety, many features are added for FBR 1&2. Doubly curved torus concept for the inner vessel is adopted to enhance the seismic buckling strength and increased number of primary pipes (from two per pump to four per pump) to achieve higher margins to core design safety limits.

Towards confirming the above design concepts for FBR 1&2, failure modes in the reactor assembly components have been

identified (Table 1) and the following detailed analyses and validation studies have been carried out.

- Structural analysis of individual components (Figure 4) to ensure compliance to codal and functional requirements
- Confirmation of pool hydraulics (Figure 5)
- Optimisation of main vessel cooling flow
- Hydraulic flow distribution studies within grid plate
- Seismic analysis of reactor assembly (Figures 6 and 7)
- Primary pipe flow analysis and core temperature analysis under one pipe rupture event
- Thermal management of top shield and reactor vault.

The results of the above detailed analyses have confirmed the
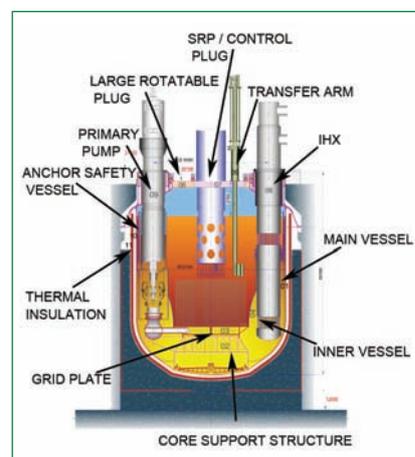
Fig. 1 *Vertical section of reactor assembly*

following.

- Inner vessel with single torus improves the hot pool mixing and gross temperature gradients in the pool
- Main vessel cooling flow rate of 200 kg/s obtained which is ½ of

| Table 1: Failure modes in reactor assembly		
Parameters	**Component**	**Failure modes**
High temperature & temperature gradients and cold shock in hot pool	Main vessel top, control plug & intermediate heat exchanger, inner vessel	Low cycle fatigue and creep damage, thermal buckling
Hot shock in cold pool	Main vessel, grid plate, core support structure & primary pipe	Creep damage
Temperature fluctuations due to thermal stratification	Core cover plate in control plug & inner vessel redan	High cycle fatigue and its effect on low cycle fatigue
Gas entrainments in free surfaces	Reactor core	Reactivity insertion
Seismic induced displacements	Core and control rods	Reactivity oscillations
Seismic induced forces and moments	Main vessel, thermal baffle and inner vessel	Buckling

**Fig. 2** *Box type roof slab in carbon steel to dome shaped roof slab in SS 304L*

Fig. 3 *Bolted grid plate with two primary pipe per header to welded grid plate with four primary pipe per header*
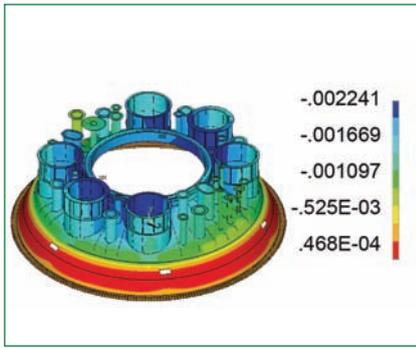
Fig. 4 *Vertical displacement plot of roof slab (normal conditions)*
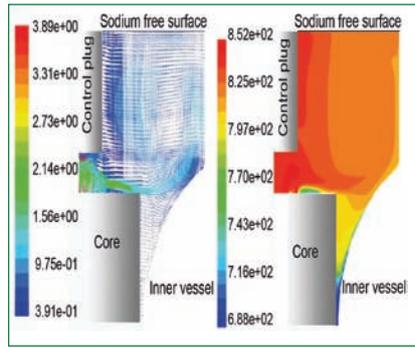
Fig. 5 *Velocity field (m/s) and temperature contours (K) in the hot pool*
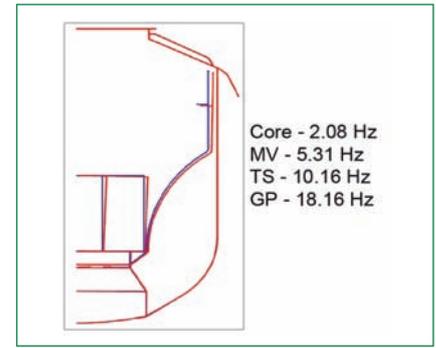
Fig. 6 *Seismic analysis of reactor assembly*

the value apportioned in PFBR

- With four primary pipes per pump, the minimum core flow ensured during one pipe rupture event is 55% which is nearly double the flow ensured in PFBR
- Temperature limits at critical locations are within the permissible limits
- Seismic analysis indicates availability of adequate margins (10-20%).

Further, to demonstrate manufacturability, transportation and handling of permanent components of reactor assembly complying with the nuclear quality and standards, it is proposed to carry out technology development for manufacture of the individual permanent components of reactor assembly of FBR-1 and subsequently integrate them either at the site or at the industry, and transport it through barge. The completed assembly will be ready for erection into the reactor pit.

Towards the technology

development, specifications for materials (23 numbers), quality assurance (16 numbers), and manufacture and integration of individual components (10 numbers) of reactor assembly along with manufacturing drawings (65 numbers) were prepared based on the manufacturing and erection experiences of PFBR components.

Sodium circuits and piping

FBR1&2 being a twin unit plant, the layout is made in such a way to accommodate both steam generator buildings (SGB) in same side of each RCB, unlike the case of PFBR. Hence, the secondary sodium piping layout is modified according to the building layout without losing the symmetricity between the two loops. The schematic arrangement of the proposed layout is shown in Figure 8.

PFBR, being a first commercial scale fast breeder reactor, SS316LN grade of austenitic steel was selected for both hot and cold

leg piping in order to eliminate the possibility of mix-up of materials. However, experience gained in PFBR has offered great confidence in overcoming the difficulty in future through design provisions and systematic care during construction. With this in background and also from cost competitiveness different materials for hot and cold leg are explored for FBR1&2.

Hot leg of piping, for which the operating temperature lies in creep regime, SS316LN is retained as in PFBR and for the cold leg where the operating temperature lies in non-creep regime, SS304LN is the candidate material for piping and fittings and hence the same is proposed for FBR1&2.

In-vessel purification (primary sodium)

In the ex-vessel concept as provided in PFBR, design features (double envelope/inerted steel cabin) are provided to take care of radioactive sodium leaks and siphoning of
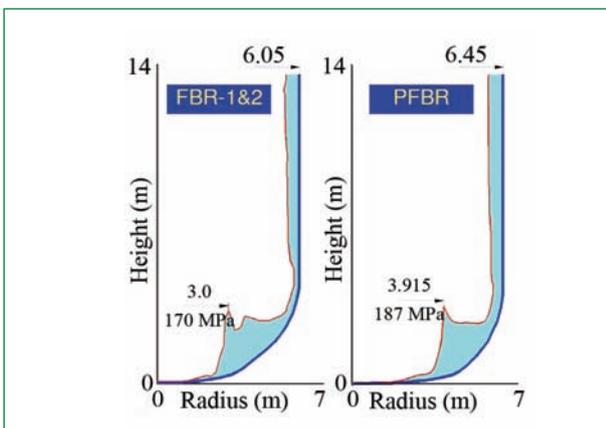
Fig. 7 *Stress distribution in main vessel under seismic events*
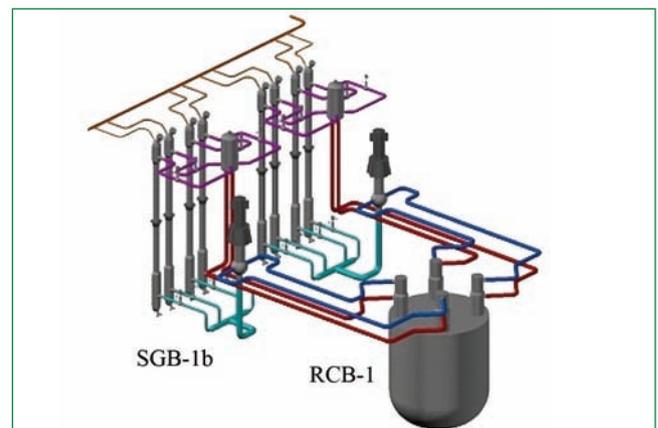
Fig. 8 *Secondary sodium piping for FBR1&2*

radioactive sodium from the reactor pool (in case of leak in purification system which goes undetected). In the in-vessel concept (Figure 9) no radioactive primary sodium is transported out of the reactor pool, therefore the possibility of radioactive sodium leak in reactor containment building is precluded and the siphoning of sodium from reactor vessel is eliminated. Hence, for FBR-1&2, the in-vessel concept is selected for primary sodium permanent purification circuit in order to enhance the safety and bring down the total cost.

The in-vessel concept (Figure 10) uses an integrated cold trap (ICT) with economizer, electromagnetic pump and flow meter, housed inside a single vessel. This assembly is located in the reactor pool and supported from the roof slab of the reactor. The electromagnetic pump takes sodium from the reactor pool and passes through the economizer and cold trap wire mesh. After purification the sodium returns to the pool through the economizer.

In the in-vessel concept, the external piping and associated cells are eliminated, which also offers reduction in RCB size. Operation of similar in-vessel concept is already proven in French fast reactor, Superphenix.

The integrated cold trap is made in two parts viz., fixed part, which comprises electromagnetic pump, economizer, cold trap cooling arrangement, instrumentation and removable part, which contains the wire mesh. The replaceable wire mesh is designed for estimated impurity ingress for two years of reactor operation. A 1:1 scale model of integrated cold trap was manufactured and being tested for its performance in sodium loop.

Decay heat removal systems

Decay heat generated in the core needs to be removed to keep the

Fig. 9 *In-vessel purification*

Fig. 10 *Assembly of integrated cold trap*
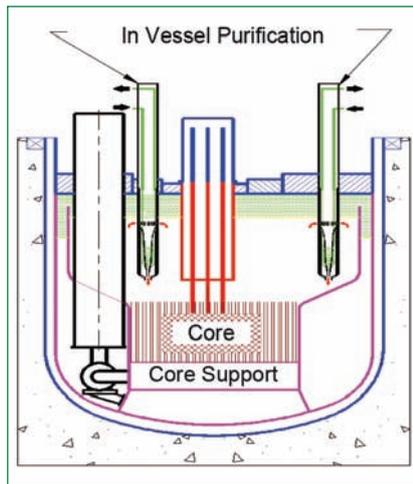
temperature within the acceptable limits, to avoid the consequences like core structural material melting, radioactivity release etc. The high reliability of decay heat removal (DHR) function with a targeted failure frequency of 10^{-7}/year is achieved through two independent diverse DHR systems in PFBR namely safety grade decay heat removal system (SGDHRS) and operation grade decay heat removal system (OGDHRS). SGDHRS removes decay heat directly from the hot pool of the reactor, while OGDHR is incorporated in steam/water system that is part of the normal heat removal path in the reactor. Decay heat removal through SGDHRS is by natural circulation and the only active component in the systems is the dampers located near to sodium to air heat exchanger. There is also in-built diversity in design
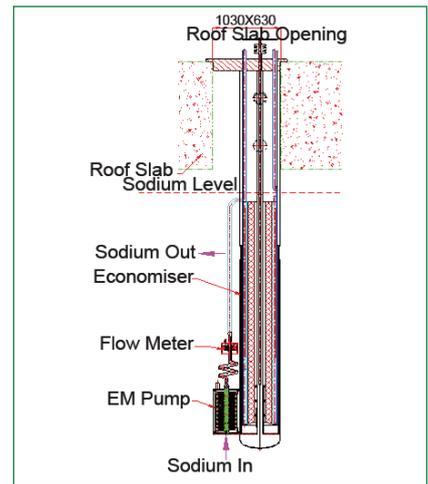
of SGDHR systems, two loops of type-A and two loops of type-B of 8 MWt capacity each.

For FBR1&2, in order to enhance the diversity and increase the reliability of DHR function, the number of SGDHR loops is increased from four to six with adequate diversity (Figure 11). One set of three DHR loops, under forced circulation cooling (6 MWt each, forced ultimate decay heat removal system - FUDHER) with two-thirds capacity under natural convection and other set of 3 DHR loops under natural circulation cooling (6 MWt each, natural ultimate decay heat removal system - NUDHER) are incorporated. This configuration provides adequate reliability as envisaged apart from facilitating the complete removal of need for separate OGDHR system as in PFBR.
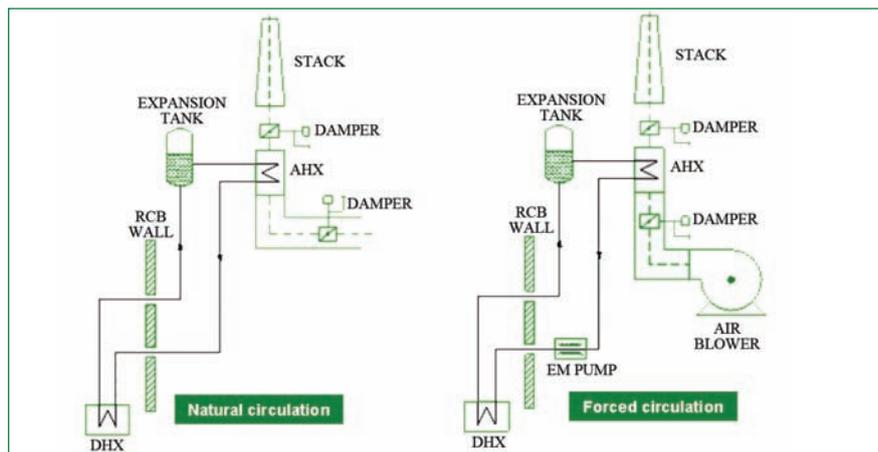
Fig. 11 *Schematic of SGDHR system for FBR 1&2*

III.2 Experimental Simulation of Sodium-cooled Fast Reactor Core Flowering due to Local Forces

PHENIX 250 MWe, French prototype sodium-cooled reactor, experienced four extremely fast and highly oscillating reactivity transients. An occurrence of such a transient triggered an automatic trip when the reactivity transient threshold was reached forcing an emergency shutdown of the reactor. In each case, the recordings from neutron chambers located beneath the vessel showed a similar signal in the form of a double oscillation as shown in Figure 1. These negative reactivity incidents in Phenix have created high impact on the Fast Breeder Reactor (FBR) programme worldwide. The reason for the above occurrence was investigated. Among various reasons, the core subassembly displacements, caused by sodium vapour explosion at a few locations where moderating materials were introduced, are considered as potential source. It

leads to the flowering and compaction of the fuel core subassemblies.

Core-flowering is a type of core-movement and it means that one subassembly expands and induces stresses on the surrounding subassemblies, causing the core to expand in radial direction. The result from core extension is displacement of the subassemblies in the core leading to an increase of the gap between the units. Small extension of the core leads to considerable decrease in the reactivity. These subassemblies are free standing and are simply supported at the bottom grid plate. The typical FBR core subassemblies are shown in Figure 2.

To assess the pressure effects, CEA – France and IGCAR were jointly working for numerical and experimental simulations by exchanging test data and computer codes. IGCAR has built a dedicated
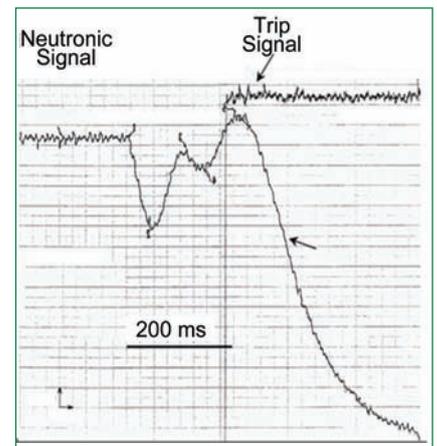
Fig. 1 *Neutronic signal variation during negative reactivity transient*

facility to induce core displacements under simulated pressure. The facility consists of a five storey building having a height of about 20 metres. The schematic of the facility is shown in Figure 3. This building houses the 1:1 model of sodium cooled fast reactor core on which the core flowering/compaction experiments will be performed. It consists of a cluster of ~130 full

Fig. 2 *Sodium-cooled fast reactor core with subassemblies and grid plate*
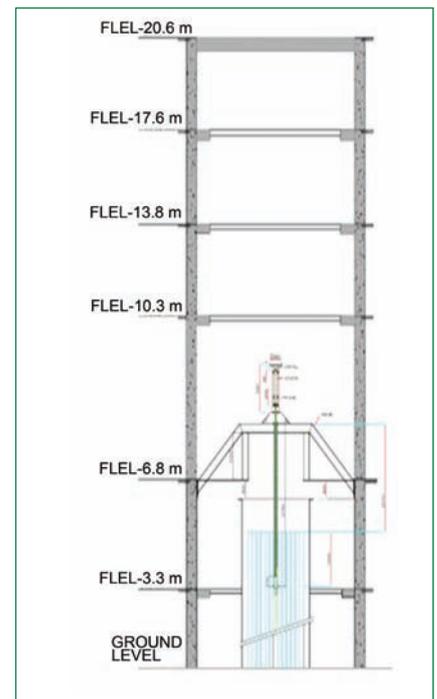
Fig. 3 *Schematic of the SFR core mechanics & dynamics studies facility*

47
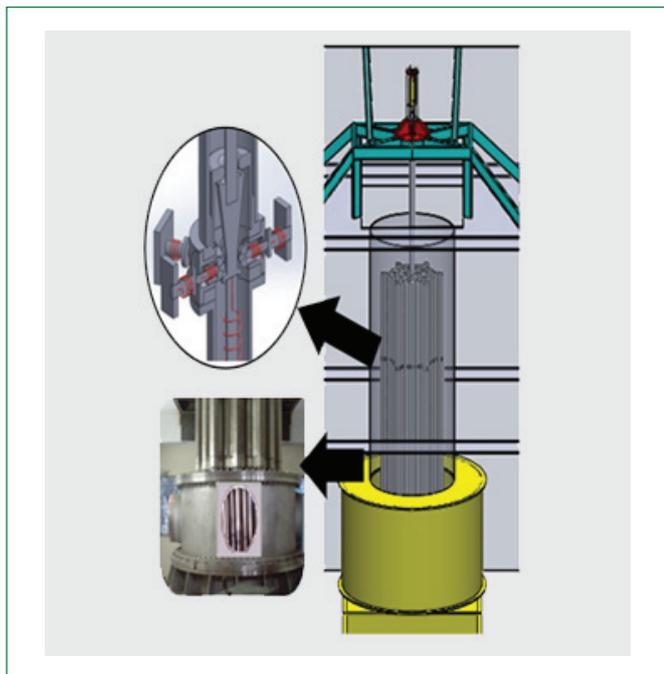
Fig. 4 *Core flowering experimental facility & its salient features*

Fig. 5 *Mock-up test carried out TBRL, Chandigarh using low density explosive*

scale subassembly meeting Phenix dimensions mounted on a grid plate as shown in Figure 2. The grid plate is of 4 m diameter plenum with all prototype features including sleeves with hard facing and dimension tolerance. This has been developed under technology development exercise. It has a loading frame with a novel system.

Towards simulating the core flowering, tests will be performed on a 1:1 model of reactor vessel by designing, manufacturing and introducing a device at the center of the core to generate mechanical core flowering. During the tests, the displacements, movements and the forces will be recorded. Load cells, LVDTs and high speed cameras will be used to measure the different parameters.

A novel mechanical device introduced at the buttons location (1440 mm from the top of the subassembly) of the core sub assemblies simulate the uniform core flowering/compaction in all the six sides of the typical subassembly. The flowering device consists of six spring back plungers which are mounted radially along a circular pipe. These plungers are pushed outwards by the downward movement of a cone as shown in Figure 4. When the cone is moved upwards, the plungers are retracted back with the help of spring. The base of the loading mechanism is welded to a 4 inch pipe which is fixed. The cone on the other hand is welded to 2 inch pipe which can be moved axially and is floating inside the 4 inch pipe. The core flowering experimental facility along with its salient features are presented in Figure 4. Hydraulic actuator along with load cell is provided for core displacement.

Neutron irradiation causes void swelling in the fuel subassemblies. Fuel subassemblies are subjected to temperature and neutron flux field along the radial and axial direction. It leads to bowing of the subassembly.

Using the same facility, experiments are planned to study swelling and bowing effects of subassembly/cluster. Using the simulated swelling and bowing subassembly it is possible to determine the fuel handling loads. Pullout force is a concern in the design of the pantograph type in-vessel handling machine.

It is also planned to carry out the transient tests on core displacements (subjected due to transient pressure developed) using low density explosive (LDE) at TBRL, Chandigarh. Mock-up tests using low density explosive has been carried out at TBRL using the seven subassembly facilities (Figure 5).

The commissioning activities of the 100 T capacity 6m x 6m size high capacity multi axis shake table are in progress at IGCAR. It can be used to capture realistically, the dynamic behaviour of the FBR core under seismic excitation using the present full scale fuel subassemblies along with the grid plate of 4 m diameter plenum with all prototype features including sleeves with hard facing and dimension tolerance (Figure 6).
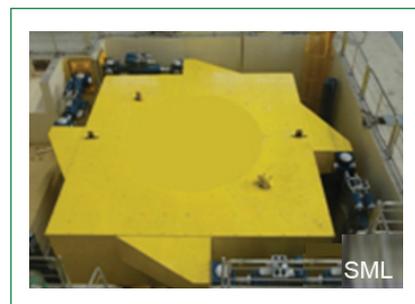
Fig. 6 *100 T shake table*

III.3 Studies for the Design of Magnetic-Coupled Robotic Device for In-service Inspection of Main Vessel of FBR I and II - Simulation & Experiments

The primary containment structure in the Fast Breeder Reactor (FBR) consists of the main reactor vessel (MV), the safety vessel (SV), and the reactor roof structure. One of the important in-service inspection (ISI) requirements for the fast reactors is monitoring the external boundary of the main reactor vessel welds for structural integrity assessment.

The inter-space between main vessel and safety vessel of the PFBR assembly is currently about 300 mm. FBR I and II would have a reduced inter-space of about 200 mm. This reduced gap requires deployment of improved techniques for carrying out in-service inspection of main vessel. In order to approach the narrow inter-space, it would be prudent to use one of the surfaces only, which is a major deviation from the current method in the in-service inspection device which clamps on to both the main vessel and safety vessel. In such a case, vacuum cups or magnets could be used on one of the surfaces.

The use of ferritic steel for the safety vessel is expected to be a major change for FBR I and II. As a natural extension, in this context, studies were initiated to take up design of an in-service inspection device for the reduced gap using magnetic principle. It was realized that both magnetic contact and magnetic field coupling with the ferritic steel safety vessel could be used to create a novel design to traverse the innards of the vessel surface. In contact-based methods, limited contact area necessitates strong magnets, though they provide easy steering. Hence, a design was required for coupling of the magnetic field with an air gap between the magnets and
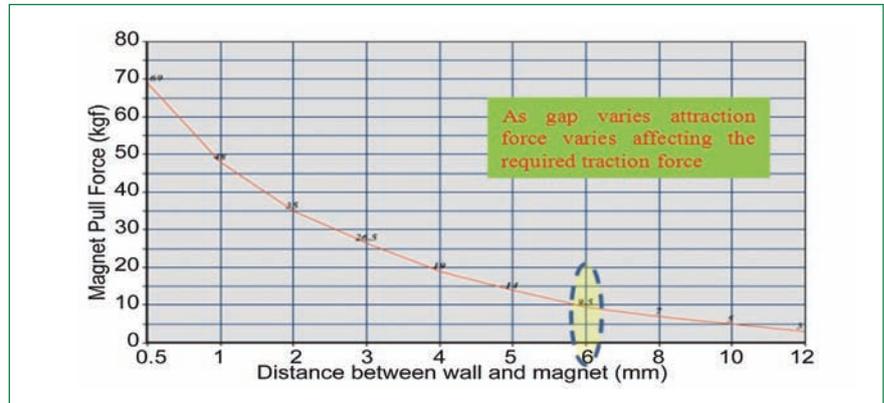

Fig. 1 *Experimental results of the investigation of magnetic pull force*

the vessel surface.

Permanent magnets have been chosen predominantly due to their high pull force to weight ratio. They also provide a constant pull force without the necessity of any external automation/control. Neodymium Iron Boron (NdFeB) magnets can be used up to operating temperatures of 160°C and have a high energy product compared to Samarium Cobalt (SmCo). A proof-of-concept, a four-wheeled vehicle design was evolved with an estimated weight of 6.5 kg. With this design in view, disc-shaped NdFeB magnets (Ø 63 mm × 10 mm) were selected, with a maximum pull force of 690 N exerted by each magnet at an air gap of 0.5 mm. Testing of the magnetic gripping module was conducted to study the magnitude of pull force required to detach by varying the air gap between the magnetic gripping module and contact surface (Figure 1).

In order to validate the concept, a four wheeled vehicle was fabricated with common rear-wheel traction. Common steering of the front wheels, though provided, was arrested within the ambit of the preliminary tests. The length and breadth of the vehicle was 300 mm

and 235 mm respectively. The height of the vehicle was 150 mm. The total weight of the vehicle, mounted with the magnets was about 6.5 kg. The magnets were mounted, within the foot-print of the vehicle, in a rectangular layout, close to the wheels. A uniform gap of 6 mm was ensured to provide the pull force of 9.5 kg by each magnet to suspend the vehicle in place. Provision has been given in the magnetic module to adjust the air gap between the magnet and the contact surface of the wall.

Experiments of the vehicle conducted

Fig. 2 *Proof-of-concept vehicle for preliminary studies*

**Fig. 3** *Vehicle with alternative wheel layout*
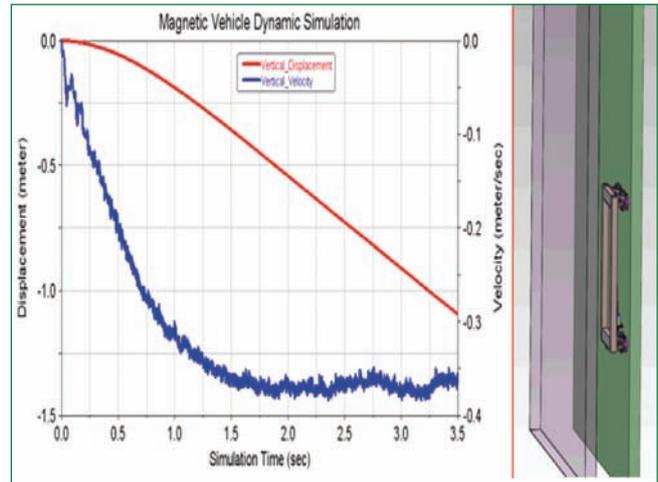
Fig. 4 *Simulation studies in multi-body dynamics tool to assess the dynamic behaviour*

in the mock-up vertical wall revealed that the vehicle could cling to the vertical wall and climb up the wall (Figure 2). The safety vessel has a cylindrical vessel with torispherical dish end. Manoeuverability of the vehicle in the torispherical region largely depends upon the layout of the wheels and hence, an alternate configuration was chosen for the wheel layout wherein the wheels are laid out in diamond shape with the leader and follower wheels along the longitudinal axis and two powered middle wheels (Figure 3).

The design was refined to change the drive layout and provide steering. The length of the modified vehicle is 600 mm and the width and height are 375 mm and 160 mm respectively. Traction is provided through a worm and worm wheel drive to the rear-wheel shaft.

Simulations were conducted on multi-body dynamics (MBD) tool to derive the drive torque over the entire vessel surface and study the dynamic characteristics of the vehicle. In these studies, each magnet was provided with an attraction force of 110 N at an air-gap of 5.5 mm. The static and dynamic coefficients of friction used were 0.3 and 0.2 respectively.

Through these simulations, it was seen that a torque of 1.3 N.m was required at each traction wheel, for a total mass of 6.5 kg of the vehicle, for the case of the vehicle climbing up vertically, against gravity on the mild steel wall (Figure 4).

The experimental and theoretical simulation data on the model of the vehicle (Figure 5) was utilized to build a scaled-down prototype assembly. Initial tests were carried out with the prototype vehicle on the vertical wall. It could be seen that the vehicle (Figure 6) proved to be stable and traction was adequate for climbing the chosen vertical wall, without any instability.
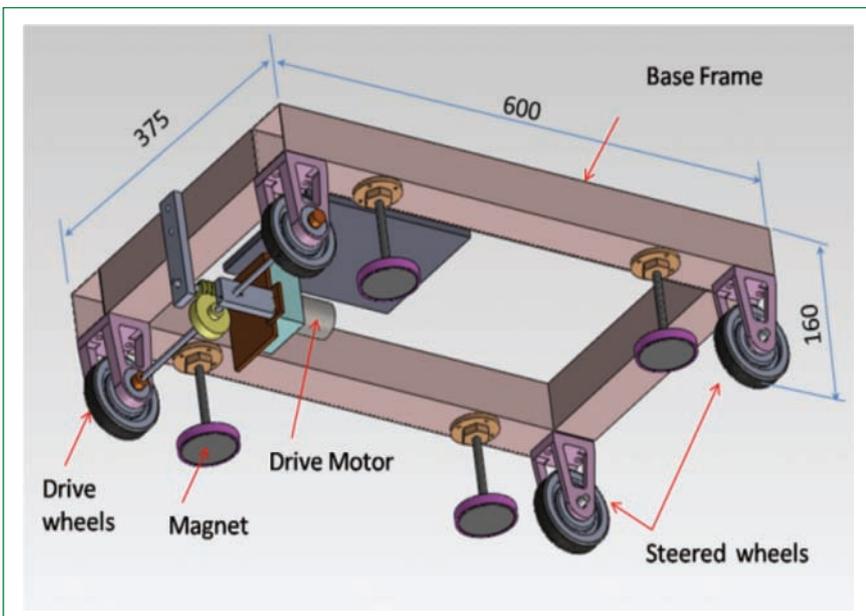

Fig. 5 *CAD model of the scaled-down prototype vehicle based on magnetic coupling*


Fig. 6 *Scaled-down prototype magnetic- coupled vehicle*

III.4   Electrochemical Hydrogen Meters for PFBR

Ten numbers of electrochemical hydrogen meters (ECHMs) are ready for installation in PFBR for steam leak detection. The schematic diagram of the electrochemical hydrogen meter is shown in Figure 1. These sensors were fabricated, assembled, calibrated and tested. Currently, the long term performance of the meters and the reproducibility are being monitored. The associated electronic units for the sensor were designed in-house and fabricated by ECIL (Figure 2). These instruments were qualified by subjecting them for the prescribed EMI/EMC tests and the environmental tests. The performance of twelve meters is being monitored simultaneously in HEXAMINI-I and HEXAMINI-II bench top sodium loops each having a sodium inventory of approximately 10 kg (Figure 3) and provisions to test six meters simultaneously.

In these loops hydrogen concentrations could be precisely controlled using the mini cold trap section of the loop. The outputs of the sensors are continuously monitored at the operating temperature of 450 °C and various tests simulating plant conditions are also continued. The testing involves (i) calibration of electrochemical hydrogen meters along with the electronics module, (ii) simulation of plant conditions such as large decrease
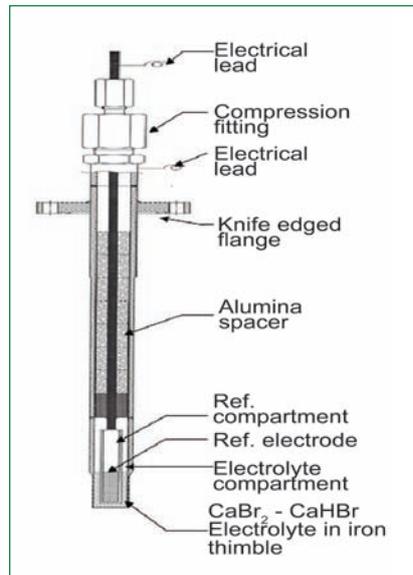
Fig. 1   Schematics of the electrochemical hydrogen meter

Fig. 2   Electronics units (a) pre-amplifier in stainless steel housing and (b) signal processing cum display unit

in sodium temperature, line heater failure, etc, and (iii) response of electrochemical hydrogen meters for meter temperature variations. The temperature coefficient of the sensors is generally ~2 (± 0.4) ppb/°C. The meters show a time lag of ~16 hours for the signal recovery during the tests simulating plant conditions such as large decrease in sodium temperature which is the time needed for the equilibration of reference electrode materials during such incidents in the plant. Typical calibration graph of a meter is shown in Figure 4.

As part of IGCAR-CEA joint research

project on fast reactor safety, one electrochemical hydrogen meter along with its electronics modules was installed in SUPERFENNEC sodium loop in Cadarache, France (Figure 5) to compare its performance along with diffusion based sensors. Sodium was filled in the loop and the temperature was raised to 450 °C. The proper working of the electrochemical hydrogen meters and its instrumentation was ascertained. Comparison of the performance of electrochemical hydrogen meters along with that of diffusion based sensors will be carried out in early next year.
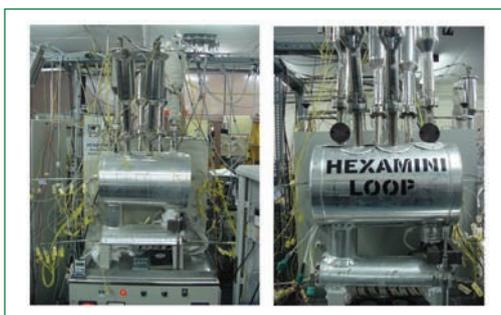
Fig. 3   Testing of electrochemical hydrogen meters in HEXAMINI sodium loops
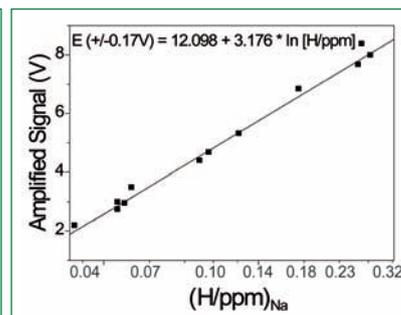
Fig. 4   Typical calibration graph of an electrochemical hydrogen meter

$$E (+/-0.17V) = 12.098 + 3.176 * \ln [H/ppm]$$
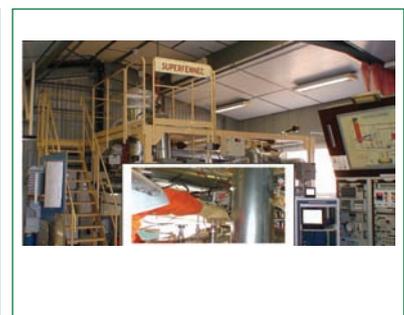
Fig. 5   SUPERFENNEC sodium loop in Cadarache, France. Inset shows the installation of electrochemical hydrogen meter

III.5 Development of Non-contact Position Sensor for CSRDM

Position of control and safety rods (CSR) needs to be monitored continuously in order to facilitate reactor power control, calibration of CSR, identify reactor anomalies, to prevent local flux peaking and to analyse stuck rod conditions. Total length of travel of CSR is 1085 mm. Continuous position monitoring of CSR of control and safety rod drive mechanism (CSRDM) in Prototype Fast Breeder Reactor (PFBR) is achieved by a draw wire type potentiometer. However, snapping of the draw wire results in falling of its associated components in the upper part and affects the availability of the mechanism. Hence, it was recommended to develop a robust non-contact type position indicator for CSRDM. Three possible alternatives were identified, namely – variable reluctance type position sensor, proximity switch based system and laser method. Variable reluctance type position sensor and proximity switch based system are in-house concepts tailor made to suit the geometrical constraints of CSRDM. Laser sensor is a generic sensor readily available in market. Performance study of these methods and their suitability for CSRDM were studied through experiments carried out in air.

Variable reluctance type position sensor

It consists of two coils wound around the mobile assembly in the region below dash pot as shown in Figure 1. Length of both the coils should be at least 1085 mm. Primary coil is excited by an alternating current source, thereby inducing e.m.f in the secondary coil. Mobile assembly
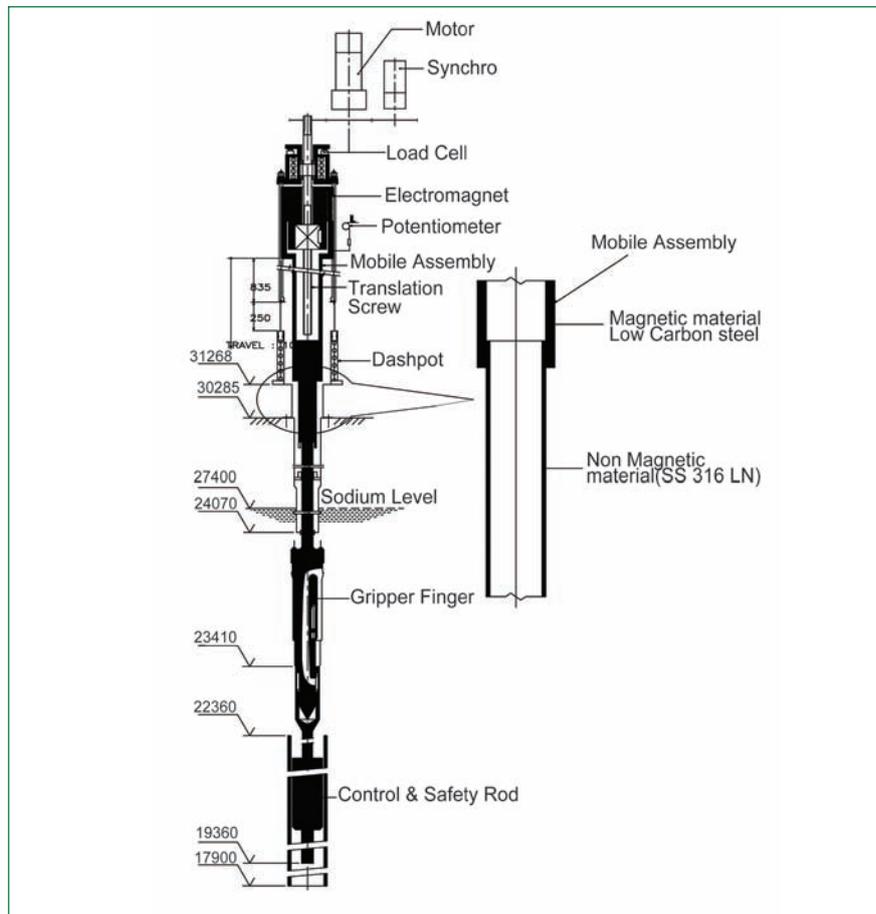
Fig. 1 Schematic of CSRDM

of CSR whose position needs to be monitored acts as the core moving in and out of the coils. The mobile assembly is made up of two hollow cylinders - a non-magnetic cylinder (SS 316 LN) axially fitted to a magnetic cylinder (low carbon steel) as shown in Figure 1. Hence movement of core into the sensor results in decrease in reluctance of the magnetic flux path, which in turn is reflected as an increase in induced e.m.f of the secondary coil. Thus, with movement of mobile assembly into the sensor, secondary output increases. The major constraint in implementing this method for CSRDM is the low space availability in the region below dashpot (available length is around 600 mm only). Hence, space in the region below the

dash pot has to be increased by elongating the length of the magnetic portion of mobile assembly to 1085 mm. Further studies are being carried out to improve the sensor design such that, the sensor can be implemented in CSRDM without much modification.

Proximity switch based system

This system comprises a large number of proximity switches fixed on the longitudinal axis parallel to the axis of movement. A minimum gap of 5 mm between each switch shall be maintained to achieve the system specified resolution. A CAM is attached to the mobile assembly of CSRDM. On sensing the presence of CAM, digital output of the proximity switch

changes to high state from low state. As the CAM moves along with the translation of mobile assembly, each switch is actuated one at a time depending on the elevation of mobile assembly. Multiple outputs obtained from all the switches need to be combined to provide position information in an easy to understand form. Hence, all the switches are connected to a resistor-diode network that generates a single analog output proportional to the position of CSR.

Laser sensor

Measurement principles used by laser sensors include – time of flight and triangulation. Among them, laser triangulation principle is found to be more suitable for CSRDM, as it can measure the position of fast moving targets with high accuracy and resolution.

Experiments were carried out on commercially available laser sensor and scaled down models of variable reluctance type position sensor and proximity switch based system. It was done to characterise the performance of each system as well as to generate operating experience.

A scaled down model of variable reluctance type position sensor with reduced length of 500 mm was manufactured and tested in air. A carbon steel rod was used to simulate the magnetic portion of mobile assembly. Primary and secondary coils were wound using enamelled copper wire (23 SWG). Primary coil was excited with a constant current source (0.1 A) with an excitation frequency of 300 Hz. The core was moved into/out of the sensor and its secondary output at various positions was noted. Experiment was done at varying frequencies in the range of 300 - 5000 Hz. Typical output characteristics of the sensor is
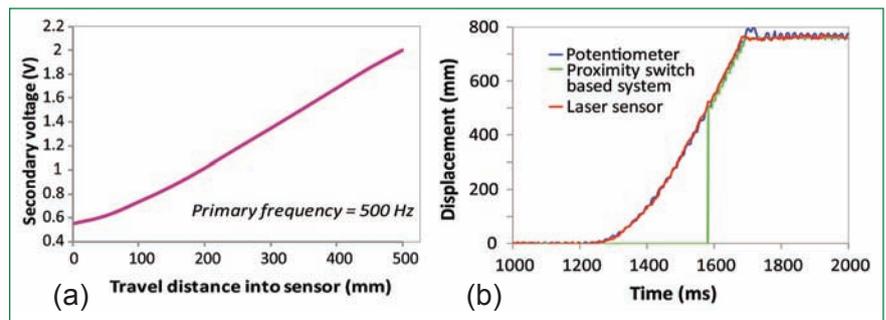
Fig. 2 *Output characteristics of (a) the scaled down model of variable reluctance type position sensor and (b) proximity switch based system and laser triangulation sensor during SCRAM action*

shown in Figure 2a. The curve is found to be fairly linear with slight non-linearity at the ends.

Testing of scaled down model of proximity switch based system with ten proximity switches and laser triangulation sensor were carried out in a dedicated test setup (Figure 3). This setup was designed to simulate both translation and SCRAM action. Total travel simulated by this setup is 750 mm. Proximity switches were arranged in such a way that it can monitor the final 250 mm of travel only. A draw wire type potentiometer was used as reference sensor. Typical output characteristics of the proximity switch based system and laser triangulation sensor obtained during SCRAM action along with potentiometer are presented in Figure 2b. Performance of proximity switch based system is found to be satisfactory with its output resolution depending on the gap between each switch. Performance of the laser sensor is found to be excellent with high level of accuracy.

The experiments carried out have demonstrated that all the three systems perform satisfactorily. However, each system has its own advantages and limitations. Variable reluctance type position sensor is very simple but the length of the CSRDM needs to be increased for its implementation. Further studies shall be carried

out to improve the sensor design such that it can be implemented in CSRDM without much modification. Proximity switch based system can be adopted for CSRDM of PFBR without any mechanical modifications to CSRDM. However, large numbers of switches are needed for achieving necessary resolution (220 switches for a resolution of 5 mm). Laser triangulation sensor is found to be meeting the design requirements. However, fixing it at the present potentiometer location in motor plate of CSRDM needs modifications which may preclude its usage in PFBR. Hence, it is recommended to continue with full scale testing and development of proximity switch based system.

Fig. 3 *Dedicated test setup that simulates CSR translation and SCRAM*

III.6   Qualification of Leak Collection System

In the secondary heat transfer circuits of FBRs, leakage of liquid sodium from the pipelines is postulated as one of the design basis accidents. The leaked sodium can undergo combustion in spray, pool or combined form, generating dense white smoke and flame leading to rise in the ambient gas temperature as well as causing a potential hazard for the plant and operating personal. To mitigate the thermal and chemical consequences of sodium fire, leak collection trays (LCTs) are designed and installed under sodium pipelines as passive fire protection system.

These leak collection trays are strategically arranged under the secondary sodium piping to collect leaking sodium into a holdup vessel and subsequently to sodium dump tank connected through a low melting fusible plug. The sodium fire will be extinguished due to oxygen starvation. To qualify the design of leak collection system for effective drainage of sodium into the dump tank without much spillage, a mock up facility was designed, fabricated and erected. The functionality and performance evaluation of this system have been studied using water as

Fig. 1 *Leak collection system- mockup experimental facility*

stimulant at various pressure and flow conditions. The water leak rate through 1 cm^2 opening and spillage characteristics as a function of water pressure was studied.

The mock-up facility consists of water source tank, leak collection tray, argon system, drain pipelines and dump tank (Figure 1). A mild steel water tank with 169 litres capacity was provided with 1" drain line. A solenoid valve with 1 cm^2 opening simulating the design basis leak is connected to the drain line of water tank. Leak collection tray was placed below the drain line at a distance of 300 mm from outlet of the solenoid valve (Figure 2). The solenoid valve simulates the pressure drop in

Fig. 2 *Solenoid valve with 1 cm^2 opening*

sodium pipeline due to surrounding insulating material. A drain pipe of 4" dia and 12 m length connecting the leak collection tray and dump tank (100 liter capacity) was provided. Before the dump tank, a valve, simulating the fusible plug along with two vent ports was installed. Two argon buffer tanks with total capacity of 800 liters designed for 5 bar pressure were fabricated and integrated to the water source tank. Pressure gauges were provided to monitor the pressure in argon and water source tanks.

Experiments were conducted by filling 130 litres of water in the source tank. The tank was pressurized by using argon gas filled in argon buffer tanks. Solenoid valve was opened
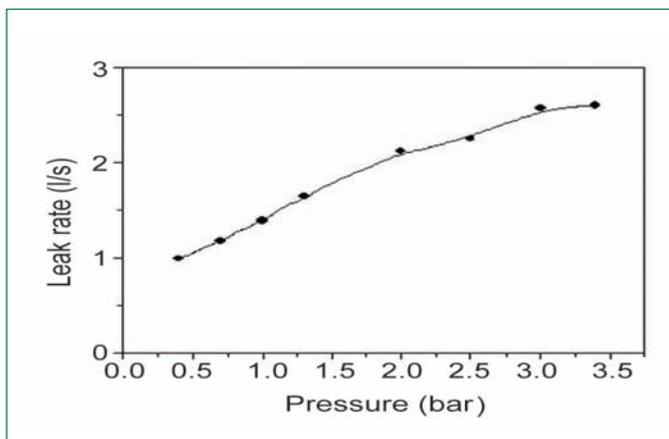

*Fig. 3 Leak rate of water as a function of water pressure*
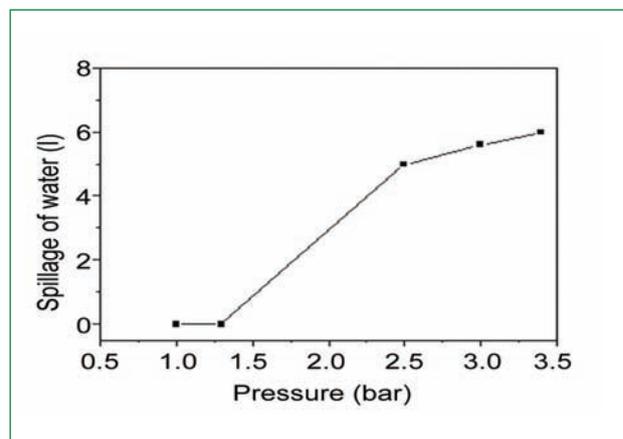
Fig. 4 Spillage of water as a function of water pressure

for exactly 40 sec and then closed. The amount of water collected in the dump tank and that was left out in the source tank were measured to estimate the water leak through 1 cm^2 opening and spillage from leak collection tray. Experiments were repeated at various pressures and corresponding leak rates (Figure 3) and spillage characteristics (Figure 4) were estimated. It was observed that the leak rate is pressure dependent and the maximum spillage of water at 4 bar pressure was measured to be about 6%.

It was also observed that the vent lines are very much required for proper drain of water through the pipelines and there was no air lock between leak collection tray and the valve. The estimated time required for melting of fusible plug is about 11 seconds. Experimental results show that the time taken for water to reach the valve (representing the fusible plug) from leak collection tray at pressure between 0.5 and 4 bar was about 29 seconds. The total holdup volume of the pipeline as well as the leak collection tray is about 356 litres. From the leak rate at each pressure, the minimum time required for overflow of water in leak collection tray was calculated (Table 1). The experimental result confirms that incase of sodium leakage from pipelines, will not lead to overflow of sodium from leak collection trays due to delay in melting of fusible plug.

Table 1: Time required to cause overflow of water in LCT as a function of water pressure

Pressure (bar)	Leak rate (l/s)	Time (s)
4.0	2.72	131
3.4	2.6	137
3.0	2.57	138
2.5	2.25	158
2.0	2.12	168
1.3	1.65	216
1.0	1.39	256
0.7	1.18	302

III.7 Feedback Experiences of Transfer Arm Testing towards Design Improvements

Transfer arm is one of the critical fuel handling machines of PFBR used for the in-vessel transfer of fresh/spent subassemblies within the core and to the in-vessel transfer position located on the periphery of the core. The machine is supported on the Small Rotatable Plug permanently and is kept parked 4 m above the core during reactor operation. Thus, it is exposed to a sodium temperature of 550 °C during reactor operation and 200 °C during fuel handling.

Transfer arm was manufactured by M/s. Larsen & Toubro, Hazira. Full scale integral testing was not carried out at the manufacturer's shop due to head room limitations. This proved costly since several modifications were required after on-site assembly at IGCAR. These include (i) provision of floating nut for guide tube hoisting mechanism, (ii) reduction in number of guides between inner and outer gripper tubes and (iii) change in actuator rod profile to enable smooth gripper finger opening/closing. Functional testing for 20 cycles was demonstrated by M/s. Larsen & Toubro. Subsequently, transfer arm was tested cyclically in air. Deep scoring marks were observed on the outer surface of gripper tube after 75 cycles. The O-ring seals between shielding sleeve and gripper outer tube got cut and the outer tube got jammed. The material combination was changed from SS-Chrome plating to colmonoy coated SS-Chrome plating at the guide locations of outer tube. The O-ring seals were changed to V-ring seals. Separate mock-up studies were conducted to validate the above design changes before implementation in the actual machine. With these changes, air testing of transfer arm for 100 cycles was successfully completed.

During air testing, it was observed that the motor brake was sluggish due to soaking of the brakes with oil leakage from the gear box, since the motor and brake were located below the main gear box. This had led to inefficient holding of gripper tube with movement of the tube downward. Also, the main gear box was very bulky. It was decided to change over to a single failure proof hoisting system with two redundant brakes. Also the gear box was replaced with

compact self locking worm gear box. Additionally, separate locking provision was made to the gripper tube to positively lock it prior to rotation of transfer arm. Also, all instrumentation were provided with an additional diverse means of indication. After incorporating these changes, transfer arm was re-assembled in a separate test vessel-5 for testing in sodium.

Sixty cycles were successfully completed at a sodium temperature of 200 °C. The transfer arm was kept in parking position and sodium temperature was raised to 400 °C and maintained for ~ 1 week before it was lowered back to 200 °C. Testing was resumed at 200 °C and gripper finger operation seized in the 62nd cycle. In-situ corrections could not release the stuck-up condition and hence transfer arm was sodium cleaned. Seizure was observed between connecting rod (connected to inner tube) and offset link (connected to outer tube). The clearance at guide locations between connecting rod and offset link was increased and the material combination was also changed from A453Gr660-SS to A453Gr660-colmonoy coated stainless steel. Similarly, slightly higher clearance was also provided between the gripper finger pin and finger bush.

The gripper assembly was tested for its functioning in a separate test setup at Structural Mechanics Laboratory (Figure 1). Tests were done at both at room temperature and at 200 °C in air. Slight scoring marks were observed in the connecting rod and actuator rod of gripper assembly. These were polished and the gripper assembly was assembled with transfer arm. The actuator rod used was of SS 410 material with hardness of 180 BHN (temporary rod made for validating gripper assembly modifications during initial testing). Hence, the actuator

rod was replaced with original A 453 Gr 660 rod of hardness 35 HRC. Slight vibrational movement of the actuator rod was observed especially during finger closing. The colmonoy coated guides for connecting rod were removed and a central guide was provided for the connecting link joining the connecting rod and the gripper actuator rod. A commercially available linear slide was used initially as the guide. With this, smooth movement of the fingers was established.

A special linear guide suitable for sodium service was designed and manufactured (Figure 2). The mating surfaces of the guides were hard chrome plated. With provision of the above guide, both connecting rod and actuator rods were made relatively free, with the guide serving to keep the connecting link nearly horizontal. Testing for 300 cycles was carried out in sodium at 200 °C. This was followed by a high temperature dwell period at 500-550 °C for ~ 1 week. Testing was resumed again at 200 °C and the performance of the machine has smooth. Tests are continuing for the remaining 300 cycles in sodium.

Considering the prototype nature

Fig. 1 *Gripper test setup at SML*

of the transfer arm and the absence of shop testing, extensive modifications were called for at site during various stages of testing to achieve the desired performance of the machine. The feedback obtained during testing has given valuable information on evolving a robust design of similar offset arm type machines for future FBRs.
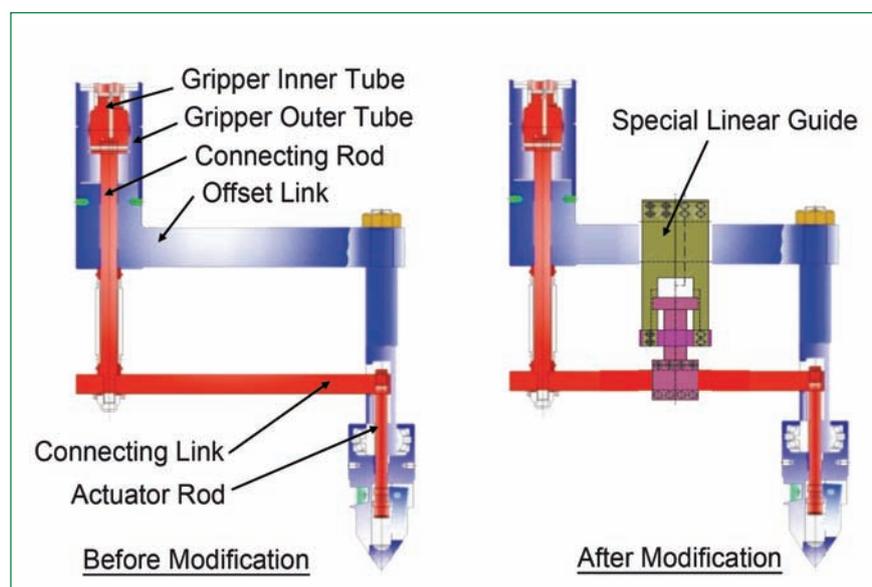

Fig. 2 *Details of special guide for gripper assembly*

III.8 Integrity of SGDHR Pipeline against Sodium Fire on Top Shield Platform Consequent to Core Disruptive Accident

During normal operating conditions, sodium leaks in primary sodium system is ruled out since all the pipelines are double walled and annular space is filled with nitrogen. But under the core disruptive accident (CDA), sodium can be ejected from reactor assembly into top shield platform (TSP) through component gap openings and can catch fire. The increase in temperature and pressure due to this fire forms the design basis loading for the containment building. However there is a concern of safety/ integrity of SGDHR pipeline during this event. Theoretical analysis of the scenario is complex due to the coupled heat and mass transfer and also chemical reactions associated with it. Hence mock-up test has been conducted at SOCA facility in SED to understand the phenomena and to develop suitable numerical model for the same.

DHR Pipeline Module consists of a cylindrical stainless steel container (0.1 m dia. and 0.1 m ht.) filled with sodium and enveloped with another cylindrical SS container (0.15 m dia. and 0.15 m ht.). The annular space is filled with nitrogen gas. Heaters were provided to maintain sodium temperature at 823 K. Three such modules have been fabricated and placed at various elevations inside SOCA experimental chamber. The schematic and photograph of a DHR module are shown in Figures 1a and 1b.

SOCA experimental facility consists of three major modules i.e., experimental chamber, sodium loop and exhaust gas treatment system. The cylindrical experimental chamber (3 m dia. and 3 m ht.) is
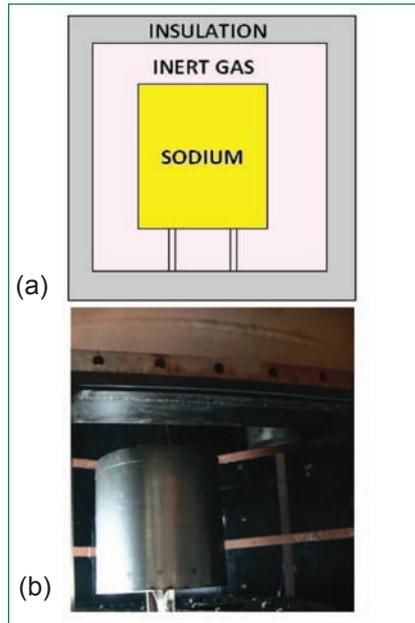
Fig. 1 DHR module (a) schematic and (b) photograph

designed for 10 bar pressure and 773 K temperature.

The sodium tank is kept inside the cylindrical shell with ring header to create the horizontal and vertical sodium jets.

The sodium release system of SOCA facility is designed to simulate the sodium ejection from the annular gaps of small and large rotating plugs during core disruptive accident. It consists of

Fig. 2 (a) SOCA chamber and (b) ring header

sodium vessel, ring header and argon system for pressurization. The jets of sodium are created by means of a ring header which contains equally distributed nozzles of 1.5 mm diameter along the circumference. The photograph of SOCA experimental chamber and the ring header are shown in Figure 2a and 2b. The dimensional details of SOCA experimental chamber are given in Table 1.

Table 1: The dimensional details of SOCA experimental chamber	
Component	Dimension
Chamber diameter	3 m
Chamber thickness	30 mm
Diameter of top and bottom head closures	3.3 m
Thickness of top and bottom head closures	100 mm
Height of the chamber	3 m
Total inner surface area of the chamber	42.4 m^2
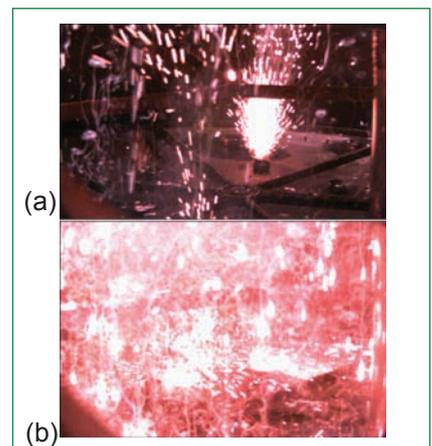
Fig. 3 Sodium spray fire scenario
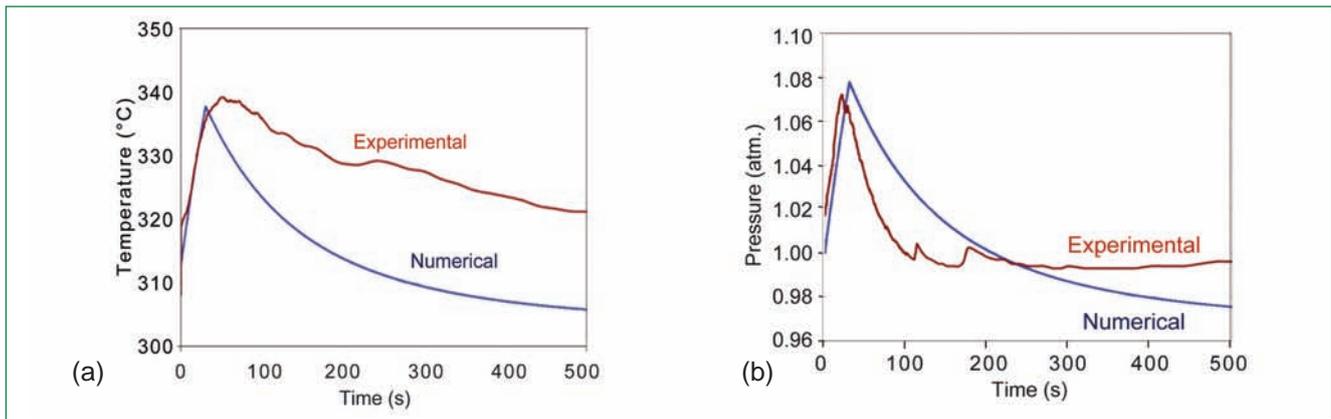
Fig. 4 *Gas (a) temperature and (b) pressure rise in SOCA chamber*

The sodium tank in SOCA facility was loaded with 5 kg of sodium and heated upto 723 K under argon atmosphere. The sodium inside the DHR modules was heated and maintained at 823 K. The sodium jet fire experiment was initiated by opening the bellow seal valve to release sodium through the nozzles of the ring header. The sodium spray was ejected for 30 seconds and continued to burn for 60 seconds. It was evident from the optical image and temperature data recorded during the sodium spray fire that the spray from the nozzles hit the bottom of the DHR module placed at 1 m above the ring header. It was also observed that sodium spray fire phenomenon (Figures 3a and 3b) was highly random and aggressive. Temperature mapping along the radial and axial directions was analysed. Rise in gas temperature in the chamber was observed to be upto 358 K and the peak pressure was 1.07 bar during the spray fire.

The experimental data of gas temperature and pressure were compared with theoretical data and are shown in Figures 4a and 4b. For 1 kg of sodium spray combustion at 773 K, the rise in gas temperature and pressure were estimated with NAFCON code as 69 K and 0.08 bar respectively NAFCON prediction of maximum temperature and pressure of gas in the chamber coincides with the experimental observation.

Based on this analysis, the increase in surface temperature of DHX pipeline module placed in the SOCA chamber was estimated using one dimensional conduction heat transfer model for composite hollow cylinder.

The estimated and measured increase in surface temperature of DHX pipeline modules are shown in Figure 5. Both experimental results and numerical prediction show that the increase in surface temperature of the DHX pipeline module under sodium spray fire is insignificant (9 K) compared to the sodium temperature inside

the module. It is also observed that there is no impact of sodium fire to the sodium kept inside the pipeline. The structural and thermal integrity of DHR module is not affected by the sodium fire.

All three DHR modules were examined after the experimental run. The DHR module after the run is shown in Figure 6. Though sodium aerosol deposition was found over the surface of the module, there was no penetration of sodium or sodium aerosol inside the module and no interaction between sodium and insulation occurred. There was no corrosion or etching observed at the surface of the DHR module. There was no leakage of sodium from the inner pipe.

It is evident that the structural and thermal integrity of DHR module is not affected by external sodium fire and there is no possibility of guard pipe rupture and release of sodium to cause secondary fire.
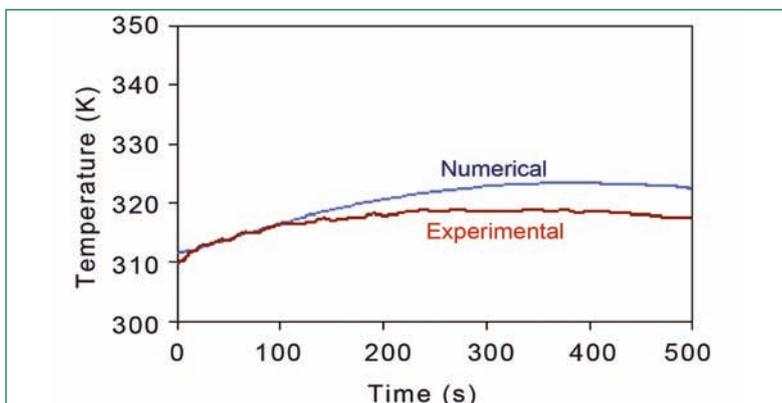

Fig. 5 *Temperature rise in surface of DHX pipeline*

Fig. 6 *DHR module after the experimental run*

III.9 Development of Sodium Pressure Measurement Device

A compact sodium pressure measurement device (SPMD) was developed to directly measure the static sodium pressure at high operating temperature. Measurement of static pressure of liquid sodium is very difficult with the conventional pressure sensors in sodium systems. This is mainly due to very high operating temperatures of the liquid sodium for fast breeder reactor (FBR) systems and requirement of high level of leak tightness due to the reactive nature of sodium with atmospheric air and moisture. The measurement of cover gas pressure wherever possible by conventional sensors gives broad idea about the sodium pressure inside the sodium loop. But many experiments in sodium and developmental activities in the field of sodium technology demand the static pressure measurement of flowing sodium. Presently, to meet the experimental requirements, the sodium pressure is being measured by a two way approach in which the sodium pressure is transmitted to the argon cover gas inside a pressure pot and this pressure is measured using conventional pressure sensors. This method involves continuous monitoring of the sodium level in the pressure pots and any errors in this method will lead to sodium leakage to the atmosphere.

The specification of sodium pressure measurement device is as follows:

Max .operating temperature: 500 °C
Max. operating pressure : 12 bar
Measurement range : 0 to 6 bar
Accuracy : ± 0.05 bar
Leak tightness : 10^{-8} Pam^3/s on helium leak testing

Leak detector : Spark plug type

Material of construction: SS316 L

Input power : DC power supply

Output : mV

Sodium pressure measurement device consists of disk, stem, sensor, bellows, bellows holder, leak detector and cover pipes. The force acting on a 30 mm diameter disk due to sodium pressure inside the pipe is transmitted to the force/strain measuring element through a 10 mm diameter stem. A two ply bellow prevents the entry of sodium to the sensor without interfering the transmission of force. To ensure this, the stiffness of the bellows will be kept to a minimum of thousand times less than that of the force transmitting mechanism. A spark plug type sodium leak detector is provided to detect any sodium entry to the sensor chamber due to the bellows failure. To ensure the centre stem axis position and to limit the expansion of the bellows during evacuation of system, a guide arrangement is provided in the stem. With respect to the variation of sodium pressure, the deflection in the bellows is negligible and this ensures good life of the bellows in service.

The total assembly will be inserted to a suitable pipe tee and sealed by welding. While introducing the device in the piping system, the pipe tee of the device can be welded with piping system as usual. There is enough gas space between sodium and the load cell and also surface area to transfer the heat to the atmosphere to maintain the temperature at sensor below the allowable limit (≈110°C). A schematic showing the conceptual design of the sodium pressure measurement device is shown in Figure 1.
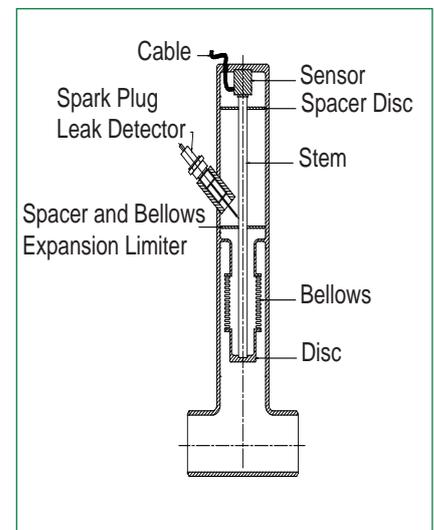
Fig. 1 *Schematic of sodium pressure measurement system*

Before introducing the device in the sodium system, the device was qualified for the sodium service at envisaged operating conditions and calibrated.

For qualification of the device, the operating conditions were simulated and tested. The device was tested with air at room temperature for the pressure range of 0 to 6 bar, water with a velocity of 4 m/s at room temperature for the pressure range of 0 to 4 bar, hot argon at 300 °C for the pressure range of 0 to 6 bar and sodium at various flow rates and operating temperature.

The sodium pressure measurement device was tested for 6 bar range
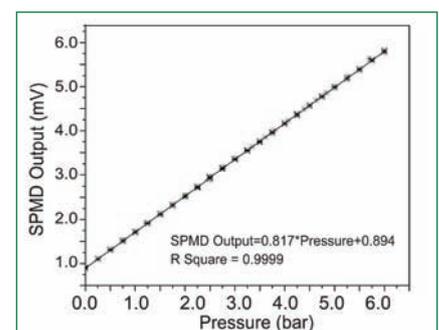
Fig. 2 *Response of sodium pressure measurement device to air pressure at room temperature*

with static air at room temperature. The testing shows that the device is with good linearity and precision. The response of the device to the pressure is shown in Figure 2.

The testing of the device in a water loop at various flow rates and pressures was conducted and the performance was evaluated. The testing confirmed that the measurement is not affected with flow rate of the flowing medium. In addition to this, the device was tested in hot argon prior to testing in sodium. The test was conducted for the pressure range of 6 bar. The linearity of the sodium pressure measurement device was maintained during the hot argon test also. There was an offset of 0.25 bar in the measurement of the sodium pressure measurement device during the hot argon test. The constant offset in the measurements is due to the differential thermal expansion among the bellows, the stem and the cover pipes which can be estimated and compensated accurately. The performance of the sodium pressure measurement device in hot argon is shown in the Figure 3.
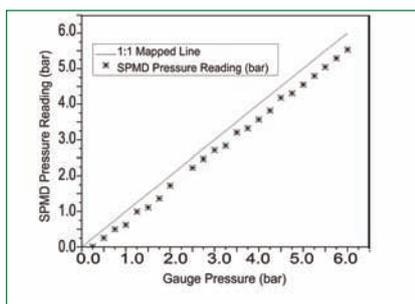
Fig. 3 *Comparison of sodium pressure measurement device output with pressure gauge reading in hot argon test*

Fig. 4 *Response of sodium pressure measurement device for sodium pressure at 350°C*

Further, the sodium pressure measurement device was tested in a sodium loop to qualify and ensure the functionality of the device in high temperature flowing sodium. The static sodium test was conducted for various temperatures in the range of 200 to 350 °C for a pressure range of 3 bar. The responses of the sodium pressure measurement device with respect to the sodium pressure at 350 °C is shown in the Figure 4.

From the hot static sodium test, the relation between sodium static pressure and sensor output of sodium pressure measurement device was established. The

device shows good linearity. The performance of the sodium pressure measurement device with respect to the sodium temperature was not affected.

The device was tested continuously for 500 hours with a sodium flow rate of 3.8 m^3/h at 300 °C. Cumulatively the device was tested for 1000 hours for various sodium flow rates and temperatures. The device was operated 10 times for thermal cycling in the temperature range of 200 to 350°C with minimum hold time of 2 hours at 350 °C. The thermal cycling did not affect the performance of the device.

III.10 Liquid Lithium Based Ultimate Shutdown System in FBRs: Reactor Physics Assessment of Concept

In the present design of FBR in India, two independent, fast acting, diverse shutdown systems (CSR and DSR) are implemented. The failure probability of the above system is ~10^{-6} /reactor-year. To increase the reliability further, addressing the beyond design base events and limit the consequences within category 4, a new concept of inherent safety called "ultimate shutdown system (USS)" has been proposed and is being investigated. This system takes care of the unprotected transient over

power (UTOP) due to uncontrolled withdrawal of absorber rods, unprotected loss of flow (ULOFA) and also ensures reactor SCRAM during seismic conditions. A liquid poison injection (LPI) system has been chosen as the potential option for ultimate shutdown system. It is to be noted that an innovative passive shutdown system called lithium injection module (LIM) is also under development in Japan and China.

Absorber material selection

The various physical and nuclear

properties like (1) liquid between 200 °C and 600 °C (2) good absorber in fast energy region (3) low radiation after irradiation (4) compatibility with sodium and steel (5) impurities (6) economic feasibility etc. have been considered for selection of absorber material. Various elements and their compounds were considered as absorber materials for the ultimate shutdown system. Lithium is chosen as the suitable candidate absorber material for ultimate shutdown system as it remains liquid between

180-1343 °C. Since lithium and sodium belong to the same chemical group, they do not interact and hence are very compatible. Even though enriched B_4C, natural B_4C and europium oxide are better neutron absorbing materials, they are not considered as they are not liquids in the operating temperature range. On comparing the PFBR flux averaged one group macroscopic absorption cross section, it is found that even with 90 % enrichment in Li-6, its absorption cross section is only 23 % of that of 65 % enriched B_4C.

Engineering design

The liquid poison injection system consists of storage tank containing liquid lithium, argon chamber which is located in the active core region and fuse plug. The fuse plug serves as an alternate passive means of actuation to perform the same function based on rise in sodium temperature. To avoid direct mixing of the liquid poison with sodium, the whole system is designed to be leak tight. The active height of liquid column in USS is 100 cm. In this study, inner diameter of lithium tube is chosen as 11.56 cm and the clad thickness is 0.2 cm. During normal operation, it is filled with argon gas.
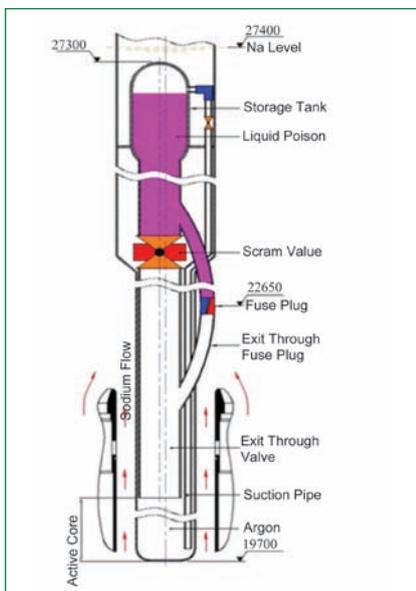
Fig. 1 Schematic of ultimate shutdown system
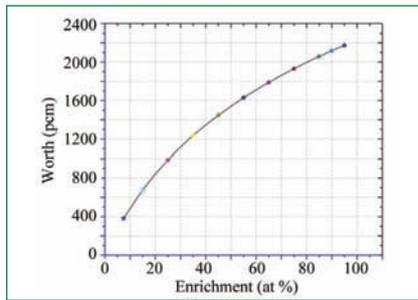
Fig. 3 Total worth of 3 ultimate shutdown system subassembly with Li-6 enrichment

The PFBR equilibrium core is chosen for the USS feasibility study. 3-D diffusion theory based IGCAR Code System (FARCOB) with Russian adjusted multigroup cross-section library ABBN-93 has been used for estimating the absorber rod worth.

The number of absorber rods, Li-6 enrichment, and their locations in the core, have to be assessed by taking into account the space availability in control plug, and requirement of extra fuel to compensate the reactivity loss due to ultimate shutdown system.

Total worth required to achieve hot and cold shutdown with 1 \$ (355 pcm) sub-criticality is 1270 pcm and 1712 pcm respectively. A 20 % uncertainty is considered in estimation of temperature and power defects in unfavorable direction.

The variation of one ultimate shutdown system subassembly worth (having 90% enriched liquid Li) at various locations is studied and shown in Figure 2. In addition, worth of three ultimate shutdown system

Fig. 2 Worth of 1 ultimate shutdown system subassembly with 90 % enriched Li-6

Fig. 4 Reference core with three ultimate shutdown system subassemblies in 5th ring

subassemblies for different enrichments is also studied by loading them in the 5th ring and is given in Figure 3. Results showed that 95% enrichment is necessary to achieve hot shutdown with (n-1) criteria, if they are loaded in the 5th ring. The optimized positions for three ultimate shutdown system subassemblies in 5th ring is given in Figure 4. The integral worth of three ultimate shutdown system subassemblies with 95 % enriched liquid lithium is shown in Figure 5. Their total worth is 2174 pcm, whereas it is 1335 pcm for two assemblies. It is sufficient to meet the hot shutdown even with two rods.

Thus, the feasibility of liquid lithium based reactor control system as a dedicated and independent ultimate shutdown system is demonstrated, based on the reactor physics assessment. For cold shutdown, more assemblies are needed, which will have more penalties on plutonium requirement. More R&D and experimental validation are necessary to finalize this concept.

Fig. 5 Integral worth of three ultimate shutdown system subassemblies in 5th ring

III.11 Design and Manufacture of Integrated Cold Trap for FBR In-Vessel Purification

For in vessel online purification of the primary sodium in future Fast Breeder Reactors integrated economiser - cold trap system which can be immersed in the hot pool of the reactor is conceptualized. The conceptual design of integrated cold trap is shown in Figure 1.

This design avoids bringing the radioactive primary sodium out of reactor vessel and leads to advantages in radiological, safety and economical aspects. Integrated cold trap will be dipped in the sodium at a temperature of 547 °C inside the hot pool of the reactor. A direct current conduction pump (DCCP) circulates sodium through the integrated cold trap.

Due to limited space availability in the reactor vessel, it is difficult to accommodate the full volume of wire mesh which is required for trapping the impurities in sodium for full reactor life span. Hence modular type replaceable wire mesh cartridges with minimum two years saturation time is planned inside the cold trap. After saturation of impurities in the cold trap, the

wire mesh has to be replaced without disturbing the entire system. The replacement of irradiated wire mesh unit will be carried out using the shielded cask for safe disposal. The other parts of integrated cold trap can be used for full reactor life span. Twin units of integrated cold trap, each with $2m^3/h$ sodium flow rate is required to purify the sodium to a reactor startup level after refueling campaign. A schematic showing the proposed location of integrated cold traps in reactor assembly is given in Figure 2.

Integrated cold trap thermal design calculations were done with a in-house developed computer code. Figure 3 gives the schematic of flow path of sodium, nitrogen and air in the integrated cold trap system.

With a sodium flow rate of 2 m^3/h, economiser is able to reduce the sodium temperature from 547 °C to 149 °C. Further reduction of sodium temperature to the cold point temperature of 110 °C is carried out by a closed nitrogen loop at a flow rate of 1.19 kg/s, 3 bar pressure and 70 °C inlet temperature. The
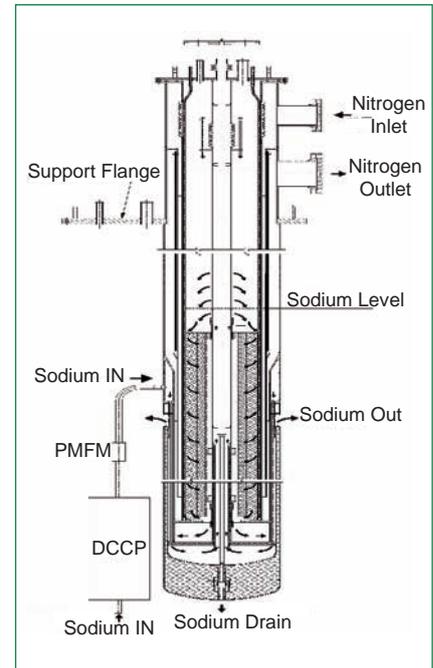
Fig. 1 *Conceptual design of integrated cold trap*

pure sodium flows back to the reactor hot pool through shell side of economiser where it gains heat and its temperature rises to 456 °C. Nitrogen temperature rises to 103 °C at the bottom most point of the cold trap and it returns to the outlet header. In the return path, the nitrogen picks up heat from the
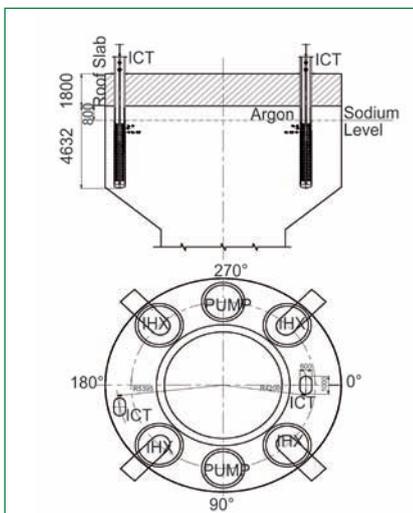
Fig. 2 *Proposed location of integrated cold trap for primary sodium purification in future FBRs*
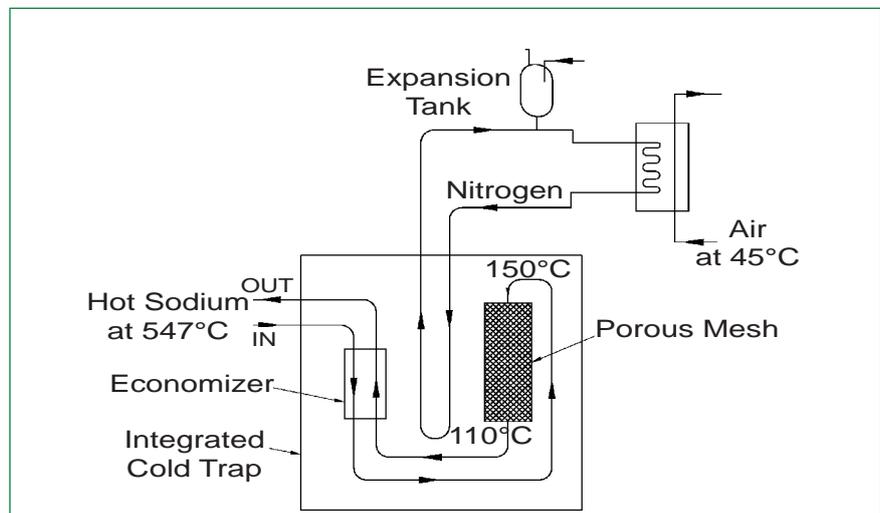
Fig. 3 *Schematic of flow path of sodium, nitrogen and air in the integrated cold trap system*

sodium at the economiser shell side and sodium in the reactor hot pool. The estimated nitrogen outlet temperature from the integrated cold trap is 174 °C. Figure 4 gives the graphical representation of various fluid temperatures along the length of the integrated cold trap.

The main components of integrated cold trap are economizer, heat exchanger, bellows and eight different shells used for making boundaries of sodium purification circuit and nitrogen cooling circuit. Design was carried out for all the components in conformance with ASME Sec VIII, Div-1 for design data as mentioned in Table 1.

Structural integrity analysis was carried out for individual components. The top tube sheet of economizer is the most critical component since it locally experiences more thermal gradient due to thermal interaction of incoming and returning sodium and nitrogen. The thermal baffles are provided in top tube sheet to reduce the thermal gradient. The tube sheet was qualified for creep-fatigue interaction. To reduce heat flow from hot sodium pool to cold sodium inside the integrated cold trap, thermal insulation is provided in between two hermetically sealed stainless steel shells. To accommodate high differential thermal expansion between the inner shell and outer shell, stainless steel bellows are provided. Analysis was carried out at nozzle junction and it was qualified for creep-fatigue interaction.

The integrated cold trap was fabricated at M/s Vividh Hi-Fab, Vadodara. To minimize the heat flux from hot pool to wire mesh region, ceramic fiber insulation was provided in a stainless steel encapsulated outer vessel. Fins were provided on the cold trap shell

| Table 1: Design data for ICT	
Design press.	2 kg/cm^2
Design basis	ASME sec. VIII, Division 1
Design temperature	550 °C
Material	AISI 316L/ AISI 304
Shell	620 mm OD; 6 mm T
Overall height	8600 mm
No. of fins	100 nos
Fin dimensions	2500 mm, 18 mm, and 2 mm
No. of tubes HX	28 numbers
Length of the HX	3000 mm
Tube dimensions	12 mm OD/ 10 mm ID

to enhance the heat transfer on the nitrogen side. For draining sodium during removal of integrated cold trap from reactor pool, a seat and plug arrangement is provided at the center of both the dished ends.

Cylindricity of each shell was controlled within the tolerance limit for maintaining the gap between shells to ensure the cooling fluid flow through the annular gaps. Fin welding were carried out in shell with restrainer arrangement and aqua purging to minimize distortion. The wire mesh (AISI 304 SS, continuous knitted type of six mesh per linear inch of grade SWG36 and SWG30) has been cleaned in tri chloro ethylene bath and required weight has been wound within the specified dimensions to achieve the required packing density. Mating parts in two seating locations of integrated cold trap have been hard faced by stellite. All necessary Non-destructive testing at various stages of fabrication have been carried out as per ASME sec V and final assembly of integrated cold trap has been completed. Nitrogen side of the integrated cold trap has been subjected to pneumatic test (Figure 5).
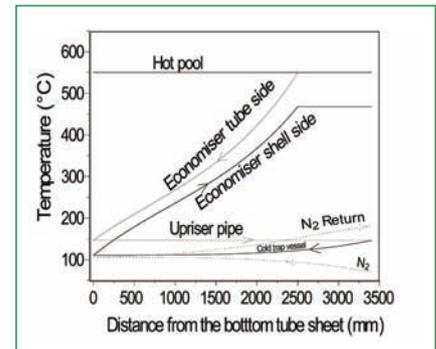
Fig. 4 *Variation of sodium and nitrogen temperatures along the length of integrated cold trap*

The integrated cold trap has been packed and held rigidly inside a steel structure and transported from manufacturer site to Engineering Hall - III.

This full scale model of integrated cold trap has to be tested in sodium at various hot pool temperatures for qualification. For testing of integrated cold trap, a sodium pool of 1000 mm diameter, 5000 mm depth with 800 mm cover gas space is required. Test vessel-3 of LCTR fulfills all the requirements for testing of integrated cold trap and work towards installation and testing is in progress.

Fig. 5 *Integrated cold trap at engineering hall-III*

III.12 Depiction of Grid Plate Melt-through Scenario by Woods Metal Simulant

During a loss of flow accident in a fast reactor the core temperature rises due to reduction in heat removal by the coolant rapidly. Eventually the fuel pins fail and depending upon the positive reactivity insertion the core can disintegrate violently.

After the expansion phase, the condensed liquid core may pierce through the grid plate, flow down under gravity, undergo fragmentation due to fuel coolant interaction, solidify and settle on the core catcher. An attempt has been made to simulate this phenomenon with woods metal water system.

A geometrical model ~ 1/10 of PFBR grid plate assembly is made with woods metal and grid plate melt-through experiments were conducted. An initial melt inventory of 20 kg woods metal is used to simulate the molten fuel. The melt temperature is 300 °C and the water column above the model bottom grid plate is kept at ~ 60 cm. The distance between the top and bottom grid plates is 75 mm and the average plate thickness is 6 mm. Melt is released at different external pressures. About

Fig. 1 Experimental facility

Fig. 2 Molten woods metal piercing the grid plate

twelve experimental runs have been completed in the experimental facility depicted in Figure 1. Subsequent to the postulated core melting event, the hot melt is expected first to hit the top of the grid plate virtually with no coolant present in the vicinity and after penetrating the top grid plate the molten core is expected to descend to the bottom grid plate. After penetrating the bottom grid plate, the hot core material will interact with the coolant in the lower plenum of the main vessel and the solidified debris will settle on the core catcher as shown in Figure 2.

Results from three experimental runs GP9, GP10 and GP11 which were carried out with identical initial

conditions except the initial pressure are highlighted in Table 1. The melt release valve operation time is less than 0.1 s. The external pressures applied to release the melt were 0 bar, 1 bar and 2 bar (gauge) for GP-11, GP-9 and GP-10 experiments respectively. Temperature histories at the top and bottom of the two wood's metal plates and chimney of core catcher are shown in Figure 3. Porosity of the debris settled on the core catcher was calculated using debris bed profile. Measurements (MMD) of debris was obtained for all the runs. The debris bed reconstructed from profile measurements is shown in Figure 4.

| S. No	Run No.	Gauge Pressure (bar)	Melt Deposit CCP (%)	Detached fines (%)	MMD (mm)	Bed Volume (cc)	Porosity	Area melted GPTop(A1) (cm^2)/ GP Bottom (A2)(cm^2)
						Table 1: Experimental results		
1	GP-11	0	71.6	0.3	1.20	2747	0.49	183/43
2	GP-9	1	29.0	4.0	0.80	1248	0.52	152/31
3	GP-10	2	27.3	11.0	0.55	673	0.26	166/13
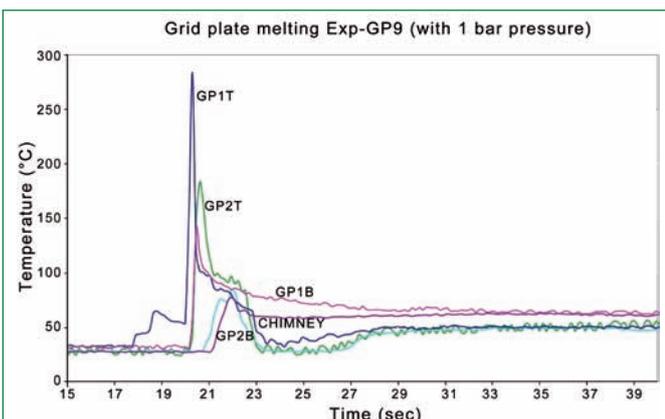
*Fig. 3 Temperature history at important locations in GP 9 run*
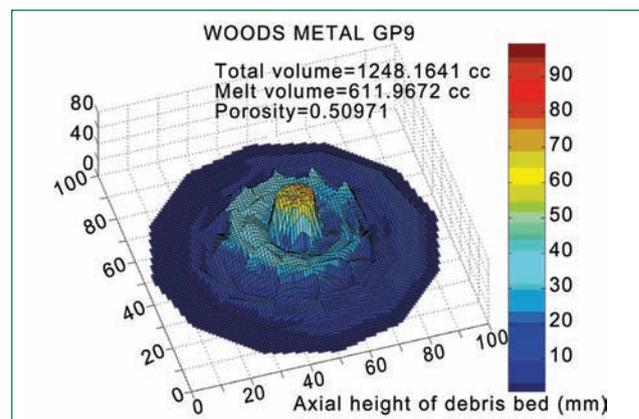
Fig. 4 Debris bed reconstructed from profile measurements

III.13 Experimental Observations of Metallic Core - Debris Characteristics in Sodium

Sodium Fuel Interaction Facility (SOFI) is aimed at studying fuel fragmentation phenomena and debris bed characteristics, towards post accident heat removal (PAHR) assessment. Experiments are conducted using melt charge in metal, oxide and other combinations for various purposes. The facility has been upgraded with specific cooling process and instrumentation requirements, for high temperature melting. In the recent series of runs, another small interaction vessel has been installed with internal filter basket and core catcher module. This innovatively designed vessel facilitates conducting experiments with lower inventory of sodium, making post-run debris retrieval comparatively easy. The new assembly is shown in Figure 1 and schematic of the complete system with melt chamber is shown in Figure 2a. Integration interface is suitably designed for individual isolation of vessel and melt chamber as and when required. The interaction vessel is pre-loaded with required quantity of sodium and heated up to 400 °C before carrying out the experiment. Recently one experiment was conducted using U-metal pellets encapsulated in steel. The melt charge was loaded inside tungsten crucible, which is used as a susceptor for efficient inductive coupling and charge isolation. The crucible configuration is shown in Figure 2b.

The charge was inductively heated to targeted temperature, and released successfully into sodium at 400 °C, inside the new interaction vessel. The rate of increase in melt temperature with respect to time, is depicted in Figure 3. After the experiment, sodium was drained to dump vessel through filter basket. Then the vessel was opened up carefully to observe accumulated debris mass along with solidified sodium, as settled inside the filter basket on the catcher plate. This has been shown in Figure 4a, which indicates the undisturbed position of debris inside the interaction vessel, before chemical cleaning of sodium. The vessel was carefully cleaned to

Fig. 1 *Experimental setup*

retrieve the catcher plate along with fragmented debris, which is shown in Figure 4b. The molten mass was found to be well fragmented during interaction with sodium. Preliminary investigation confirms population of finer debirs on the bed. However, detailed analysis is being carried out for size spectrum and mass mean diameters (MMD) of the formed debris bed for this run.
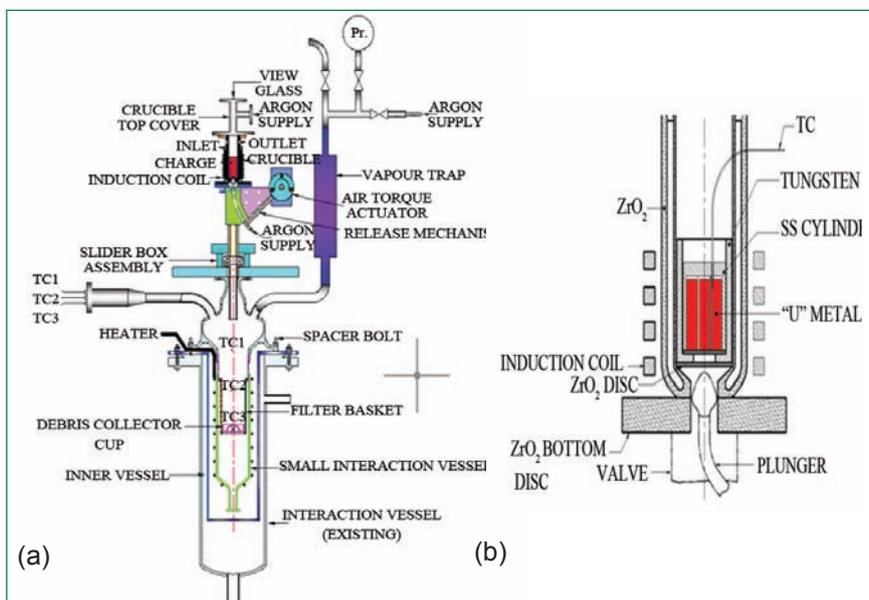

**Fig. 2** *Schematics of (a) facility and (b) cold crucible frame*
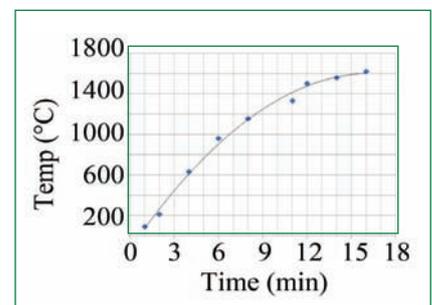

Fig. 3 *Charge temperature vs time*
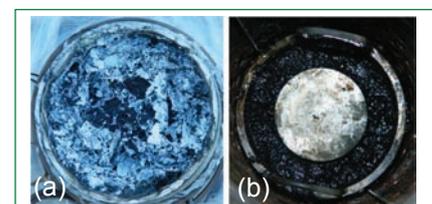
Fig. 4 *(a) Debris along with sodium and (b) cleaned debris on catcher*

# III.14 High Temperature Under Sodium Ultrasonic Imaging

Under sodium viewing at high temperatures is an important requirement in sodium cooled fast reactors (SFR) for navigation during structural inspection. Under sodium viewing is also needed to locate and identify loose parts, if any, under sodium, when required. As sodium is opaque, optical techniques are not suitable and ultrasonic based techniques can only be used for any internal inspection/viewing under sodium. Conventionally, ultrasonic imaging is done using XY raster scanning of the ultrasonic transducer. However, due to space constraints within the reactor, this may not be possible. As an alternative, θ-Z scanning is explored in the present study for high temperature under sodium viewing application.

Towards the development of ultrasonic methodology for under sodium ultrasonic viewing using θ-Z scanning, a systematic under sodium ultrasonic experiment was carried out, after gaining sufficient experience from under water studies. Under sodium ultrasonic scanner (Figure 1) and suitable software were developed for acquisition of ultrasonic signals in θ-Z mode and their on-line/off-line processing. Various tools and objects of different

shapes and dimensions were placed in a specimen cage (Figure 2), which was inserted in the Sodium Test Vessel-I at Hall-III in IGCAR, hanging from the top flange on which the under sodium ultrasonic scanner was placed. Under sodium ultrasonic experiments were carried out using an ultrasonic transducer provided by CEA, France.

The ultrasonic transducer was placed at a distance of ~450 mm from the sample cage and the signals were acquired at a step of 0.12° and 1 mm in θ and Z directions, respectively. Ultrasonic signals were acquired at various temperatures in the range of 180 to 400° C. The acquired signals were processed using specifically developed software in LabVIEW for generating C-scan image slices corresponding to different planes oriented at different angles. The C-scan slices were then ensembled to generate the 3D images, after applying suitable corrections for the angle at different depths, for enhanced viewing of the objects.

Figure 3a shows the photograph and Figure 3b the ultrasonic 3D image obtained for the set of elbows of different diameters placed in the cage. The photograph and the ultrasonic image generated for a
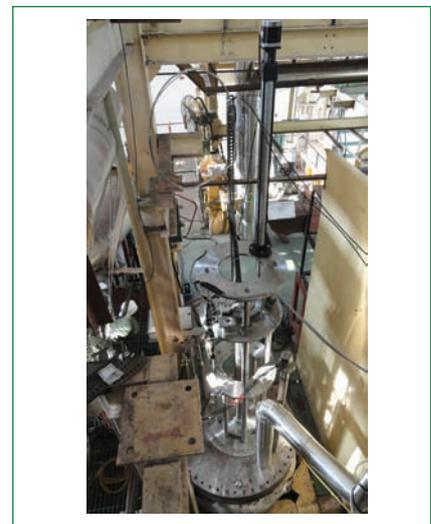
Fig. 1 *Under sodium ultrasonic scanner mounted on sodium test vessel - I at Hall – III*

plier and a hammer on a plate are shown in Figure 4. This corresponds to a condition of objects fallen on the ground. Even though the objects are placed on an inclined plate with respect to the ultrasonic beam, the image from the view normal to the plate is generated and shown in Figure 4, which can be used for any dimensional measurements.

The present study demonstrates that the methodology developed for under sodium ultrasonic imaging using θ-Z scanning can be employed for imaging of reactor internals in SFRs.

Fig. 2 *Cage structure showing mounting of various tools and objects for under sodium ultrasonic imaging*
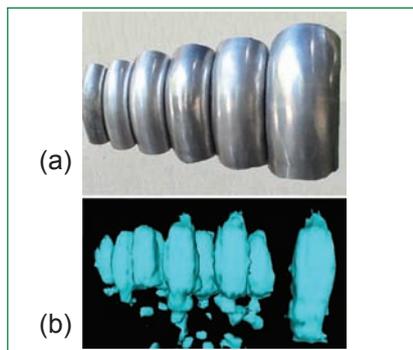
Fig. 3 *(a) Photograph and (b) under sodium ultrasonic 3D-image of a set of elbows of different diameters*
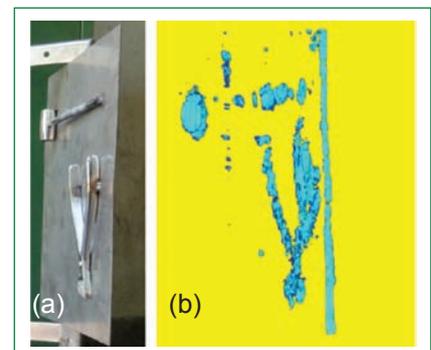
Fig. 4 *(a) Photograph and (b) under sodium ultrasonic 3D-image of a plier and a hammer placed on a plate simulating objects fallen on the ground*

III.15 Design & Development of Ex-vessel Discrete Sodium Level Probe

Mutual inductance type level probes are used for level measurement in fast breeder reactors and sodium experimental facilities. Both continuous and discontinuous mutual inductance type level probes are based on changes in mutual inductances of coils of the probe due to presence of sodium in vicinity of the probe.

Both continuous and discontinuous mutual inductance type level probes need insertion of the probe inside the vessel for measuring the level of liquid sodium, hence require free head room space above the vessel for their insertion into the pockets. These sensors also require temperature compensation as electrical conductivity of sodium changes with temperature. To avoid insertion of level probe in vessels for measuring sodium level, as a developmental activity, a non invasive type ex-vessel discrete level probe is designed, simulated and tested. Ex-vessel level probe consists of one primary winding and two differentially connected secondary windings wound on a magnetic core. The probe is placed outside a stainless steel vessel in which presence of sodium is to be detected. Primary winding carries alternating high frequency excitation current, which produces an alternating magnetic field which passes from one leg to another leg of magnetic core through stainless steel vessel and sodium. This magnetic field links with secondary coils and produces voltage in the secondary coil. When sodium is present in vessel at the position where the level probe is placed, additional eddy currents are generated in sodium due to primary magnetic field. These circulating eddy currents generate their own field which opposes the primary magnetic field resulting in reduction of total flux linkage with secondary winding facing the stainless steel vessel. Hence there is a reduction in secondary winding voltage facing stainless steel vessel in comparison to secondary winding facing air. The sensitivity of level probe is defined as ratio of difference between secondary voltage with full sodium level and secondary voltages with no sodium level to secondary voltages with no sodium level . Schematic of ex-vessel level probe is shown in Figure 1.

$$Vs = Vs_2 - Vs_1$$

Sensitivity

$$= \frac{Vs(\text{with Na}) - Vs(\text{No Na})}{Vs(\text{No Na})} \times 100$$

Vs = Output of differentially
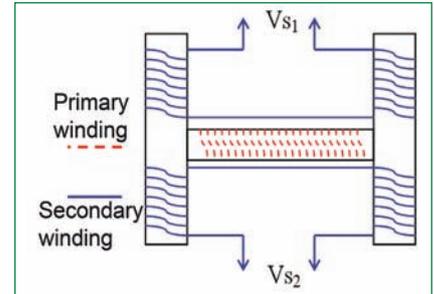
Fig. 1 *Schematic of ex-vessel level probe*

connected secondary windings.

$Vs(\text{with Na})$ = Output of differentially connected secondary windings with sodium in stainless steel vessel.

$Vs(\text{No Na})$ = Output of differentially connected secondary windings without sodium in stainless steel vessel. Schematic of level probe is shown in Figure 1.

Experimental results

Ex-vessel level probe was tested in test pot-1 of thermal shock test facility. Sodium temperature was varied from 200 to 500 °C. Level probe output was recorded for full sodium and nil sodium conditions. Frequency of input current to primary winding of probe is varied from 100 Hz to 3000 Hz to select the optimum frequency at which level probe shows maximum sensitivity. Variation in level probe output with frequency for primary current of 100 mA is shown in
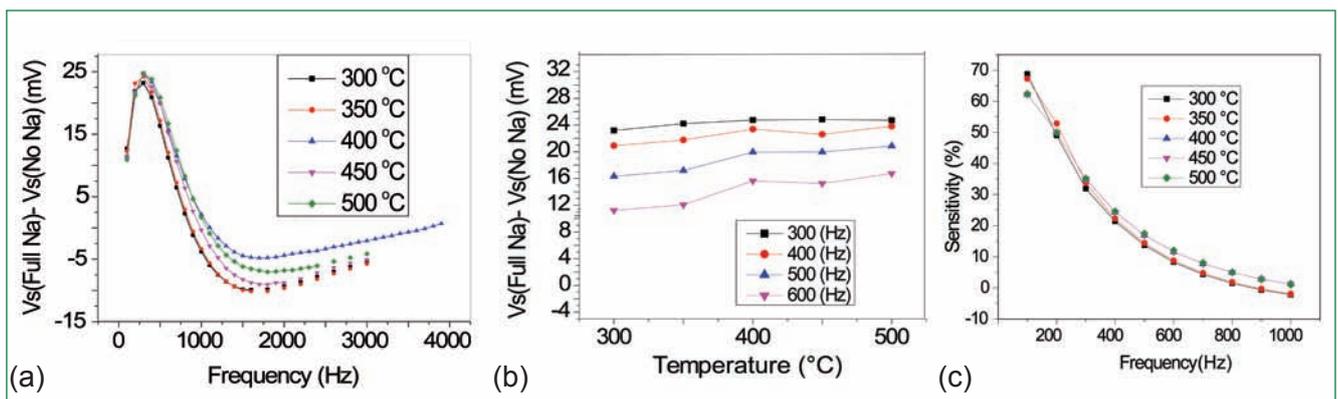
Fig. 2 *Variation in level probe (a) output with frequency, (b) output with temperature and (c) sensitivity with frequency*
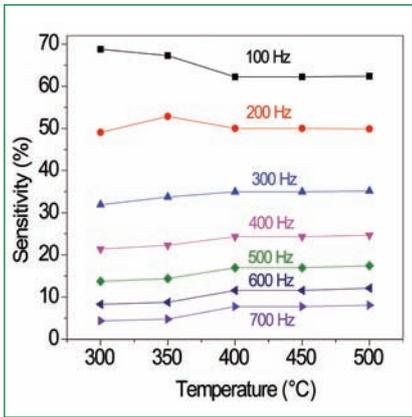
Fig. 3 *Variation in level probe sensitivity with temperature*

Fig. 4 *Magnetic flux density at (a) 100 Hz and (b) 1000 Hz*

Figure 2a. Sodium temperature is varied from 300 to 500 °C. It can be seen that level probe output shows maximum change at 300 Hz. Variation in level probe output at different frequencies for different temperatures is shown in Figure 2b. Plot of level probe sensitivity with frequency and temperatures are shown in Figure 2c and Figure 3 respectively

Analysis of ex-vessel level probe

Two dimensional finite element model of ex- vessel level probe is simulated in COMSOL to optimize the design and study the effect of frequency and sodium temperature on level probe sensitivity. Magnetic flux path and its direction along with depth of penetration of magnetic flux in stainless steel vessel with sodium at 100 Hz and 1000 Hz is shown in Figure 4a and Figure 4b. It can be seen that with increase in supply frequency, depth of penetration of magnetic flux reduces. Comparison between analysis and experimental results is shown in Figure 5. Due to neglecting of eddy currents in magnetic core in modeling, sensitivity of level probe obtained through modeling is higher than experimental results.

Ex-vessel level probe for sodium level measurement

Three numbers of ex-vessel level probes with H shape magnetic core are required for measuring level of liquid sodium in SILVERINA loop at discrete locations. Three numbers of ex-vessel level probes along with their supporting mechanisms were fabricated and tested at room temperature. One probe each was installed in each test pot of SILVERINA. Probe in test pot-1 was tested for sodium level detection. Probe output changed from 25 to 39 mV due to presence of sodium at probe location.

Ex-vessel level probe for NaK level measurement

FBTR has NaK bubbler and NaK tank which do not have NaK Level probe. NaK level was required to be detected for record purpose. An ex-vessel level probe with H shape magnetic core was fabricated for measuring level of NaK in NaK bubbler in FBTR. NaK bubbler consists of stainless steel wall of 4 mm thickness and stainless steel mesh. Ex-vessel level probe was placed outside the stainless steel wall to monitor the NaK level. Three designs with different dimensions were fabricated, analyzed and compared. It was seen that probe with 10 mm central limb gave better sensitivity. Probe output increased from 48 mV to 65 mV due to presence of NaK at probe location in NaK bubbler. Presence of NaK was also detected in NaK tank with stainless steel wall of thickness of 1.5 mm. Probe output increases from 56 to 62 mV due to presence of NaK at probe location in NaK tank. It was established that ex-vessel level probe can be used for measurement of NaK level at discrete locations.
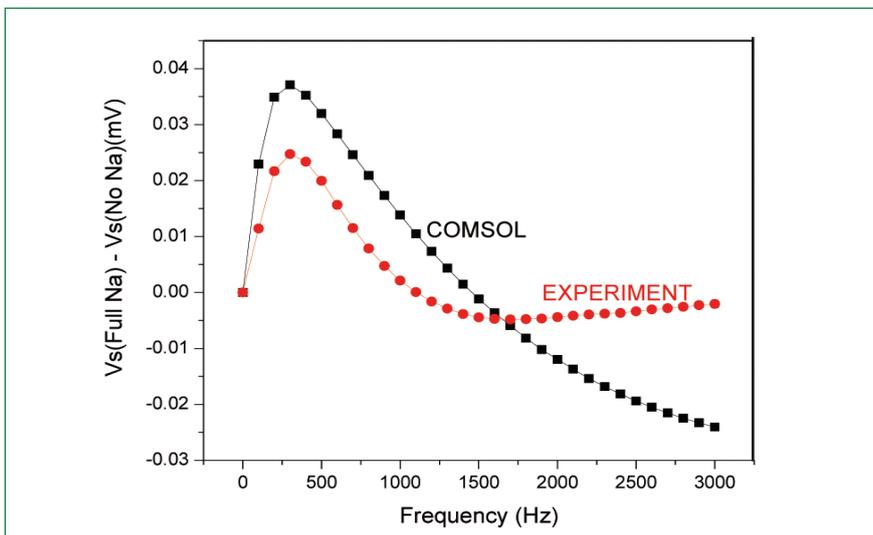
Fig. 5 *Comparison between finite element model analysis and experimental results*

III.16 Design and Development of Sodium Submersible Annular Linear Induction Pump

Electromagnetic pumps have been used for pumping sodium in auxiliary circuits of FBRs and also in various experimental loops. In these electromagnetic pumps the windings are in contact with ambient air which cools the winding. To meet the requirement of sodium draining from reactor pool a submersible annular linear induction pump has been designed and manufactured. DC conduction pump was the other option but it was not opted because of its bulkiness and requirement of higher size AC to DC converter power supply needed for pump operation. To overcome this constraint sodium submersible annular linear induction pump was conceptualized.

Conventional electrical insulation can withstand temperatures up to 220 °C whereas in requirement of sodium draining from reactor pool the winding temperature can go as high as 600 °C. Therefore, it was decided to use mineral insulated (MI) cable for making winding of annular linear induction pump due to proven record of MI cable in high temperature and high radiation environments. Design of an annular linear induction pump of capacity 2 m^3/h and 4 kg/cm^2 was done using the equivalent circuit approach. The design of submersible annular linear induction pump is different from design of normal annular linear induction pump since the requirement of long length of MI cable becomes an
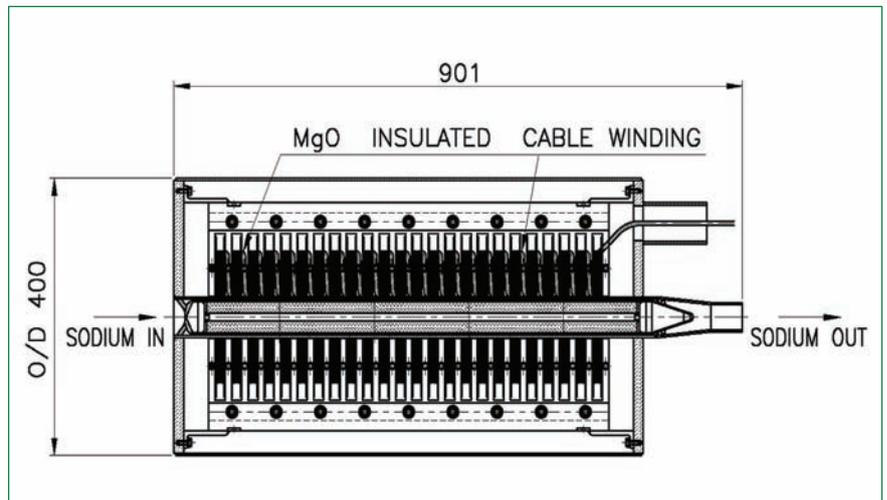
Fig. 1 Schematic of sodium submersible annular linear induction pump

additional constraint. A single length of 100 meters mineral insulated cable is needed for making the pump coils. The schematic drawing of designed submersible annular linear induction pump is shown in Figure 1.

Development of pump involved indigenous development of mineral insulated cable for such application as per IGCAR specification. This was successfully completed in collaboration with Indian industry. Thereafter, fabrication of pump as per IGCAR drawings was taken up. The main challenge was fabricating the winding with a single cable and keeping unilateral direction of traveling magnetic field. Stainless steel plates were provided on either side of the winding for keeping the coil in place. Special fixtures as well as support arrangements were made for fabricating the winding. The fabricated winding is shown in Figure 2.

After fabricating the winding, laminations were inserted in the slots. About ten numbers of lamination stacks were used. The winding along with lamination is shown in Figure 3. The completed submersible annular linear induction pump with outer stainless steel casing is shown in Figure 4. Insulation resistance test at 1000 V DC and HV test at 2.5 kV was done on the fabricated annular linear induction pump and found satisfactory.

The design and fabrication of submersible annular linear induction pump is a technological achievement since it is the first time that an annular linear induction pump has been made using mineral insulated cable for high temperature sodium environment without any external cooling provisions. Sodium testing of the manufactured submersible annular linear induction pump is planned shortly.
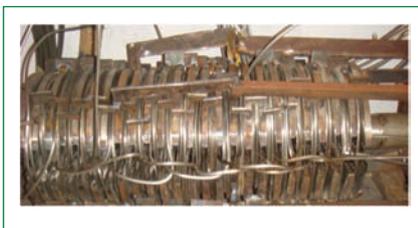
Fig. 2 *MI cable winding of submersible annular linear induction pump along with fixtures and support*

Fig. 3 *Submersible annular linear induction pump with MI cable winding and CRGO laminations*

Fig. 4 *Manufactured submersible annular linear induction pump with outer stainless steel cover*

III.17 In-sodium Thermal Striping Experiments in Fatigue Loop of INSOT Facility

A new test set-up has been commissioned in fatigue loop of INSOT Facility for conducting thermal striping experiments simulating the fuel-blanket interface to measure the temperature fluctuations on the surface due to mixing of non isothermal streams in sodium. In-sodium experiments are required to validate the computational analysis of the mixing phenomena. The test set-up was operated with two streams of sodium impinging on a instrumented plate with definite temperature difference of 150 °C. The data generated from these basic studies are very useful for validation of numerical code.

Thermal striping experiments were conducted with the axis of cold and hot nozzles in parallel and perpendicular to the axis of the instrumented plate thermocouples (Figure 1). The sodium jet temperature through hot nozzle was maintained in the range of 450 to 550 °C and sodium temperature through cold nozzle in the range of 300 to 400 °C with sodium flow rates ranging from 0.171 m³/h up to 0.738 m³/h.

Fatigue loop of INSOT has been modified for integrating the thermal
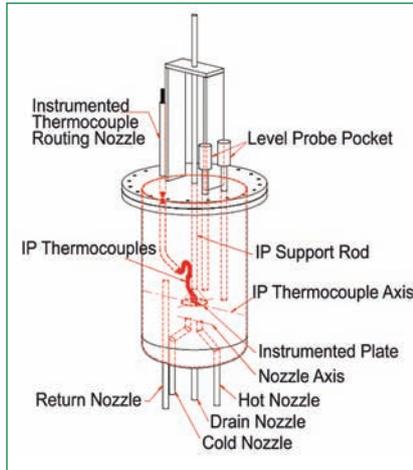
Fig. 1 *Isometric view of IP assembly & orientation of hot/cold nozzles in thermal striping test vessel*

Fig. 2 *IP assembly showing the embedded thermocouples*

striping test set-up (TSTS) consisting of sodium thermal striping test vessel (TSTV) with the testing mechanism and the connecting pipelines in test section-2. The temperature measurement during the thermal striping experiments is done with thirteen numbers of 0.50 mm stainless steel sheathed thermocouples embedded in an instrument plate (IP) (Figure 2).

Instrumented plate is fixed to an actuation mechanism erected on the top flange of the thermal striping test vessel (Figure 3) for enabling the vertical adjustment of

the instrumented plate inside the test vessel.

The commissioning works for the thermal striping test set-up have been carried out systematically.

Experiments conducted

The first in-sodium test was carried out for a duration of 120 minutes and test data from the embedded thermocouples on the instrumented plate, cold, hot sodium inlet nozzles and mixed outlet pipeline of the thermal striping test vessel were acquired in real time using a portable data acquisition system with high precision data

Fig. 3 *Top flange assembly showing routing of thermocouples to the IP and internal baffles*

Fig. 4 *View of thermal striping test set-up during conduct of experiments*

Fig. 5 *Time series plot of temperature*
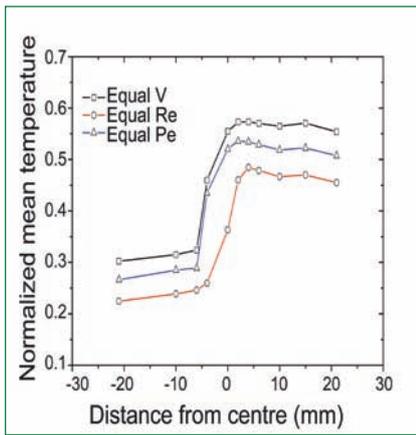
Fig. 6 *Normalized mean temperature distribution*
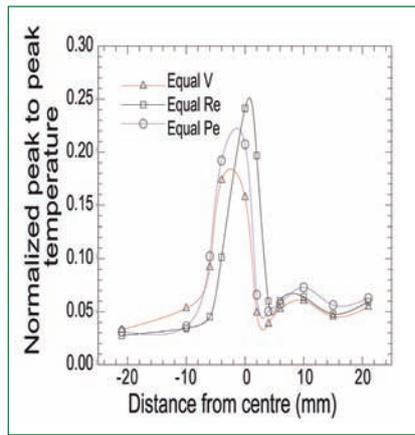
Fig. 7 *Peak to peak temperature distribution*
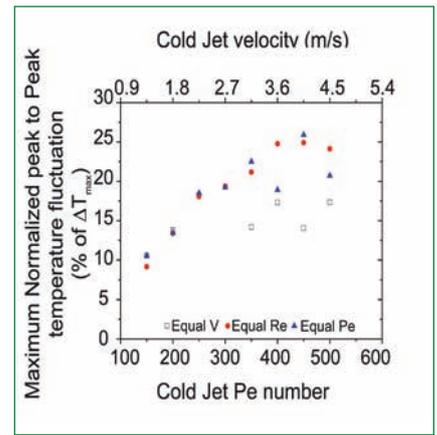
Fig. 8 *Variation of maximum peak to peak temperature fluctuation with cold jet Pe number*

sampling. The readings were taken with different frequencies of 50, 100, 500 and 1000 Hz at eight vertical positions of the instrument plate. The distance between the nozzle and instrument plate from 85 to 155 mm was successively varied in steps of 10 mm with reference to the hot and cold nozzles for each reading. In the second thermal striping test set-up campaign the temperature was sequentially raised in steps of 20°C per hour to 450°C in the hot nozzle while maintaining the cold nozzle at 300°C. Four numbers of thermal striping experiments were conducted at different sodium flow rates of 0.124, 0.249, 0.372 and 0.498 m³/h maintained in both the hot and cold nozzles. In the third thermal striping test set-up campaign the temperature was raised in steps of 20°C per hour to 550°C in the hot nozzle and to 400°C in the cold nozzle. Twenty six numbers of thermal striping experiments were conducted at various combinations of flow rates of sodium in the hot and cold nozzles up to 0.738 m³/h. Fourth campaign of thirty one thermal striping experiments has been completed with a perpendicular orientation of instrument plate assembly with respect to nozzles. The overall performance of the thermal striping test set-up (Figure 4) during the

conduct of the thermal striping experiments were satisfactory.

The governing dimensionless parameters derived from non dimensional form of governing equations related to temperature fluctuation in the mixing zone are Reynolds number (Re) and Peclet number (Pe). The temperature fluctuations in the mixing zone are dependent on these numbers. Accordingly, the parametric studies have been carried out with the details provided in Table-1; where, V is velocity of sodium jet at the nozzle exit and subscript 'h' and 'c' stands for hot and cold flow respectively. Hot and cold sodium flow rates have been controlled to maintain the conditions described in Table 1.

The analysis of the experimental data acquired has been carried out. A typical time series plot of temperature measured in the centerline of the two jets and at an elevation of 85 mm from the nozzle exit is shown in Figure 5. The mean temperature and peak to peak value of temperature (T_{p-p}) fluctuations as seen by each thermocouple have

been expressed in normalized form is shown as follows.

$$T_{mean}^{*} = \frac{\left(\hat{T} - T_c\right)}{\left(T_h - T_c\right)}$$

$$\Delta T_{p-p}^{*} = \left(\frac{\Delta T_{p-p}}{T_h - T_C}\right)$$

The normalized mean temperature distribution is shown in Figure 6.

The normalized peak to peak temperature distribution is shown in Figure 7. It can be seen from this figure that peak to peak temperature fluctuation is maximum when Re ratio between hot and cold jet is equal and decreases with increasing Re ratio. The maximum normalized peak to peak temperature distribution against cold jet flow rate and Pe number is shown in Figure 8. From this figure it can be seen that, the maximum peak to peak temperature fluctuation initially increases with Pe number. However, this gradually becomes insensitive to Pe number at higher values of Pe. More experiments are also planned to find out the threshold value of Pe where temperature fluctuation becomes independent of the Pe number.

Table1: Details of parametric studies			
Parameter	V_h/V_c	Re_h/Re_c	Pe_h/Pe_c
Equal V	1.00	1.18	1.06
Equal Re	0.85	1.00	0.90
Equal Pe	0.94	1.11	1.00

III.18 Development of 18Cr ODS Steel Cladding Tubes for Future FBRs – Microstructural Characterisation

The ferritic/martensitic steels are qualified for irradiation resistance upto 200 dpa due to their inherent void swelling resistance. However, their low creep strength at temperatures above 873 K restricts their application as a fuel cladding material in FBRs. Oxide dispersion strengthening increases the creep resistance of ferritic/martensitic steels beyond 873 K while retaining the inherent advantage of low void swelling. IGCAR's roadmap for the development of advanced cladding materials for FBRs using oxide fuel envisages the development of 9-18Cr oxide dispersion strengthened ferritic/ martensitic steels. In India, closed fuel cycle technology has been adopted in order to allow faster deployment of fast reactors. Reprocessing of the spent fuel to recover the fissile materials is necessary to reduce the doubling time. Compatibility of the fuel cladding material with the reprocessing medium is essential. Reprocessing of spent fuel requires that the chromium content in ODS steel shall be as high as 18 wt.% to minimize the dissolution of the irradiated cladding material in nitric acid.

Development of 18Cr-ODS steel is far more complex and challenging as compared to the 9Cr-ODS steel. The nominal chemical composition of $Fe-0.025C-18Cr-2W-0.3Ti-0.23$ Y_2O_3, has been chosen for the cladding tube. Prealloyed steel powder and nanosized yttria particles were mechanically milled, compacted, hot extruded and cold pilgered through four different stages to achieve cladding tubes of the desired dimensions. Optimisation of intermediate heat treatments between pilgering steps, necessary to soften the work hardening in the
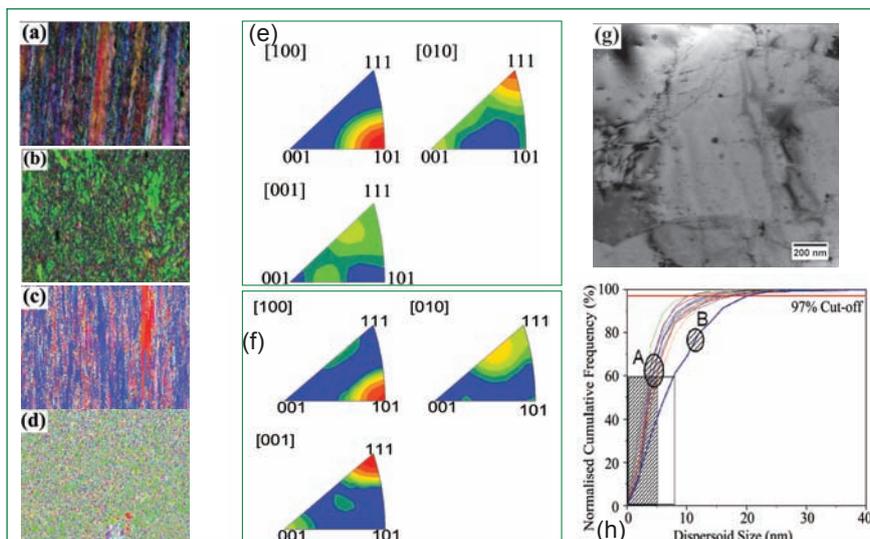
Fig. 1 *(a – b) EBSD orientation maps corresponding to LS and TS of the 12mm dia stage 1 tube, (c – d) EBSD orientation maps of LS and TS of the final stage 4 6.6mm dia clad tube, (e-f) IPF for stage 1 and stage 4 ODS tubes, (g) typical TEM BF micrograph of the ODS clad tube and (h) dispersoid size distribution during various stages of fabrication (A) and in final annealed tube (B)*

material and qualification of the tubes at various stages of thickness reduction by pilgering, was carried out by extensive microstructure and microtexture analysis. A unique two-step heat treatment methodology (1323 K for 1h in the 1st step and a progressively increasing temperature in the 2nd step) was evolved as a result of these studies, which was successful in the suppression of recrystallization and ferrite grain growth. Figures 1a and 1b show the EBSD generated orientation maps for the longitudinal and transverse sections (LS & TS) of the tube after the 1st stage of pilgering. Figures 1c and 1d show the LS and TS maps after the 4th stage of pilgering, i.e. the final size. In Figures 1a to 1d the Red, Green and Blue colors represent <001>, <101> and <111> pole normal directions. Elongated grains are seen in the LS images (Figures 1a and 1c) and the refinement of grain sizes is clear in the TS images (Figures 1b and 1d). Figure 1e and 1f show the inverse pole figures (IPF) for the stage 1 and 4, respectively.

The pole concentrations along preferred directions indicate a strong α-fibre and a relatively weak γ-fibre texture for the stage 1 tube which changes to near equal strengths for the α and γ-fibre textures for the stage 4 tube. Design of heat treatments to modify the deformation fiber texture to a more favorable recrystallization is under study. Figure 1g shows a typical bright field (BF) transmission electron microscope (TEM) micrograph of the ODS tube with 1.5 – 40 nm sized Yttria-titania complex dispersoids in a ferrite matrix. Figure 1h sums up the dispersoid size distribution of the ODS tubes during various stages of fabrication as inferred from detailed transmission electron microscope studies. This figure shows that about 60% of the dispersoids have sizes ≤ 5 nm while 97% of the dispersoids have sizes ≤ 15 nm. This dispersoid distribution and the ferrite matrix microstructure are acceptable for the application as clad tubes. Further studies to alter the deformation fibre textures through controlled recrystallization are in progress.

III.19 Prediction of Ductile Crack Initiation and Growth from Tensile Data for Type 316L(N) Stainless Steel

For numerical prediction of fracture parameters using material data from simple tests such as tensile test, it is essential to define an appropriate damage criterion. A new local damage approach based on plastic strain equivalent to uniform strain available from tensile test and grain diameter of the material has been proposed for prediction of crack initiation in 316L(N) stainless steel. 2D (plane strain and plane stress) and 3D finite element method (FEM) simulations were carried out for compact tension specimen (CTS) geometry with blunt notch of different a/W ratios under mode-I type of loading.

Figure 1 shows 3D finite element mesh of compact tension specimen used for simulations. The various elastic-plastic fracture parameters were estimated using a strain-based criterion, i.e., the equivalent plastic strain (ε_{pe}) at a characteristic distance, l_c (=2 times grain size) reaches a critical value set as ε_u, the uniform equivalent strain in a uniaxial tensile test (Figure 2). The elastic-plastic fracture toughness (J_{Ic}) and crack tip opening displacement (CTOD) results from finite element model analysis were within 8% of the values obtained from experiments on compact tension specimen. Also, the stretch
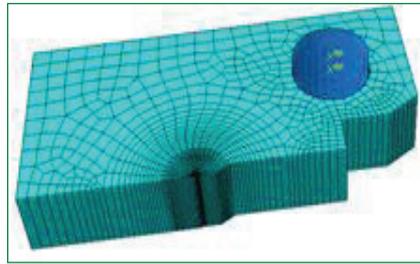
Fig. 1 *One-fourth 3D finite element mesh for compact tension specimen*

Table 1: FEM predicted and experimental J_i values			
a/W	Predicted J_i (N/mm)		$J_{SZW,\ exp}$ (N/mm)
	SZW	$J_{integral}$	
0.4	289	295	~270
0.5	288	275	
0.6	301	286	
0.7	289	292	

zone width predicted from the finite element model studies was comparable (within 5%) to those obtained from scanning electron microscopy of the fracture surface. The J_{Ic} estimated from finite element model based on stretch zone width (SZW) and J domain integral values corresponding to critical CTOD were in good agreement with each other for different a/W ratios (a: crack length and W: specimen width) and also with the experimentally obtained values (Table 1). The failure criterion based on ε_u is attractive since it is better defined and easier to obtain from the experimental data compared to the fracture strain.

In order to predict crack propagation and therefore the J-R curve, the stress triaxiality factor TF=σ_h/σ_{eq} (σ_h: hydrostatic stress, σ_{eq}: von Mises equivalent stress) was introduced. Crack propagation in a ductile material requires a hydrostatic stress in addition to an accumulated

plastic strain. Therefore, beyond crack blunting the critical strain criterion for crack propagation has been modified taking into account the stress triaxiality. A bonded node at the crack tip is allowed to de-bond when the local damage D (defined as D= ε_{pe}.TF) reaches a critical value. Based on comparison of a number of 2D finite element model crack growth results, the critical damage was taken as 1.2 times ε_u. The load versus displacement plots predicted using this damage criterion were in good agreement with those obtained experimentally (Figure 3). The finite element method predicted J contour integral and the experimental J-R curves are in close agreement (Figure 4). Thus, the damage criterion for crack propagation chosen in this study leads to a good prediction of J-Δa curves and can be used for crack growth analysis in components with different stress triaxiality conditions.
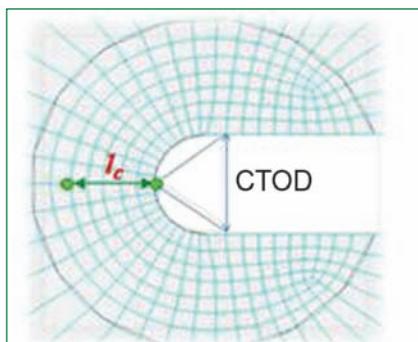
Fig. 2 *Typical mesh at crack tip with l_c highlighted*
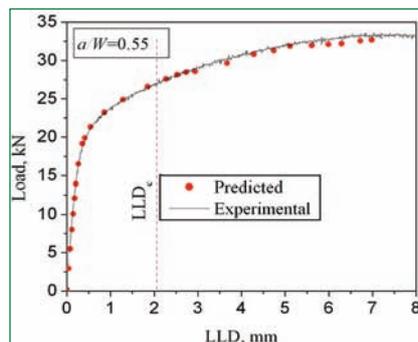
Fig. 3 *Comparison of experimental and predicted load vs. LLD plots*
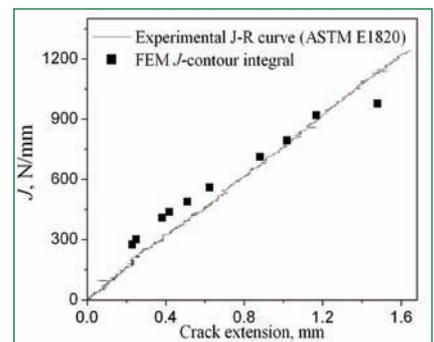
Fig. 4 *Experimental and FEM predicted J-R curves*

III.20 Modeling, Prediction and Validation of Thermal Cycle, Residual Stress and Distortion in Type 316 LN Stainless Steel Weld Joint

A detailed thermo-elasto-plastic analysis using finite element model was carried out to study the thermo-mechanical behavior of 316LN stainless steel during autogenous TIG welding on 3 mm thick plate. The welding simulations were performed using finite element package SYSWELD. The numerically predicted thermal cycles and temperature distribution were validated using infrared (IR) thermography. Figure 1 a and 1b compares the temperature distribution predicted by finite element model with that of infrared thermography measurements at 70 and 140 seconds respectively. The model predictions of the surface and bulk residual stress profiles were validated using X-ray diffraction (XRD) and ultrasonic testing (UT) respectively and are shown in Figures 2a and 2b. Distortion analysis was also performed and validated using digital height gauge measurement at 15 mm and 50 mm from the weld centerline as showing Figures 3a and 3b respectively. There was good
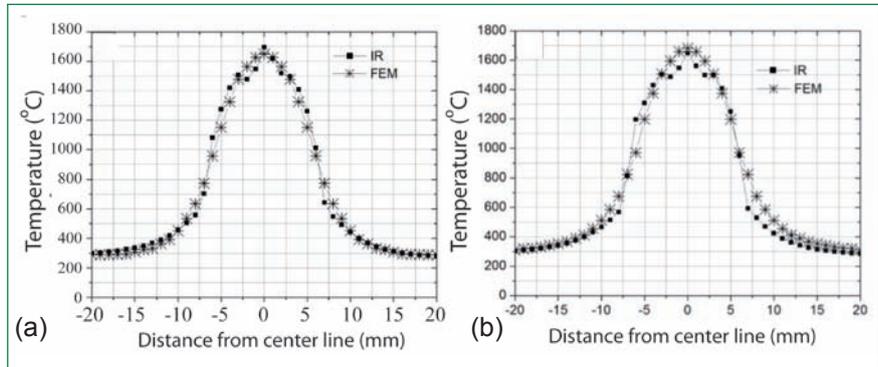
Fig. 1 *Comparison between finite element model predicted and infrared thermography measured temperature distribution at (a)70 s and (b)140 s*

agreement between the model predictions and the experimentally observed values of temperature, residual stresses and distortion. Therefore, the numerical modeling in combination with non-destructive methods provides an efficient approach for predicting the effect of welding process on the weld attributes.
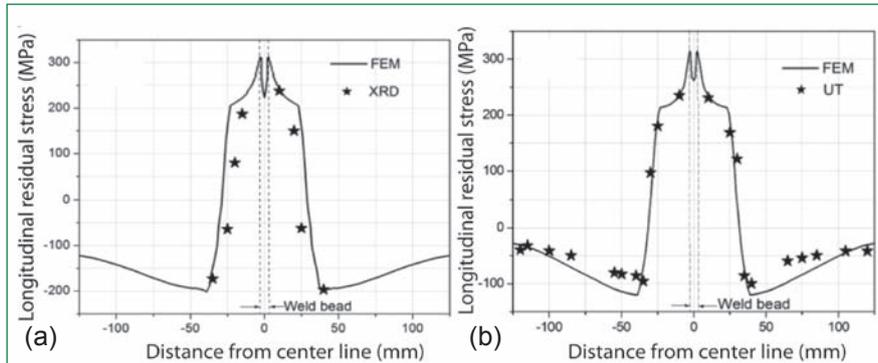
Fig. 2 *Residual stress profiles (a) finite element model vs X-ray diffraction and (b) finite element model vs ultrasonic testing*
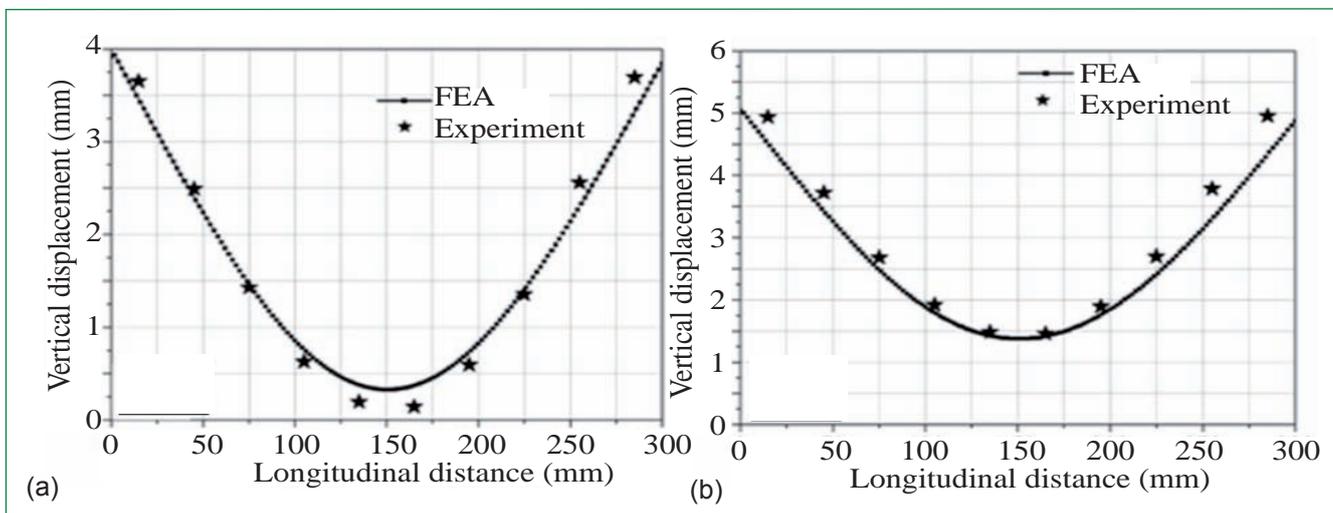
Fig. 3 *Distortion comparison (a) at 15 mm (b) at 50 mm*

III.21　Effect of Nitrogen Content on the Mechanical Properties and Corrosion Behaviour of 316LN SS

The selection of structural materials for reactor assembly components of sodium cooled fast reactors (SFRs) is governed by high temperature mechanical properties such as creep, low cycle fatigue (LCF), creep-fatigue interaction (CFI) and compatibility with liquid sodium coolant. For PFBR, type 316L(N) stainless steel (SS) alloyed with 0.07 wt.% N and ~0.025 wt.% C was used as the structural material. With a view of increasing the design life of future SFRs from 40 to 60 years, efforts were made to develop a nitrogen enhanced 316LN SS with superior high temperature mechanical properties. Using PFBR grade type 316L(N) SS as the basic chemical composition, the influence of nitrogen content on tensile, creep, low cycle fatigue, stress corrosion cracking, fracture, and fatigue crack growth behaviour have been studied for different nitrogen contents in the range of 0.07 to 0.22 wt.%.

Mechanical properties

Tensile properties have been studied between room temperature and 1123 K. Yield and ultimate tensile strength were found to increase linearly with increase in nitrogen content (Figure 1). Creep properties have been studied at 823, 873
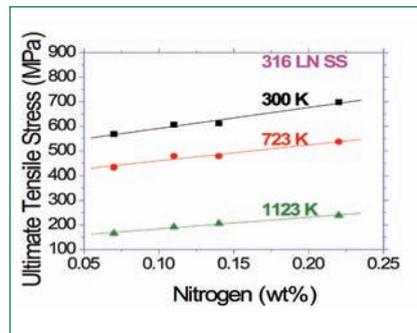
Fig. 1　Effect of nitrogen content on ultimate tensile strength

and 923K at various stress levels in the range of 140 - 350 MPa for rupture time upto 33,000 hours. Creep rupture strength increased significantly with increase in nitrogen content (Figure 2).

The extent of internal and surface creep damage decreased remarkably, with increasing nitrogen content, resulting in the increased creep rupture strength. The beneficial effect of nitrogen on the low cycle fatigue life was found maximum for a nitrogen content of 0.14 wt.% (Figure 3). Increase in fatigue life upto 0.14 wt.% N has been attributed to the enhanced planar slip of dislocations and slip reversibility. The reduction in fatigue life beyond 0.14 wt.% N content has been attributed to high

Fig. 2　Effect of nitrogen on creep rupture strength

matrix hardening and the decrease in residual ductility. The dislocation substructure was characterised by cells (Figure 4a) at lower nitrogen content and high density of planar slip bands (Figure 4b) at the highest nitrogen content. Based on these studies, nitrogen content in nitrogen enhanced 316LN SS has been optimized at 0.14 wt.%. This material has been named as NE316LN SS. The tensile and creep data have been analyzed according to RCC-MR nuclear code procedures in order to generate the design curves.

The time independent allowable stress S_m (Figure 5a) and the time dependent allowable stress S_t (Figure 5b) were found to be much higher than the RCC-MR values.
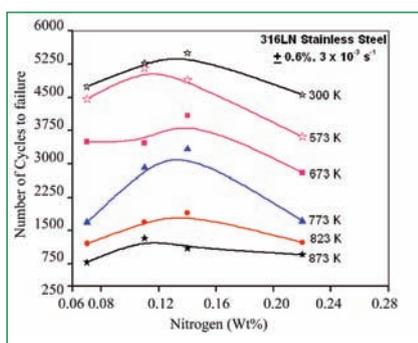
Fig. 3　Effect of nitrogen on low cycle fatigue life
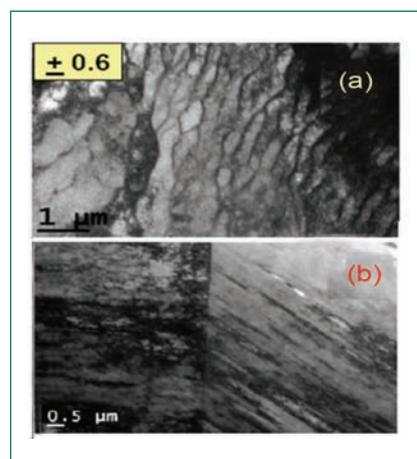
Fig. 4　Dislocation substructure in low cycle fatigue tested 316LN SS containing (a) 0.07 wt.% and (b) 22 wt.% N
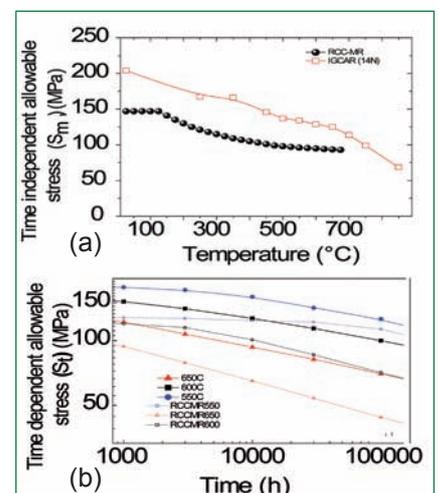
Fig. 5 (a) S_m and (b) S_t curves for NE316LN SS

Typically, S_m value at 873 K was higher by 35% while S_t value at 873 K for 1,00,000 h was higher by 40%.

Stress corrosion cracking

Stress corrosion cracking (SCC) studies were carried out in acidic sodium chloride medium using constant load technique. It was observed that stress corrosion cracking resistance increased with increasing nitrogen content in as-received condition. X-ray photoelectron spectroscopic (XPS) studies showed that enrichment of nitrogen took place in the passive film which increased the stability of the passive film. This increased the stress corrosion cracking resistance of nitrogen containing stainless steel. (Figure 6). On cold working, SCC resistance decreased as compared to mill-annealed stainless steel. However, with increasing nitrogen content SCC resistance increased for cold worked stainless steel. Beneficial effect of nitrogen on SCC resistance was observed for sensitized stainless steel only up to the solubility limit of nitrogen, beyond which, large amount of Cr_2N nitrides got precipitated.

Corrosion fatigue

The corrosion fatigue behaviour was investigated in boiling 5M NaCl + 0.15M Na_2SO_4 + 2.5 ml/l HCl solution at a stress ratio of 0.5 and a frequency of 0.1 Hz in mill-annealed and sensitized conditions. The stress range was varied by varying the maximum and minimum stress. The number of cycles to failure decreased with increasing mean stress in both the conditions. 316 LN SS with 0.22 wt.% N showed better creep-fatigue resistance than the steel with 0.07 wt.% N at all values of mean stress in the mill-annealed condition (Figure 7).

Fatigue crack growth behavior

The effect of nitrogen on fatigue crack growth (FCG) behavior of
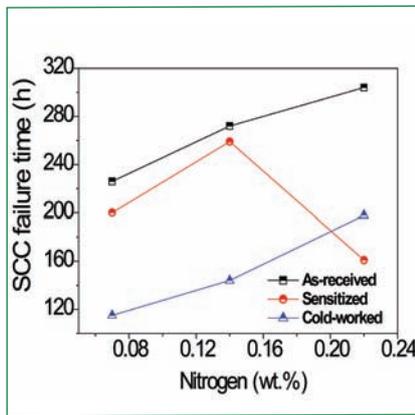
Fig. 6 SCC failure time obtained using a constant load test

316LN SS has been studied at room temperature. Extensive crack closure due to martensite formation was observed in the Paris regime for the steel containing 0.07% N. The steel containing 0.14% N had the highest intrinsic fatigue crack growth threshold (Figure 8). The improved fatigue crack growth thresholds at 0.14% N is attributed to the lower slip irreversibility. A new model that quantifies slip irreversibility in terms of fracture surface roughness and crack tip stress intensity factor as well as the yield strength of the material (through the plastic zone size) has been proposed. The fractions of slip irreversibility estimated using this model were found to correlate inversely with the threshold stress intensity factor range. The present model explains the fatigue crack growth resistance in threshold

Fig. 7 Creep-fatigue behaviour in as-received and sensitized conditions

regime as a function of nitrogen content.

Quasistatic fracture

Elastic plastic fracture toughness ($J_{0.2}$) values were higher at all test temperatures (298-823 K) for 0.14 mass% nitrogen steel (Figure 9). The same trend was observed in the average stretch zone width measured on the tested specimens (at 298 K ~260, 366 and 138 μm) and the tensile properties. Thus the variation in toughness could be correlated to the deformation behavior.

Based on resistance to low cycle fatigue, stress corrosion cracking (in sensitized condition), fracture, fatigue crack growth behaviour, adequate tensile and creep resistance, 316LN SS with 0.14%N is recommended for sodium cooled fast reactor applications.

Fig. 8 FCG results with crack closure correction
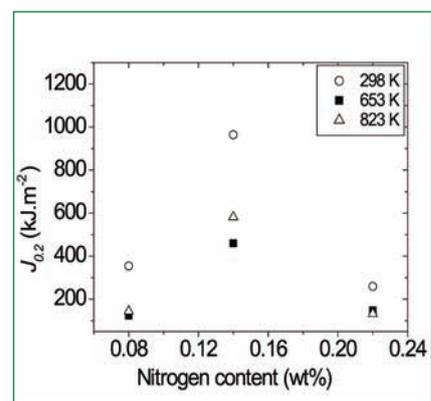
Fig. 9 Fracture toughness variation with nitrogen content

III.22 Plasma Sprayed Alumina Coating on Inconel 600 Rings for Fast Reactor Neutron Detector Application

High temperature fission chamber (HTFC) neutron detectors, whose outer shell/ring, made of Inconel 600 require to be coated with high electrical resistant alumina for application in PFBR. As per the specifications, the ceramic coated Inconel ring should withstand one hundred controlled thermal cycles at the maximum temperature of 923 K in argon atmosphere. The insulation resistance should be greater than 10^{13} ohm at room temperature and greater than 10^8 ohm at 923 K. Initial trials using plasma sprayed alumina coating on Inconel 600 rings with and without NiCrAlY bond coat failed within a few cycles during thermal cycling. Therefore, further studies were taken up to develop thermal shock resistant plasma sprayed alumina coatings with high electrical resistance.

The poor thermal cycle life and adhesion strength of the coating were attributed to oxidation at the interface of sprayed coating and metallic substrate. Therefore, deposition of an oxidation resistant bond coat between the top ceramic coat and the substrate as well as the coating technique employed are crucial to achieve maximum thermal cycling life and adhesion strength.

Inconel 600 samples of size 20×20×6 mm polished up to 600 grit emery paper were used as substrates. Ni-50%Cr bond coat of 50 μm thickness was deposited by high velocity oxygen fuel (HVOF) technique on these substrates. Top alumina coating of 250 μm thickness was deposited by atmospheric plasma spray process. Subsequently, plasma spraying was carried out on Inconel 600 collars/ring components of neutron detectors. The surface morphology of plasma sprayed alumina coating over Inconel 600 with Ni-50%Cr bond coat exhibited typical splat type of morphology with relatively dense surface without any microcracks (Figure 1). The cross section micrograph also showed that the coating was relatively dense. X-ray diffraction analysis on plasma sprayed alumina coating revealed well-crystallized γ and α phases of Al_2O_3.

Thermal cycling tests conducted in air on two sets of coated samples and collars/rings at 923 K revealed that the coated samples performed well without spallation or delamination even after one hundred cycles. No weight change was observed on the coated samples and rings after thermal cycling. Figure 2 shows the photograph of plasma sprayed alumina coated rings after 25, 50 and 100 thermal cycles, which performed well without any spallation. Even though the thermal expansion coefficient of NiCrAlY bond coat and Ni-50%Cr bond coat are similar, the thermally grown oxide on Ni-50%Cr bond coat is chromia while that over NiCrAlY bond coat is alumina. The oxidation resistant chromia, forming with Ni-50%Cr bond coat could have improved the thermal cycle life. Adhesion test was carried out as per ASTM C 633–01 on the as-sprayed sample and also after thermal cycling. The adhesion test results revealed higher adhesion strength of 38, 35.3, 33.4 and 31.9 MPa respectively for the as-sprayed coating and after thermal cycling for 25, 50 and 100 cycles respectively.

The insulation resistance of plasma sprayed alumina coated Inconel 600 samples (after 100 thermal cycles) measured with 600 V applied voltage was found to be ~10^{11} ohm at room temperature and ~10^8 ohm at 923 K. The insulation resistance at 923 K satisfied the acceptance criteria. Apart from insulation resistance, the plasma sprayed alumina coating developed on Inconel 600 exhibited good thermal cycle life combined with adequate adhesion strength. The present results suggest that plasma sprayed alumina coatings over Inconel 600 could be used for critical components like neutron detectors exposed to high temperature in fast breeder reactors.
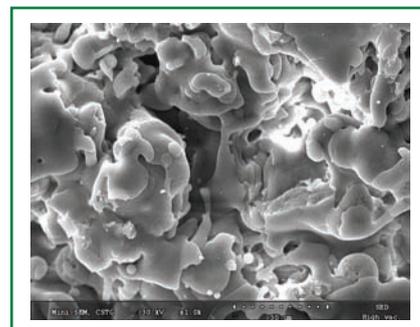
Fig. 1 *Surface morphology of plasma sprayed alumina-coated Inconel 600*
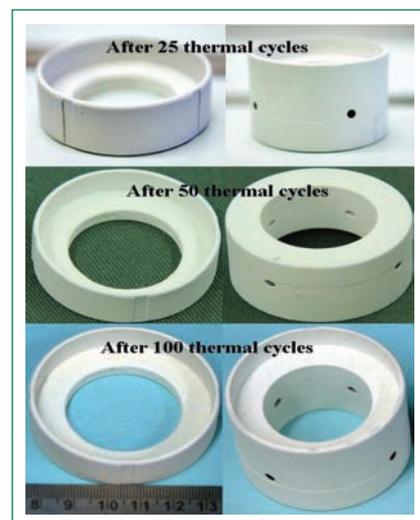
Fig. 2 *Photograph of plasma sprayed alumina coated Inconel 600 collars/rings*

III.23 Validation of Computer Code PREDIS against PHENIX End of Life Natural Convection Test

A validated accident analysis code is essential for a safe design of a nuclear reactor. An in-house computer code PREDIS is used to study the transient behavior of both small and medium sized fast breeder reactors. The kinetics portion of the code has been validated against SEFOR reactor transient and FBTR rod ramp experiment. The flow coast down has been validated with BN-800 Coordinated Research Project (CRP) and European LOFA benchmark up to onset of boiling. In 2009 various experiments were conducted by CEA in PHENIX reactor before its decommissioning, and are called PHENIX end of life (EOL) Tests. One important experiment among them was the natural convection test and the details of the experiment were shared with IGCAR as part of a Coordinated Research Project of IAEA and also by CEA-IGCAR collaboration. The unprotected phase of PHENIX natural convection test is simulated using PREDIS code and compared with the experimental results.

The main objective of the natural convection test conducted in PHENIX was to check transition to natural convection in case of loss of flow accident as predicted by computer codes. PHENIX is a pool type sodium cooled fast reactor with a nominal power of 560 MWt/250 MWe. During the natural convection test the operating power was reduced to 120 MWt for safe operation since one out of three secondary sodium circuits was out of operation at that time. The experiment was initiated by manual dry out of the two steam generators without SCRAM which results in an unprotected loss of heat sink transient. The present study involves only the first part of the test before the manual SCRAM. The 450s long transient is analyzed using PREDIS code considering the increase in inlet coolant temperature as the accident initiation. Since PREDIS models only the core region, the change in inlet temperature from 360 to 405 $^\circ$C is taken as input for the transient simulation.

The code PREDIS assumes a 2-D cylindrical model for the reactor core with hexagonal cross section for the subassemblies. The entire reactor is divided into several radial cylindrical rings depending on the flow zoning of the reactor. PREDIS uses a single pin model, all heat transfer calculations are done for a representative pin in the ring. The height of the core is divided into several axial meshes due to the variation in linear heating rate. A point kinetics model is assumed for neutronics calculations. In the considered transient, there is no external reactivity in the system and hence net reactivity of the system could be approximated to be a sum of feedbacks, fuel expansion, doppler feedback, grid plate expansion, vessel expansion and the apparent insertion of control rods due to core expansion are the various feedback mechanisms considered for the study.

For the simplicity of calculation of the whole core is divided into fourteen axial and nine radial zones. The radial and axial expansion of the core is considered as a sum of two components. The fuel removal worths per mesh calculated using first order perturbation theory is used to find reactivity change due to expansion of each mesh. The fuel removed from each fixed mesh due to expansion is assumed to be added at the boundaries viz. the core and axial blanket, core 1 and core 2 and core 2 and radial blanket.

While calculating the fuel expansion feedback, 90% of the fuel is assumed to have a closed gap and the rest 10% an open gap as recommended by CEA. This is because of the fact that the fuel clad gap depends on the burn-up level of the fuel which varies spatially due to the flux shape. When the gap is closed, presence of clad restricts the free expansion of fuel in the axial direction so axial expansion of fuel is assumed to be same as that of clad after the closure. Therefore 90% of the fuel is considered to be expanding with the steel and the rest 10% expands with the rise in fuel temperature. Doppler feedback is calculated using Doppler constants for each mesh and are added up.

Apparent insertion of control rods due to axial expansion of core is calculated from the axial expansion of the pins in the first ring. All the pins near to control rods are assumed to have closed gap and hence steel temperature is used for calculating expansion.

The temperature rise at the hot pool was found to be less than 10 $^\circ$C therefore the control rod drive expansion feedback is neglected but the vessel expansion feedback is considered. Following the evolution of the core inlet temperature, the vessel is slowly heated up by the increasing temperature in the cold pool. The vessel temperature is assumed to follow the core inlet temperature with a time delay. Since the vessel is fixed at the top of the roof slab the expansion of vessel results in a downward motion of the core. The absorber rods are also fixed at the top slab and hence
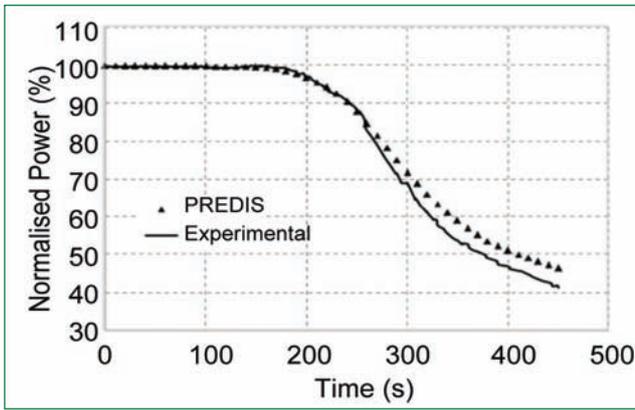
Fig. 1 Variation of reactor power with time
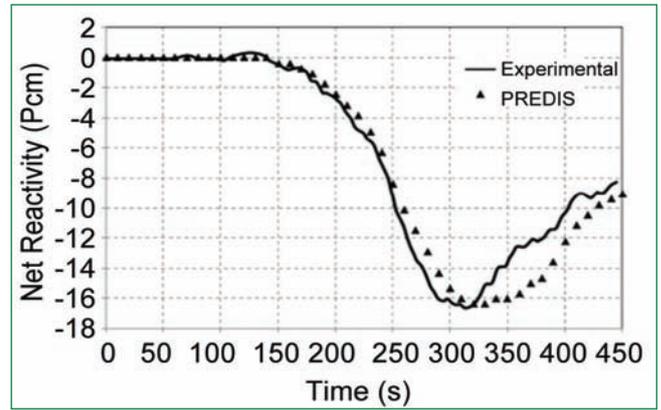
Fig. 2 Variation of net reactivity with time

the core downward motion results in removal of absorber rods and a negative reactivity feedback. The vessel expansion coefficient and time delay is chosen as 0.5 pcm/°C and 130 s respectively based on the experimental reactivity.

The kinetic parameters and various perturbation worths used as input for PREDIS are calculated by IGCAR-2D code system using ABBN93 cross section set. The accident is initiated because of the increase in inlet coolant temperature due to reduction in heat removal in the secondary circuit. Grid plate temperature increases with rise in coolant temperature. The resultant expansion of grid plate gives rise to a negative feedback which is the most important feedback in the considered transient. The reactor power starts dropping due to the negative feedbacks from grid plate expansion and fuel axial expansion. The response in reactor power is compared with the experimentally observed curve in Figure 1. The average fuel temperature in the core region also drops due to power drop giving rise to positive Doppler feedback. In blanket region fuel temperature increases due to the rise in coolant temperature. A negative Doppler is found in blanket due to the broadening of ^{238}U capture resonances with increase in temperature.

The net reactivity is calculated as the sum of all the feedback effects and compared with the experimental curve in Figure 2. The transient had been analyzed earlier using TRACE code of FAST code system at Paul Scherrer Institute (2012) and the results were reported. The code TRACE has been extensively verified in the past against data from other evaluated codes like ERANOS and various experiments related to fast reactor systems. TRACE results are taken as the reference for comparing PREDIS results. All the reactivities of components are plotted and compared with the TRACE calculated results in Figure 3.

The nature of evolution of system temperature with time is same with both code systems. In the core region fuel temperature decreases due to reduction in power while in the blanket region a rise in temperature occurred and is attributed to the rise in coolant temperature. The clad temperature shows a similar trend as the inlet coolant temperature. The temperatures calculated by PREDIS is less than that calculated by TRACE. In case of fuel, PREDIS calculated a higher value in core and lower one in blanket region compared to TRACE (Figure 4).

The PHENIX natural convection test is used for evaluating the transient analysis code PREDIS. The code could predict the transient with good accuracy and the results agreed with the test results. All the major reactivity feedbacks considered are well in agreement with the TRACE calculated values. This study ensures the transient analysis capability of PREDIS in simulating mild transients.
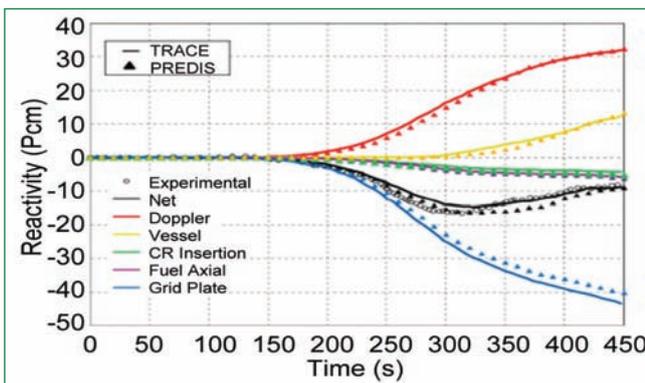
Fig. 3 Variation of reactivity components against time
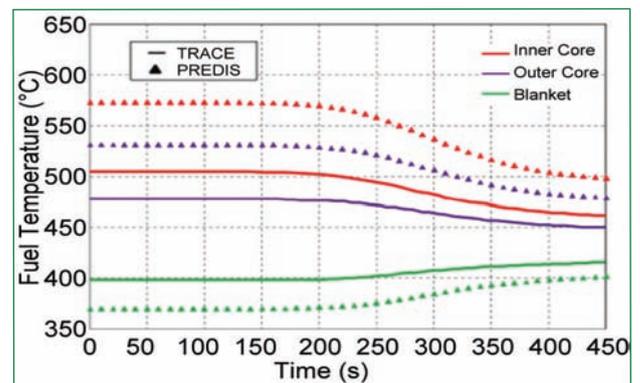
Fig. 4 Variation of fuel temperature with time

III.24 Design, Development & Testing of Switch Over Logic System with Read-back Facility for Safety Related I&C Systems of FBRs

In Safety Class-II and fault-tolerant non-nuclear safety systems of FBR, diversified dual real-time computers (VME and cPCI bus based systems) with switch over logic system is being implemented. Signal from field sensors (analog/digital) are duplicated and connected simultaneously to both VME & cPCI systems for processing and generating identical output signals as the application software running on both the systems are also similar. These output signals are used for control, alarm annunciation, interlock, lamp indication purposes and is routed through switch over logic system to final control element. Switch over logic system (Figure 1) plays an important role in checking healthiness of both VME & cPCI system and sending healthy system's output to the plant.

Fig. 2 (a) Switch over logic board
(b) ORing logic board
(c) P1 backplane and
(d) P2 backplane

It is a stand-alone system with high reliability and availability. The switch over logic has been implemented using highly reliable MIL grade hermetically sealed relays. Based on SG9 comments, ONLINE status of each channel is indicated through redundant contact available as part of 4-pole-double-throw (4PDT) relay. Latching type of relay is used in our design for each channel to maintain default routing status irrespective of power supply condition to SOLS.

System overview

The design of SOLS consists of one switch over logic board (Figure 2a) with maximum of nine ORing logic boards (Figure 2b) all housed in 19" high 6U card frame mounted on specially designed P1 backplane (Figure 2c) and P2 backplane (Figure 2d).

The switch over logic board receives health status from both VME & cPCI system and sends command to ORing logic boards mounted over backplane to route healthy system's output to the plant. Depending on system healthiness, ORing logic board helps in routing output signals generated by VME or cPCI system. The switch over action takes place automatically depending

Fig. 1 Switch over logic system

on health status from real-time computer systems. Provision has been made to route manually any healthy system's output to the plant during maintenance or periodic surveillance. Each ORing logic board can route 15 output signals of analog, digital or potential free contact type generated from real-time computer system to the final control element in the plant.

Testing of SOLS

The SOLS operating states are tested for normal mode, transition phase and power failure condition. Failure of relay to switch its position is now detected through ONLINE status declared by SOLS which is qualified after checking all channel status through read-back facility. This helps plant operator to initiate maintenance action in less time to reduce system downtime and improve upon system availability. A state transition diagram is shown below in Figure 3.

Fig. 3 State transition diagram of switch over logic system

III.25 Design & Development of 32 bit Soft-Core Processor based Remote Terminal Unit for FBRs

Distributed digital control systems (DDCS) architecture is followed for plant control and operation in FBRs. Remote terminal units (RTUs) installed in several LCCs situated near to field sensors acquires analog/digital signals data from sensors; processes and generates control outputs for control elements. These systems send data to process computer, local display stations kept in the same LCC or other LCC and to various other peer level DACs on LAN. This mandates the need of multiple sockets TCP/IP Ethernet communication support for embedded systems used in FBRs. Also, since the designed life of NPPs is around 40-60 years, there is a strong need for addressing the component obsolescence issues in designs. Existing RTUs are 8-bit microcontroller based systems where the ethernet communication is done by external hardware (Wiznet modules) as shown in Figure 1, which has serious limitations on number of simultaneous connections (sockets supported); and obsolescence of such hardware is always an issue.

Conceptual design

For addressing the above challenges FPGA based RTU design is done with the entire digital logic of the board implemented using one FPGA device. Soft-cores are used for processor (MicroBlaze), EMAC (TEMAC), UART and DDR controllers. Real time operating system (RTOS) along with software TCP/IP stack is ported to the processor, which finally enables us to implement entire logic inside FPGA along with multiple socket support. This also enables the design to be more immune to obsolescence as the FPGAs are less prone to obsolescence and moreover the same design can always be ported to next generation of same FPGA family. This concept is explained in Figure 2.

Design validation and results

To prove this concept a development board was used to demonstrate the multi-socket TCP/IP communication. A MicroBlaze processor based FPGA design was developed using Xilinx tools. Configuration of RAM memory, instruction cache, clock and other IP cores (like TEMAC, DDR controller, UART) was done using Xilinx platform studio tool. The bit file was generated and exported to eclipse based software development environment (Xilinx SDK). Board

Fig. 1 *Wiznet module*

support package was developed with lwIP TCP/IP stack configured to xilinx kernel. Application software was developed demonstrating the multiple sockets TCP/IP communication with the client PC as shown in Figure 3.

Performance achieved

Xilinx provides open source iperf software for testing TCP TX/RX throughput. The achievable throughput with MicroBlaze processor's cache size of 32k in socket mode during transmit was 46 Mb/s and during receive it was 27.4 Mb/s.

Product development

A 8ch analog input, 16ch Digital input and 8ch relay output universal RTU board was designed with this idea. This design included the gigabit ethernet interface, USB UART interface, watchdog & power supply monitoring circuitry. Block diagram of the schematic design is shown in Figure 2. The final assembled and tested board is shown in Figure 4.

Fig. 2 *Block diagram of microblaze based RTU*

Fig. 3 *Multiple socket output on a client software*

Fig. 4 *32-bit soft-core RTU board for 8ch Analog Input, 16ch digital input & 8ch relay output*

III.26 Embedded System of Under Water Trolley I&C for Spent Fuel Transportation

The fuel subassemblies of Fast Reactors are transported to the storage bay in a systematic manner after its usage. The spent or failed fuel subassemblies kept in the outer ring of the core for cooling and then moved to the washing facility where nitrogen and steam are used to wash the sodium deposits over the subassembly. The effluent is monitored for fission products. If fission products are present, then the fuel subassembly is declared to be faulty and kept in a container. After washing, under water trolley (UWT) is used to transport the spent fuel subassemblies or container with failed fuel subassemblies from spent subassembly exit port (SSEP) of fuel transfer cell to spent subassembly storage bay (SSSB). Under water trolley operations has to be controlled remotely by highly reliable embedded system as it handles radioactive materials.

The under water trolley I&C system is designed and developed to operate the trolley from handling control room (HCR) panel or console, or from fuel building local control center (FB LCC). It monitors the position of the under water trolley continuously and issues motor control signals for safe operation of under water trolley. It provides the necessary indications, alarms and displays in handling control room and fuel building local control center.

Under water trolley instrumentation

The drive system of under water trolley consists of a drive motor, reduction gear, wire rope and drum. The drive motor is powered using a variable frequency drive (VFD) system. Limit switches are provided to indicate whether the trolley reached its destination, to lock the trolley with linear actuator

and to know the status of open/close condition of valves. The trolley position is continuously monitored by two independent and diverse position sensors, viz., a draw-wire potentiometer and a synchro.

Under water trolley instrumentation and control architecture

The under water trolley instrumentation and control system is built with two identical subsystems, a relay-based switch over logic system and appropriate power supply modules in a 19" 42U standard cabinet. The system architecture is shown in Figure 1. All the input signals are connected to both the subsystems. Both the subsystems do the processing as per the control logic and send the outputs to routing logic. The health statuses of the subsystems are sent to switch over logic circuit, which in turn directs the routing logic to route the outputs of the desired subsystem to the field. All the hardware requirement for under water trolley instrumentation and control are designed in-house, so that the complete system is open & amenable

for verification &validation (V&V).

Under water trolley operations

A three-way station selector switch is mounted on the console to select the operating station. Under water trolley operations are performed by "computer guided" sequence or "manual" sequences. under water trolley can be operated in high speed (31.4 mm/s) or low speed (6.24 mm/s) using variable frequency drive . The various operations to be performed using the under water trolley includes:

- Open SSEP valve
- Load fuel subassemblies/ container
- Close SSEP valve
- Unlock under water trolley
- Move towards SSSP
- Unload fuel subassemblies/ container
- Move towards SSEP and
- Lock under water trolley.

For permitting each of these operations, there is a set of safety interlocks to be checked. For example, before the subassembly/container is loaded into the trolley, it is to be ensured that the trolley is
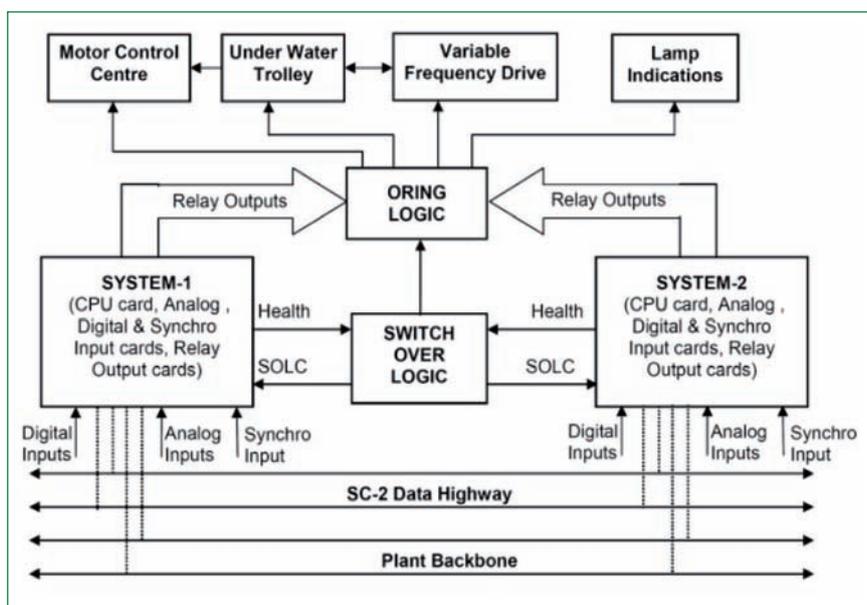

Fig. 1 Under water trolley instrumentation and control architecture

positioned and locked beneath the loading port.

Design methodology

A disciplined development methodology which has control in each phase is followed for embedded system of under water trolley instrumentation and control as shown in Figure 2. Each phase in the design flow is verified by an independent V&V group.

Under water trolley instrumentation and control system functions

The under water trolley instrumentation and control software performs the following functions.

- Scans the input signals
- Performs engineering unit conversion on analog signals
- Receives soft inputs/commands
- Implements safety interlocks
- Generates control outputs
- Provides necessary indications/alarms
- Transmits data every one second
- Checks for hardware healthiness using the diagnostic features provided on the CPU and I/O cards
- Detects failure of the software itself by the watchdog timer
- Provides provision for safe termination of operation in case of system failure any abnormal conditions or network failure.

The sequence of operations performed by the embedded system is shown in Figure 3. The scan cycle is 200 ms. The complete software is written in C with MISRA C compliance. This improves the reliability and testability of the software system.

DDCS interface

The embedded system of under water trolley instrumentation and control is connected to the process computer through safety Class-II data high way and display stations of FB LCC, HCR console and
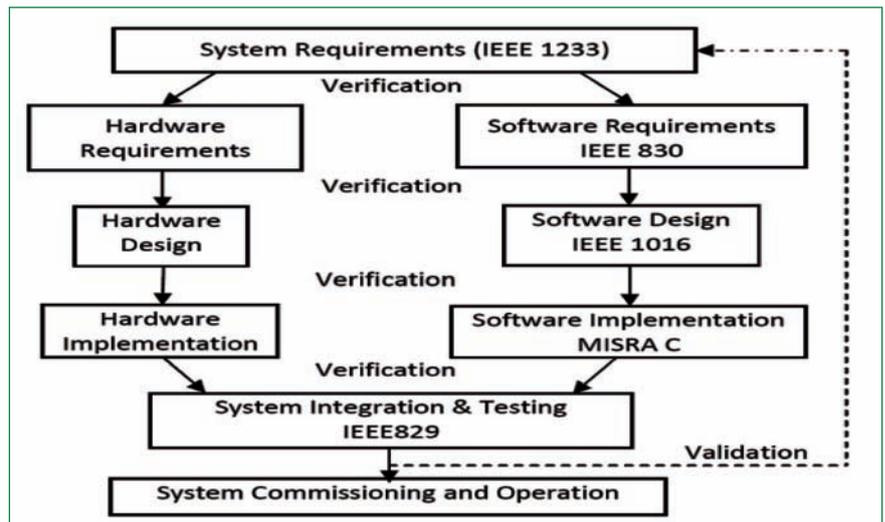
Fig. 2 *UWT instrumentation and control design methodology*

panel through plant backbone. The data packets are sent to display stations and Information packets are received at every 1 second. Command packets are received as and when it is initiated.

Integration and testing

UWT operations from console, panel of HCR and FB LCC are simulated and tested with the appropriate test cases. Static analysis of the code is carried out with in-house developed static analyzer and commercially available tools. Dynamic analysis is carried out by instrumental code. The system is verified at each stage. Installation and commissioning is being carried out.
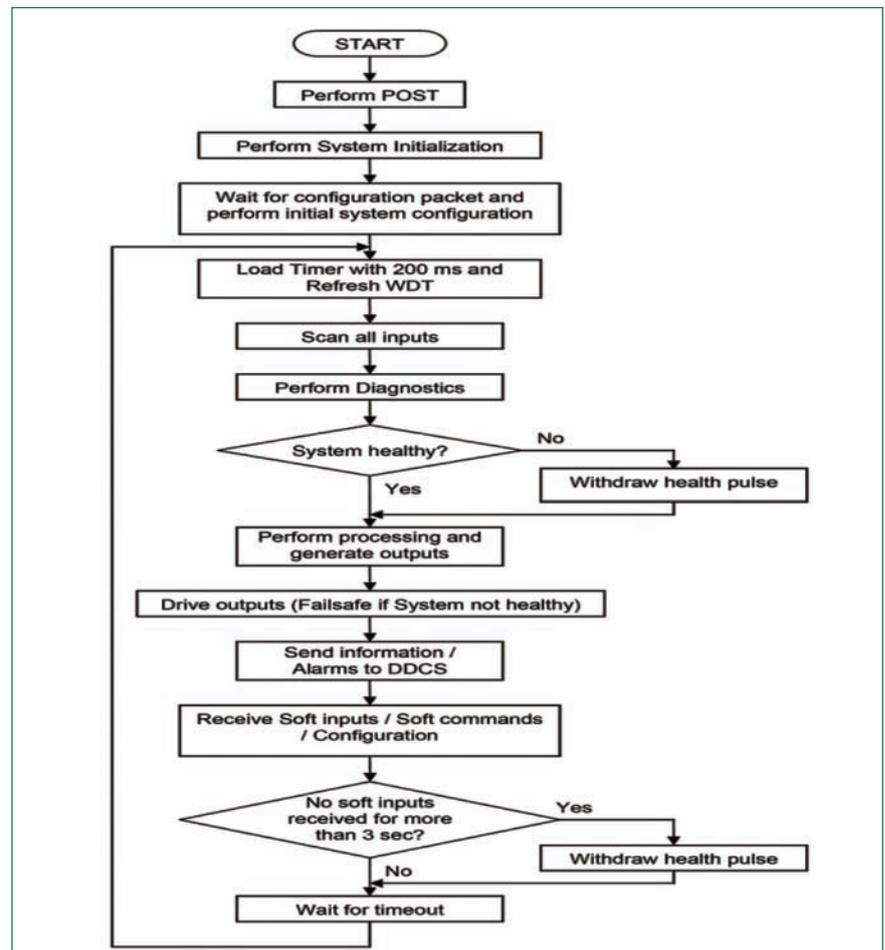
Fig. 3 *Flowchart for the UWT instrumentation and control system*

III.27 Design and Development of Application Specific Integrated Circuits for Fast Breeder Reactors

The instrumentation and control systems of a Nuclear Reactor can be broadly classified as:

a. Safety critical systems

b. Safety related systems

c. Non-nuclear safety systems

Safety systems (i.e. safety critical and safety related systems) are primarily responsible for the safe and efficient operation of the reactor. Further, these instrumentation and control systems should also undergo stringent qualification tests like electro-magnetic compatibility, environmental and seismic. After deployment, the systems need to be maintained at least for a period of 15 to 20 years. The instrumentation and control systems consist of hardware and software modules. The hardware modules (CPU board, various input/output boards and fine impulse test system) were designed and developed using programmable logic devices (PLDs). The hardware modules developed have been tested extensively in the field for their performance in Fast Breeder Test Reactor. The performance of these designs was found to be satisfactory. Based on the field experience gained, PLDs are used extensively in the hardware modules of the safety instrumentation & control systems of Prototype Fast Breeder Reactor (PFBR).

However, as PLDs are rapidly evolving and becoming obsolete in a short span of time (typically 5-6 years), compared to the reactor's life time of about 40 years, to tackle the obsolescence problem, it was decided to explore the feasibility of fabricating ASICs using Indian foundry for some of the proven digital designs used in safety systems designed using PLDs. As a first step, two designs were selected for ASIC fabrication and the details are as follows:

32-bit error detection and correction ASIC

Error detection and correction (EDAC) provides detection & correction of single-bit errors, detection of all double bit errors for both hard and soft errors in memory devices. It supports partial-word-write operations, parity generation and checking on data bus. EDAC is used for ensuring the data integrity of the main memory of the 32-bit versa module European (VME) central processing unit (CPU) card. Currently, FPGA version of this EDAC ASIC has been used in VME CPU card which is being used in real time computer (RTC) based instrumentation and control systems for Prototype Fast Breeder Reactor (PFBR).

Figure 1a shows the Graphic Data System Information Interchange (GDS-II) of EDAC ASIC, Figure 1b shows the EDAC ASIC and Figure 1c shows the target VME CPU card used for testing the EDAC ASIC.

Glue logic ASIC for VME relay output card (ROC)

ROC ASIC for VME relay output card is designed for custom integration using standard ASIC technologies. It is fully compliant to the VME specification supporting A16 address and D16 data modes. Unique features includes diagnostic read/write register, reconfigurable watchdog timer, relay contact read-back and clock fail detection for ensuring fail safe operation of safety systems in Nuclear Power Plant. VME bus timing is guaranteed by using a system clock of 16 MHz.

Figure 2a shows the GDS-II of ROC ASIC, Figure 2b shows the ROC ASIC and Figure 2c shows the target VME Relay Output Card used for testing ROC ASIC.

Designs were modeled using Verilog HDL. Comprehensive test suites were developed for exhaustive verification and sign off at foundry. Design, fabrication, packaging and target testing has been completed. These ASICs were also successfully tested for dry cold, dry heat and temperature cycling environmental qualification tests as per Indian Standard (IS) - 9000. This developmental activity has proved that ASICs are feasible to be designed, developed and fabricated in association with Indian semiconductor foundry and a promising choice for use in safety instrumentation and control systems of future fast reactors.
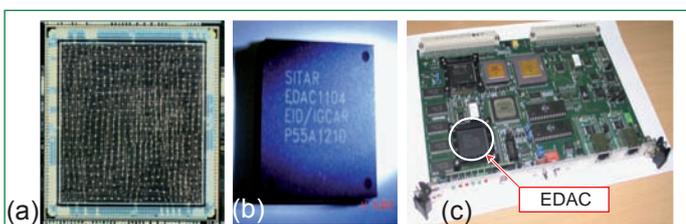

Fig. 1 EDAC (a) ASIC GDS-II, (b) ASIC and (c) ASIC testing on VME CPU
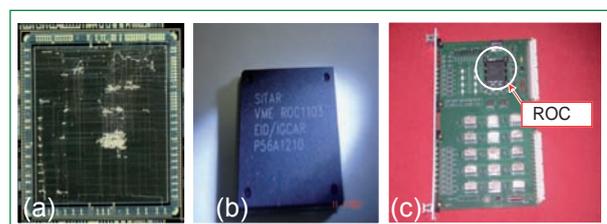

Fig. 2 ROC (a) ASIC GDS-II , (b) ASIC and (c) ASIC test card

III.28 Reliability Analysis of Control Logic of SGDHRS Dampers

In PFBR, decay heat is removed through one of the following heat transport systems: (1) safety grade decay heat removal system (SGDHRS) and (2) operational grade decay heat removal system (OGDHRS). OGDHRS is the normal heat transport path for operational as well as DHR functions. However when there is a failure of OGDHRS due to component failures in secondary or steam water circuit or loss of offsite power (LOP), SGDHRS is called into operation to remove decay heat.

In the present analysis the probability of damper failing to open on demand is calculated. The present report models the control logic and actuators for both electrical and pneumatic dampers of SGDHR system in detail with a Bayesian updated estimator for mechanical part. The SGDHR system consists of four identical Decay Heat Removal loops of each 8 MWt heat removal capacity at a hot pool temperature of 820 K. The decay heat exchanger transfers heat from radioactive primary sodium to intermediate sodium. The air heat exchanger dissipates heat from intermediate sodium to atmospheric air. The intermediate sodium flow by natural convection is obtained by placing the thermal centre of air heat exchanger ~ 41 m above the thermal center of decay heat exchanger. The drive force for the flow of air over the finned tubes of air heat exchanger is obtained by providing a stack of height 30 m. During normal plant operation, to minimise the heat loss, pneumatic and motorised dampers provided at the inlet and outlet of air heat exchanger are kept crack open permitting certain amount of natural circulation in the SGDHR circuit to
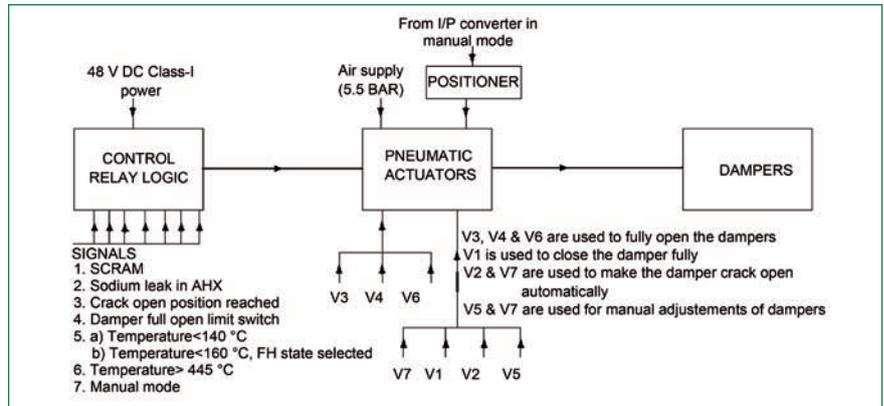
Fig. 1 *Control logic for pneumatic dampers*

enable smooth change over to decay heat removal mode when required. The air dampers are opened on auto mode when the SGDHR system is required for decay heat removal. The dampers can be opened by manual command from the control room. If manual operation from control room also fails, dampers can be opened manually by sending operators to the damper site.

On failure of control power supply, the pneumatic and electric dampers are driven to fully open position. On failure of pneumatic supply, the pneumatic operated dampers are driven to full open and on failure of electrical power, motorised dampers will remain "stay put". It is admissible to raise the reactor power to full power only when all the four loops are available. In other words, if one safety grade decay heat removal system loop becomes

unavailable during normal operation of the reactor on power, reactor is shutdown through the controlled shutdown mode. Pneumatic and motorised dampers (2 x 50% area) are provided on either side of the exchanger in the air circuit. The dampers located downstream are used as open/close device and has no control function. The dampers located upstream are used for control of air flow.

The damper control logic for pneumatic and electric dampers in block level are shown in Figures 1 and 2. Relay logic has various relays to implement the damper open/close logical conditions with relays in fail safe configuration. System boundary considered for this analysis extends from the SCRAM signal contact in the control logic of electrical and pneumatic damper to the mechanical part
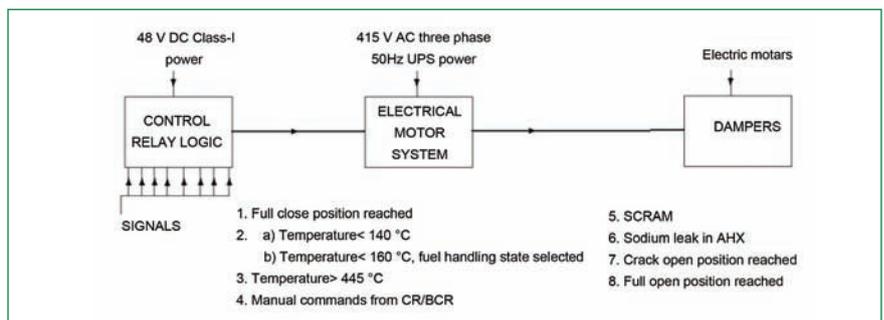
Fig. 2 *Control logic for electric dampers*

of damper. It includes relay logic and relay contacts, power supply, actuators, valves and mechanical part of the damper. The success criteria considered for this analysis is the damper moves from partial open/closed position to full open position.

The support systems considered for this analysis are Class-II power supply for the motor of electrical dampers and compressed air system for pneumatic dampers. Failure of Class-I control power supply is not modeled as it is fail safe. The damper opening logic system of safety grade decay heat removal system is modeled using fault tree analysis using the immediate cause approach. The fault trees were developed from ladder logic diagrams. The fault tree top event is damper failure to open on demand and spurious closure of damper. A portion of the fault tree developed for pneumatic damper is shown in Figure 3. The analysis was carried out using RISKSPECTRUM software. All components in the system are periodically tested. Failure of
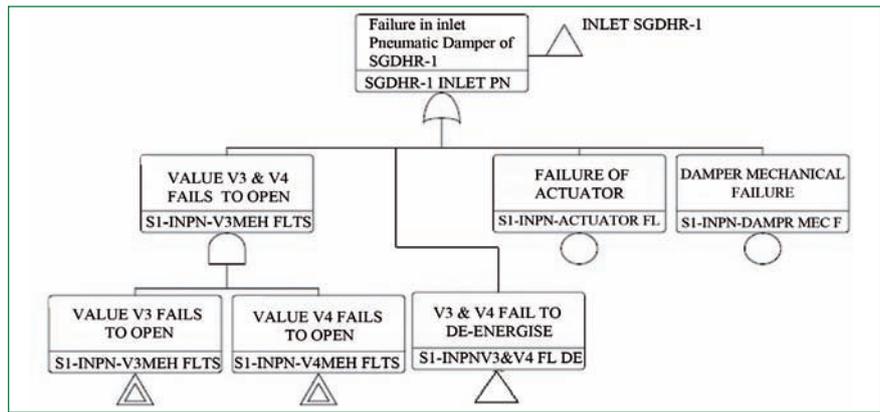

Fig. 3 Schematic fault tree for pneumatic damper

Class-I control power supply will lead to opening of dampers. Since the unavailability of any one division of Class-I power supply is 1.2 E-06, the number of damper openings due to control power supply failure when there is no demand is negligibly small. Common cause failure analysis is carried out using beta factor model. A beta factor of 10% is used for valves, 5% for divisions of Class-II power supply and a beta factor of 5% for relays. Operator intervention is considered for operating the Class-II division bus coupler in the present analysis.

A sensitivity study on damper control logic reliability on test interval was

carried out. When the test interval for damper logic is increased to 7 days, the contribution of relay contacts to damper failure probability is ~14% in the case of electrical dampers and ~11% for pneumatic dampers. In all other cases the contribution of relay contacts to damper failure probability is less than 10%. The probability of failure of damper to open on demand is 1.6E-03 for electrically operated dampers and 1.4E-03 for pneumatically operated dampers. The failure probability is dominated by the failure in mechanical part of the dampers and to a lesser extent by the failure of motors in electrically operated dampers.

III.29 Reliability Evaluation of Emergency Diesel Generator System by Fault Tree Analysis

The availability of alternating current (AC) electrical power is essential for the safe operation of Nuclear Power Plants (NPPs) and prevention or mitigation of accidents. Offsite power sources normally supply the essential power from the electrical grid when the plant is connected. If the plant loses offsite power, highly reliable emergency diesel generators provide onsite AC electrical power. A total loss of AC power is referred as "station blackout" occurs as a result of complete failure of

both offsite and onsite AC power supplies. Unavailability of power can have a significant adverse impact on a plant's ability to achieve and maintain safe-shutdown conditions. Station blackout probability is highly sensitive to emergency diesel generator performance, and diesel generator unavailability can significantly increase the station blackout risk. Thus the detailed reliability evaluation of diesel generators set is very important. One such study is carried out by fault tree analysis method based on

the function flow diagram of each diesel generator subsystem.

Reliability modeling of diesel generator system

The analysis has been done on a typical diesel generator set taking one of the recent diesel generator set ordered for PFBR plant as reference. The boundary of the diesel generators train applied in this analysis is shown in Figure 1. This includes diesel engine, electrical generator, starting air system, diesel fuel oil system, cooling water system, lube oil system, charge air

and exhaust gas system, governor system, generator excitation and voltage regulator system, engine and generator control logic systems. The comprehensive reliability model of the diesel generator system is established based on the reliabilities of individual subsystems. Two failure modes of diesel generator i.e. "fail to start on demand" and "fail to run" were considered and analyzed separately. Fault tree of diesel generator system was developed and evaluated in ISOGRAPH software package.

Diesel generators fault tree was constructed with "diesel generator fail to function" as the top event and diesel generator "fail to start" and "fail to run" as the sub events. The main fault tree was divided into sub trees and each sub trees represent the failure of each subsystem. Each sub trees were developed further to reach up to represent the subsystem failure in terms of component failures. The failure rate or failure probability data for components were taken from generic reliability data sources. Failure data for some components were adopted from events reported in literature. The analysis was carried out with the assumption that all component failures are non-repairable and their distribution is exponential.

The basic events involving the failure of components, which are required to operate only at the time of diesel generator start (e.g. valve opening on demand, relay operation on demand), were modeled as 'fixed model' (fixed failure probability) in ISOGRAPH. This model is used in sub trees coming under diesel generators 'fail to start' mode of failures.

The components which are continuously working whether diesel generator is running or not (e.g. control panel power supply unit) were modeled as 'dormant' events and their unavailability is
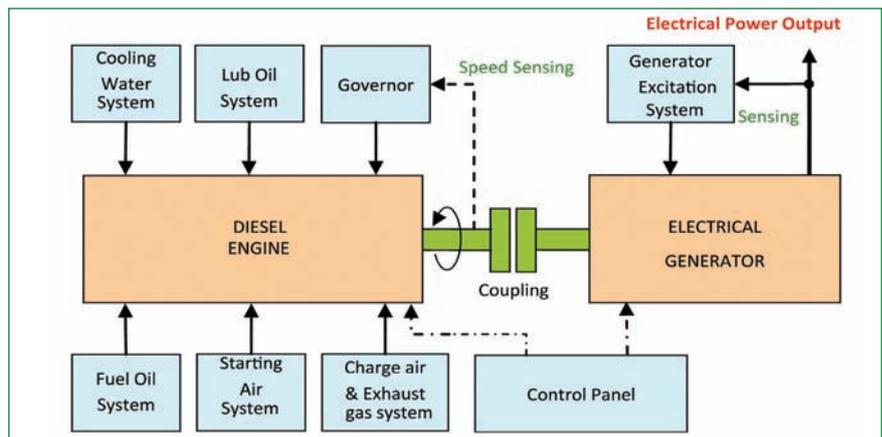
Fig. 1 *Diesel generator system boundary*

defined as

$$Q(t) = \frac{\lambda}{\lambda + \mu}(1 - e^{-(\lambda+\mu)t})$$

where,

Q = component unavailability

λ = component failure rate

τ = inspection interval

MTTR = mean time to repair

'Constant failure and repair rate model' was used to model the component failures which are dependent on the operation time. The unavailability of a component represented by this model are given by

$$Q = \frac{\lambda.\tau}{2} + \lambda.MTTR$$

where,

Q = component unavailability

λ = component failure rate

μ = component repair rate
      (1/MTTR)

Common cause failure parameters are applied for redundant component groups (e.g. redundant air starting valves in diesel generator starting system). Beta factor modeling was used for this purpose and generic common cause failure model parameters were mainly taken from "common cause failure parameter estimations update 2010" by USNRC. Whenever common cause failure model parameters are not available for a redundant group of components, beta factor of 5% was assumed. These factors were provided in event modeling window of ISOGRAPH.

Diesel generator reliability results

Diesel generator subsystem fault tree models were evaluated for assessing the equivalent diesel generator failure rate. All diesel generator subsystems including fuel oil system, lube oil system, engine, electrical generator etc were analyzed. From the analysis it is found that diesel generator 'fail to start' and 'fail to run' rates are 2.27E-03 per demand and 7.93E-04 per hour respectively. Diesel generator subsystem wise equivalent failure rate is given in Table 1.

Table 1: DG subsystem wise equivalent failure rate			
S L No	Subsystem	Failure rate / probability	
		Fail to start	Fail to run
1	Fuel oil system	1.06E-05	4.14E-04
2	Starting air system	5.51E-04	--
3	Cooling water system	3.00E-05	1.15E-04
4	Charge and exhaust gas system	1.63E-05	1.17E-05
5	Lub oil system	2.00E-05	7.92E-05
6	Engine	2.02E-04	1.14E-04
7	Governor	2.86E-04	1.29E-05
8	Electrical generator	5.38E-04	2.18E-05
9	Generator excitation system		1.86E-05
10	Control logics	6.15E-04	5.90E-06
	Total	2.27E-03	7.93E-04

Diesel generator fail to start probability is mainly contributed by starting air system and control logics system. Starting air system failure probability is dominated by failure of solenoid operated valve for changing the fuel rack position followed by common cause failure of main air starting valves. Control logic system failure is caused by failures of various relays.

Diesel generator fail to run is mainly contributed by fuel oil system followed by cooling water system and engine. Fuel oil system failures are dominated by fuel injector failures and fuel pump failures. Lube oil and cooling water system failures are dominated by failure of lube oil pump and cooling water pumps.

Reliability analysis of diesel generator to start and operate successfully up to its mission time is performed for different mission times of 1, 4, 8 and 24 hours. Unreliability of diesel generator in performing its function for different mission times is given in Table 2.

Table 2: DG mission time unreliability	
Mission time (hours)	Unreliability
2	0.003
4	0.005
8	0.009
24	0.021

From the above studies, it is established that diesel generator reliability to operate successfully up to its mission time is within targeted reliability of 0.975 even for scenario demanding continuous operation of diesel generator for 24 hours.

III.30 Rationale behind Design and Development of MDFR-500 and Core Design Options

IGCAR has identified thrust areas to be pursued simultaneously for the development of a robust indigenous metal fuel programme. Important among these include; carrying out key irradiation R&D with metal fuel in FBTR, embarking on design and development of metal fueled fast reactors, demonstration of pyro based metal fuel reprocessing program on prototypic scale etc. Towards R&D of the irradiation programme and detailed PIE, an elaborate road map involving testing of metallic fuel pins is evolved taking into consideration the operating conditions and core features of FBTR. Further, apart from pin level testing in FBTR, full subassembly based testing could also be realised as an additional confirmatory measure with possible availability of PFBR for testing of metallic fuels at a later date. It is planned to pursue the irradiation R&D programme with both sodium and mechanical bonded metallic fuels. While the reprocessing of mechanical fuel could be through the already proven aqueous reprocessing route, the sodium bonded metal fuel requires pyro based reprocessing program to be demonstrated on a prototypic scale

and hence, identified as a thrust area.

As a part of the design and development of metal fuel fast reactor, conceptualization of a 500 MWe Metal fuel Demonstration Fast Breeder Reactor (MDFR-500) has been undertaken. Considerable experience gained through operation of FBTR, apart from other several sodium test loops, coupled together with the successful indigenous design and development of 500 MWe PFBR, which is under advanced stage of construction, provide adequate

technological base for undertaking the challenging task. The design of the sodium cooled, pool type, MDFR-500 reactor system is proceeded through adopting proven design concepts as envisaged in MOX fueled FBRs and important variants are incorporated with due consideration to experience gained during safety review, manufacturing and construction of PFBR with a view to improve the overall economics and enhance the plant safety. The conceptualization of the reactor assembly (Figure 1) that forms part of the NSSS is
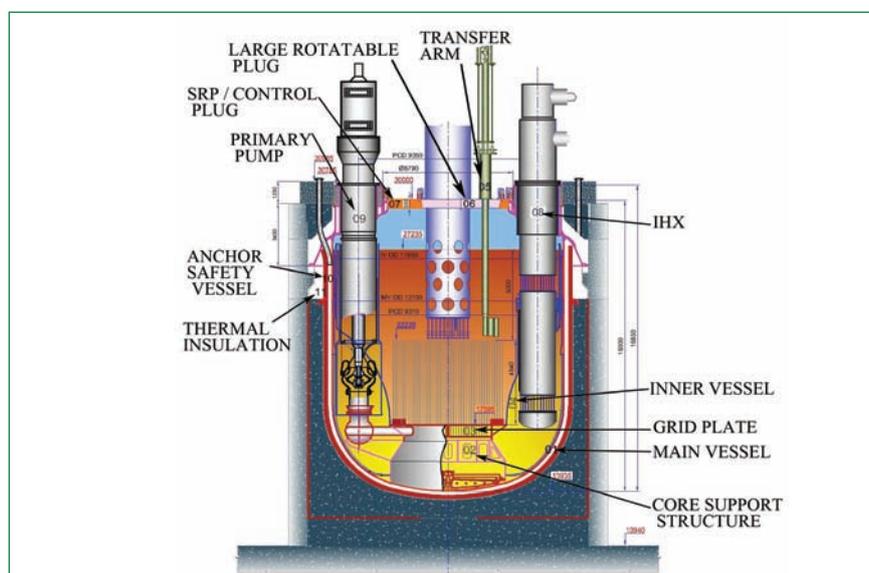

Fig. 1 Vertical section of reactor assembly

completed along with other major heat transport components such as sodium pumps, intermediate heat exchangers, steam generators, sodium storage tanks etc. The in-vessel and ex-vessel fuel handling schemes have been finalized taking in to consideration specific requirements for handling spent fuel with sodium bonding.

Towards maximizing the breeding ratio, several design options and fuel composition were evaluated with based on a common adaptable fuel pin and subassembly configurations that can accommodate either mechanical or sodium bonded in order that either of the options would not call for any change in the reactor assembly and the associated fuel handling components. Also, this helps in adapting a suitable design commensurating with the maturity in the reprocessing technology i.e either pyro or aqueous based technology.

Fuel composition for sodium bonded pin is U-20w%Pu-10w%Zr and for mechanical bonded is U-15w%Pu. Fuel is slid into T91 clad of diameter 6.6 mm with 0.45 mm thickness. Mechanical bonded pin will additionally have Zr-4 as a liner of 150 μm thickness between fuel and the clad.

Active core of 1000 mm is sandwiched between blanket materials on either side for 300 mm each. Blanket material for sodium bonded pin is U-10 w%Zr and for mechanical bonded it is U metal. Uranium may be deeply depleted. The bond medium is sodium in the case of sodium bonded and helium for mechanical bonded fuel pin. Fuel and blanket materials are each provided with 75% smear density. In the case of mechanical bond, two semi-circular shaped longitudinal grooves are provided in fuel and blanket to accommodate swelling. In mechanical bonded pin, clad, liner and fuel are co-swaged together to create a perfect mechanical bonding amongst the three layers.

While the fission gas plenum can be provided only at the top for sodium bonded pin, it can be provided either at the top and/or bottom for the mechanical bonded fuel pin. In order to have unified design, the current design incorporates fission gas plenum for both the options. Plenum length is chosen based on the fission gas induced stress on the clad for a cumulative damage fraction limit of 0.25 for a target peak burn-up of 100 GWd/t. For sodium bonded pin, plenum space is also provided for accommodating the expelled sodium across the fuel and blanket column when the fuel and blanket makes contact with the clad due to its swelling and also to house an initial excess sodium level above the core to provide necessary bonding for the length of axial extrusion of the core. The pins are fitted with end plugs at both the ends and welded. A spacer wire made of T91 material is wound helically over the pin and welded at the top end plug. The pin length is 3.3 m and is shown in Figure 2.

The subassembly consists of fuel pin bundle and shield at the top and as well at the bottom. Due to the absence of bottom plenum and because of the relatively harder neutron spectrum in the metallic core and from the consideration of limiting dose on grid plate to 1 dpa, about 50 cm ferro boron (FeB) is provided as the lower axial shield in MDFR-500 for the design life of 60 years. Other components like foot assembly, head assembly, etc.,
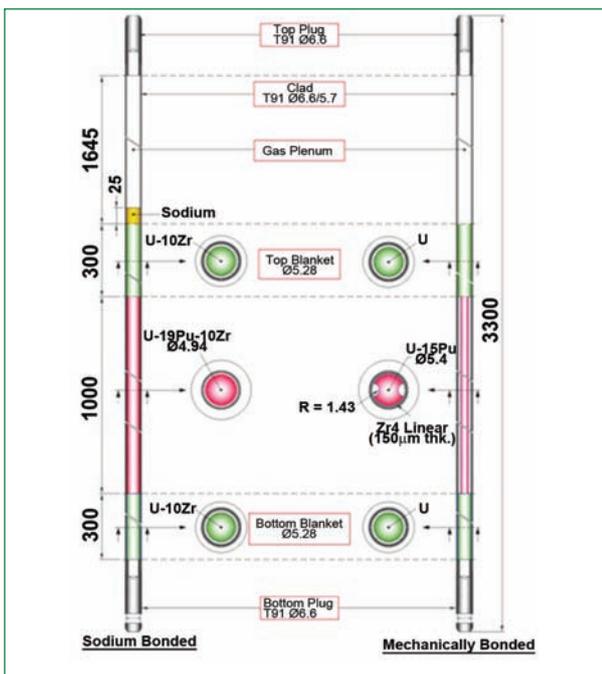

Fig. 2 *Metal fuel pins*
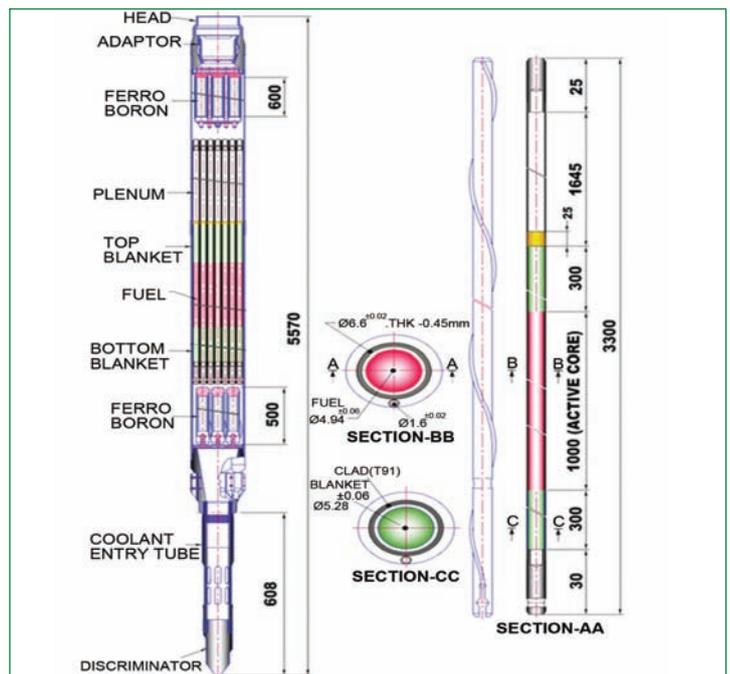
Fig. 3 *MDFR-500 fuel subassembly (typical)*

remain the same as in the case of MOX fuel subassembly. Due to longer fuel pin and incorporation of lower axial shield, subassembly is 5.57 m long. A typical metal fuel subassembly which can house either sodium or mechanical bonded pin is shown in Figure 3.

The physics parameters of MDFR core are being finalized for both the types of subassembly designs. While breeding ratio of greater than 1.3 is achievable in the core, all efforts are being directed towards reducing the sodium void coefficient initially to that MOX fuel subassembly with a final target of nil sodium void coefficient. Based on experiments carried out in KAMINI, ferro boron (FeB) is identified as the bulk radial shield material. The selection of FeB facilitates in reducing the radial shield thickness and thus brings down the number of radial shield rows. The safety aspects of different cores are also being assessed in parallel towards finalizing the core designs for both sodium bonded and mechanical bonded options.

III.31 Achievements in Advanced Solid Mechanics Relevant to SFR

The design and performance of Commercial Fast Breeder Reactor depends greatly on the level of implementation of advanced solid mechanics. Solid mechanics plays an important role in the design, manufacturing, operation, reliability and life prediction of reactor component. The area of application of solid mechanics in structural analysis can be attributed to different fields' namely structural design, structural integrity assessment, material modeling, and structural dynamics.

The objective of R&D projects with reference to sodium cooled fast reactor is to quantify design margin and safety margin. The precise determination of available margins requires exact modeling of parameters governing the behavior of the component. The operating environment of reactor consists of the thermal hydraulics of molten sodium metal, nonlinear dynamics of reactor component and their interaction with surrounding fluid, complex material responses at elevated temperature. Therefore a series of problems in the field of solid mechanics have been taken up as collaborative project with IIT Kanpur.

Thermal ratcheting in cylindrical pipes due to axially oscillating temperature front

Studies related to the evaluation of thermal ratcheting in reactor component have been performed. Component where fluctuating sodium free level exists such as main vessel or radial thermal gradient with primary stress such as fuel pin are prone to thermal ratcheting and every component must respect the ratcheting limits for the entire life of the component. The phenomenon gets further complicated by the complex cyclic behavior of austenitic stainless steel. This problem is solved in two parts. The first part deals with the solution of transient heat transfer equation with time varying boundary condition. It was solved using in house code as well as commercial codes for confirmation. Second part deals with the development of theoretical model based on the upper bound shake down theorems. A general procedure is developed to predict the shakedown corresponding to given deformation shape and it could further be utilized setting up design rules against ratcheting.

Dynamics of a single fuel subassembly in a loose bearing

The reactor core of the fast breeder reactor consists of 1258 subassemblies which comprises of fuel blanket, reflector and shielding subassemblies. Each of these subassemblies are supported at the bottom by inserting the subassembly into the sleeve provided in the grid plate. The smooth movement of the subassemblies during the loading and unloading are ensured by providing clearance fit between the foot of the subassembly and the grid plate sleeves. For exact prediction of the response of the subassemblies under dynamic excitations such as seismic loading conditions, the exact boundary conditions between the subassembly foot and the grid plate sleeves is to be modeled by considering the effect of clearance and the presence of the fluid in the interspace. This interesting and challenging problem is addressed through a collaborative project with IIT Kanpur titled "dynamics of single fuel subassembly - effect of the nonlinearity introduced due to clearance". In this work, mathematical model for a single PFBR subassembly is developed which is capable of simulating the effect of clearance between subassembly and sleeve. The differential equations for predicting the response under forced/base excitation is developed by introducing the effect of clearance in the form of hertian spring and the presence of fluid in the clearance space is modelled by equivalent nonlinear spring. Figure 1 shows the supporting arrangement

and schematic of the assumed mathematical model. Three different sets of approximating functions have been used for formulating the response viz Fourier series, the set of polynomial and the cantilever model superposed on a linear function. The validity of the approximate formulation is verified by comparison of the results obtained using approximate analysis with exact modal analysis. It is found that the approximation involving cantilever modes superposed on a line give results with high accuracy. So this approximation is used for the response calculation of the subassembly under forced excitation. To model the impact of the subassembly with the sleeves hertzian 3/2 power law springs are used.

To validate the proposed model, experimental investigations are carried out by developing a set up which consists of a long hollow pipe representing the subassembly which is connected to another smaller pipe which represents the subassembly foot as shown in Figure 1b. The smaller pipe is inserted in a cylindrical cavity containing fluid representing the sleeve portion. Experiments are performed with different fluids in the interspace between sleeve and the subassembly foot. Subassembly responses are recorded using accelerometers and strain gauges. It is observed that the response of the subassembly largely remains the same with different fluids. Comparison of experimental observations and numerical results shows fairly good match. The formulations developed in this work can be easily implemented in the commercial finite element software for further studies.

Understanding parametric Instability in fluid filled thin walled vessels

The fast breeder reactor consists
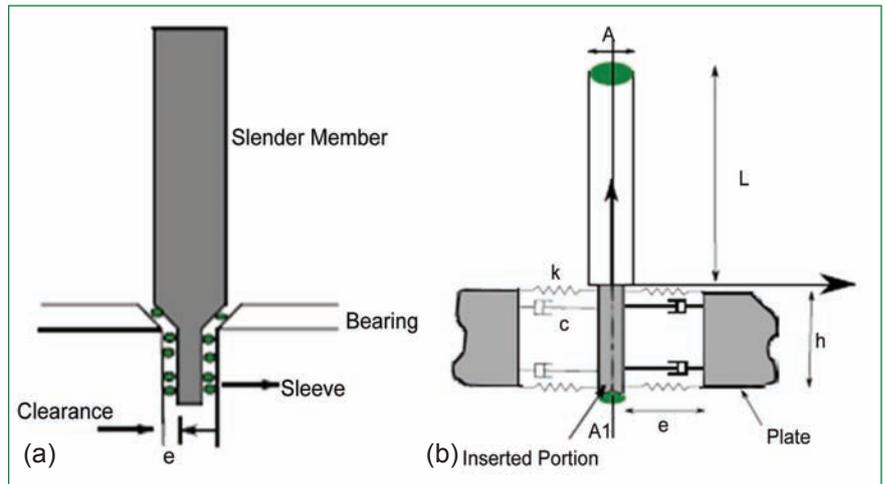
Fig. 1 *Modeling of fuel subassembly (a) mounting of subassembly in sleeve and (b) assumed mathematical model*

of two thermal baffles inside main vessel one is outer baffle and the other is inner baffle. These two baffles are used to cool main vessel below creep region. The annular space between main vessel and outer baffle is called feeding collector and that between outer and inner baffles is called restitution collector. The cold sodium is sent through this feeding collector, thereby cooling main vessel, then over flows the outer baffle and joins the restitution collector. The radial gap for the feeding collector is very less (i.e. 100 mm) and the flowing sodium in the gap is incompressible. Hence the added mass of sodium in this gap is very large. So the natural frequency of the outer baffle with fluid structure effect is low.

With the above background when the seismic excitation takes place there will be very high pressure rise in the gap of feeding collector. This high pressure will act external to the outer baffle and internal to main vessel. This high pressure acting external to the outer baffle will produce buckling of the outer baffle. The pressure in the feeding collector is not static which can be analysed using any commercial finite element model codes. But the pressure is dynamic nature which needs some detailed study. This particular study

was undertaken by IIT-Kanpur. The governing differential equations for dynamic buckling of baffle have been derived for general purpose. After that the proper boundary conditions of PFBR have been applied and then the appropriate solutions for critical buckling loads are obtained.

After completing the above project for critical buckling load of thermal baffle, the same problem of seismic excitation due to baffle response is undertaken by IIT-Kanpur. This new project is going to be a complete study for the dynamic buckling of thermal baffles under seismic excitation with the effect of fluid structure interaction.
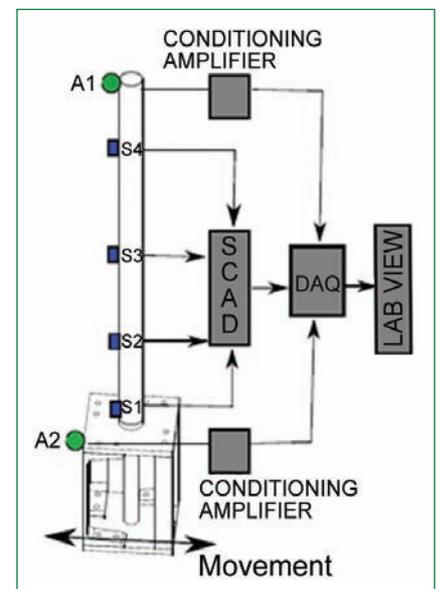

Fig. 2 *Experimental setup*

III.32   Electroextraction of Boron from Boron Carbide

High-density pellets of boron carbide, containing boron enriched in ^{10}B isotope (~67 at.%) will be used in the control rods of the India's first prototype fast breeder reactor (PFBR). Boron carbide powder is synthesized by a high temperature reaction between boron and carbon. The powder thus obtained is subsequently hot pressed to produce high-density boron carbide pellets. An exhaustive physicochemical characterization of boron carbide pellets was carried out to ascertain the suitability of these pellets for control rod applications in fast reactors. Those pellets which do not meet the technical specifications are rejected (~10 %) during quality control. Synthesis of isotopically enriched boron (^{10}B > 20 at. %) is a time consuming and energy intensive process. It is advantageous to recover the enriched elemental boron from those boron carbide pellets which are rejected for not meeting the chemical specifications of nuclear grade boron carbide. There is a need to develop a methodology to recover isotopically enriched boron (^{10}B > 20 at. %) from these rejected pellets.

A pilot plant facility was established to study the viability of electroextraction process for the large scale extraction of boron from boron carbide.

An electrolytic cell designed and fabricated for the electroextraction of boron from boron carbide is shown in Figure 1. The electrolytic cell consisted of a cylindrical vessel (height: 710 mm, OD: 273 mm) made out of inconel-600. A liner made up of nickel (purity ~ 99 %) was placed inside this vessel. A high-density (ρ = 1.84 g cm^{-3}) graphite crucible (height: 300 mm, OD: 240 mm) was used as the container for the
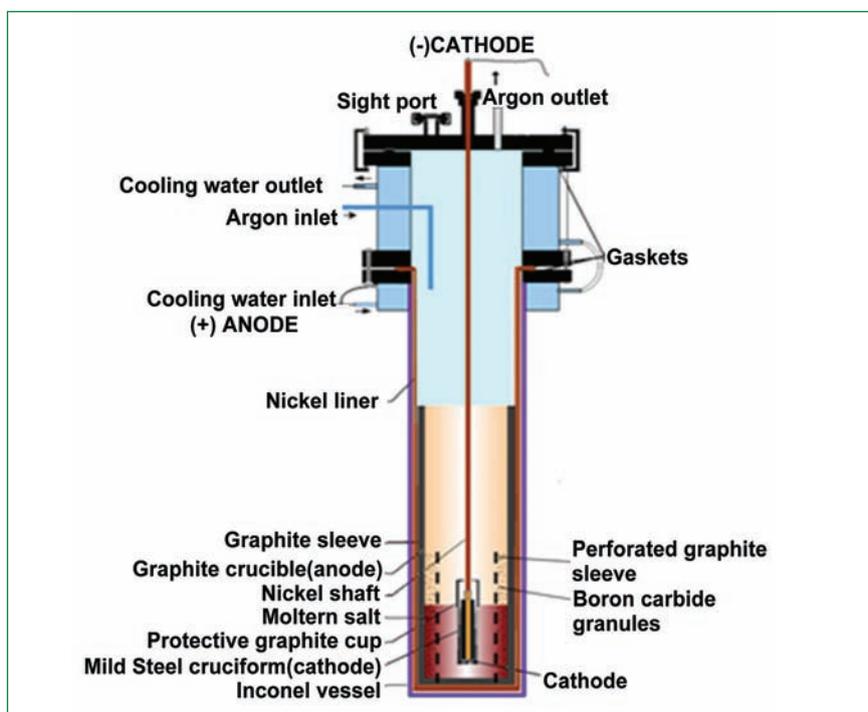

Fig. 1 Electrolytic cell

molten salt mixture. It was placed inside the nickel liner. A graphite sleeve (having the same height as that of the graphite crucible) was placed over the graphite crucible to prevent corrosion of the nickel liner by salt vapours. A perforated graphite sleeve (OD: 150 mm) was placed inside the graphite crucible. The annular space thus created between the graphite crucible and the perforated graphite sleeve was filled with granules of boron carbide which acted as the consumable anode. In addition to this, boron carbide granules were placed in the form of a layer (50 mm thick) at the bottom of the graphite crucible.

A mixture of KCl (40 wt. %), NaCl (40 wt. %) and KBF$_4$ (20 wt. %) salts was used as the electrolyte. Electroextraction was carried out by applying a potential of 1.5 V at 1073 K. During the electrolysis, boron was electrodeposited on mild steel cathode.

Elemental boron of~92 % purity was electroextracted from

boron carbide. The product was characterized for its physicochemical properties (bulk density, specific surface area and size distribution of the particles). The powder exhibits near bi-modal distribution of sizes with more than 50 vol. % of the particles having sizes in the range of 1 to 30 μm. The x-ray diffraction (XRD) pattern of the electroextracted boron showed that the powder is partially crystalline in nature. The major crystalline phase was found to be β-rhombohedral. The morphology (SEM) of the particles shows the particles to be irregular in shape. The crystalline nature of the sample was further confirmed by transmission electron microscope (TEM) analysis of boron. The average size of the particles vary from 25 nm to 40 nm. It has thus been established that molten salt electroextraction process can be used for the recovery of enriched elemental boron from enriched boron carbide scrap generated during the production.
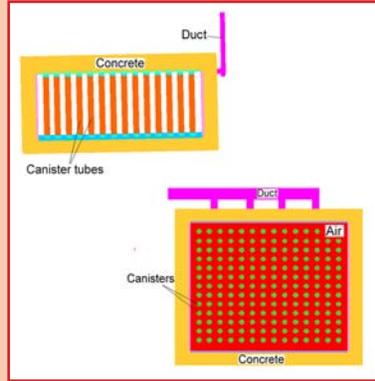
Fuel Cycle

IV.1 Fast Reactor Fuel Cycle Facility

Financial approval for the project, Fast Reactor Fuel Cycle Facility (FRFCF), to close the fuel cycle of Prototype Fast Breeder Reactor has been received. The work on this mega project is being piloted by Indira Gandhi Centre for Atomic Research with technical support from Bhabha Atomic Research Centre and Nuclear Fuel Complex. Approval of Atomic Energy Regulatory Board for the construction of Fast Reactor Fuel Cycle Facility has been obtained. Basic infrastructure like approach roads, construction power supply system, workshop, storage and construction office space has been created at the site to facilitate speedy commencement of the construction work.

Two major construction work tenders have been issued. These are in an advanced stage of processing for release of work orders to contractors. Prequalification of contractors for
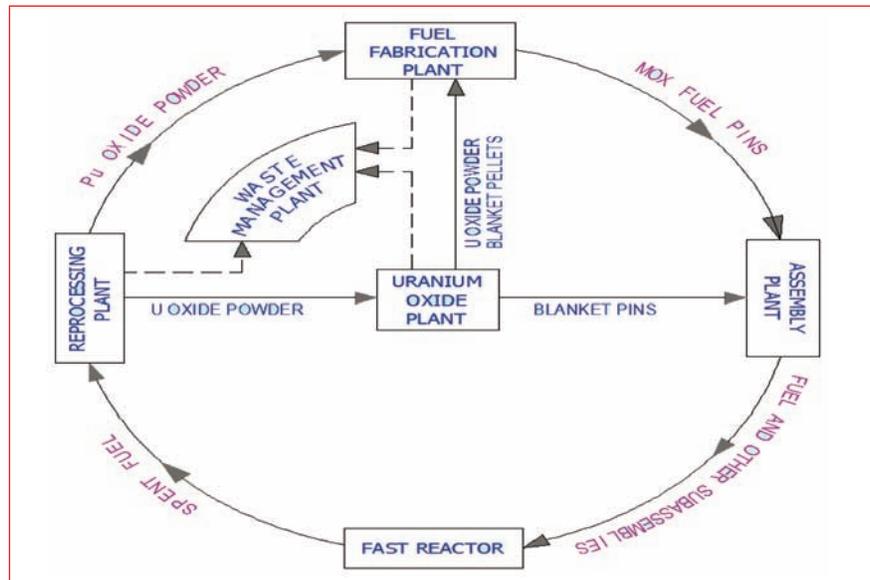
Fig. 1 Process flow diagram of the fast reactor fuel cycle facility

construction of the plant buildings has been completed. Tenders for the plant building constructions have been prepared and are ready for issue. Procurement action for large value materials like lead and stainless steel has been initiated.

Resources needed for initiating work on all fronts for achieving fast progress are being mobilised.

Successful commissioning of Fast Reactor Fuel Cycle Facility will herald launching of work on the second stage of nuclear power plants based on plutonium fuel and pave the way for achieving energy security of the nation.

Process flow diagram and perspective view of the Fast Reactor Fuel Cycle Facility are shown in Figures 1 and 2.

LEGEND:
1. ADMINISTRATIVE BUILDINGS
2. CENTRAL WORKSHOP
3. CENTRAL STORES
4. MAIN POWER STATION
5. AIR CONDITIONING PLANT
6. FUEL RERPOCESSING PLANT (FRP)
7. WASTE MANAGEMENT PLANT (WMP)
8. CORE SUBASSEMBLY PLANT (CSP)
9. FUEL FABRICATION PLANT (FFP)
10. REPROCESSED URANIUM OXIDE PLANT (RUP)
11. TRAINING CENTRE
12. CANTEEN
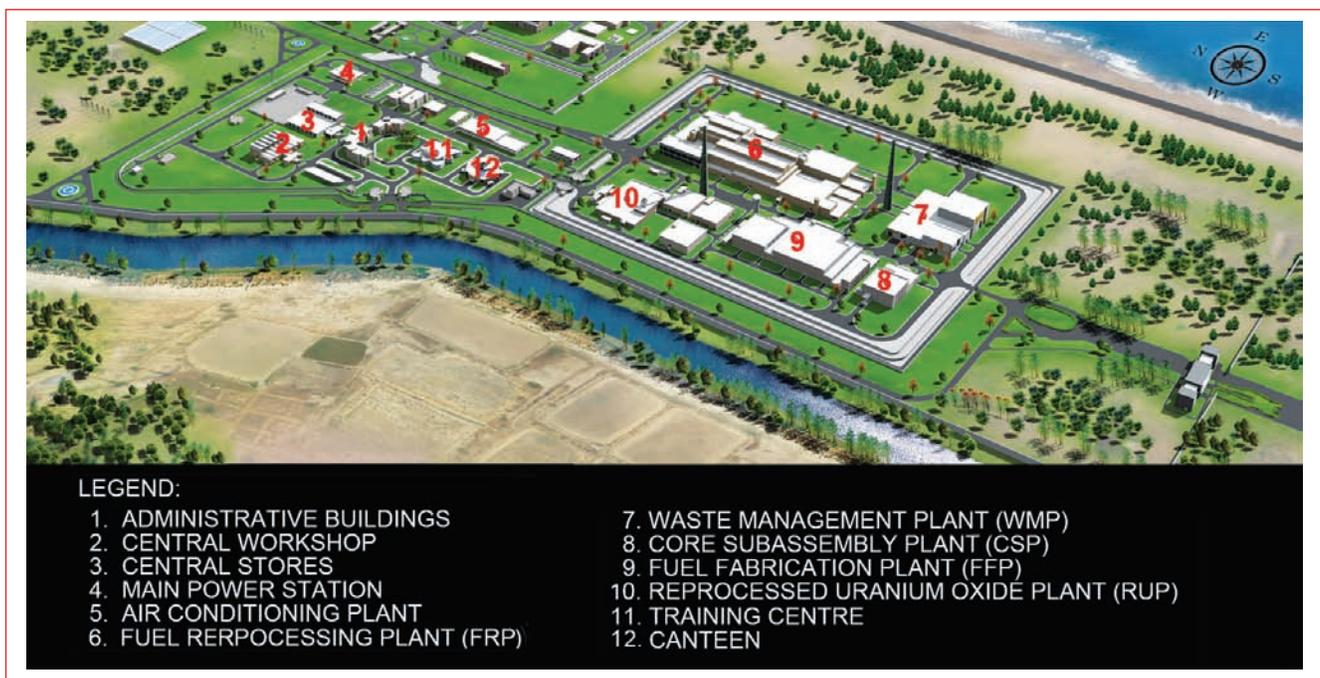
Fig. 2 Perspective view of the fast reactor fuel cycle facility

IV.2 Burn-up Measurements on (U,Pu) Mixed Oxide Fuel using HPLC-Mass Spectrometric Methods

The atom percent burn-up of a fuel is the number of fissions per 100 initial heavy element atoms. Burn-up is a measure of energy produced and is an important parameter for the study of fuel performance. The measurement of the burn-up of a nuclear reactor fuel subjected to high burn-up is challenging due to the high levels of radioactivity associated with the fuel. The isotope dilution mass spectrometric technique (IDMS) and HPLC (high performance liquid chromatography) based techniques earlier developed in our laboratory for rapid and accurate determination of the burn-up, measure the concentration of a selected fission product (burn-up monitor) and that of the residual heavy elements present in the spent fuel to deduce the burn-up. The criteria for choosing a particular fission product monitor stems from the desired nuclear properties such as fission yield, neutron absorption cross section, decay constant and its migration in the fuel matrix.

The determination of burn-up of uranium-plutonium mixed oxide (MOX) spent fuel was carried out using its dissolver solution by HPLC and mass spectrometric methods. The pure fractions of neodymium, uranium and plutonium required for mass spectrometric studies are conventionally obtained using time consuming traditional ion-exchange chromatographic technique. However, to reduce the separation time, radiation exposure and waste volume generation, these metal ion fractions were rapidly isolated employing HPLC technique. The MOX dissolver solution was injected into the HPLC system for the isolation of desired fractions of
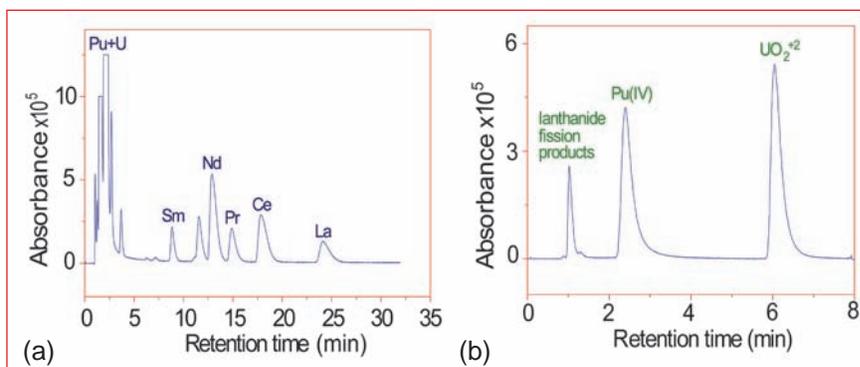
Fig. 1 *(a) Direct injection of MOX dissolver solution into HPLC for the separation and determination of lanthanide fission products and (b) separation and determination of uranium and plutonium in dissolver solution of MOX fuel by reversed phase chromatography ; detection: post-column reaction with arsenazo(III) at 655 nm*

fission products and actinides. For the first time, this procedure for separating the elements required for burn-up determination has been developed in our laboratory. The fractional fission and the atom percent fission were computed based on these measurements.

The burn-up measurements of MOX fuel pellets were carried out on a test irradiated fuel, discharged from Fast Breeder Test Reactor (FBTR). The U-Pu mixed oxide fuel with 29 ± 1 % PuO_2 (76% ^{239}Pu in total plutonium) and UO_2 enriched in ^{233}U (53.5% ^{233}U in total uranium) was used. One of the irradiated fuel pellets was dissolved in 11 M HNO_3 medium in the hot cells. An aliquot of the dissolver solution containing uranium, plutonium and fission products in HNO_3 medium was directly injected into the HPLC system with appropriate dilutions.

All the three fractions (uranium, plutonium and neodymium) obtained from HPLC separation were analysed by isotopic dilution thermal ionization mass spectrometric (ID-TIMS) measurements. In the present work, neodymium fraction was obtained by its isolation from

other lanthanide fission products using dynamic ion exchange chromatographic technique, whereas pure fractions of uranium and plutonium were obtained using reversed phase chromatographic technique. In the dynamic ion-exchange experiments, the reversed phase monolith column was modified using an ion-pairing reagent, camphor-10-sulfonic acid (CSA). The fission product monitor, neodymium was separated from other lanthanides using α-hydroxyiso butyric acid (α-HIBA). The mobile phase 0.02 M CSA+ 0.1 M α-HIBA, (pH adjusted to 3.1) was employed for the separation. Figure 1a gives the chromatogram showing the lanthanides present in the dissolver solution separated from each other as well as resolved from uranium and plutonium. The fission product monitors, neodymium/lanthanum, present in the dissolver solution were well separated from uranium (UO_2^{+2}) and Pu(IV). The concentrations of lanthanum, cerium, praseodymium and neodymium in the dissolver solution were determined using a calibration plot. Figure 1b (Mobile phase: 0.1 M HIBA, pH:

3.75) gives the chromatogram for the separation of uranium and plutonium present in the dissolver solution using reversed phase chromatographic technique with a monolithic C18 column and HIBA as the mobile phase.

Identical separation procedures were followed after the addition of spikes viz. ^{238}U, ^{239}Pu and ^{142}Nd. The pure neodymium, uranium and plutonium fractions obtained from chromatographic separations were evaporated to near dryness and re-dissolved in 1:1 M HNO$_3$ medium. This procedure i.e. dissolution of fractions in HNO$_3$ medium was repeated three times to minimize the organics (CSA and HIBA) during the loading of neodymium, uranium and plutonium fractions for TIMS analysis.

For determining the burn-up by HPLC technique, the following methodology was employed. The fission product lanthanum is mainly formed as mono isotopic (^{139}La) and allows the use of chemical technique for its assay. However, the lanthanum yields (y) for ^{239}Pu and ^{233}U fissions differ by ~11 %. Similarly, use of praseodymium (^{141}Pr) results in a difference in the "y" between ^{239}Pu and ^{233}U fissions by ~20 %. The neodymium isotopes produced in the fission are ^{143}Nd, ^{144}Nd, ^{145}Nd, ^{146}Nd, ^{148}Nd and ^{150}Nd for both ^{233}U and ^{239}Pu fissions. The total neodymium yield is 16.41 % and 17.43 % for ^{239}Pu and ^{233}U respectively, differing by about 6 %. Thus, using total neodymium as fission product monitor can be regarded as a better option than using praseodymium or lanthanum. Further, the difference in "y" gets minimized by employing fractional fission contributions from ^{233}U and ^{239}Pu for computing atom % burn-up. The fractional fission data was deduced from mass spectrometric measurements. The atom % burn-up was estimated to

be 10.7 by HPLC technique.

The isotopic compositions are given in Table 1 and Figure 2. Since the test fuel is a combination of plutonium recycled from thermal reactor and uranium enriched in ^{233}U to provide more fissile content, the fissions would be mainly contributed by ^{239}Pu and ^{233}U. Since one of the criteria for choosing a burn-up monitor is uniform fission yield from various sources of fission, different isotopes of neodymium were examined for deducing burn-up for this type of test fuel and the pair ^{145}Nd + ^{146}Nd having closely similar fast fission yields from ^{233}U (5.65 %) and ^{239}Pu (5.59 %) was chosen. The ratios of neodymium isotopes i.e. [^{145}Nd + ^{146}Nd] / [^{150}Nd] are widely different for these two sources of fission (12.12 for ^{233}U and 5.48 for ^{239}Pu). Hence, the mass spectrometric data for these isotopes have been chosen for computing the fractional fissions. The fractional fission contributions of ^{233}U and ^{239}Pu towards total fission are 54.2 % and 45.8 % respectively. The atom % burn-up deduced from the concentrations of uranium, plutonium and neodymium was 10.8 (total neodymium as monitor),

10.9 (^{148}Nd as monitor) and 10.9 ($^{145+146}$Nd as monitor).

The possible sources of error in the computed burn-up are those arising from assay of fission product monitor and that of heavy elements, data on the fission yield of the fission product monitors and computation of fractional fissions. The overall uncertainty arising from the individual contributions to the atom percent fission could be well within 3 %.

| Table 1: Isotopic composition of uranium, plutonium and fission products in the dissolver solution		
Element	Isotope	Composition (%)
Uranium	^{238}U	55.09
	^{233}U	43.23
	^{234}U	1.25
	^{235}U	0.397
	^{236}U	0.036
Plutonium	^{239}Pu	72.80
	^{240}Pu	24.27
	^{241}Pu	1.56
	^{242}Pu	1.14
	^{238}Pu	0.23
Neodymium	^{143}Nd	29.23
	^{144}Nd	23.81
	^{145}Nd	18.75
	^{146}Nd	15.06
	^{148}Nd	8.69
	^{150}Nd	4.46
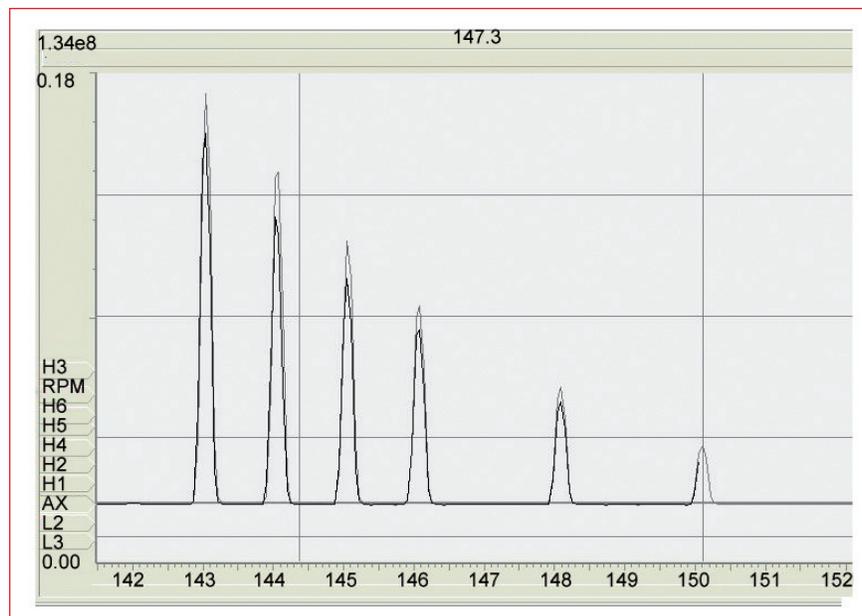
Fig. 2 *Isotopic composition of neodymium obtained from dissolver solution of MOX fuel*

IV.3 Solubility of TBP in Various Aqueous Solutions of Fuel Reprocessing

Tri-n-butyl phosphate (TBP) diluted with hydrocarbon is the most widely used solvent in PUREX (plutonium uranium extraction) process for the separation of uranium and plutonium from fission products, in the reprocessing of spent nuclear fuels. In the Interim-23 process, 5% TBP is used as the solvent for the separation of ^{233}U from irradiated thorium. Presence of trace amount of TBP in the aqueous waste solutions generated in the PUREX process is undesirable because it leads to violent exothermic reactions when the aqueous solutions are concentrated by evaporation. Several industrial accidents have resulted from the reaction of heated solutions containing TBP with nitrates or nitric acid. A concentration of as low as 5 mg/l of TBP and its degradation products is considered safe in the evaporator feed solutions, if the concentration factor is about ten times. Solubility data for TBP in aqueous medium (either for pure TBP or TBP in inert diluents) are incomplete in literature. Therefore, it is essential to generate solubility

data for TBP in pure form and TBP (diluted with hydrocarbon diluent) in different concentrations of nitric acid, in the presence of heavy metal ions and various fission products at room temperature. The solubility of 5, 20, 30 and 100% TBP in various nitric acid concentrations (0–15.7 M), the effect of uranium concentration on the solubility of TBP in 4 M HNO$_3$ and the effect of various fission products on the solubility of 30% TBP in 3 to 4 M nitric acid have been determined and the results are discussed.

Effect of nitric acid concentration

The solubility of TBP in varying concentration of nitric acid was determined by gas chromatography (GC). The peak area obtained in each case was compared with the calibration graph (Figure 1) constructed by injecting known volume of standard TBP solutions in n-dodecane. The graph is linear with the R^2 value of 0.996. The relative standard deviation was 5% at 2 ppm and 2% at 200 ppm of TBP.

Solubility curves generated for 5, 20 and 30% TBP at different
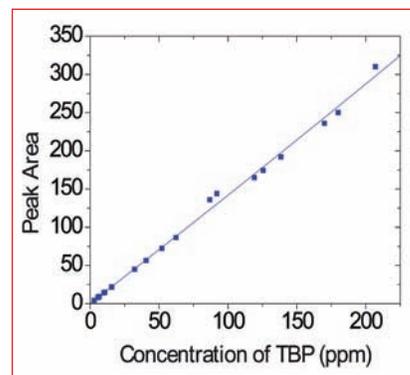
Fig. 1 *Calibration graph for dissolved TBP*

concentrations of nitric acid varying from 1 to 15.7 M are plotted in Figure 2 and the solubility curve for 100% TBP in nitric acid is shown in Figure 3.

Solubility of TBP in water is reported to be 1.54 mmol/l at room temperature. This solubility predictably decreases when inorganic solutes are added to water. Figures 2 and 3 reveal that a minimum solubility exists at about 8–9 M nitric acid. The decrease in the concentration of TBP in the aqueous phase at low acidities is due to the fact that in this range the dissolution of TBP takes place mainly as a result of transition of
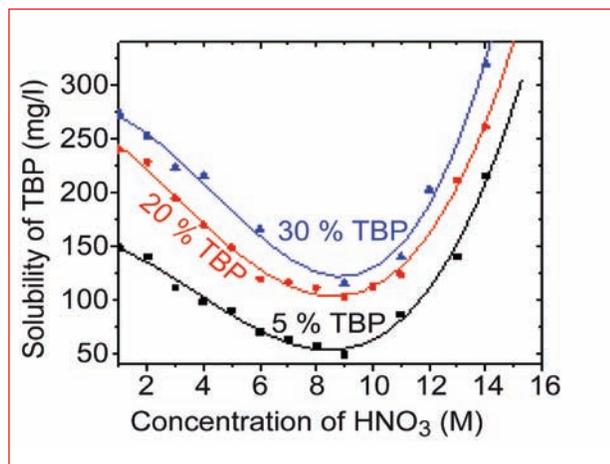
Fig. 2 *Solubility curves for 5, 20 and 30% TBP at various HNO$_3$ concentrations*
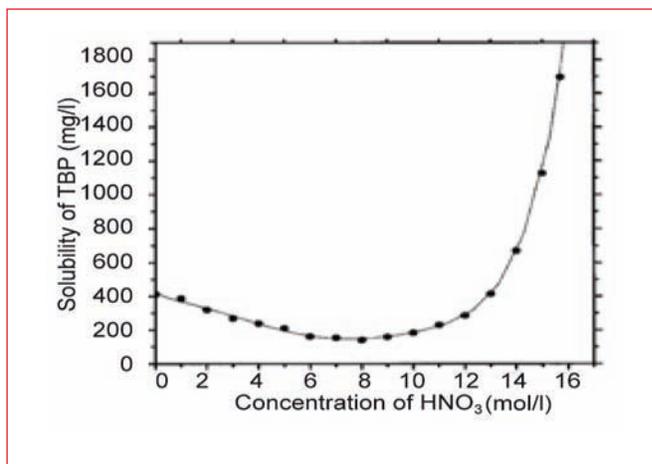
Fig. 3 *Solubility curve for 100% TBP at various HNO$_3$ concentrations*
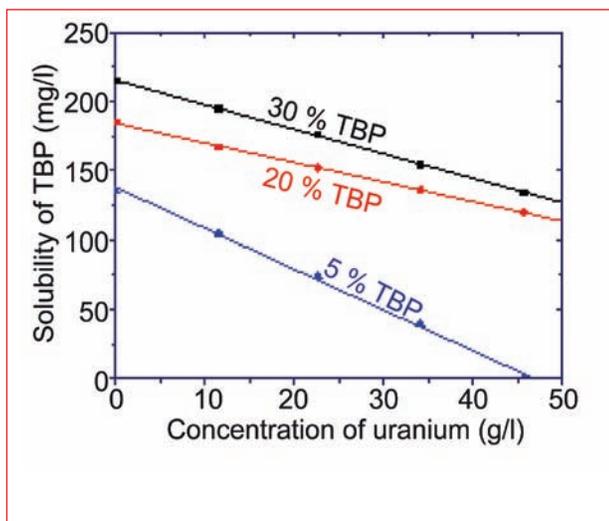
Fig. 4 Solubility of 5, 20 and 30% TBP as a function of uranium concentration
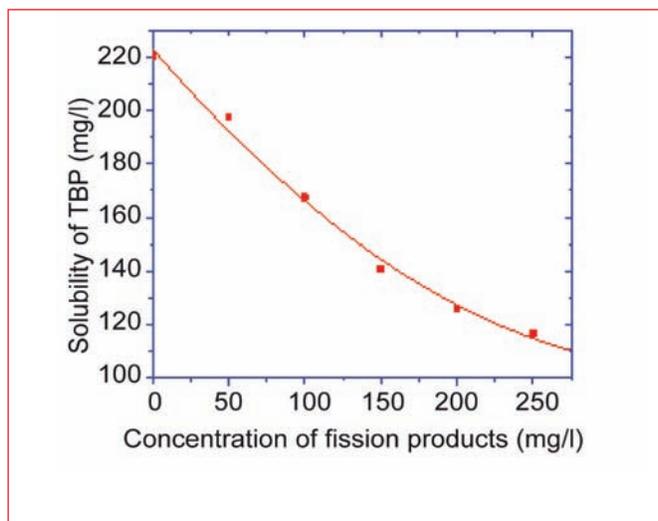
Fig. 5 Solubility of 30% TBP in a simulated waste solution in 4 M HNO$_3$

free TBP molecules into aqueous solutions. Formation of compounds by the acid and TBP makes a small contribution to the solubility in this region.

With increase in nitric acid concentration interaction of TBP molecules with nitric acid significantly increases resulting in the increase of monosolvate concentration, which finally leads to the increased solubility in higher acid concentrations.

Effect of uranium concentration

The solubility of varying concentrations of TBP as a function of heavy metal ion (uranium) concentration in 4 M nitric acid is shown in Figure 4. The general trend is that the solubility of TBP decreases with increasing

concentration of uranium in all cases (5, 20 and 30% TBP). In the case of 5% TBP, when the concentration of uranium was increased to 46 g/l the solubility of TBP reached a value below the detection limit of gas chromatography, which was about 2 ppm. This is due to the fact that the TBP available to dissolve into the aqueous phase was insufficient. In the other two cases (20 and 30% TBP), sufficient quantity of free TBP was available to have significant solubility (119 and 134 ppm TBP respectively) in 4 M nitric acid for the same concentration of uranium.

Effect of fission products

The solubility of 30% TBP in a synthetic waste solution in 4 M

HNO$_3$, simulating the composition of fission products in high active liquid waste streams that would be generated in the reprocessing of FBTR Mark-I fuel, which had undergone a burn-up of 150 GWd/t and with the cooling period of one year revealed that the solubility of TBP decreases with increasing metal nitrate concentration (Figure 5).

The data generated on the solubility of TBP indicate that the concentration of nitric acid and presence of heavy metal ions and fission products have a significant effect on TBP solubility in aqueous phase. These data would serve as the base line for controlling the concentration of TBP while treating the waste solutions.

IV.4 Characterization of Submicron Dispersion in Product Streams of Centrifugal Extractor

Centrifugal contactors are vital for a variety of solvent extraction operations especially for fast reactor fuel reprocessing. During turbulent couette mixing, a good dispersion is

obtained, which is allowed to settle in a centrifugal settling field operating typically at 80-200 g. In the normal case, practically all the dispersion is settled and entrainment in the

continuous phase is less than 1% for satisfactory operation. The carry over depends on the extent of formation of micron size particles while mixing. Generation of micro-sized drops

can be explained on the basis of (i) non-linear drop dynamics, (ii) severe inter-particle collisions resulting in the formation of tiny segments during drop breakup and (iii) tearing of colliding drops by tiny sharp edges on the machined surfaces of stationary as well as rotating bowl.

To study primarily the hydrodynamics and related phenomena for the 40 mm centrifugal extractor, dilute acid (equivalent to acidified water) was used. Since the operations were conducted in the operable zone having entrainment much below the permissible limit of 1% (flooding limit), presumed effect of acidity on the entrainment was not significant. To prevent the entry of any foreign particle, the aqueous product stream was to be analyzed with dynamic light scattering technique and the aqueous feed solution was prepared with millipore water and filtered through a hollow-membrane based filter.

The 40 mm centrifugal extractor having annular mixing zone was in-house designed and fabricated indigenously. It's rotor was coupled to a miniature 3-phase alternating current motor fed by a variable frequency drive (VFD) device. Aqueous and organic phases were fed by two valveless metering pumps. Aqueous phase pumping was started first and at the outset of exit of aqueous from aqueous product port, organic phase pumping was started. Drop size samples were taken after reaching the steady state which was checked by volume input-output balance.

Two series of experiments were conducted. In the first series of experiments, total throughput and rotational speed were fixed at 200 ml/min (12 l/h) and 3000 rpm respectively. The phase flow ratio, organic to aqueous (O/A) was varied at several levels like 0.1, 0.3, 0.5, 1, 3, 5 and 10. In the second series of experiments, total throughput and organic to aqueous ratio were fixed at 200 ml/min (12 l/h) and 1 ml/min respectively. The rotational speed was varied from 2000 to 3600 rpm.

Micro-drop size measurement

The samples were analyzed by a dynamic light scattering (DLS) instrument with a fibre-optics based remote probe. The instrument was repeatedly calibrated by checking against an aqueous suspension of 100 nm gold-coated polystyrene nano-spheres. It had the measurement uncertainty of ±1 nm.

Table 1: Other phase carryover by TOC method for two extreme organic to aqueous cases*		
Ratio	Dispersed Phase	Entrainment ppm
0.1	Organic	250
10	Aqueous	550
Average of three determinations		

Parameters such as fluid temperature, density and characteristic viscosities were incorporated in the system before recording the particle size distribution.

The results of the two series of experiments shown in Figures 1a and 1b revealed that the drop size distribution has bi-nodal shape indicating one primary and one secondary peak. Primary peak is essentially due to high energy dissipation during mixing resulting in the formation of ultra-fine drops of dispersed phase into the continuous phase. These ultra-fine drops are difficult to settle completely. Since mechanism of attrition of bigger drops as well as tearing of colliding drops by surface imperfections may contribute to these events, it requires a detailed study of drop dynamics in sub-micron region for complete understanding of this phenomenon.
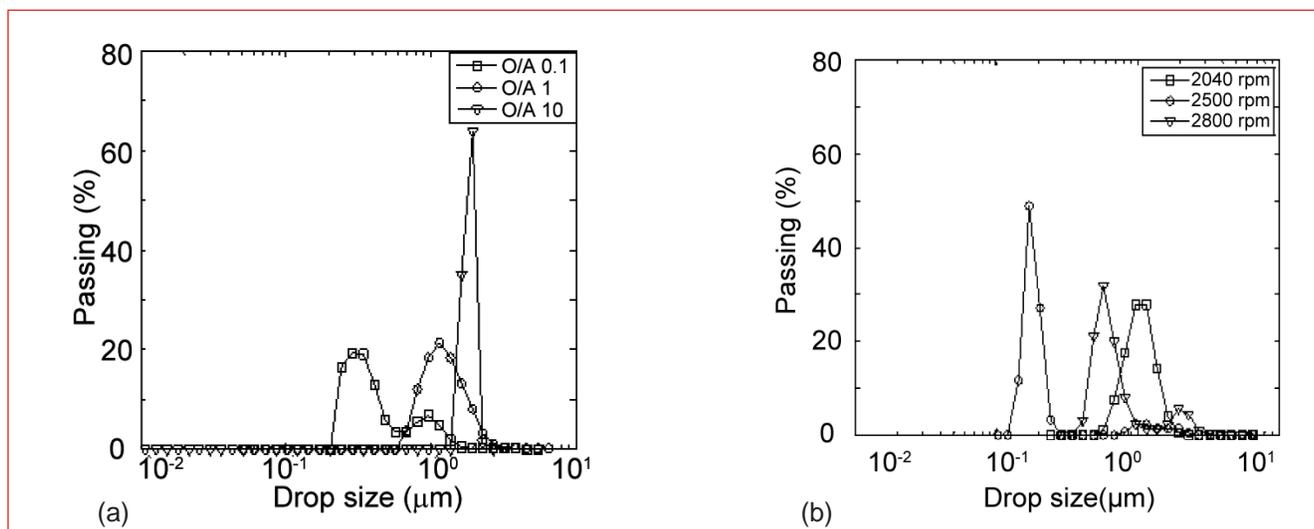
Fig. 1 *(a) Experimental drop size distribution of micro-sized organic entrainment at different organic to aqueous in the aqueous phase (Total throughput: 200 ml/min; speed of rotation: 3000 rpm) and (b) variation in the sizes of entrained organic drops with varying rotor speed*

IV.5 Control and Diagnostics of Motors of Centrifugal Extractors using Variable Frequency Drives with Vector Control

Centrifugal extractors are used for solvent extraction operations in CORAL. Each centrifugal extractor has 16 stages and each stage is driven by an electrical motor. Custom built 3-phase squirrel cage induction motors are used for this application.

Process requirements

The speed of each stage is to be maintained between 3000 and 3600 rpm. If the speed of any stage falls below 3000 rpm, the entire centrifugal extractor needs to be tripped. As the centrifugal extractor is located within the hot cell having high radiation and acid vapor, there are practical problems associated with the measurement of the speed of each stage using conventional speed sensors.

Variable frequency drives

Variable voltage and variable frequency drives (VVVFD) are used for this application and the speed is indirectly monitored using the current of each motor. The VVVFDs operate in sensor-less vector control (SLVC) mode which provides tighter speed regulation. The speed is estimated from the torque component of the current vector. The torque required for the load is automatically adjusted to achieve tighter speed regulation.

Figure 1 is the speed response of the motors with respect to current. The speed is almost constant (slip is <10%). Information on the operating voltage, frequency, current and power factor are sensed by the VVVFD. From these parameters, the speed is estimated based on load characteristics of the motor. A separate setup was used to obtain the characteristics of the motor
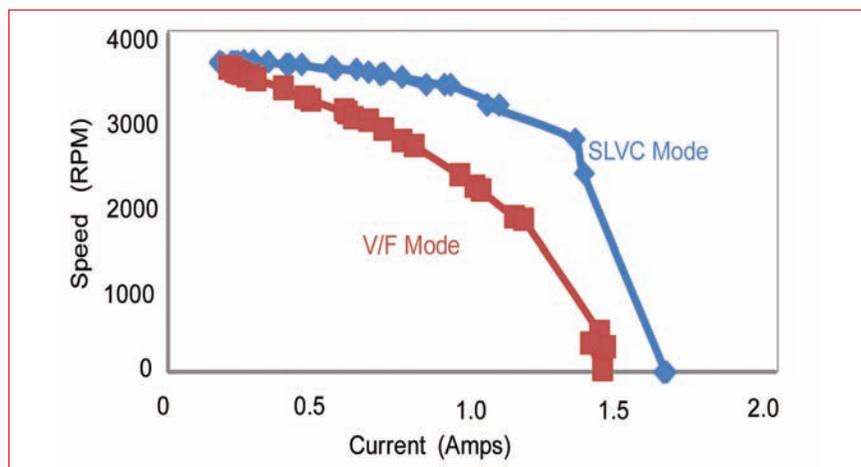
Fig. 1 *Speed response of the motors*

under various loads. The speed of each stage is estimated by simply monitoring the current of motor from the drive, thereby avoiding the separate speed measurement system.

Motor diagnostics

Besides estimating the speed, other diagnostic information of the motor is also derived from the VVVFD. This includes motor stalling, overload, disconnection, single phase open, mechanical vibration, earth fault and high resistance at connector. Table 1 indicates the range of motor parameters for various motor fault conditions.

In addition to these on-line parameters, the VVVFD can carry out off-line diagnostics also. Using the VVVFD analog and digital signal I/Os, the full centrifugal extractor motor bank is configured to trip whenever any fault is detected by any of the stage.

Operator interface

The VVVFDs are in communication with a human machine interface (HMI) that serves as an operator interface. The communication protocol of VVVFDs is modbus on RS-485. The HMI has various

screens for operation, diagnostics and configuration. The live parameters of all the sixteen motors are available on a single screen.

Operating experience

After incorporating individual VVVFD for each motor of the centrifugal extractor, there has been a significant improvement in the overall operating performance of the plant. Earlier, the motor operation was checked manually using in-cell cameras, which was very cumbersome. The operation is made much easier with the incorporation of this system.

PF	I_{torque} (A)	$I_{magnetic}$ (A)	Message
<10 <20	<0.2 >0.5	<0.05 >1.0	Stopped Stalled
<45->30	<0.2	<0.5	Mechanical connection fault
<75	<0.2	<0.5	Normal running
>75	<0.2	<0.05	Not connected
<75	>0.2	>0.4	Phase open

Table 1: Motor diagnostics - online error decoding

IV.6 Design Temperature Limits for FRFCF Storage Cells: Enhancement of Natural Convection Cooling and Constraints on Operation Flexibility

Decay heat producing hull wastes will be compacted inside canisters and stored in dedicated concrete cells. Several canisters will be stored inside a cell. Since the storage time extends over several years, it is envisaged to cool the cells by natural convective flow of air. Each canister transfers the decay heat produced inside to surrounding mainly by thermal and gamma radiation. A small fraction is transferred by convection also. Canisters are stored inside metallic tubes. Each tube can accommodate several canisters. Heat generated in the canisters will be transferred by the natural convective flow of air in the cell to the outer surface of tubes. The air contained between the canisters and tube is stagnant due to the small annular clearance. Knowledge of the generated heat distribution among various structural parts in the cells including gamma heating of concrete walls is obtained through detailed reactor physics calculation. Heat produced by the canisters has to be limited such that it can be removed by the natural convective flow established through the cell without exceeding the limit on concrete wall temperature, viz., 65 °C. Thermal hydraulic analysis of canister storage cell has been carried out to estimate the limiting heat source of canisters and the requirement of elevation difference between supply and exit air passages in the cell for gaining the required natural convection flow through the cell.

The maximum canister loading rate of the cell is ~24 per year. It takes ~21 years for the cell to be fully loaded. The maximum and minimum age of canisters at the time when they
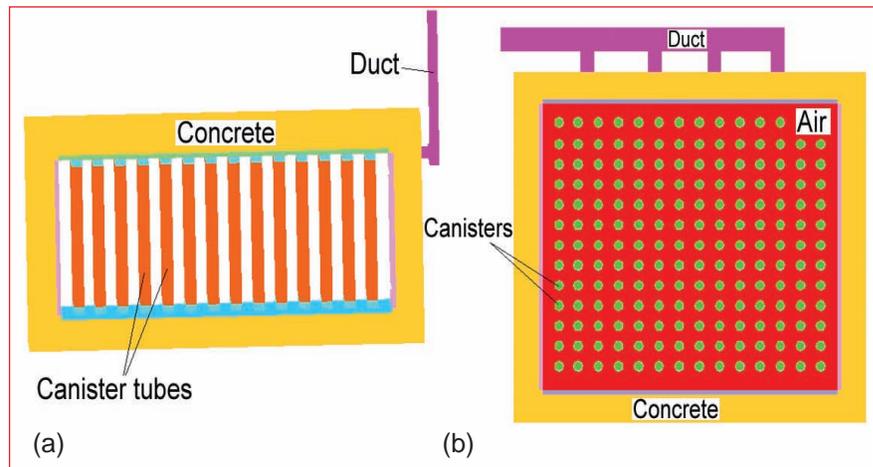

Fig. 1 *Schematic of (a) the three dimensional model and (b) top view of the storage cell*

are fully loaded for the first time will be 21 years and zero year respectively. Decay heat loads of fresh and 21 years aged canister are ~1250 W and ~10 W respectively. When high power canisters are located close to the concrete walls of the cells, the concrete surface would get heated up due to thermal radiation as well as gamma flux reaching it directly. To avoid this, high power canisters are recommended to be located in the central region of the cell and low power canisters in the periphery of the cell. With this scheme, fresh load of canisters arriving at the cell will always occupy positions in the central region and they will be moved to peripheral location after sufficiently longer duration so that their decay power reduces to comfortable levels. Even though this scheme requires shuffling of canisters inside the cell once, it helps in enhancing the thermal load bearing capacity of the cell several folds. There is a large economic benefit without compromising on the safety.

As already mentioned, canister mainly transfers heat to its

surroundings by thermal and gamma radiation. Therefore, to reduce the radiation heating of concrete walls, it is desirable to provide a concentric coolant tube around each of the canister storage tube so that the cooling air driven by natural convection flows predominantly through the annulus. Air flow exiting through individual tubes reach a common duct which in turn is connected to exhaust stack through filter banks. In order to avoid the temperature dilution of exit air from the cell by mixing with other gas streams reaching the common exhaust stack, the insulated exhaust duct from the cell is to be connected to the common stack at its upper most elevation. This avoids the reduction in buoyancy induced driving head due to temperature dilution of exhaust air at lower elevations. To avoid excessive heating of bottom floor of the cell by conduction from hot canisters mounted over it, an insulation layer is recommended to be provided between the canisters and concrete floor.

Analysis has been carried out for validation of the concept in
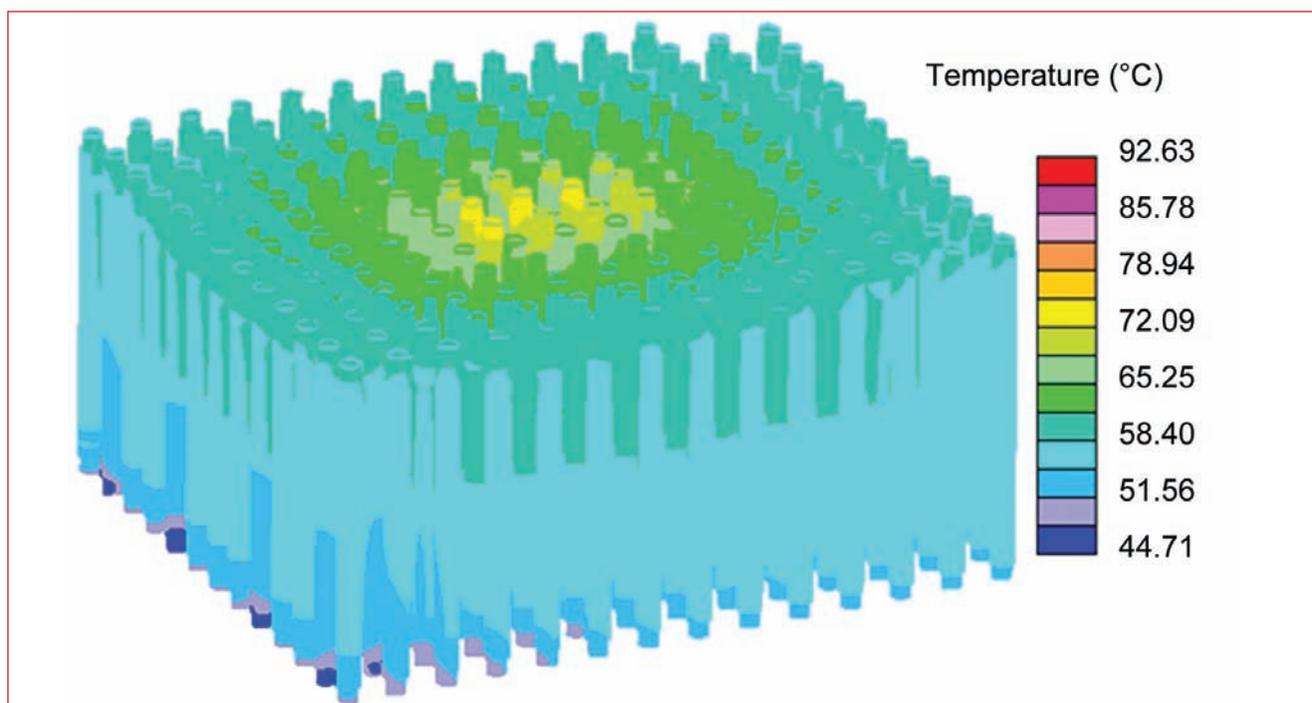
Fig. 2 *Temperature distribution in tubes inside the cell*

two stages. First stage involved several parametric studies using a two dimensional model assuming cosine heat generation distribution inside the cell to arrive at the suitable shuffling scheme. Based on the case identified to be feasible through axi-symmetric analysis, detailed three dimensional analysis was performed to estimate realistic temperatures of various parts. Three dimensional model of storage cell is shown in Figure 1. Heat generation is modelled as volumetric heat source in canister volumes. Flow entry is considered at the bottom of the cell and flow exit from stack is considered at an elevation above the entry by a value arrived at from the two dimensional calculation. Pressure drop offered by the filter banks is modeled as that corresponding to maximum choked condition. Heat generated in concrete walls due to gamma heating is considered in the model. The conjugate thermal analysis considers heat transfer by all the three modes. The outer surface of concrete walls (1.5 m thick) above the ground level and

ceiling are modeled with combined natural convective and radiation heat transfer to the ambient air. Radiation heat transfer within the cell is modeled using discrete transfer model with internal view factor calculation. Temperature dependent density of air is modeled using ideal gas relation such that buoyancy driven flow can be simulated. Turbulence is modelled using standard k-ε model. The analysis is carried out using general purpose computational fluid dynamics code.

It is seen from the analysis that based on the heat load and natural convective cooling possible through the stack, canisters stored externally (before bringing to cell) for one year can be stored at the cell by meeting the requirement of limiting temperature for concrete structures. In order to avoid excessive heating of concrete surfaces by thermal radiation and direct gamma heating, the high heat generating canisters are recommended to be located at the central region and they can

be moved to the periphery after their decay power reduces to comfortable levels after six years. Further, twenty four filter banks (double the number normally provided) are recommended in the discharge for enhancing natural convection and thereby, to increase the margin between the limit and operating temperature. It is also required to insulate the exhaust duct connection from cell area to the location of joining with the stack at 75 m height. Maximum value of concrete temperature predicted in this case is 61.4 °C. Predicted temperature distribution in the tubes inside the cells is shown in Figure 2. In case, the canisters are cooled for four years externally before loading them in the storage cell, then the cooling arrangement for them can be simplified without the need for (i) cooling tubes, (ii) additional filter banks and (iii) canister shuffling. Further, the discharge duct connection to the stack can be lowered to 40 m above suction duct such that the maximum concrete temperature achieved is 62 °C.

IV.7 Fabrication of Qualified Sodium Bonded Metallic Fuel Pins Containing U-19Pu-6Zr Metal Slugs for Test Irradiation in FBTR

As a part of the effort to develop metallic fuels for use in future FBRs, a campaign has been planned to assess the irradiation behavior of sodium-bonded U-19Pu-6Zr metallic fuel pins in FBTR.

Development and casting of metal fuel slugs of suitable composition was carried out and U-19Pu-6Zr metal slugs were supplied by BARC. Further fabrication of sodium bonded fuel pins containing fuel slugs for irradiation studies was carried out at our Centre.

For the fabrication of sodium bonded metallic fuel pins, a negative pressure argon atmosphere glove box train consisting of double and single module glove boxes along with automatic pressure control, independent gas recirculation and purification is in operation. Several fuel pins containing U-6Zr and 14EU-6Zr fuel slugs have been fabricated and encapsulated in special capsules. These fuel pins are undergoing irradiation in FBTR.

The U-19Pu-6Zr metal slugs

Fig. 1 *Metrology and inspection of U-19Pu-6Zr fuel slugs*

contained in stainless steel tubes and housed in a magazine was received from BARC. The tubes containing metal slugs were taken into the glove box by bag-in process. To retrieve the metal slugs, the tubes were cut at suitable location using a tube cutter by placing the tubes on a jig. As the metal slugs were very brittle in nature, they were carefully handled. The metal slugs were subjected to metrology for inspection on length, diameter, straightness and weight (Figure 1). The fuel slug was qualified earlier by eddy current testing at BARC.

The fuel pin consists of blanket (U-6Zr), fuel slug (U-19Pu-6Zr) and the resultant annulus between the slug and the inside of the tube is filled with sodium to provide a thermal bond. The level of sodium above the slug is 20±0.5mm. The clad tube and the end plugs are made out of modified 9Cr-1Mo (ASTM A 387 Grade 91) material.
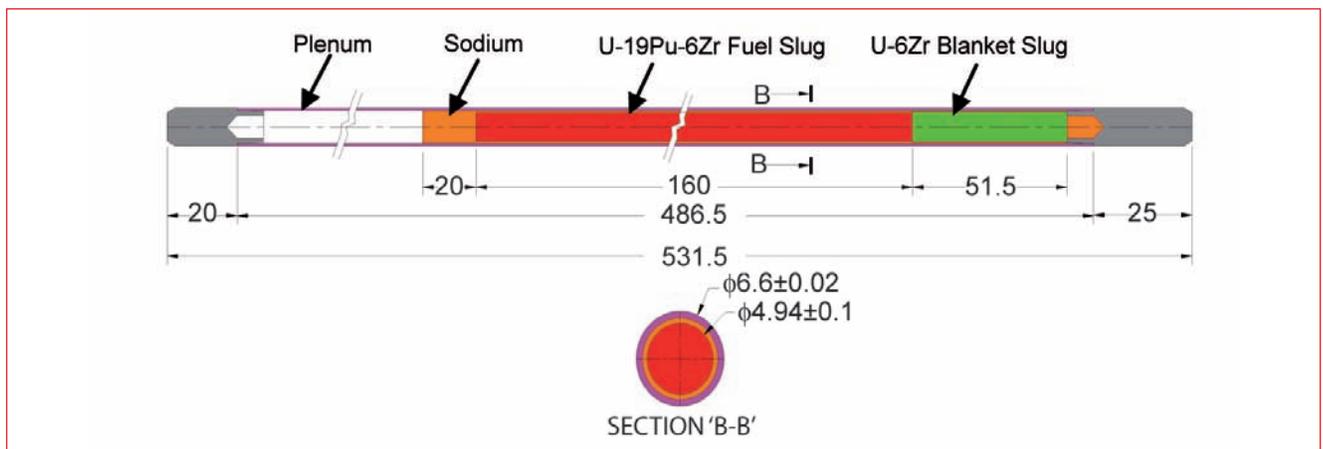

Fig. 2 *Schematic showing fuel pin internals*
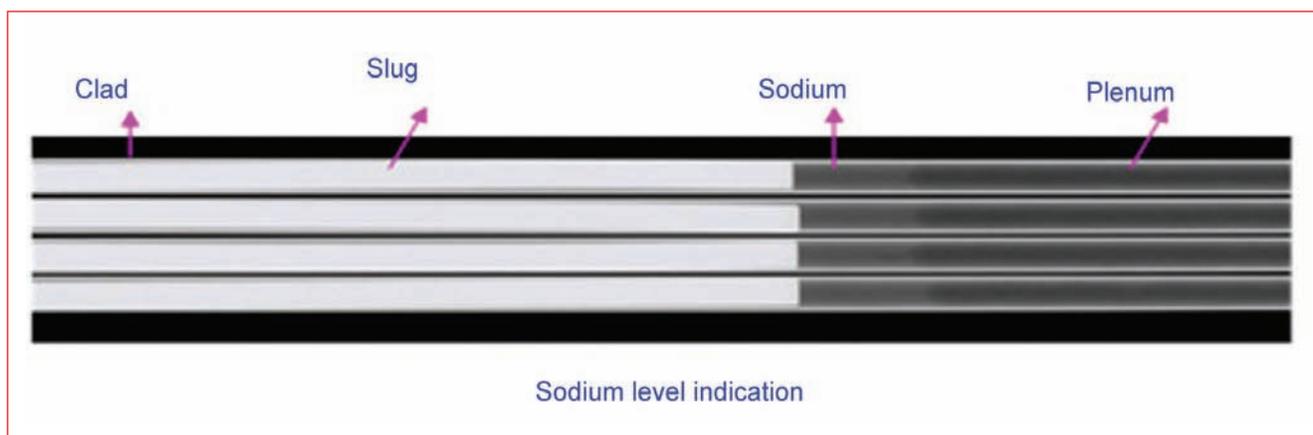
Fig. 3 *'X' radiography showing fuel pin internals and sodium level*

T91 clad tubes are of 0.45 mm wall thickness and 6.6 mm outside diameter. The fuel slug of length 160 mm is the fuel column. A blanket, U-6Zr of length 49 mm is placed at the bottom. A plenum gap of 228 mm is provided at the top (Figure 2).

In a glove box, one end closed clad tube is loaded with measured quantity of sodium. It was carried out by the extrusion of sodium in cylindrical form to suitable diameter smaller than the tube ID. The sodium wire is then pneumatically injected into the clad tube by inserting the polyethylene tube containing sodium through a guide sleeve. The polyethylene tube and the PTFE (polytetrafluoroethylene) sleeve avoid mouth contamination of clad tube during sodium addition which may cause defective welds during closure welding. The clad tube with sodium wire is placed in a tubular furnace and heated to 423 K for melting and settling of sodium.

The qualified fuel slug was inserted into the clad tube by levitation method to prevent mouth contamination. The clad tube was then transferred into a furnace for settling the sodium by heating to 423 K and vibrated by a power oscillator with amplifier. The settling process ensures that the slug is seated at the bottom of the tube, the bond sodium rises along

the annulus between the fuel slug and the clad displaces majority of the voids. The cooling arrangement is designed to freeze the annular sodium progressively from bottom to top.

The end cap closure welding is done in a specially developed leak tight welding chamber by automated pulsed TIG (tungsten inert gas) process. The chamber is pressurized with helium at 1.2 bar (g). Weldability of thin walled clad tube to end plug (mod.9Cr-1Mo) without preheating was studied. The weld joint was subjected to postweld heat treatment at the temperature of 1033±10 K for 30 minutes in a furnace housed in the glove box. The welding power supply, its control panel, vision system and the furnace control are placed outside the glove box. Real time capturing of weld parameters were carried out. The weld joint was qualified by visual examination, helium leak testing (10^{-15} MPa m^3/s max) and X-radiography. The welds were characterised by metallography before & after the production of welds. The top end plug welded fuel pin is subjected to helium leak test (HLT) to check the integrity of weld. Then the pin is subjected to the sodium bonding operation. The process consists of holding the fuel pin in an unrestrained condition at 823 K for 1 hour with

simultaneous application of vertical electromechanical vibration.

Sodium bonded metallic fuel pins of U-19Pu-6Zr (6 Nos.) were fabricated and qualified. The quality of the weld, plenum gas pressure and purity were ascertained with the help of tests performed on set-up and process test pins that were welded prior to and after the actual fuel pin welding. The actual fuel pins were subjected to dimensional inspection, helium leak test and full length X radiography to ascertain the integrity of internals as well as the weld joint and length of the sodium level above fuel slug (Figure 3).

Neutron radiography (NR) and eddy current testing (ECT) were carried out on the U-19Pu-6Zr metallic fuel pins prior to encapsulation into irradiation capsules to record pre-irradiation data. cerium examination of the metallic fuel pins was aimed at obtaining images of internal details such as dimensional variations of slugs, sodium level, voids in sodium (if any), fuel-clad gap and in-homogeneities within the slug. Eddy current testing was carried out to examine the slug, sodium and fuel clad regions for any in-homogeneities and to compare with the observations of neutron radiography. The accepted fuel pins were transferred to IDEAS for capsule construction.

IV.8 Studies Related to Pyrochemical Reprocessing of Metal Fuels

Development of molten salt electrorefining based pyrochemical reprocessing for treating the spent U-Pu-Zr fuels is in progress. The demonstration of all unit operations in the engineering scale and evaluation of thermochemical data of LiCl-KCl in presence of fission products are important aspects of the development. Studies on electrorefining of U-Zr alloy slugs from sodium bonded pins were carried out in the engineering scale facility. Basic electrochemical and thermochemical studies related to pyrochemical reprocessing have also been carried out.

Studies using sodium bonded pins with U-6Zr alloy

Chopping of sodium-bonded U-6Zr fuel pins was carried out in the engineering scale inactive demonstration facility. A total of eleven fuel pins were chopped using a single-pin chopper inside the inert atmosphere containment box. The chopped fuel pin segments are shown in Figure 1a.

The LiCl-KCl-UCl$_3$ electrolyte which had been used for earlier electrorefining runs was used for the electrorefining of these U-Zr alloy segments. About 730 grams of chopped fuel pin segments were loaded in the anode basket. These contained about 16 grams of bond sodium. Electrorefining was carried out at constant potential (-1.2 to -1.7 V vs Ag/AgCl ref. electrode) mode at 773 K. A total of 591 gram of uranium was electrodeposited on the cathode during the electrorefining run. The sodium from the chopped fuel pin dissolved in LiCl-KCl eutectic as NaCl during electrorefining. A typical uranium deposit is shown in Figure 1b.
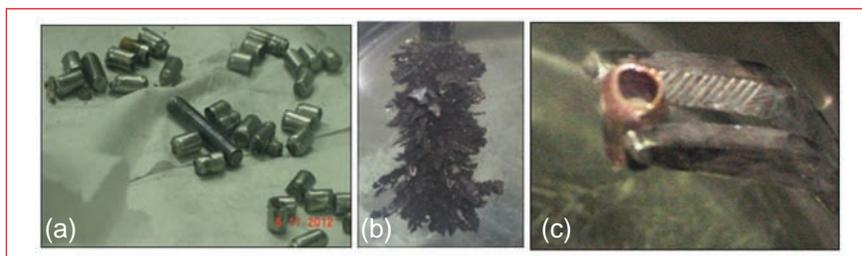

Fig. 1 *(a) Chopped U-6Zr fuel pin segments, (b)uranium electrodeposit from a typical electrorefining run and (c) chopped fuel pin after electrorefining*

The residual clad after electrorefining shown in Figure 1c indicates the complete removal of U-Zr .

The uranium metal deposit obtained in different runs were subsequently vacuum distilled to remove the occluded salt and uranium was consolidated by induction melting. The average separation factor of zirconium in the cathode deposit during various electrorefining runs was found to be ~1700.

Basic electrochemical studies

Electrochemical studies were carried out using transient techniques such as cyclic voltammetry, chronopotentiometry and convolution voltammetry on the behavior of uranium and typical fission products like samarium, lanthanum and neodymium at various inert and active electrodes in LiCl-KCl eutectic to elucidate the reduction mechanism. The cyclic voltammograms of samarium tri chloride at molybdenum as working electrode are shown in Figure 2a.

The reversibility of the redox couples was evaluated using various methodologies followed by the estimation of diffusion coefficient, transfer coefficient and heterogeneous rate constant. The underpotential deposition of uranium, neodymium and lanthanum was observed at gallium electrode due to the formation of intermetallic compounds of these metals with gallium (Figure 2b). The Gibbs energy of formation of these intermetallic compounds was also measured by open-circuit chronopotentiometry in the temperature range 698-798 K.

A computer code DIFAC (Diffusion of Actinides in Electrorefiner) was developed as a part of modelling the electrorefining process. The code was used to model the anodic
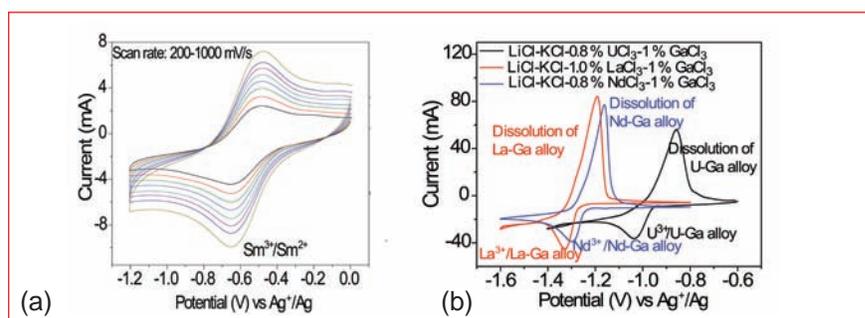

Fig. 2 *(a) Cyclic voltammogram of SmCl$_3$ at a molybdenum electrode;T=729 K and (b) cyclic voltammograms of U^{3+}, Nd^{3+} and La^{3+} at Ga electrode in LiCl-KCl eutectic; T=723 K*
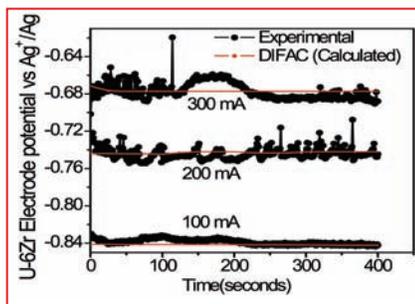
Fig. 3 *Experimental and calculated potential profiles (using DIFAC code) during anodic dissolution of U-Zr alloy;T=808 K*

Fig. 4 *(a) Calculated isothermal contours and liquidus projection of LiCl-KCl-UCl$_3$, (b) isothermal contour and liquidus projection of LiCl-KCl-NdCl$_3$ and (c) isothermal contour and liquidus projection of LiCl-KCl-PrCl$_3$*

dissolution of uranium, zirconium and U-Zr alloy in LiCl-KCl eutectic at various current densities. The experimental and calculated anode potentials during anodic dissolution of U-Zr alloy are shown in Figure 3.

Phase diagram studies

Experimental determination of phase diagrams of molten salts and thermodynamic modelling of the salt systems are essential for evaluating how the thermochemical properties of LiCl-KCl change due to the loading of fission products during the course of electrorefining. Thermodynamic modelling of LiCl-KCl-UCl$_3$ was carried out using the CALPHAD methodology incorporating phase diagram data, electromotive force data and estimates for enthalpy of mixing at T=1113 K along various isoplethal sections in the ternary phase field. The optimization of the system was done using the PARROT module of ThermoCalc software. The calculated liquidus projection of LiCl-KCl-UCl$_3$ is shown in Figure 4a.

Rare earth elements are the major fission products in the spent fuel; therefore, it is necessary to understand the interaction of RECl$_3$ (RE: Nd, Pr) in the LiCl-KCl medium. No literature was available on the phase diagram of these ternary systems. Hence, a detailed study on these systems by differential thermal analysis(DTA) technique was taken up. Samples with ternary compositions covering the entire phase field were prepared inside dry

argon atmosphere glove box and loaded inside hermetically closed iron capsules. These samples were analysed by differential thermal analysis. In the absence of any quarternary compounds in these systems, the contours of the liquidus surface projection of these ternary systems were deduced by using the liquidus temperatures obtained from the heating curves and the liquidus data of the constituent binary systems which are shown in Figure 4b and 4c, respectively.

Recovery of actinides from spent salt

To reduce the fission product contents of the refabricated fuel and to recycle the electrolyte for minimizing the solid waste generation in the process, the eutectic salt is purified by actinide drawdown process. An experimental facility was set up in argon glove box to demonstrate and study the extraction behavior

of actinides from molten salt using lithium-cadmium alloy. It consisted of a single stage continuous extractor with four tanks, one each for salt feed, salt collection, cadmium feed and cadmium collection respectively. All the vessels and transfer lines were maintained at 773 K using resistance heaters covered with insulation (Figure 5). Extraction experiments were carried out with uranium and cerium solute in eutectic salt.

Exhaustive electrolysis is an alternative electrochemical route for the recovery of actinides from spent salt using Li-Cd as counter electrode. Laboratory scale runs were carried out for the recovery of uranium from LiCl-KCl-UCl$_3$ using Mo as working electrode. A typical electrolysis indicated that uranium could be completely removed from the electrolyte from an initial concentration of 3 wt.% .
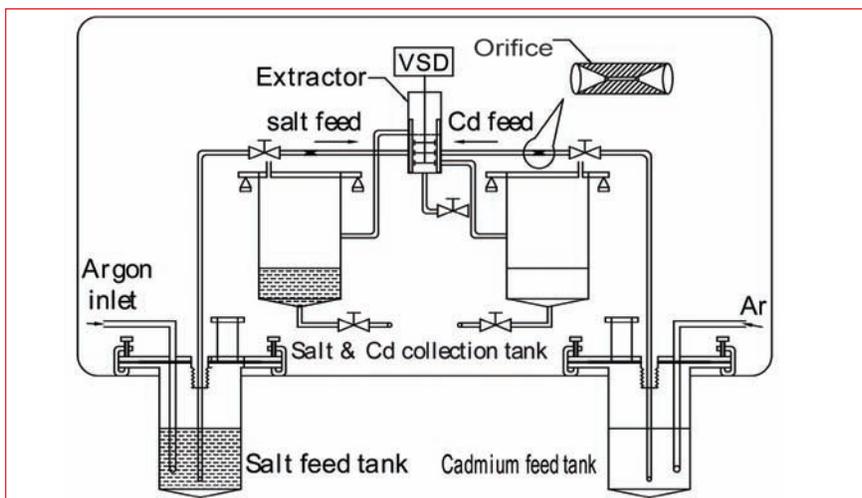
Fig. 5 *Schematic of actinide drawdown process equipment*

IV.9 Performance Evaluation of Mechanisms and Experiments in Ambient Temperature Electrorefiner

Ambient temperature electro refiner (ATER) facility has been setup with an objective to gain experience in remote operation and automation systems for electrorefining. The experience gained in this facility will be helpful in improving the design of electrorefiner meant for reprocessing of spent metallic fuel of future fast reactors. The set up was commissioned and cyclic operations of different systems were carried out. This facility will also be used for design modification and testing of components of the high temperature electrorefiner (HTER).

The ATER facility consists of an assembly station, electrorefining station, scraping station and tilting station. Besides, it also has three electrodes, electrode subassemblies, process panel, mini crane, support structure, pneumatic system and gripper system. Figure 1 shows the aerial view of ATER. Two cathodes, one anode and a stirrer will be used for operation. Anode is a porous cruciform basket filled with copper rodlets. Cathode-1 is a solid rod of 75 mm diameter. Cathode-2 is a ceramic crucible with a holder. There are three electrode subassemblies corresponding to the three electrodes.

During operation, cylindrical copper rodlets of 6 mm diameter and 6 mm length are loaded in the anode. Acidified copper sulphate solution is used as electrolyte. By applying a DC potential, copper from the anode will be electro transported through the electrolyte and gets deposited on cathode-1. The dendritic deposit of pure copper will then be scraped and collected in a vessel.

The electrode subassemblies will be moved between different stations for each batch operation with the help of a crane. Each electrode subassembly and the electrode assembly stations have electrical drives and pneumatic drives to perform the various functions. Provision exists for operation of the system in manual and auto modes.

Twenty cycles of individual operation of anode, cathode-1, cathode-2, refining station, tilting station and scraping station were carried out. Performance was checked and was found satisfactory. Subsequently, 192 full cycles of operation were carried out. The operation of the system was found to be trouble free.

Electrorefining experiments in ATER were divided into four phases. The first phase was a hydrodynamic study to find out suitable stirrer. The second phase was to find out the effect on current density due to rotation of anode. The third phase was to determine the current efficiency and throughput and the last phase was to calculate the cell constant.

LiCl-KCl eutectic molten salt is used as the electrolyte in HTER. Hence the hydrodynamic experiments in ATER were conducted using water as the simulant fluid as kinematic viscosity of water at room temperature is similar to the kinematic viscosity of molten salt at 773 K. Experiments were conducted to determine the mixing time using different stirrers at different RPMs (revolutions per minute). To determine the mixing time suitable tracer was introduced near to the anode and conductivity of the solution was continuously monitored at three locations. Two

Fig. 1 *Aerial view of ATER*

types of radial stirrer i.e. double roushton type and cage type were examined for different RPM. From the studies it was concluded that cage type stirrer at higher than 120 RPM is suitable for electrorefining operation.

During the second phase of experiments the cathode potential was maintained at 1 V with respect to a calomel reference electrode. Experiments were conducted with stirrer rotating at 0, 90 and 160 RPM, cathode-I rotating at 20 RPM and anode with and without oscillation. From the experiments it was seen that the current density is high at the stirrer rotation of 160 RPM and is independent of anode rotation. The third phase experiments are for determining the current efficiency and throughput of complete electrorefiner cycle which is in progress. In this phase, approximately 2 kg of copper dendrite will be deposited in the solid cathode.

The fourth phase experiment is aimed at determining the cell constant of ATER. The cell constant depends on the geometry of the electrodes and distance between them. Since the geometry and distance between the electrodes in ATER will be approximately the same as that of HTER, this experiment helps in determining directly the cell constant of HTER.

IV.10 A Versatile Monazite Ceramic Host for Nuclear Waste Immobilization

Crystalline ceramics such as synthetic monazites (rare earth orthophosphates, e.g., $CePO_4$) are considered as alternative matrices for the immobilization of the high level radioactive waste (HLW). It is a single phase crystalline material with excellent chemical and radiation stability. The crystal structure of monazite (e.g., $CePO_4$) is monoclinic with four formula units per unit cell. The structure of $CePO_4$ is composed of nine-coordinated cerium atoms linked together by distorted phosphate tetrahedra. An interesting property of the monazite crystal structure is that all the atoms occupy the general crystallographic sites thereby giving the atoms a high degree of freedom to move around in cohesion, without disturbing the crystal symmetry. It is this flexibility of monazite crystal structure that makes it possible to accommodate chemically diverse (different size and charge) cations (nearly 20 in number) of the HLW into its crystal structure (cerium site), a unique feature of the monazite ceramic. The average valence of the HLW elements needs to be +3 for immobilization in monazite as the cation valence in monazite is +3.

In the present work, an attempt is made to identify and synthesize a versatile monazite phase that can accommodate cations of different valencies without requiring coupled substitution for charge balance, so that it can accommodate HLW of different compositions even if the average cationic valence differs from +3.

Among the lighter rare earth (lanthanum to gadolinium) phosphates that crystallize in the monazite crystal structure, $CePO_4$
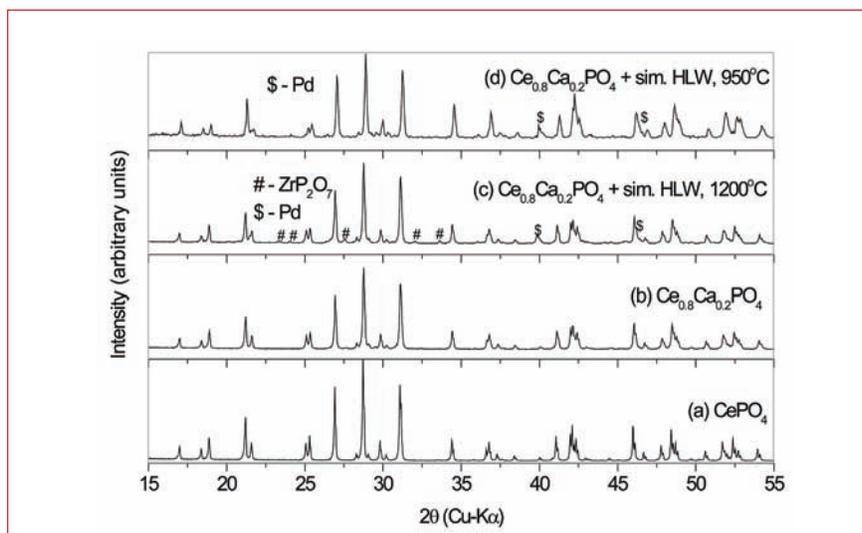
Fig. 1 *XRD patterns of (a) $CePO_4$, (b) $Ce_{0.8}Ca_{0.2}PO_4$, (c) and (d) $Ce_{0.8}Ca_{0.2}PO_4$ with 20 wt.% simulated HLW oxide sintered at 1473 and 1223 K respectively*

has additional flexibility due to the multiple valence states (+3 or +4) of cerium. When a cation of valence less than +3 replaces Ce^{3+}, then a corresponding number of Ce^{3+} gets oxidised to Ce^{4+} to maintain the charge neutrality of the lattice. But, it may not be possible to accommodate, without coupled substitution, cations of valence greater than +3 in $CePO_4$ as cerium. does not exhibit +2 valence; also the PO_4 tetrahedra are highly covalent and cannot allow cation vacancies or oxide ion interstitials.

As cerium exists in mixed valence state in calcium doped $CePO_4$, it can accommodate cations of any valence by initiating the internal redox reaction, viz., $Ce^{3+} -> Ce^{4+} + e^-$, as required by the incoming cation, in order to maintain the charge neutrality of the lattice. The oxidation and reduction among the Ce^{3+} and Ce^{4+} present in calcium doped $CePO_4$ will assist in accommodating HLW of different compositions in the structure even if the average valence of the HLW elements is other than 3. Thus, Ca-doped $CePO_4$ is expected to be a versatile ceramic host for

the immobilization of HLW. The solid solution studies for calcium in $CePO_4$ showed that single phase monazite could be prepared only up to 20 % replacement of the cerium. site. Therefore, the monazite phase, $Ce_{0.8}Ca_{0.2}PO_4$ is selected as the versatile ceramic host.

The synthesis, characterization and waste loading characteristics of the versatile monazite phase $Ce^{3+}_{0.6}Ce^{4+}_{0.2}Ca^{2+}_{0.2}PO_4$ were examined using simulated waste.

Monazite compounds $CePO_4$, $Ce_{0.8}Ca_{0.2}PO_4$ and $Ce_{0.8}Ca_{0.2}PO_4$ with 20 wt. % simulated HLW were prepared through a solution chemistry route by mixing stoichiometric amounts of the appropriate solutions of the cations. Calcination was done at 573 K to get nanocrystalline precursor. Sintered pellets were prepared by heating at 1473 K. The theoretical density of the sintered pellet was around 92%. X-ray diffraction characterization showed the formation of single phase monazite (Figure 1). In the case of simulated waste loaded $Ce_{0.8}Ca_{0.2}PO_4$ small amount of impurity phases were also

observed. The impurity phase was not observed when the sintering was done at 1223 K.

X-ray photoelectron spectroscopic characterization showed cerium to be in mixed valence state (+3 and +4) in $Ce_{0.8}Ca_{0.2}PO_4$ displaying both the features of $CePO_4$ (Ce^{3+} reference) and CeO_2 (Ce^{4+} reference).

The charge compensation mechanism operating in the versatile monazite phase, $Ce_{0.8}Ca_{0.2}PO_4$, when an aliovalent cation replaces Ce^{3+} ion is demonstrated by preparing the compound $Ce_{0.6}Ca_{0.2}U_{0.2}PO_4$. XPS characterization revealed that in $Ce_{0.6}Ca_{0.2}U_{0.2}PO_4$ cerium exists in single valence state of +3. When calcium alone is doped in $CePO_4$ i.e., in $Ce_{0.8}Ca_{0.2}PO_4$, the Ce^{3+} get oxidized to Ce^{4+} in order to maintain charge neutrality of the lattice and when uranium is doped in $Ce_{0.8}Ca_{0.2}PO_4$ (i.e.,

in $Ce_{0.6}Ca_{0.2}U_{0.2}PO_4$), the Ce^{4+} generated gets reduced to Ce^{3+} and the presence of equal atomic proportion of U^{4+} and Ca^{2+} keeps cerium in +3 state. This clearly demonstrates the charge compensation mechanism operating in the versatile monazite phase, $Ce_{0.8}Ca_{0.2}PO_4$ and therefore, can accommodate different HLW compositions.

Sintering studies carried out for the simulated waste form using a home-built quartz push-rod dilatometer system showed that the sintering starts at as low a temperature as 973 K (Figure 2). A theoretical density of 93% was obtained for the pellet sintered at 1223 K for one hour in air. Thus, the simulated waste loaded $Ce_{0.8}Ca_{0.2}PO_4$ shows high sinterability at a relatively lower temperature.

Chemical durability studies on the
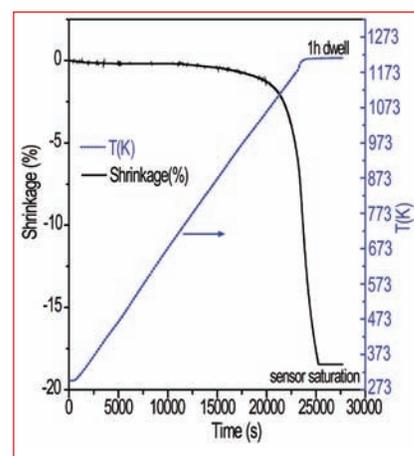
Fig. 2 *Dilatometric sintering curve for $Ce_{0.8}Ca_{0.2}PO_4$ with 20 wt.% simulated HLW oxide*

sintered pellet of the simulated waste loaded $Ce_{0.8}Ca_{0.2}PO_4$ were done by leaching with de-ionized water in an all-quartz soxhlet apparatus as per the material characterization test procedure (MCC-5) for 28 days and the leach resistance of the simulated waste form was found to be better than that of the reference borosilicate glass waste form.

IV.11 Single-cycle Partitioning of Trivalent Actinides from HLLW and Recovery of Americium by Extraction Chromatography

PUREX process has been adopted for the recovery of uranium and plutonium from the spent nuclear fuel. The raffinate rejected after the extraction of U(VI) and Pu(IV) is known as high-level liquid waste (HLLW). Since the trivalent actinides (Am(III) and Cm(III)) are inextractable by the PUREX solvent, they are rejected to HLLW. Partitioning of trivalent actinides from HLLW followed by transmutation of them into short-lived or stable products (P&T strategy) is vital for the long-term safe management of HLLW. The current strategy for partitioning involves a two-cycle solvent extraction, in which the trivalent lanthanides and

actinides are co-extracted from HLLW, followed by the recovery using dilute nitric acid in the first-cycle. The mutual separation of lanthanides and actinides from dilute nitric acid medium is then carried out in the second-cycle. Several reagents have been proposed for the co-extraction of lanthanides and actinides as well as for their mutual separation.

In the recent past, development of a single-cycle process for the separation of trivalent actinides from HLLW is receiving increased attention. Unlike the conventional two-cycle process, this approach uses, in general, a combination of extractants comprising of reagents

employed for trivalent actinide partitioning and lanthanide-actinide separation. In this context, we studied the feasibility of using tetra-bis(2-ethylhexyl)diglycolamide (TEHDGA) and bis(2-ethylhexyl) phosphoric acid (HDEHP) extractants in n-dodecane (nDD) for the separation of Am(III) directly from simulated HLLW (100 GWd/Te). Synergistic extraction of Am(III) and Eu(III) from nitric acid medium followed by selective stripping of Am(III) from organic phase was observed. Based on the optimized conditions, a mixer settler run was performed to evaluate the feasibility of using these extractants for the separation of Am(III) directly from

fast reactor simulated HLLW.

For mixer-settler studies, the organic phase employed was 0.1 M TEHDGA – 0.25 M HDEHP/n-DD and the aqueous phase was simulated HLLW from fast reactor fuel reprocessing (FR-SHLLW) spiked with $^{(152+154)}$Eu(III) and ^{241}Am(III) tracers. The organic and aqueous phases were assayed for $^{(152+154)}$Eu(III) and ^{241}Am(III) radioactivity and the other metal ions were determined by the analysis of the aqueous phase (FR-SHLLW) using ICP-AES. Our studies indicated that Eu(III) was extracted quantitatively in 4 stages, whereas Am(III) exhibiting lower distribution ratio than Eu(III), required ~11 stages for complete extraction. Lanthanides and other metal ions were determined by the analysis of these metal ions in aqueous raffinate. All the lanthanides along with Mo(VI) and Y(III) are extracted quantitatively from FR-SHLLW and Fe(III) is extracted to the extent of 80%. Other metal ions including Zr(IV) and Pd(II) were rejected to raffinate.

Recovery of Am(III) from the loaded organic phase was carried out by using an aqueous formulation, 0.05 M DTPA (ditheylenetriamine penta acetic acid)- 0.5 M citric acid at pH 3, developed for stripping of Am(III) from other lanthanides present in organic phase. Selective stripping and quantitative recovery of Am(III) from loaded organic phase was observed in 4 contacts. However, it was necessary to understand the stripping behavior of Eu(III) and other lanthanides during the recovery of Am(III). Analysis of the aqueous and organic phases indicated that the contamination of Eu(III) in the Am(III) product was about 5%. Similarly, the stripping of other lanthanides in the Am(III) product was less than 10%. Our studies, thus, indicated the
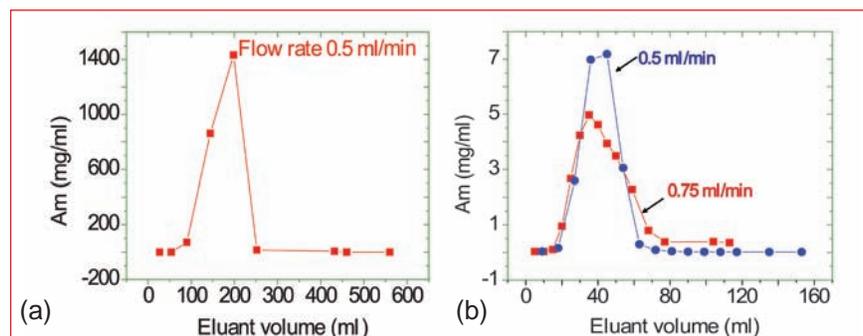
Fig. 1 *Elution profile of Am(III) (a) using 0.01M HNO$_3$ from CMPO-XAD support. Americium was eluted with about 175 ml of 0.01M HNO$_3$ and (b) with 0.1M citric acid at different flow rates from CMPO/XAD support. Americium was eluted with ~40 ml of citrate solution*

feasibility of separating Am(III) from FR-SHLLW as well as other lanthanides in a single-cycle processing step. However, marginal contamination of some lanthanides such as La(III), Ce(III), Pr(III) and Nd(III) was observed (~10%). Nevertheless, the stripping of other lanthanides (having very large neutron absorption cross section) in the Am(III) product was negligible. Our results, thus confirms the possibility of separating Am(III) directly from fast reactor HLLW in a single-cycle processing step, for facilitating the transmutation of americium.

In an another study, acidic liquid waste effluent generated during the continuous solvent extraction (SX) runing in counter-current mode with 1.1M TiAP/HNP solvent and a feed solution containing U(VI), Pu(IV) and Am(III) were taken up for recovery of americium. It contained Am (III) at a concentration of ~0.3 mg/ml in 1.6 M HNO$_3$ and the total volume of the raffinate solution was about two litre. An extraction chromatographic technique based on octyl (phenyl)-N,N-diisobutyl carbanoyl methyl phosphine oxide (CMPO) as the stationary phase was employed for the recovery of Am(III). 50 wt% CMPO/XAD-7 resin was employed as the extraction chromatographic support material for the recovery of Am. The chromatographic resin material was

prepared by impregnating CMPO with XAD-7 support in the presence of a diluent followed by evaporation of the volatile solvent. The distribution ratio for the extraction of Am(III) from 3M HNO$_3$ with 50 wt% CMPO/XAD-7 resin was measured. Similarly, distribution ratios were also measured for americium from a solution with 0.01M HNO$_3$ and 0.1M citric acid (pH: 3.4).

The acidity of the feed solution was adjusted to 3M HNO$_3$ prior to loading. The feed solution was processed in three batches and loaded till 5% Am breakthrough was obtained in the eluate. The loaded Am(III) was initially eluted with 0.01M HNO$_3$ **(**Figure 1a), which resulted in the generation of large aqueous volume. Subsequently, 0.1M citric acid (pH adjusted to 3.4 with dilute ammonia) was used to elute Am(III) **(**Figure 1b). The loaded americium was eluted as a sharp band and column performance was found to be much better compared to the one obtained with dilute HNO$_3$. The formation of Am(III)-citrate complex was mainly responsible for the better performance of citric acid based system. These studies have established that Am(III) can be efficiently recovered from acidic waste solutions as a concentrate using extraction chromatographic technique with CMPO as the stationary phase, XAD-7 as the support material and citric acid as the complexing agent.

IV.12 Design and Commissioning of Field Instrumentation and PLC-SCADA System for DFRP Waste Tank Farm (WTF)

Waste tank farm (WTF) is meant for storage of radioactive liquid wastes before transferring to waste immobilization facility. The functions of waste tank farm instrumentation and control (I&C) include monitoring tank liquid parameters (level, density, pressure and temperature) and liquid transfer operation.

I&C design of waste tank farm

I&C architecture is based on PLC-SCADA and control panel (CP) as shown in Figure 1. It has been designed to ensure reliable and safe operation.

Instrumentation for measurement of process parameters

Purge method is used to measure tank liquid level and density. Differential pressure transmitters and T-type thermocouples are used for measuring liquid pressure and temperature respectively.

Liquid transfer and other operations

Liquid waste transfer among tanks is done using steam ejectors. Steam is controlled by air operated valves (AOV) which in turn are controlled by solenoid valves (SV). The other operations include sampling and sparging.

PLC and SCADA

The field instruments are connected to the PLC. All operations and interlocks are implemented in the PLC program. PLC is connected to redundant SCADA servers through ethernet. SCADA provides the operators with
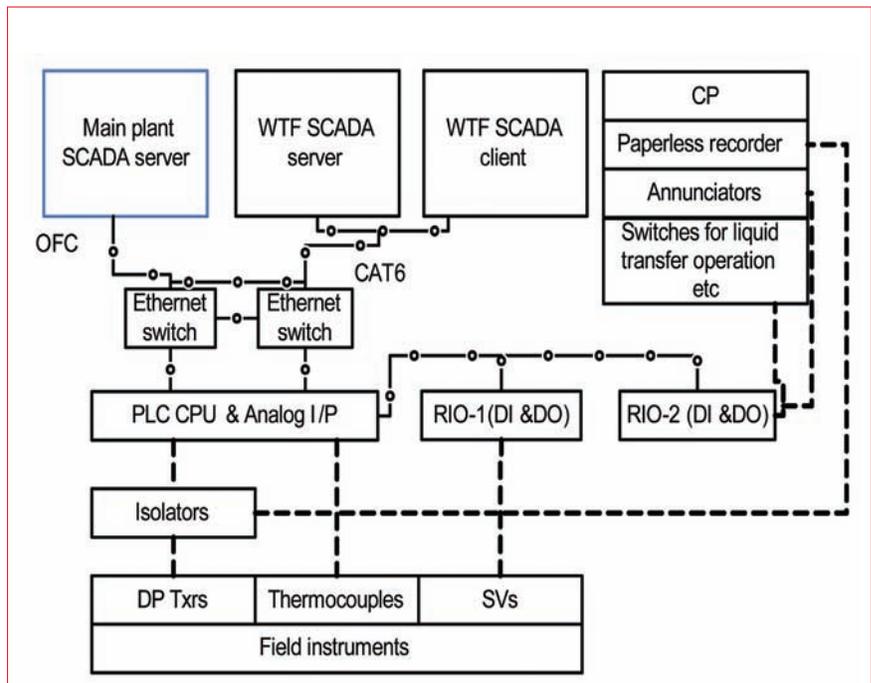
Fig. 1 *DFRP waste tank farm instrumentation and control architecture*

the interface to view all plant parameters and carry out the operations. The SCADA also provides trend graphs, alarms, reports etc. to the operator.

Control panel

Control panel houses paperless recorders for monitoring of selected process parameters, alarm annunciators and key operated switches for steam ejector based transfers. Control panel front fascia is shown in Figure 2.

Instrumentation and control of ventilation

Status of off gas exhaust fans and dampers are provided on control panel and in SCADA. Remote start/stop switches of fans are provided on control panel . Instrumentation is also provided for off-gas equipment.

Supplementary monitoring room

DFRP main control room acts

as secondary monitoring for waste tank farm and vice versa. Continuous monitoring of waste tank farm signals in DFRP main plant control room (MCR) is through optical fiber communication link.

Commissioning

All field instruments are ensured of their performance by various acceptance tests at every stage. After cabling and providing electrical supply, integration of field instruments with PLC, SCADA and control panel was carried out with detailed tests.

Fig. 2 *Control panel*

IV.13 Studies on the Development of Sol-Gel Process for Fuel Fabrication

High density pellets of (U, Pu) mixed oxide (MOX) are fabricated through powder metallurgical processes that involve preparation of powders of these oxides, mixing, their consolidation into pellets and sintering. These processes lead to the generation of aerosols inside the glove boxes in which they are handled. Production of microspheres through the sol-gel process – an advanced process-involves handling only solutions and sols rather than solids and powders and is more amenable for remotization and significantly reduces the radiotoxic burden.

The actinide elements Am, Np, and Cm (collectively called as minor actinides) with a long half life that are present in the spent fuel (in relatively small quantities) need to be transmuted into short lived radioactive nuclides (*eg. by* incorporating them in a conventional fuel) in order to reduce the radiotoxic burden to the environment. Hence, the fabrication of MOX fuel pellets containing minor actinides is an important aspect of the research on fast reactor fuels. Since minor actinides are highly radiotoxic materials a special purpose remote handling facility is being developed in our laboratory for fabricating these fuels.

Broth preparation and the preparation of acid deficient plutonium nitrate solution are critical steps in the preparation of $(U,Pu)O_2$ MOX microspheres. In order to optimize the conditions for the preparation of the acid deficient plutonium nitrate solution trial experiments were carried out. Subsequently by using this solution $(U, 21\%Pu)O_2$ microspheres were prepared by

using the internal gelation method. These microspheres were dried and calcined at 773 K in air. The dried microspheres were found to be defect free and free flowing. The photograph of the dried $(U, 21\%Pu)O_2$ microspheres is shown in Figure 1a.

In order to optimize the parameters for the preparation of microspheres containing americium, trial experiments were carried out. Urania microspheres containing about 5% of americium oxide was successfully produced by using the external gelation technique. The wet microspheres were washed and dried in a glove box facility (Figure 1b). This experiment has established the possibility of making microspheres impregnated with americium, an important step towards fabrication of a sphere-pac fuel pin containing minor actinide elements.

Porous TiO_2 microspheres find application in the removal of plutonium from the carbonate medium by column chromatography. Internal gelation process is an excellent route for the preparation of mono-dispersed microspheres. So far no systematic study has been carried out on the gelation chemistry for the preparation of TiO_2 microspheres through the internal gelation method. Hence, systematic studies on the preparation of TiO_2 microspheres through internal gelation was taken up. The key parameters that influence the gelation process were identified and optimized. In the internal gelation process hexamethylene tetramine (HMTA) and urea are used as gelating agents. A solution containing $TiOCl_2$ along with a mixture of the gelating agents,
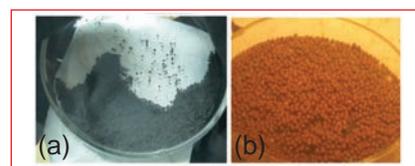
Fig. 1 *(a) Calcined product of (U, 21%Pu)O₂ microspheres and (b) green (U, 5% Am)O₂ microspheres*

called as the broth was used in these experiments. In the present study, while the concentration of HMTA and urea were fixed at 0.5 M and 1.75 M respectively, the concentration of titanium was varied from 0.6 M to 1.4 M. The duration required for observing a sudden rise in the viscosity of the broth during heating was measured at different rates of heating. The gelation temperature was found to be a strong function of the heating rate. However, the temperature required for gelation for a given composition of the broth is more relevant in arriving at the optimum conditions for gelation. In the present study, the gelation temperature of various compositions of broth was determined at four different heating rates (1.62, 2.17, 3.35 and 4.21 K min^{-1}).

A linear least square regression analysis of these data was carried out. Extrapolation of the variation of the temperature of gelation to zero heating rate yielded the temperature at which gelation would occur in this broth. This temperature could be taken as an index for comparing the characteristics of broths with different compositions. This could also be regarded as the "equilibrium gelation" temperature. The dependence of this onset temperature on the concentration of Ti in the broth was found out by a series of experiments. A least square regression analysis of

these results yielded the following expression. Equilibrium gelation temperature (˚C) = 14.6 + 20 [Ti].

This concept is being used for the first time in determining the gelation temperature.

Gelation experiments were carried out with broths of different compositions using a 1.8 m gelation column. It was found that the compositions with equilibrium gelation temperature in the range of 30 – 35° C ([Ti] = 0.8, 1.0 and 1.2) yielded good crack free microspheres after heat treatment.

IV.14   PLC Web Server Module as a Diverse System for a Reprocessing Plant SCADA System

In a nuclear fuel reprocessing plant, plant signals are digitized using distributed PLCs which provide the information over plant local area network (LAN) to redundant SCADA servers. This information is in turn communicated from SCADA servers to the control room operator display stations over LAN. In the event of failure of SCADA server, the plant information will not be available to the operator in the control room. Redundant SCADA servers though provide high availability, still can have potential common mode failure due to lack of diversity among them. Hence a provision of diversified distributed remote web server part of each remote PLC system, completely independent of SCADA servers, is desirable from plant safety and operation point of view. Even when the control room is uninhabitable ,these PLC based remote web servers can provide plant information at remote locations using panel PCs (running browser clients) located in PLC racks. In addition, these PLC based web servers also send plant data to dedicated display stations located in control room running browser software. These PLC based web servers are realized using redundant ethernet modules with HTTP server software running in them plugged into central processing unit (CPU) backplane of PLC as shown in Figure 1. This ethernet based web server module is hot swappable and can be plugged into any available slot in the CPU backplane. It also provides real-time peer-to-peer communications. This ethernet module supports non web based functions also. Using the web page development software the web pages are developed as static pages with tag name, alarm status, engineering units, etc. The text boxes and indication lamps are associated with corresponding memory address of PLC tags. The pages are then loaded into the ethernet based web server module. At every scan interval, the PLC-CPU module reads plant signals using PLC input/output cards and sends values in engineering units to the PLC web server module. In turn the PLC web server module updates the remote browser client with values in real time.

The hardware and software tools used for development, viewing web pages, etc., are independent of those used for the development of redundant SCADA servers and control room display stations. The

Fig. 1 *PLC web server module mounted in PLC rack*

screenshot of a browser based display giving plant information, running on dedicated display stations in control room, received from these PLC based remote web servers is as shown in Figure 2. Thus, diversified PLC based remote web server implemented for the first time in DFRP ensures plant availability and safety even under situations like non availability of main SCADA servers and control room display stations. It also helps periodic surveillance as well as monitoring of process even when control room is uninhabitable.
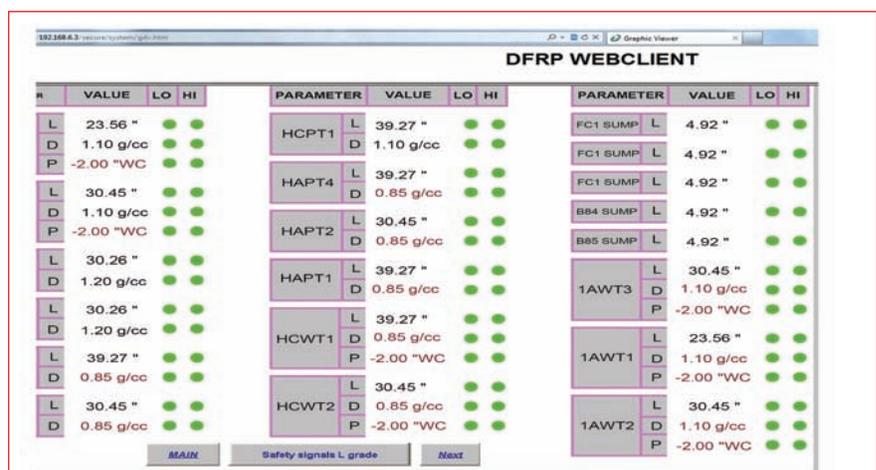

Fig. 2 *Web client displaying process parameters & alarms in real-time*

IV.15 Development and Qualification of Activated Flux for Tungsten Inert Gas (TIG) Welding of Titanium

Titanium is used as a structural material for the fabrication of dissolver vessel for the aqueous reprocessing of spent fuel of Fast Breeder Reactor. In fabricating titanium equipments, tungsten inert gas (TIG) welding process is a preferred choice owing to superior weld quality. The main objective of the present study is to develop a suitable activating flux and its qualification for activated flux tungsten inert gas (ATIG) welding of titanium. The oxide based activated flux which is used for TIG welding of steel and stainless steel is not suitable and effective for welding of titanium. Hence, there was a need to formulate a suitable flux which is effective for titanium welding.

The flux formulation was optimized by carrying out many trials of bead on plate welding on ASTM grade-2 titanium plate using single and multi-component flux powders (Figure 1a). ATIG welding of titanium using this flux produces a very narrow weld bead with depth to width ratio of about 1.25 compared to 0.25 of conventional TIG welds produced using same welding parameters (Figure 1d). The welding arcs captured using high speed camera showed arc constriction and overall arc size reduction in ATIG welding (Figure 1b) compared to TIG welding (Figure 1c). This is a proof of mechanism of arc constriction by the use of flux which increases the arc energy density and therefore, weld bead penetration. As the welding progresses, the flux is vaporized by the arc heat on the leading side and there will be no flux on the trailing side of the arc. Therefore, there is no sign of arc constriction on the trailing side

and the arc is similar to that in conventional TIG welding.

The welding parameters were optimized using this developed flux to achieve full penetration in 6 mm thick titanium plate without addition of any filler metal. ATIG weld joints were prepared using 6 mm thick titanium plates with square-butt joint geometry. The weld joints were qualified by radiography. The root bend and face bend tests passed 4T bend radius as per ASME Section IX requirements with bend angle of 180°. In transverse tensile testing, the weld joints fractured in the weld metal with tensile strength of 398 MPa and sufficient ductility. The tensile strength of the weld joint is similar to the base material tensile strength of 402 MPa and is also well above the minimum specified tensile strength of 345 MPa for ASTM grade-2 titanium base material. Therefore, the tensile properties of the ATIG weld joints of titanium are acceptable as per ASME section IX. The failure in the weld metal could be due to the presence of coarse and columnar primary

Table 1: Corrosion rate (mpy) of Ti and its ATIG weld joint		
Phases ↓	Ti base material	ATIG weld joint
Liquid	15.17	11.90
Vapour	0.37	0.62
Condensate	0.30	0.76

β grains found in the weld metal. Hardness measurements across the weld joint showed no noticeable variation in hardness in the base metal, heat affected zone and weld metal, which is preferable. Three phase corrosion test in liquid, vapour and condensate phase of the weld joints in 11.5 molar boiling nitric acid showed improved corrosion resistance compared to the base material (Table 1). It is concluded that an activated flux for TIG welding of titanium has been successfully developed as the weld joints passed all the qualification tests required according to ASME section IX.
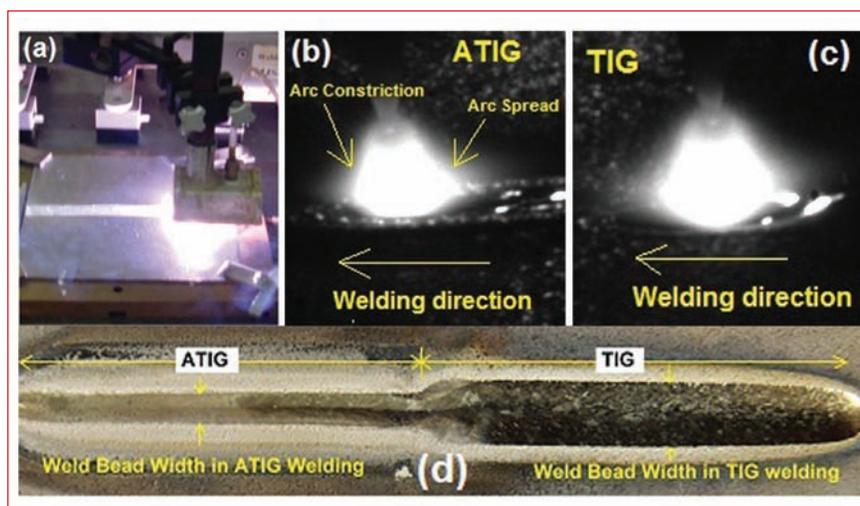

Fig. 1 *(a) ATIG welding in progress, (b) & (c) arcs captured by high speed camera in ATIG & TIG welding process respectively and (d) weld bead profile in TIG and ATIG welding for same welding parameters*

IV.16   Positron Annihilation Studies on Cesium Loaded Iron Phosphate Glasses

Iron phosphate glasses (IPG) are potential matrices for immobilisation of high level nuclear wastes rich in alkali oxides, sulphates and chrome oxides which are poorly suited for vitrification in borosilicate glasses. The low melting temperatures of IPG compared to borosilicate glasses make it suitable for loading radioactive wastes like ^{137}Cs which are extremely volatile at high temperatures. Iron phosphate glasses with a nominal composition of 40 mol% Fe_2O_3 : 60 mol% P_2O_5 is said to accommodate ~ 50 wt% of cesium, while maintaining excellent chemical durability. Exploring the waste loading capacities of these glasses becomes crucial in deciding their suitability as a waste matrix. In this context we have attempted to use positron lifetime spectroscopy to follow the microstructural evolution of open volume defects in IPG as cesium gets progressively loaded in the matrix.

IPG (40 mol% Fe_2O_3 : 60 mol% P_2O_5) and Cs doped IPG (5, 12, 18, 26 and 35 mol% Cs_2O) were prepared by mixing appropriate quantities of Fe_2O_3, $NH_4H_2PO_4$ and Cs_2CO_3 in an inert atmosphere argon glove box, taking care to maintain an FeP ratio of 0.67 and an O/P ratio of 3.5. The mixtures were initially heated at 873 K and then slowly taken up to their respective melting temperatures. The melts were then quenched on to SS dies, to yield the respective glasses. X-ray diffraction measurements were carried out for all samples. Broad features characterize the amorphous nature of the samples.

Positron lifetime measurements were carried out on both IPG and Cs loaded IPG pellets using BaF_2 based fast-fast lifetime spectrometer
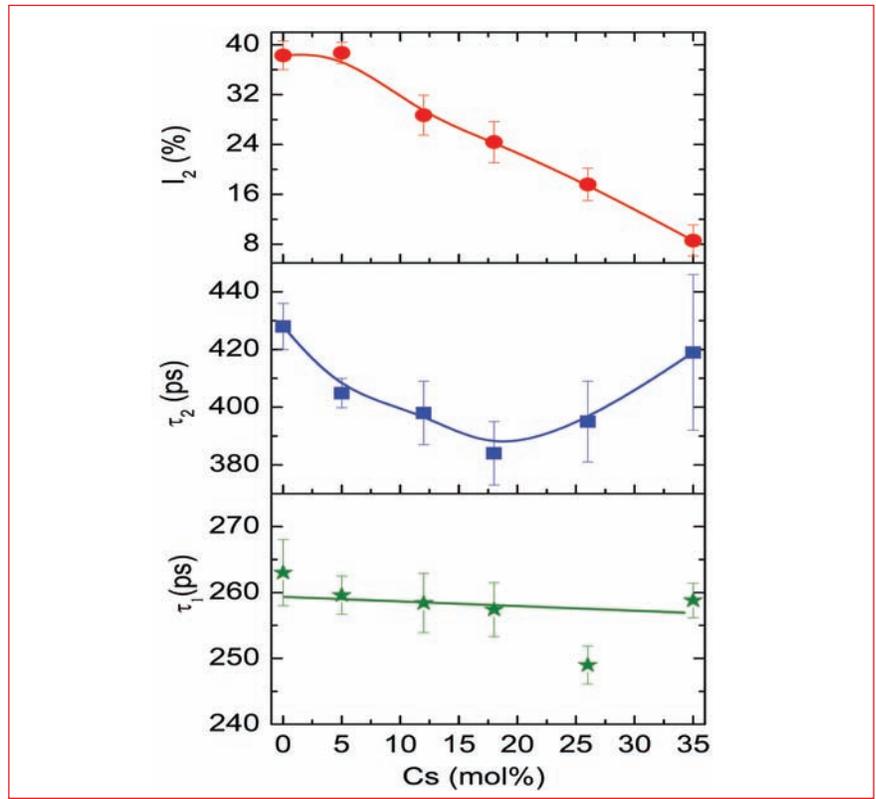

Fig. 1   *Variation of resolved lifetime components τ_1, τ_2 and I_2 as a function of cesium loading in 40 mol% Fe_2O_3:60 mol% P_2O_5 glass*

having a time resolution of 260 ps. About 10^6 counts were accumulated at the peak for each positron lifetime measurement. The experimental spectra were then analyzed to extract resolved lifetime components and their intensities. Ab-initio positron lifetime calculations based on atomic superposition method were carried out for $Fe_3(P_2O_7)_2$ - the parent crystalline counterpart of 40 mol% Fe_2O_3:60 mol% P_2O_5 glass. In an attempt to model the nature of the defects present, appropriate cluster of atoms were removed creating voids and lifetime calculations were performed in an unrelaxed configuration.

Figure 1 shows the variation of the positron lifetime components τ_1, τ_2 and its intensity I_2 as a function of Cs loading. The as-received IPG exhibits two lifetime components,

τ_1 (263 ps) corresponding to the reduced bulk lifetime and τ_2 (428 ps) corresponding to the defect lifetime. IPG consists predominantly of $(P_2O_7)^{4-}$ linkages interspersed by FeO_6 octahedra/tetrahedra. This glassy network also consists of voids which act as trapping centres for positrons and give rise to a defect lifetime τ_2. The calculated bulk lifetime (τ_b) in crystalline $Fe_3(P_2O_7)_2$ is 321 ps. The experimental value of 263 ps for τ_1 can be theoretically accounted for annihilation in the bulk. In order to understand the nature of defect corresponding to τ_2 value of 428 ps, positron lifetime values were computed for various defect and defect cluster configurations. A void, created by removing a cluster of one phosphate (1P + 4O atoms) unit with a radius of 2 Å, is found to give a lifetime value of 425 ps which closely
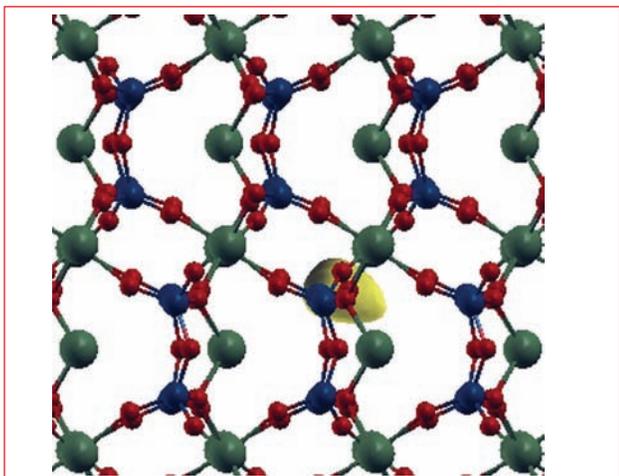
Fig. 2 *Positron density profile around a PO₄ void in crystalline Fe₃(P₂O₇)₂. Atoms are shown as spheres with Fe in green, P in blue and O in red. The maximum positron density, shaded in yellow, is at the void*
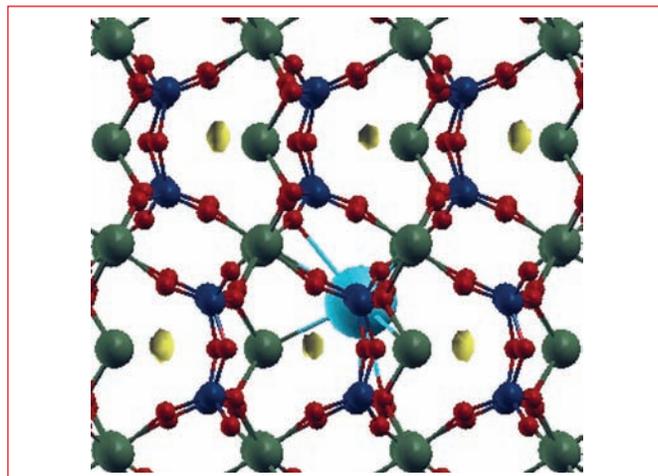
Fig. 3 *Positron density profile after putting Cs (blue colour) in the void. The maximum positron density shaded in yellow is now not localized at the void instead resides in the interstitial regions*

matches with the experimental defect lifetime. Figure 2 shows the positron density distribution being localized in the void. Hence the lifetime component τ_2 corresponds to positron annihilating in voids. Accordingly, the intensity I_2 is a measure of the void concentration.

As cesium gets progressively loaded into the glass, resolved lifetime components show interesting variations as seen in Figure 1. τ_1 remains constant at nearly 260 ps. However, τ_2 shows a marginal decrease upto 18 mol% of Cs_2O and is seen to increase again for higher Cs loading which indicates a reduction in void size upto 18 mol% Cs loading, beyond which the void size increases back to undoped value. However, the void intensity I_2 decreases linearly from 40 to 8% with increased Cs loading. It is interesting to note that the glass transition temperature (T_g) exhibits a maximum for ~21 mol% Cs loaded iron phosphate glass after which the T_g is observed to drastically decrease.

In order to understand the decrease in the defect intensity (I_2) upon Cs loading, lifetime calculation was performed by putting one Cs atom at the centre of the void. The calculated void lifetime value of 425 ps decreases to the bulk value of 321 ps upon filling the voids with Cs. This is illustrated in Figure 3, showing delocalization of the positron density profile upon filling the void with cesium. Thus, the decrease in defect intensity can be understood in terms of depletion of the available voids or open spaces as cesium concentration is progressively increased.

Cs is known to be a network modifier in phosphate glass. There are two structurally distinct composition ranges for network modifier ion concentrations. At lower levels of Cs loading, available terminal oxygen concentrations allow for formation of isolated Cs polyhedral as shown in Figure 4a. At higher Cs concentrations, shortage of terminal oxygen leads to formation of edge/corner sharing Cs polyhedra as shown in Figure 4b. The change over concentration is known to vary with coordination number of the modifier atom. Sudden changes in macroscopic properties such as glass transition temperature coincide with this concentration driven transition in modifier bonding from localized polyhedra to modifier substructures.

These concentration dependent local structure differences may be responsible for the observed variations in defect lifetime as seen in Figure 1. Our recent Raman scattering studies also show such local structural changes associated with Cs loading. Synchrotron based EXAFS and X-ray scattering studies are in progress, which can give better insights to understand the local structure of Cs loaded iron phosphate glasses.
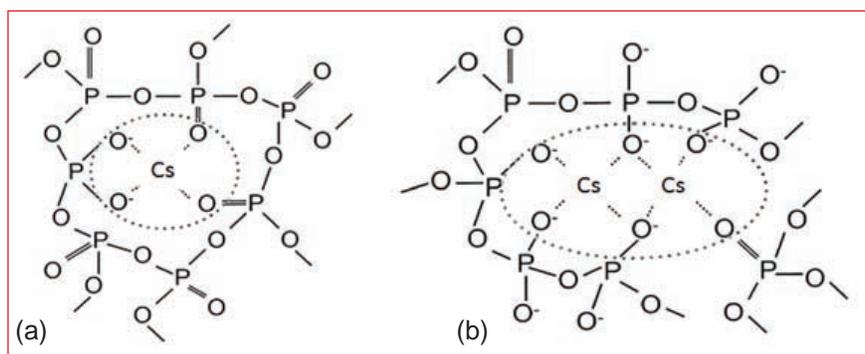
Fig. 4 *Schematic model showing (a) isolated Cs polyhedral and (b) edge sharing Cs polyhedra formation with available terminal oxygen*
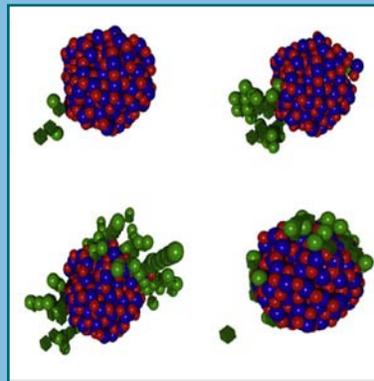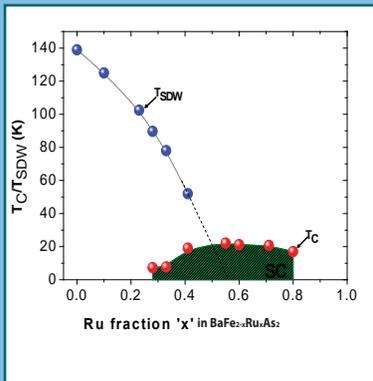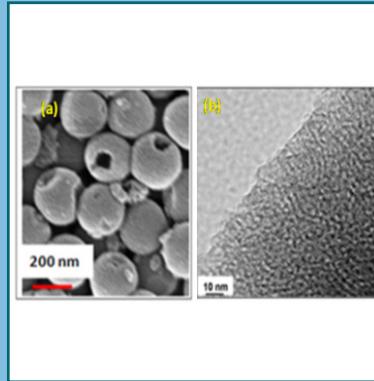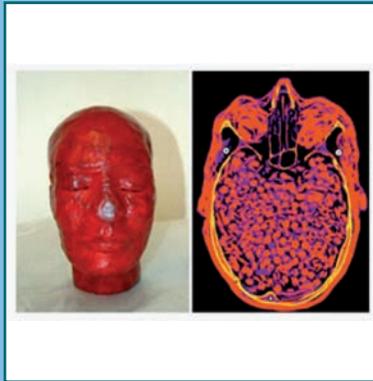
CHAPTER
5

Basic Research

V.1 Innovative and Fundamental Studies on Sodium Fire

Sodium leaks may pose serious threat to the operation of fast reactors due to high chemical activity of sodium with air and water. A few innovative and small scale experiments are being carried out to study the possible consequences of small sodium leaks, sodium interaction with structural concrete and sodium reaction with water/steam in the steam generator. Salient features of the experiments and important results are highlighted.

Small sodium leak experiments

All the sodium piping is provided with detectors for indicating sodium leak. However, the leak rates below 100 g/h can not be detected. The sodium coming out during small leak may plug the defect or may react with thermal insulation and form corrosive products on the piping material. This may cause sudden failure of the piping without any prior indication. Hence, to investigate sodium leaks through small defects in piping, an experimental study is undertaken. The setup consisting of a sodium holdup vessel and enclosure to collect the leaked sodium is installed as shown in Figure 1.

Sodium vessel is designed for 5 bar at 600°C and provided with a bottom nozzle having 0.3 mm
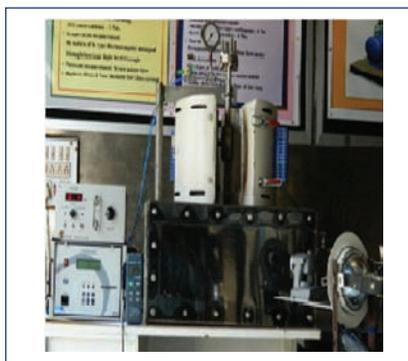
Fig. 1 *Schematic of setup*

opening as shown in Figure 2.

The enclosure is provided with sodium collecting pan, a precision balance, argon circuit with oxygen monitoring and other necessary instrumentation.

A series of experiments were carried out with 25 g of sodium at 500°C and various pressures viz., 1, 2, 3, 4 bar and gravity. When sodium holdup vessel is at 500 °C, the nozzle tip temperature reaches about 120°C allowing the sodium to leak in the collection pan kept in the enclosure. The enclosure is maintained at low oxygen concentration to prevent reaction of sodium. After each run, the weight accumulated on pan is recorded to estimate the average leak rate.

A few important results of experiments are shown below in Figures 3 and 4, for both draining

Fig. 2 *Sodium holdup vessel and release nozzle opening*

under gravity and pressure. In many of the runs the sodium flow was observed to be stopped due to self-plugging of the release nozzle by sodium oxides. This plugging phenomenon was also found to be random. Under gravity, leak rate is found to vary between 24 to 30 g/h (Figure 3).

Sodium leak rates under pressurized release were found to be 800, 1250 and 3600 g/h at 1, 2 and 4 bar respectively.

The plugging phenomenon was observed in most of the experiments after few grams ejected out under gravity and also under pressurization. The experiments were then extended for establishing unplugging conditions viz., where the plug gets broken and sodium flow is resumed. The unplugging has been consistent at a vessel tip
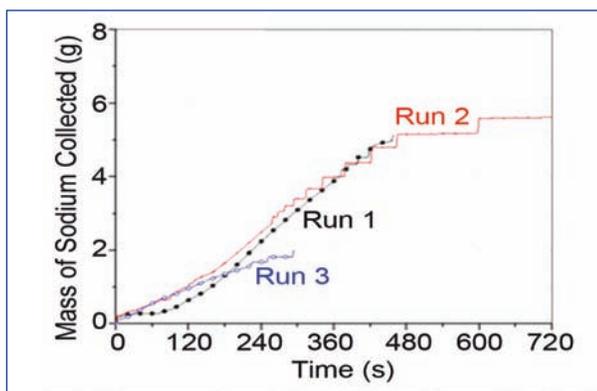
Fig. 3 *Leaked sodium through 0.3 mm dia. opening under gravity*
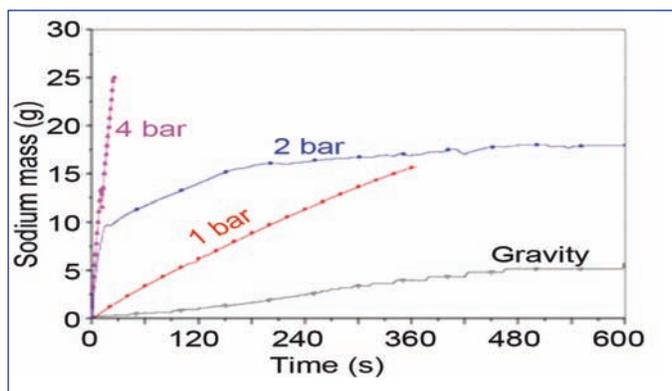
Fig. 4 *Sodium leak rate with pressure*

temperature of 290 to 300 °C and an applied pressure of 4-5 bar.

From the above results, it is inferred that the sodium leak rates are well above 100 g/h for pressure cases and hence they may be well detectable by the detectors before the defect aggravates to cause a large failure. Moreover, the sodium piping is maintained about 400 °C under 4 bar pressure, hence possibility of plugging may be remote. However, in the realistic scenario of small sodium leak in secondary systems of FBRs, sodium will react with thermal insulation in presence of air. Hence, an experimental loop is being setup to investigate sodium insulation reaction and its effect on sodium piping.

Sodium concrete interaction studies

During sodium leak incident in the secondary sodium circuit the sodium will be ejected out under pressure and may interact with the underlying structural concrete. The reaction is exothermic and apart from temperature and hydrogen release, it causes degradation of concrete. A sacrificial layer is provided on the concrete used in the steam generator building. However, the depth of layer has to be suggested for different orientations viz., for vertical walls and flooring.

To study the effect of sodium interaction on impinging, flowing and stagnant surfaces, an experiment was conducted. With limestone concrete specimen with similar composition of sacrificial layer for PFBR concrete. The propagation of thermal and chemical reaction in the concrete specimen and external and internal damage of concrete block are being evaluated.

Experimental setup consists of sodium supply tank and piping mounted with heaters and necessary instrumentation. The concrete sample placed in a cubical experimental chamber of 140 m^3 volume. About 2 kg of sodium at 550 °C was released onto the specimen at 25 g/s drain rate. About twenty five thermocouples were positioned inside the specimen at various depths (5 mm, 25 mm and 45 mm from the surface) for studying the temperature distribution. High speed video imaging, online gas analysis were deployed during the run for measuring concentration of O_2, CO, CO_2 and CH_4. The setup and sodium impingement scenarios on the concrete are shown in Figure 5.

The sodium temperature on the surface of concrete specimen is shown in Figure 6.

Sodium temperature at impingement and sloping zone has seen peak (800 °C) in the initial period but

Fig. 5 *Schematic of setup and scenarios during run*

reduced to below 200 °C within short time. The temperature in the stagnation zone was observed to be increasing gradually above 600 °C indicating accumulation of burning sodium.

Temperature distribution in the block at various depths is shown in Figure 7. Maximum temperatures in the block at 5 mm, 25 mm and 45 mm depth from the surface are observed to be 120, 80 and 60 °C respectively.

Preliminary post-test analysis indicated no noticeable visual damage on the specimen. However, the specimen is being subjected to non destructive testing (for crack and sodium penetration depth), rebound hammer test and destructive testing for assessment of loss of strength and depth of sodium penetration. The outcome will be vital in developing sodium resistant concrete for future applications.
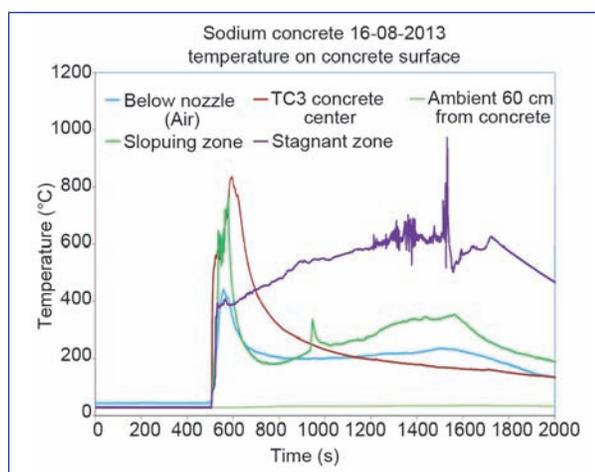
Fig. 6 *Sodium temperature on the concrete surface at three zones*
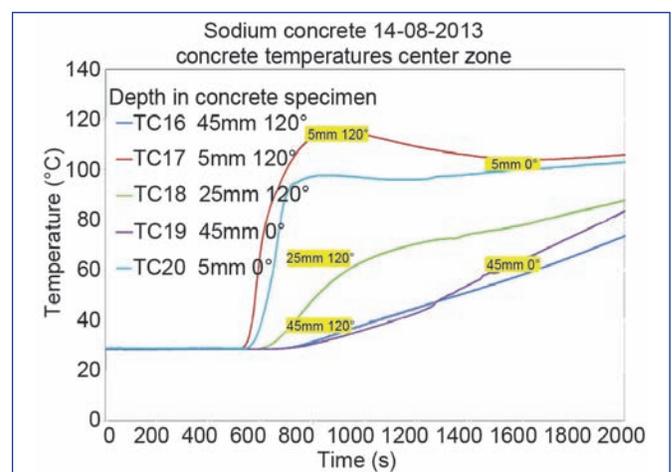
Fig. 7 *Temperature distribution in the concrete block at various depths*

Fig. 8 *Sodium water reaction setup*

(a) (b)

Fig. 9 *Scenarios during sodium water interaction*

Sodium interaction with steam/water

During a water/steam leak into sodium in the steam generator of fast breeder reactor, there will be a reaction between sodium and water releasing hydrogen along with a pressure pulse. To investigate the mechanism of sodium steam interaction and consequent temperature, pressure raise, experimental setup has been installed.

Sodium water reaction setup consists of a water injection system and a cubical test chamber as shown in Figure 8.

The test chamber is provided with a heater mounted cup to create a sodium pool, inert gas purging system, gas monitoring system and a piezoelectric type transient pressure sensor with a range of 0-500 psi at 10 mV/psi sensitivity. Water injection system is connected to a water supply tank though a solenoid valve and a needle type release nozzle. The nozzle is initially placed above sodium pool and will be immersed during the run by a piston valve type arrangement and a pneumatic actuator. This prevents the chance of injection line blockage by sodium.

Few experiments were conducted by injecting water at about 6 ml/minute into 10 g of sodium pool at 350 °C. The reaction was captured with high speed camera

and the scenario is as shown in the Figure 9.

Transient pressure pulse in the interaction chamber was monitored and indicated in Figure 10.

A new setup is being installed to study the effects of pressure pulse propagation in a closed system.

The setup for steam sodium interaction comprises of a steam vessel designed for 4 bar and 300 °C which can generate about 100 ml steam and test chamber similar to that of sodium water setup. A pressure safety valve is provided for the steam vessel to prevent system over pressurization. The steam release line is provided with a solenoid valve to facilitate steam release from vessel to enclosure as shown in Figure 11.

Pressure gauges and thermocouples are mounted at different locations on the steam line to monitor pressure and temperature of steam. Thermocouples are provided adjacent to the nozzle within the sodium to record the interaction

temperature.

The enclosure is equipped with a pressure transducer to record any pressure pulse generated. Heaters are mounted on the steam vessel. The atmosphere inside enclosure is maintained inert by argon purging. Provisions are there for enclosure for gas sampling, inert gas purging and evacuation purposes.

Preliminary experiment has indicated that the steam ejected is driving out the sodium from the cup of the sodium pool and investigating the reaction between steam and sodium is difficult in open system. Hence, a setup with closed sodium vessel is being installed with an in-sodium pressure probe for measuring transient pressure in the sodium pool. A high pressure steam injection setup which will simulate steam sodium interaction at pressures upto 200 bar (simulating tube rupture in steam generator) is also being setup to study the pressure pulse propagation in the connecting systems.
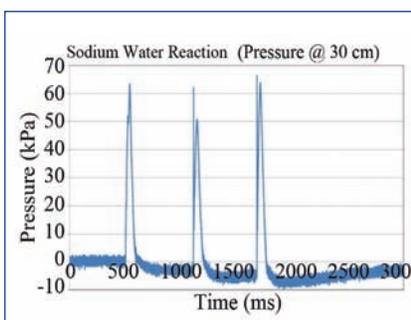
Fig. 10 *Pressure pulse obtained during sodium water reaction*

Fig. 11 *Setup to study sodium steam interaction*

V.2 Radiation Induced Defect Centers in Borate Based Thermoluminescent Materials

Boratebased thermoluminescent (TL) phosphors are gaining more importance for dosimetry applications in the recent times because of the ease of synthesis in bulk quantities, simple glow curve structure, increased neutron and gamma sensitivity, near tissue equivalence and simple thermal treatment procedure for reuse. The understanding of the radiation induced defect centers in these phosphors is necessary to explain thermoluminescent mechanism in these phosphors. The information about the charge traps though vital to explain the thermoluminescent process, cannot be obtained from the thermoluminescent measurements alone. Hence in this study an attempt has been made to explain the thermoluminescent process by identifying the defect centers formed upon irradiation using infrared (IR) and electron paramagnetic resonance (EPR) spectroscopic studies.

Four different borates viz., lithium tetra borate (LTB), magnesium tetra borate (MTB), zinc metaborate (ZMB) and cadmium tetra borate (CTB) were investigated in this study. In all the borate systems studied, the presence of tetrahedral (BO_4) and trigonal (BO_3) networks have been elucidated using infrared spectroscopy. The infrared spectrum of a typical borate system (LTB:Mn) is shown in Figure 1.

Further to identify and characterize the defect centers formed upon gamma irradiation in these phosphors, it is necessary to have an idea of the possible defect forming centers from the knowledge of the structural characteristics. The schematic representation of the possible radiation induced defect centers in borates is illustrated in Figure 2. When boron (3 valence electrons) is present in tetrahedral arrangement the extra electron required for charge compensation is taken from the surrounding cations and hence act as a negative point defect. Such point defects act as hole traps and are termed as 'boron oxygen hole center' denoted as BOHC. The oxygen which acts as the trap bridges two different borate networks. The non-bridging oxygen can also be looked upon as another negatively charged point defect which can trap a hole in the absence of any nearby charge compensating cations at the interstitials. The possible electron trap centers that can result upon gamma irradiation are the boron electron center (BEC) which arises if two cations (R, R') of same valency, but different electron affinity are present in the lattice. In such cases the electron can be trapped at the antibonding orbital of R'–O bond. Also the interstitial cations can themselves serve as electron trap. Oxygen vacancies which may be formed for charge compensation due to the addition of dopants to the lattice during synthesis may also act as electron trap centers.
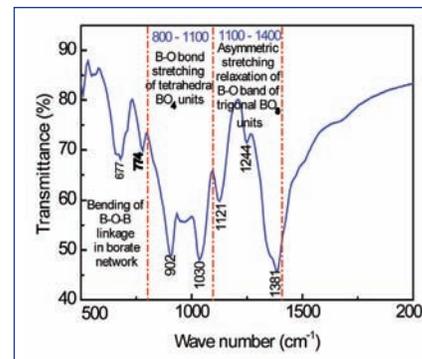
Fig. 1 *Infrared spectrum of LTB:Mn*

Most of the defect centers (electron and hole traps) formed upon irradiation are paramagnetic in nature. Hence, to identify the paramagnetic radicals formed in these borates and to establish their relevance to thermoluminescent, EPR measurements were carried out on unirradiated, gamma irradiated and phosphors irradiated to gamma dose and annealed at different temperatures from 50 to 300°C for one hour duration. Figure 3 shows the typical EPR signals recorded for manganese (Mn) doped LTB under different conditions. Unirradiated LTB:Mn shows a single broad and unresolved EPR signal (Figure 3(1)) centered at g=2 characteristic of Mn^{2+} ions in the matrix. The broad and unresolved

(a) R, R', R" - B,Li,Mg, Gd, Mn, Zn, Cd (Network formers)
C - Network modifiers - Li, Mg, Zn (interstitial)
(b)
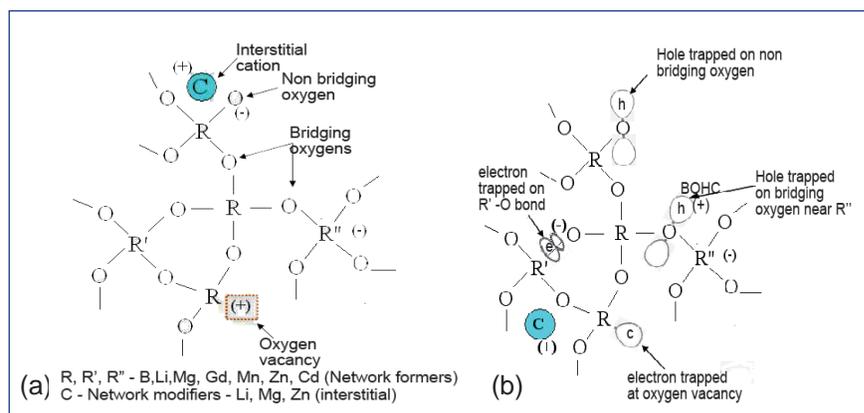
Fig. 2 *Possible defect centers in borate based phosphor showing the different types of radiation induced paramagnetic centers and their relationship with pre-existing radiation defects in the lattice (a) before and (b) after irradiation*

response is characteristic of Mn–Mn interactions (dipolar or exchange coupled).

In the case of irradiated LTB:Mn phosphors, two paramagnetic radicals were observed. Center 1 with a g-value characterized by 2.0043 is identified as 'boron oxygen hole center' (BOHC), which is a hole trapped on an oxygen ion that links two BO_4 units. Center 2 with a g-value characterized by 1.9988 is identified as an electron trapped at an oxygen vacancy (O_v^-). Thus upon gamma irradiation the holes are trapped in the bridging oxygen atoms and the electrons are trapped at the oxygen vacancies. When this irradiated phosphor is heated linearly from room temperature to 450 °C, an intense orange red thermoluminescent emission characteristic of Mn^{2+} was observed at a temperature around 270 °C. To find the relevance between the thermoluminescent glow peak at 270 °C and the paramagnetic radicals, the thermal decay of these radicals was measured from the decrease in the EPR signal intensity of the phosphors annealed to different temperatures (Figure 4). It was observed that both the centers were stable up to around 200 °C and there was a sudden drop in the signals beyond that temperature. Also the thermal activation energy of both the paramagnetic centers was determined using the relation,

$$ln[-ln(1 - \Delta I/I)] = c - \frac{E_a}{kT}$$

where I is the intensity of the signal in irradiated phosphor, ΔI is the amount of decrease in EPR signal after each annealing temperature (T), c is a constant and E_a is the thermal activation energy.

The activation energy for the thermal destruction of BOHC center and O_v^- centers were found to be 1.29±0.013 eV and 1.32±0.021 eV
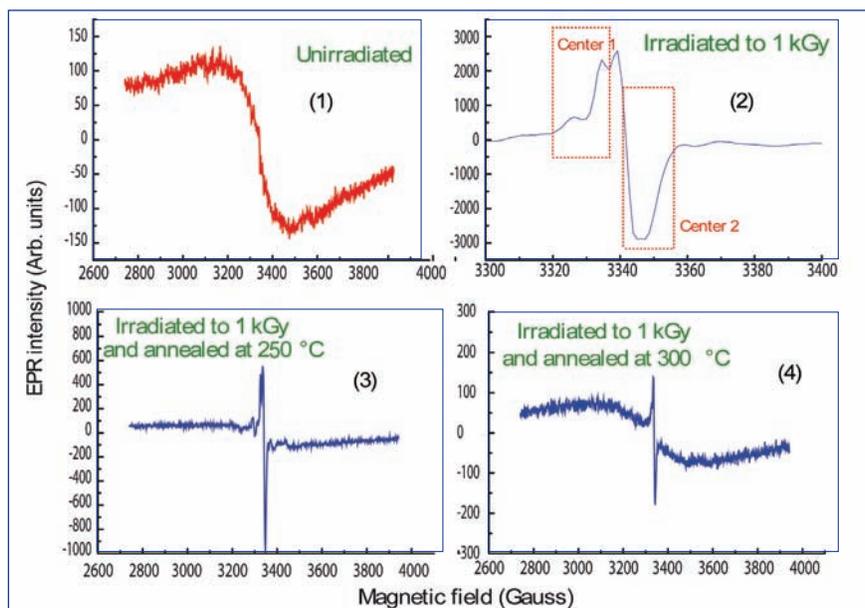
Fig. 3 EPR spectrum (first derivative) of $Li_2B_4O_7$:Mn phosphor under different conditions

respectively. From the kinetic analysis of thermoluminescent, the trap depth was determined as 1.27±0.028 eV. This confirms that these two centers are responsible for thermoluminescent in LTB:Mn phosphor. Based on the above analysis, the following model is proposed for the mechanism of thermoluminescent in LTB:Mn phosphor.

Upon irradiation,

$$Li_2B_4O_7 : Mn \rightarrow BOHC, O_V^-$$

Upon heating,

$$BOHC \rightarrow h$$

$$O_V^- + h \rightarrow O_V^* \rightarrow (Mn^{2+})^*$$
$$\rightarrow Mn^{2+} + h\nu \ (\textbf{TL})$$
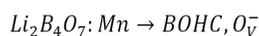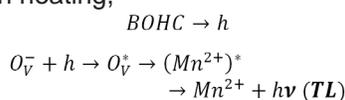
That is, upon irradiation electrons are trapped at oxygen vacancies and holes are trapped at bridging

oxygen of the two BO_4 tetrahedra where, the B^{3+} is replaced by Mn which causes the B-O bond of the two tetrahedral units to be much weaker. Upon heating, the holes are released from BOHC center and recombines with the electrons trapped at oxygen vacancies. This recombination energy is non-radiatively transferred to the nearby Mn^{2+} ions substituted for Li^+ ions and the excited Mn^{2+} ions gives it characteristic emission in the orange red region (580 nm).

Similarly, the trap centers responsible for thermoluminescent in the other borate phosphors were also studied and the defects identified using EPR are shown in Table 1.
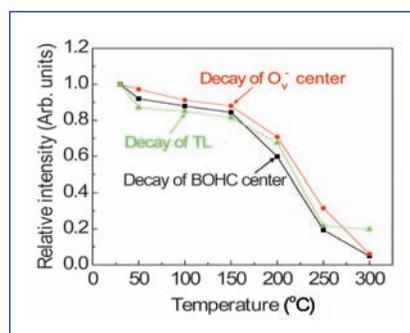
Fig. 4 Thermal decay of thermoluminescent and paramagnetic trap centers in LTB:Mn phosphor

Table 1: The paramagnetic radicals observed in other phosphors			
P	Center	g-value	Activation (eV)
MTB	BO_3^{2-}	2.0150	1.18±0.015
	O_v^-	1.9981	1.19±0.042
ZMB	BO_3^{2-}	2.0168	1.48±0.045
	O_v^-	1.9974	1.53±0.012
CTB	BO_3^{2-}	2.0127	1.05±0.025
	BEC	2.0024	1.02±0.032

V.3 Detection of Cations using Magnetic Nanoemulsions

Excess or deficiency of the heavy metal ions such as Fe^{3+}, Zn^{2+}, Cu^{2+} and intracellular ions like Na^+, K^+, Ca^{2+} and Mg^{2+} in human body fluids can lead to various biological disorders. Therefore, periodic monitoring of cations is a prerequisite for studying the physiological functions, diagnosis of diseases and the prevention. Similarly, heavy metals bound to proteins and nucleic acids can cause severe health hazards to human and animals. Most of the present techniques for detection of toxic cations at low concentrations are expensive, complex in design, non-portable and involve data interpretation. Other major drawback of some of the existing sensors is their slow response and poor sensitivity.

A simple sensor is developed for detection of cations in ppm levels, using magnetically polarizable nanoemulsions that consist of octane-based ferrimagnetic nanoparticles of ~10nm size, an ionic surfactant and water. The oil-in-water nanoemulsion is prepared using a simple emulsification procedure. For cation sensing, the nanoemulsion is illuminated with a fiber optic based white light source and the Bragg peak is monitored as a function of cation concentration. For visual detection, the color of the sample is recorded for different concentrations of ions. For quantitative measurement, the reflected Bragg peak   is recorded using a fiber based reflection probe.

Figures 1a to 1d shows the Bragg
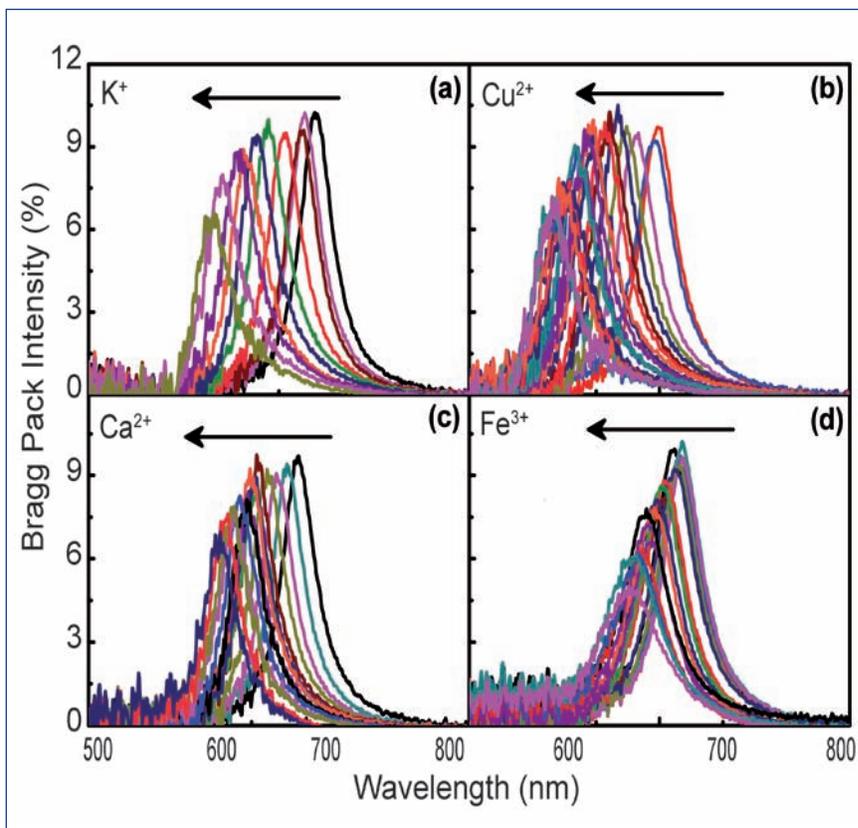
Fig. 1 *The Bragg peaks (λ_{max}) for different concentrations of (a) K^+, (b) Ca^{2+}, (c) Cu^{2+} and (d) Fe^{3+} (Arrows indicate increasing concentration of ions)*

peak (λ_{max}) for various cations where the λ_{max} monotonically blue shifts with increasing ion concentrations. The diffraction peaks are symmetric and narrow in all the cases, which indicate
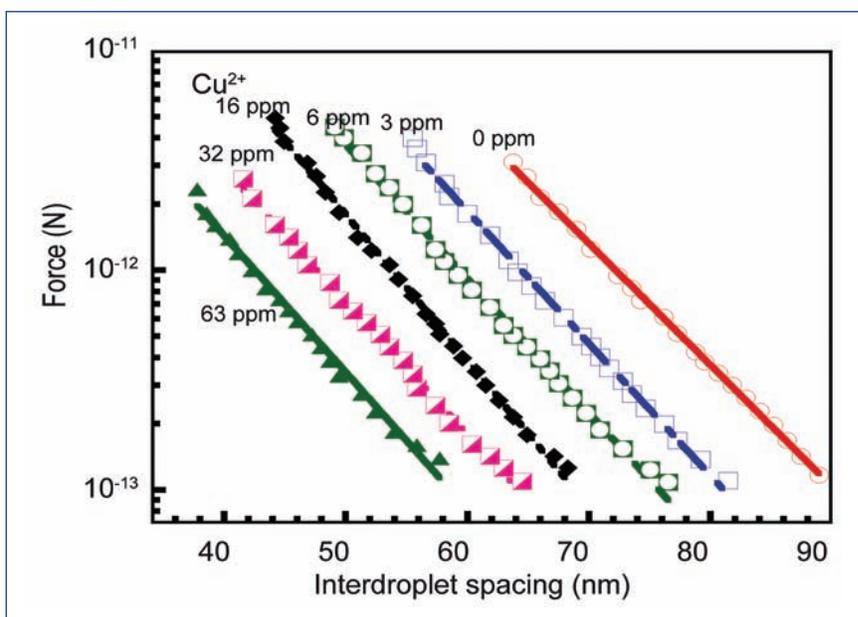
Fig. 2 *The force-distance profiles for different concentration of Cu^{2+} cation (The solid/dashed lines show the theoretical fit)*

that the 1-D ordering is stable irrespective of the concentration of cations. For K^+, the shift in the λ_{max} was 146 nm as the concentration of ions is increased from 0 to 319 ppm, where the observed lattice spacing reduction was ~55 nm. For Cu^{2+} cations, the shift in the λ_{max} was 83 nm as the concentration of ions is increased from 0 to 51 ppm. Though the overall shifts in the λ_{max} in both the cases are akin, the slopes were different for different cations. The different slopes indicate the selectivity for various ions.

Figure 2 shows force-distance profiles in the presence of Cu^{2+} cation of different concentrations. In all cases, the force profiles are found to decay exponentially with the inter-droplet spacing. From the force distance curve, the first interaction distance ($2L_0$), which is defined as the distance at which the force value is 2×10^{-13} N and the K^{-1} that describes the spatial extension over which the perturbation due to an electrical double layer extends.

In the case of Cu^{2+}, the $2L_0$ for 3, 6, 16, 32 and 63 ppm are 74, 69, 62, 55 and 51 nm, respectively. The average value of the Debye length for the K^+ and Cu^{2+} ions is ~7 nm. The decay length does not change much but the magnitude of the force increases significantly, which indicates an increase in the surface potential.

These results show that $2L_0$ values are very sensitive to diffusion of the ions into the double layer. However, no significant variation in the decay length is observed with added ions. The decay length calculation using electrostatic theory is found to be inaccurate for multivalent ions due to the complex
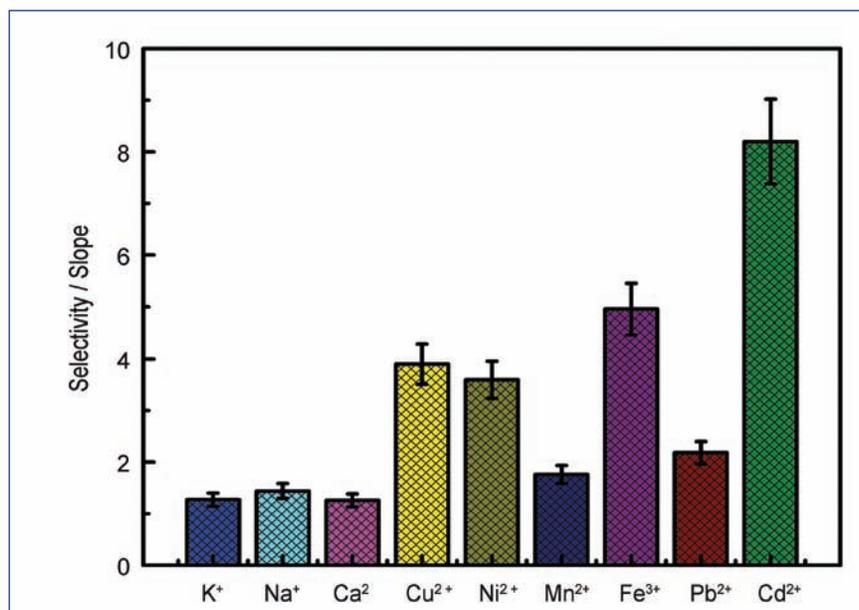
Fig. 3 *Selectivity for different cations*

many-body potential between the spheres. At smaller interdroplet spacing, only the counter ions are expected to contribute to the electrostatic screening because of strong repulsion between other spheres. With increase in the concentration of ions, the $2L_0$ decreases by several nanometers. Interestingly, the experimental force profiles follow electrostatic theory, irrespective of the concentration of added cations. The non-retarded van der Waals attraction is effective only at high salt concentrations and at very small surface separations. The structuring of water at the hydrophobic surface in presence of ions and directional binding of molecules can also lead to changes in $2L_0$.

To check the selectivity of this approach for different metal ions, the variation in the slopes of λ_{max} shift versus metal ion concentrations is compared (Figure 3). Interestingly, the slopes were different in all the cases, which confirm the selectivity of the nanofluid in recognizing different metal ions in solutions. The sensor shows highest slope change for Cd^{2+}. Among the studied

cations, the sensor shows highest sensitivity and selectivity for Cd^{2+}, with minimum threshold detection limit of 0.3 ppm. Selectivity in mixed ion conditions, was established by fixing the Cd^{2+} concentration (1 ppm) and varying the K^+ ion concentration ratio from 0 to 15. Even at 1:15 ratio (Cd^{2+}:K^+), the sensor shows selectivity for Cd^{2+}.

In conclusion, a novel, inexpensive and ultrasensitive approach for detection of metal ions in ppm levels is demonstrated for the first time. The sensor produces visually perceptible color changes, in the presence of metal ions, due to changes in the lattice periodicity of one-dimensional array of droplets. Alteration of the diffused electric double layer in presence of cations causes a large blue shift in the diffracted λ_{max}. The concentration of the metal ions is found to be directly proportional to the shift in the λ_{max}. Because the emulsion used is easy to produce, inexpensive, portable and allows rapid detection of several metal ions, it can be used as a tool for metal ion recognition.

V.4 The Study of Magnetism and Structure Across the Spin Density Wave Transition in $BaFe_{2-x}Ru_xAs_2$ Single Crystals

The last five years, condensed matter physics research is witness to intensive efforts in a class of superconductors, termed the FeAs superconductors. In the copper oxides, superconductivity occurs by doping holes and electrons into an anti-ferromagnetic insulator, whereas, in the FeAs superconductivity occurs at the expense of an itinerant anti-ferromagnetic spin density wave (SDW) ground state, either by the application of external pressure and by chemical substitution.

FeAs superconductors occur in several varieties, viz., LaOFeAs (1111), $BaFe_2As_2$ (122), LiFeAs (111) and more recently in the $CaFeAs_2$ (112) variant. In all of these systems, detailed phase diagrams have been reliably measured, because of the possibility of synthesis of single crystals. The striking properties of these superconductors has been their large critical fields, H_{C2}, a very high critical current density, J_C, unconventional superconductivity and the role of magnetic fluctuations in mediating the Cooper-pair interactions. Magnetism that

happens to be a competing ground state, is stripe like and is associated with very strong magneto-phonon coupling, leading to nematic fluctuations.

Of all the super conducting (SC) families indicated in the above paragraph, $BaFe_2As_2$ has been most well studied, since single crystals can be grown relatively easily in this system. We have synthesized single crystals of a variety of the substituted $BaFe_2As_2$ samples, using no flux. This method of synthesis yields smaller crystals, but are bereft of ferromagnetic impurity phases. We have in the course of our studies discovered superconductivity in ruthenium substituted $BaFe_2As_2$ system for the first time and have established its phase diagram. These crystals have been extensively used in the study of their properties, viz., critical field H_{C2} and critical current J_C. The critical fields were measured in the magneto-resistance set up while the critical current was obtained by measuring magnetization, in the vibrating sample magnetometer.

Here, we focus on the study of

magnetism and structure across the spin density wave transition in under doped $BaFe_{2-x}Ru_xAs_2$. The phase diagram of the $BaFe_{2-x}Ru_xAs_2$ system determined from resistivity versus temperature measurements on single crystals grown in our laboratory without flux is shown in Figure 1a. It is evident from the figure that SDW transition that occurs at 135K in the pristine $BaFe_2As_2$ sample depletes with increase in ruthenium substitution. At x=0.3, superconductivity emerges but vanishes beyond x=0.8. Associated with the paramagnetic to SDW transition is a structural transition from tetragonal to orthorhombic symmetry. As illustrated by this phase diagram, magnetic, structural instabilities are correlated with superconductivity. While in several systems the structural transition precedes the SDW transition, in the ruthenium substituted phase diagram there is a simultaneous occurrence of these transitions.

We have carried out structural characterization of powdered single crystals of the $BaFe_{2-x}Ru_xAs_2$
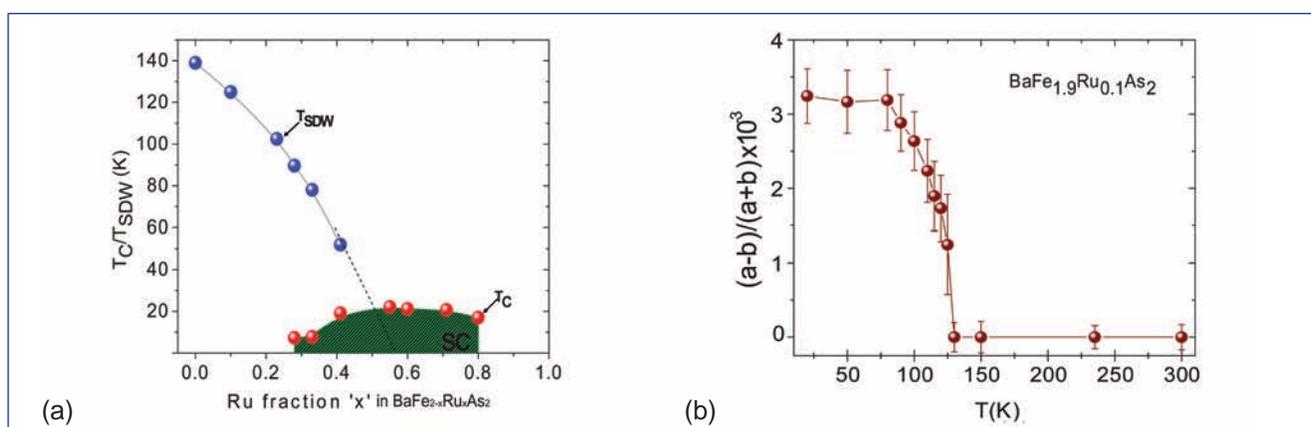
Fig. 1 *(a) Phase diagram showing the spin density wave and super conducting phases, obtained from resistivity of $BaFe_{2-x}Ru_xAs_2$ single crystals and (b) the orthorhombic distortion obtained from temperature dependent structure data for x=0.1*
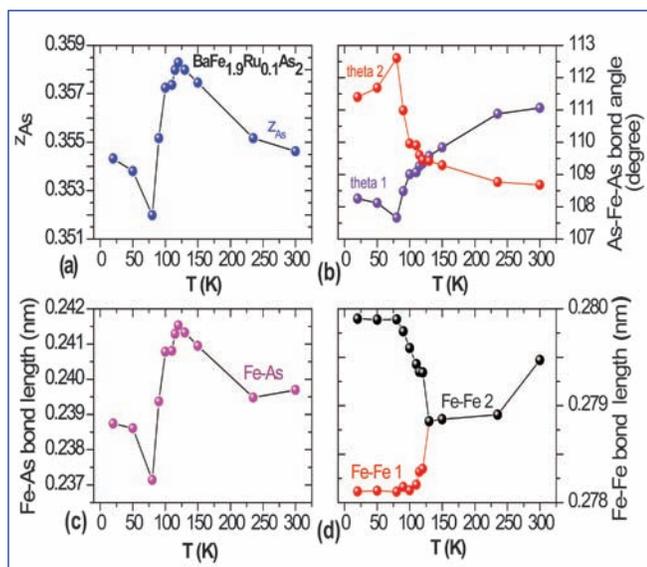
Fig. 2 *The variation in the arsenic position Z_{As}, As-Fe-As bond angles, Fe-As and Fe-Fe bond lengths as a function of temperature*
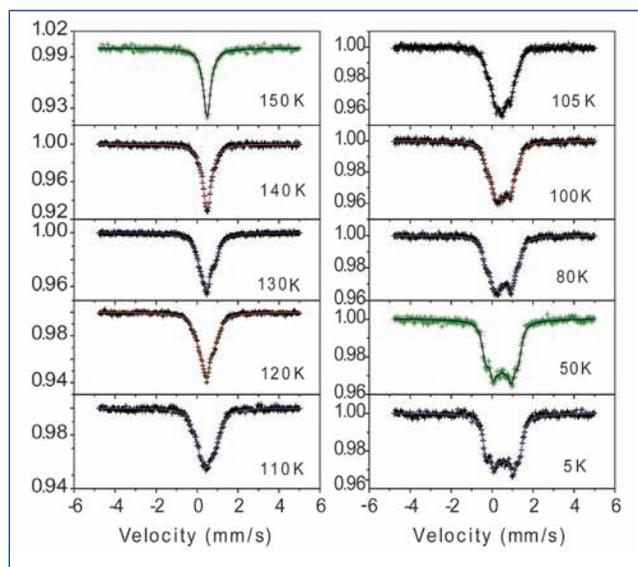
Fig. 3 *Mössbauer data measured at temperatures indicated in $BaFe_{1.9}Ru_{0.1}As_2$ single crystals*

system, using synchrotron radiation measurements. Shown in Figure 1b is the orthorhombic distortion obtained measurement of x-ray diffraction across the structural/ magnetic transition for ruthenium fraction x=0.1. It is evident from the figure that the orthorhombic distortion starts appearing at the structural transition. From Rietveld refinements of the structural data as a function of ruthenium substitution, structural parameters Z_{As} and As-Fe-As bond angles, were obtained. Our studies indicate that Z_{As} decreases with ruthenium substitution and tetrahedral angle expand and contract with ruthenium substitution. In Figure 2 we show how the structural parameters vary as a function temperature for a sample with ruthenium fraction of x=0.1. Interestingly, we see from Figure 3 that the structural parameters show anomalies at the structural transition in order to respect the magnetic ordering, as is evident from the temperature dependent variation of the Fe-Fe bond lengths. The magnetism of the compounds has been investigated by low temperature Mössbauer spectroscopy. The low temperature

data show broadening that has been analysed in terms of hyperfine-field distribution. The results of Mössbauer spectroscopy indicate that with ruthenium substitution the local magnetic moment decreases, before the stabilization of the superconducting ground state. Mössbauer spectroscopy has been measured as function of temperature for two ruthenium fraction, x=0.1 and x=0.5. Shown in Figure 3 is the Mössbauer spectrum taken as a function of temperature

for the x=0.1 sample. The data was analysed in terms of a local magnetic field distribution. The variation of the local field distribution as a function of temperature is shown in Figure 4. It is evident from the figure that hyperfine field distribution is finite well above the magnetic/structural transition. This implies that nematic or orbital ordering fluctuations occur well above the magnetic transition, which are detected as the presence of local ordering of moment by Mössbauer spectroscopy.
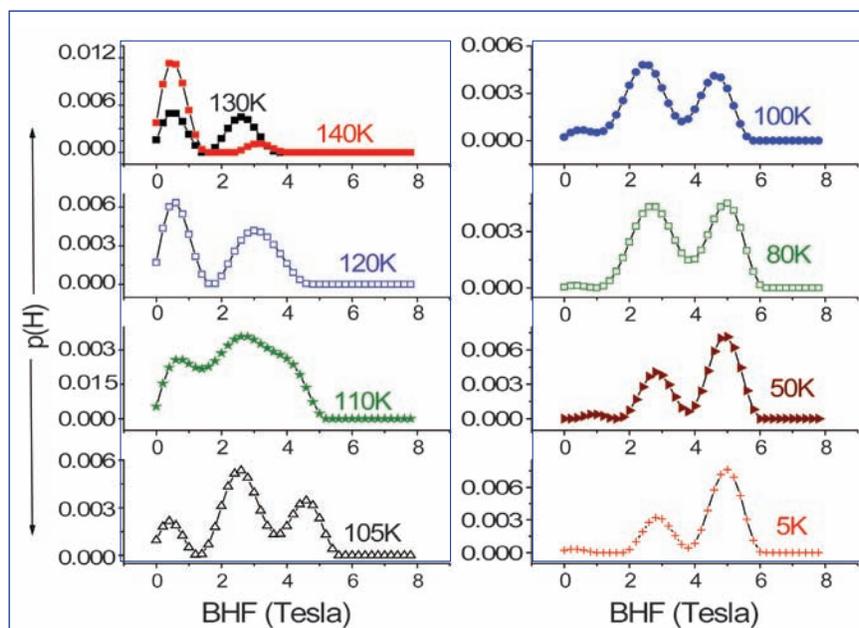
Fig. 4 *Internal hyperfine field (BHF) variation as a function of temperature in $BaFe_{1.9}Ru_{0.1}As_2$ single crystals*

V.5 A Novel Phase of Osmium Carbide Realized under Extreme Conditions of Pressures and Temperatures

A major area of research in high pressure science has been in the search for new super-hard materials with improved chemical and thermal stability comparable to that of diamond. Synthesis of novel phases of partially covalent compounds of transition metals (TM) and low atomic number (Z) elements, such as borides, carbides, nitrides and oxides is one of the methods being explored to obtain compounds with exceptional mechanical properties. The basic principle is to have maximum valence electron charge density, basically contributed by the transition metal and forming p-d hybridized covalent bond between carbon and transition metal, leading to enhancement in hardness. Among the transition metals, osmium has the highest valence electron charge density of 0.572 electrons/Å^3. Also, osmium has the least compressibility among transition metals and is comparable to that of diamond. Synthesis of OsC in hexagonal structure (WC) has been reported more than fifty years ago. However, there are no subsequent confirmatory

results on synthesis of this compound. Theoretical calculations suggest WC type structure to be mechanically unstable. Detail calculations on mechanical properties of OsC in nine different structure types have been reported. The three structures which have been proposed to be stable are: NiAs (cubic) > FeSi (cubic) > CoSn (hexagonal) in decreasing order of stability.

The enthalpy of formation of carbides and nitrides of latter transition metals (along the period in the periodic table) are positive and low compared to that of the early transition metals, and hence are not easily formed. As pressure is known to change the electronic structure considerably and enhance the chemical reactivity of elements, it may be possible to synthesize these novel carbides and nitrides under extreme conditions of high pressure and temperature, which otherwise are not possible by the conventional methods. Synthesis at extreme conditions of P and T in general results in the formation of compounds in dense phases,

which are preferable in the quest of novel super hard materials.

Laser heated diamond anvil cell (LHDAC) facility set up in our laboratory is used to carry out the high pressure-high temperature (HPHT) synthesis experiments. The LHDAC setup consists of a Mao-Bell type diamond anvil cell (DAC) into which a CO_2 (λ = 10.6 μm, 120 W, CW mode) laser beam is focused to heat the pressurized sample. Sample assembly for LHDAC experiment is very crucial and has to be optimized for efficiently converting the incident infra red laser beam into heat concentrated on the sample without much dissipation. A stainless steel gasket is preindented to a thickness of ~80 μm and a through hole of diameter ~150 μm is drilled at the centre. The gasket is mounted on the piston diamond and pelletized sample of size ~100 μm is placed in the gasket hole. The rest of the sample chamber is filled with liquefied argon or nitrogen, which function as pressure transmitting medium (PTM). Along with the
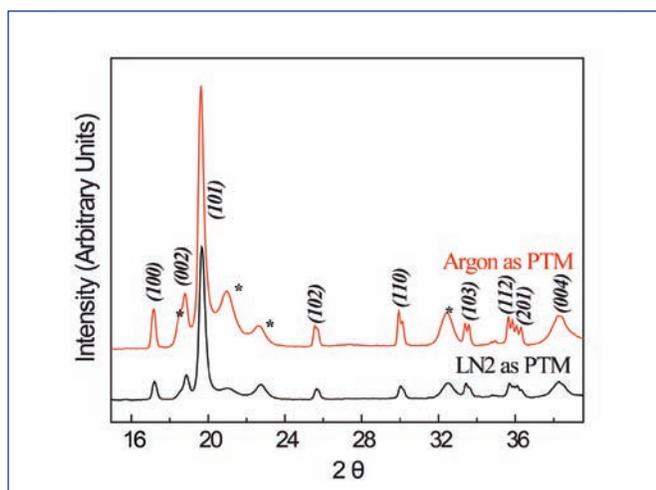

Fig. 1 XRD patterns of Os+C at ambient
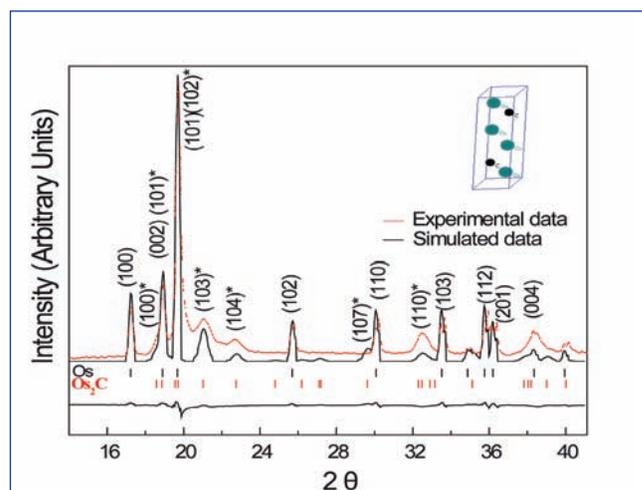
Fig. 2 Experimental and simulated XRD plots
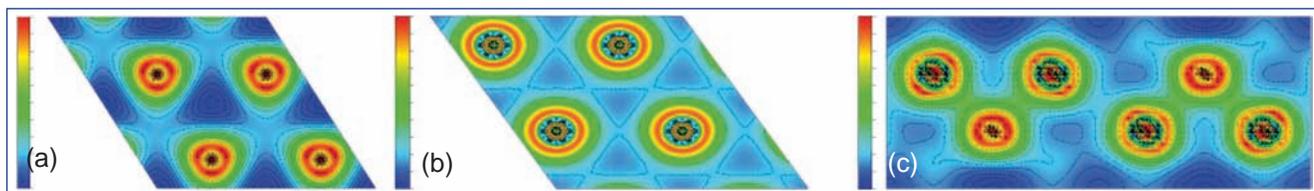
Fig. 3 *Electronic charge distribution (a) on (001) plane between carbon atoms, (b) on (001) plane between osmium atoms and (c) on (110) plane between osmium and carbon atoms*

sample, a small chip of ruby (~10 μm) is loaded for pressure estimation by ruby fluorescence technique. Temperature of the sample is measured by spectroradiometric technique. The laser heated samples are characterized by in-situ high pressure X-ray diffraction (HPXRD) technique in angle dispersive geometry.

The sample assembly is standardized by including optimum ratio of osmium and graphitic carbon, both 99.9% pure. Os:C in the ratio 1:3 is loaded into the DAC with liquefied nitrogen as PTM. The sample is pressurized to ~8 GPa and heated by focusing the infra red laser. A persistent glow seen on the sample indicated that the coupling of the laser to the sample to be very good. Temperature of the hot microscopic sample is found to be ~2000 K. In-situ HPXRD on the laser heated sample indicates consumption of osmium, but new distinct reflections from a possible new phase are not observed. This could be due to the very small volume fraction of the synthesized compound, and also may be due to attenuation of diffracted signal by the diamond anvil. To reduce attenuation by diamond, ambient pressure XRD pattern of the sample is obtained by passing the X-ray beam through the piston diamond alone (Figure 1). Three distinct new reflections are seen at 21.03°, 22.74° and 32.55° 2θ. The observed new reflections do not correspond to earlier reported WC type OsC. To rule out the possibility of reaction of nitrogen with osmium and also for reproducibility, HPHT

experiments starting from osmium and carbon mixture are carried out in cryogenically loaded argon pressure transmitting medium. The results obtained using liquefied nitrogen and argon are identical, except for intensities. This clearly indicates the formation of a novel osmium carbide. Lattice determination is carried out using POWD, and a hexagonal lattice with a= 2.536 Å, c = 12.526 Å and V = 69.8 Å^3 is obtained with good figure of merit. TEM on the retrieved sample is performed and is seen that reflections seen in XRD are also observed in electron diffraction measurements.

Identification of the crystal structure of the synthesized osmium carbide is a non-trivial task, due to inherent limitations with high pressure experiments. The structure types suggested by calculations do not correspond to the observed XRD. Recently, high pressure synthesized Ru$_2$C (hexagonal, space group 164, $P\bar{3}m1$), Re$_2$N (hexagonal, space group 194, P6$_3$/mmc) and Re$_3$N (hexagonal, space group 187, $P\bar{6}m2$) have been reported and these structures are considered as candidate structures and evaluated by carrying out first principle electronic structure calculations. Phonon dispersion and phonon density of states for the candidate structures indicates Os$_2$C in space group 164 to be mechanically unstable. Between Os$_2$C (194) and Os$_3$C (187), the volume correspondence between calculated and experimental values suggest the novel synthesized osmium carbide to be Os$_2$C with space group

194 (P6$_3$/mmc). The simulated pattern for Os$_2$C along with experimentally obtained pattern, shown in Figure 2, match very well. Bulk modulus is calculated to be 418 GPa, which is less than that of pure osmium (423 GPa). The electronic band structure and density of states for Os$_2$C is computed. DOS at E$_F$ is mostly dominated by d-states of osmium implying Os$_2$C to be metallic.

The high pressure synthesized sample is in powder form and sample quantity is only few micro grams, thus retrieval of the sample for hardness measurement is not possible. A semi-empirical method has been used to estimate hardness from the structural details. For the proposed structure of Os$_2$C, hardness is estimated to be 22.1 GPa. Origin of hardness can be understood from the crystal structure and electronic charge distribution of Os$_2$C projected in different planes, shown in Figure 3. In the case of Os$_2$C, the Os-C bond distance is the shortest and the Os-Os and C-C bond distance are same. From the inset shown in Figure 2, the structure can be thought of as a layer of carbon intercalated between osmium layers. From Figure 3, it is seen that charge distribution between C-C and Os-Os is significantly less than that between Os-C. This leads to incorporation of covalent bonding between Os-C, thereby enhancing hardness. Formation energy of carbon rich phases of osmium carbide is unfavourable than that of Os$_2$C. Thus synthesis at further higher pressures may result in formation of OsC with significant improvement in mechanical properties.

V.6   Anomalous Vibrational and Structural Behavior of PbFCl at High Pressure

PbFCl belongs to the family of minerals called matlockites that find a variety of technological applications such as constituent phosphors (upon rare earth doping) in x-ray image storage detectors, neutron detectors and as luminescent pressure markers in high pressure experiments. The matlockites also have very interesting physical properties on account of their layered tetragonal structure

The mixed halide PbFCl crystallizes in a tetragonal structure (space group: P4/nmm, Z=2) at ambient pressure and temperature, with layers of ions arranged along the c-axis in the sequence: F^--Pb^{2+}- Cl^--Cl^--Pb^{2+}-F^-. Presence of the weakly bonded Cl^- bilayer in this layered arrangement allows consideration of PbFCl as analogous to a molecular solid, even though all bondings are purely ionic. The unit cell can be visualized as composed of two PbFCl 'molecules' that are weakly bound. As a consequence, they are highly compressible, like molecular solids, and flaky with cleavage planes perpendicular to c-axis.

Factor group analysis of the P4/nmm space group symmetry for the bimolecular structure yields in a division of the eighteen degrees of freedom into modes of the following symmetries:

$$\Gamma_{18} = A_{1g}(1)+ A_{1g}(2) + B_{1g} + E_g(1) + E_g(2) + E_g(3) + 3A_{2u} + 3E_u$$

where all the A_{1g}, B_{1g} and E_g constitute six Raman active optic modes, $2A_{2u}$ and $2E_u$, are four infra red active modes and A_{2u} and E_u are two acoustic modes. Here we report results of high pressure Raman spectroscopy (HPRS) experiments
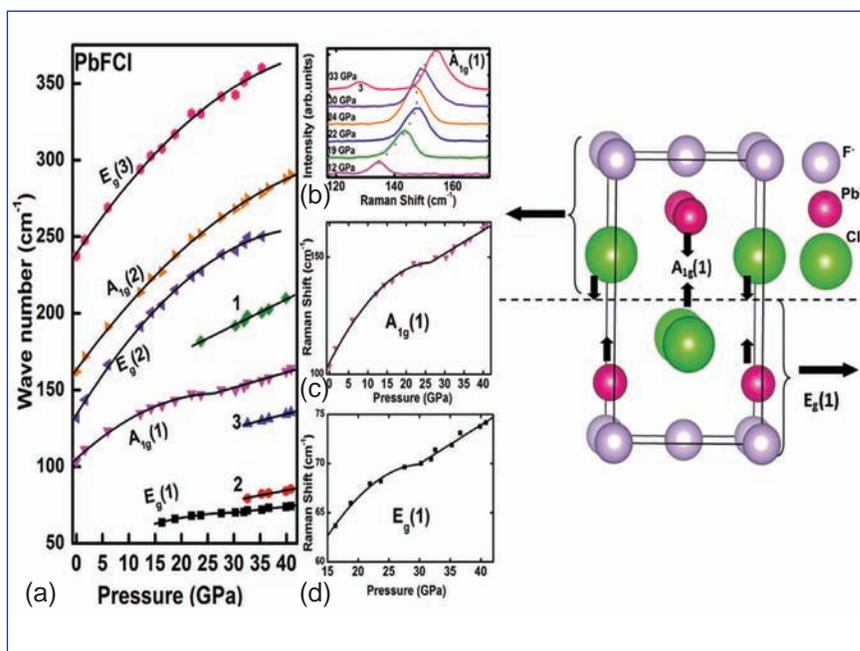
Fig. 1 *(a-d) Sublinear pressure variation of Raman modes showing instability of the rigid layer modes $A_{1g}(1)$ and $E_g(1)$; (right) unit cell of PbFCl depicting the two rigid-layer vibrational modes*

done on powder samples of PbFCl synthesized by solid state reaction method. All expected modes, except B_{1g}, were intense enough to be studied as a function of pressure. Of these the two low-frequency vibrational modes, $A_{1g}(1)$ and $E_g(1)$ are "rigid-layer (RL) modes". The rigid-layer modes uniquely describe the relative motion between the two rigid molecular units in the unit cell along directions parallel to the c-axis ($A_{1g}(1)$) and perpendicular to it ($E_g(1)$), and are therefore sensitive to any changes in the interlayer bonding. It was observed that while all Raman modes varied sublinearly and monotonously with increasing pressure, the two rigid-layer modes exhibited instability at ~24 GPa and ~31 GPa respectively, above which they started varying linearly and with higher slope, $\partial\omega/\partial P$. Further, a new Raman mode emerged at ~181 cm⁻¹ and 24 GPa. Also, the intensity of

the $A_{1g}(1)$ mode showed a large increase above this pressure. These indicated onset of structural distortion of the tetragonal cell and an increased interlayer coupling. Above ~33 GPa, two new modes appeared at frequencies below the $A_{1g}(1)$ mode and consistent with the expected modes of a monoclinically distorted phase with space group $P2_1/m$.

High pressure X-ray diffraction studies performed up to ~47 GPa confirmed the occurrence of the structural transitions with decreasing crystal symmetry. The unusual behavior of the rigid-layer modes and accompanying changes in Raman spectra is consistent with a picture in which the structural distortion involves destabilization of the tetragonal unit cell following a gradual change in the bonding nature from layer-like (2D) to non-layer like (3D) involving the Cl^- bilayers along the *c* direction.

V.7 Dynamics in Thermo-responsive Microgel Crystals Undergoing Melting

Colloidal dispersions of monodisperse particles exhibit crystalline ordering with lattice constants in the visible region and the time scales governing the Brownian dynamics of colloidal particles ranges from micro seconds to several seconds. Hence, static light scattering and dynamic light scattering are the appropriate techniques to study their structure and dynamics respectively. Larger length scales and the slower dynamics give easy access to the experiments, making colloids as ideal model systems for investigating universal phenomena such as melting/freezing and glass transition. Apart from fundamental interest, colloidal crystals have found many applications like Bragg filters, optical switches, sensors etc.

Colloidal suspensions of hard-spheres are known to freeze into a face-centered cubic (fcc) structure at a volume fraction, $\phi = 0.5$ whereas charge stabilized

suspensions undergo freezing into a body-centered cubic-structure (bcc) at much lower ϕ ~0.005. Aqueous suspensions of thermo-responsive poly (N-isopropylacryl-amide) (PNIPAM) microgel particle constitute yet another interesting colloidal system where the particle size is tunable by varying the temperature, T. Figure 1 shows variation of particle size with T and at T ~34°C sudden collapse in size is due to the volume phase transition of these particles. At room temperature dense suspensions of PNIPAM microgel particles crystallizes into a fcc structure. Upon heating, these crystals melt into a liquid like order.

The melting of crystal into liquid is a classic example of first order phase transition and is identified using well known Lindemann criterion and Hansen-Verlet criterion. Both these criteria are based on static properties and have been found to be applicable for colloidal systems. Though colloidal systems

mimic atomic systems in structural ordering, they differ in dynamics. In atomic systems, the dynamics is ballistic whereas Brownian motion governs the dynamics in colloidal systems. Realizing this fact, Löwen *et al* have proposed yet another phenomenological dynamical criterion for colloidal liquids undergoing freezing into colloidal crystals. The dynamical criterion states that the ratio of long time self diffusion coefficient (D_L) to the short time self diffusion coefficient (D_S), at the freezing point, is a universal number (D_L/D_S ~0.1). The dynamics in colloidal liquids (i.e. liquid like-ordered suspensions) is characterized by short-time (D_S) and long-time (D_L) diffusion coefficients and as the colloidal liquid freezes into a colloidal crystal, it is the long-time diffusion that decreases and slows down near freezing. Thus monitoring D_L helps in identifying the freezing transition and D_S sets the scale to
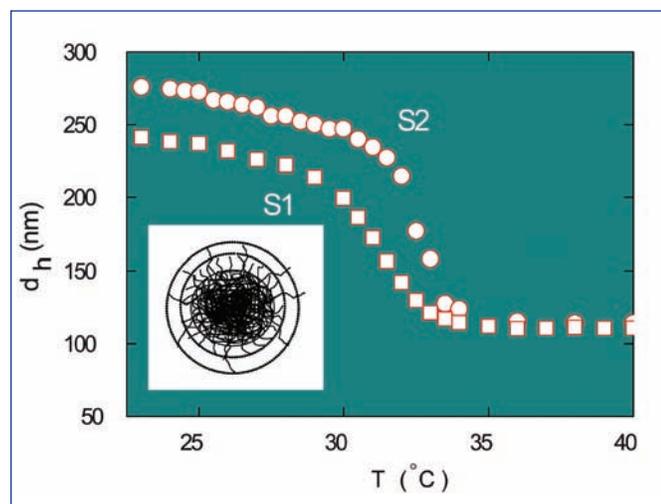
Fig. 1 *Hydrodynamic diameter, d_h of PNIPAM microgel particles as function of T measured under dilute condition of samples S1 and S2. inset: schematic of the internal structure of the PNIPAM microgel particle showing dense core and shell of dangling polymer chains*
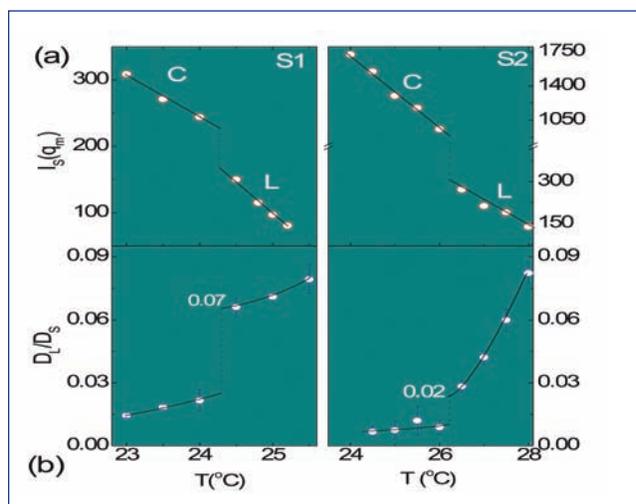
Fig. 2 *(a) Bragg peak intensity, $I_s(q_m)$ and (b) D_L/D_S, measured as function of T for samples S1 and S2. Lines drawn are guide to the eye. Dotted lines represent melting transition of PNIPAM crystal (C) to liquid like order (L) upon melting*

measure the value of D_L at freezing/melting. Thus Löwen's criterion is a measure of the value of D_L (in units of D_S) at freezing/melting and is the dynamical analog to Lindemann criterion which is based on static properties of the system.

Dynamical criterion has been verified experimentally and through simulations for freezing of hard-sphere and charge stabilized colloidal suspensions. Unlike hard-sphere and charge stabilized colloidal particles, PNIPAM microgel particles are inhomogeneous in density (dense core and rare shell of dangling polymer chains: Inset in Figure 1), compressible/deformable and porous in nature. We verify the applicability of the dynamical criterion for melting of the crystal of such inhomogeneous particles by studying the dynamics across the melting. It is found that the ratio D_L/D_S at melting of dense PNIPAM microgel crystal deviates considerably from 0.1. We attribute this deviation to the entanglement of the dangling polymer chains of PNIPAM microgel particles and evidence the presence of an entanglement by observing the subdiffusive dynamics at short time

We have synthesized monodisperse PNIPAM microgel particles having diameters of 238 and 273 nm in aqueous medium and using them prepared PNIPAM microgel crystals having volume fraction of 0.49 (S1) and 0.79 (S2) at 23°C respectively. The Bragg peaks from these crystals have been captured and Bragg peak intensity is monitored as a function of temperature using static light scattering (Figure 2a). The sudden fall in the intensity of the peaks at 24 and 26°C for samples S1 and S2 respectively is due to melting transition. By performing dynamic light scattering measurements across the melting of crystals the mean square displacement
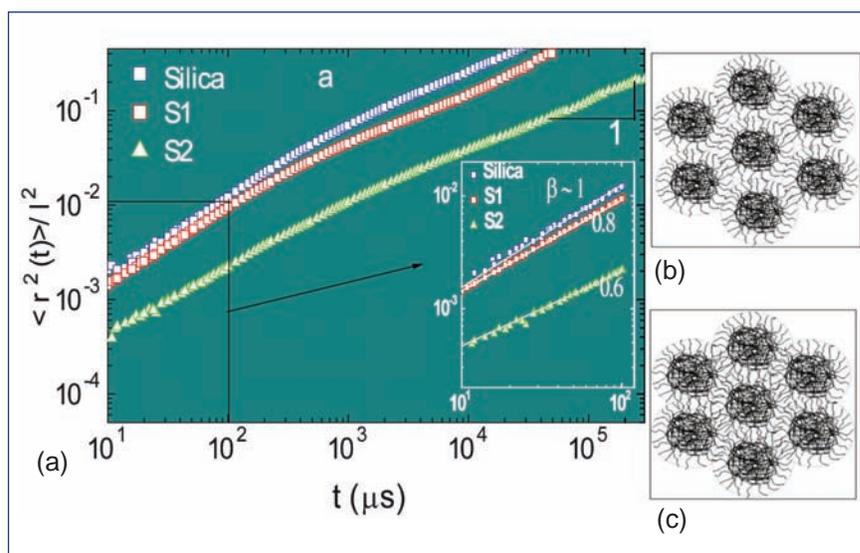
Fig. 3 *(a) Mean square displacement versus t close to the melting transition of sample S1 and S2 and close to freezing of shear melted silica suspension. Inset: MSD at shorter times; Continuous lines are fits of MSD to t^β. Schematic representation of PNIPAM microgel particles depicting the overlapping/entanglement of dangling polymer chains of neighboring PNIPAM particles with (b) less overlap in sample S1 and (c) more overlap in sample S2*

(MSD) of PNIPAM microgel particles have been obtained. D_L and D_S are determined by analyzing the long time and short time data of the MSD. The ratio D_L/D_S at melting is found to be 0.07 and 0.02 for samples S1 and S2 respectively (Figure 2b) indicating violation of dynamical criterion in dense thermo-responsive microgel suspensions.

We understand the deviation from 0.1 in dense PNIPAM Microgelsuspensions by carefully analyzing the MSD behavior at short-times as D_S sets the scale to measure the value of D_L at freezing/melting. The measured MSD as function of time for PNIPAM microgel samples S1 and S2 close to their melting are shown in Figure 3a and for comparison we also show the MSD of charged silica particles in a dilute shear melted silica suspension. At long times, usual diffusive behavior is observed (mean square displacement, $<r^2(t)> \propto t^\beta$ with $\beta = 1$ as shown in the Figure 3a) for all the three samples. Whereas MSD at short-times shows unusual

behavior. For silica suspension the particle diffusion at short times is diffusive (i.e. $\beta \sim 1$) but in the case of PNIPAM samples S1 and S2 it is sub-diffusive ($\beta < 1$) and the value of β depends on the volume fraction (inset in Figure 3a).

The subdiffusive dynamics at shorter times is due to the entanglement of dangling polymer chains of PNIPAM microgels (shown schematically in Figure 3b and 3c). The low value of D_L/D_S arises due to over estimation of D_S assuming the diffusive motion of PNIPAM microgel at shorter times. The dynamical criterion for freezing is proposed for the colloidal liquids where the particles undergo diffusive motion at short as well as at long times. Since the short time motion of the particles in dense PNIPAM microgel liquids close to melting/freezing is sub-diffusive, there is no suitable scale for scaling D_L. Thus present study constitutes a strong evidence for entanglement of dangling polymer chains of neighboring PNIPAM particles and their influence on particle dynamics in dense suspensions.

V.8 Brillouin Scattering Studies of Acoustic Phonon Modes and Central Peak in Pb(Sc$_{1/2}$Ta$_{1/2}$)O$_3$ Single Crystal

Relaxor ferroelectrics (RFE) are characterized by a broad and frequency dependent maximum in the dielectric susceptibility as a function of temperature, broad distribution and divergence of relaxation time on cooling with no macroscopic change in crystal structure. The origin of the complex behaviour exhibited by RFEs is found to be due to the nucleation and growth of the polar nanoregions (PNRs) that begin to appear at a temperature, the so called Burns temperature T_B. Brillouin scattering studies in these systems directly revealed the dynamical features of the PNRs such as the slowing down of their relaxation time and the coupling between the polarization fluctuations and acoustic phonon modes through the appearance of central peak (CP) and softening of the acoustic phonon mode.

Pb(Sc$_{1/2}$Ta$_{1/2}$)O$_3$ (PST) is a complex perovskite material that exhibit varied ferroelectric behaviour depending on the degree of B site ordering. A spontaneous relaxor to ferroelectric transition accompanied by a change in the structure from cubic to rhombohedral below T_c, has been observed in these systems. Here, the anomalous behaviour of acoustic phonon across the phase transition by Brillouin light scattering for a partially ordered PST single crystal has been studied. Single crystals of PST were grown by a flux method. Brillouin light scattering measurements were performed on (100) surface of the crystal in back scattering geometry using a high contrast 3+3 pass Sandercock tandem Fabry-Perot interferometer. Measurements were carried out in the FSR ranges of 75 and 400 GHz
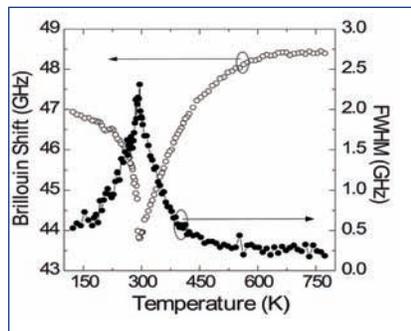
Fig. 1 *Temperature dependences of Brillouin shift (open circles) and the width (FWHM) (closed circles) of the LA phonon mode of PST*

Fig. 2 *$1/\tau$ as a function of reduced temperature $(T_c - T)/T_c$ for LA phonon; points are the experimental data and the solid line is the fit*

in the temperature range of 800 to 100 K using Linkam (THMS 600) cryostat.

The spectra were fitted with Voigt function with the fixed Gaussian width. The temperature dependence of Brillouin shift of LA phonon mode and its width (FWHM) are shown in Figure 1. Above 600 K, the Brillouin shift and FWHM of LA phonon mode is almost constant independent of temperature mainly governed by the lattice anharmonicity. Below 600 K, the LA phonon mode begins to deviate from the normal high temperature behaviour and exhibit marked softening with decrease in temperature. Further, the frequency of LA phonon exhibits a sharp minimum at 295 K, the transition temperature T_c. As shown in Figure 1, the width of the phonon mode begins to show a gradual increase at 450 K with a sharp maximum at T_c.

Above T_c, the gradual softening of the frequency followed by the gradual increase in the width of the LA phonon reveals that the polarization fluctuations are the dominant dynamic mechanism.

The dynamic fluctuation contribution is a characteristic of an $P^2\varepsilon$ - type quadratic coupling squared in order parameter and linear in strain. Since the structural phase transition is accompanied by the transition from relaxor to normal ferroelectric phase, bilerar coupling (linear in polarization and strain) between polarization and strain becomes a dominant mechanism of the coupling. The sharp damping maximum for LA phonon at 295 K can be connected with the Landau-Khalatnikov (LK) like relaxation mechanism, associated with the bilinear coupling. In LK coupling mechanism, the relaxation rate of the polarization can be calculated from frequency and the width of the LA phonon. The calculated relaxation rate of the polarization relaxation is given in Figure 2. The relaxation time τ_o=0.22 ps for PST is of similar order of magnitude as the relaxation time observed for typicalorder-disorder ferroelectrics. For instance, τ_o is 0.13 ps for KH$_2$PO$_4$ and 0.10 ps for triglycine sulfate. This suggests that an order-disorder type of mechanism predominates the structural phase transition.

V.9 Tribological Properties of Ultrananocrystalline Diamond Films

Materials with grain size refined to nanometer scale have great potential for several mechanical applications that range from micro electro mechanical systems (MEMS) to macroscopic abrasive coatings for cutting tools used in industrial applications. For these applications, diamond coatings are useful due to their unique mechanical properties. Furthermore, ultra nanocrystalline diamond (UNCD) films with such unique characteristic are superior to microcrystalline diamond film in several ways. These characteristics usually accrue from surface smoothness, fracture toughness, high electrical conductivity, low thermal expansion coefficient and high chemical inertness. All these basic features of ultra nanocrystalline diamond films cause improved tribological properties such as low friction and high wear resistance to manifest. Hence, such films are technically reliable for micro electro mechanical systems and other micro/macroscopic device applications.

Ultra nanocrystalline diamond films were synthesized in two different plasma gas mixtures such as 1.5% H_2/Ar/CH_4(UNCD$_{1.5}$) and Ar/CH_4(UNCD$_{Ar}$) used in plasma media at constant substrate temperature of 550°C. Plasma chemistry dependent grain/grain boundary microstructure, chemical composition and associated tribology characteristics of these films were investigated with respect to change in normal loads.

The bright-field transmission electron microscope analysis of UNCD$_{1.5}$ film is shown in Figure 1a.
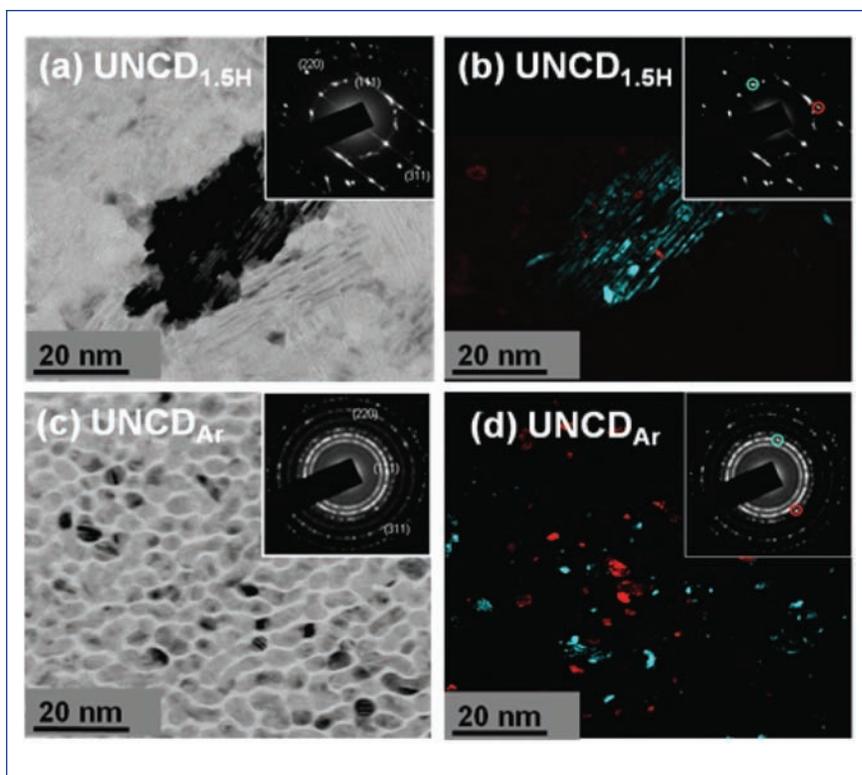
Fig. 1 *(a) and (b) The bright field TEM image and the corresponding dark field TEM image (inset shows the selected area electron diffraction patterns of the corresponding micrographs) of UNCD films grown using Ar/1.5% H_2/CH_4 plasma, (c) and (d) the bright field TEM image and the corresponding dark field TEM image (inset shows the selected area electron diffraction patterns of the corresponding micrographs) of UNCD films grown using Ar/CH_4 plasma*

This reveals that there is formation of large clusters of small grains. The selected area electron diffraction (SAED) patterns in inset of Figure 1a show (111), (220) and (311) diffraction rings. These rings ensure that the clusters are indeed constituted by ultra nanocrystalline diamond grains. The streaks oriented along (111) direction indicate that the large clusters contain (111) planar defects (stacking faults). In addition, dark field imaging was used to reveal the grains and their size distribution. The dark field image of UNCD$_{1.5H}$ films (Figure 1b) was obtained by selecting two different regions of selected area electron diffraction pattern (e.g., red, and

green circles in the inner (111) ring in the inset of Figure 1b. In this way, by using the objective/diffraction aperture, the dark field image of some grains from (111) reflection was acquired. The dark field image clearly shows elongated clusters of grains (green region) with a size of 40-80 nm. These green and red regions in grains correspond to the green and red circles of inner (111) ring in the selected area electron diffraction pattern shown in inset of Figure 1b. Consequently, the presence of 1.5% H_2 in the Ar/CH_4 plasma causes formation of large dendritic grains devoid of grain boundaries. Interestingly, the removal of 1.5% H_2 from the Ar/CH_4 plasma modifies the microstructure

of the films profoundly. The bright field transmission electron microscope analysis of UNCD$_{Ar}$ film is shown in Figure 1c along with selected area electron diffraction patterns in the inset of Figure 1(c). It is seen that the clusters contained in the UNCD$_{Ar}$ films are constituted by spherical grains of size ~5 nm. These sizes are normally uniform. Grain boundaries of around ~1 nm in thickness are clearly observed. This indicates that the grain boundaries possess distinctly different structure from that of grains. Detailed examination of the selected area electron diffraction further reveals the presence of extra diffraction rings besides the (111), (220) and (311) rings. This additional feature corresponds to c-diamond lattice of 3C diamond structure. It is observed from the dark field image of UNCD$_{Ar}$ films (Figure 1d) that the green colored spherical grains show a grain size of about 5 to 7 nm and the red colored grains correspond to a grain size of 10 to 12 nm.

Friction coefficient of diamond films yields high value in ultra high vacuum and nitrogen atmospheres. However, low and ultra-low friction behavior of diamond films, particularly exhibited under humid environments, are assumed to be due to either re-hybridization or passivation of interacting dangling bonds formed during sliding. Transformation of diamond to graphite or a-C is influenced by shear forces, frictional heating and presence of oxygen and water vapor. All these factors cause reduction in friction coefficient. Consequently, passivation of dangling covalent bonds brings about low friction and wear of diamond in moist environments containing hydrogen or water molecules. Low/ultra-low friction behavior is explained in
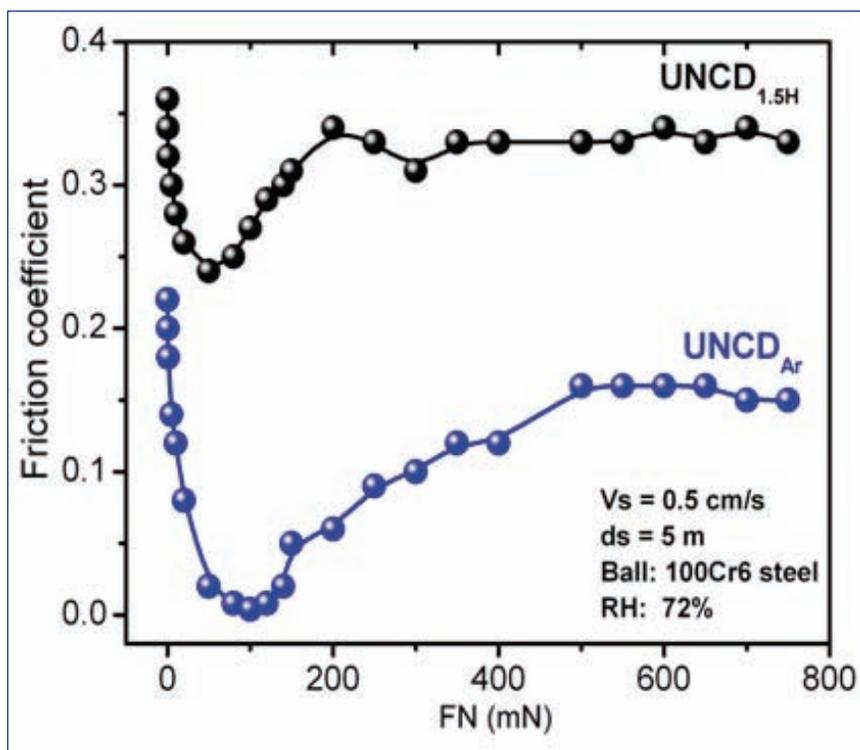
Fig. 2 *Load dependent friction coefficient of UNCD$_{1.5H}$ and UNCD$_{Ar}$ films*

the terms of plasma chemistry dependent grain/grain boundary characteristics such as volume fraction, chemical bonding and composition. Load dependent friction coefficients of both these films are presented in Figure 2. In UNCD$_{1.5H}$ film, the crystal size is larger and the grain boundary volume fraction is smaller. If the grain boundary volume fraction decreases, the amount of t-PA chains which contains hydrogen atoms/molecules are reduced, this possibly does not sufficiently passivate the activated dangling bonds, thereby resulting in high surface energy. Similarly, UNCD$_{1.5H}$ film contains less amount of lubricious boundary phase fraction of sp^2 bonded a-C. This is once again related to plasma chemistry, which signifies entrainment of less volume fraction of grain boundaries. In this condition, the shear activated sliding resistance of grain boundary is high and the friction behavior is largely dominated by grains. Large grain sizes of UNCD$_{1.5H}$ film

fractures easily from the boundary-grain interface due to evolution of shear strain during tribo-test.

During low load friction test, the capillary induced adhesion dominates and at high load, plastic deformation model of friction operates yielding high value of friction coefficient for both the ultra nanocrystalline diamond films (Figure 2). However, at intermediate loads, the elastic model of friction operates, which brings out low value of friction coefficient. Low friction coefficient with a value of 0.024 is observed for UNCD$_{1.5H}$ film. An ultra-low friction coefficient with a value of 0.004 is measured for UNCD$_{Ar}$ film at certain specific intermediate loads. Such low friction coefficient and wear depth are mainly caused by surface chemical passivation of dangling covalent bonds during sliding. This occurs at moderate loading range of 80-120 mN. However, at low load of 5 mN, the friction coefficient is high due to action of capillary condensation force.

V.10 Gas Sensing in VO$_2$ over Metal – Semiconductor Transition Regime

Vanadium dioxide is a smart material which undergoes a semiconductor to metal phase transition (SMT) near room temperature of 68°C. This transition is accompanied by large modifications in its optical and electrical properties which suggest its use in window coatings, infrared sensors, optoelectronic memories and switches. Bulk vanadium dioxide crystals exhibit a first order structural phase transformation from a monoclinic (S.G. P2$_1$/c) to tetragonal (rutile, S.G. P4$_2$/mnm) structure which accompanies the semiconductor to metal phase transition. It is also of great interest in condensed matter physics because it is a classic strongly correlated electron system.

Due to its semiconducting nature near room temperature, the possibility of gas sensing with VO$_2$ has been explored. Though there have been numerous reports on V$_2$O$_5$ as gas sensing material, there are very few gas sensing reports on VO$_2$. We have utilized the low resistance of VO$_2$ nanostructured films in the semiconducting region near room temperature and optimized its gas sensing performance specifically towards detecting methane over the semiconductor to metal transition regime.

Preparation of stoichiometric VO$_2$ requires precise control of deposition parameters due to the possibility of formation of other thermodynamically stable oxides like V$_2$O$_3$ and V$_2$O$_5$. We have adopted a two-step synthesis approach using pulsed dc magnetron sputtering and post-deposition oxidation to obtain nanostructured VO$_2$ films. Nanostructured films of metallic

vanadium were deposited on sensor substrates (Au interdigitated electrodes pre-patterned on alumina) using pulsed dc magnetron sputtering technique. The pulse power was 160 W at 100 kHz and base pressure was 3×10^{-6} Torr using Ar$^+$ plasma. The substrate temperature was maintained at 350°C during the deposition time of 40 min. These samples were then oxidized in an annealing chamber at 550°C in O$_2$ environment where the flow was maintained at 20 sccm at a partial pressure of 0.2 Torr. The oxidation was performed for 3 hours to achieve an oxide layer thickness of 450 nm.

Recently, vanadium dioxide films are also grown by vapour transport method. Vanadium dioxide powders as precursor is taken in a alumina boat and heated in a tube furnace with argon as carrier gas. The substrate is kept at a distance of 1 cm from the source downstream. The temperature of deposition is optimized between 850-900°C.

Temperature versus resistance measurements were carried out in Linkam stage in the temperature range from 0 to 100 °C. The film is heated and cooled at various rates from 10 to 25 °C/min. From Figure 1, it is observed that the resistance drops over two orders of magnitude around 68°C while heating and around 58°C during cooling. The small hysteresis width of the film (< 10°C) showed good stoichiometry of the films. The film resistance was reversible for different heating/cooling rates and was similar without deviations confirming the good quality of the film.

The morphology of these samples were studied by field emission scanning electron microscope
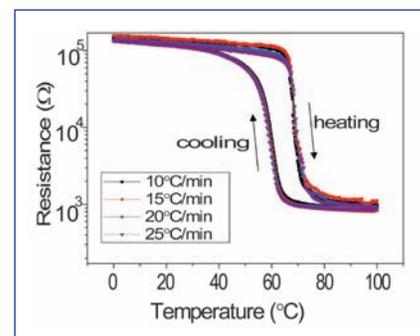
Fig. 1 *Semiconductor – metal transition in VO$_2$ for different heating/cooling rates*

(FESEM; Zeiss Supra 55) operated in secondary electron imaging mode. The films synthesized by pulsed dc magnetron sputtering possessed rod type morphology as observed in Figure 2. The layered structure present in the nanorod bundles is evident from the figure. The rods were 150-200 nm in diameter and a few microns in length. The rods appear in bunches which are held together by van der Waal's forces. By contrast, the films synthesized by vapour transport consisted of micron sized cauliflower- like structures as shown in Figure 3.

The gas sensing experiments
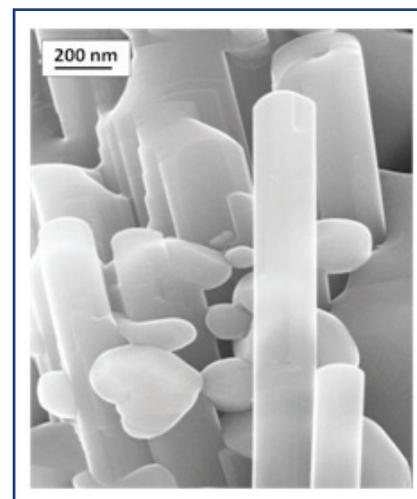
Fig. 2 *Field emission scanning electron microscopy image of VO$_2$ nanorods*

were carried out in a custom built exposure facility system. It consists of a double walled stainless steel chamber containing a PID controlled hot stage upon which the sample is mounted. The gas flows are set from mass flow controllers and the sensor response upon exposure to gases is manifested as resistance changes, which is recorded in a standard two probe method using a multimeter. Commercially procured gas mixtures of ultra high pure grade CH_4 diluted in nitrogen carrier gas was used along with synthetic air in background. These gases were further passed through moisture traps to remove any residual humidity. The concentrations were varied in the range from 50-500 ppm at operating temperatures of 25, 50, 100, 150 and 200°C. The sensor response (S) expressed in % is defined as ratio of change in resistance upon exposure to gas to the initial resistance $(\Delta R/R_0) \times 100$ where $\Delta R = (R_0 - R_{gas})$, R_{gas} is the resistance upon exposure to gas and R_0 is the initial resistance.

Figure 4a shows the response transient (resistance versus time) at three different temperatures for various concentrations of methane for sputtered film. It can be observed from the resistance transients that upon exposure to CH_4, the resistance of the VO_2 sensor decreases. From the slopes of the transient plots, it can be inferred that the response time (time taken by the sensor to reach 90% of initial resistance) and recovery times (time taken to recover 70% of final resistance) are very short for sensing performed at 50°C in its semiconducting state. The response and recovery times increase as the temperature is raised.

It is of particular interest to note that the response decreases slightly as the operating temperature is increased as shown in Figure 4b. This can be attributed to the formation of metallic state in the sample above the semiconductor-metal transition temperature. Above 150°C, the increasing resistance in the metallic state may produce sufficient hindrance that prohibits any observable sensing. A maximum response value of 1.4% has been obtained for lowest detection limit of 50 ppm of CH_4 at lowest operating temperature of 50°C.

Test conducted with nanostructures synthesized with vapour transport method also gave promising results. Figure 4c shows the plot of response (S) of the sensor versus operating temperature. The temperature is varied from room temperature semiconducting state
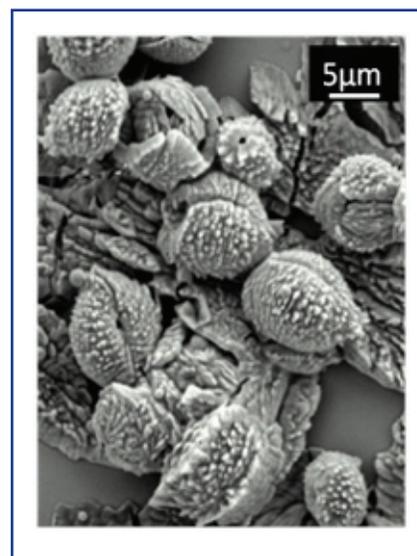
Fig. 3 *Field emission scanning electron microscopy image of VO$_2$ cauliflowers*

to 100°C in its metallic state. It is seen that the S value increases initially and reaches a maximum near the transition temperature of 68°C then drops down in its metallic state. This confirms that the semiconducting state of VO_2 is suitable for sensing over the metallic state.

Thus a novel gas sensing material based on VO_2 has been developed. Various operating conditions have been optimized for films and nanostructures. It has been shown that the methane sensing properties are promising below the transition regime in the semiconducting state. More efforts are on to improve the sensor response.
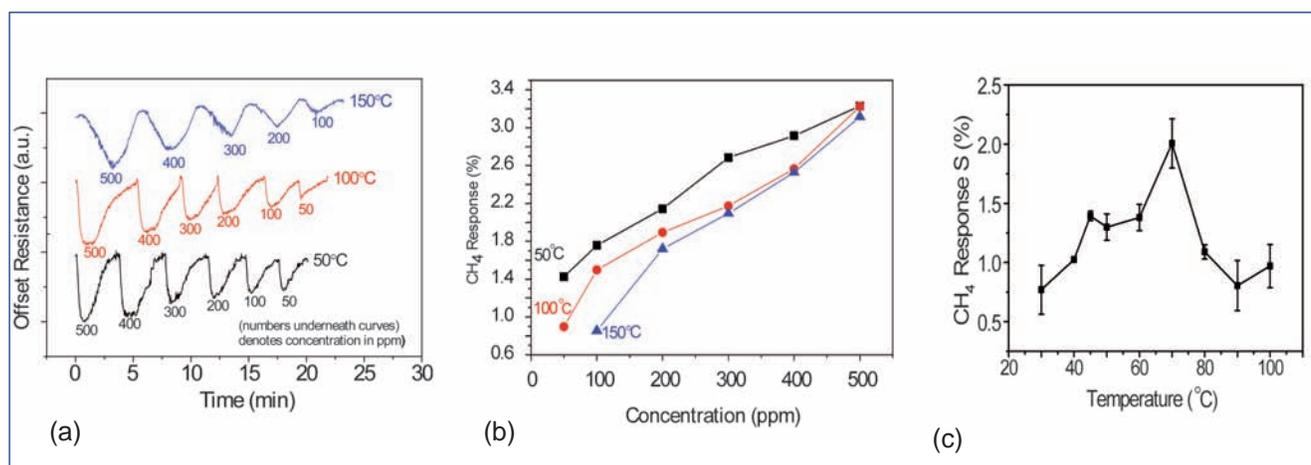
Fig. 4 *(a) Response transient at 50,100, 150 °C for various concentrations of methane for sputtered film, (b) response versus concentration for sputtered film and (c) response versus operating temperature for CVD film*

V.11 Custom-designed High Temperature Hall Measurement Facility for in-situ Probing of Gas Sensing Mechanism by Metal Oxides

Semiconductor oxides exhibit change in conductivity in the presence of trace levels of oxidizing or reducing gases and this property has been exploited for applications as gas sensors. The conductivity in turn depends on both carrier density and mobility. Measurement of Hall voltage is the only direct technique known for deriving the carrier density and mobility of semiconducting oxides. Conventional Hall measurement

systems work either in air or vacuum and they cannot be deployed for studies both at high temperatures and in presence of analyte species. We designed and set up a high temperature Hall measurement system in order to investigate the carrier density changes during the interaction of semiconducting oxides with analyte molecules.

The Hall measurement system uses a programmable commercial

van der Pauw Hall measurement card with a switch system, a current source capable of sourcing 1 nA to 1 mA current, a multimeter to measure the pico-volts to milli-volts along with pico-ammeter to measure the actual current flowing through sample. The specially designed sample probe with a built-in heater capable of giving a maximum temperature of 400 °C and which can withstand against any chemical attack is
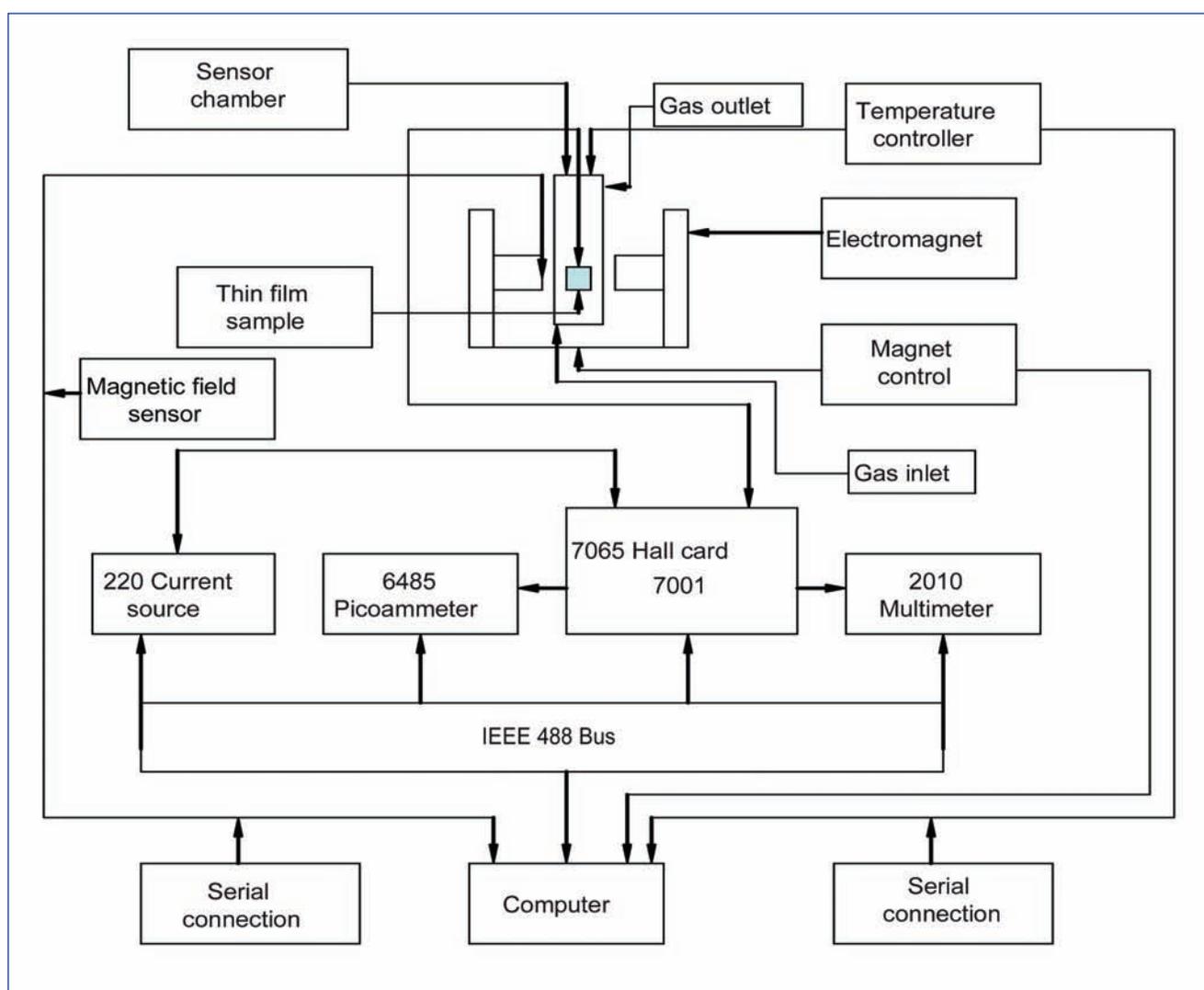
Fig. 1 *Schematic diagram of the high temperature Hall measurement system for in-situ measurements of changes in carrier density and four probe resistivity during analyte - semiconducting oxide interaction*

the salient feature of the system. A flat rectangular chamber made of SS 316L (non magnetic) was designed to fit into the pole gap of the electromagnet with a magnetic field of 1 Tesla within the pole gap was designed. All the instruments were integrated as shown in Figure 1 and a software program was written in-house for four probe resistivity and Hall voltage measurements.

Thin film of indium oxide was chosen as the model compound and the modulations in carrier density/mobility during its interaction towards NO_x in the range of 200 to 400°C were investigated. Air containing the specified concentration of NO_x was introduced into the chamber using mass flow controllers and the measurements were made after equilibration. To avoid the voltage signal arising from the deviation from the orthogonality of the magnetic field and current directions, the polarities of the current and magnetic fields were reversed through the software program and the average value was used in the calculation of four probe conductivity, carrier density and mobility. The plot of logarithmic conductivity (four probe) of In_2O_3 as a function of inverse temperature (Arrhenius plot) in air and air containing 25 ppm of NO_x are shown in Figure 2(a). The conductivity exponentially decreases with decrease in the temperature in air and air containing 25 ppm NO_x, exhibiting Arrhenius type behavior. The conductivity in 25 ppm NO_x is lower than in air. However, below 200°C, the conductivity falls at a faster rate in 25 ppm NO_x showing the deviation. The plot of carrier

density as a function of temperature also shows a decrease in conductivity both in air and 25 ppm of NO_x in air (Figure 2b). The significant difference in electron affinity of NO_2 (220 kJ/mol) and O_2 (42 kJ/mol), is ascribed as the reason for NO_2/NO to get chemisorbed on In_2O_3 surface at much lower temperatures and the reduction in the carrier density thereby localizing the conduction electron on the surface. The plot of mobility as a function of

temperature is shown in Figure 2c. At high temperatures, the mobility is similar in both the atmospheres, whereas at low temperatures, the mobility is largely affected due to the presence of NO_x, which corroborates with the trend in conductivity values (Figure 2a).

This investigation demonstrates the use of the high temperature Hall measurement system in understanding the mechanism of NO_x sensing of In_2O_3 thin films.
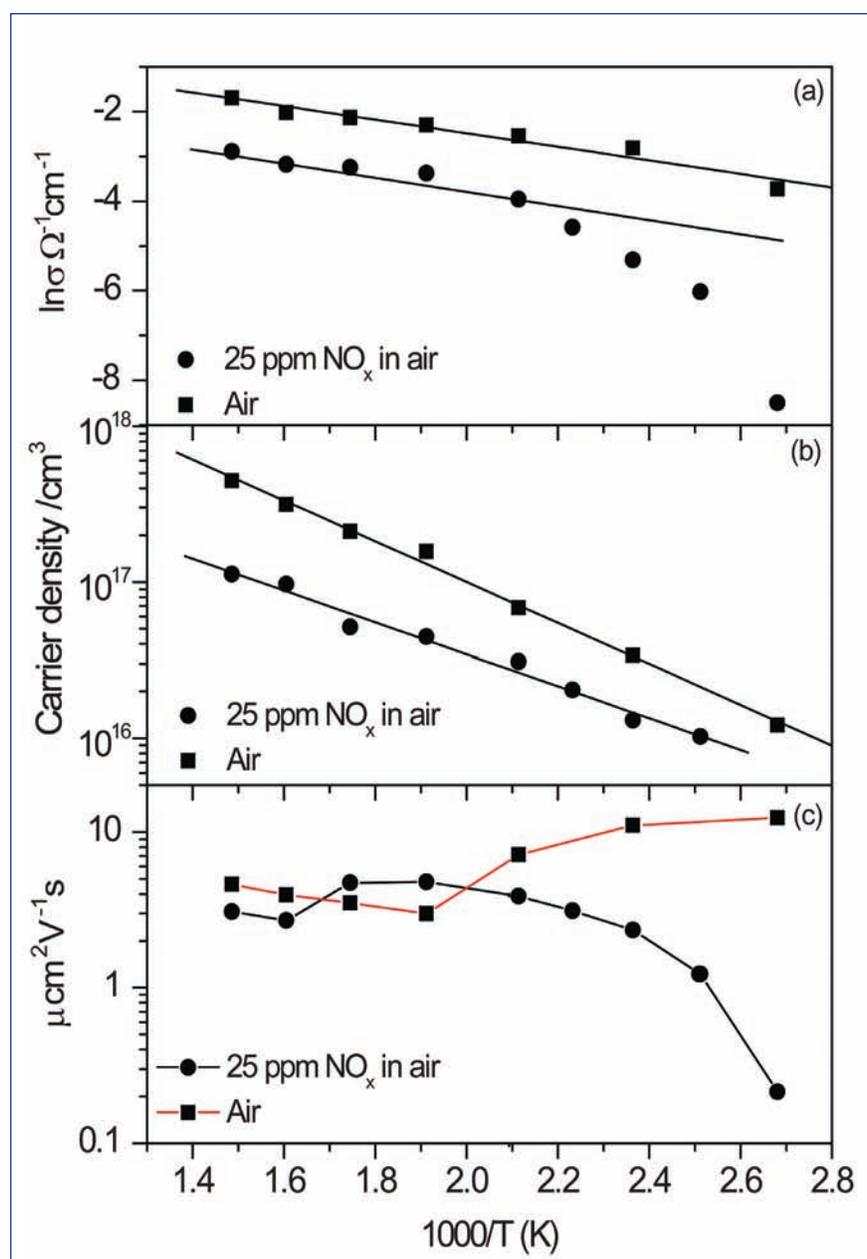
Fig. 2 *The plot of (a) conductivity, (b) carrier density and (c) mobility as a function of temperature for 25 ppm of NO_x in air at 350°C during the interaction with In_2O_3*

V.12   Optical Waveguide in Nonpolar GaN Nanowires

Group III nitride based GaN nanowires have emerged as potential building blocks for nanoscale electronic and optoelectronic devices. Controlling diameter and surface morphology of GaN nanowires play a crucial role in defining electrical, optical and electromechanical properties, for its use in light emitting diode (LED), high electron mobility transistor (HEMT), chemical sensor and nano-electromechanical (NEMS) devices.

In the conventional polar c-axis oriented GaN materials, polarization induced electric fields parallel to the growth direction causes the reduction in external quantum efficiency of white light emitting diode. Whereas the nonpolar $[10\bar{1}0]$ and $[11\bar{2}0]$ oriented GaN materials have attained intense research interest due to the absence of polarization induced electric fields. However, the low energy nonpolar planes of GaN are generally susceptible to defects and impurities and reported to form morphological distortion leading to drastic modification of physical properties including poor performance in optical properties.

We report the O free growth of nonpolar GaN nanowire. By reducing the O contamination to a critical level, we were able to synthesize and reproduce size selective growth of nanowires with uniform size and shape. Along with the perfection in architectural features, we have also demonstrated improvement in the optical properties of the nanowires in the formation of waveguide showing far field emission.

GaN nanowires were grown on Si(100) in chemical vapor deposition technique at 900 °C using Au catalyst assisted vapor-liquid-solid
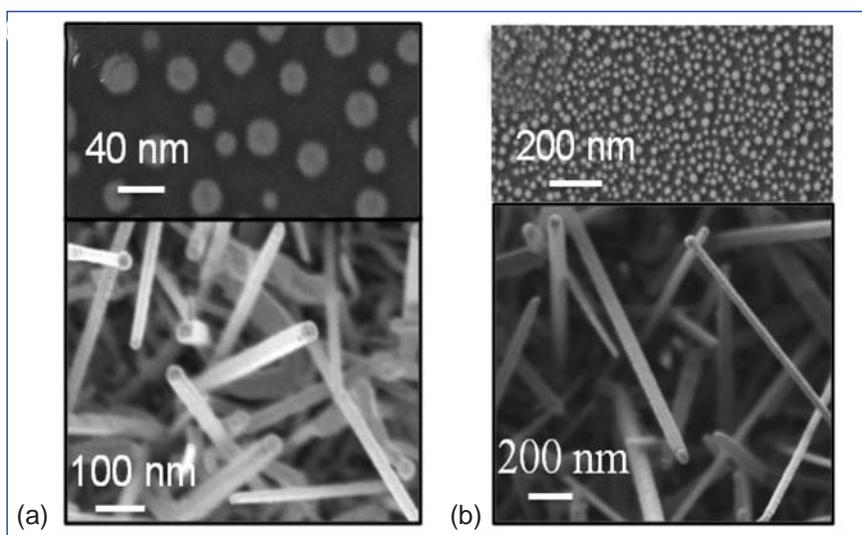
Fig. 1 *(a) Au catalyst of 30($\pm$5) nm and uniformly grown nanowires of diameter 40($\pm$5) nm and (b) Au catalyst of 40($\pm$5) nm and uniformly grown nanowires of diameter 55($\pm$5) nm*

(VLS) process at atmospheric pressure. Ga metal (99.999%, Alfa Aesar) is used as precursor with mixture of ultra high pure (UHP) Ar+H_2 (5N) as carrier gases and 5N pure NH_3 as reactant gas for the growth. Nanowires were grown for a duration of 60 minutes by purging 10 sccm of NH_3 as reactant gas and 20 sccm of carrier gas. For O reduced condition, nanowires were grown at oxygen partial pressures of 1.2×10^{-4} Torr (< 1 ppm O_2) using catalytic Au nanoparticles of
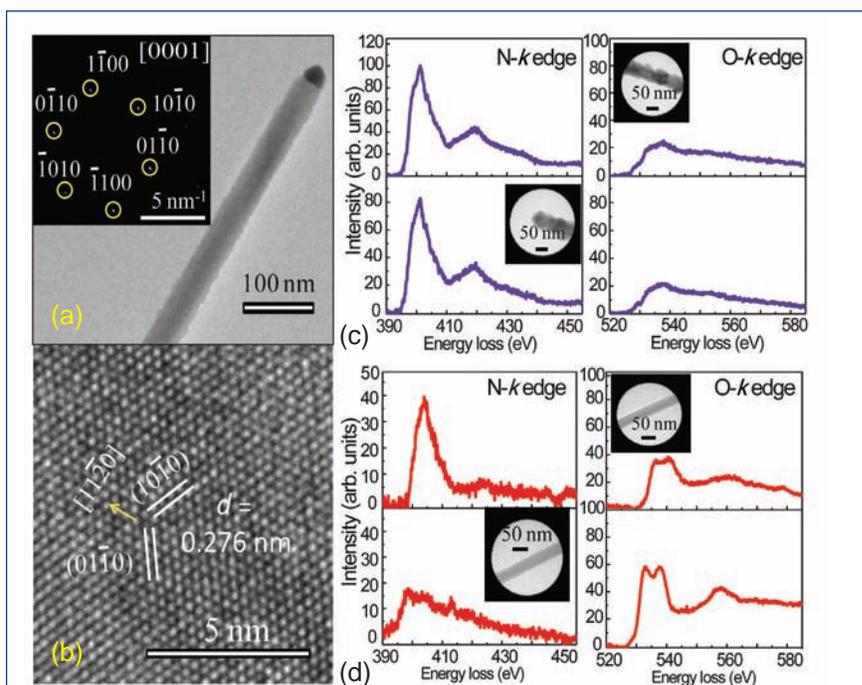
Fig. 2 *(a) Smooth uniform nanowire with Au catalyst at tip. Insets shows wurtzite GaN phase, (b) High resolution image showing crystalline plane of GaN. EELS spectrum for N-and O k-edge of GaN nanowires grown in, (c) O reduced and (d) O rich condition. Inset shows the region of the nanowires studied for checking uniformity of composition along the wire length*

different average size for realizing size control in the growth process.

Nanowires grown in O reduced condition show smooth and homogeneous surface morphology and uniform size distribution all over the sample with a growth rate of 3 µm/h. Diameter of the nanowires exactly follows the size of the catalyst particle 30($\pm$5) nm at the tip and having uniform shape and size distribution ~40($\pm$5) nm with homogeneous surface morphology along the wire, as shown (Figure 1a) in the field emission scanning electron microscopy (FESEM; SUPRA 55 Zeiss). Au nanoparticles of size distribution ~40($\pm$5) nm were used for demonstrating size selective growth of nanowires with uniform shape and surface morphology with bigger sizes of 55($\pm$5) nm (Figure 1b).

A typical nanowire grown in O reduced condition shows transmission electron microscopic (TEM; LIBRA 200FE Zeiss) image of a perfect rod like shape with uniform surface morphology (Figure 2a) and having an Au catalyst particle at the tip. The SAED (selected area electron diffraction) pattern (inset Figure 2a) reveals that the nanowire is single crystalline wurtzite phase of GaN with zone axes [0001]. Interplanar spacing of 0.276 nm shown in the high resolution transmission electron microscope (HRTEM) image (Figure 2b), corresponds to the nonpolar {10$\bar{1}$0} planes of wurtzite GaN with a growth direction along [11$\bar{2}$0]. HRTEM assisted electron energy loss spectroscopy (EELS) study of nanowires are analyzed by collecting the *k*-edge emission of N and O. The concentration ratio of N to O, n_N/n_o is found to be ~1.2 along the nanowire (Figure 2c), showing dramatic reduction in O concentration and homogeneous
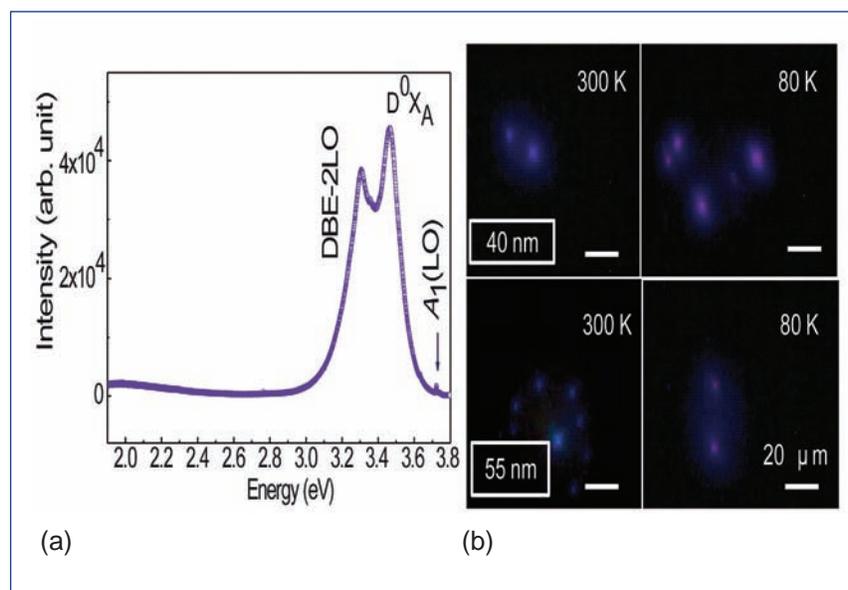
Fig. 3 *(a) Photoluminescence of GaN nanowires at 80 K, (b) far field bright violet emission spots at 300 K and 80 K on the nanowires of average diameter 40 nm and 55 nm*

incorporation of N into crystalline planes of GaN than that compared to 0.09-0.20 along nanowires grown in the O rich condition (Figure 2d).

Photoluminescence (PL; Renishaw inVia) study at 80K show a strong bound exciton band D^0X_A at 3.47 eV with a phonon replica of donor bound exciton with longitudinal optical mode (DBE-2LO) band around 3.34 eV (Figure 3a). Absence of yellow band (~2.2 eV) and strong emission of DX band are the implication of high optical quality GaN phase.

These GaN nanowires are used as waveguide for observing far field excitation-emission process (Figure 3b) at room temperature (300 K) as well as 80 K with bright violet emission spots corresponding to the D^0X_A band around 3.47 eV (357 nm) of PL emission (Figure 3a). GaN is reported to have very high refractive index of 2.7 at 357 nm wavelength. These emissions are observed to come out of the ends of nanowires through the available open space while other ends are at the excitation with laser light. Condition for a nanowire to function as a single-mode optical

waveguide, is 1≈$\pi d\sqrt{(n_1^2-n_2^2)}/\lambda$ < 2.4, with 1 being the realistic lower limit. For diameter, *d* of our nanowires ~40($\pm$5) and 55($\pm$5) nm at wavelength, λ =357 nm; n_1 ~2.7 and n_2 = 1 are the refractive indices of the nanowire around 357 nm and surrounding medium of air, respectively, we can get the minimum value close to 1.

In conclusion, size selective nonpolar wurtzite GaN nanowires with uniform surface morphology are grown by reducing the O concentration to background level. Electron energy loss spectroscopic measurements confirm little variations in the O concentrations along the nanowire grown in O reduced condition. High resolution transmission electron microscopic analysis reveals that the nonpolar nanowires are grown along [11$\bar{2}$0] with side facets (10$\bar{1}$0). Far field bright multiple violet emission spots form nanowires, grown in the O reduced condition, show formation of single-mode waveguide in these samples. The results pave the way for commercialization of ensembled GaN nanowire devices for optoelectronic applications.

V.13 Gas Phase versus Low Temperature behavior of Trimethylphosphite/Dimethoxymethane with HCl - A Matrix Isolation Infrared Study

Matrix isolation (MI) infrared technique has been used in the study of conformations in molecules, weak intermolecular interactions such as hydrogen bonding and spectroscopy of unstable species such as radicals, ions and the intermediates formed during chemical reactions. Understanding the interaction of organic phosphates with acids such as nitric acid is important, as it holds the key to unraveling the complex and interesting chemistry of the phosphates, in fuel reprocessing. Towards this end, we have studied reactions of some model compounds such as trimethyl phosphite (TMPhite) and dimethoxymethane (DMM) with hydrochloric acid (HCl). The interactions between these molecules were followed by

(a) Co-depositing the gaseous molecules with the matix gas at low temperatures

(b) Pre-mixing of the gaseous molecules along with the matrix gas and then depositing at low temperatures

Ab initio computations were carried out at B3LYP/6-311++G(d,p) level of theory using Gaussian suite of programs to arrive at the structures, interaction energies and vibrational frequencies of these molecules and their adducts.

Trimethyl phosphite with HCl

When TMPhite and HCl were co-deposited using nitrogen matrix through a twin-jet nozzle and annealed, new features were observed in the HCl stretch and P-O stretch region of TMPhite which are shown in Figure 1b. The experimental observation together with computations revealed that the

new features can be assigned to the first higher energy adduct of the TMPhite and HCl. The structure of the adduct is shown in Figure 2a. When TMPhite and HCl were pre-mixed with nitrogen gas and then deposited at 12K, new features were observed which are different from those obtained when TMPhite and HCl were co-deposited through

a twin-jet nozzle. The intense product features observed in the pre-mixed experiment agree well with the features of CH_3Cl in Argon matrix which is shown in Figure 1c. It is therefore clear that in the gas phase, TMPhite reacted with HCl to yield CH_3Cl, following a nucleophilic substitution (Arbuzov reaction), a reaction that is apparently frustrated
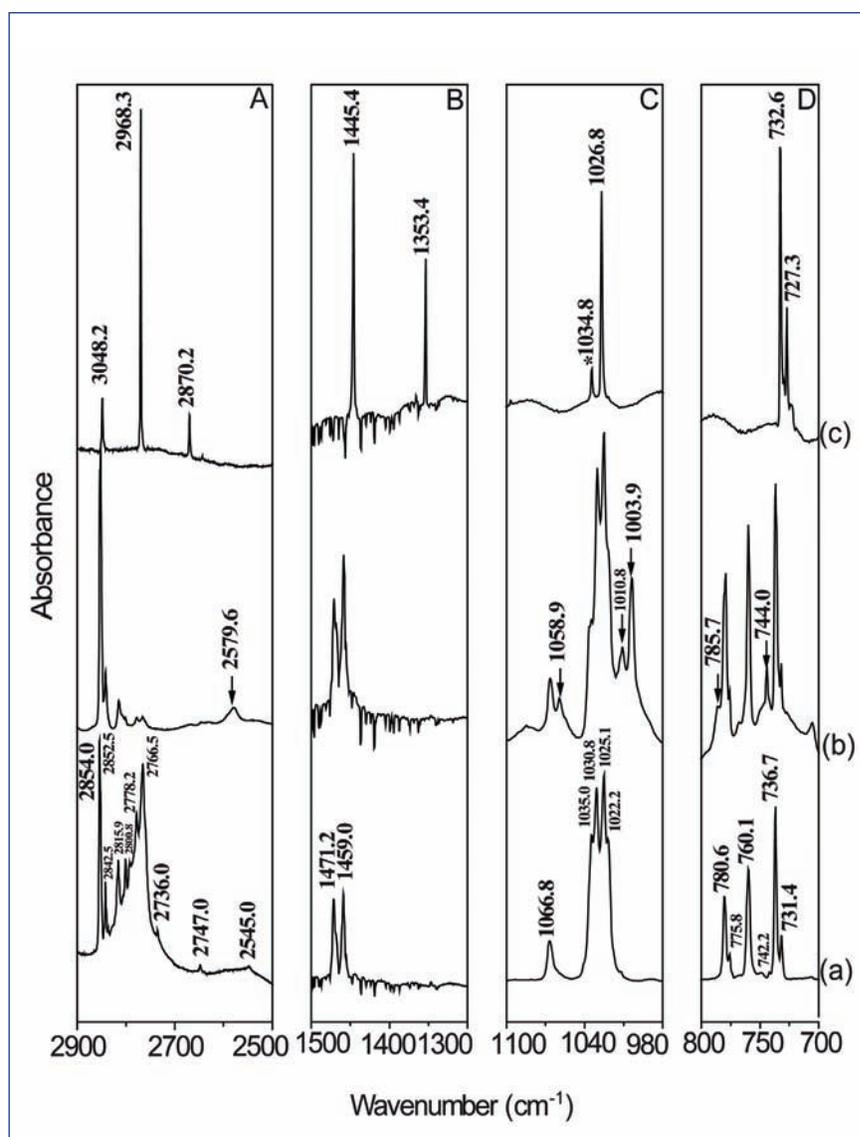
Fig. 1 *Comparison of gas phase vs matrix isolation infrared spectra of TMPhite with HCl in a N_2 matrix. Trace (a) shows the infrared spectra of HCl (Grid A) TMPhite (Grid B,C,D) alone, trace (b) shows the infrared spectra of TMPhite-HCl adduct and trace (c) shows the infrared spectra of CH_3Cl product formed due to the gas phase reaction of TMPhite and HCl, in N_2 matrix*

in the matrix. Figure 2a shows the schematic of the reaction between TMPhite and HCl in the gas phase.

Dimethoxymethane with HCl

Pre-mixing of DMM and HCl with argon in the gas phase and then deposited at 12 K resulted in a nucleophilic substitution reaction and yielded products, cis-chloromethyl methyl ether (cis-CMME) and methanol as shown in Figure 3c. On the contrary, when DMM and HCl were co-deposited using argon matrix and then annealed, produced a hydrogen bonded alkoxy adduct (Figure 3b) probably the intermediate in the gas phase nucleophilic substitution reaction. The formation of the alkoxy adduct was evidenced by the shifts in the vibrational frequencies of the DMM and HCl submolecules. The nucleophilic substitution reaction
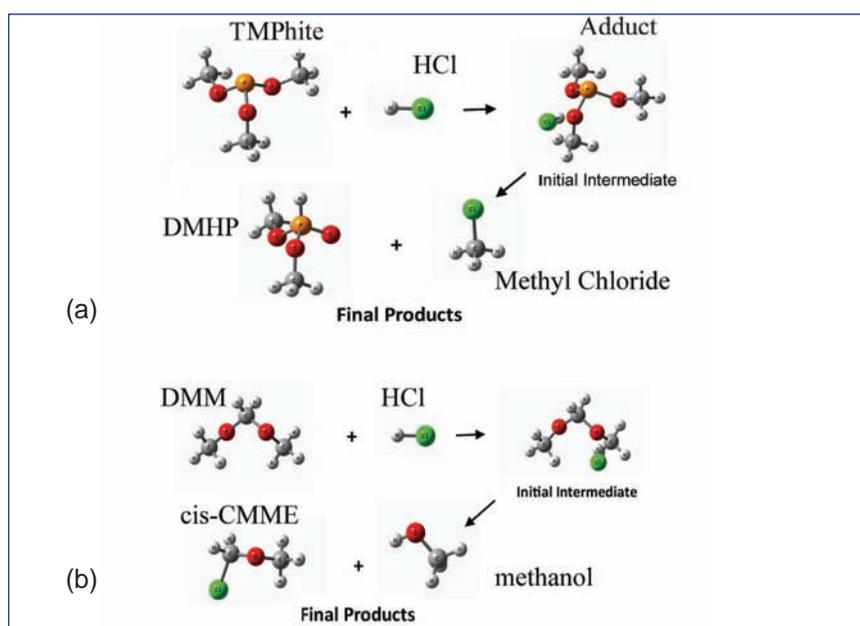
Fig. 2 *Schematic of the gas phase reaction and the hydrogen-bonded intermediate (adduct) trapped in matrix isolation experiments (a) TMPhite-HCl and (b) DMM-HCl*

between DMM and HCl is prevented in the low temperature matrix probably due to the cage effect in the matrix. Figure 2b shows the schematic of the reaction between DMM and HCl.
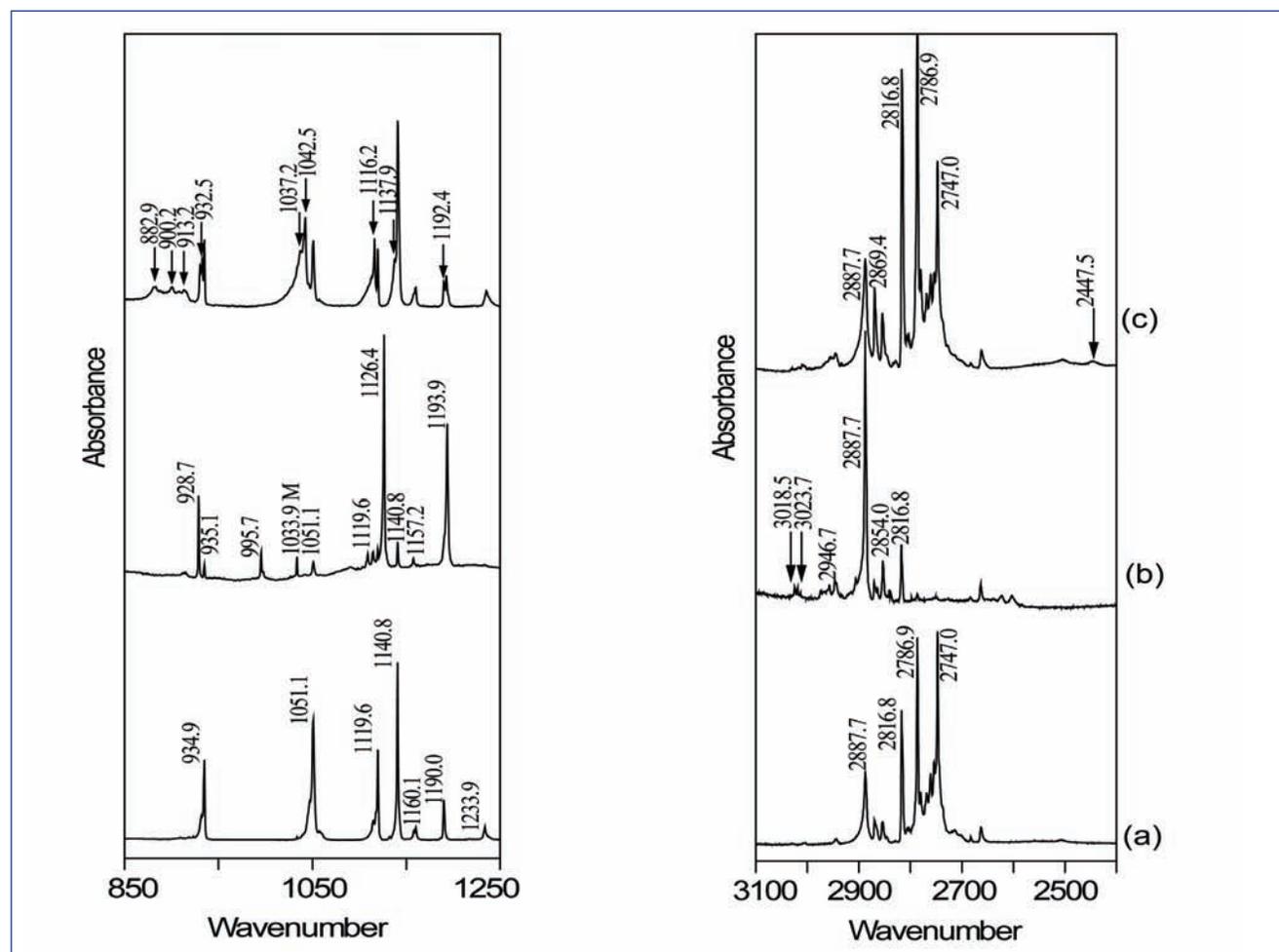
Fig. 3 *Comparison of gas phase versus matrix isolation infrared spectra of DMM with HCl in Ar matrix. Trace (a) shows the DMM alone spectra, trace (b) shows the cis-CMME product formed due to the gas phase reaction of DMM and HCl and trace (c) shows the infrared spectra of DMM-HCl adduct*

V.14 Simulating Radiation Damage in a bcc-Fe System with Embedded Yttria Nanoparticles

Oxide dispersion strengthened (ODS) steels have excellent structural and chemical stability, high creep resistance and are stable under intense neutron radiation. Many experimental studies have been carried out on oxide dispersion strengthened alloys, but the role of embedded nanoparticles in improving the stability is still not clear. The focus of this work is on identifying the role of yttria nano-particles by performing a molecular dynamics study on a simplified model system of a single yttria nano-particle embedded in Fe matrix.

The simulation is carried out by embedding a ~2.22 nm diameter spherical yttria particle at centre of a 40×40×40 bcc-Fe cell. The system contains 127,867 atoms. Periodic boundary conditions are used in all directions. Fe-Fe interaction is represented by Finnis-Sinclair potential. A weakly attractive Morse potential for Fe-O, repulsive Ziegler-Biersak-Litmark potential for Fe-Y and a fixed charge Coulombic potential splined to ZBL is used for Y-Y interactions. Y-O and O-O interactions are modelled by Buckingham potential combined with a fixed charge Coulomb interaction. Fixed charges are given only to yttria atoms. Eight different primary knock-on (PKA) Fe atoms between 16 to 57 Å from yttria particle center are started towards the particle in sixty six different directions each, with 1 keV energy, for 30 ps simulation time.

Damage created by the primary knock-on in the system is studied by quantifying the total number of Frenkel defects produced, by comparing the initial and current
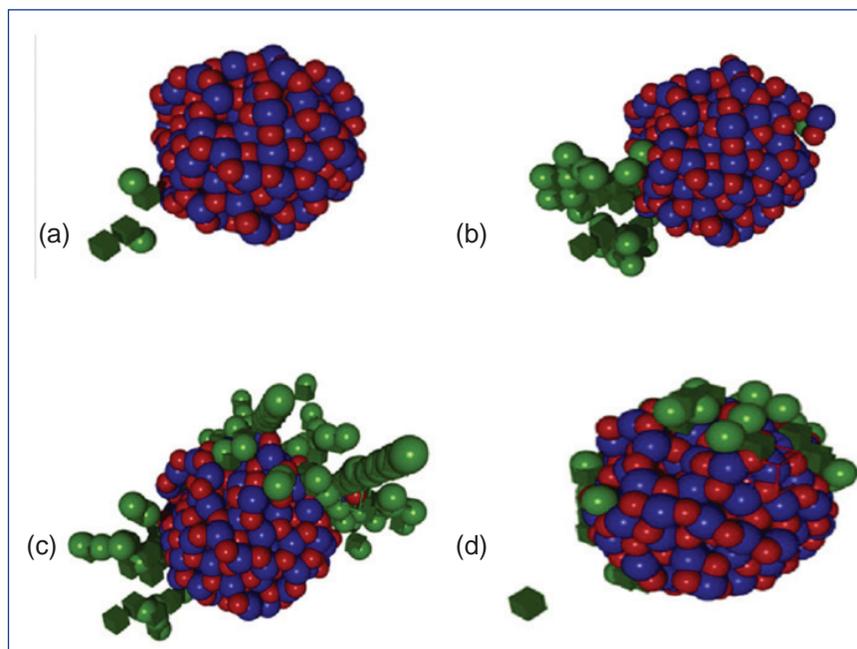
Fig. 1 *Snapshots of 1 keV collision cascade showing defect attraction to the nanoparticle during cascade relaxation process for (a) 0.025 ps, (b) 0.1ps, (c) 0.25 ps and (d) 1.25 ps. Blue spheres are Y and red are O atoms. Green spheres are Fe interstitials and green cubes Fe vacancies. Defects are seen to enter (b), come out of the yttria particle (c) and reside at the Fe-yttria interface (d). Fe atoms that remain on lattice sites are not shown*

states of the system at various time steps. If an atom is not found within 0.9 Å radius of the original crystal position, that position is marked as vacancy. If an atom has moved more than 0.9 Å and does not occupy any vacant site, it is marked as interstitial.

Figure 1 shows the 1 keV collision cascade generated for one of the cases. Effect of yttria is to limit the cascade volume when compared to an equivalent damage cascade in pure Fe system. A key feature is that Fe atoms can relocate to positions within the particle during the ballistic phase of the cascade if it has enough energy to penetrate the particle. These Fe atoms are eventually ejected from the particle to reside at the interface. This may be a feature of the potentials used.

The kinetic energies of all Fe atoms

that enter and exit again from the nanoparticle during the cascade show that the nanoparticle can absorb very large amounts of energy without permanent displacement of yttria atoms. The particle absorbs kinetic energy which otherwise is used for producing more Fe defects and releases the energy slowly over a long time scale by converting it to atomic vibrations, thus allowing for higher mobility of the defects in the region. Partial amorphisation of particle structure takes place during this process but after large times it becomes similar to that before irradiation. When cascade is initiated close to a nanoparticle, it acts as a block to propagation of collision cascade. This resilience might lead to the oxide dispersion strengthened material being more radiation resistant than pure metal.

V.15 High Temperature X-ray Diffraction of Magnetron Sputtered Zr Based Coatings

Zr based hard coatings are of great interest in a number of technological applictions due to their improved tribological, corrosion, mechanical and physical properties. The addition of Al progressively modifies the texture and improves the resistance against oxidation and also increses significantly the hardness of the coatings. Zr, ZrN and alloyed films of ZrAlN have been prepared on Si substrate using pulsed DC magnetron sputtering. High temperature X-ray diffraction (HTXRD) is used to study phase stability and to determine the coefficient of thermal expansion (CTE) of the coatings. HTXRD experiments were carried out using an INEL XRG – 3000 diffractometer with glancing angle incidence (ω) of 5° and Cu K_α radiation. Buhler HDK 2.4 high temperature camera with tantalum as a heating holder was used for the high temperature measurements in the two theta range 20 to 90° at 2.8 x 10^{-6} mbar with the heating rate of 10 K/min, with a step size of 100 K from room temperature to 1373 K. Samples were kept on a tantalum base and were heated in the temperature range of 300-1373 K and XRD patterns were recorded simultaneously. After heating up to 1373 K, samples were cooled to room temperature with a rate of 50 K/min. Lattice parameters were calculated from HTXRD patterns and from the lattice parameter data, average coefficients of thermal expansion was determined. HTXRD pattern of Zr films deposited on Si indicates that Zr films were stable up to 773 K and the films tend to oxidize to form monoclinic ZrO_2 and promote interdiffusion and finally resulting in the decrease of film thickness beyond 773 K. $ZrSi_2$
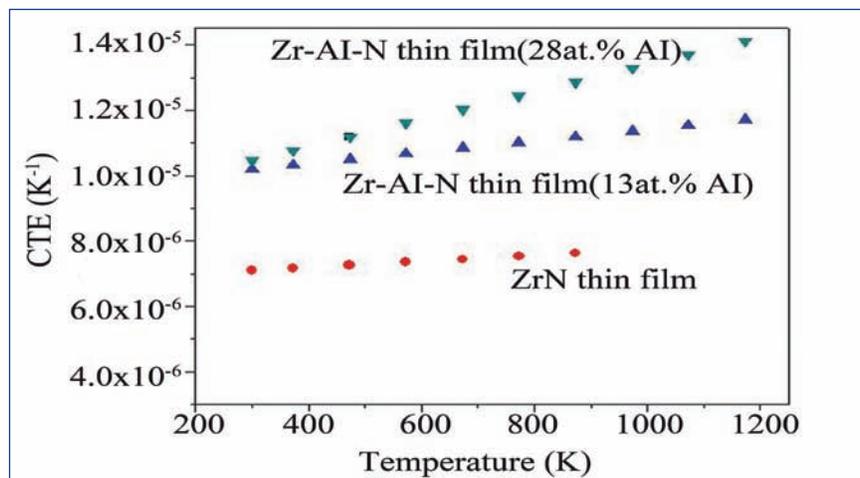
Fig. 1 *A comparative plot of zirconium based films*

phase was also noticed at higher temperature. The average thermal expansion coefficient zirconium film up to 873 K was calculated using first order derivative of lattice parameter and average CTE values are found to be $\alpha_{Ta}(K^{-1}) = 5.63 \times 10^{-6} + 1.08 \times 10^{-8} \times (T)$ and $\alpha_{Tc}(K^{-1}) = 6.2 \times 10^{-6} + 7.36 \times 10^{-8}(T)$ along the a and c axis, respectively and it is higher than of CTE of the bulk Zr (5.7×10^{-6} K^{-1}). HTXRD pattern of ZrN thin films deposited on Si substrates indicates that ZrN film is stable up to 973 K and the film tends to oxidize to form monoclinic ZrO_2 and promotes interdiffusion and finally resulting in the $ZrSi_2$ beyond 973 K. The average thermal expansion coefficient of ZrN film up to 973 K was calculated using first order derivative of lattice parameter and found to be $\alpha_T (K^{-1}) = 6.81 \times 10^{-6} + 9.26 \times 10^{-10} x(T)$. The phase stability and linear thermal expansion behaviour of alloyed ZrAlN thin films with different Al concentration $Zr_{0.34}Al_{0.13}N_{0.53}$, and $Zr_{0.25}Al_{0.28}N_{0.47}$ were investigated. The HTXRD patterns of $Zr_{0.34}Al_{0.13}N_{0.53}$ and $Zr_{0.25}Al_{0.28}N_{0.47}$ in the temperature range of 300-1473 K show that addition of 13 at.% of Al did not promote the formation of any oxide

phase of Zr. However, there is a slight inter-diffusion of the film as is evident from the reduction in the peak intensities of (200) and (311) reflections. Second order polynomial fit was used for the non linear fitting of the lattice parameter. It was found that the ZrAlN thin film was stable up to 1373 K and there was no signature for the formation of any secondary phase. The lattice parameter of $Zr_{0.34}Al_{0.13}N_{0.53}$ was found to be: $a_T(Å) = 4.513 \times 10^{-10} + 4.381 \times 10^{-15} (T) + 3.922 \times 10^{-19}(T^2)$ in the temperature range 300-1373 K and the average linear thermal expansion coefficient is found to be: $\alpha_T (K^{-1}) = 9.3 \times 10^{-6} + 2.7 \times 10^{-9} (T)$. Lattice parameter of $Zr_{0.25}Al_{0.28}N_{0.47}$ was also calculated from the HTXRD and It was found to be: $a_T(Å) = 4.454 \times 10^{-10} + 4.139 \times 10^{-15}(T) + 9.416 \times 10^{-19} (T^2)$ in the temperature range 300-1373 K and the average linear thermal expansion coefficient was found to be: $\alpha_T(K^{-1}) = 10.01 \times 10^{-6} + 1.9 \times 10^{-9}(T)$. The CTE values of alloyed ZrAlN thin films were found to be higher for the 13 and 28 at. % of Al alloyed films of ZrAlN than that of the ZrN films (7.2×10^{-6} K^{-1}). A comparative plot of Zr based films is shown in Figure 1.

V.16   Recovery of Platinum from the Residue of Direct Oxide Electrochemical Reduction Process

Direct oxide electrochemical reduction is a new method by which metal oxide can be converted to metals. This process is being studied for conversion of uranium oxide to uranium. In this process solid uranium oxide is used as the cathode against a platinum anode. LiCl-1wt% Li_2O is used as the molten electrolyte and the cell is operated at 650 °C. During this process, the platinum electrode is partially consumed and goes into the molten salt forming a residue. A quick analysis of the residue has revealed that the platinum content varied between 10-95% for different campagins along with other impurities such as U, Fe, Cr, Ni and Mn in parts per million level. Being a precious material, it is required to recover the platinum from the used salt residue.

Dissolution of the residue in aqua regia was found to be incomplete. Hence, an analytical procedure using chlorination of the platinum residue was standardized for the recovery of platinum. Recovery of platinum involves three steps. In the first step, chlorination of residue was carried out so that platinum forms chloroplatinate which is easily soluble in aqua regia. In the second step, platinum was precipitated as platinum sulphide and in the final step, the platinum sulphide was heated at 800°C to give platinum metal.

It is observed that chlorination of residue in presence of admixtures helped its speedy dissolution in aqua regia. Two admixtures LiCl-KCl eutectic and NaCl were used in our studies. The residue sample was mixed with admixtures in a quartz vessel and chlorination was carried out using chlorine gas.
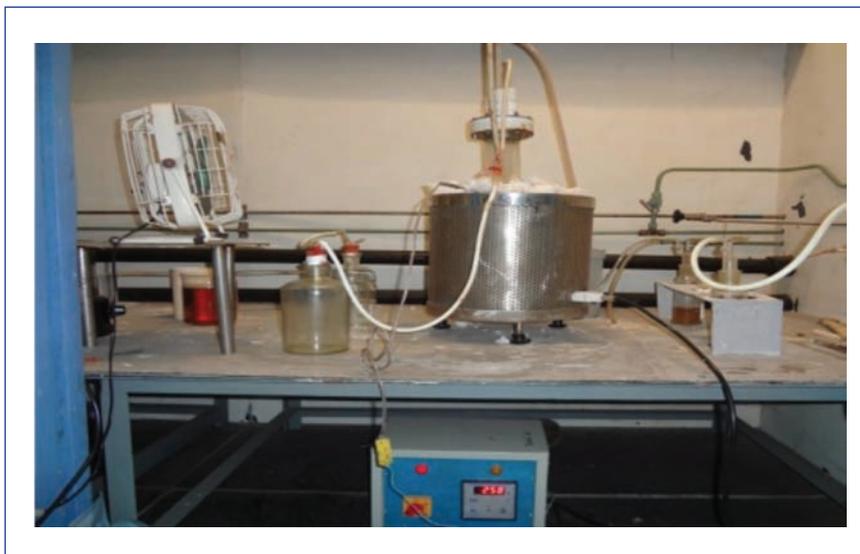
Fig. 1 *Schematics of chlorination setup*

Various process parameters such as ratio of the sample to admixture, temperature and duration of chlorination were optimised. A sample to admixture ratio of 1:25, temperature of 600°C and 3 hours duration were found to be the optimum conditions for chlorination. Figure 1 gives the schematic diagram of the chlorination set up used in our experiments. The effluent gas from the chlorination setup was allowed to pass through a saturated solution of sodium hydroxide. Completion of dissolution was assertained by analyzing the solution using Inductively coupled plasma/optical emission spectrometry (ICP-OES).

After the dissolution of residue, pH was adjusted to one and platinum was separated as platinum sulphide by the addition of 5% sodium sulphide solution. Recovery of platinum was determined by analysis of platinum sulphide using ICP-OES and it was found to be around 95%. Pure platinum was recovered by heating the platinum sulphide. The recovery of platinum by heating step was also confirmed by analysis using ICP-OES.

The above chlorination procedure was applied to residue samples from different runs of direct oxide electrochemical reduction process and the details of platinum recovered in three different samples are given in Table 1.

Table 1:Amount of platinum recovered from the residue samples of direct oxide electrochemical reduction process		
Experiment	Sample weight. (g)	Platinum recovered (g)
1	0.5	0.31
2	0.2	0.04
3	0.2	0.02

V.17 Effect of Alloying Elements on Dispersion and Structure of Oxide Nano Particles in Model ODS Alloys

Oxide dispersion strengthened steels combine the irradiation swelling resistance of ferritic steel with the high creep resistance required for long-term operation in a high-temperature reactor. These novel alloys require mechanical alloying to disperse nano-scale strengthening oxides of yttrium and titanium throughout the steel. Understanding the character and distribution of these oxides is critical to understanding and developing these alloys to their full potential. There is a broad consensus on the dispersion strengthening mechanisms in ODS alloys by introducing nano particles into the matrix, whereas a detailed understanding of alloying elements in refining the size distribution, number density, crystal structure and composition of the nano-oxide particles is still to be obtained. The size of the oxide nanoparticles in ODS alloys ranges from 1 nm to 50 nm and the particles with different crystal structures are found to be Y_2TiO_5 (Orthorhombic, Hexagonal), $Y_2Ti_2O_7$ (cubic), $YTiO_3$ (orthorhombic), $Y_2Ti_2O_6$ (orthorhombic) and in other possible phases depending on alloying element concentration and processing method.

Three model ODS alloys ($Fe-0.3Y_2O_3$, $Fe-0.2Ti-0.3Y_2O_3$ and $Fe-14Cr-0.2Ti-0.3Y_2O_3$) were prepared by using mechanical
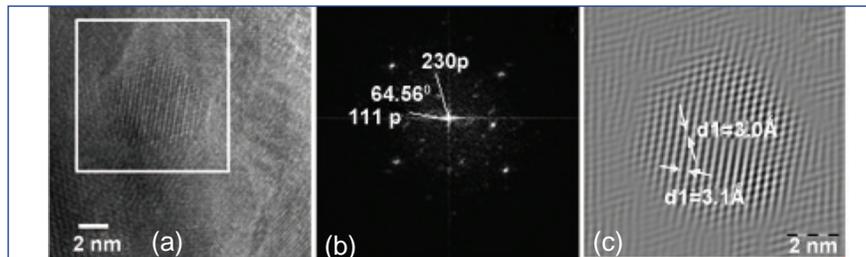
Fig. 1 (a) HRTEM images obtained from alloy $Fe-0.2Ti-0.3Y_2O_3$ with an embedded particle, (b) FFT taken from the highlighted region in (a) containing the particle indexed for various planes and angles and (c) Inverse FFT image showing lattice planes of different d-spacing of orthorhombic Y_2TiO_5
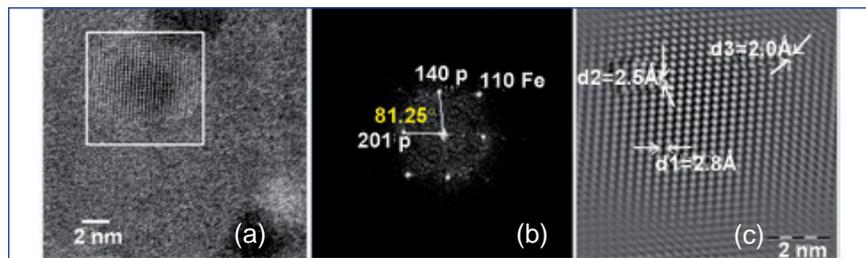
Fig. 2 (a) HRTEM images obtained from alloy $Fe-14Cr-0.2Ti-0.3Y_2O_3$ with an embedded particle, (b) FFT taken from the highlighted region in (a) containing the particle indexed for various planes and angles and (c) Inverse FFT image showing lattice planes of different d-spacing of orthorhombic Y_2TiO_5

alloying and hot extrusion method. The samples were characterized with LIBRA 200FE (Carl Zeiss) high resolution transmission electron microscope.

In all three alloys, several low magnification images are taken and the measured average size and number density of the oxide particles are tabulated in Table 1. The presence of Ti refines the dispersed particles finer whereas Cr addition does not alter the size distribution. Figure 1 and Figure 2 shows typical high resolution transmission electron microscope (HRTEM) images of the oxide particles for the alloys $Fe-0.2Ti-0.3Y_2O_3$ and $Fe-14Cr-0.2Ti-0.3Y_2O_3$. Several high resolution transmission electron microscope images were recorded and crystal structure of nano oxide particles determined. Figure 3 shows that in the

alloy $Fe-0.2Ti-0.3Y_2O_3$, ~62.5% of the particles indexed were orthorhombic Y_2TiO_5 and this number goes up to ~ 84.6 % in case of the alloy $Fe-14Cr-0.2Ti-0.3Y_2O_3$. This makes the impression that presence of Cr favors the formation of the orthorhombic Y_2TiO_5 phase as compared to the fcc $Y_2Ti_2O_7$.
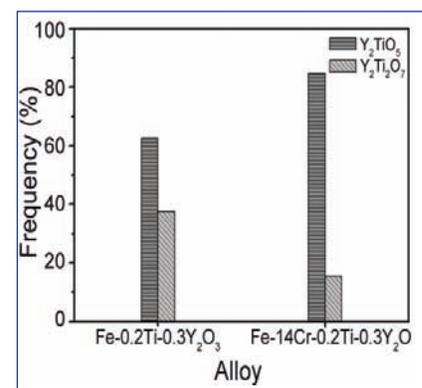
Fig. 3 The crystal structure of the oxide particles for alloys $Fe-0.2Ti-0.3Y_2O_3$ and $Fe-14Cr-0.2Ti-0.3Y_2O_3$

Table 1: The number density and average size of oxide particles in ODS alloys			
N, (d)	$Fe-0.3Y_2O_3$	$Fe-0.2Ti-0.3Y_2O_3$	$Fe-14Cr-0.2Ti-0.3Y_2O_3$
N (m^{-3})	3.4×10^{21}	4.3×10^{21}	5.3×10^{20}
(d) (nm)	14.3	7.6	10.9

V.18 Characterisation of Mechanical Behaviour of Advanced Ultra Super Critical Boiler Materials

The successful indigenous development of 304HCu austenitic stainless steel (304HCu SS) and modified nickel-base Alloy 617 (Alloy 617M) seamless boiler tubes of 52 mm diameter with wall thickness of 9.5 and 11.9 mm, respectively, for the National Mission Program on Advanced Ultra Super Critical thermal power plant technology development, was reported last year. For 304 HCu, the process flow sheet was optimized based on detailed microstructural characterisation and a new heat was produced. Extensive characterisation of the mechanical behaviour of both these advanced high-temperature boiler tube materials has been carried out.

Compared to the tensile properties of Alloy 617 reported in literature, the indigenous Alloy 617M has higher yield strength (YS) and ultimate tensile strength (UTS) at all the test temperatures, while its tensile ductility is lower below 873 K (600ºC) and higher above 873 K (Figure 1). The YS of indigenous Alloy 617M is better than the minimum specified in VdTÜV (German) standard.

The variation of creep rupture life with applied stress at different

Fig. 1 *Variation of tensile properties with test temperature of indigenous Alloy 617M tube material (a) tensile strength and (b) tensile ductility*

temperatures (Figure 2) shows that indigenous Alloy 617M has better creep properties compared to internationally reported data. The indigenous 304HCu SS has creep rupture strength well within the ±20% scatter band and is close to the mean value of internationally reported data (Figure 3) except at 600 °C where it is close to the lower bound of the scatter band.

Low cycle fatigue tests on Alloy 617M and 304HCu SS at 973K (700ºC) show that the number of cycles to failure decreases with increase in strain amplitudes from

±0.25 to ±0.6% (Figures 4 and 5).

Ambient temperature (25ºC) quasi-static fracture toughness tests were carried out on indigenous Alloy 617M and 304HCu SS. $J_{0.2}$ for Alloy 617M is 417 kJ/m^2 (Figure 6) while J_{Ic} for an equivalent grade of Alloy 617 from different methods of crack length estimation is reported as 250-439 kJ/m^2. The lower band corresponded to potential drop method as used in the present study. The results for Alloy 617M can be considered as conservative, but comparable with reported values. $J_{0.2}$ values for indigenous

Fig. 2 *Variation of creep-rupture life with applied stress of indigenous Alloy 617M tube material at 760ºC*
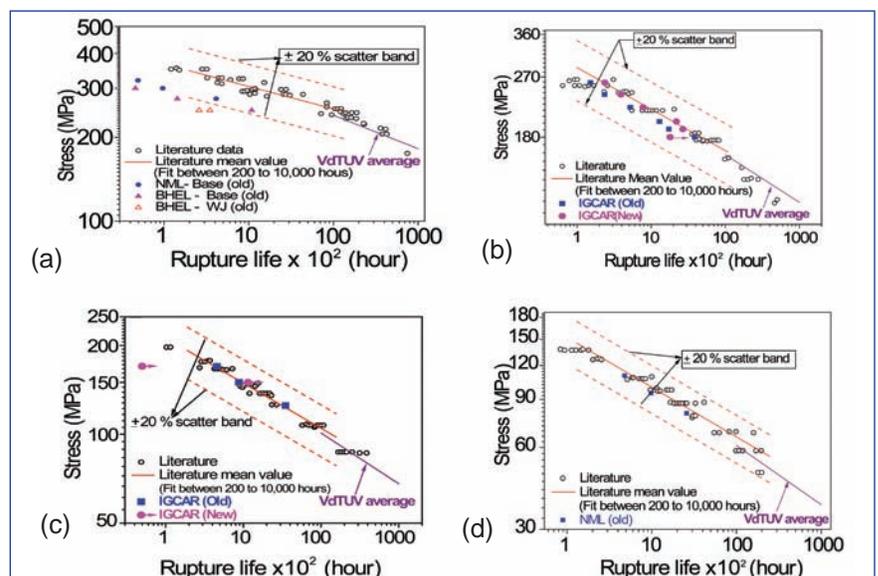
Fig. 3 *Variation of creep-rupture life with applied stress of 304HCu SS indigenous tube material and its weld joint (WJ) at (a) 600ºC, (b) 650 ºC, (c) 700 ºC and (d) 750 ºC*
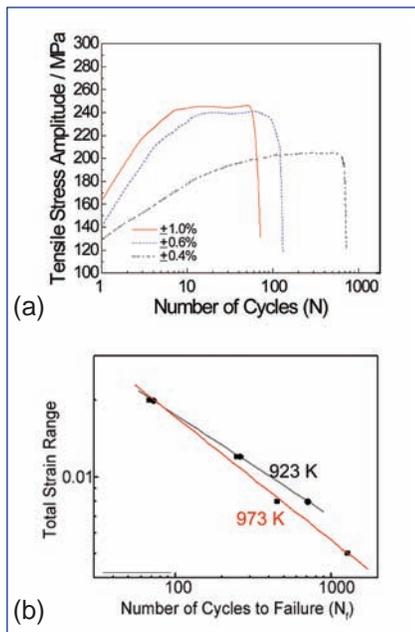
Fig. 4 *(a) Cyclic stress response curves at 650ºC (923K) and (b) strain-life plot at 650 and 700ºC (923 and 973K) of indigenous 304HCu tube material at 3×10⁻³ s⁻¹ strain rate*
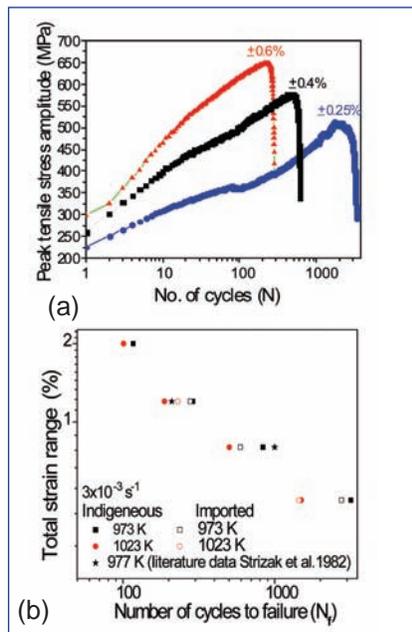
Fig. 5 *(a) Cyclic stress response curves and (b) strain-life plot of Alloy 617M tube material at 700ºC (973K) and 3×10⁻³ s⁻¹ strain rate*
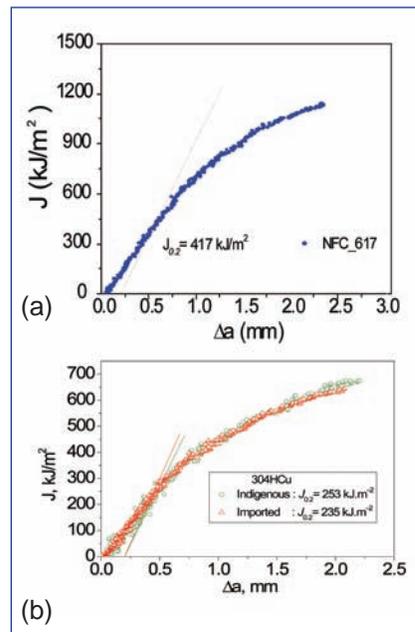
Fig. 6 *J-R curve for the tube materials at ambient temperature (25ºC) (a) indigenous Alloy 617M (b) indigenous and imported 304HCu SS*

(253 kJ/m^2) and imported (235 kJ/m^2) tubes of 304HCu SS are comparable (Figure 6b). For 304HCu SS (indigenous), the fatigue crack growth (FCG) threshold at room temperature is 7.5 MPa.m$^{1/2}$ (Figure 7) which is

comparable to the reported value of 8.7 MPa.m$^{1/2}$.

Ageing led to a significant decrease in the Charpy impact energy of both the materials. For the 304HCu SS, the decrease was ~40% while for Alloy 617M, it was ~60% for type-A with notch in the circumferential direction and ~55% for type-B with notch in the radial direction

(Table 1).

The results of the ongoing detailed characterisation of the mechanical behaviour of the 304HCu SS and Alloy 617M tube materials have given confidence that these properties are comparable to internationally reported values as also codified values in the VdTÜV standard.
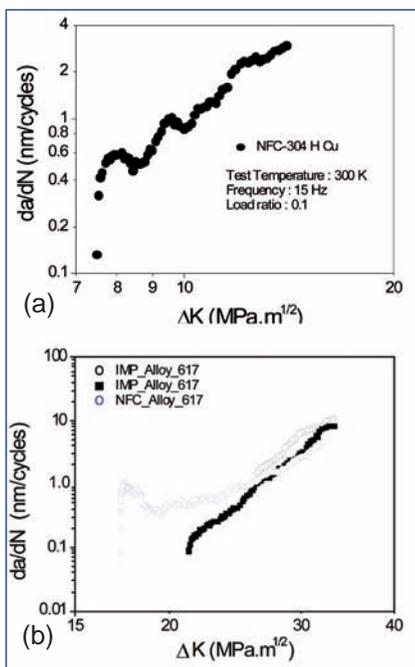
Fig. 7 *Fatigue crack growth plot at ambient temperature (25ºC) for (a) indigenous 304HCu SS tube material and (b) indigenous and imported Alloy 617M*

Table 1: Results of Charpy V-notch impact test at ambient temperature for the indigenous 304HCu SS and Alloy 617M tube materials before and after ageing

Material	Spec. size (mm)	Notch orientation	Charpy energy (Joules)	
			Measured	Full-size Equv.*
304HCu SS (Unaged)	5×5×55 (notch: 1mm)	Type-A (circum.)	33 ± 1	272 ± 6
		Type-B (radial)	34 ± 1	276 ± 4
304HCu SS (700°C/1000 h)		Type-A (circum.)	21 ± 0	168 ± 2
		Type-B (radial)	22 ± 3	175.5 ± 4.5
Alloy 617M (Unaged)	10×10×55 (notch: 2 mm)	Type-A (circum.)	327.5 ± 0.5	-
		Type-B (radial)	269.5 ± 4.5	
Alloy 617M (750°C/1000h)		Type-A (circum.)	133.0 ± 3.0	
		Type-B (radial)	121.5 ± 1.5	

* For 304HCu SS, Charpy energy obtained from sub-size specimens converted to full-size equivalent using empirical formula: C_v(full-size) = KC_v(sub), with K=8*

V.19 Challenges in Manufacture of Thermal Mixer for the Ultra Supercritical Test Facility

Thermal mixer is a critical component in Advanced Ultra Supercritical Power Plants. It is planned to study the fireside corrosion of high temperature alloys that is used at elevated temperatures. The thermal mixer was designed and manufactured as per ASME Section VIII-Division-1. It is used to cool the high temperature and high pressure steam from the test loop by mixing it with the low temperature and low pressure steam. The thermal mixer is working at high pressure and temperature; hence, it requires careful selection of material, fabrication techniques and non destructive examinations to ensure integrity of the different parts. It consists of inlet cone, supporting cones, central piece, perforated shell, cold inlet pipe and outlet cone. All the parts were made of AISI 316LN material.

The machining of austenitic stainless steel parts requires careful selection of cutting tools, use of specially designed fixtures to suit the requirements and optimum machining parameters due to high strength and work hardening characteristic of the material. The inlet and outlet cones have integrated concentric cones in each with uniform annular gap of 46.5 mm and to a depth of 175 mm as seen in Figure 1. It was machined as a single piece. With the constraints of cutting tool approach and large amount of material removal, machining of the concentric taper grooves to form cones was a challenging task. The central piece dimensions of length 548 mm, outer diameter 323.8 mm and thickness 31.23 mm was machined from hollow bar. Special cutting tools were designed and fabricated for machining internal
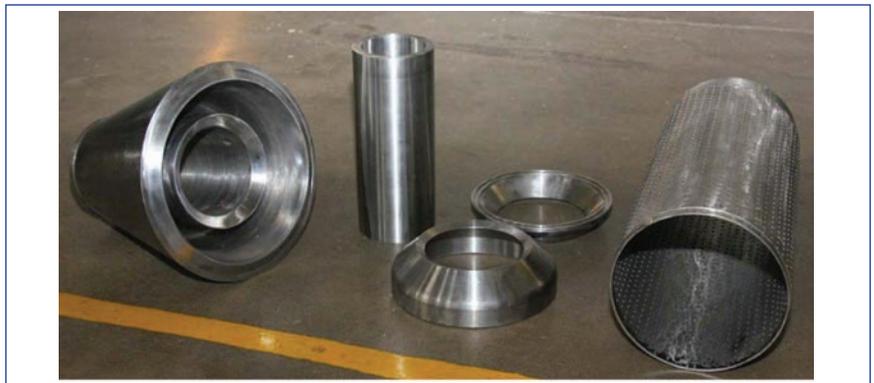
Fig. 1 *Machined part*

bores, outer diameters and internal taper deep groves forming. The thermal mixer parts were machined with close dimensional, geometrical tolerances and surface finish to achieve good weld fit up and concentricity within 0.5 mm.

The perforated shell of thickness 3 mm, outer diameter 217.56 mm with 1575 numbers of holes of diameter 5 mm with triangular pitch of 15 mm was rolled, fabricated and machined to achieve the required dimensions.

The machined components were assembled as per approved weld sequence and assembly procedure. The wall thickness of cones and central piece is 31.23 mm. It involves more amount of weld-metal deposition due to high thickness. In the fabrication of austenitic stainless steel components, weld distortion and dimensional control are challenging task. High wall thickness weld requires huge amount of weld metal deposition

and this leads to weld distortion. In order to minimize the weld distortion, the weld joint design was modified from single bevel to unequal double bevel with narrow gap. Also, combination of suitable welding processes were selected, low heat input was maintained, distortion control techniques and welding fixtures were used. Gas tungsten arc welding process was used for root & stabilising pass weld and shielded metal arc welding process for subsequent weld passes. Care was taken to maintain the cleanness in every pass during welding (Figure 2).

Liquid penetrant examination was carried out after root and final pass welding. Ultrasonic examination was carried out to ensure the soundness of the weld joints. Finally, hydrostatic test of the thermal mixer was carried out at 101 bars (g) and fabrication of thermal mixer was completed successfully (Figure 3).

Fig. 2 *Inlet/outlet cones and perforated shell in assembled condition*

Fig. 3 *Thermal mixer*

V.20   Characterisation of Creep-fatigue Interaction and HAZ Microstructure in INRAFM Steel

Extensive research pertaining to melting of four heats of 9Cr-RAFM steels containing tungsten and tantalum in the ranges 1-2 wt.% and 0.06 - 0.14 wt.% respectively and detailed characterization of their physical and mechanical properties and microstructural investigations, led to the development of India specific RAFM steel having 1.4 wt.% tungsten and 0.06 wt.% tantalum. The steel is designated as Indian Reduced Activation Ferritic Martensitic (INRAFM) steel. Studies on cyclic stress behaviour of the steel are important as the pulsating nature of operation of ITER in which the test blanket module (TBM) fabricated out of the steel will be tested. Studies on nature of microstructure in heat affected zone (HAZ) are important as fusion welding is a major joining technique that will be adopted for fabrication of test blanket module. In this report, the aspects of creep-fatigue interaction and thermal ageing behaviour of weld joint of the steel are highlighted.

Effect of application of hold on CFI behaviour of INRAFM steel

Application of hold in either tensile or compressive direction decreases the fatigue life of the steel (Figure 1). Also longer the duration of hold application, lower is the fatigue life under creep-fatigue interaction. It is deduced that during the application of hold at peak strain, creep effects are dominant and this has an effect on coarsening the initial microstructure. Hence, under combined creep and fatigue loading in a given cycle, the rate of coarsening of the microstructure is accelerated. Another important aspect observed during the present

study is the phenomenon of stress relaxation occurring during creep-fatigue interaction. This is an important aspect that could provide useful information on damage and deformation behaviour of materials. Interestingly, it has been observed that life under creep-fatigue interaction at 823 K, is inversely proportional to the amount of stress relaxed. The reason for decease in fatigue life with increase in the hold duration is ascribed to the increased amount of plastic strain accumulated during the extended period of hold application, larger substructural changes and coarsening of carbides. It is also clear from Figure 1 that application of compressive hold in peak strain has far more damaging effects on fatigue life than application of equivalent period of tensile strain, at least for short duration such as 10 min. Analysis of fractographs and longitudinal sections of the failed samples indicated oxidation assisted crack initiation and propagation. At long holds, creep has a dominating influence on dictating fatigue life. Under short holds, negligible creep effects
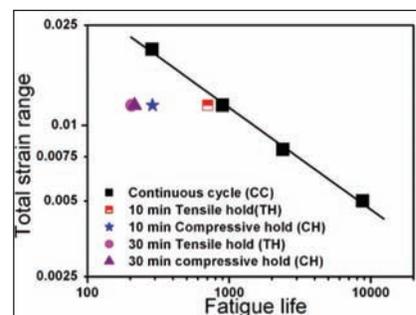
Fig. 1 *Effect of the direction of application of hold and duration of the hold applied on fatigue life of INRAFM steel at 823 K*

are expected and predominantly surface oxides have a deteriorating effect on fatigue life. Oxygen diffuses ahead of the crack tip and causes cracking of oxides during subsequent loading. Crack tip remains open and hence blunted under tensile hold, whereas the crack remains closed and hence is sharp under compressive hold. Subsequent unloading just after the compressive hold, breaks the thin oxide layer and the crack progresses in the metal matrix promoting faster damage in the material. This is the reason why one observes that compressive hold is more deleterious than tensile hold in this material.
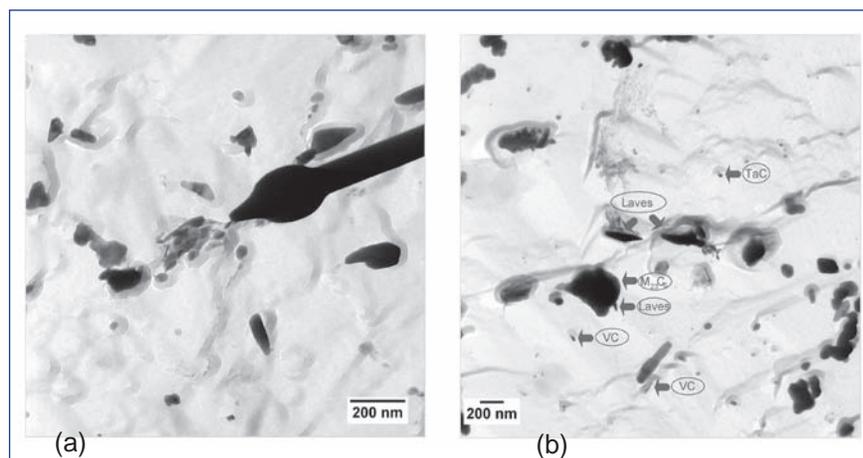
Fig. 2 *Micrograph of FGHAZ region in INRAFM steel aged at 823 K showing (a) fine precipitates of Laves phase after 5000 hours aging and (b) coarse laves phase after 10000 hours aging*

Early precipitation of laves phase in the heat affected zone of INRAFM steel weldment

The microstructural variations across a weldment (weld, heat affected zone and base metal) of INRAFM steel on prolonged thermal exposure has been studied in an autogenous bead-on-plate welds made by TIG welding. The heat affected zone in 'as welded' condition consisted of the precipitate-free coarse and fine grained regions (CGHAZ and FGHAZ). On aging at 823 K for 5000 and 10000 hours, the INRAFM steel showed the presence of fine

acicular precipitates in addition to $M_{23}C_6$ and a few undissolved pre-existing MX precipitates, which have been identified as Laves phase. The Laves phase is fine with an average size of 40 nm at 5000 hours, which coarsens after 10000 hours of aging (Figures 2a and 2b). Comparison of the size of Laves phase between that formed in the base metal and heat affected zone after 5000 hours of aging, suggests that it formed first in FGHAZ. Earlier investigation reveals no formation of Laves phase in the RAFM steel with 1 wt.% W. The formation of Laves phase in the

HAZ of INRAFM steel in contrast to 1W steel is attributed to the higher W content and abundant precipitation of carbide during high temperature exposures. The high depletion of carbon in the FGHAZ due to high growth rate of carbides, reduces the availability of supersaturated carbon leading to early precipitation of Laves phase in the vicinity of the coarse carbide. It is well known that the formation of Laves phase is detrimental to fracture toughness. Hence, it can be concluded that FGHAZ is the weakest region in the weldment during thermal exposures at temperatures around 823 K.

V.21 Tensile, Low Cycle Fatigue and Creep-Fatigue Interaction Properties of Grade 92 Steel

Grade 92 steel (9Cr-1.8W-0.5Mo-VNb) is one of the creep strength enhanced ferritic martensitic steels developed as a candidate material for use in steam generators of sodium cooled fast reactors and piping systems of fossil power plants. The mechanical properties of this material depend to a large extent on the heat treatments employed, hence an effort has been made at our Centre to optimize the normalizing and tempering treatments for this material for enhanced mechanical properties.

Effect of normalizing and tempering heat treatments on tensile strength

The steel was subjected to normalization at 1313, 1333 and 1353 K for 30 minutes and subsequently tempered at 1013, 1033 and 1053 K for 60 minutes. Tensile tests on the heat treated steel specimens were carried out at a nominal strain rate of 3×10^{-3} s^{-1} over a temperature range of 300 to 923 K. The variations of ultimate tensile strength with test

temperature of the steels at different heat treatment conditions are shown in Figure 1. Tensile strength of the steel increased with the increase in normalization temperature; whereas it decreased with increase in tempering temperature. The decrease in tempering temperature increased the tensile strength of the steel much more appreciably than that of increase in normalizing temperature.

Tensile strength of the material is governed by the mean free

path of dislocation motion. Microstructural features of martensitic transformation induced dislocation substructure and subgrain (martensitic lath) and intra and inter-granular precipitation of carbides and carbonitrides of the tempered martensitic grade 92 steel are expected to change the dislocation mean free path appreciably to impart different tensile strength, as observed (Figure 1). Estrin and Mecking work hardening analysis has been used
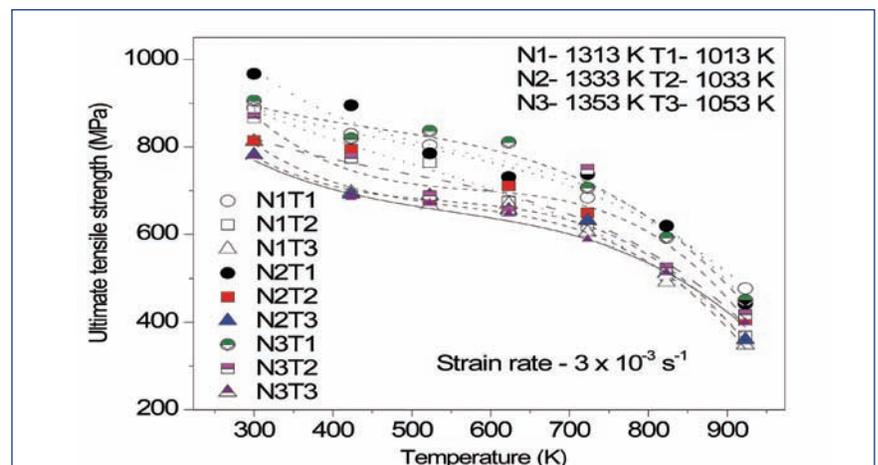
Fig. 1 *Variation of ultimate tensile strength of the steel with temperature, showing the effects of normalizing and tempering heat treatments*
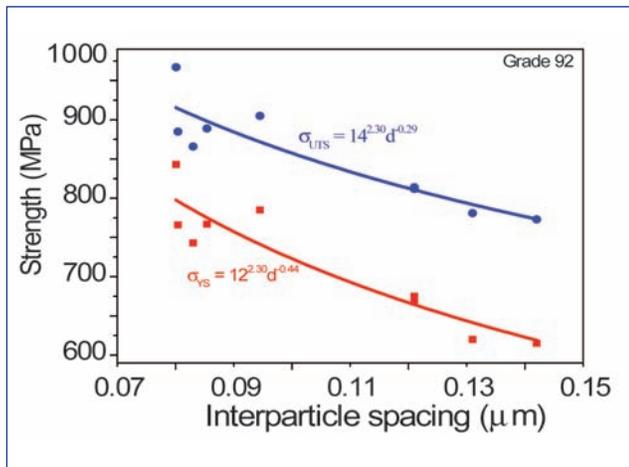
Fig. 2 *Variation of tensile strength of the steel at 300 K with inter-barrier distance to dislocation motion*
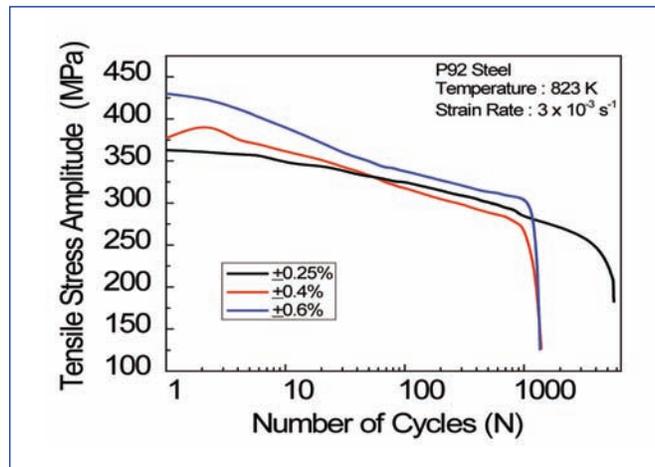
Fig. 3 *Cyclic stress response of P92 Steel at 823 K (strain rate : 3 x 10^{-3} s^{-1})*

to estimate the mean free path of dislocations. According to the analysis, when the mean free path of the dislocations is constant and given by mean inter-barrier spacing, a plot of $\sigma\theta$ versus σ^2, where σ is the true stress and θ is the work hardening rate, should be a straight line. The intercept of this line on $\sigma\theta$ axis is given by $\alpha^2 b^2 G^2/2bd$, where G is the shear modulus, b is the Burgers vector, α is the dislocation strength factor, and d is the inter-barrier spacing. The inter-barrier spacing was calculated for each heat treatment condition using α = 1.2, G = 83 GPa and b = 2.48 x10^{-10} m taken from literature. The inter-barrier spacing obtained from the above was plotted against yield strength and ultimate tensile strength of the steel at 300 K, as shown in Figure 2. There exists an inverse relation of yield strength and ultimate tensile strength with inter-barrier spacing.

Low cycle fatigue properties

The low cycle fatigue tests on P92 steel were performed as per ASTM E 606 standards under fully reversed total axial strain control mode employing a triangular waveform. Tests were conducted at 823 K and 873 K at a constant strain rate of 3 ×10^{-3} s^{-1} with strain amplitudes varying from ±0.25% to ±0.6%. The cyclic stress response of the alloy exhibited a continuous softening at the temperatures of this investigation. Typical cyclic stress response of the alloy is given in Figure 3. The fatigue life of indigenous P92 steel as a function of temperature is given in Figure 4a. The fatigue life of the alloy decreased with increase in strain amplitude and temperature.

Creep-fatigue interaction behaviour

Although creep strength is a primary concern and many efforts have been made for evaluating it, consideration of the interaction of creep and fatigue damage is also important in evaluating the integrity of components that will experience a range of cyclic loading. Creep fatigue interaction tests were conducted by introducing hold times at peak tension and compression strain in the range 0-10 minutes at 823 K and 873 K. The cyclic stress response of the steel was similar to continuous cycling tests, exhibiting a continuous softening behaviour. The fatigue life of the alloy is found to decrease with the introduction of hold time and life further decreased with increase in the duration of hold time (Figure 4b). In line with literature, fatigue life of the alloy was minimum when a compression hold was introduced. In general, fatigue life of the alloy decreased as continuous cycling > tension hold > compression hold.
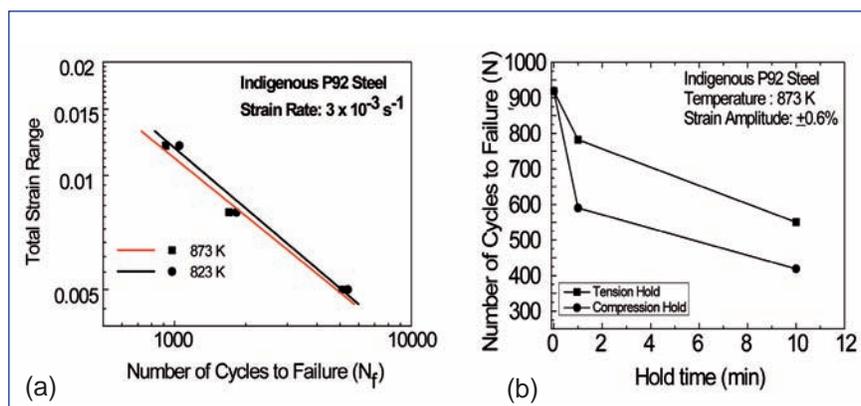
Fig. 4 *(a)Variation of fatigue life as a function of temperature and (b) hold time*

V.22 Thermal Stability Characterization of Magnetic Fe-0.55Si-0.28Mn-0.045C Iron Alloy

In the design of India's 500 MWe prototype fast breeder reactor, an iron base alloy of nominal composition Fe-0.55Si-0.28Mn-0.045C (mass%) has been selected as the candidate material for the electromagnet of diverse safety rod drive mechanism. This material, henceforth called magnetic iron has to serve the purpose of an electromagnet, which under normal operating conditions holds the diverse safety rod, by magnetic forces of attraction. Upon called to perform, the magnet is de-energized by switching off the exciting current and thereby allowed to fall freely into the reactor core. Considering the typical operating temperature and other design considerations such as holding capacity requirement of the magnet, indigenization of material development etc., a Fe-base alloy with permissible levels of magnetic impurities and with a Curie temperature of about 1032 K (759°C) has been chosen for this purpose. Various physical and mechanical properties of this material are being characterized for the purpose of generating a comprehensive database. In this context, high temperature phase stability and heat capacity parameters were characterized using calorimetry.

The preliminary characterization of the alloy has been done using X-ray, optical microscopy and transmission electron microscopy (TEM), which revealed the presence of a small fraction of $(Fe, Mn)_3C$ type carbide phase (Figure 1). The differential scanning calorimetry (DSC) thermogram obtained at the slow scan rate of 3 K/min (Figure 2) clearly shows the presence of four distinct endothermic thermal events. The first peak at about 1032 K is due to transition from ferromagnetic to paramagnetic ferrite. The second peak at 1133 K is due to α (bcc) $\rightarrow \gamma$ (fcc) phase change. The third peak at 1662 K is due to $\gamma \rightarrow \delta$ (bcc). Finally the largest endothermic peak occurs at 1795 K, which is due to melting of the alloy. The values of enthalpy change corresponding to $\alpha \rightarrow \gamma$, $\gamma \rightarrow \delta$ and $\delta \rightarrow L$ transformations are also estimated as 16.02 ± 2, 21.72 ± 2, and 258 ± 18 J g^{-1} respectively. The isothermal inverse drop calorimetry measurements of enthalpy increment $(H_T - H_{298.15})$ over the
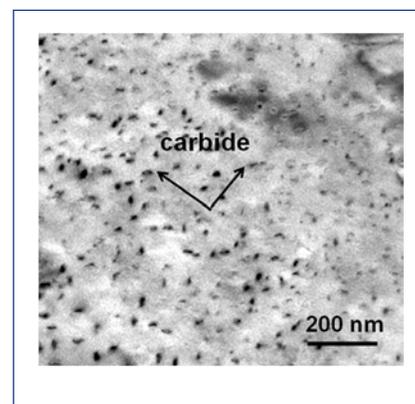
Fig. 1 *Transmission electron microscopy micrograph of magnetic iron*

temperature range 300-1523 K clearly revealed both the Curie transition and $\alpha \rightarrow \gamma$ phase changes in $(H_T - H_{298.15})$ vs temperature plot (Figure 3). Further, from the enthalpy increment data, the heat capacity has been evaluated by a non linear regression fitting. The magnetic contribution to the heat capacity has been separately calculated using a phenomenological model. It is found that magnetic effects contribute substantially to the heat capacity of α-ferrite phase (Figure 4). The change in C_p associated with magnetic transformation is estimated to be 0.7 J g^{-1} K^{-1}
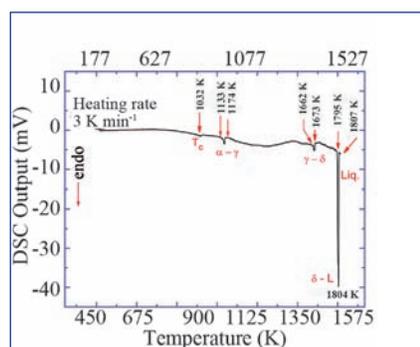
Fig. 2 *DSC thermogram at 3 K min⁻¹ for magnetic iron*
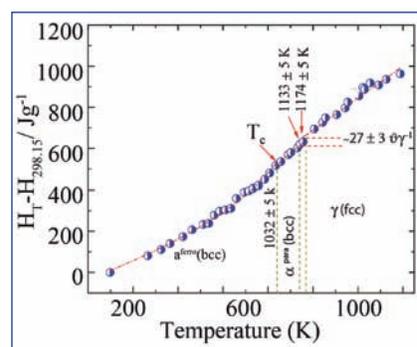
Fig. 3 *Enthalpy increment variation with temperature for magnetic iron*
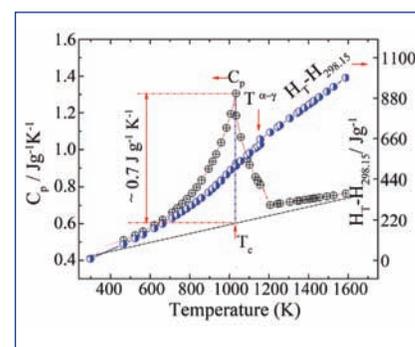
Fig. 4 *Heat capacity data together with enthalpy increment for magnetic iron*

V.23 Inhibitor Loaded Nanocontainer based Hybrid Coatings for Corrosion Protection of Modified 9Cr-Mo Ferritic Steel

A novel corrosion protective coating was developed based on 2-mercaptobenzothiazole (MBT) loaded hollow mesoporous silica (HMS) nanocontainers which can offer both active and passive functionalities and thereby exhibiting self-healing ability. The MBT loaded HMS nanocontainers were mixed with silane-zirconia hybrid sol and applied on modified 9Cr-1Mo steel by dip coating process. The corrosion protection efficiencies of pure hybrid coatings (CS) and that with inhibitor loaded nanocontainer mixed coatings (CS-NI) were compared.

The HMS spheres were synthesized by sol-hydrothermal method. The field emission scanning electron microscope (FESEM) image (Figure 1a) of the monodispersed HMS spheres (average diameter ~200 nm) reveal that these are hollow. The uniform and well defined hexagonal mesostructure was revealed by high resolution transmission electron microscope (HRTEM) image (Figure 1b). The loading and release properties of HMS spheres were investigated using UV-visible spectroscopy. The encapsulation of MBT into the pores of HMS was confirmed, by the decrease in intensity of the absorption maxima after the interaction of the MBT molecules with HMS and absence of new band

(Figure 2a). The loading efficiency of MBT in the HMS was found to be 72 %. The concentration of MBT in the releasing medium increased with time and reached equilibrium after 10 hours (Figure 2b). The rate and amount of release of MBT depended on pH and decreased in the order acidic > alkaline > neutral, confirming the stimuli responsive intelligent releasing property of HMS spheres.

Using electrochemical impedance spectroscopy (EIS), changes in the total impedance (Z) and phase angle (θ) were monitored as a function of frequency and immersion times in 0.05 M NaCl for CS and CS-NI coatings. The total impedance (at 10^{-2} Hz) of CS was $2.2 \times 10^5 \, \Omega \, cm^2$ after immersion in 0.05 M NaCl for 0.5 hours and decreased to $4.64 \times 10^4 \, \Omega \, cm^2$ after 72 hours (Figure 3), which can be attributed to the absorption of water and electrolyte. The Bode phase angle plot after 72 hours immersion clearly showed three time constants with a well evolved one at the lower frequency indicating corrosion.

The addition of MBT loaded HMS nanocontainer into the coatings brought significant changes in the impedance pattern (Figure 4). The Z values at 10^{-2} Hz decreased continuously from 0.5 to 48 hours of immersion in NaCl solution; the Z value of 1.1×10^5 for 48 hours of immersion increased to 1.3×10^5
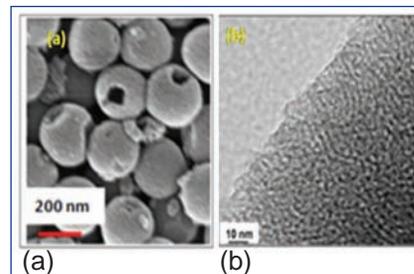
Fig. 1 *(a) FESEM and (b) HRTEM images of HMS spheres*

after 72 hours. As the immersion time increased, the inhibitor gets released from the nanocontainer and a new interfacial layer is formed, which results in the continuous increase of the theta value in the Bode phase angle plot from 24 to 72 hours and increase in the total impedance. The Bode plots for CS-NI had only two time constants; the third one indicating corrosion initiation was absent. The above mentioned results suggested a possible self healing ability of the coatings.

Thus, the EIS results confirmed the superior corrosion resistance of mod. 9Cr1Mo steel under silane-zirconia hybrid coating mixed with inhibitor loaded nanocontainers. The impregnated mechanically stable nanocontainers sealed the micro cracks and pores present in the hybrid barrier coating and enhanced the corrosion protection efficiency of CS-NI by the release of entrapped inhibitor molecules, therein demonstrating the "self-healing" ability.
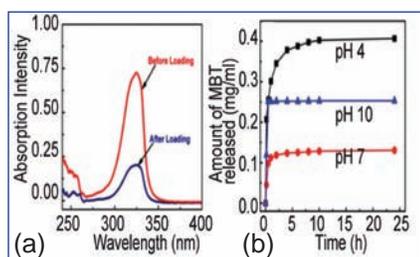
Fig. 2 *(a) UV-vis spectra of MBT solution (b) releasing behavior of HMS*
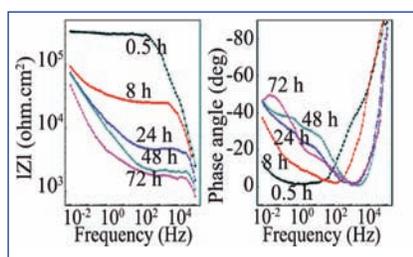
Fig. 3 *EIS of CS during immersion in 0.05 M NaCl solution*
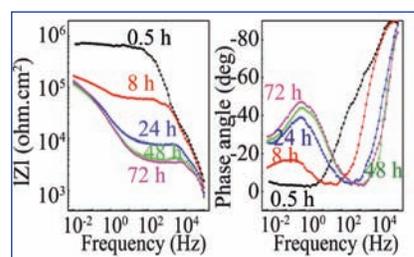
Fig. 4 *EIS of CS-NI during immersion in 0.05 M NaCl solution*

V.24 Wavelet Analysis of Acoustic Emission Signals Generated during Tensile Deformation of AISI type 316 Stainless Steel

Acoustic emission (AE) technique is widely used for studying deformation and fracture behavior in materials. The AE signals are transient elastic waves generated by rapid release of energy from localized sources in a material. The AE generated during tensile deformation can be used to discriminate different types of sources. The AE signals detected by using piezoelectric transducer contain a wealth of information about the nature of the AE sources responsible for their generation. The signals also contain valuable information from one or multiple sources, which may sometimes overlap.

The response from AE sensors is characterized by parameters such as ringdown counts, events, peak amplitude distribution and RMS value. In general, any acoustic event gives rise to a wave train. The time domain parameters mentioned above have limitations in treating AE signals as wave packets. Many of the useful information get averaged, while transforming a signal from one domain to another. These problems can be successfully overcome by the introduction of time-frequency distributions. Among them, wavelet transform (WT) offers unique merit to resolve these signals in time and frequency domains and can be very useful to extract significant information for identification and characterisation of the AE sources. In view of this, in the present investigation, an attempt is made to use the wavelet transform based AE signal processing approach to study the deformation and fracture behavior of AISI type 316 austenitic stainless steel (SS). It focuses on the energy criteria because of the different distribution of energy in each component that can be related to the deformation and fracture behavior.

Flat specimens in the solution annealed condition were tested at ambient temperature (298K) at different strain rates (5.6×10^{-4} s^{-1} to 2.8×10^{-2} s^{-1}). The AE signals were recorded by piezoelectric wideband (frequency 100-1000 kHz) sensor and AE Disp system. The resultant waveforms were processed through wavelet transform using wavelet Db-12. The resultant wavelet coefficients are further analysed for energy distribution. In this work, in order to find energy distribution contained in different components, the ratio of energies at different levels to the total energy were considered. Figure 1 shows one typical wavelet analysis of AE signal obtained at the maximum strain rate (2.8×10^{-2} s^{-1}). As can be seen from the figure, maximum energy concentration during yielding region is observed at 230-270 kHz (Figure 1a) while during work hardening at 550-630 kHz (Figure 1b) and during necking region at 170-210 kHz (Figure 1c). The low frequency response before and during yielding is due to dislocation activity, and that during necking is related to ductile fracture process. The higher frequency response at higher strain levels beyond yielding is due to reduced rate of dislocation activity.

The variation of engineering stress (MPa) and corresponding frequency (kHz) component as well as the variation of engineering stress (MPa) and corresponding energy content as a function of loading time have been analysed. Increase in energy concentration and occurrence of higher frequency signals with increase in strain rate has been observed and is attributed to increase in the rate of source activation of AE signals. This study has shown that energy distribution of wavelet coefficients of AE signals generated during tensile testing can be advantageously used for understanding the deformation and fracture behavior in materials.
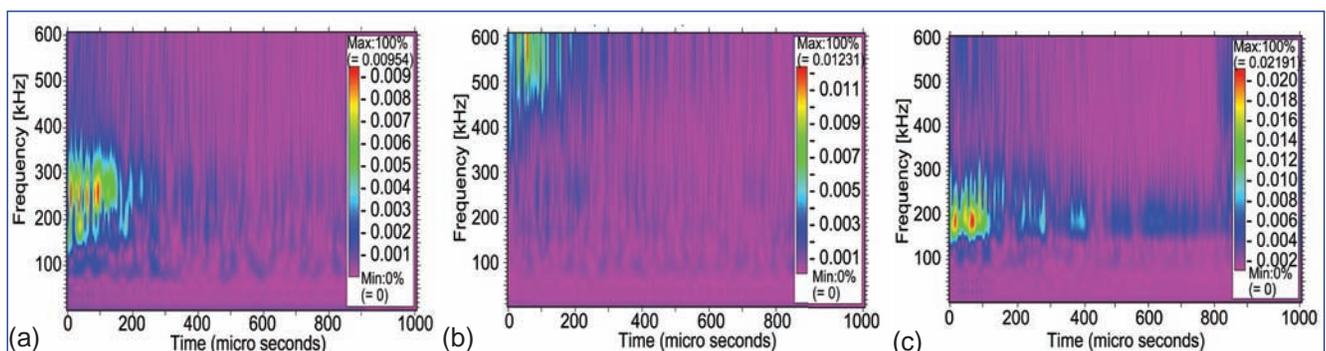
Fig. 1 *Wavelet analysis (2D color contour diagram of wave transform coefficients)-frequency with maximum energy versus time (a) 230-270 kHz during yielding, (b) 550-630 kHz during work hardening and (c) 170-210 kHz during necking for testing at maximum strain rate (2.8×10^{-2} s^{-1})*

V.25 Bulk Nanocrystalline TiTaNb Alloy Synthesized by Cryo-rolling

Bulk ultra-fine (nanocrystalline) grain (UFG) structured materials can combine very high strength together with their functional properties, such as the exceptionally high corrosion resistance in the Ti5Ta1.8Nb alloy, a candidate material for reprocessing applications. Their synthesis involves the top-down approach, in which coarse grains (~5 μm or more) have to be severe plastically deformed and fragmented down to nanocrystalline sizes. Commonly used techniques such as the equal-channel angular pressing, equal channel angular extrusion and the high pressure torsion are difficult to upscale. Therefore, a rather simple method, viz., multipass cryo-rolling, was adopted; the material was dipped in liquid nitrogen prior to each rolling pass up to true strains ~2.3 resulting in a grain size reduction from 5 μm down to 10 nm (Figure 1a

and 1c). Detailed XRD and electron microscopy studies after various levels of rolling strains indicate that the successive steps of rolling induce hardening and formation of dislocation cell structure (Figure 1b) followed by a critical strain leading to the formation of nanocrystalline grains. Aberration corrected HRTEM studies (Figure 2a) revealed tiny edge dislocations (A) and nano-twins (B) within a grain in the UFG material. The spurious contrast and directional streaking along atomic columns (Figure 2a), is under study through theoretical simulation of the projected potential and invoking strain along the atomic columns. Grain boundary characterisation by HRTEM revealed well-defined steps which are clear signatures of dislocation annihilation. Precision electron diffraction (PED) studies in a TEM (see Figure 2b), revealed significant increase in coincident site

lattice (special) boundaries after grain fragmentation. Microtensile test results showed nearly 3-fold increase in yield strength by grain fragmentation.

The cryo-rolled materials exhibited two Hall-Petch regimes (I and II in Figure 2c; σ_Y: Yield Stress & d: grain size) with significantly different Hall-Petch parameters (k_{HP}). This difference in k_{HP} was rationalized based on variation in dislocation density (ρ), estimated using the XRD based modified Williamson-Hall approach. Decrease in dislocation density beyond a critical strain at which the cellular structure (Figure 1b) was formed, is in line with the grain fragmentation model conceptualized.

Three phase hot-nitric acid corrosion test on the UFG Ti alloy exhibited no deterioration of the material's extraordinary corrosion resistant properties due to grain fragmentation.
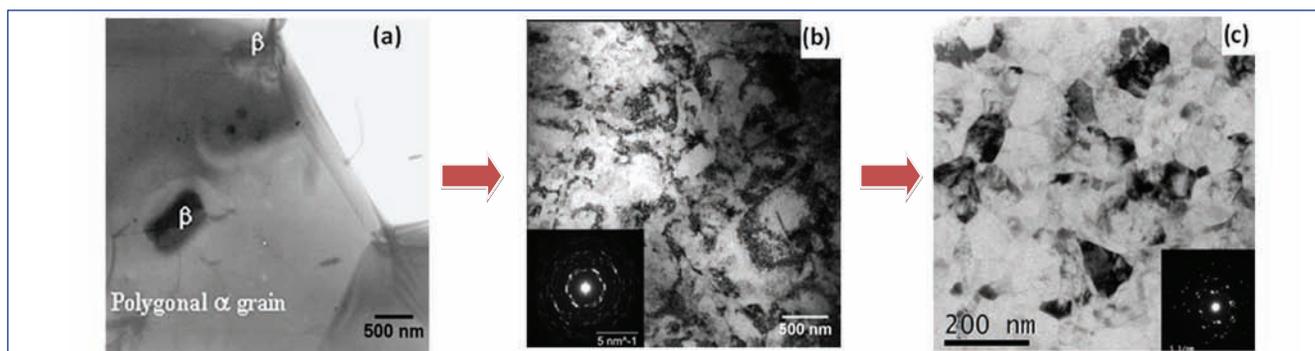
Fig. 1 Microstructural transformation in a coarse grain TiTaNb alloy during cryo-rolling
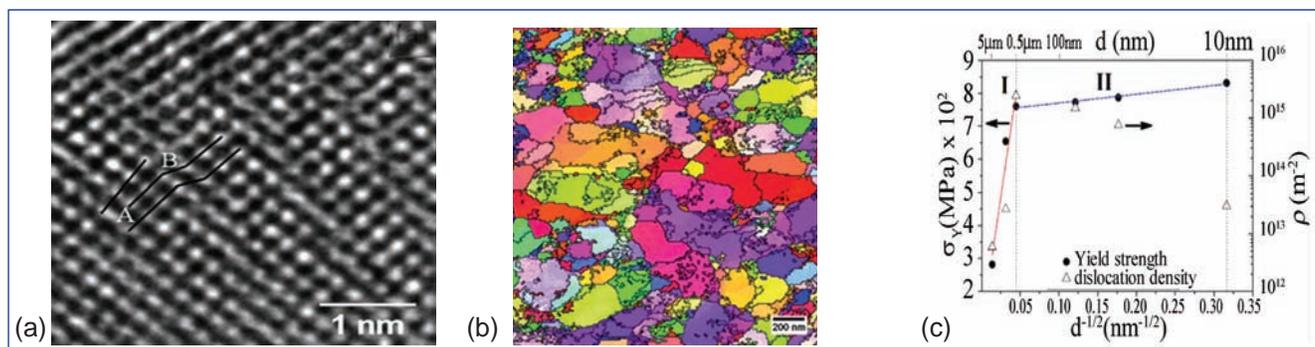
Fig. 2 *(a) Aberration corrected HRTEM, (b) precision electron diffraction orientation imaging microscopy and (c) mechanical property – dislocation density correlation in UFG TiTaNb alloy to understand Hall-Petch regimes I and II*

V.26 Measurement of Annular Air-gap using Active Infrared Thermography

Accurate measuremet of air-gap between planar and concentric cylindrical geometries is required on many occasions. Though qualitative results are sufficient in most of the applications, in some cases e.g. nuclear fuel pins, quantitative information on the annular gap between the fuel pellets and the cladding tube is essential, as it influences the heat transfer. Non-destructive measurement of air-gap is desired. X-ray radiography, eddy current and ultrasonic techniques have certain limitations. Radiography technique cannot detect micron sized air-gaps due to limited resolution, while eddy current technique is slow as it requires scanning of the whole pin surface using a point probe. Further, it is prone to electromagnetic coupling related noise. Ultrasonic technique can only detect gap-closure i.e. contact conditions and also require the use of couplant. In this work, infrared thermography based experimental procedure has been reported for measurement of micron sized annular air-gaps. This is fast, convenient, accurate, non-contact and does not require complicated data analysis.

Annular air-gaps of various dimensions are simulated using outer hollow cylinders made of aluminum and solid stainless steel inserts of varying diameters. The specimens are externally heated using a hand held hot air-gun for approximately 3-5 minutes till the temperature of the specimens reached ~150°C, which is based on temperature decay time, transverse dimensions and thermal diffusivity of the object under consideration. After the heating is stopped, thermal images are acquired for about 10 minutes using an infrared camera. Temperature decay over a region of interest (ROI) is studied as a function of time. For avoiding the viewing angle effects, caution is adopted while selecting the region of interest to exclude the pixels on the two edges of the cylindrical surfaces (Figure 1). Temperature decay during the cooling cycle follows an exponential profile in all the cases where the decay constant is found to be air-gap dependent. The rate of temperature decay is fastest for the empty cases (without inserts) and lower for smaller air-gaps.

During temperature decay, the core of the system (which is at a higher temperature) is surrounded by a cooler skin layer. The thickness of the skin layer increases with time and after a transition time (theoretically estimated as 83 s) internal thermal transients can be neglected and temperature of the whole body decays as a function of time only. During this period (experimental time scale is several times higher than the transition time) the rate of temperature decay is predominantly determined by a single time constant which is the product of two lumped parameters namely thermal resistance (inverse of the product of convective heat transfer coefficient and surface area) and thermal capacitance (product of the density, specific heat and volume). Biot number is a dimensionless quantity which signifies the relative contribution of the conduction and convection modes of heat transfer and for the present system it is theoretically estimated as 0.027 which is far less than unity, confirming that the temperature variation across the body is negligible compared to the body-air temperature difference and conduction resistance of body
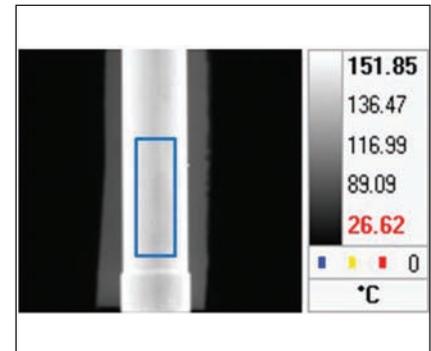
Fig. 1 *A typical IRT image of a specimen and the region of interest is shown using a blue rectangle*

is negligible. This enables analysis of the system in terms of a single time constant. It is observed that the time constant of temperature decay increases with decreasing annular air-gap as the thermal capacitance increases. An empirical relationship between the inverse of time constant of temperature decay (τ^{-1}) and annular air-gap is established as shown in Figure 2. For small air-gap values (up to 650 µm), the data is fitted with a straight line. Using this calibration curve, unknown air-gaps up to 20 µm are measured with ± 6.2% error. The applicability of this procedure is limited to the small air-gap region only, essentially because, for larger air-gaps, convection currents cannot be neglected and a simple lumped system of analysis is inadequate.
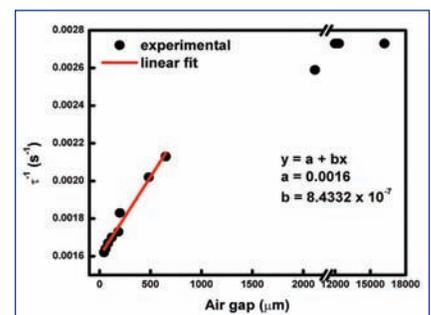
Fig. 2 *Calibration curve between the inverse of time constant of temperature decay and annular air-gap*

V.27 Experimental and Computational HRTEM Characterization of V-4Ti-4Cr Alloy

V-Ti-Cr alloys are potential candidate materials for high performance structural applications in fusion power systems due to their favourable mechanical and physical properties at elevated temperature. Worldwide, the researchers mainly focussed on the V-Ti-Cr system with an emphasis on compositions in the range of V-(4-10)Ti-(4-5)Cr for first wall/blanket module application of fusion based thermo-nuclear reactors.

In the present study, the phase structural information has been attempted through heuristic approach of alloy design. Thermodynamic calculations have been carried out through Miedema model for the entire V-Ti-Cr alloy system. Miedema model is based on the mutual behaviour of the formation enthalpy of the amorphous phase and that of the solid solution phases. If, for a particular composition, the enthalpy of formation of the solid solution phase is smaller than that of the amorphous phase then the solid solution phase will stabilize for that composition.

The enthalpy - composition plot for the ternary V-Ti-Cr system indicate the stability of the solid solution phase for V - (4-10)Ti - (4-5)Cr composition range, which is also in agreement with the atomic size variation which is well within the 12% size variation limit. An alloy with a composition of V - 4Ti - 4Cr has been considered as the reference composition for the present study and has been prepared by melting the highly pure V, Ti and Cr in a water cooled vaccum arc melting unit.

For initial phase identification, X-ray diffraction studies have been carried out which confirm the structure is
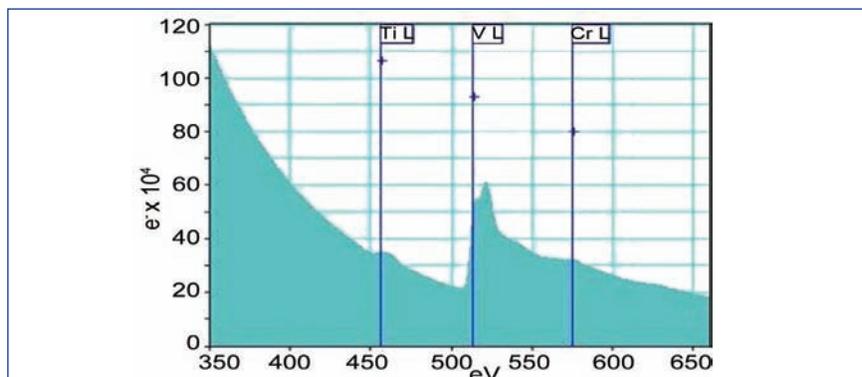
Fig. 1 *EELS spectra from a portion of the V-4Ti-4Cr alloy*

of BCC type. The lattice parameter of the alloy has been determined as 3.0356 Å from the Nelson-Riley method. Micro-chemical characterization of the alloy has been attempted through electron energy loss studies (EELS) and is shown in Figure 1. For elemental quantification, power law method has been adopted for the background correction and the quantification results are in accordance with the alloy composition. The relative quantification for V, Ti and Cr have been determined as 91.36 wt%, 4.14 wt% and 4.50 wt% respectively.

For detailed structural information high resolution transmission electron microscope (HRTEM) studies have been performed and one typical phase contrast micrograph from a portion of the

specimen is shown in Figure 2. Power spectrum confirms that the micrograph is of [001] type of zone axis pattern. For further confirmation, the phase contrast image simulation has been carried out for pure V through the multislice method, as shown in Figure 3. The positions of the atomic columns and the channels have been shown in the image.

From the present studies it is concluded that solid solution phase is the stable phase for V-4Ti-4Cr alloy. No oxide impurities has been detected through EELS. Comparison between the experimental phase contrast image with that of the simulated thickness-defocus map confirms 14% increase in the lattice spacing from that of pure body centered cubic vanadium.
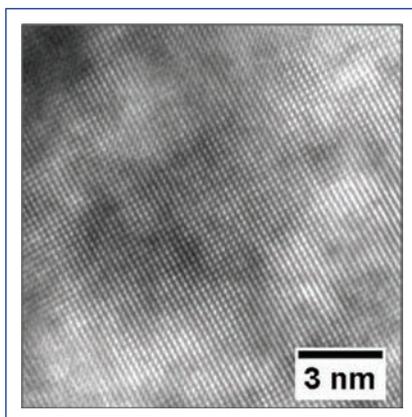
Fig. 2 *Phase contrast micrograph for a portion of the alloy showing the lattice fringes along [001] ZA*
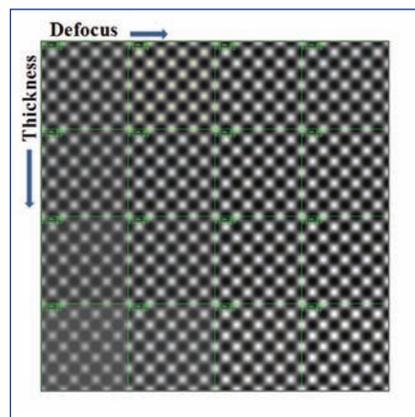
Fig. 3 *Phase contrast simulated image showing the thickness – defocus map for pure V*

V.28   Atomic Scale Study of Annealing Effects in Eurofer-97

Eurofer-97 alloy is a ferritic martensitic steel mainly consisting of Fe and Cr (9%) used as structural material in fission and fusion reactors. This reference material can withstand high neutron fluence under temperature and coolant conditions required in a fusion reactor based on magnetic confinement of plasma.

These alloys after homogenization are subjected to final heat treatment in terms of normalization (annealing at 900 °C) followed by tempering (760 °C). It is important to understand the changes in microstructure of these alloys due to heat treatments at elevated temperatures. This study is motivated to look at atomic scale the changes if any in the local structure and magnetic properties of Eurofer alloy subjected to annealing treatments in a controlled manner using Mössbauer spectroscopy.

Mössbauer spectra obtained in the sample subsequent to Normalized and tempered (N&T) condition and after annealing treatment at different temperatures are shown in Figure 1. Mössbauer spectrum in the N&T condition of the sample could be de convoluted in to three six line patterns with the values of hyperfine fields close to 33 Tesla characteristic of α-Fe. Thus the observed six lined pattern of the Mössbauer spectrum in as N&T condition shows the ferromagnetic ordering and hence is consistent with the ferritic nature of the Eurofer sample. Annealing at 1000 °C results in an appearance of a singlet along with a six line pattern in the Mössbauer spectrum as high as 7% of Fe atoms are associated with non-magnetic and cubic sites. Occurrence of non-magnetic and cubic sites is understood to be due to the occupation of Fe atoms
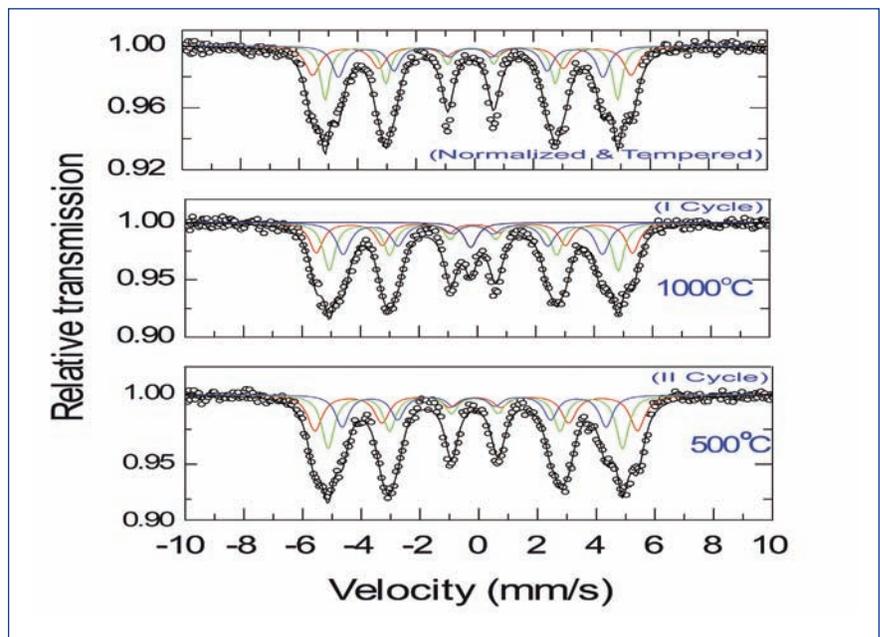
Fig. 1 *Mössbauer spectra obtained in Eurofer at 300 K subsequent to annealing treatments as mentioned*

at austenitic phase (i.e) $M_{23}C_6$ precipitates. Similar results have been reported on modified 9Cr steel using positron annihilation and acoustic studies.

Results are presented in terms of the variation of magnetic hyperfine field $<B_{hf}>$ with annealing temperature in Figure 2. In the I cycle of heat treatment there is a reduction in $<B_{hf}>$ subsequent to annealing at 1000 °C associated with 7% of Fe atoms occupying non-magnetic and cubic sites in the matrix attributed to the formation of $M_{23}C_6$ precipitates. In the II cycle beyond 500 °C there is an increase in the value of $<B_{hf}>$ which is due to disappearance of a singlet with all the Fe atoms associated with the ferritic matrix. This is understood to be due to dissociation of the fine $M_{23}C_6$ precipitates following the annealing beyond 650 °C. Annealing beyond 700 °C there is a decrease in $<B_{hf}>$ attributed to the reformation of $M_{23}C_6$ precipitates. These precipitates are likely to have

formed at grain boundaries with the associated diffusion of carbon atoms from matrix to grain boundaries and vice versa with the above heat treatments. This study might be useful for an understanding of the annealing induced changes in local structure and magnetic properties and correlation with bulk properties in Eurofer-97.
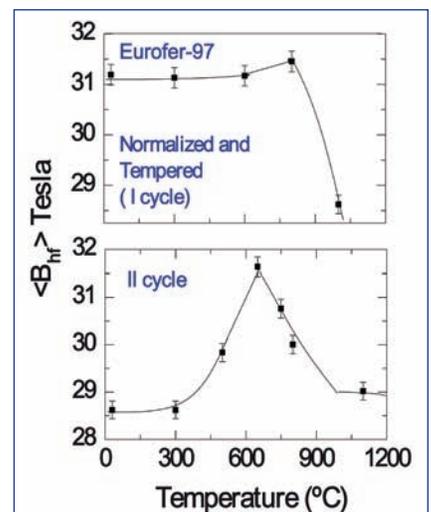
Fig. 2 *Variation of mean hyperfine field $<B_{hf}>$ with annealing temperature*

V.29 Synthesis, Characterisation and Gamma Attenuation Studies of Epoxy based Materials towards Phantom Development

In-vivo monitoring is an essential requirement of radiological safety of occupational radiation workers. Detection of inhaled fission and activation products are relatively easy because they emit high energy gamma rays (e.g. ^{137}Cs, ^{60}Co). There exists a problem with the detection of low energy photons emitting radionuclides (e.g. isotopes of U, Pu, and Am) as the photons are attenuated by tissues surrounding them. These radionuclides are prominent in nuclear fuel cycle and primarily alpha emitters with long half- life inhaled during unusual occurrences are retained in the body for long time. So, effective dose per unit intake is high.

The calibration of the whole body counting system is carried out with a realistic torso phantom to establish the response to a known amount and type of radioactive material. Presently available phantoms are either from LLNL, USA or JAERI, Japan. The LLNL phantom corresponds to the reference Caucasian adult while the JAERI is based on the reference Japanese adult. Though the Reference Adult Man of Japan is considered to represent the Asian population, there are differences in the description of Adult Indian. In view of these observations it has been proposed to develop lung phantom corresponding to reference Indian adult. Polyurethane foam (for soft tissues) and Epoxy resin (for hard tissues) selected as base materials. Three batches of epoxy resin based materials have been synthesized in our Centre towards phantom development. Based on

Table 1: Elemental compositions for all batches of synthesized epoxy resin system

	%N	%C	%H	%O
Mean (%)	3.56	68.72	10.23	17.49
Std. Dev.	0.16	1.81	0.48	2.48

Table 2: Thickness and density of epoxy resin

Disc ID	Thickness	Density (g/cc)
1_2	1.16 cm	0.84
3_1	0.92 cm	1.29
3_2	0.78 cm	0.85

their elemental composition and properties. Epoxy resin Araldite CY-205 and hardener Jeffamine T-403 were selected as starting materials. Accurately measured quantities of liquid epoxy resin, hardener were poured into a reaction vessel (1000 ml) and given a short manual mix. A twin bladed rotor was passed through the central stirrer gland and connected to the variable speed electric stirrer. The components were then thoroughly mixed for 30 minutes by ensuring that the blades of the rotor were deep in the fluid. After 30 minutes the mixture poured into moulds. The samples were left at room temperature for 15-20 hours to complete the hardening process. The synthesized materials have been characterized for its elemental composition, thermal stability, density and types of functional groups present in the final product using different characterization methods. Elemental compositions of all sets are given in the Table 1. The densities of all the epoxy material sets were determined to be in the range (0.84 -1.29 g/cm^3). Their thermal stability was found to be 300°C.

To know the attenuation properties of the synthesized materials, gamma attenuation studies have been carried out. For these studies, three discs from the batches were used.

Table 2 shows their dimensions. In order to understand the gamma attenuation behavior below 100 keV, ^{133}Ba and ^{241}Am sources were used and the measurements were obtained using planar HPGe detector. ^{152}Eu source was used for studying the gamma attenuation behavior above 100 keV, and the measurements were taken using coaxial HPGe detector. The source was kept over a lead disc of 12 mm thickness and having 1.6 mm hole drilled in the center. The lead disc with the hole in the center was used to get unidirectional beam from the source. A setup was arranged to place the samples in fixed location. In this arrangement fixed gap is available between source position and detector. At first the counts due to ^{133}Ba, ^{241}Am and ^{152}Eu sources were measured by keeping the sources at 45 mm above detector surface. Later the sample was introduced between the source and detector surface and the measurements were taken. Reduction in counts was observed due to the sample. From the reduction pattern (at low energy < 100 keV), it is observed there is a reduction in counts from 5 % to 26% depending upon energy and thickness of the samples (Figure 1a). At higher energies (>100 keV) the measured attenuation (5% to 22%) is due to energy, thickness and density of the

sample (Figure 1b).

Attenuation properties of any body tissue depend upon its elemental composition and density. The elemental composition and density of the synthesized materials are different from actual lung tissue hence difference in attenuation properties. Steps are being taken to achieve similar elemental composition and density by introducing proper additives and foaming agents during synthesis.
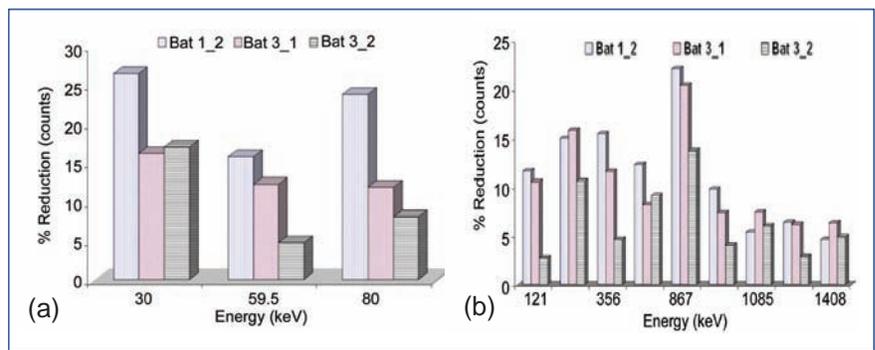
Fig. 1 *Gamma attenuation in terms of % reduction in counts at (a) low energy and (b) high energy (Bat 1_2 is 1st batch second sample, Bat 3_1, Bat 3_2 are 3rd batch first and second samples)*

V.30 EURODOS Intercomparison Exercise on Monte Carlo Modeling of Skull Phantom

Recently whole body counting facility participated in an international validation exercise i.e., EURODOS. As a part of inter comparison exercise on Monte Carlo modeling for the in vivo monitoring of ^{241}Am in skull phantom, conducted by faculty of Nuclear Science and Physical Engineering, Czech Technical University in Prague, a study on "how close the Monte Carlo simulation is to real measurement for real geometry in skull measurement of ^{241}Am" was made. ^{241}Am is a bone seeker and skull accounts for 33 % of the total bone content of the body.

VOXEL phantoms

As a part of this exercise, three VOXEL phantoms representing three different skull phantoms were received in the form of MRI images. The skull phantoms are (1) Candu Senior Republic (CSR), (2) Bone Phantom Americium (BPAM) and (3) Buendesamt Fur Strahlenschutz (BFS). Information pertaining to the location of a particular material in the phantom was extracted from these images and converted into input file for Monte Carlo N-particle code simulation using an in-house FORTRAN program.

The CSR phantom was made up of plaster and polyurethane with surface distribution of the ^{241}Am activity. The BFS phantom is a human skull having uniform distribution of 2.4 kBq ^{241}Am on inner surface and 3.0 kBq on outer bone surface (Figure 1). The skull cavity is filled with tissue-equivalent wax in the form of small spheroids and the outside of the skull is covered with tissue-equivalent wax.

The skull phantom consists of one-half (bilateral slice) ^{241}Am contaminated bones on the left side, and one-half blank, un-contaminated bone on the right side. The activity of the complete skull is 621 ± 8 Bq. The skull is casted in ICRU muscle equivalent tissue.

Monte Carlo simulation tasks

A total of three tasks pertaining to modeling of given skull phantoms with specified HPGe detectors of different configuration and also in different measurement geometry have been executed. In the entire exercise ^{241}Am spectrum has to be generated with the energies and the yield factors provided by the organiser. Whole body counting

facility used Monte Carlo N-particle code for simulation in this exercise. From the simulated spectrum, the detection efficiency values were estimated for 59.4 keV peak.

Task-1: This task is a simple one, where all the input parameters needed for simulation were well defined, complete detector configuration was provided. Based on that the given planar HPGe detector was modeled over the top of the CSR phantom and ^{241}Am spectrum was simulated. The simulated spectrum matched very well with measurement of the evaluator as shown in Figure 2. The simulated efficiency value 4.89×10^{-3} cps/Bq is closely matching with geometric mean value $(4.936 \times 10^{-3}$ cps/Bq$)$ of the simulated efficiency values reported by all participants.
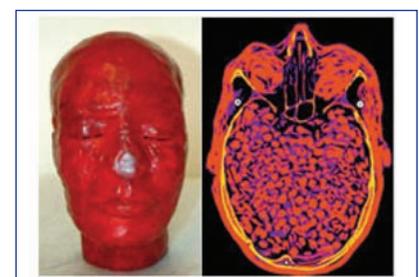
Fig. 1 *Physical BFS phantom with a MRI image slice*

Task-2: In this task, a coaxial HPGe detector model and type only was provided along with detector dimension details. In order to valid the participant's detector modeling, the organizer provided a measured ^{241}Am spectrum obtained for point source geometry with actual detector. Many of other detector configuration details required for modeling the detector were collected from detector data sheet and then the detector is modeled. First, ^{241}Am spectrum for the point source geometry was simulated. The simulated spectrum matched very well with measured spectrum given by organizer validating our detector modeling. After this validation, we proceeded with the phantom measurement simulation. This part had sub tasks of modeling the three phantoms in different counting geometry.

(1) The detector is placed over the CSR phantom in a geometry same as in Task -1

(2) The detector was positioned infront of the forehead of Bfs phantom (Figure 3)

(3) The detector placed over the BPAM phantom.

Task-3: As per third task participant has to optimise the number of detectors and geometry for better efficiency and also the geomety should be practically applicable to routine monitoring. Four HPGe detectors one on the top, one on each left, & right side and one on the back of the BFS phantom were placed and simulation done

Table 1 gives all the simulated efficiency factors obtained in this exercise.

Phoswich detector simulation

Since, suitable calibration phantom for skull measurement of ^{241}Am is not available, whole body counting facility Phoswich system is not having calibration factors for bone measurements. The Phoswich detector along with CSR & BFS virtual phantoms was modeled and efficiency factors were simulated. The simulated spectrum of Phoswich detector along with planar HPGe detector spectrum is shown in Figure 4. The simulated efficiency factors of Phoswich HPGe detectors described in this exercise were compared.

Results and discussion

A total of 16 laboratories took part in the exercise. So far only the Task-1 results were evaluated by the organizer.

The actual measured efficiency factor for Task-1 is 5.5×10^{-3} cps/Bq. The simulated efficiency factor by WBCF, IGCAR is 4.89×10^{-3} cps/Bq. The geometric mean of efficiency values reported by all participants is 4.93×10^{-3} cps/Bq. IGCAR simulated values is less by 11% compared with actual measured value. But within 1% of participant's geometric mean value. The deviation in simulated values by participants may be due to the

Table 1: Simulated efficiency factors			
Task	Phantom	Detector	Efficiency (CPS/Bq)
1	CSR	Planar HPGe	4.89e-03
1	CSR	Phoswich	4.10e-02
1	BFS	Phoswich	3.05e-02
2	CSR	LOAX HPGe	8.55e-03
2	BFS	LOAX HPGe	4.66e-03
2	BPAM	LOAX HPGe	4.68e-03
3	BFS	4 LOAX HPGe	2.80e-02

difference between reality and parameters used in simulation. This can be only be verified with repeated measurements.

Simulation of IGCAR Phoswich detector with CSR & BFS phantom showed that the efficiency factor obtained for Phoswich system (Table 1) is one order higher than that of HPGe detectors. Phoswich simulation helped in establishing calibration factors for measuring ^{241}Am in skull.

The results of this exercise has given us confidence in Monte Carlo N-particle code simulation of skull voxel phantoms for ^{241}Am measurements using HPGe/ Phoswich detectors. In addition to this, Whole body counting facility could establish calibration factor for Phoswich system for the measurement of ^{241}Am in skull without any physical phantom.
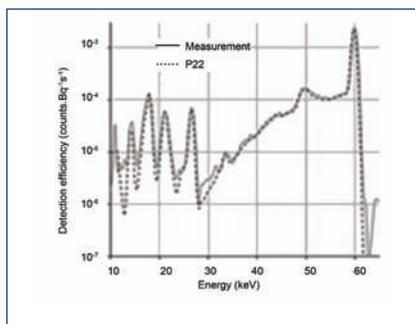
Fig. 2 *Comparison of simulated and organizer measured spectrum of task 1*
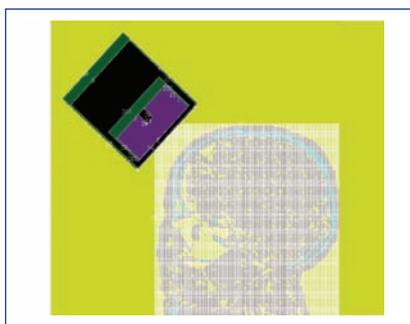
Fig. 3 *Counting geometry for task-2 BFS phantom*
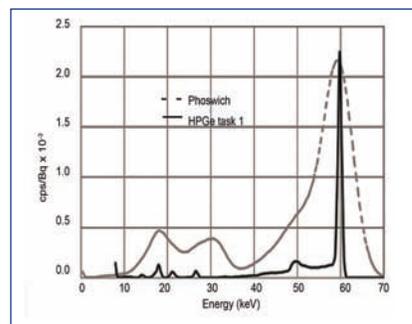
Fig. 4 *Comparison of simulated spectrum (CSR phantom) of Phoswich and planar HPGe*
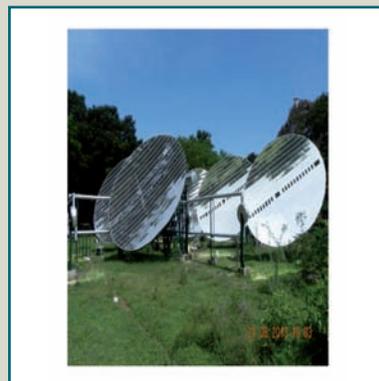
CHAPTER 6

Infrastructure and Facilities

VI.1 Commissioning of High Temperature Mass Spectrometer inside Glove Box and Studies on U-Ga Alloys

A high temperature quadrupole mass spectrometer (HTQMS) has been setup on the floor of a glove box with a view to conduct vaporization studies on radioactive and air sensitive samples. (Figure 1) In this set up, the samples were contained in a small crucible called, Knudsen cell and the cell was heated by electron bombardment. The vapour molecules produced are effused through a tiny orifice (diameter of about 0.5 mm). Ionisation of the vapour was effected by electrons emitted from an oxide coated iridium filament and the mass analysis was carried out by a quadrupole analyser. The ion currents were measured by pulse counting method. A pneumatically operated shutter imposed between the Knudsen cell chamber and the ion source helps to differentiate whether the ions detected emanate from the Knudsen cell or due to ionization of background molecules. The temperature of the Knudsen cell was measured by a disappearing filament pyrometer focused onto a black body hole provided at the bottom of the cell.

There have been few problems which were hindering the objective of commissioning this facility inside argon atmosphere glove box that would permit vaporisation studies on radioactive samples: (i) space constraint between the front panel of glove box and a linear motion drive used for shutter operation, making it impossible to remove/replace the drive during maintenance. This was overcome by providing a suitable port in the glove box panel and a special adapter with modified

Fig. 1 *High temperature quadrupole mass spectrometer inside glove box*

dimensions for the port. (ii) the electron bombardment furnace assembly is lowered into a 50 cm pit inside the glove box during sample change operations and it was very difficult to lift the heavy furnace and place it on the glove box floor for any furnace related maintenance work. Suitable modifications were made to facilitate this operation. Few more modifications and all the required mechanical and electrical work relating to installation of flow meter, oxygen sensor, spot welding apparatus, normal supply, exhaust and emergency exhaust lines were completed. Subsequently, the glove box was closed, leak testing was carried out and the leak rate was brought down to desired levels both in positive and negative pressure modes.

Before taking up vaporization studies on radioactive samples using this facility, studies on uranium-gallium system was taken up to get familiarised with various mass spectrometric operations with glove box completely closed. Thermodynamic properties of these

alloys are essential from the point of view of molten salt reprocessing for recovery of uranium from spent fuel. The recovery is carried out by equilibrating the spent fuel with Ca-Ga mixture whereby actinide-gallium compounds are formed. A knowledge of vaporization behavior of these compounds is required for a better understanding of the stabilities of these compounds. For mass spectrometric studies, samples belonging to the biphasic region (U_2Ga_3+UGa_2) were used. Ga^+ was the ion produced in the mass spectra of equilibrium vapour and the corresponding neutral species was ascertained to be Ga(g). The apparent enthalpy of vaporization of Ga(g) over (U_2Ga_3+UGa_2) was derived from the slopes of log(I^+(Ga)·T vs. 1/T plot and the mean of slopes obtained from six runs is given as (at T= 1239 K): (356.1±6.2) kJ/mol. From the partial pressures derived, a combined pressure-temperature relation was obtained by least squares fitting of all the points (81 data) from the individual runs.

VI.2 Design and development of SQUID based Vibrating Sample Magnetometer (SQUID VSM)

A SQUID based vibrating sample magnetometer (SQUID VSM) has been developed at IGCAR which combines the high sensitivity offered by the SQUID with the high speed of measurement offered by the conventional VSM. SQUID magnetometer capable of measuring magnetization of materials in the temperature range 4.2 - 300 K and at high magnetic fields upto 7 Tesla was developed earlier at IGCAR using a home built SQUID sensor and its associated readout electronics. The SQUID magnetometer offers considerably higher sensitivity compared to any other magnetometers such as vibrating sample magnetometer (VSM) and alternating field gradient magnetometer (AFGM). In spite of its high sensitivity, however, the speed of measurement is very slow since a full flux profile has to be recorded at each value of temperature (T) and magnetic field (H); this is considered as a major disadvantage of the SQUID magnetometer. In order to enhance the measurement speed, the existing SQUID magnetometer has now been modified into SQUID VSM using a home built sample vibrator unit. In addition to enhancing the measurement speed, the SQUID VSM enables higher system sensitivity to be attained by the use of phase sensitive detection techniques using a lock-in-amplifier referenced at vibration frequency for measuring the SQUID output, which suppresses incoherent noise.

Figure 1 illustrates the working principle of the SQUID magnetometer as well as SQUID VSM. The main components of the SQUID magnetometer are the SQUID sensor and its associated room temperature flux locked
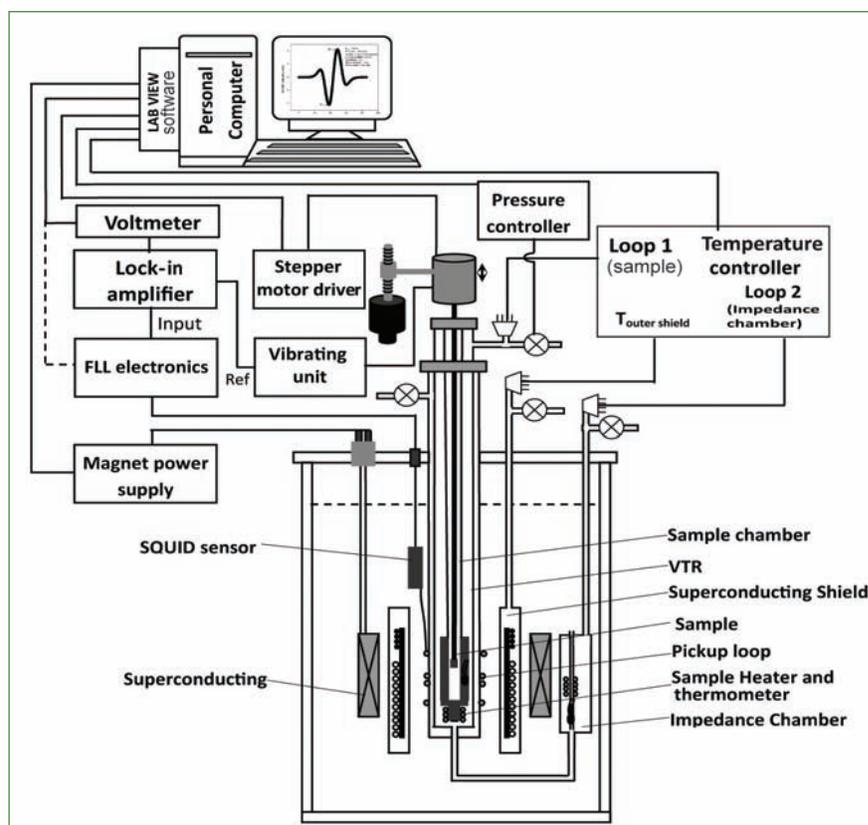
Fig. 1 *Schematic diagram of the SQUID based vibrating sample magnetometer*

loop (FLL) readout electronics, superconducting pickup loop in the form of an axial wire-wound gradiometer which is inductively coupled to the SQUID, variable temperature regulator (VTR) to set the sample temperature to the desired value and hold it constant, a superconducting magnet to produce a uniform magnetic field, superconducting shields to trap a stable magnetic field in the vicinity of the sample and thus provide a relatively quiet magnetic environment around the sample, and a stepper motor driven sample transport assembly to move the sample slowly across the superconducting pick up loop. In the SQUID based VSM there is an additional sample vibrator unit to vibrate the sample at fixed frequency and fixed amplitude.

The conventional SQUID

magnetometer operates by moving the sample slowly across the pick up loop in order to record the flux profile without any sample vibration. Whenever there is a change of magnetic field gradient in the vicinity of the pickup loop, screening current is induced in the pickup loop which is inductively coupled to the SQUID. The SQUID, in conjunction with the flux locked loop electronics, gives rise to a measurable change in the output voltage, which is proportional to the change of magnetic field gradient in the vicinity of the pickup loop. In this way, if the magnetic moment of the sample changes with temperature, there is a change of field gradient in the vicinity of the pickup loop, which is detected by the SQUID. The SQUID output voltage is recorded with respect to the positional coordinates of the specimen and the magnetic
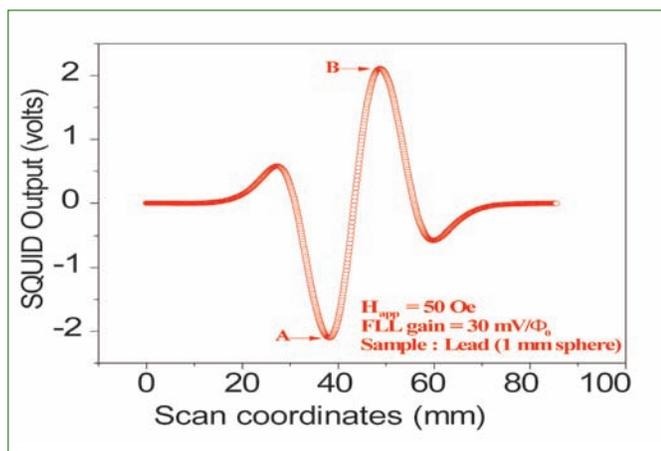
Fig. 2 *SQUID output as the sample is moved slowly across the pickup loop, while vibrating with a fixed frequency of 20.3 Hz and a fixed amplitude of 1 mm*
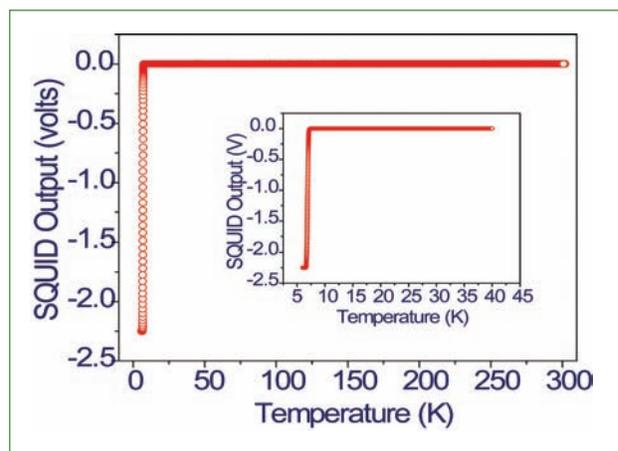
Fig. 3 *Superconducting transition of the lead sphere. (The inset shows the closer view of the transition)*

moment is subsequently derived from this measured flux profile. Measurements over an extended range of temperature and magnetic field tend to be slow since a full flux profile has to be recorded at each value of temperature and field.

In the case of SQUID VSM, the sample is vibrated with a fixed vibration frequency of 20.3 Hz and a fixed amplitude of about 1 mm. The home built sample vibrator incorporates electronic feedback circuits to maintain the amplitude of vibration constant. Initially, the vibrating sample is slowly moved across the superconducting gradiometer only once to identify the location of the sample where the output of the SQUID VSM is maximum. Subsequently, the sample is located at this position where the sensitivity is maximum and the temperature of the sample is swept at a rate of 1 K/min to 3 K/min as desired by the user using a temperature controller. The SQUID output is fed to the lock-in amplifier and is phase sensitively detected with respect to the reference frequency of the sample vibration. The lock-in amplifier output, which is proportional to the magnetization of the sample, is measured as a function of temperature of the sample. SQUID VSM increases the measurement speed significantly since a full flux

profile is not recorded at each value of temperature and magnetic field. If the magnetization of the sample is desired to be measured over the temperature interval of 5 to 300 K with a temperature increment of 1 K, the conventional SQUID magnetometer may take more than a day to complete the measurement. In contrast, this measurement can be completed in less than a couple of hours using a SQUID based VSM.

For testing the SQUID VSM, a lead sphere was loaded as a sample and its temperature was maintained below its superconducting transition temperature. The lead sphere was moved slowly across the pickup loop while vibrating at a fixed frequency of 20.3 Hz and a fixed amplitude of 1 mm. This initial scan serves to identify the location of the sample where the output of the SQUID VSM is maximum. Subsequently the sample is located at the fixed position where the sensitivity is maximum (either at A or at B in Figure 2) and sample temperature is swept across the desired range, while the sample vibrates around the fixed position. The output of the SQUID sensor is phase sensitively detected using a lock-in-amplifier. Figure 3 shows the variation of the lock-in-amplifier output as a function of temperature of the lead sphere. As the temperature of the sample is increased,

SQUID VSM output shows a step change at the superconducting transition temperature (T_c), reflecting the Meissner effect in the superconducting state. Above T_c, the change of magnetization in the normal state is extremely small with further increase in temperature. These measurements also confirm the fact that the vibration amplitude of the sample is indeed constant when the temperature of the sample varies from 5 K to 300 K; it may be noted that this is an important requirement while designing the vibrator unit during the construction of SQUID based VSM. Figure 4 shows the photograph of the SQUID based VSM developed at IGCAR. Successful development of SQUID VSM at IGCAR augurs well for the design and development of other SQUID based measuring systems in future.

Fig. 4 *Photograph of the SQUID based VSM*

VI.3 Characterization of cMUT MEMS Devices using Nano Vibration Analyzer

MEMS(microelectromechanical systems) based capacitive micro-machined ultrasonic transducers (cMUT) are the devices used to transmit and receive ultrasonic waves in air and have potential to be an alternative to piezo transducers. It is a device with two plate-like electrodes of a capacitor, in micron dimensions, fabricated though standard IC fabrication process. During operation it is biased with a DC voltage and simultaneously driven with an AC signal to vibrate one of the plates. It can be used as both as ultrasonic transmitter (electrostatic force is responsible for vibration in membrane to transmit the waves in surrounding medium) and as receiver (deflection of membrane due to pressure of ultrasonic waves, resulting in capacitance change). At IGCAR, these devices are being fabricated, in collaboration with IISc, Bengaluru and CEERI, Pilani, for reactor safety vessel in-service inspection. The fabricated devices are characterized for their dynamic response using nano vibration analyzer (NVA) and are discussed here.

Figures 1a and 1b shows the block diagram and photograph of the experimental setup used for the dynamic characterization of the cMUT devices using nano vibration analyzer, respectively. The wafer containing cMUT devices is placed on X-Y stage (Figure 1c). Two tungsten microprobes, monitored through another USB camera, were used to apply the biasing voltage to the cMUT under characterization. This was done by precisely placing the tungsten tips on contact pads
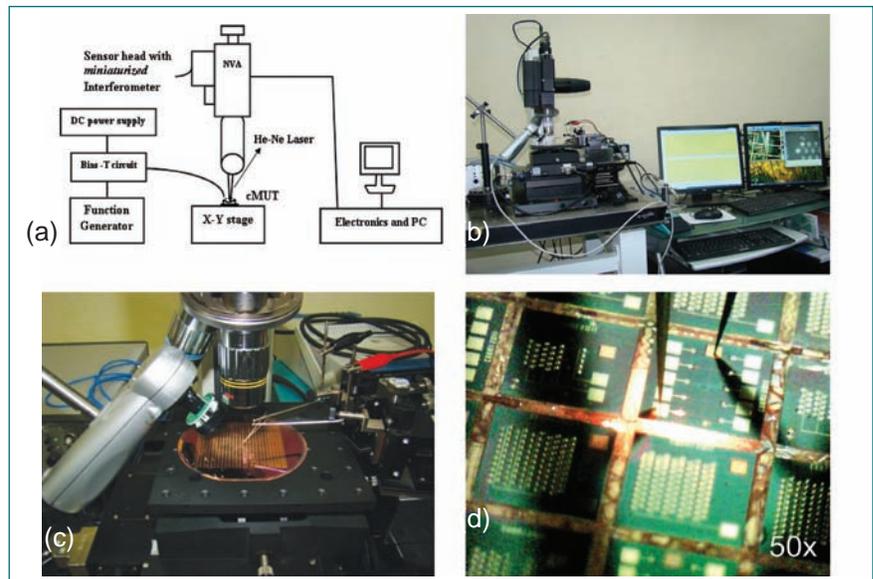
Fig. 1 *(a) Block diagram, (b) photograph of the experimental setup used to measure the natural frequency of the cMUT cells using nano vibration analyzer, (c) Two tungsten microtips, monitored by another USB camera, were used to apply the biasing voltage and AC signal to the cMUT under characterization and (d) Magnified view of the wafer containing the cMUT cells*

of the device (Figure 1d). AC signal was applied using a function generator and a high voltage power supply was used to provide the DC biasing. To estimate the natural frequency of the cMUT cell, the function generator frequency was varied in steps and amplitude of vibration was recorded using nano vibration analyzer at each frequency. From the frequency versus amplitude plot resonant frequency and Q-factor of the device is estimated.

A typical frequency response of a cMUT cell is shown Figure 2a. The applied voltage is 100V DC and 4V AC. From this plot, cMUT natural frequency and Q-factor is estimated to be 1.54 MHz and 32 respectively. Also, a typical response of an array of 1x5 cells is shown in Figure 2b. Similar measurements were carried out on several cMUT cells on the wafer. These devices are being diced and packaged for further characterization.
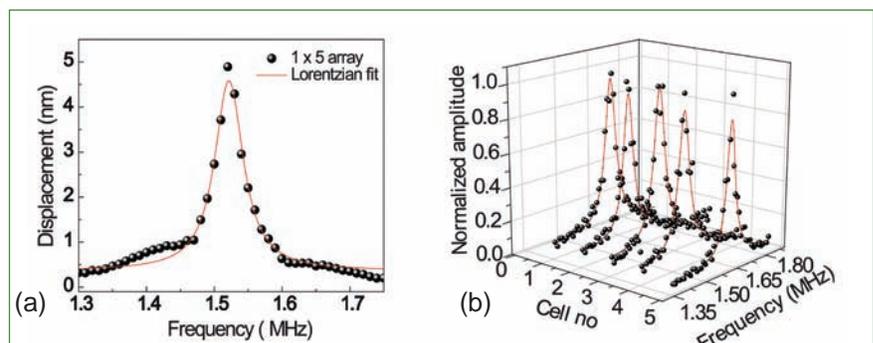
Fig. 2 *Frequency spectrum of (a) single cMUT cell and (b) 1x5 array measured using the setup shown in Figure 1. Resonance frequency of the cells is ~1.5 MHz with a Q-factor of ~28*

VI.4 Design Simulation of Semiconductor Neutron Detector

Semiconductor neutron detectors have advantages over the conventional helium-3 gas based detectors due to their insensitivity to microphonics, smaller size and low power requirements. These detectors are generally fabricated in a planar configuration by coating a layer of neutron-to alpha converter material (^{10}B, ^6LiF) onto a semiconductor PIN diode (Figure 1a). The charge particles created in the converter material impinge on the PIN diode and create electron-hole pairs which provide the electrical signal. However, the neutron detection efficiency of the planar configuration devices is < 5%, because of the conflicting thickness requirements of the converter layer. To increase the efficiency, 3D neutron detectors are being configured (Figure 1b). The basic configuration of the 3D detector consists of a common PIN diode, which is micro structured and then back filled with ^{10}B. These detectors are to be fabricated through a collaborative project between IGCAR and CeNSE, IISc.

Ahead of any device fabrication there is a need for modeling and simulation to predict the device performance. In particular, for a semiconductor neutron detector design, modeling is required to study the ion energy deposition and predict the intrinsic thermal-neutron detection efficiency. Monte Carlo simulation can be used to estimate these parameters with proper particle tracking and ion energy-deposition functions. In the present work, 3D and planar neutron detector efficiency calculations are carried out using Monte Carlo simulation method based on the Shultis-McGregor methodology.
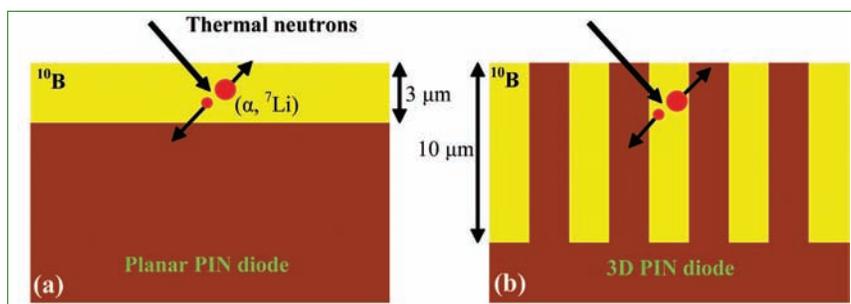
Fig. 1 *(a) Planar semiconductor neutron detector with ^{10}B as converter material. The impinging neutrons undergo reaction with ^{10}B and produce charged particles. In this configuration, only one of the charged particle gets detected and (b) 3D configuration of the neutron detector, where micro trenches are created in PIN diode, and filled with ^{10}B. The increased efficiency of the 3D detectors is due to the fact that both charged particles, deposit their energy in PIN diode*

In this method, the detector is represented by a unit cell, which when replicated in space, will form the entire detector. A parallel neutron beam, perpendicular to the detector face, is assumed to uniformly illuminate the face of the unit cell. Reaction ions produced in the unit cell are tracked through the cell and the energy deposited in Si and ^{10}B are estimated. The fraction of neutrons incident on the unit cell that lead to the deposition of energy in the silicon above some lower level discriminator (LLD) setting, yields the detector efficiency. Figure 2a shows the variation in detector efficiency with $^{10}B/Si$ width ratio in a trench cell of 4 µm wide. The trench depth is 10 µm and lower level discriminator

is 300 KeV. From this figure it is clear that when ^{10}B width is about 70% of the unit cell, the efficiency is maximum. Now, the simulation is repeated for planar diode configuration which is achieved by setting the ^{10}B /Si width ratio in the unit cell to one. Figure 2b shows the variation of efficiency of a planar diode with ^{10}B thickness. Although efficiency increases initially with increasing ^{10}B thickness, it reaches a maximum at ~3 µm and thereafter it decreases. Further simulation on the efficiencies of different 3D microstructure design parameters and possibility of enhancing the efficiency in planar configuration are being carried out.
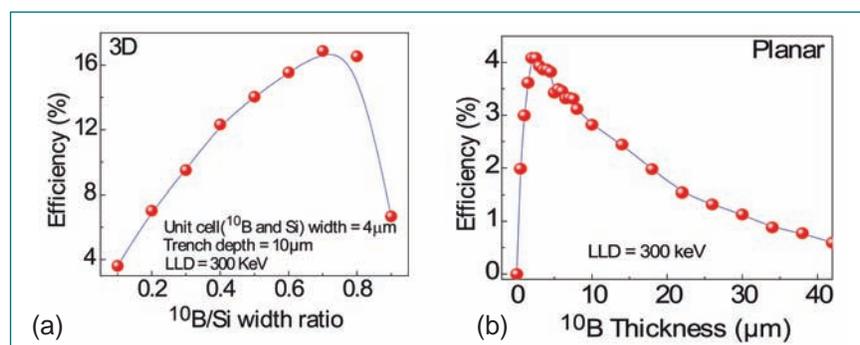
Fig. 2 *(a) Variation of neutron detector efficiency with $^{10}B/Si$ width ratio in a unit cell of 3D trench (depth = 10 µm) structure and (b) Efficiency of a planar diode with ^{10}B thickness. For both the cases LLD = 300 KeV*

VI.5 Development of Thin Film Plastic Scintillators for Radiation Detection

Plastic scintillator consists of a solid solution of organic scintillating molecules in a polymerized solvent. They have wide ranging applications in the field of radiation detection and measurements. Generally a base monomer along with the scintillator and wave length shifter (organic molecules) is polymerized and molded in to required shape and size. This is a very delicate process and requires specialized systems.

A simple method for preparing thin film plastic scintillators was developed. Polystyrene (AR grade) beads were dissolved in xylene (AR grade) along with PPO and POPOP (Scintillation grade). Well dissolved mixture was coated on transparent cellulose acetate sheets to have various wet thicknesses (120 to 960 μm) of scintillating medium using thin film wire coaters. The coating was allowed to dry in room temperature. After the drying process thickness of the coating was measured at several places using standard micrometers to ensure the uniformity of coating.

The scintillator was coupled to the standard PM tube assembly and counting system and the detection efficiency of the scintillator was measured for various β-sources. Light absorption and emission characteristics of the scintillators were studied using

Fig. 1 *Efficiency for β - sources with thickness*

standard fluorimeter setup. Radio luminescence of the scintillators was also studied in the fluorimeter using ^{90}Sr-^{90}Y β-source. Table 1 shows the measured dry film thickness obtained for different wet film thicknesses. The reduction in film thickness is due to the evaporation of the solvent used. Figure 1 shows variation in efficiency for different β-energy sources with respect to increasing film thickness.

It was observed that 720 μm wet film thickness (176 ± 22 μm dry film thickness) yields acceptable efficiencies for beta sources. The measured efficiencies were in the range of 75 to 95 % of that of commercial 250 μm thick plastic scintillator (Eljen make PVT based plastic scintillator). Photo luminescence emission

spectrum of prepared films showed an intense emission peak at 420 nm which is very much similar to that of commercial PVT based scintillator. Figure 2 shows the radioluminescence (smoothened by 10 point moving average) observed in the prepared and commercial scintillators. As observed in emission spectrum, in radio luminescence also the peak was in 420 nm. For 720 μm coating thickness the light yield was ~75 – 95% of that of commercial PVT based plastic scintillator whereas the same was 65 to 85% for 960 μm coating thickness. Test results of the prepared scintillators are encouraging and further efforts are on to increase light yield by optimizing the weight percentage of each constituent.

Table 1: Measured dry film thickness obtained for different wet film thicknesses			
Wet thickness (μm)	Trials	Dry thickness (μm)	Ratio
240	3	69 ± 6	3.54
480	3	127 ± 18	4.02
720	4	176 ± 22	4.16
960	4	234 ± 35	4.24
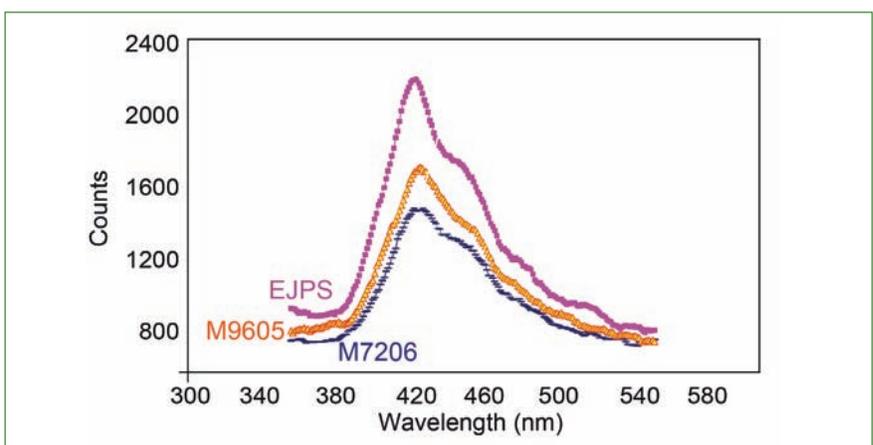
Fig. 2 *Radio luminescence observed in plastic scintillators*

VI.6 Development of Indigenous BF$_3$ based Passive Waste-Drum Assay System

Assay of waste drums to quantify the plutonium content in alpha bearing wastes is mandatory before transferring the waste to waste management facilities. A BF$_3$ based system for assay of plutonium by passive neutron detection has been developed with the co-ordinated efforts of radioactive facilities in IGCAR and ECIL. The system was commissioned in Radio Metallurgy Laboratory (RML). It is an indigenous alternative to the imported ^{3}He based waste assay system available in IGCAR.

The system consists of sixteen BF$_3$ detectors arranged in a circular geometry with associated nuclear electronics (Figure 1). The design of assay system was done jointly by IGCAR and ECIL, Hyderabad and was manufactured by ECIL.

Each detector is a BF$_3$ based proportional counter (90% ^{10}B) with 1000 mm length and 50 mm diameter. Detectors are filled with BF$_3$ gas at a pressure of 600 torr and have a sensitivity of 100 cps/nv. High density polyethylene is used as the moderating medium to improve the detection efficiency of neutrons generated by the spontaneous fission of actinides. The assay system is designed to accommodate a standard drum of 600 mm diameter and 900 mm height. A separate drum holding trolley with castor wheels is provided to move the drum, to and from the assay system.

Nuclear electronics for the sixteen channel BF$_3$ detectors consists of a pre-amplifier, shaping amplifier and TTL convertor. Low voltage and high voltage power supplies are provided respectively to the pre-amplifier and the detector. The BF$_3$ sensors generate TTL pulses proportional to number of neutrons received and are fed to the microcontroller module for processing. The microcontroller is interfaced with a computer through RS232 communication which responds to control commands from the user interface. After data acquisition and processing, the microcontroller sends the results to the computer for further analysis and storage.

Individual detectors were tested using a Am-Be neutron source for determining the voltage plateau and operating voltage. Each detector was tested at bias voltages in the range 500 mV to 3V to fix the threshold bias voltage to obtain maximum signal to noise ratio. It was found that the optimum operating voltage and the bias voltage are 2075 V and 1.5 V respectively.

Active wastes usually contain strong gamma emitters. In order to test the gamma tolerance of the BF$_3$ detectors, individual detectors were exposed to a 11.89Ci ^{60}Co source in presence of the neutron source. The distance from BF$_3$ detector to gamma source was varied to get different gamma dose rates at the detector surface. It was concluded from the tests that the count rate of the detectors does not show any significant increase until

Fig. 1 *Photograph of the waste assay system with BF$_3$ detectors*

gamma dose rate exceeds 10 R/hr (Figure 2).

The waste assay system installed at RML was subjected to various performance tests such as long term stability test and statistical tests. Performance tests on the detectors have indicated that the net counts from all the detectors (Figure 3) are in the acceptable range. The system was calibrated with a standard plutonium source. The calculated efficiency of waste assay system is 10.5% and the minimum detectable limit (MDL) is 25 mg of research reactor grade Pu which has less ^{240}Pu content. These values are comparable with that of the ^{3}He based system.

Waste drums assayed in the BF$_3$ based system were also assayed in ^{3}He based system for comparison. Variation in the plutonium content between the two systems was within 10%. The BF$_3$ based assay system is performing satisfactorily.
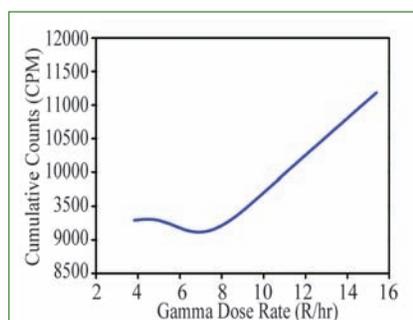
Fig. 2 *Gamma tolerance of BF$_3$ detectors*
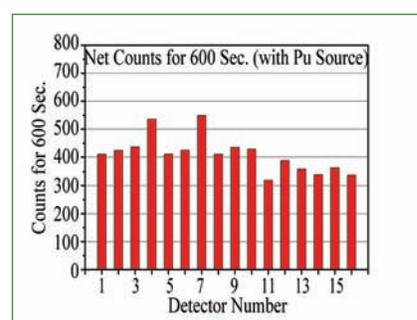
Fig. 3 *Histogram showing the response of sixteen detectors*

VI.7 Assay of Waste Drums with Alpha Containing Solid Waste for Fissile Material and Fission Products

Radioactive solid waste generated during the reprocessing of fast reactor fuels has to be assayed for alpha as well as gamma before sending to CWMF for disposal. Until now, such assay has not been carried out for solid waste generated by reprocessing plants in India. The solid waste is contained in drums of 200 liter capacity.

The spontaneous emission of neutrons (passive neutrons) by plutonium is used for assaying the plutonium in the waste drums. A complete system based on passive neutron counting technique using ^{3}He detector is being used in CORAL for quantifying plutonium. Waste drums with surface dose rates up to 20 mS/h can be assayed by this system. A similar unit with BF_3 detector has also been developed.

Gamma activity in the drums due to fission products are assayed by high resolution gamma spectrometry (HpGe). The drum is placed in the drum positioning system which consists of a drum rotating and vertical movement mechanism. The control is by a PLC with operator interface. The system is shown in Figure 1.

The detector is surrounded by lead shield and a 25 mm dia collimator is used to optimise the distance between the detector and the drum.

Distance between the detector and drum has been optimized in such a way that the detector has to see the entire width of the drum.

The drum is vertically divided into five vertical segments of 160 mm
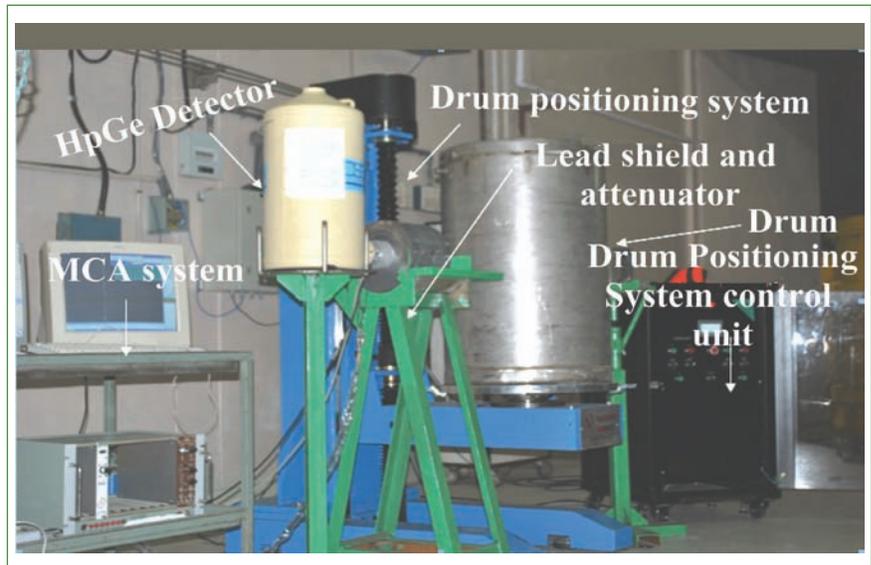
Fig. 1 *System for assay of fission products in solid waste drums*

based on calibration with ^{152}Eu source. Since the detector is seeing the entire drum horizontally (600 mm), vertically also it will see the drum for 600 mm. But the segment size is 160 mm. Hence, neighboring segment contribution has to be eliminated. In order to eliminate the effect of neighboring segments on the counts, a detailed mathematical optimization is carried out by employing an intense multi energy gamma emitting nuclide such as ^{152}Eu. The factor for each energy was obtained.

The waste present in the drums may have material of different densities and hence, the effect of densities on the attenuation of gamma ray is studied by keeping the source behind the drum. A MATLAB program has been written for this purpose. The segment and attenuation corrected counts are used for calculating the fission products. Eight spectra for every 20 mm height of the drum were taken. Average CPS corresponding

to different energies of ^{152}Eu is used for calculating the efficiency of the detector.

Fission products present in the drum is quantified in the individual segments employing segmented gamma scanning using HpGe detector after eliminating neighboring segment contribution and attenuation correction. Fission products present in the five segments are added to get the value in the entire drum. Results of the assay of one of the typical solid waste drums is given in Table 1.

Table 1: Fission products in the waste drum	
Nuclide	mCi
^{137}Cs	0.669
^{134}Cs	0.005
^{154}Eu	0.098
^{125}Sb	0.206
^{106}Ru	2.021

VI.8 Development of Microcontroller based Automatic Radioactive Sample Loading Assembly for ICP-AES in Lead Mini Cell

Analytical characterization of radioactive materials for trace and minor metallic constituents is essential. Of the conventional analytical methods, inductively coupled plasma atomic emission spectrometry (ICP-AES) is widely selected as the technique of choice to perform the analysis of radioactive materials. An automatic sample dispenser is designed and integrated with the ICP-AES instrument to facilitate the measurement of sample and blank consistently and reproducibly. (Figure 1).

To carry out the analysis of radioactive solutions particularly high-level liquid wastes, a lead mini cell facility has been commissioned. The maximum activity that can be handled in the cell is 1 curie equivalent of ^{60}Co. The cell is maintained at a pressure of -20 to -40 mm water column with respect to ambient. All the operations inside the cell will be carried out using master slave manipulators. A high resolution ICP-AES is commissioned in the lead mini cell. In this system, the sample solution to be analyzed is pumped from the mini cell to the ICP source for ionization using a peristaltic pump. In the normal operation of ICP OES, for each analysis 1 ml of active solution followed by a blank solution will be drawn into the ICP source at one minute intervals. Changing of active solution to blank solution within this short time is practically not possible with master slave manipulators. To overcome this difficulty, a new sample loading assembly and its microcontroller-based instrumentation suitable for active glove box has been designed, developed and commissioned.
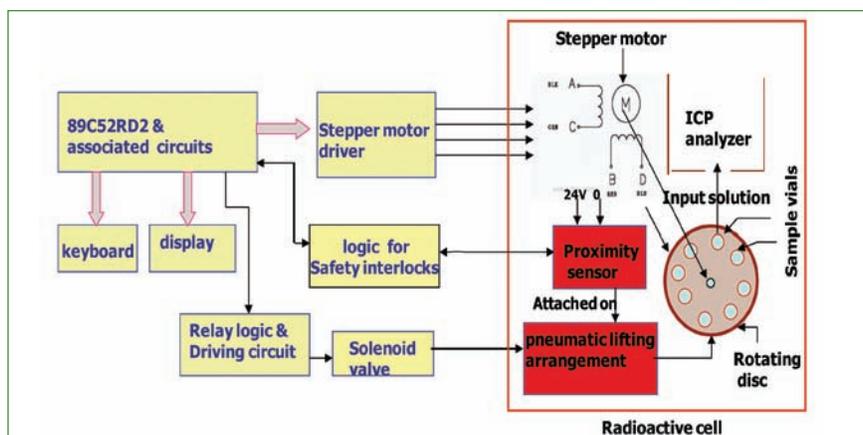
Fig. 1 *Block diagram of the system*

The sample loading assembly is a circular platform made of nylon, fabricated for holding eight sample vials. Sample and blank vials are stored alternatively in the platform. It is programmed to rotate in such a way that the selected sample vial will be aligned exactly with the ICP source first and subsequently lifted, so that; the sample solution will be drawn into ICP. The same operation is repeated for blank. The entire automatic operation is completed within a minute. The instrumentation provides controls for rotation of disc for selecting the required vials, sample lifting mechanism and safety interlocks. The instrumentation also provides four user programmable speeds with offset adjustments for fine-tuning in both forward/reverse directions from the front panel keyboard. The introduction of sample into ICP source is achieved by a pneumatic lifting mechanism. The microcontroller ensures safe operation of lifting the sample using a solenoid valve with suitable limiting conditions. Further, the system provides necessary safety interlocks to avoid any accidental falling of sample vial causing the breakage and spillage of active solutions. All the operational features are programmed and executed through a front panel keyboard and a LCD display panel. The user interactive firmware software is developed in C language and embedded in the microcontroller

The sampling unit has been installed in the lead minicell. Necessary feed through wiring for signal transmission, power supply between the sample loading assembly in the minicell and the control instrumentation (shown in Figure 2) outside the cell are implemented. The performance was evaluated by carrying out analysis of mimic vials and standard solutions. Presently the facility is being used routinely for the analysis of radioactive neptunium solution using ICP-AES.

Fig. 2 *Sample changer inside radioactive cell*

VI.9 Precision Machining and Laser Welding of Critical Components

Laser beam welding is a high energy process that offers advantages like deep and narrow weld, minimum distortion, and minimal heat affected zone. Precision machining of components enables production of defect-free laser welds. Many critical components needed in Fast Reactor Programme, which are difficult or not possible to fabricate using conventional welding techniques, have been successfully fabricated using Nd-YAG laser welding system. Some of these works are highlighted below:

Development of pressurized capsule with attachment of thermocouple

Pressurized capsules are small size capsules made of cladding tubes filled with argon at high pressure, and are used to determine the in-reactor creep behaviour of clad materials. It is proposed to identify the creep rupture in the pressurized capsules using thermocouples attached to the gas-region of the pressurized capsules (Figure 1). These joints are critical in nature since they should withstand the high temperature and the associated high pressure exerted by argon during irradiation. SS316 sheathed thermocouple of 1 mm diameter with sheath thickness of about 0.18 mm was successfully attached to the gas region of the pressurized capsule using laser welding. The welding parameters selected were such that the sheath material was not punctured and at the same time sufficient weld penetration was achieved. Pressurized capsules filled with argon at 60 bar pressure at room temperature and welded with thermocouples to the gas region were tested in an electrical

furnace at 700°C and found to be performing without any failure.

Laser welding of ultrasonic transducer housing for under sodium scanner of PFBR

In PFBR, for safe fuel handling operation, it is to be ensured that no subassemblies project above the core surface within 100 mm of plenum. Ultrasonic imaging is adopted to view the projection of subassembly heads, if any. For this purpose ultrasonic transducers (UT) operating upto 180°C in sodium are required to be developed. It is required to weld the nickel based UT housing of 0.5 mm wall thickness with a crystal mounting cap. Laser welding was adopted for this application. Weld interface of UT housing and crystal mounting cap was machined with close tolerances. The weld joint with the required leak tightness of 1×10^{-8} std. cc/s was achieved after several standardizing trials. Since the UT housing has a rectangular cross section with centre offset circular bore, a special fixture was designed and fabricated to mount the housing for welding. Ten numbers of UT housings have been successfully welded with crystal mounting caps for the transducers for use in under-sodium imaging (Figure 2).

Laser welding in extended spark plug type leak detector (ESPLD)

In PFBR, in the case of sodium leak from the main vessel, it will be
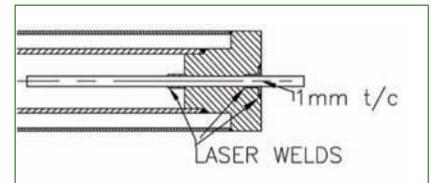
Fig. 1 *Pressurized capsule with central thermocouple*

collected in the inter-space between the main vessel (MV) and the safety vessel (SV). Extended Spark Plug type Leak Detector (ESPLD) is used as a diverse method of sodium leak detection and it is introduced in the inter-space of MV and SV. In the development of ESPLD, four critical weld joints were required to be made. Due to the small size of the sensor, laser welding was preferred. The sensor is attached to a 25m long mineral insulated (MI) cable of 1.5 mm diameter. It was essential to design and fabricate a fixture to restrict the relative movement between the MI cable and the sensor while welding, to avoid cracks. Another challenging task was to reduce the core diameter of MI cable in the region of the circumferential laser weld, from 0.8 mm to 0.6mm precisely. Using a specially designed and fabricated fixture, the MI cable was held between the head stock and the tail stock of a lathe, and uniform reduction in diameter was carried out using a diamond tool facilitating the successful circumferential laser weld. These laser welding operations enabled development of ESPLDs (Figure 3).

Fig. 2 *UT housing welded with crystal mounting caps and the weld profile*

Fig. 3 *Laser welded ESPLDs*

VI.10 Performance Evaluation of Soft PID algorithm for Automatic Control of Plugging Indicator in Bi-Metallic Sodium Loop

VME bus based real time computer (RTC) system is used for plugging indicator control of Prototype Fast Breeder Reactor. Proportional - integral - derivative (PID) algorithm is required to control the Plugging Indicator which is implemented in software and the PID parameters are kept as configurable in run time. Performance of this soft PID algorithm was evaluated by deploying the VME system in Bi-Metallic sodium (BIM) loop of FRTG for the control of plugging Indicator.

BIM loop is in operation in Engineering Hall-I, to study the carbon transfer behaviour and its influence on the mechanical properties of the materials (namely Mod. 9 Cr-1 Mo and SS 316 LN) used in the secondary sodium circuit of PFBR. This loop consists of EM pump for sodium circulation, material samples in sample holders, cold trap, plugging indicator and nickel tube sampler in the sodium purification circuit.

Plugging indicator (PI) is a device used to measure the purity of the sodium. Impurities such as sodium oxide and sodium hydride get dissolved in sodium at higher temperature. When the sodium temperature is lowered the dissolved impurities get precipitated. This principle is used for sodium purification and purity monitoring. By decreasing the temperature of sodium flowing through the plugging indicator (Figure 1), plugging of the orifices takes place due to impurities in sodium. When the sodium flow through the orifice drops to 80% of the initial flow, the temperature measured at the orifice of the plugging indicator is called as
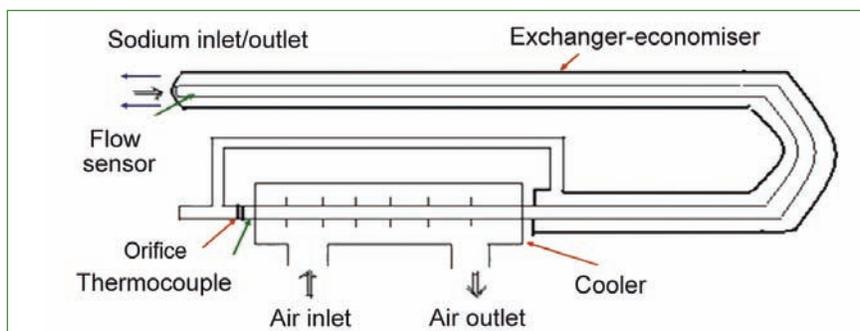
Fig. 1 *Plugging indicator*

plugging temperature which gives the indication about concentration of impurities in sodium. Figure 2 shows the block diagram of plugging indicator control system.

Plugging indicator can be operated in 'manual' or 'auto' mode. In 'manual' mode, signal for the control valve is given by the RTC system based on the value obtained from Graphical User Interface (GUI). In 'auto' mode, the plugging indicator can be operated in continuous/discontinuous mode. Mode selections are accomplished through GUI.

In the continuous mode, partial plugging of orifice corresponding to 95 lph (or set value) through PI is maintained. The nominal flow through plugging indicator is 100 lph. Speed of the blower is automatically adjusted by the RTC system so that the orifice is always kept partially plugged. If the impurity level increases/

decreases, sodium flow tends to reduce/increase and hence the corresponding control signal output is adjusted in order to maintain 95 lph. The temperature corresponding to 95 lph is recorded as plugging temperature.

In discontinuous mode, sodium temperature is gradually lowered to the plugging temperature by varying the air flow to the PI. The temperature corresponding to drop in flow by 2% is taken as the plugging temperature. To prevent sudden plugging of the orifice plate, the rate of cooling is maintained at 5°C/min up to 200°C or selected value. Below 200°C, the sodium is cooled at a slower rate of 2°C/min till the blower trips. This cycle is repeated once in four hours (or set value). In both the modes of operation, blower is tripped when the flow reaches 80 lph or plugging temperature reaches 110 °C.

Two types of software namely
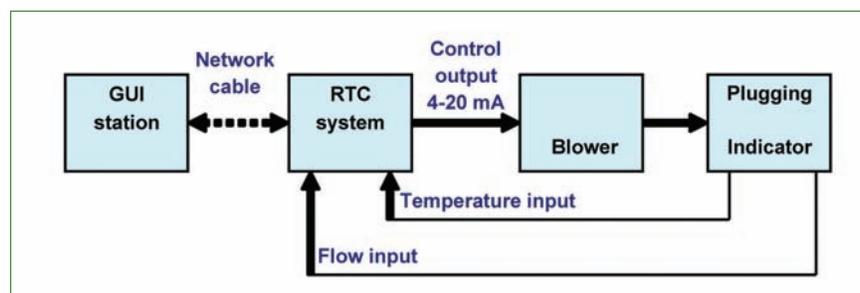
Fig. 2 *Block diagram of plugging indicator control system*
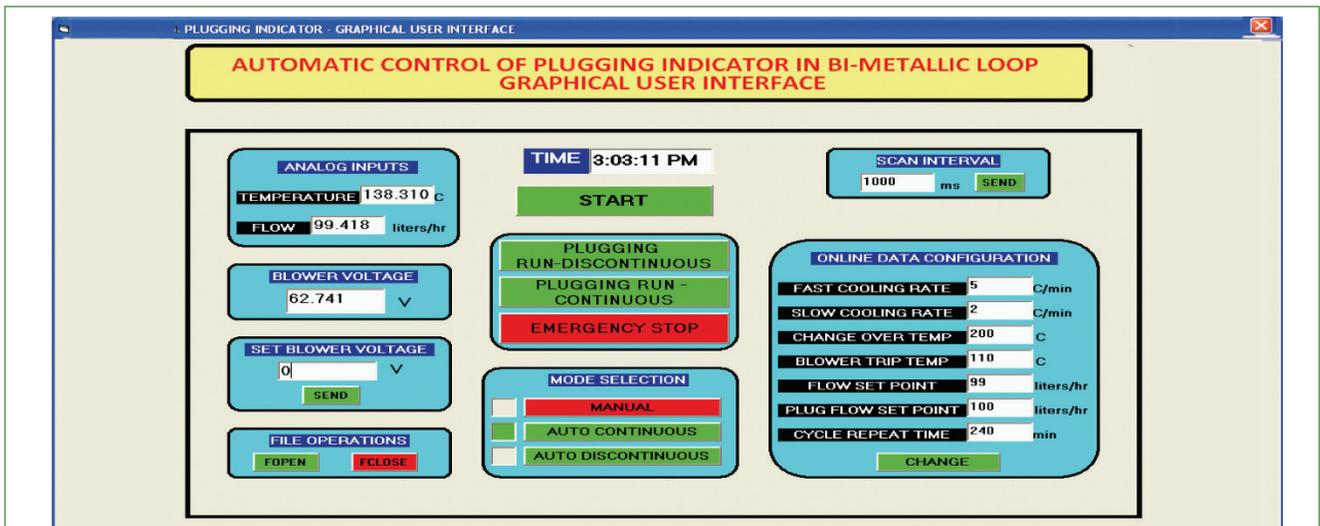
Fig. 3 *GUI screen shot*

control software and GUI software is used for plugging indicator control. Control software was developed using Tasking C cross compiler and is embedded in CPU card of RTC system. This software receives PI modes and set points from the GUI station using TCP/IP protocol. This software scans the temperature and flow inputs, executes the control algorithm, generates analog output and sends the information to GUI station for storage and display purposes. Soft PID based control algorithm generates 4-20 mA control output for controlling the control valve from 0 to 100%. The P,I,D component of control output is calculated as per the following algorithm:

Control output

$$= ((P+I+D) * 0.16) + 4.0$$

P = Kp * Proportional error

I = Ki * Integral error

D = Kd * Derivative error

Kp, Ki, Kd are P,I,D constants which

are configurable in run time.

GUI software was developed using Visual Basic 6.0. Screen shot of main form of the GUI is shown in Figure 3. Main form has the following features: display for temperature and flow values, provision to change the PID constants, set points, cooling rates etc during run time.

PI experiments were carried out by changing the cold point temperature (CPT) of cold trap from 110 °C to 190 °C (dissolving the impurities in the cold trap). Plugging temperature corresponding to different CPT was recorded. Auto discontinuous mode was started with the PID constants of 0.5, 0.05 & 0 respectively. CPT and the loop flow were kept at 160 °C and 100 lph respectively. The plugging run plot obtained for these PID constants showed fluctuations in temperature profile. Hence the PID constants were changed as 0.5, 0.01 & 0 respectively. Figure 4 shows discontinuous plugging run

plot when CPT was 160 °C.

Auto continuous mode was started with the PID constants of 5, 0.01 & 0 respectively. CPT was kept at 150 °C and the loop flow was maintained at 100 lph. Plugging run plot obtained for these PID constants showed fluctuations in temperature profile. Hence the PID constants were changed as 5, 0.005 & 0 respectively. Figure 5 shows continuous plugging run plot when CPT was 160 °C.

Soft PID algorithms for continuous and discontinuous mode were successfully tested at BIM loop. P and I constants for both the modes were tuned and arrived at the optimum control action. Based on the experiments, it can be concluded that the continuous mode of operation gives the preliminary data that there are impurities in the loop. The exact plugging temperature can be obtained from the discontinuous plugging run.
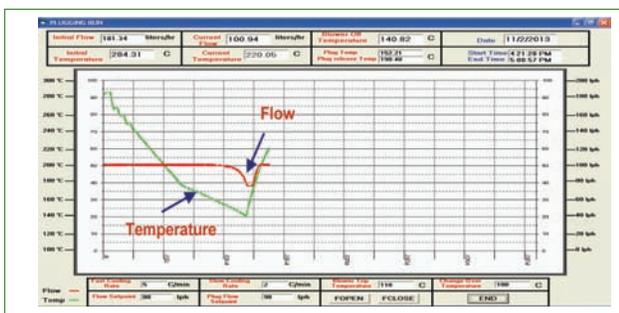
Fig. 4 *Plugging run plot–auto discontinuous mode*
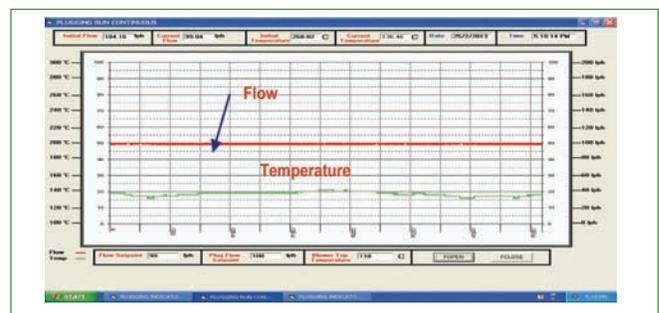
Fig. 5 *Plugging run plot–auto continuous mode*

VI.11   EMI/EMC Pre-Compliance Test Facility

Electromagnetic interference (EMI) is defined as the unwanted coupling of electromagnetic signals from one system to another which leads to the impairment or degradation of electronic system. Ability of equipment or system to function as designed without degradation or malfunction in an intended operational electromagnetic environment is called as electromagnetic compatibility (EMC). Qualification of electronic systems for EMI and EMC requirements is mandatory as per AERB safety guide. In order to reduce the design cycle and enhance the quality of design with respect to EMI/EMC requirements, Electronics & Instrumentation Division (EID) has established pre-compliance level EMI/EMC test facilities.

The EMI/EMC test setup contains ground reference plane, horizontal coupling plane and vertical coupling plane. An earth pit was laid exclusively for EMI/EMC test facility and multipoint earthing was provided through a copper bus-bar to connect the ground reference plane to the earth electrode in the earth pit. The following test facilities are currently operational at EID.

Electrostatic discharge (ESD) (IEC 61000-4-2): This test is to evaluate the performance of electrical and electronic equipment when subjected to ESD. In addition, it includes ESD which may occur from personnel to equipment in contact. The ESD is to be applied to the equipment under test (EUT) from ± 2 kV to ± 8 kV in contact discharge mode and ± 2 kV to ± 15 kV in air discharge mode. Figure 1 shows

Fig. 1 *ESD test in progress*

the snapshot of ESD test.

Electrical fast transient (EFT): (IEC 61000-4-4). This test is intended to demonstrate the immunity of electrical and electronic equipment when subjected to types of transient disturbances such as those originating from arcing contacts in switches and relays. The EFT is to be applied to the EUT from ± 0.5 to ± 4 kV in power port and ± 0.5 to ± 2 kV in signal port.

Surge: (IEC 61000-4-5). Surge is a transient wave of electrical current, voltage or power propagating along a line or a circuit and characterized by a rapid increase followed by a slower decrease that can be generated either by switching transients or by lightning transients. The test levels are from ± 0.5 to ± 4 kV for open circuit voltage and ± 0.25 to ± 2 kA for short circuit current.

Conducted RF: (IEC 61000-4-6). This test is to evaluate the functional immunity of electrical and electronic equipment when subjected to conducted radio-frequency disturbances in the range of 150 kHz to 80 MHz.

Power frequency magnetic field: (IEC 61000-4-8). This test is to demonstrate the immunity of equipment when subjected to power frequency magnetic fields. Tests are carried out for short duration (1000 A/m for 3 s) and for

Fig. 2 *Power frequency magnetic field test in progress*

continuous magnetic field (10 A/m, 30 A/m and 100 A/m). Figure 2 shows the snapshot of power frequency magnetic field.

Pulse magnetic field: (IEC 61000-4-9). This test is intended to demonstrate the immunity requirements of the equipment when subjected to impulse magnetic fields. The test levels for pulse magnetic field test are 100 A/m, 300 A/m and 1000 A/m.

Voltage dips & interruption: (IEC 61000-4-11). This test is intended to demonstrate the immunity of electrical and electronic equipment when subjected to voltage dips and short interruptions of power supply. The test voltage levels are 70%, 40% and 0% of nominal voltage for 500 ms, 200 ms and 5 sec.

Conducted emission (CE): (CISPR 11, Class A). CE is the radio frequency noise present in the physical wiring or traces of an electrical system. CE measurement is carried out for the frequency band of 150 kHz to 30 MHz.

The EMI/EMC test facility was widely used and nearly 50 tests were performed, over a period of eight months in the year 2013, on various electronic systems in deployment mode. It is also planned to augment the laboratory with additional test facilities.

VI.12 Development of Digital Signal Processing (DSP) Algorithms for Condition Monitoring System of Rotating Equipment

Condition monitoring system (CMS) helps in doing preventive maintenance on rotating equipment (motors, fans, pumps, etc) in a very cost effective way. Presently these CMSs along with their sensors are to be imported at high cost with no design details being available for maintenance. Hence a CMS developed with efficient Digital Signal Processing algorithm will provide valuable import substitution.

Faulty bearings contribute to most of the failures in rotating equipment. 90% of the rolling elements bearing faults are from either inner race (IR) or outer race (OR) faults. The fancy with bearing faults is that the bearing fault frequency does not depend on the equipment rather it depends on the mechanical construction of the bearing.

When bearing faults occur, each rolling element keeps on hitting the fault on every rotation. This causes sharp peaks at periodic intervals, but they are of low energy. These signals are modulated by a number of high frequency harmonic components resulting from the structural response to individual impacts. Along with that, a lot of other vibrations and noises also occur. Due to this, the characteristic bearing fault frequency signal is lost in the noise and an efficient noise filtering is required for characteristic fault frequency retrieval.

Fast Fourier transform

There are various Condition Monitoring methods already in practice for analysis and detection of bearing faults in Induction Motors. An effective DSP algorithm that brings out the fault signatures in a very early stage itself is required. These fault signatures are looked out for in the frequency domain. The Discrete Fourier transform, or the fast Fourier transform (FFT) as it is commonly called, is used to see the vibration signal in the frequency domain.

Figure 1 shows the just the direct FFT of the acquired vibration data of Outer Race fault. It is noted that peak is not visible at the characteristic fault frequency.

Discrete wavelet transform

If the noise type and frequency are known, different filters can be used for denoising. However in vibration analysis for bearing faults, neither the noise type nor the frequency range is known. For such application Wavelet transform has been widely used, due to its extraordinary time-frequency representation capability.

Five-level decomposition with DWT based on Daubechies-4 wavelet is done on the filtered signal. The input signal is divided with respect to frequency bands by this decomposition. The FFT plots of the details which constitute our interested area of frequencies are
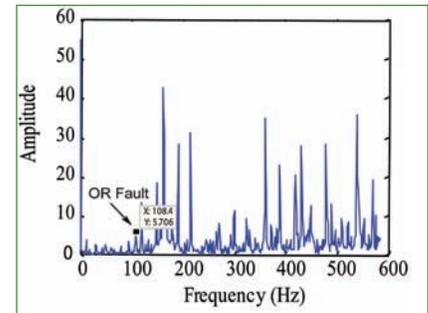
Fig. 1 *FFT of OR fault signal*

plotted in Figure 2. It can be seen that though the OR fault's characteristic frequency is seen it is hidden in between other noises.

Morphological operation

The basic concept of morphological signal processing is to modify the shape of a signal, by transforming it through its intersection with another object, the structuring element.

The morphological operator selected for filtering of vibration signals for fault diagnosis is Self-Complimentary Top Hat. The Figure 3 shows the Morphological operated signal. The peaks corresponding to the rotating frequency (F_r), the fault frequency and their harmonics are clearly visible in these figures. These frequency peaks are observed only after the signal is morphologically filtered.

When compared to FFT and DWT, Morphological operation on the vibration signals brings out the fault frequencies easily and effectively.
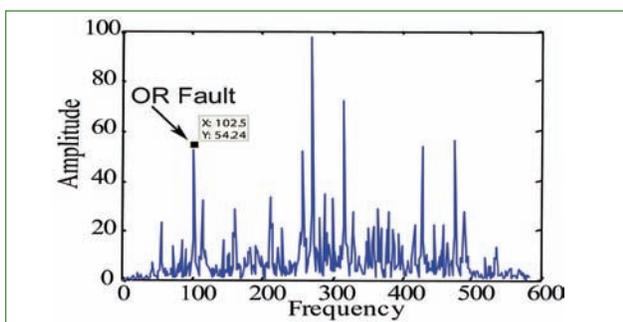
Fig. 2 *DWT denoised OR fault signal*
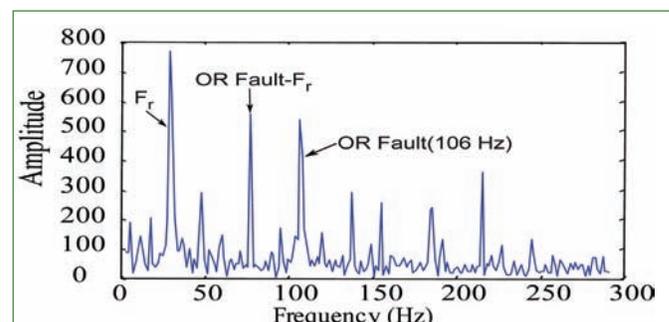
Fig. 3 *Morphologically filtered OR fault signal*

VI.13 Ductility Behavior Study of Beam Column Joint with Fly Ash Concrete

Fly ash has emerged as a novel engineering material with considerable promise as binder in the manufacture of concrete. In this investigation, reinforced concrete beam-column joints with and without fly ash were tested in the reversed lateral load testing frame for studying ductility behavior. In the study 40% of ordinary Portland cement is replaced with Class F fly ash. Ductility is the capacity to undergo inelastic deformation and absorb energy. The capability of the joint under reversed lateral loads had to be established so that the joint experience substantial inelastic deformations in tension and compression in the presence of axial compressive loads, similar to those during earthquake.

Eight numbers of reinforced concrete beam-column joints with and without fly ash were tested (four numbers were tested at 28 days and four numbers at 56 days). Out of the eight specimens, four controlled specimens were cast without fly ash (CBC0%) and the other four specimens were cast with 40% fly ash (CBC40%). The materials used in the mix were Ordinary Portland Cement (OPC-43 grade), river sand, coarse aggregate, Fly Ash (F grade) and potable water. Conplast (SP430) super plasticizer was incorporated in the mix to increase the workability. Water-cement ratio of 0.45 and 0.75% super plasticizer was used for OPC reinforced concrete beams .The same water-cement ratio and 1.3% super plasticizer was used for fly ash concrete beams. Fe500 grade steel was used for longitudinal reinforcements, stirrups and ties. Columns and beams were made with M30 grade concrete.

The height of the column was 1000 mm and of size 150 mm x 150 mm. The span of the beam was 1500 mm and of size 150 mm x 200 mm. Reinforcement details for the beam-column is shown in Figure 1.

The reversed lateral load test set-up consisted of a loading frame with hydraulic jack of 200 kN to apply constant axial compressive load and a hydraulic actuator of capacity 200 kN with a stroke length of ± 100 mm to apply reversed lateral load on the specimens.

The loading frame was used to apply a vertical axial load through steel rollers placed with the support of steel plates in between the jack and the column head. The vertical load was chosen to a design compression of 20% axial resistance found from analysis. The experimental set-up is shown in Figure 2.

A steel reaction frame supported the actuator providing lateral load to the specimen. Instrumentation included linear voltage displacement transducers for lateral displacement measurement at the top of the column and one load cell attached to actuator was used for the measurement of reversed lateral loads. Linear voltage displacement transducers was connected to a data logger and readings were captured by
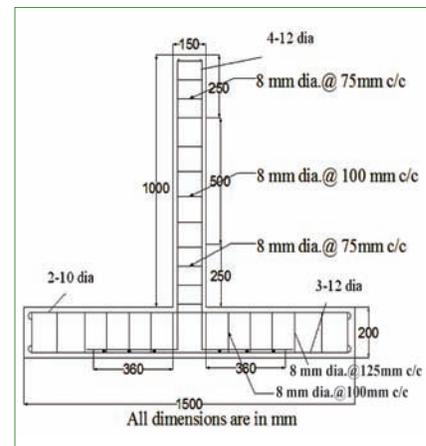
Fig. 1 *Test specimen*

a computer at every load interval was realised until failure of the specimens.

In all the specimens, failure was due to concrete crushing at the beam-column junction and minor cracks were noticed along the height of the column. The failure pattern of beam – column joint subjected to lateral loading is shown in Figure 3.

Figure 4 shows the experimental hysteretic curves of the beam-column joint with fly ash when tested at 56th day.

In Figure 5 the trajectory of load-displacement of all the specimens with and without fly ash tested at 56th day is shown.

The displacement at yield and failure of the specimens and hence displacement ductility was obtained from the peak lateral load

Fig. 2 *Test setup*
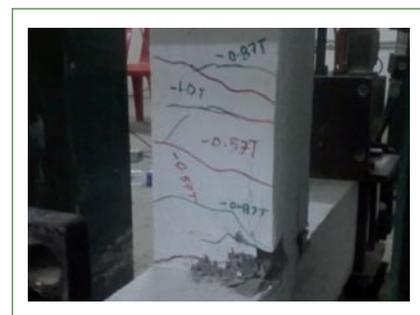
Fig. 3 *Failure pattern*

versus lateral displacement curves. Table 1 shows displacement ductility of the test specimens. Displacement ductility is the ratio of displacement at ultimate load to displacement at yield load. A ductility ratio of 3-5 is adequate for structural members subjected to earthquake loads.

The energy absorbed by all specimens during reversed lateral loads was calculated as area under the hysteretic loop for each cycle. It was observed that the energy absorption capacity of specimens with fly ash were as good as specimens without flyash.

Hence, it is concluded that reinforced flyash concrete beam-column joint is ductile and ductility behavior is not effected due to replacement of cement with flyash.
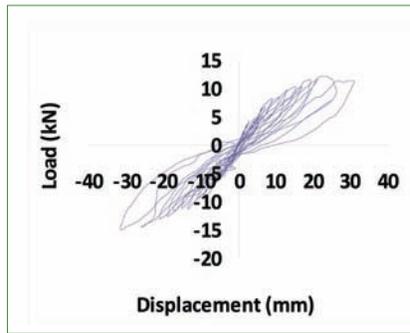
Fig. 4 *Hysteretic curve @56 days*
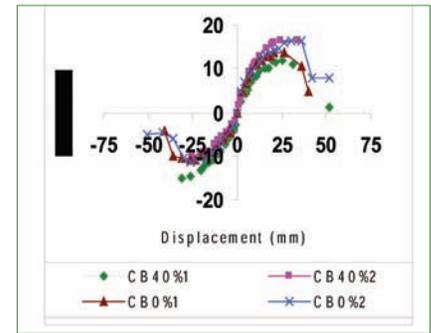
Fig. 5 *Load-displacement curve*

Table1: Displacement ductility					Average Ductility Ratio
Specimen Series	Displacement (mm)				
	Yield		Ultimate		
	Upward	Downward	Upward	Downward	
CBC0% -28	6.2	6.8	31.2	36.0	5.2
CBC40%-28	6.6	6.2	33.0	33.4	5.2
CBC0%-56	6.6	5.4	35.6	30.2	5.5
CBC40%-56	5.8	5.9	31.5	31.2	5.4

VI.14 Development of Charts for the Design of Arbitrary Shaped Column

Generally the axial load and moment carrying capacity of a concrete column section is expressed as an interaction curve between axial force and bending moment. Depending on the magnitude of the axial force in the column section, the maximum moment would vary as determined by the interaction chart. For the design of reinforced concrete columns of standard shapes such as rectangle and circle, the design interaction charts are readily available in literature. For more complex shapes such as L, T, Y, and hollow rectangular sections, the design axial – moment interaction charts have to be developed from the fundamental principles. The conventional approach is time consuming, laborious and is valid only for a predetermined arrangement and area of steel reinforcement.

Figure 1a depicts the arbitrary shaped column section as designed by conventional approach. Figures 1c and 1d indicate the strain and stress block diagram respectively. By considering the neutral axis at a given position, force and moment equilibrium equations are solved to obtain the axial load capacity and the corresponding moment capacity.

The equilibrium equations based on conventional approach would be,

$$\int b(y).dy.f_c(y) + \sum A_{sc}.f_{sc}$$
$$- \sum A_{st}.f_{st} = P_{cap}$$

and

$$\int b(y).y.dy.f_c(y) + \sum A_{sc}.f_{sc}.y_1$$
$$+ \sum A_{st}.f_{st}.y_2 = M_{cap}$$

where,

'b(y)' is width of section at distance *'y'* from neutral axis, *'A_{sc}', 'y$_1$'* and *'A_{st}','y$_2$'* are areas of steel reinforcements and distances of bar from neutral axis at compression and tension zones respectively, *'f_c'* is the concrete stress corresponding
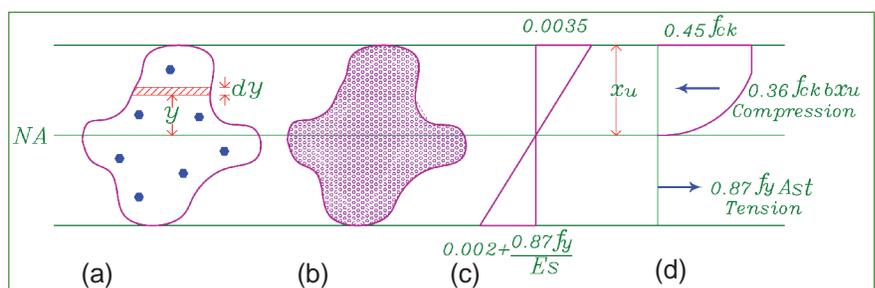
Fig. 1 *(a) Arbitrary shaped column section, (b) grid point mesh, (c) strain diagram and (d) stress black diagram*
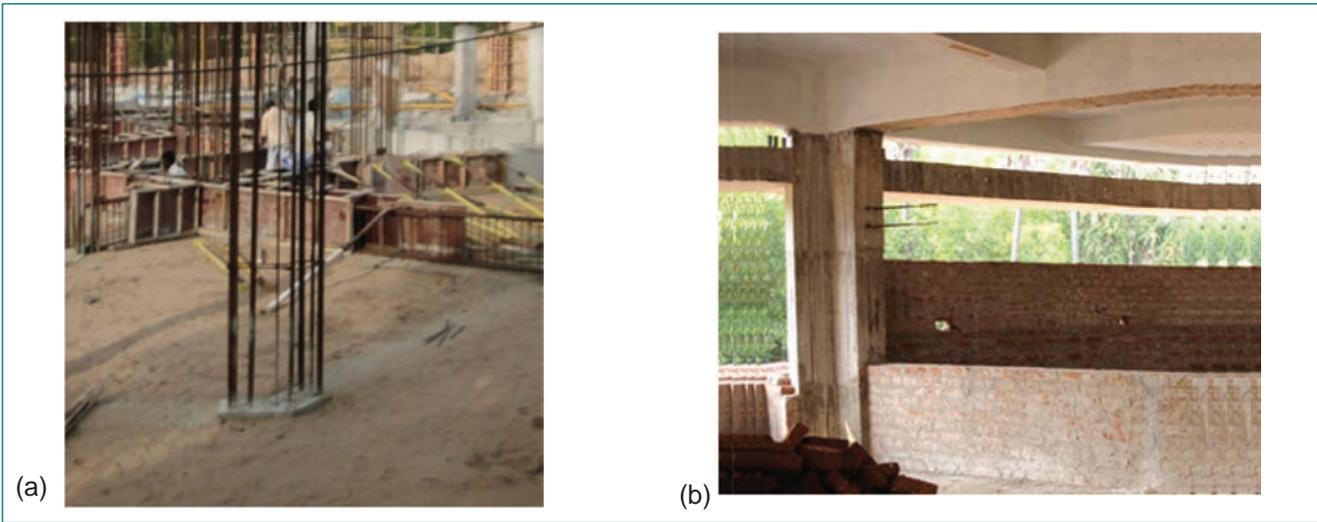
Fig. 2 *Angular shaped column used in IFFRM building (a) plinth level and (b) after completion*

to distance *'y'*, *'f$_{sc}$'* and *'f$_{st}$'* are the steel stresses in compression and tension respectively and *'P$_{cap}$'* and *'M$_{cap}$'* are the axial load and moment capacities of the section.

The above equation can be solved by integration for simple shapes, but the procedure would become cumbersome for complex shapes. To circumvent the problem, numerical integration technique has been developed based on finite grid point meshing and computer software has been developed based on this method in Visual Basic. Figure 1b shows the column section with the area sub divided into grid points with finite area. The equilibrium equations based on this approach would be,

$$\sum a.f_c + \sum A_{sc}.f_{sc}$$
$$- \sum A_{st}.f_{st} = P_{cap}$$
and
$$\sum a.f_c.y_c + \sum A_{sc}.f_{sc}.y_1$$
$$+ \sum A_{st}.f_{st}.y_2 = M_{cap}$$

where, *'a'* is the area of grid point and *'f$_c$'* is the stress in compression corresponding to the grid point location.

By this method, one can carry out design of any arbitrary shaped column sections for bending based on both Indian and AERB standards. In this method, data on the arbitrary column section is input in the form of coordinates of the vertices from which the sides of the polygon are generated. Based on grid meshing, the polygon is subdivided into a number of grid points enclosed by the polygon edges.

By considering the neutral axis at different positions along the depth and width, force and moment equilibrium equations are solved to obtain the points along the axial - moment interaction curves.

The computer program is GUI based and is endowed with written-from-scratch graphical features to enable plotting of polygon shape showing grid point mesh and also the biaxial moment - axial interaction curves. Batch mode operation is also supported in the software to run multiple column design problems in a single mouse click. Mesh density of 50 x 50 sub divisions provided as default is found to be satisfactory for most sections. For thin walled sections, the mesh density can be increased and appropriate mesh size can be chosen by making convergence trials. The advantages of this technique are that any arbitrary shaped cross section and any arbitrary pattern of steel reinforcement with different bar diameters can be designed.

Figures 2a and 2b show photographs of the angular shaped column in Integrated Facility for Fusion Reactor Materials building with the column up to plinth level and after completion respectively and Figure 3 shows the corresponding axial-moment interaction curve as obtained from the computer program.
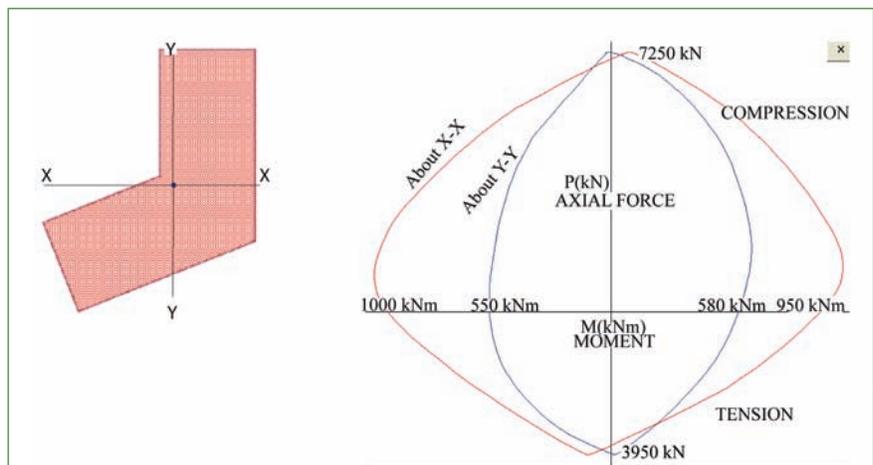
Fig. 3 *Axial force- moment interaction curves for angular column*

VI.15 Evolution in Thermal and Mechanical Properties during Radiation Degradation of Poly-tetrafluoroethylene – Lead Composites

Application of polymer materials in nuclear spent fuel reprocessing plants required should possess good radiation as well as chemical resistance. Radiation resistant polymers like PEEK, neoprene, polyurethane, EPDM etc., which are being used in the reprocessing plants have low chemical resistance when compared to Teflon (Poly-tetrafluoroethylene, PTFE). PTFE is extensively used under severe conditions because of its resistance to high temperature and to most of the chemical solvents. However, the radiation stability of PTFE is very poor. Its mechanical properties degrade at very low radiation doses even under vacuum. To employ PTFE in reprocessing plants, the radiation resistance of PTFE requires to be improved. One of the methods to improve the radiation resistance of a polymer is by blending with a metal or ceramic component. As lead has good radiation attenuation property, PTFE-Pb powders were blended, sheets of composites were fabricated and the effect of Pb on the radiation resistance of the composites was investigated.

The materials used for the preparation of composites were PTFE powder as the polymer matrix and lead powder as filler material. Lead and PTFE powders were mixed homogeneously at different weight ratios (0, 5, 10 and 15 % Pb) and 2 mm thick sheets were fabricated using a hydraulic compression moulding press at 673 K and 140 bar. The composite samples were irradiated in a gamma chamber with ^{60}Co source in ambient air at 5 kGy/h dose rate and at room temperature up to the radiation dose of 50 kGy.

Enthalpy of melting (ΔH_m) and enthalpy of crystallization (ΔH_c) of irradiated and unirradiated PTFE-composite samples were measured (Figures 1 and 2) using a differential scanning calorimeter (SETSYS TG-DTA-DSC, France) in argon atmosphere.

The samples were heated to 703 K, soaked for 5 min. for stabilization and cooled. Crystallization process was recorded from molten state during cooling. The heating and cooling rates for all the specimens were 10 K/min. The effect of radiation on molecular weight and crystallinity of PTFE was calculated from the DSC

data. Tensile strength of pure PTFE and PTFE-Pb composites, before and after exposure to different gamma doses, was measured using Universal Testing Machine (Figure 3).

It is reported in literature that the heat of crystallization of a polymer is closely related to its molecular weight and Equation (1) can be applied for PTFE.

$$M_n = 2.1 \times 10^{10} \times \Delta H_c^{-5.16} \qquad (1)$$

where M_n is the number average molecular weight and ΔH_c is the heat of crystallization in Cal/g. Table 1 shows the decreasing tendency of molecular weight of PTFE with radiation which can be attributed to intensive chain scission reaction of PTFE at increased doses.

Degree of crystallinity (X) in percentage was calculated from the enthalpy of melting data using Equation (2).

$$X (\%) = (\Delta H/H_f) 100 \qquad (2)$$

where H_f is the heat of fusion of fully crystalline PTFE, which value is reported as 57.3 Cal/g.

PTFE achieves better degree of crystallinity during irradiation process. With longer exposure to radiation dose, the molecular weight
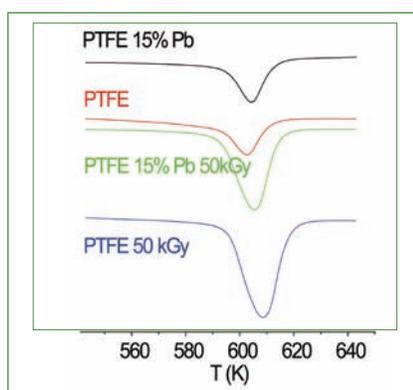
Fig. 1 *Melting peaks of PTFE and PTFE-15Pb composite by DSC*
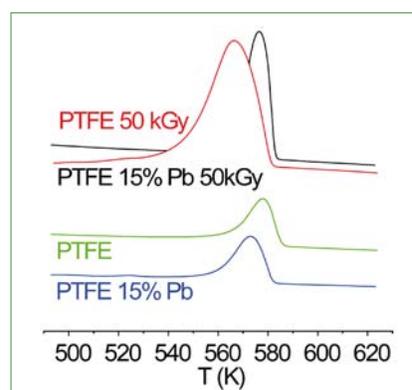
Fig. 2 *Crystallization curves for PTFE and PTFE-15Pb composite*

Table 1: Radiation effect on molecular weight and degree of crystallinity in PTFE			
Dose (kGy)	ΔH_c (Cal/g)	M_n	X (%)
0	9.2	2.21×10^5	16.1
1	10.9	0.91×10^5	19.1
5	11.8	0.61×10^5	20.6
10	14.5	0.22×10^5	25.2
50	16.6	0.10×10^5	29.0

Fig. 3 *Universal testing machine*

Table 2: Radiation effect on the tensile strength of PTFE and its composites with Pb

Dose (kGy)	Tensile strength (MPa)			
	PTFE	PTFE-5%Pb	PTFE-10%Pb	PTFE-15%Pb
0	8.0	10.7	11.0	13.0
1	7.1	9.5	9.8	11.5
5	6.5	9.0	9.5	10.8
10	5.8	8.0	8.7	10.2
50	2.1	6.4	7.5	9.8

of PTFE decreases owing to chain scission reaction and facilitates crystallization. Smaller polymer chains offer less hindrance in the regular arrangements or orientation during the crystallization process because of better mobility and lower intra as well as intermolecular entanglement.

Owing to greater degree of crystallinity with radiation dose, both ΔH_m and ΔH_c were observed to increase for pure PTFE and for the composites. However, incorporation of lead shows a decrease in the rise of ΔH_m and ΔH_c in comparison to pure PTFE. This is attributed to the lower mobility of the polymer segment during crystallization due to the hindering effect of lead particles. The percentage increase in ΔH_m and ΔH_c values of PTFE composites (irradiated up to 50 kGy) with lead content plotted in Figure 4 reveals that the radiation attenuation property of lead suppresses the radiation damage of PTFE, thereby imparting stability to PTFE against gamma radiation.

Tensile strength values determined for PTFE and its composites with lead are listed in Table 2.

Lead enhances the structural strength of PTFE, which is reflected in the increased tensile strength.

Figure 5 shows the percentage decrease in tensile strength with radiation dose for PTFE and its composites.

It is evident from Figure 5 that 50% reduction in the tensile strength for pure PTFE occurs at 30 kGy. Addition of 15% Pb to PTFE aided in decreasing the reduction in tensile strength to 20% and the reduction was within 50% even at 50 kGy. Thus, the reduction in the tensile strength of PTFE during exposure to gamma rays is suppressed significantly because lead acts as excitation energy sink.

Irradiation of PTFE and its composites with Pb (5, 10 and 15 wt.%) by gamma rays (up to 50 kGy) revealed a decrease in the molecular weight and increase in the crystallinity of PTFE with increase in

the dose due to the enhancement of the enthalpy of crystallization as well as melting. When the percentage of lead in the composites increased from 5 to 15 wt.%, the values of ΔH_m and ΔH_c decreased gradually. Tensile strength of PTFE and PTFE-Pb composites decreased with radiation. However, the decrease in tensile strength owing to radiation was inhibited by the lead filler in the composite due to its action as an excitation sink, thereby reducing the radiation damage on PTFE. Hence, lead (15%) can be loaded as a filler material in the fabrication of PTFE components and coatings for the plant to increase the radiation resistance of PTFE, after ascertaining the corrosion resistance of PTFE-Pb composites.
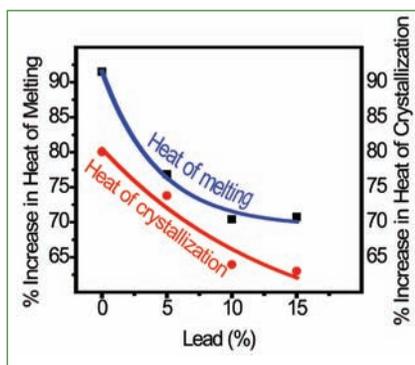
Fig. 4 *Percentage increase in ΔH_m and ΔH_c against Pb content in irradiated PTFE-Pb composites; radiation dose: 50 kGy*
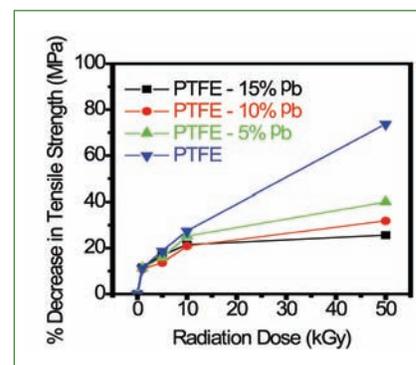
Fig. 5 *Percentage decrease in tensile strength at different doses*

VI.16   Site Characterization of DAE Complex at Kalpakkam using Soft Computing Techniques

Site characterization is an imperative task in every geotechnical engineering project. Geotechnical engineers use laboratory and in situ tests for site characterization. It is never possible to know the detailed geotechnical properties at every location beneath an actual site because, in order to know it, one would need to sample and/or test the entire subsurface profile. So, one has to predict geotechnical properties at any point of a site based on a limited number of tests. This article presents genetic programming (GP) and minimax probability machine regression (MPMR) for prediction of standard penetration test (SPT) value (N) at any point in DAE complex, Kalpakkam. (The SPT N value is the number of blows required to achieve a penetration of 300 mm, after an initial seating drive of 150 mm with a standard sampler into soil using repeated blows of a 63.5 kg hammer falling through 760 mm.) The basic concept of MPMR has been taken from minimax probability machine classification algorithm by G.R.G. Lanckriet. It has been successfully adopted for modeling different problems. 95 N values have been used to develop the GP and MPMR.

Figure 1, shows the locations of SPT tests. A comparative study has been carried out between the developed GP and MPMR models

Genetic programming

GP is developed based on the Darwinian principle by John Koza. In first step, an initial population of equations is created. In second step, each equation was executed to determine the fitness value. Then, 'parents' are selected through
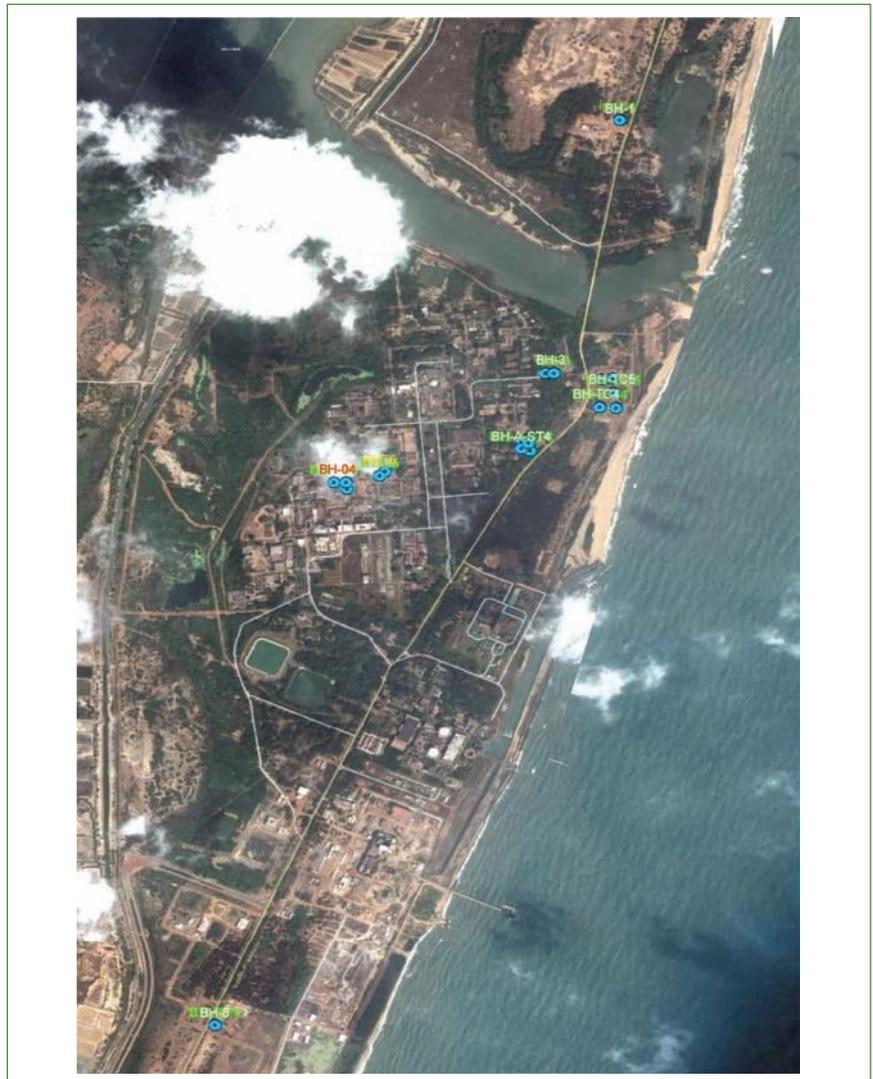
Fig. 1 *Bore hole locations*

tournament. New off springs are produced through the process of reproduction, mutation and crossover. A number of offspring are created in generations. The best equation that appeared in any generation is the solution of the problem.   To develop the above mentioned GP, 66 datasets out of 95 datasets have been adopted for training dataset. The remaining 29 datasets have been used for testing dataset. The purpose of the training dataset is to develop the GP model. Testing dataset has been used to verify the developed GP. In this study, latitude (L_x), longitude(L_y)

and depth (d) has been taken as input of the GP model. The output of GP is N. GP has been programmed by using MATLAB.

Minimax probability machine regression

MPMR does not assume any distribution of the available data for prediction of output variable. MPMR models the regression function in the following way.

$$y = \sum_{i=1}^{m} \beta_i K_i(x_i, x) + b$$

Where *y* is output, *x* is input, m is number of datasets, K(x_i,x) is kernel function, β_i is weighting coefficients and *b* is bias. In this problem, input
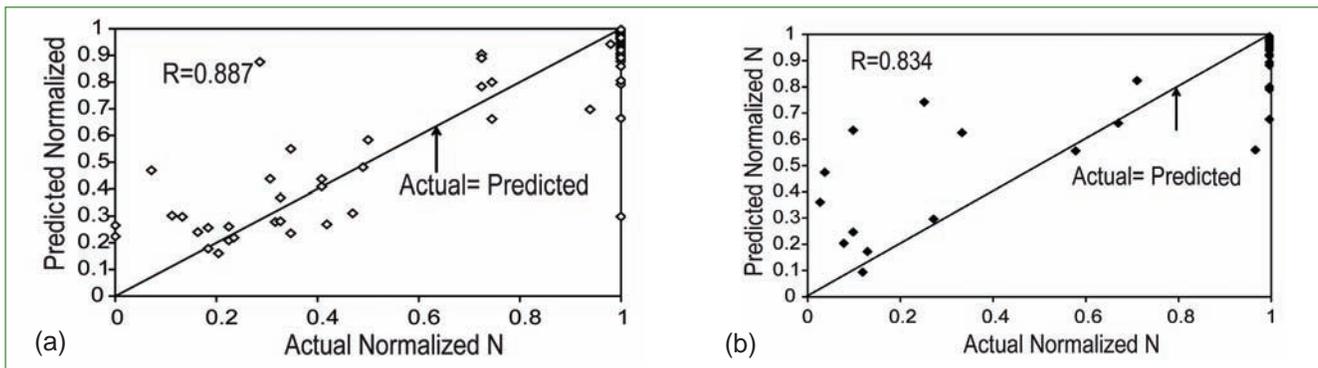
Fig. 2 *Performance of training dataset for the (a) developed GP and (b) GP model*

variables are L_x, L_y and d. The output of MPMR is N. So, x=[L_x, L_y, d] and y=[N]. MPMR uses the same training and testing dataset as used by the GP model. The datasets are normalized between 0 and 1. Radial basis function,

$$K(x_i, x) = \exp\left[-\frac{(x_i - x)(x_i - x)^T}{2\sigma^2}\right]$$

where σ is the width of radial basis function, has been adopted as a kernel function. MPMR has been constructed using MATLAB.

For GP, the size of population is kept 600. Number of generation is set to 200. Maximum depth of tree is kept 6. The final GP gives the following equation for prediction of N.

$$N = 3.29L_x - 0.06L_y + 6.80d^2L_x^4 - 3.06L_x^2 + \frac{0.06L_x^2}{d} - \frac{0.012L_y}{d} - 3.97dL_x^2 - \frac{0.15}{d} + \frac{0.003}{d^2} + \frac{0.2L_y}{L_x^2\left(9.08L_x - \dfrac{L_x}{d}\right)} + 0.89$$

The above equation has been used to determine the performance of training and testing dataset. The performance of GP and MPMR

has been assessed in terms of coefficient of correlation(R). For a good model, the value of R will be close to one. Figures 2a and 2b show the performance of training and testing dataset respectively. The value of R is not so close to one for training as well as testing dataset.

For MPMR, the design values of σ has been determined by trail and error approach. The developed MPMR gives best performance at σ =0.4. The performance of training and testing dataset has been determined by using the design values of σ. Figures 3a and 3b depict the performance of training and testing dataset respectively. It is observed from Figures 4 and 5 that the value of R is close to 1 for training as well as testing dataset.

Therefore, the developed MPMR proves its ability for prediction of N value. The developed MPMR produces better R value than the GP model. So, the performance of MPMR is better than the GP model. Normalization of data is not required for developing the GP

model. However, normalization of data is essential to develop the MPMR model. Figure 4 depicts the predicted surface of N value at a depth of 1.5 from the developed GP. Figure 6b represents predicted surface of N value at a depth of 1.5 from the developed MPMR.

This article describes GP and MPMR models for prediction of N value at any point in DAE complex, Kalpakkam.

The MPMR model gives better performance than the GP model. With this model, for given latitude and longitude within DAE complex, subsoil properties like safe bearing capacity, liquefaction potential, shear capacity etc. can be evaluated.

(a)

(b)

Fig. 4 *Surface of N value at a depth of 1.5 m from the (a)GP model and (b) MPMR model*

Fig. 3 *Performance of (a) training and (b) testing dataset of the MPMR model*

VI.17 An Integrated Meteorological Observational Facility at Kalpakkam

Site specific meteorological observations are essential in understanding boundary layer turbulence and atmospheric dispersion for radiological impact assessment studies. At the tropical coastal site Kalpakkam the atmospheric stability and diffusion characteristics vary as per the prevailing flow and meteorological conditions. In order to understand the spatial and temporal plume dispersion characteristics under various seasonal conditions a network of meteorological observational systems have been setup at this coastal site. The observational network at Kalpakkam include three 50 metres instrumented micrometeorological towers, portable masts, ultrasonic anemometers, Doppler SODAR, GPS Radio-Sonde and automated weather stations. They provide continuous measurements of meteorological parameters and turbulence fluxes. The instruments are distributed in a range of 40 km to capture the spatial variation in the parameters and mesoscale systems. Three meteorological towers of height 50 m are set up across the coast i.e., one near the coast (Edaiyur, Kalpakkam), second at Anupuram about 5km away from the coast and third one at an inland site away from the coast (Jeppiar Nagar Satyabhama University). For acquisition of real time data and visualization at our Centre a rugged, user-friendly data-acquisition system was designed around an industrial embedded computer platform. Tower data can be transferred to a central server located through radio frequency transmission and network file transfer protocol.

Meteorological Towers are designed as per the IS 800 standards, for maximum wind load and maximum wind speed at 65 m/s. All the meteorological towers (Figure 1) are equipped with slow response sensors (Cup anemometers, Wind wanes) to measure the wind speed and direction at 2, 8, 16, 32, and 50 m levels. The temperature and humidity sensors are installed at 2, 16, and 50 m levels. The data from these sensors are recorded continuously and averaged at 10 minutes and 1 hour intervals.

The data from the tower system to the central server is communicated in real-time through communication

Fig. 1 *Meteorological towers in stalled at Edaiyur and Anupuram sites*

system. Figure 2 shows the complete radio frequency network.

The system has been in continuous use in the field and has been providing meteorological data input to the real-time dispersion model of a Decision Support System for radiological emergency. Figure 3 depicts the real time observations during the Thane cyclone.

The diurnal variation of wind speed and wind direction at different levels on 50 metres tower at Anupuram for a typical day is shown in Figure 4.

A Doppler Acoustic SODAR (Sonic Detection And Ranging) is installed at Edaiyur site within DAE site region (Figure 5a) and the instrument has been set up in a continuous measurement mode. This instrument works on the principle of scattering of sound
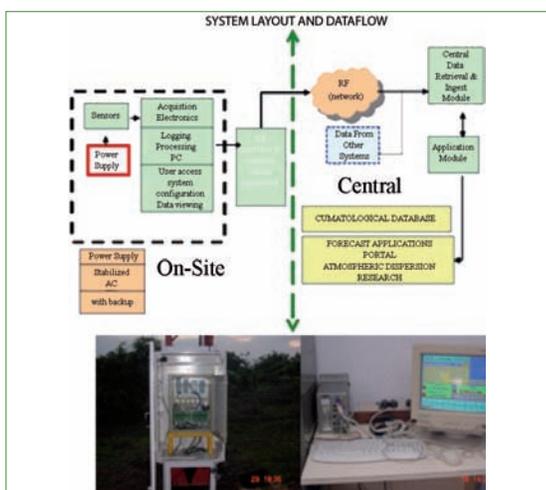
Fig. 2 *Transmission of real-time met data through RF network*
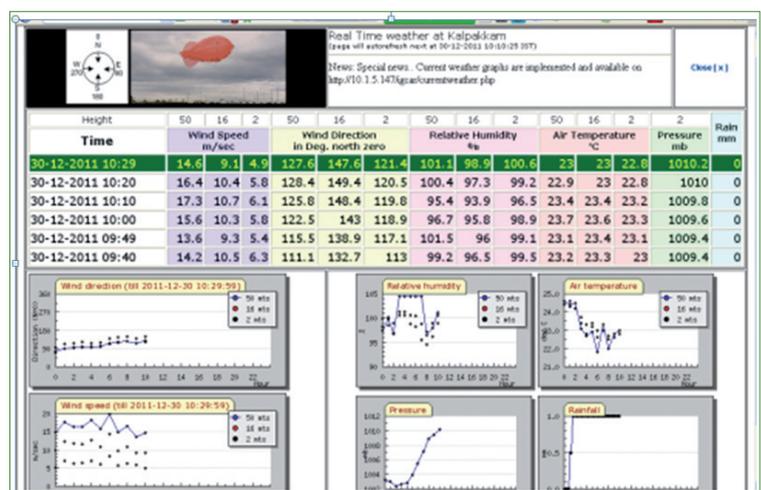
Fig. 3 *Real-time observations during "thane cyclone" 30th December, 2011*
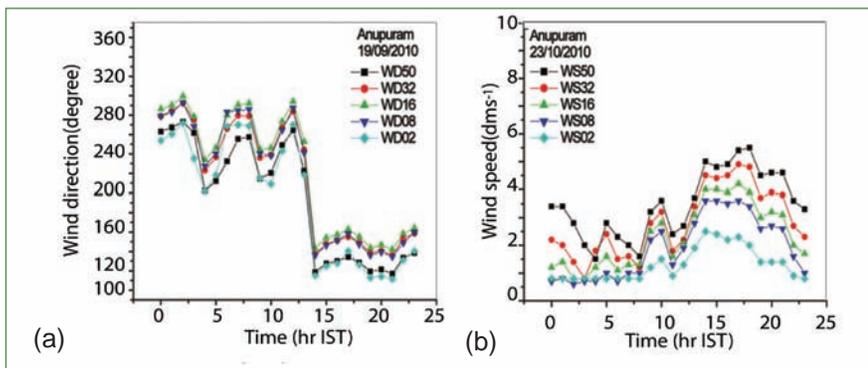
Fig. 4 *Diurnal wind speed and wind direction at different levels on a 50 m tower at Anupuram*

Fig. 5 *(a) Doppler SODAR installed at Edaiyur, IGCAR and (b) sonic anemometer flux measurements*

waves by atmospheric turbulence. It measures the wind speed at various heights above the ground, and the thermodynamic structure of the lower layer of the atmosphere.

The SODAR is used to infer boundary layer properties such as mean wind speed, direction and diffusion parameters upto about 0.5 km height. A typical wind data measured with SODAR is shown in Figure 6.

The vertical profiles from SODAR permit to identify local low-level circulations and to distinguish the seasonal winds up to 300 m AGL. The SODAR also gives data on surface layer turbulence statistics and turbulence kinetic energy. The back scatter echogram from SODAR gives qualitative information of stable, unstable and thermal boundary layers.

The turbulent quantities (fluxes, fluctuating components of winds, temperature etc.) are measured with fast response sensors called Ultra Sonic Anemometers (USA). A sonic anemometer (Figure 5b) uses sound to measure horizontal and vertical components of wind
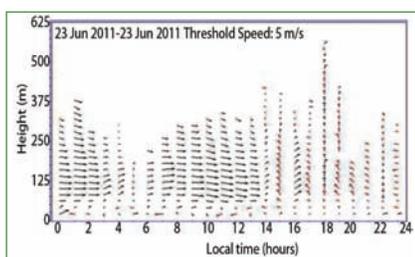
velocity, wind direction and acoustic virtual temperature. To gather these measurements three portable masts each of 10 m height are installed within IGCAR site. The raw data collected at a frequency of 10 Hz for u, v, w and tv (virtual temperature) are used to analyze the fluxes and spectra of wind components. Frequency (f) weighted spectra of u-component and w-component calculated for a 3-h period on SW monsoon synoptic winds shows approximate $f^{5/3}$ behavior. A typical u and w spectra is shown in Figure 7 which indicates large eddies present in the u-spectrum. The peak of the spectra corresponds to the mixing length.

A network of automated weather stations (AWS) was set up by ISRO under the PRWONAM (Prediction of Regional Weather with Meso-net Observations and Modeling) project. The AWS (Figure 8) is a 4.5 m mast fitted with wind anemometer, wind

wane, air temperature, humidity sensors, and automatic rain gauge for continuous measurement of meteorological variables

A GPS Sonde ground station is successfully set up at Kalpakkam in collaboration with ISRO as part of IGBP (ISRO Geo-sphere Bio-sphere Programme) The ISRO GPS Sonde named as 'Dr. Pisharoty Sonde' has a GPS receiver and is operable with battery power (Figure 8). This system is used to collect vertical profiles of winds, temperature and humidity up to the entire troposphere of atmosphere. The position of Radio Sonde balloon is tracked by the GPS navigation system.

The network of instruments facilitated to conduct a number of boundary layer field experiments (CABLE-2001-2002, ARMEX, ICARB 2006, and RRE-2010) and to characterize the flow field and dispersion at this site. The meteorological information is regularly used in the analysis of dispersion estimates for design purpose as well as in theoretical studies.

Fig. 6 *Time-height wind profile measurements by SODAR, IGCAR*

Fig. 8 *Sonic anemometer wind spectral (u, w component) analysis (on 17/09/10 from 00-03 hrs IST)*

Fig. 9 *AWS and GPS balloon system at Kalpakkam*

VI.18   Studies on Sodium Aerosol Dispersion in Open Environment

In a sodium cooled fast reactor (SFR), in the event of category- 4 leakage of sodium in the secondary loop, the hot sodium over-flown and spread over the entire area of steam generator building results in large amount of sodium fumes/aerosols. The sodium aerosols are composed of sodium hydroxide, sodium carbonate and sodium bi-carbonate following the reactions with moisture and CO_2. The sodium hydroxide, which is formed instantaneously, is highly corrosive and damages the vulnerable components in steam generator building and causes severe damage to the human upon contact (threshold limiting value for the inhalation hazard for the hydroxide species is 2 mg/m^3). As the aerosols get released into the atmosphere, they will be transported by the wind in the downward direction and get deposited along the path. If sodium aerosols remain in hydroxide form and cause exposure to humans, it is hazardous, but if it is in carbonate form, the concern is reduced to a great extent. So the quantity of sodium aerosols and quantitative information on chemical species present in the aerosols in a given sodium fire event is important for SFR safety studies. Hence it is proposed to undertake a study on atmospheric dispersion of sodium aerosols. The study comprises of (i) burning 50 kg sodium in a open environment, (ii) release of aerosols through a 10 m stack, (iii) measurement of aerosol parameters in the downwind direction upto 1 km, (iv) apply the results for particulate dispersion codes in order to validate the model and (v) evolve a suitable model to predict site specific dispersion characteristics for a given sodium fire event.

Fig. 1 Sodium burning facility

The study was conducted in two phases. The phase-1 was conducted as a feasibility study in which, 5 kg of sodium is burnt in open environment, aerosols were released at the ground level and sampling was carried out upto 50 m distance.

The phase-2 experiments were conducted by burning 50 kg sodium in an exclusive facility and aerosols were made to release through 10 m chimney (Figure 1). A mandatory safety report was prepared for (i) sighting the facility, (ii) sodium burning procedure and release of aerosols and (iii) sampling characteristics and the same was duly got approved from the IGC-Safety Committee. As per the site meteorological data analysis of long term observations, sodium burning facility was constructed at Edaiyur bridge side for the release of sodium aerosols to study the dispersion characteristics upto 1 km range when the wind direction is from south.

The aerosol sampling was carried out by using both off-line and real time instruments which include (i) filter paper sampling system (low volume, high volume and large flow rate), (ii) chemical speciation sampling system, (iii) Impactor, (iv) fall out collection trays,

Fig. 2 Layout for aerosol samplers

(v) quartz crystal microbalance (QCM) and (vi) optical particle counter (portable powered with battery). Important weather parameters were obtained from a meteorological observation station, which is already in operation at the site. Based on weather condition, a sampling layout is drawn which is of 30° field sector with central line at 170°N having origin at the release point. The sector is divided into various arcs of radii 50, 100, 200, 300, 400, 500, 600 and 700 m and sampling stations were earmarked using GPS coordinate system (Figure 2). The sampling stations were identified using GPS instrument and about 110 samplers (in total) were deployed in the field.

The aerosol sampling systems such as, low volume, high volume, and chemical speciation samplers were powered with UPS (uninterrupted power supply) source and their operation was controlled by radio frequency network. The large flow

Fig. 3 Sodium aerosol release
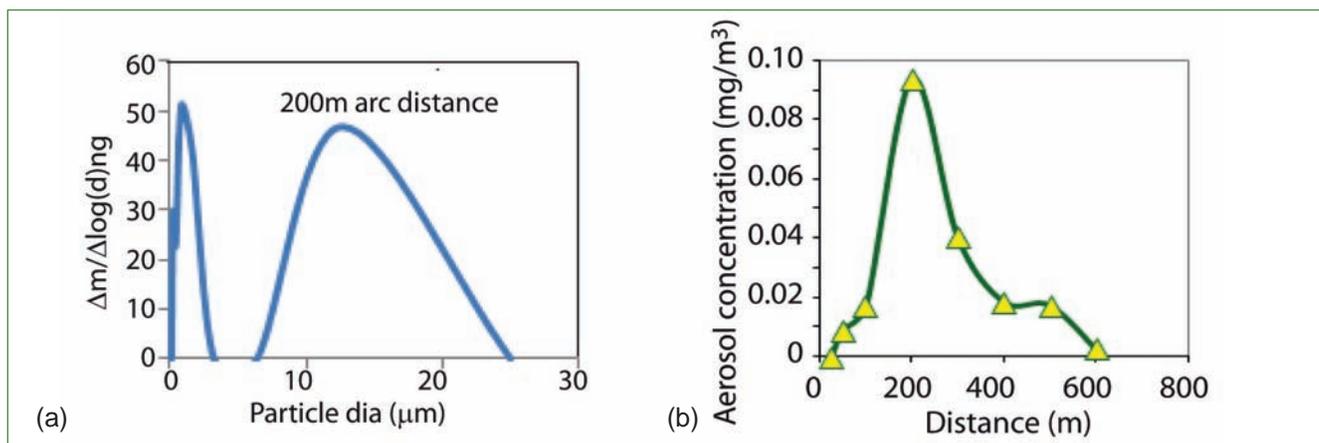
Fig. 4 *(a) Mass size distribution and (b) at 200 m distance and aerosol concentration as function of distance*

rate samplers and QCM were powered with mains power supply.

A trial experiment with 5 kg sodium burning, followed by two experiments with 50 kg sodium burning were carried out. The first burning experiment was carried out during the summer season (May 21, 2013) and the second experiment was conducted during autumn season before the on-set of NE monsoon (October 01, 2013). Figure 3 shows the photograph of the aerosol release through the chimney.

It was found that about 30-40% of sodium was burnt with release rate of ~3 g/s. The particle size distribution was measured as bimodal with lower mode around 1-3 µm and upper model above 10 µm along the downwind direction (Figure 4 a). The highest aerosol mass concentration of $0.9 \, mg/m^3$ was measured at 200 m distance from the release point (Figure 4b). The theoretical prediction by FLEXPART (particle dispersion model) (Figure 5a and 5b) was found to be close in all measured points (100-600 m distance) except at 200 m location where measured value is twice that of predicted value. The aerosol deposition on the ground between 50-700 m distances was found ~ 7% off the total quantity of aerosol release. Considering the wind velocity as 6.6 m/s (at the time of experiment) within 100 s the 90% of the species remain converted as carbonate. However, the reported chemical species was bi-carbonate species.

Two experimental runs were conducted successfully and theoretical prediction of sodium aerosol dispersion by using both FLEXPART and GPM model has been compared with experimental values. Further experiments (two runs) are planned after NE monsoon in March, 2014 to obtain site specific particle dispersion model including lateral dispersion.
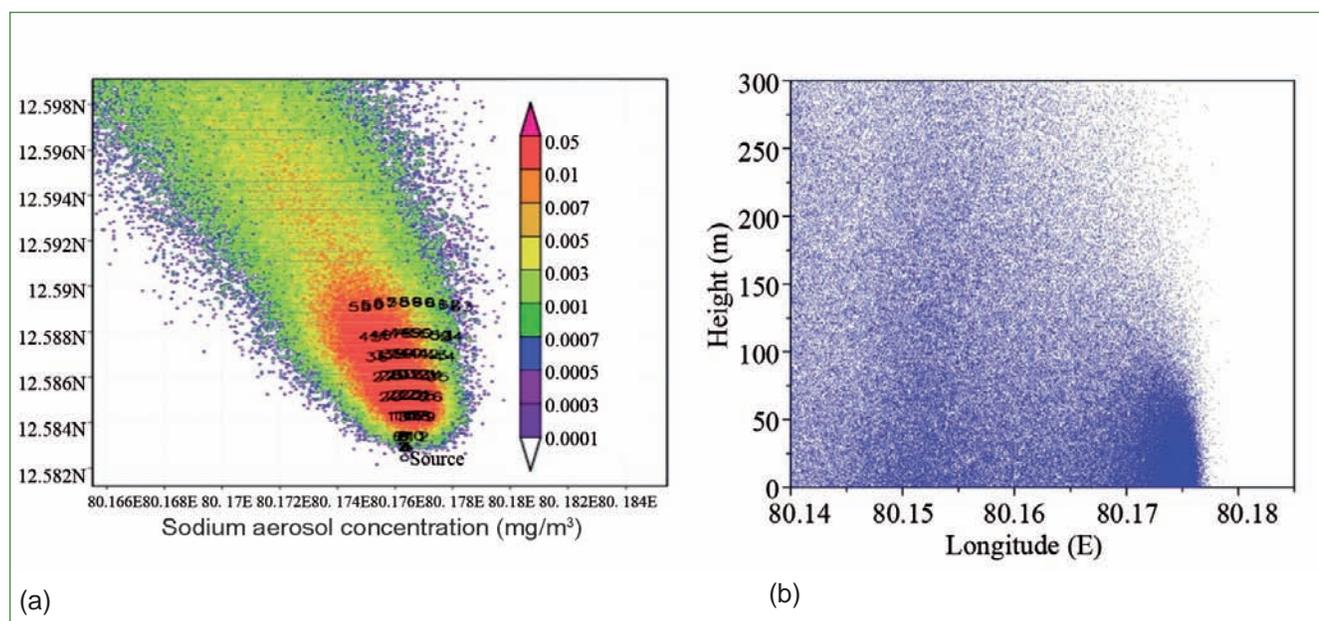
Fig. 5 *FLEXPART prediction: concentration on the ground and vertical particle distribution (a) sodium aerosol concentration (mg/m³) and (b) cross section along the aerosol plume*

VI.19 Environmental Radiation Monitoring in Ocean Side of Kalpakkam Coast

DAE site Kalpakkam, encompassing several operating nuclear facilitates is enclosed in a strip of land between the Bay of Bengal on the east and Buckingham Canal on the west. Approximately about 50% of the Emergency Prone Zone (EPZ) area around the plant lies in the Bay of Bengal. In order to assess the radiological impact of routine and accidental releases from a nuclear installation, it is necessary to know the concentration of radionuclides and dose rate profile in both, land and ocean areas surrounding the nuclear island. As the land program is in operation on 24x7 basis by using continuous radiation data loggers (gamma tracers), a unique dose rate measurement campaign has been conducted for the first time, on the sea side using gamma tracer (GT) instrument.

The main objectives of the radiation measurements over the Bay of Bengal is to generate baseline dose rate around the Kalpakkam site, These measurements are part of the regulatory requirements and the data was used as input during the process of MoEF clearance of major projects at Kalpakkam.

A GT is a GM detector based unit, having built-in power supply, battery operated and a data logger. It is portable and enclosed in a hermetically sealed weather proof casing. The system can operate with its internal battery for a period of 3 to 4 years. The sensitivity of the instrument is 2.6 cps/mGyh^{-1} and the measuring range is 20 nGyh^{-1} - 10 mGyh^{-1}. The archived data can be transferred through IR-transceiver DataGATE module (embedded Web Server) and analyzing software

Fig. 1 *Survey covered at Kalpakkam an extent of about 6 km into sea and about 18 km across*

was used for the analysis of the data gathered for their graphical visualization.

In this campaign, two GTs were used; one to measure the radiation level over the sea and at the other inside the water at about 10 meter depth. During the measurement, instrument is immersed in the sea for five mintues to measure the radiation levels at a rate of one minute. The boat was anchored at selected locations as indicated in the Google Map and dose rate measurements were obtained. The measurement started from the location 1 at Sadras and proceeded as indicated through the continuous line in Figure 1. The survey covered an extent of about 5 km into the sea and about 18 km across.

Figure 2a shows the installed GT on the boat surface to measure the dose rate above the water level. Figure 2b shows the photograph of the gamma tracer being lifted from the ocean after making measurement at one of the location.

The archived data of one minute from the GT is downloaded through an infrared reader onto a laptop. The data can be easily downloaded
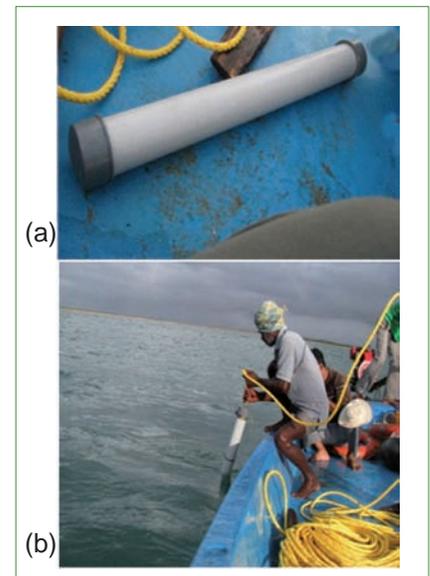
Fig. 2 *Gamma tracer (a) placed on the boat and (b) lifted from the water*

by giving default IP address and net mask address of network interface card and DataGATE module.

The observed dose rate levels of Bay of Bengal of Kalpakkam region over the ocean was found varying in the range of 50-60 nGyh^{-1} and at 10 m depth varying in the range of 35-40 nGyh^{-1}.

It is observed that the dose rate values over the ocean are found less when compared to land measurements (Figure 3). It is due to the contribution from the terrestrial components is less on the ocean surface whereas the contribution from the cosmic ray is less at 10 m depth.
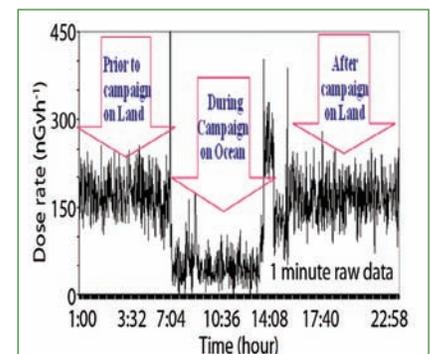
Fig. 3 *In-situ dose rate measurements*

VI.20   Phosphorus Speciation in the Coastal Sediments of Kalpakkam Coast

Sediment plays an important role in the overall nutrient dynamics of the coastal marine ecosystem. It is known that the sediment of the coastal system can act as an internal source of nutrients for the overlying water column. Among other nutrients, phosphorus has been recognized as the most essential and critical nutrient in the terrestrial as well as coastal aquatic environments for controlling marine primary productivity. Though, a considerable amount of work on physico-chemical characteristics of Kalpakkam coastal waters has been carried out, studies on nutrient content in sediment in particular are lacking. To bridge this gap, a work programme on phosphorus in marine sediment has been initiated. Thus, a study was designed with the following objectives: (1) to investigate the distribution pattern of major P species (LoP- Loosely bound P; AlP- Aluminium bound P; FeP- Iron bound P; CaP- Calcium bound P) in the surface sediments, (2) to find out the bioavailable fraction of P and (3) contribution of organic P (OP) to the total P (TP) content.

To find out the distribution of various fractions of phosphorous in the marine sediment during pre-northeast monsoon period samples were collected from ten locations (Mamallapuram-M1 & M3; Edaiyur backwater- E1 & E3; MAPS Jetty- J1 & J3; Sadras backwater- S1 & S3; off Palar river- P1 & P2) covering ~80 sq. km of the inner shelf coastal region (Figure 1a). Sedimentary parameters such as sand, silt, clay and organic carbon percentage were analyzed in order to find out their relation with various phosphorus fractions. The sediment was found to be predominantly sandy in nature
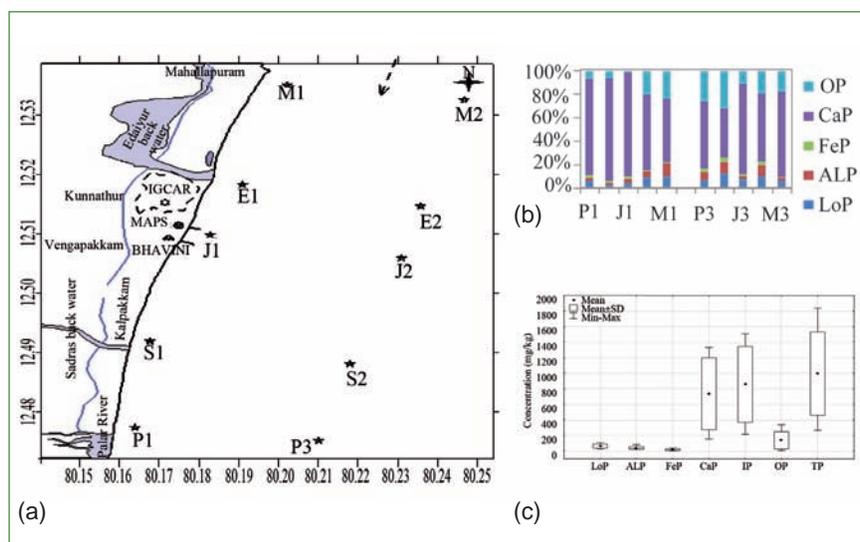
Fig. 1 *(a) Map of study area with sampling locations, (b) percentage contribution of different fractions of phosphorus and (c) variations in contents of different fractions of phosphorus in the coastal sediment of Kalpakkam*

with low silt and clay content. Contribution of LoP to TP was 7.5% at 63.6±27.2 mg/kg. Except Edaiyur transect, the LoP values increased towards off shore region with comparatively high mud percentage as compared to the near shore locations. AlP ranged from 21.9 to 84.8 mg/kg and it contributed 5.3% of TP content. The spatial variation of FeP increased towards offshore except at Sadras and MAPS Jetty, which showed reverse trends. FeP constituted 2.1% of the TP content. As Fe/Al-P concentrations were directly proportional to the amount of fine grain sediment, the low levels of Fe/Al-P found in this coastal area were therefore attributed to the sandy nature of the sediments. CaP was found to be the dominant form of fraction of P in this region, with most of the value exceeding 70% (average 68.7%) of TP. The spatial distribution of CaP fraction showed decreasing trend towards offshore except in the Mamallapuram transect. The IP content was found to be the dominant portion as compared to the OP content at this

location and contributed 83.7% of the TP. OP contents (avg. 16.3%) showed increasing trend towards offshore except in the Edaiyur transect. The TP contents ranged from 268.5 to 1839.0 mg/kg with an average of 997.8±535.4 mg/kg. The present study area being an open shallow coastal environment that supports turbulence and mixing, LoP and OP can be considered as potentially bioavailable fractions, which contributed from 5 to 44% (average 23.8%) of the TP during the present study. The order of abundance of the major forms of P in the marine surface sediments of Kalpakkam was as follows: CaP > OP > LoP > AlP > FeP (Figures 1b and 1c). Results of the present study on P content in Kalpakkam coastal sediment were found to be significantly lower than that of Mumbai coast and indicated relatively clean nature of Kalpakkam coastal sediment. The present study encourages future intensive research to elucidate the role of different seasons in speciation of phosphorus in Kalpakkam coastal sediment.

VI.21 Shoreline and Beach Profile Studies along Kalpakkam Coast

Shoreline or coastline is the boundary between land and sea which keeps changing its shape and position continuously due to the prevailing dynamic environmental conditions. Coastline changes have attracted more focus in recent times since they act as important environmental indicators that directly affect coastal economic development and land management. The change in shoreline is mainly associated with waves, tides, winds, periodic storms, sea level change, erosion, accretion and human activities. Waves change the coastline morphology continuously and form the distinctive coastal landforms. Similarly, the beach profile is equally important because it acts as an effective natural mechanism, which causes waves to break and dissipate their energy. Thus, monitoring changes in shoreline and beach profile helps to identify the nature and processes that caused these changes in any specific area, to assess the human impact and to plan management strategies.

A study was carried out at Kalpakkam coast from February 2012 to March 2013 to find out monthly shoreline and beach profile changes. Three parameters such as shoreline variability, cross-shore beach profile measurement and grain size distribution were monitored on monthly basis. In our study, shoreline refers to the first berm during spring low tide, while moving from foreshore to backshore. The change in beach profile was measured every month during spring low tide between the high water line of landward shift and seaward shift. About 18 km of the coastal belt from south end

of Kalpakkam Township to north of Mamallapuram was covered during this study. Totally 28 cross shore profiles were taken during every month. The data collected was processed by using Trimble and Arcview GIS software. Results showed a significant monthly change in shoreline positions during the study period (Figures 1a to 1e). On an average the change in beach width varied about 40-50 m. A minimum distance of about 10m was observed between the boundary wall and the shoreline near the north of Edaiyur backwater mouth (Figure 4), whereas, the maximum distance between the boundary wall and the shoreline (~40 m) was observed at Kalpakkam Township. Maximum variation of the shoreline position was observed at north of MAPS Outfall area. Change in beach volume and beach width for every beach profile was calculated by the help of BMAP software (Beach Morphology and Analysis Package). The results showed that the beaches along this coast varied from extremely gentle to slightly steeper slope, showing dissipative to reflective nature of the beach. Monsoonal changes were found to be the main reason behind such observations. Grain size was analyzed by sieving beach sand in automatic sieve shaker in half phi (Φ) interval. Grain characteristics such as central tendency, sorting, kurtosis and skewness were estimated using GRADISAT software. The mean grain size distribution of the beach sediments observed was coarser to fine. The spatial mean size distribution showed foreshore sediments having coarse grains than back shore and mid-shore. The beaches were found to be well sorted, moderately
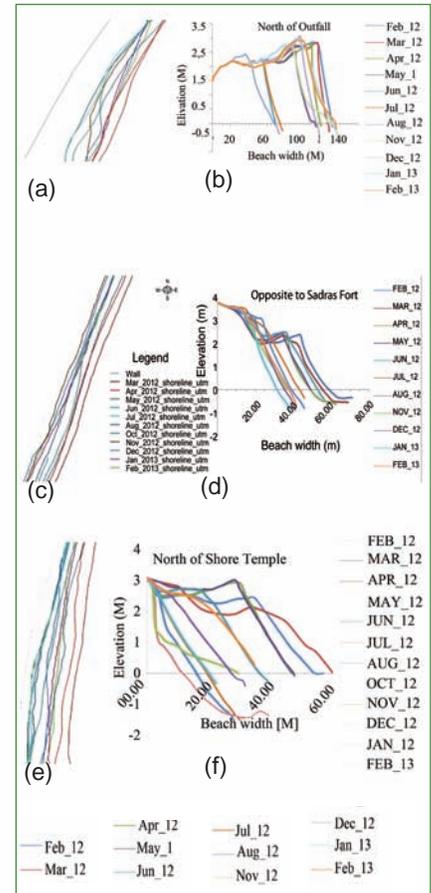
Fig. 1 *Variations in shoreline and cross-shore beach profiles near (a)&(b)outfall of MAPS, (c)&(d)Sadras Fort, Kalpakkam coast and (e)&(f)Shore Temple, Mamallapuram*

well sorted and moderately sorted sediment environments. Sediments were identified as fine skewed to coarser skewed with platykurtic, mesokurtics and leptokurtic charters.

Fig. 4 *Beach erosion near Edaiyur watchtower and seepage of seawater through the IGCAR boundary wall*

VI.22 Integrated Distress Alarm System for Radiological Facilities of DAE Kalpakkam Testing Facility

DAE Kalpakkam complex being a multi facility site, AERB recommended for an Integrated distress alarm system (IDAS) comprising all the nuclear facilities like MAPS, FBTR, RCL, RDL, KARP, WIP, PRP, BHAVINI etc. with connectivity to main control room (MCR) and auxiliary control room (ACR). Towards this SES/ EIRSG has developed TCP/IP based nodes using ARM processor LPC2478 with ALARM, TEST and ACK input switches, hooter and LED outputs. All these nodes will be placed at various radiological facilities and will be connected to dual redundant main control room and auxiliary control room servers and communicate with each other over ethernet local area network as per the architecture shown in Figure 1. The functionality of the input switches when pressed is as follows.

ALARM

The corresponding node LED indicating the threat location glows and hooter sounds in remaining
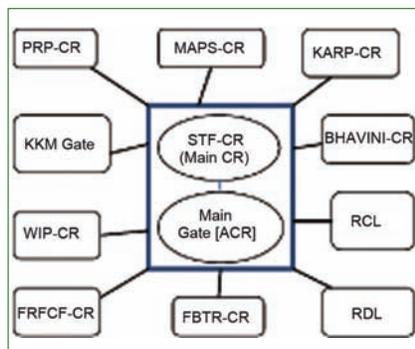
Fig. 1 *Architecture diagram of Integrated distress alarm system*

Fig. 2 *Distress alarm system demonstration with two nodes*

nodes other than the originating (where it was pressed) node.

TEST

The healthiness of the nodes is checked.

ACK

The threat scenario is acknowledged and hooter mutes in the acknowledged node but the LED continues to glow.

On the graphical user interface(GUI) screen of main control room and auxiliary control room server personal computers all these nodes are displayed by means of labels

with background colour indicating the status. GREEN indicates that the node's connectivity is fine; RED indicates a threat in that node; YELLOW indicates that the node is not connected to the server personal computers. This system with three nodes was designed, fabricated and functionality was demonstrated to High Level Security Committee (HLSC). HLSC consented for fabrication of distress alarm modules for all the radiological units within the complex.

VI.23 Development of Knowledge Management Portal

Knowledge Management (KM) has various dimensions like people, process, technology, knowledge and return on investment. Technology is the visible dimension of KM and is implemented in the form of a portal. To make the portal more effective it needs to be integrated with the work processes. As a prototype, development and implementation of such a portal has been

undertaken in Computer Division (CD) and integrated with many work processes. The usage of the portal can be extended to other divisions of IGCAR. This portal is expected to streamline the work processes, act as repository of knowledge and thus enabling knowledge preservation, enhance the knowledge sharing culture and hence improving the overall performance of the division. The portal is web based, and all

employees of CD are made users with different privilege levels. The portal facilitates the users to view, edit and upload their knowledge assets and carry out various divisional activities.

The KM portal commissioned in the Intranet and linked to IGCIMS, the IGCAR information & knowledge management system. The specific modules pertaining to CD are protected by username/password.

The overall structure of the portal is depicted in Figure 1 and the major modules implemented are discussed in the following sections.

Document management

This module provides the facility for the users to upload their documents, based on the defined knowledge taxonomy along with the required meta data. The uploaded documents can be viewed by the users based on access privilege (All/Division/Section) specified by the author of the document. A facility has been provided to view and rate the documents. The average rating of the document and the number of people accessed the document are displayed in the documents table. Multiple rating of the document by the same user is prevented. Document search facility is also provided to search the desired document based on year, document type and author.

Expertise management

This module shows the consolidated information of the employee which consists of publications details, monthly reports, projects handled, indents/work orders, projects guided etc. Knowledge sharing index based on documents uploaded to the portal and knowledge utilization index based on the documents accessed is also displayed.

Monthly reports

Online submission of monthly reports is facilitated by monthly reports module. Using this module, users can log their daily work. Daily logs can be used for preparing monthly reports. This monthly report can be viewed by the respective employees and their reporting officers only. The user can access all his/her monthly reports at any point of time to prepare annual or quarterly reports. The section heads can view the monthly reports
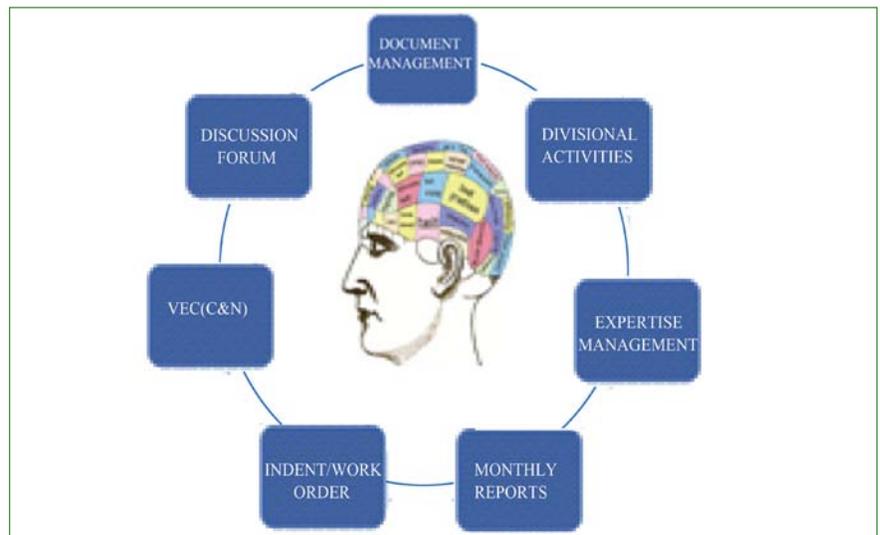
Fig. 1 *The overall structure of the portal*

of their respective sections. Division Head, Group Director and Director, IGCAR can access the monthly reports of all the employees.

Discussion forum

This module facilitates an online discussion between the employees of CD. The forums are created based on defined knowledge taxonomy and knowledge sharing communities. The members of the forum can post a new topic and allow the remaining members to post their views. A mail alert facility has been provided to send an alert email to corresponding employees of that forum, whenever a new topic is posted.

VEC (computers & networks)

This utility to facilitate the indentors to prepare the VEC form. The indentors have to enter their IC number to log in and fill the VEC form and upload the soft copy of the indent. They can also check the status of the indents submitted to the VEC. The uploaded VEC forms with scan copy of the indents can be viewed by the VEC members. The VEC members can access the previous VEC meeting details like the indents submitted and their status. Facilities are provided for the VEC secretary to update the status of the indents and to prepare the VEC meeting minutes.

Data and information management

Various data and information management utilities have been developed to keep track of the activities of Computer Division. This includes divisional activities in module, indents/work order module, annual maintenance contracts (AMC), expenditure of Computer Division, gate pass module, PRIS-G projects module and research scholars/project students module.

In addition to the above modules, facilities are provided to upload divisional quarterly progress reports, divisional meetings MOMs, Motivational documents etc. In the portal home page information regarding monthly reports, extra hours of CD employees, indenting officers list etc. are provided. Visitor counter is implemented. User feedback module and help file are provided. Modules to keep track of the visitors to CD, meetings that take place in CD meeting room are also developed. The details of CD vision committee, community of practice and CD Knowledge Module task force are also provided in the portal. The portal is used by many employees of IGCAR in addition to employees of CD. The usage statistics indicates more than 1000 usages per month.

VI.24 Introduction of Solar Steam as an Alternate Energy Source at IGCAR for Auxiliary System Application

To overcome the large deficit in supply and demand of electrical energy, harnessing the abundant solar energy available as conventional energy source is one of the alternative. Solar concentrator was introduced in IGCAR as a step towards this direction. Parabolic solar dish (Figure 1) is installed at Southern Cafeteria (SC) for the production of steam which is utilised for the cooking purpose.

The solar rays are focussed by means of parabolic concentrator to an absorber coil and the heat energy is utilised for cooking applications at the Southern Cafeteria, IGCAR. The present system has been designed considering the various aspects including the available technology and maintainability. The system replaces 18 kW electric heater and is expected to result in an annual energy saving of 21600 units apart from reducing green house gas emission.

Solar incident radiation in Tamilnadu is about 1 kW/m^2. It varies from morning to evening and from one season to another season. After taking a conservative value for the incident solar radiation, around 80 m^2 reflector area is provided by the solar grade mirror which is required to generate equivalent of 18 kW electrical output. This is provided by five numbers of reflectors with each having 16 m^2 reflective area. These reflectors capture, reflect back and focus the solar radiation to an absorber disc (containing absorber coils) through which cold water is circulated. The steam generated in the absorber coils is led to steam drum. The steam pressure depends on the temperature and is limited by automatic control. The

system is capable of producing 25 kg/h steam if minimum required solar radiation is present. The steam pressure is limited to 9.5 kg/cm^2 by defocusing action. A pressure regulator maintains the downstream pressure to 3.0 kg/cm^2 and directly fed to steam cooking vessels of 250 litre capacity. The solar concentrator installed at SC is shown in Figure 1.

The major components of the system are parabolic reflectors & its PLC based tracking system, solar absorber coils, Steam drum and pressure regulating system.

Solar grade mirror made from low iron content float glass has been utilised for the manufacture of parabolic reflectors. It provides reflectivity of about 0.92 without any appreciable degradation for ten years. It has silver reflective coating to ensure better reflectivity. A gearbox with AC motor and PLC system is used to move all reflectors from east to west direction from morning to evening time to ensure that reflectors continually face the solar incident radiation. Tracking system is automatic in E-W direction. N-S seasonal adjustments have to be done manually. The chemical control of the water is being maintained by the softener plant. The softener plant reduces hardness below 10 ppm (Figure 2).

The softened water is pumped to the steam drum by feed water pump and it operates based on the drum level. The water from stem drum flows through the absorber coils and picks up heat and flashes to steam drum. The steam pressure is controlled by the PLC system and ultimately limited by the pressure relief valve. A data logging system is

Fig. 1 *Solar dish at southern cafeteria*

provided to monitor and record the solar incident radiation and other critical parameters. UPS supply is provided to this system with a back up storage of thirty minutes.

The control and instrumentation system is designed to protect system against abnormal events. In case water level drops below the desired level, system will turn to safe configuration. The safety valve in the steam drum is set at 10.5 and 11 kg/cm^2. The system is tested, commissioned and is in operation to meet the steam requirement of SC. The system can replace the conventional steam producing system in order to meet auxiliary steam requirement of Centre.
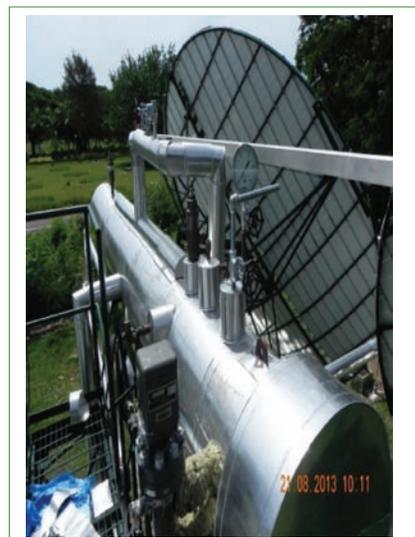
Fig. 2 *Steam drum and its auxiliaries*

VI.25   Improved Electrical Protection System with Enhanced Safety Features by the Introduction of Numerical Relays

The introduction of numerical relays in place of conventional electromechanical relays (EMR) created a revolution in the electrical protection system. IGCAR has taken a systematic approach in a phased manner towards this. In 2006, after initial trails and successful implementation, it was decided to introduce it in other substations. Thus the 33 kV new central switching station (NCSS-2), 33 kV & 11 kV central switching station (CSS), PDC-V & DFRP substations were provided with numerical relay for protection.

The latest version of the numerical relays are of programmable type and provide complete protection in addition to control and monitoring. It improves the reliability of protection and enhances the capability of trouble shooting and fault diagnosis. The communication capability of these relays helped for remote monitoring and data transfer. It offers an added advantage of multi-function capability and multiple characteristics. Numerical relays offer several advantages in terms of protection, fault diagnosis, logics etc. In case of instantaneous over-current relay there is no intentional time delay and circuit breaker trips instantly. In case of normal inverse, very inverse, extremely inverse and long inverse over-current relays, the inverse current-time characteristics are stored in the memory of microprocessor in tabular form called look-up table. Special logics could be developed and implemented in IGCAR with

the help of numerical relays to achieve better relay coordination. Tripping time could be brought down and spurious tripping could be avoided by proper current discrimination.

In case of graded protection the fault clearing time is more and can cause damage of the equipment involved namely, transformer, cable, cable joints, switchgear etc. This is a major disadvantage in providing grading in protection system. There is no way to overcome this problem with electromechanical relays. When using numerical relays, location of fault can be identified with the help of communication between numerical relays. Maximum tripping time of 60 ms instead of 1.3 seconds could be achieved by establishing communication between numerical relays for fault occurring anywhere in the system.

With different types of relay characteristics, it is possible to provide better matching of protection characteristics since these characteristics are stored in the memory of the microprocessor. Step value for current, voltage and time is very less and hence sensitive setting is possible.

The auto resetting feature of relay is an added advantage of numerical relay compared to electromechanical relays. Numerical relay is having the added advantage of compactness in size and uses indication on liquid crystal display.

The microprocessor based relay enables easy interface with

Fig. 1 *Central switching station panel with numerical relay*

digital communication equipment and usage of optical fibre cable for communication. As the relay hardware consists of standard modules, maintenance is easy. The burden offered by the relay is low and hence the burden on the current transformer. It is possible to achieve precise setting and fast response with these relays.

By combining several functions in one devise, numerical relays offer cost advantage compared to electromechanical relays. However the relay had other limitations such as common mode failure which make the protection ineffective. The relay may operate for the externally-sourced transients also. Figure 1 shows the central switching station panel with numerical relay.

VI.26 Six Sigma Approach for Quality Management System in HEPA Filter Testing Facility

Six Sigma is a methodology for pursuing continuous improvement in customer satisfaction and profit. It is a management philosophy attempting to improve effectiveness and efficiency. Under a Six Sigma programme, members of the laboratory are assigned specific roles to play, each with a title. The members of the laboratory are defined as viz. team member, team leader and owner. The defined methodology adopted for its operation is PDCA (Plan Do Check and Act) cycle. The technical tool adopted in the management is (i) Identify the customer requirement, (ii) Define a process map, (iii) Review of data/ process, (iv) Implementation (v) Improve effectiveness and efficiency by route cause analysis and (vi) Analyze and include peripheral inputs. This highly structured format is necessary in order to isolate and eliminate variation or defects in the operation, which results fail safe mechanism for the goal it sought for.

Six sigma approach for QMS in HFTL

The Policy

HFTL is committed to provide services in the field of testing HEPA filter banks, Clean rooms and Iodine Filter banks in various facilities with high credibility and integrity, which consistently satisfy the needs and expectations of our centre. The objectives are met by the involvement of all the staff with a well defined series of procedures which streamlines a fail proof system.

The organisation

The owner is the Head of the Division, the Team leader is OIC and he is designated as Quality Manager and the team member comprises of Technical Manager and Technical coordinators.

Process map

High level of quality in testing is achieved through adoption of a system of standard procedures and protocols prescribed by relevant international standards and codes. All personnel of HEPA filter testing laboratory follow systematic and uniform procedures as documented. The quality management system has been documented in four levels. Level 1: Quality manual, which describes the policies, defines the methodologies for operation of the laboratory quality management system. Level 2: Procedures, which describe who and how any activity is carried out. Level 3: Work instructions, which give the step by step instructions to be followed on testing and calibration. Level 4: Lists, formats and records to demonstrate its process.

Implementation

Implementation of process is carried out by PDCA cycle. The effectiveness of implementation is relay on the performance of the instruments. Instruments are procured with proper calibration certificates (traceability). Every year these instruments are calibrated at Fluid Control Research Institute, Palakkad, a NABL accredited laboratory. These instruments undergo inter comparison tests with other similar instruments of same nature within this laboratory or in the similar testing laboratory (Aerosol Test Facility, Centralized Waste Management Facility).

Continual improvement and elimination of variation

This is the process by which feedback from the customer is received and the needs of the customer are fulfilled. The laboratory maintains a run chart in which every process element is observed over a time, like (i) integrity of filter bank, (ii) variation of pressure in the duct and its effect on instrument reading, (iii) flow rate of the instrument etc. These process elements are taken care while doing measurements in order to eliminate the variation if any observed.

Peripheral inputs

This is a roll-up of sub processes which add value to the process. In this context, one of the key processes is to allow the customer to visit and witness the testing process and receives the inputs from the customer. HFTL implements this procedure during all its activities (in-situ testing and testing conducted in test rig).

Quality management(QM)

QM is a process to get recognition of the competence of a laboratory for specific tests and measurement. In this context, the laboratory has obtained ISO 9001:2008 certification for its effective demonstration of services through quality system elements. The laboratory has advanced further and obtained accreditation against IS/ISO/IEC 17025 by NABL (National Accreditation Board for Calibration and Testing Laboratories), India. The accreditation is the process to reflect the technical competency for the specific tests and/or measurements indicating, approved procedure, relevant acceptable national/ international specifications, range of measurement, accuracy of test results/measurement, uncertainty, etc. The distinct component for the compliance of IS/ISO/IEC 17025 laboratory management system is proficiency testing program (demonstration of measurement capability at frequent intervals) in accordance with nodal agency. The measurement capability is explained in terms of Z-score. HFTL is regularly participated proficiency

testing with CWMF. Besides, laboratory accreditation involves an independent assessment by technical experts for its performance along with assessment for the effective implementation of management system. The HFTL members and team leader are qualified with IS/ISO/IEC 17025

laboratory management system and trained for the estimation of uncertainty in measurements as per NABL procedure. The laboratory obtained NABL accreditation in December 2013, for the period of two years and had undergone two rounds of audit so far. The laboratory is first of its kind (HEPA filter bank

testing) to get NABL accreditation in India and incidentally first laboratory in IGCAR. The goal doesn't stop here; the next step is to comply with the requirements of Asia Pacific Laboratory Accreditation Cooperation (APLAC) for the international recognition.

VI.27 Entrainment and Impingement Study of Marine Fauna at Cooling Water Screens of MAPS

Nuclear power plants are one of the major users of cooling water during the process of power generation. The cooling water systems of coastal power plants have always been an important subject of study for biofouling as well as for the environmental issues such as entrainment and impingement. The entrainment of marine organisms is a concern for power plant operation because of the accumulation and clogging of the cooling circuits by these organisms. In order to understand the entrainment and impingement of marine fauna at the cooling water system of Madras Atomic Power Station (MAPS), a pilot study programme for eight months (March to October 2013) period was carried out. In this regard entrapped fauna were recorded on hourly scale at three cooling water screens of MAPS on weekly basis. The entrained specimens were categorized, weighed and observed for impingement effect.

The study shows that the major entrained groups of animals were jellyfish, crab, fish and prawn. Apart from above, a few lobsters and sea snakes were also observed as entrained entity. The numerical count of the total observations during the study period shows jellyfishes are the largest entrained group covering around 52 % of numerical counts and constituting almost 95% of biomass recorded during the study period
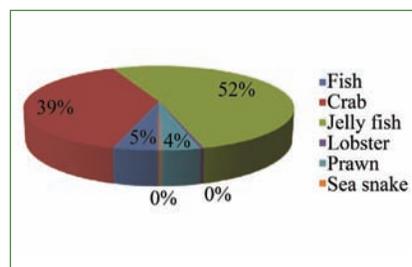
Fig. 1 *Faunal abundance of impinged organisms at MAPS cooling water system*

(Figures 1 and 2). The monthly data analysis shows large scale jellyfish entrainment during March, April, August and October (Figure 3). This is mostly due to the jellyfish bloom at Kalpakkam coast during this period. The next entrained group is crab, which numerically accounts for 39% and on biomass counts for 4% of the total entrained fauna. A total of 13 species of crabs are observed as entrained groups, of which species Menippe rumphii (Fabricius, 1798) and Charybdis lucifera (Fabricius, 1798) account for more than 90% of entrained crabs. Both the crab species have no commercial value as found from the local fisher folk. The next entrained group is fish which accounts for 5% of numerical count and mere 1% of biomass. Totally 21 number of fish species are observed. Razorbelly scad is the commonly entrained fish species. These few entrained fishes are generally small in size and have less commercial value. The other entrained group such as

Fig. 2 *Impinged faunal biomass at MAPS cooling water system*

prawns, lobsters and sea snakes are rare observations and negligible in biomass count, comprising less than 1% of entrained biomass. The monthly study trend (Figure 3) shows crab impingement declines from March to October. In case of fish the highest impingement is observed during the month of July. Similarly full moon and new moon days show more faunal impingement than other normal days of sampling.

The present data when compared with the impingement data from other coastal power plants, shows that the impinged fish biomass at MAPS cooling water system is much less than the other temperate and tropical power plants.
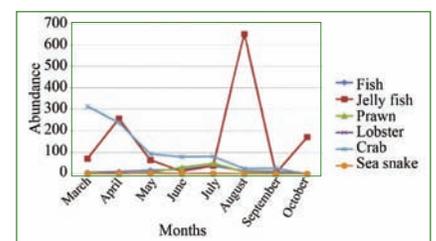
Fig. 3 *Monthly faunal abundance of impinged marine organisms*

VI.28 Seismic Qualification of PHWR Rupture Discs: Challenges and Experiences

Atomic Power Projects at Kakrapara (KAPP-3&4) 700 MWe and Rawatbhata (RAPP-7&8) 700 MWe are under construction. In this reactor, calandria vessel, moderator and the associated auxiliary piping systems are provided with appropriate rupture discs to relieve over-pressure in the system. Shake table experiments are carried out towards improving the structural integrity of this rupture disc assembly under seismic conditions. This rupture disc assembly has been manufactured by M/s. BS&B Safety Systems (India) Limited for the NPCIL projects (KAPP 3&4 and RAPP-7&8). It is made up of ASTM-A-240 type 316SS material. After visual inspection and burst pressure test qualification at the factory, one representative rupture disc assembly has been randomly selected from the tested lot further for seismic qualification as per the approved test procedure.

Seismic qualification experiments cover the resonance test followed by five operating basis earthquake (OBE) condition. These tests were conducted at the Structural Mechanics Laboratory (SML) using the tri-axial servo hydraulic shake table. The rupture disc assembly used in the seismic qualification experiment was a pre-bulged for 15NB, 1", 2" and 4" size rupture disc and pre-bulged and pre-scored type for the 20" size rupture disc. The rupture disc assembly was kept in position using with the appropriate holder arrangement. A typical rupture disc along with its holding arrangement is shown in Figure 1. The inlet of rupture disc assembly housing is connected with a
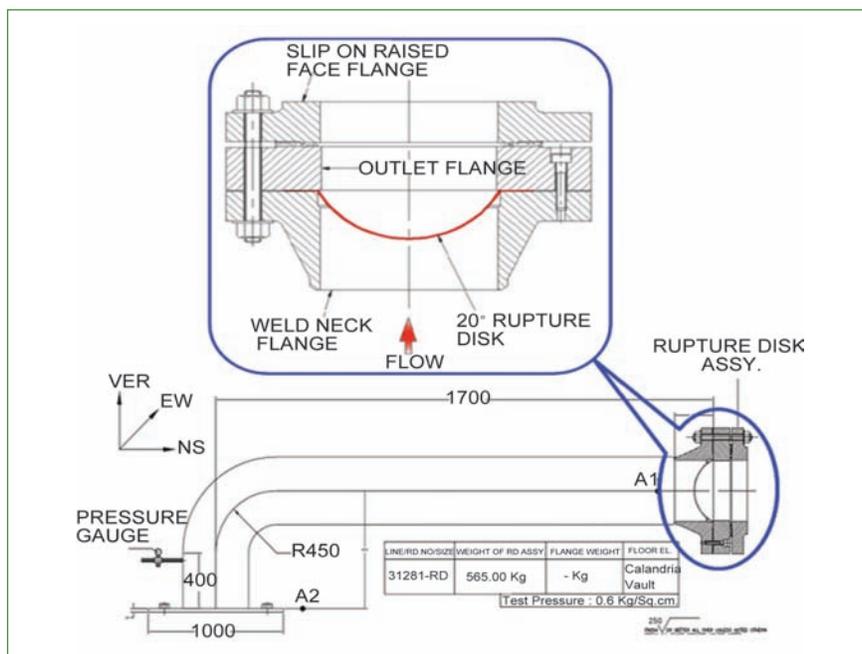
Fig. 1 *Typical rupture disc and its holding arrangement*

welded neck flange with weld edge preparation suitable for butt welding with respective pipes. The outlet side of this rupture disc assembly is connected with one outlet flange and adjacent to that a Slip On Raised Face Flange (SORF) is attached as shown in Figure 1.
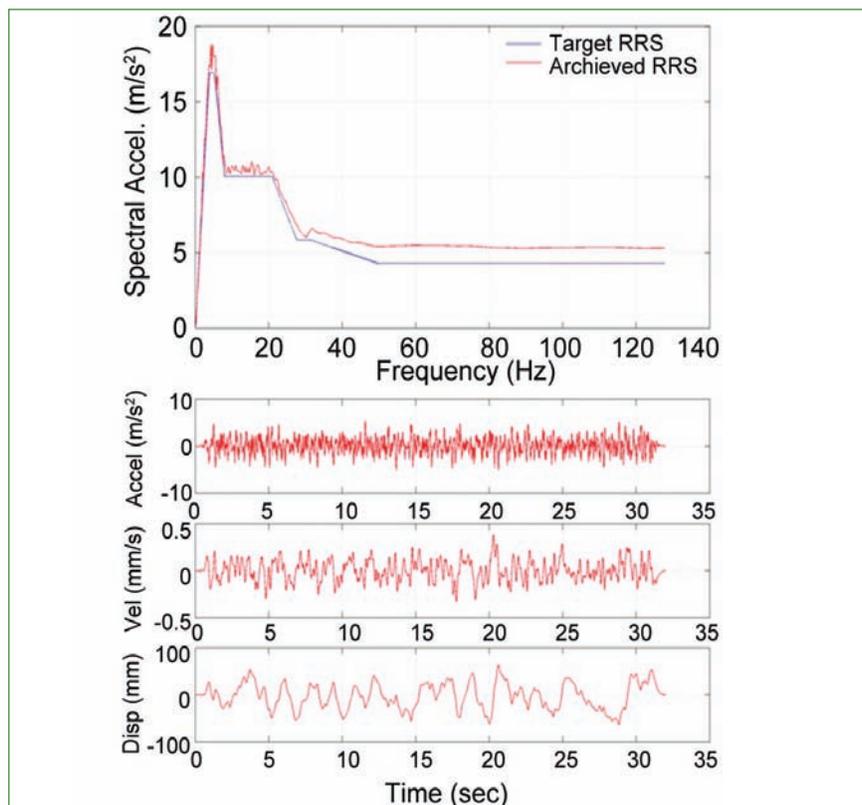
Fig. 2 *Typical spectrum compatible time history generation (TRS enveloping RRS)*

Selected rupture disc in each size has been tested for the seismic qualification. The tested rupture discs were reverse buckling in type.

The other details about the size, test pressure and burst pressure of the tested rupture disc are tabulated and given in Table 1.

The test has been conducted as per IEEE Std 344-1987: IEEE. It is the recommended practice for seismic qualification of Class 1E equipment for nuclear power generating station. The enveloped and broadened operating basis earthquake required response spectra (RRSs) for which the equipment is to be qualified for the reactor building (RB) have been used for the testing the RDs. It covers two orthogonal horizontal directions (N-S and E-W) and in the vertical direction at 5% damping. The test response spectra [TRS] for 5% damping shall envelope 10% more than the RRS for the frequency range given in the envelope floor response spectrum. The typical case is presented in Figure 2. The TRS has been generated as per Clause 7.6.1.2 & 7.6.3.1 of IEEE 344. For the purpose of comparison of TRS with RRS, TRS are calculated for a damping value of 5%. The shake table maximum peak acceleration equal to the zero period acceleration [ZPA] of the RRS. The TRS is enveloped the RRS considering only frequencies of the shake table motion time history lying within the RRS region (Figure 2). The respective spectrum compatible time history has been generated for all the three directions of operating basis earthquake is used for the experiment. These two horizontal and one vertical spectrum compatible time history motion applied simultaneously for the shake table experiment.

The seismic qualification experiments include the resonance
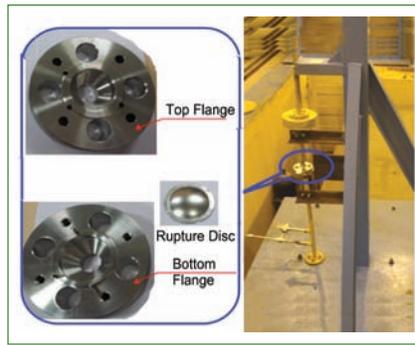
Fig. 3 *Experimental setup for the 15 NB rupture disc (small size)*

search test followed by five operating basis earthquake . The resonance search test conducted in all the three mutually perpendicular directions without pressurising the system in the upward direction (from 1 to 50 Hz) and in the downward direction (from 50 to 1 Hz). It is done by base excitation as per the clause 7.1.4.1 of IEEE 344. Subsequent to the resonance search test RDs have been subjected to five operating basis earthquake tests. While testing the RD's for operating basis earthquake qualification, the systems have been pressurised up to the respective test pressure condition as given in Table 1. Depending upon the size of the rupture disc appropriate test arrangement has been fabricated to simulate the realistic condition towards seismic qualification. The test arrangement for the small size RD (15 NB) and the large size RD (20") tested are given in Figures 3 and 4 respectively.

Tri-axial accelerometers are mounted one very close to rupture disc assembly and the other one at the support location towards capturing the test response. Seismic qualification of thin RD, which has a very less margin between the test pressure and the burst pressure was the challenge faced during this experiment. Finally very high precision small range pressure gauge was deployed for maintaining

Table 1: The test parameters about the tested rupture discs		
Size	Test pressure (kg/cm^2 - g)	Burst pressure (kg/cm^2 - g)
15 NB	0.6	0.80 - 0.90
1"	11.0	12.35 - 13.65
2"	11.0	12.35 - 13.65
4"	0.6	1.90 - 2.10
20"	0.6	1.33 - 1.47

very small test pressure, which is very close to the burst pressure. Additional supports provided which is very close to the rupture disc have been recommended for the size of 15 NB towards meeting the seismic qualification criteria. All other RD's (1", 2", 4" & 20") satisfy the applicable seismic design requirements without any additional supports.

Based on the performance found before, during and after the qualification experiments, it is certified that the above rupture disc assemblies met the specified seismic qualification criteria subject to meeting the post burs test as per approved NPCIL test procedure. Since this rupture disc assembly has completed type tests for five operating basis earthquake cycles the same will not be used in the reactor application.

Fig. 4 *Experimental setup for the 20" rupture disc (large size)*

VI.29 Innovative Standalone Instrumentation and Control Device for High Resolution pH and Oxidation Reduction Potential Measurement

An innovative approach in digital potentiometry using pulsating sensor based instrumentation is deployed to develop high resolution pH and oxidation reduction potential (ORP) monitoring device. The basic concept in designing such instrument is direct conversion of emf developed near electrode and electrolyte (here sample or test solution) interface to digital pulse frequency using a specially designed voltage to frequency converter (VFC). The relation between frequency and pH is obtained by calibration of the instrument with appropriate buffer solutions. Such a relation is used in the system software to convert frequency to pH which is displayed on the LCD monitor. For measurement of ORP, appropriate electrodes are chosen and the unit has to be operated in mV mode to give direct ORP reading in mV unit. Proper care is taken to design this instrument to meet the following requirements (i) input voltage from -1.0 to +1.0 V in order to cover the entire range of application, (ii) high input impendence, (iii) stable output frequency with respect to change in ambient temperature during measurement and (iv) high precision (<0.1 % RSD) & high resolution (0.01 mV).

In order to meet the above criteria an electronic circuit designed with a high precision VFC and a programmable instrumentation amplifier (IA) is used to measure the low voltage from the sensor in terms of frequency. A buffer is used at the sensor end to strengthen its signal and to prevent the IA from loading the sensor circuit. The circuit is designed to give a frequency output
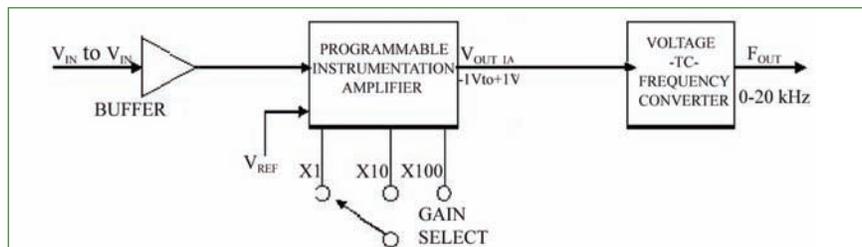
Fig. 1 *Block diagram of instrumentation*

linear to the voltage input so that the voltage measurement can be done with any frequency measuring device. The circuit includes a high precision VFC which has a very low non-linearity error of 0.005% at 100 kHz of operation and a low offset programmable gain instrumentation amplifier whose gain can be digitally selected to 1, 10 and 100. The block diagram of the circuit is shown in Figure 1. The sensor output which varies from -1 to +1V, is fed to a unity gain buffer circuit (also called as voltage follower circuit). Although the voltage gain of a buffer is unity, it provides considerable current gain and thus power gain. This output is amplified using a programmable IA. The output of IA is given by:

$$V_{OUT\ IA} = (V_{IN} + V_{REF}) * Gain$$

In this circuit V_{REF} is kept as zero volt. The user has to select the appropriate gain depending upon the output signal received from the sensor. The VFC is configured in bipolar mode providing an output frequency of 0-20 kHz corresponding to an input signal range of ±1V. The passive components of the VFC circuit must have low temperature coefficients, in order to reduce the drift in output with temperature. The output of the VFC varies linearly with $V_{OUT\ IA}$. In some of the instruments control device is also provided in order to measure as well as control pH of

solution whenever it is needed.

For pH measurement any glass electrode with reference calomel electrode commercially available is used with a BNC connector. The specific features of this pH meter are (i) can be used from 0 – 14.0 pH with resolution of 0.01 pH, (ii) calibration holds for a long time (~1 month), (iii) provision for temperature compensation, (iv) long distance signal transmission (~100 meter), (v) precision: < 0.3% RSD in entire pH range and (vi) Besides pH measurement the instrument can be used for concentration measurement of any other ion using suitable ISE. With highly satisfactory performance in many laboratory measurements such pH meter has been deployed in quality control laboratory of Madras Atomic Power Station. The photograph of pH meter is shown in Figure 2. In near future such pH meter will be deployed in FBTR for both offline and online measurement of pH.

Fig. 2 *Photograph of pH meter*

VI.30 A Novel Technique for Isotopic Assay of Heavy Water in Light Water and Heavy Water Mixtures using Digital Conductometry

Isotopic determination of heavy water finds importance in quality control of heavy water in Pressurised Heavy Water Reactors (PHWRs) as well as in heavy water production plants. Towards this a high resolution digital conductivity measurement technique has been developed for quick determination of heavy water concentration in 0-100% range using ~1 ml of sample solution with reasonable precision.

The sensing methodology is based on slight difference in the degree of dissociation of a weak acid in water and heavy water media which are isotopically different. This leads to gradual decrease in conductivity of weak acid in water and heavy water mixtures with gradual increase in heavy water content of the medium. Based on this concept the methodology was designed to monitor conductivity of a specific weak acid produced in-situ in water and heavy water mixtures of different proportions. The conductivity shift in the aqueous medium after and before formation of weak acid is a measure of isotopic purity of heavy water in the water and heavy water mixture. Appropriate precautions are taken to overcome the effect of impurities and temperature which can suppress the small shift in conductivity.

The methodology was developed by using a PTFE mini conductivity cell with a pair of stainless steel electrodes of appropriate geometry in order to measure heavy water concentration using ~1 ml of sample containing a homogeneous mixture of light water and heavy water of different proportions. To this, appropriate amounts of mannitol and boric acid solutions from the respective working standards were added in order to generate weak acid (boron mannitol complex). Before each addition the conductivity of solution was monitored online. All measurements were conducted at constant solution temperature. A polynomial relation was established using shift in conductivity and concentration of heavy water which was further used for determination of heavy water concentration of unknown sample. The conductivity measurement was carried out using a high performance pulsating sensor based conductivity monitoring instrument. The conductance cell was placed onto a specially designed logic gate oscillator and it was connected to the parallel port of PC via power supply cum signal routing unit which contained optical isolator and line buffer for signal input to PC. In this case the conductance cell constituted the resistivity part of the LGO whereas a fixed capacitor was placed as the capacitive part. The output of the LGO is a train of digital pulses of 5 V amplitudes from which, the frequency is computed. The digital pulse frequency is directly related to conductivity of solution. The relation between conductivity and pulse frequency is determined by calibration of conductivity cell. The schematic of conductivity cell with block diagram of instrumentation and the schematic diagram of oscillator circuit are illustrated in Figures 1 and 2, respectively.

The advantage of adopting this innovative conductivity measurement technique is that the primary signal from the sensor end is in direct digital form which
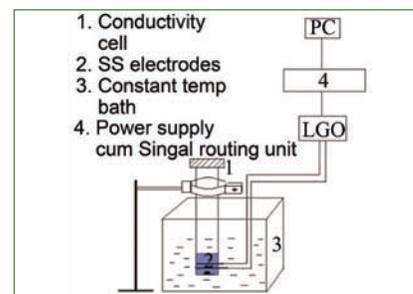
Fig. 1 *Block diagram of instrumentation*

simplifies instrumentation for analog to digital conversion. The signal loss during long distance transmission is practically neglected and it possesses excellent noise immunity. The high precision, high resolution and fast response following digital conductometry approach enabled to deploy this technique for such crucial application. Using our indigenously made data acquisition system the online data in graphic form is recorded and filed for the future use. A second degree Polynomial relation between frequency and %D_2O was established in high concentration range (>40 to 100%) with R^2 0.99934 and a linear relation was obtained in low range (0 to 40%) with R^2 0.99994. These relations were used for determination of percentage composition of heavy water of samples in the entire range of concentration (0% -100%) with reasonable precision (relative standard deviation, RSD: ≤ 1.5%). The accuracy in measurement is ≤ 1.75 %. The results obtained from the present technique agreed well with those from refractometry and infrared spectroscopy.
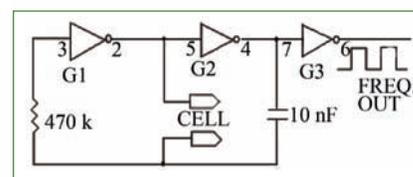
Fig. 2 *Schematic of logic gate oscillator circuit*

VI.31   Value added Information Services with Advanced Digital Library Infrastructure

Scientific Information Resource Division (SIRD) has adapted itself to the modern developments in information processing and knowledge sharing. In upgrading the digital library infrastructure at regular intervals to incorporate the latest technologies, which make its resources and services up-to-date.

Value added services in SIRD

To enhance the information resources usage, SIRD has adopted many value additions in it's information services to patrons.

- Advanced radio frequency identification (RFID) based circulation system, self check-in and check-out stations, shelf and inventory management readers and electronic article surveillance gates

- Various institutional repositories are provided to patrons like IGC publications, research articles, knowledge management documents of fast reactor, image archives etc

- Initiatives have been taken to build knowledge domains on various aspects of nuclear technology which aims
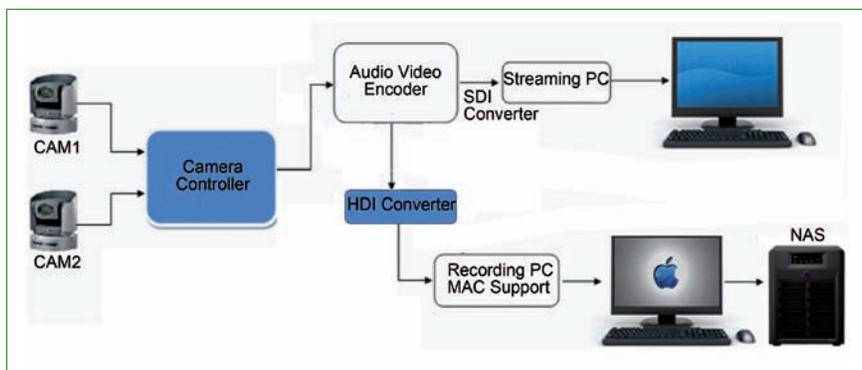
Fig. 1 Live video streaming architecture

to empower meaningful information retrieval.

Live streaming at SIRD, IGCAR

SIRD provides information as part of knowledge management initiative and has implemented the live and on-demand video streaming solution. Live streaming architecture is given in Figure 1. This aims the live streaming and capturing the technical events, symposium, eminent lectures, speeches etc. which are happening in the Sarabhai Auditorium of our Centre. Users can view the live video streaming on their desktop through intranet. These videos are uploaded in to storage area network based server(NAS) along with necessary metadata entry for

future retrieval. On-demand video streaming (off-line stream) is also provided so that the viewers can watch it at any time that suits them as shown in Figure 2.

The live video streaming facilitates creation of a dynamic video library and forms the part of organisational knowledge management. The eminent lectures, speeches and technical programmes happening in auditorium are not only streamed into user desktops, but also archived for future retrieval. With the latest high definition cameras and high performance streaming/storage servers, it is possible to have very efficient live streaming solution for the organizations. Figure 3 shows the live streaming setup at Sarabhai Auditorium.
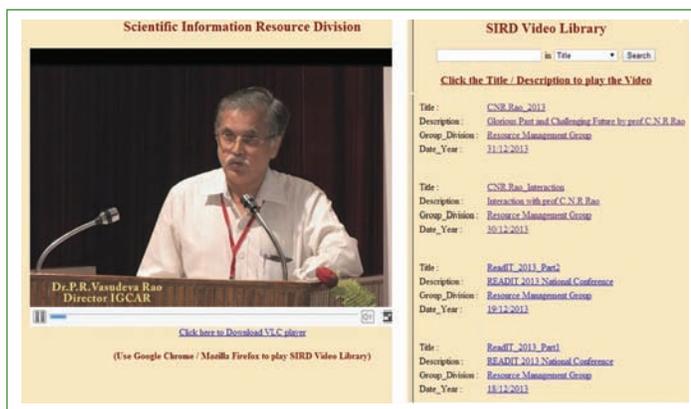
Fig. 2 On demand streaming of videos
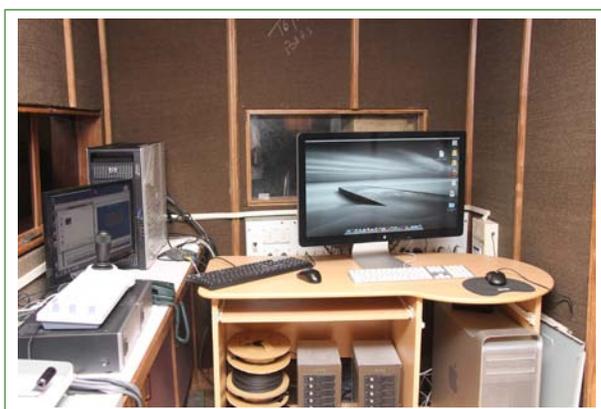
Fig. 3 Live streaming setup

VI.32   Development of Semantic Web Based Knowledge Management Portal for Nuclear Reactor Domain

Capturing the knowledge available in each domain and preserving it for the future is one of the prime objectives of knowledge management. One of the shortcomings to be addressed in this context is the lack of precision. This can be effectively eliminated by knowledge representation. In the present era this can be overcome by enabling the machine to process the available knowledge. As it is not an easy task to teach machines to comprehend natural languages, the way the information is provided to the machine has to be analysed. This is realisable by semantic web, which is an extension of current web where machine can understand the concept and process the knowledge. A initiative has been taken to develop the requisite knowledge representation for nuclear reactor domain. As a case study knowledge representation for the Fast Breeder Test Reactor (FBTR) is carried out by collecting the knowledge available from various resources.

Semantic web technology is realized through ontology. Ontology is a formal and explicit specification of a shared conceptualization. It is used to tap the knowledge of any particular domain to avoid ambiguity of terms. The major advantage with use of ontology is that it provides a globally unique identifier for all concepts. Ontology describes the concepts in a particular domain and the relationships that exists within them. It helps to share common understanding of the structure of information among the users, enable reuse and analyse the domain knowledge. For any given domain, controlled vocabulary (keywords) from that domain is taken for knowledge representation. In this respect, Resource Description Framework (RDF), Web Ontology Language (OWL), eXtensible Markup Language (XML) F-logic, ObjectLogic etc. are some of
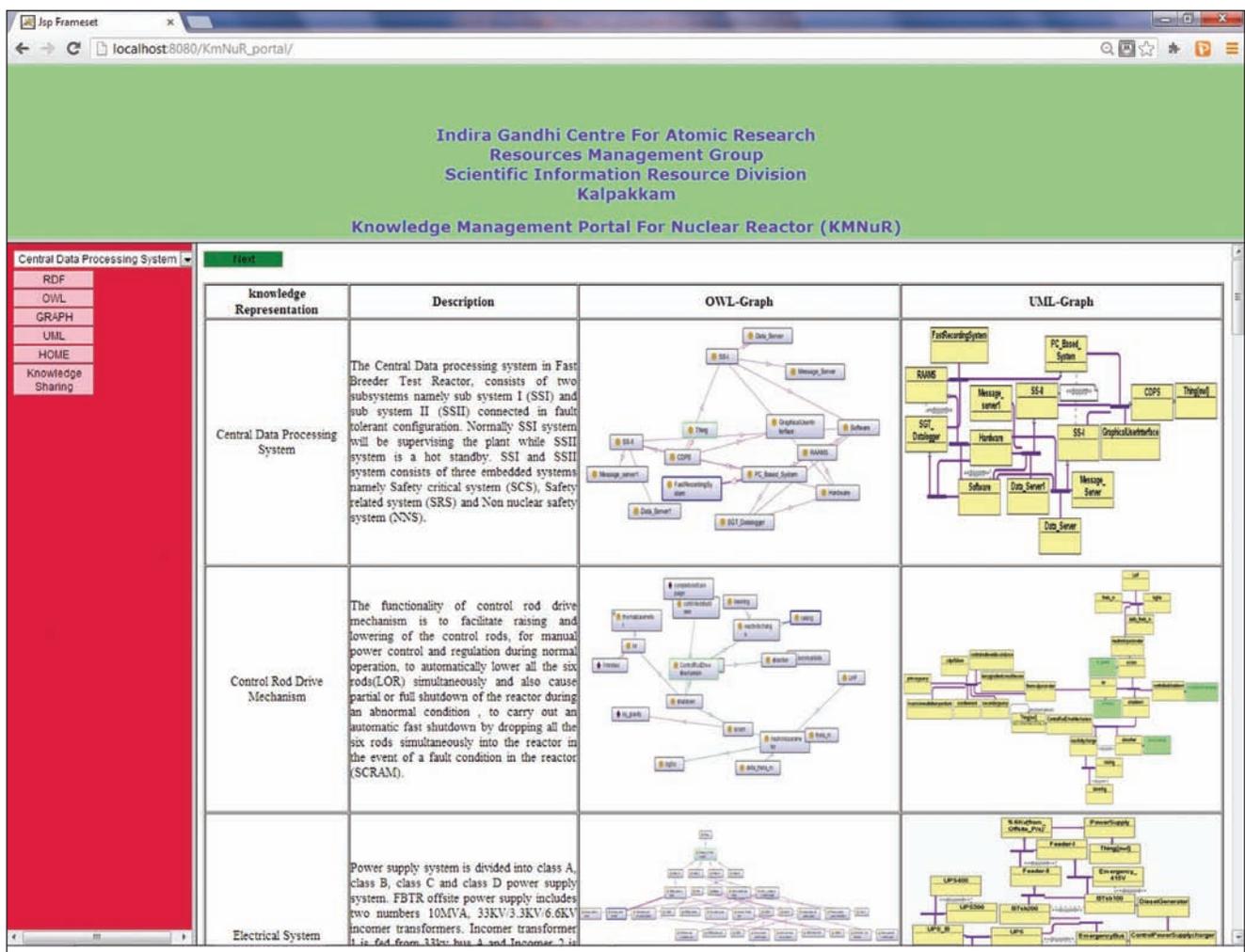
Fig. 1 *Main screen of knowledge management portal for nuclear reactor showing the knowledge representation of each system, its description, OWL_graph and UML_graph*

the languages used to feed the collected knowledge on a particular domain, to the machine.

The designed semantic web based knowledge representation portal is christened as KMNuR (Knowledge Management for Nuclear Reactor). The objective of the portal is to develop an ontology that would enable effective usage of the contents being made available to the user. The knowledge pertaining to FBTR is obtained from data sources like journals, books, internal reports, existing data in IAEA, open archives and from nuclear experts, that has been stored in machine readable languages as specified above.

The KMNuR web portal is a client/server architecture having user interface in the front end and database at the backend. The front end of the user interface, developed using the java web application allows the user to get the requisite knowledge about the FBTR from MySQL database at the backend. Net Bean IDE and GlassFish server are used for developing the Java web based application and publishing the web application, respectively. It employs tools like Protégé Integrated Development Environment (IDE) for ontology development and Ontology Editor for Compact UML-style OWL

Graphic Notation (OWLGrEd) for Unified Modeling Language (UML) generation.

The screen shot of the main page of KMNuR portal is shown in Figure 1. The left side frame of the web portal lists out the names of systems such as reactor core, control rod drive mechanism, primary sodium system and the parameters such as nuclear flux, gamma ray source, reactor steady state etc. related to FBTR.

When the user selects a particular system it provides information about it on the right side frame. RDF or UML graph or OWL buttons have been provided in the portal for enabling the user to view the acquired knowledge. Since the UML images are complex, a provision for zoom has been made to get an enlarged image. The overall aim of the KMNuR portal is to integrate and infer the semantic knowledge required by the users while carrying out tasks in the domain of nuclear reactor. By clicking the "Knowledge Sharing" menu in the KMNuR web portal, an user can upload new knowledge to the system. The user has to furnish details like title of knowledge uploaded, authors contributing the knowledge, details of the knowledge, RDF, OWL and UML format of the corresponding knowledge. Once the relevant data

is furnished, then it is submitted to the database for approval by clicking the "Submit the Knowledge" button. These data are then stored in the database. Once the administrator approves the knowledge it is added to the web portal. In KMNuR web portal, whenever the user inputs a knowledge it will be cross checked with the existing knowledge for similarity, to avoid any redundancy in the portal. If the user has submitted knowledge that is having new information then it is added to the web portal for reuse and sharing. In this effort, a Quick Mapping Evaluator (QME) program has been developed for ontology mapping. QME allows the user to select the required ontology alignment algorithm for extracting the shared knowledge. Ontology matching algorithm has been developed that aids the agent program to filter and collect the knowledge for the search, reuse and share thereby giving relevant answers to the user query. For uploading a new knowledge, OWL knowledge available in KMNuR portal is utilized. If the knowledge is not already available in the portal, the approval_status field in the knowledge database is updated. Thus the ontology matching algorithm aids the portal to avoid duplicates.

VI.33   Introduction of New e-Services in IGCAR

As part of e-governance initiative at IGCAR, a project was taken up to develop an online system which connects the functions of Administration, Accounts, Stores, Purchase and budget monitoring with all the users of IGCAR. This online system providing e-services to all the employees of IGCAR, is

termed as Automated Workflow Management System (ATOMS). This system is operational since 2010 and various services are being added periodically in the domains indicated. During the year 2013, new services have been introduced in the ATOMS, like a procedure for streamlining

the works undertaken by various agencies in the Centre, generation of quit order towards manpower accounting and monitoring of revenue budget, whose details are given in the following paragraphs.

Works Procedure

The researchers of the Centre,

working in various R&D facilities, request for execution of civil, electrical, mechanical or air conditioning works to be taken up in order to setup new facility or maintain the existing facilities. The works procedure involves a work requisition, creation of a technical sanction and finally issue of a work order (Figure 1). All these processes have been automated.

The requisition procedure includes details to describe the nature, time required and fund availability for the work. This enables to assign the work to the specialized engineer to take it forward. The automation of this procedure has facilitated ease of information transfer and also structuring of the information. Before initiating any major or minor works, it is mandatory to obtain a technical sanction to certify the purpose and allocate budget for the execution of the work. The technical sanction generation has been automated. As the requisitioner, agency performing the work, budget approval etc. is brought in one loop by virtue of automation, it helps in speedy issue of sanction. After completing the tendering process and identifying the contractor, work order has to be issued towards execution of the work. The work order form is filled online and the work order can be generated incorporating necessary conditions and clauses, case by case, is done very quickly. Printing in the appropriate format is done subsequently.

Quit Order: In order to effectively account for total manpower in the organization, entries must be made in the database at the time of joining and when the employee quits the organization, due to any event like superannuation, transfer etc., the quit order is generated. There are about 14 events leading to the separation of employee from the organisation. All the quit order
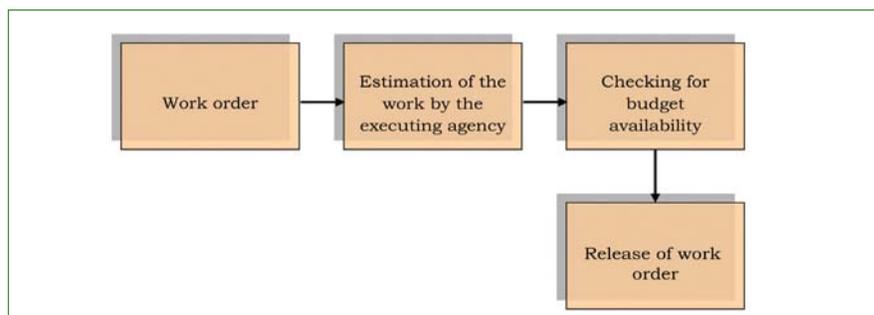
Fig. 1 *Work flow for work order generation*

forms pertaining to these events have been included and the quit orders are now generated using this automated system.

Revenue Budget Monitoring: The revenue budget is used to operate and maintain the facilities established through the capital projects. The annual revenue expenditure of IGCAR is to the tune of Rs. 280 Crores. It includes administrative expenses like salaries, travel etc., apart from Supplies & Materials (S&M) and Minor Works, which constitute about 18% of the total revenue expenditure, which is spent by the individual groups towards operating and maintaining their facilities. Since the fund available under revenue budget is scarce, a need to monitor the group-wise utilization was suggested. In order to implement, the group-wise

monitoring, the following exercise was carried out.

- Identification of revenue budget coordinator within each group
- Allocation of head of account codes to each group
- Allocation of funds to each group under S&M and minor works
- Providing the online group-wise allocation, expenditure, commitments and balance fund availability. A program was developed and hosted on plan website to show the summary and expenditure up to voucher level.

This online revenue budget monitoring mechanism helps the budget coordinators to prioritize their requirements within the allocated/available funds. It also helps towards limiting the expenditure under revenue within the approved BE/RE at the Centre level.

Fig. 2 *Screen shot of revenue budget summary*

CHAPTER
7

Awards/
Publication/
News & Events

Awards & Honours

Indira Gandhi Centre for Atomic Research had been chosen by St. John Ambulance (India), Tamil Nadu State for a Special First Aid Award in recognition of its contribution towards imparting training on First Aid to departmental employees.

IGCAR has won the AERB's Fire safety award for the Year 2012

IGCAR House Magazine " TRIVENI " has been selected for "RAJBHASHA GRIH PATRIKA PURASKAAR " for the year 2012-13 by DAE. The award will be given on the eve of "All India Official Language Conference" being organized at "The Institute of Mathematical Sciences (IMSc)-Chennai' during 16-17 January, 2014.

Dr. C. S. Sundar, MSG has been elected as APAM Academician by Asia Pacific Academy of Materials.

Dr. P. Chellapandi, RDG was awarded the "National Design Award - 2013" by National Design and Research Forum, Institution of Engineers (India) for his outstanding contributions on December 20, 2013 during the 28th Indian Engineering Congress at Chennai.

   He has been awarded the 2009 VASVIK Award by Vividhlaxi Audyogik Samshodhan Vikas Kendra, Mumbai for his contributions in the field of Mechanical & Structural Sciences and Technology.

Dr. U. Kamachi Mudali, MMG & RpG has been elected as "Fellow of ASM" by the Board of Trustees of ASM International, USA for outstanding contribution in the development and application of corrosion-resistant advanced materials and coatings for critical uses in nuclear and related industries in 2013.

   He is appointed as Member of Editorial Board of the Indian National Academy of Engineering, INAE, 2013.

   He has been conferred with prestigious "Fellow Honour" of National Association of Corrosion Engineers (NACE), USA, for his outstanding contributions in corrosion science, engineering and technology of materials used in nuclear and allied industries including academic contributions.

   He has been appointed as Member of Journal of Coating Science and Technology.

   He has been elected as "Honorary Fellow" by Electrochemical Society of India 2013.

Dr. Shaju K. Albert, MMG has been elected as "Fellow of IIM" by the Council of Indian Institute of Metals.

Dr. A. K. Tyagi, MSG has received the "Eminent Mass Spectroscopist Award - 2013" from Indian society for Mass Spectrometry (ISMAS) in recognition of his outstanding contributions in the area of Secondary Ion Mass Spectrometry.

Dr. S. Venugopal, MMG has been awarded the D.Sc. Degree by the University of Madras for his thesis entitled "Contribution to the Optimization of Parameters for Mechanical Working and Controlling the Development of Micro Structure during Hot Working of Metallic Materials".

Dr. D. Sornadurai, MSG has received the "Recognition Award -2013" from International Centre for Diffraction Data (ICDD), USA in recognition of his outstanding contributions towards solving crystal structures of many new materials and publishing them in standard powder diffraction files of PCPDF-4+2013 database.

MOON Quality Circle of Fast Reactor Technology Group, IGCAR with members Shri A. T. Loganathan, Shri D. Kuppuswami, Shri K. Mohanraj, Shri T. V. Maran, Shri A. Clement and Shri B. Babu has won Gold Medal in the Chapter Convention for Quality Circles (CCQC-2013) held at Easwari Engineering College, Chennai during October 5-6, 2013. Shri K. Mohanraj and Shri D. Kuppuswami won the First prize in debate. Shri A. T. Loganathan won the Second prize in QC Poster Competition Award.

DAE Awards

Department of Atomic Energy has instituted annual awards for excellence in Science, Engineering and Technology in order to identify best performers in the area of Research, Technology Development and Engineering in the constituent units (other than Public Sector Undertakings and Aided Institutions). The Young Scientist, Young Engineer, Young Technologist, Homi Bhabha Science and Technology Award and Scientific and Technical Excellence Award fall under this category. Group Achievement awards for recognition of major achievements by groups have also been instituted. Life time Achievement Award is awarded to one who has made significant impact on the DAE's programmes. They are the icons for young scientists and engineers to emulate. The awards consist of a memento, citation and cash prize.

The recipients of the Awards from IGCAR for the year 2012 are:

Scientific and Technical Excellence Award : Shri G. Padmakumar, FRTG
Shri Sanjay Kumar Das, RDG

Young Applied Scientist/Technologist Award : Shri Shiv Prakash Ruhela, FRTG
Shri Prashant Sharma, FRTG

Young Engineer Award : Shri Sanjay Kumar Pandey, RDG
Ms. Diptimayee Samantaray, MMG
Shri J. Kothandaraman, RpG

Meritorius Technical Support Award : Shri M. Arumugam, ROMG
Shri S. Selvam, ESG
Shri R. Devarajulu, MMG
Shri C. Ambujakshan Nair, FRTG
Shri M. Chandrasekaran, ROMG

Meritorious Service Award : Smt. Saroja Gopal, Presently at DAE, Mumbai
Smt.S. Viji, Director's Office

Group Achievement Award:

Design, Development and Manufacture of Titanium Dissolver for Fast Reactor Fuel Reprocessing
Shri B. M. Ananda Rao, RpG, Group Leader

Shri M.V.Kuppusamy, Shri Navtesh Bajpai, Shri Saju T Abraham, Shri D Kuppusamy, Shri C. B. Rajeev, Shri G. Kaliamoorthy and Dr. B.Venkatraman from EIRSG, Shri T. Karthikeyan, Dr. R.Mythili, Dr. Arup Dasgupta, Dr. Saroja Saibaba, Dr. M.Vijayalakshmi, Shri Harish Chandra Dey, Dr. Arun Kumar Bhaduri, Shri T.Nanda Kumar and Dr. U. Kamachi Mudali from MMG, Shri Sanatana Maharana, Shri S.Solomon Nesakumar, Shri S.K.Gupta, Shri T. Dinesh, Shri V.Muralikrishnan, Shri H.Humayoun and Shri A.Ravisankar from RpG

Design, Manufacture and Deployment of Passive Neutron based Alpha Waste Drum Assay System
Shri R. Amudhu Ramesh Kumar, RpG, Group Leader

Shri C.R.Venkatasubaramani from CG, Smt. R.Akila from EIRSG, Shri M. Geo Mathews, Shri E.Balu, Shri A.Palanivel and Shri P.Sivakumar, Shri Padi Srinivas Reddy, Shri K.K.Shimjith, Shri R.Anbarasan, Shri V.Anandha Narayanan, Shri Akhilesh K Nair, Shri K.Stanley, Shri Saptarsi Chaterjee, Kum.S.Usha, Shri Ch.U.Bhanu prasad, Smt.S.Poongodi, Shri N.T.Bineesh. Smt.P.Dhanalakshmi, Kum.S.Eswari and Smt.V.Ramya from RpG

Integrated top shield test facility and validation of thermal design of PFBR top shield
Shri Sriramachandra Aithal, RDG, Group Leader

Shri N. Vijayan Varier, Shri Vimal Kumar and Shri Makrand B Rajhans from TCQCD, Shri P. Jagannathan from EIRSG, Shri C. Sivathanu Pillai, Shri K. Velusamy, Shri V. Venkatachalapathy,

Shri Vasa Trinadh Gopi, Shri G. Ramnathan and Shri P. Palani from ESG, Shri S.K. Samantaray, Shri P. Ramamoorthy and Shri T. Kumaran from FRFCF, Shri V. Rajan Babu, Shri P. Puthiyavinayagam, Shri V. Balasubramaniyan, Shri K. Krishnaprasad, Smt. R. Vijayashree, Shri S. Raghupathy, Dr. K. Velusamy, Shri R. Gajapathy, Shri U. Parthasarathy, Shri B. Madhavan, Shri S. Saravanan, Shri M. Sakthivel, Shri Govind Kumar Mishra, Shri V. Pradeesh, Shri E. Balasundaram, Shri C. Raghavendran, Smt. P. Swetha, Shri G. Venkataiah, Shri S. K. Rajesh, Shri M. Babu Rao, Shri R. Manu, Shri S. Ramesh, Shri A. Sivakumar, Shri V. Devaraj and Shri P. Raja from RDG

Design, Construction, Commissioning and Licensing of Interim Fuel Storage Facility
Shri P. V. Kumar, then FRFCF & ESG(C), Group Leader

Shri G. Srinivasan, Kum S. Usha, Shri S. Varatharajan, Shri P. R. Swaminathan, Shri M. Elango, Shri R. V. Ramesh, Shri P. Ravi, Shri S. Baskaran, Shri S. Domesan, Shri A. Thandavamoorthy, Shri M. Uthaman, Smt. Liji Jacob, Shri N. Gopalakrishnan, Shri A. P. Abdul Mustak, Kum S. Meena, Shri V. J. Ramalingeswara Rao, Smt. V. Jayachitra, Shri K. G. Subramanian, Shri N. Sampath Kumar, Shri S. Sarangarajan, Shri E. Ramesh, Shri R. Shanmugavel, Shri Kalyana Rao Kuchipudi, Shri D. Devaraj, Shri P. Ragothkumar and Shri S. Rama Rao from ROMG, Smt. Thilakavathy, Smt.V.Gandhimathi, Shri Harikumar, Shri R J Paul Surendranath, Shri Nadarajan and Shri K Vasudevan from ESG, and Dr. M T Jose, Dr. N Suryamurthy, Shri R. Sarangapani and Shri P Arumugam from EIRSG. The award is also shared by Shri A C Wali, Shri A V G Reddy and Shri B Ravinder from FRF, NFC.

Performance Testing of Primary Ramp and Primary Tilting Mechanism of the Inclined Fuel Transfer Machine of PFBR.
Shri B. K. Sreedhar, FRTG, Group Leader

Shri N. Murugesan from CG, Shri G. Ramesh, Shri Krishna Tripathi, Shri P. Rajasekar, Shri M.P. Prabhakar, Shri G. Vijyaraghavan and Smt Alka Kumari EIRSG, Shri G. Kempulraj, Shri B.S. Ramesh Babu, Shri V. Praveen Kumar, Shri M. Krishnamoorthy, Shri V. Rajendran, Shri N. Chockalingam, Shri K. Narayanan, Shri C. Muthuswamy, Shri K.M. Natarajan, Shri R. Raj Kumar Bharathi, Shri S. Manimaran, Shri R. Manikandan, Shri Mohamed Shijas. B, Shri J. Abilash, Shri R. Murugapandian, Shri M. Pradeesh and Shri M. Tulasi from ESG, Shri B.K. Nashine, Shri G. Padmakumar, Shri B. Babu, Shri G. Vijayakumar, Shri S. Chandramouli, Shri V. Ramakrishnan, Shri P. Vijaya Mohana Rao, Shri C. Asokane, Shri S.C.S.P. Kumar Krovvidi, Shri Nilayendra Chakraborty, Shri S. Ignatius Sunder Raj, Shri P. Madan Kumar, Shri R. Rajendra Prasad, Shri A. Ashok Kumar, Shri K. Jayagopi, Shri Rakesh Kumar Mourya, Shri J. Saravanan, Shri T.V. Maran, Shri M. Anbuchelian, Shri Shiv Prakash Ruhela, Shri Y.V. Nagaraja Bhat, Shri R. Nirmal Kumar , Shri S. Krishnakumar, Shri D. Laxman, Shri S. Sureshkumar, Shri Gautam Kumar Pandey, Shri D. Muralidhar, Shri S. Ravishankar, Shri S. Alexander Xavier, Shri Parmanand Kumar, Shri N. Venkatesan, Shri K. Mohanraj, Shri C. Rajappan, Shri P.C.V. Murugan, Shri N. Sreenivas, Shri L. Egambaram, Shri R. Iyyappan, Shri N. Mohan, Shri G. Anandan, Shri A. Sudarsana Rao, Shri A. Kolanjiappan, Shri R. Ramalingam, Shri R. Shanmugam, Shri C. Adikesavan, Shri K. Karunakaran, Shri R. Krishnamurthy, Shri M. Sambamurthi, Shri P. Bakthavatchalam, Shri C. Ambujakshan Nair, Shri A.T. Loganathan, Shri A. Govindarajan, Shri M.T. Janakiraman, Shri P. Ganesan, Shri A. Kulanthai, Shri S. Shanmugam, Shri D. Kuppuswami, Shri P. Sonai, Shri P.R. Ashokkumar, Shri P. Varadan, Shri N. Thulasi, Shri K. Arumugam, Shri A. Anthuvan Clement, Shri V. Gunasekaran, Shri M. Kathiravan, Shri M. Karthikeyan, Shri Shaik Rafee, Shri S. Rajkamal Singh, Shri K. Srinivasa Rao, Shri N. Mariappan, Shri K.H. Anub, Shri H. Rafiq Basha, Shri K. Ganesh, Shri Ashish Tiwari, Shri L. Mohanasundaram, Shri L. Muthu, Shri P. Pothi, Shri P. Lakshmayya, Shri K. Palani, Smt. J. I. Sylvia, Smt. S. Nagajothi, Smt. Shanthi Rajendran, Smt. M. Chandra and Shri M. Mohana FRTG, Dr. U. Kamachi Mudali and Shri T. Nandakumar from MMG, Dr. P. Chellapandi, Dr. K. Velusamy, Shri S. Raghupathy, Shri K. Madhusoodanan, Shri Jose Varghese, Shri A. Venkatesan, Shri C.S. Surendran, Shri M. Rajendrakumar, Shri N. Subramanian, Shri Juby Abraham, Shri Ram Kumar Maity, Shri P. Lenin, Shri E. Balasundaram from RDG. The award is also shared by S. Roy, P.K. Limaye, M. Dev, Jit Pal Singh, Somesh Rai and R.J. Patel from RD&DG, BARC.

Design, Development, Verification & Validation of Hardware & Computer based Systems for Instrumentation & Control of PFBR
Shri S. A. V. Satya Murty, EIRSG, Group Leader

Shri N. Murali, Shri R. Jehadeesan, Shri M.L. Jayalal, Shri D. Thirugnana Murthy, Shri N. Sridhar, Shri K. Palanisami, Smt. T. Sridevi, Shri G. Venkat Kishore, Smt. L. Srivani, Shri Md. Najam Anwer, Shri Manoj Kumar Misra, Smt. K. Kameswari, Smt. T. Suguna, Shri M.A. Sanjith, Shri N. Satheesh, Smt. Saritha P. Menon, Shri T. Gokulakrishnan, Shri J. Selva Solomon, Shri A. Nageswaran, Smt. E.M.T. Sirisha, Shri Rajesh Vadarevu, Shri Alok Kumar Gupta, Shri Raghavan Komanduri, Shri R. Kanagarajan, Shri P. Shanmuganathi, Shri G. Prabhakara Rao, Shri P. Sahoo, Shri A. Shanmugam, Shri R. Ramakrishnan, Smt. P. Parimalam, Shri R.P. Behera, Shri M. Manimaran, Shri M. Kasinathan, Shri Mahesh Kumar Patankar, Shri M.S. Chandramouli Sharma, Smt. N. Malathi, Shri R. Ananthanarayanan, Shri M.P. Rajiniganth, Shri K. Praveen, Shri Aditya Gour, Shri A. Santhana Raj, Shri Anindhya Bhattacharya, Shri P. Manoj, Shri A.D. Arun and Smt. V. Lalitha from EIRSG, Shri B. Sasidhar Rao from FRFCF, Shri K. Madhusoodanan, Shri S. Lekshminarayanaswamy, Shri A. Venkatesan, Shri C.P. Nagaraj, Shri Tanmay Vasal, Shri M. Sivaramakrishna, Shri M. Sakthivel, Shri R. Dheenadhayalan, Shri N. Subramanian, Shri Chandrakant Upadhyay, Shri Govind Kumar Mishra, Shri Ankit Kumar, Shri R. Varuna, Ms T. Somavathi, Shri V. Pradeesh, Ms. A. Nisha, Shri E. Balasundaram and Shri N. Anandakumar from RDG, Shri V.J. Ramalingeswara Rao, Smt. K. Vinolia and Smt. Gowri Lakshmanan from ROMG. The award is also shared by Dr. K.P. Sarkar, Shri Geetha Santhakumar, Shri Ramesh B Adelli, Shri Anup Suryawanshi, Shri Dinesh Maurya from BARC

Quasi-non-destructive measurement of the isotopic ratio of boron in irradiated B4C pellets from FBTR control rods using a home-built refelectron time-of-flight mass spectrometer
Dr. M. Joseph, CG, Group Leader

Dr. N. Sivakumar, Dr. P. Manoravi, Shri A. Ananthakumar, Shri M. Saravanan, Shri R. Rajaram, Shri G. Rajendra Prasad and Shri Y. Ravi from CG, Shri V. Anandraj from MMG

Setting up of an inert atmosphere glove box train facility and fabrication of qualified sodium bonded metallic fuel pins containing U-6 Zr, EU-6Zr, U-Pu-Zr metal Slugs for test irradiation in FBTR
Dr. V. Ganesan, ROMG, Group Leader

Shri G. Ravisankar, Shri A. Ananthakumar, Shri M. Saravanan, Shri G.Rajendra Prasad, Shri Y. Ravi, Shri R.Lavakumar, Shri Abhishek Kumar Yadaw, Shri A. Manivannan, Shri G.Nandha Kumar, Shri M.Masanam, Shri G.Lakshmanan, Shri R.Kumaran, Shri A. V. Vinod, Ms. R. Jayashree, Shri G. Saravanan, Shri A. Senthamilselvan, Shri P. Ravisankar, Shri S. Maharajan, Shri D. Vijayakumar, Shri R. Parthiban, Shri A. Praveen and Shri R. Padmanaban from CG, Shri K. Krishna Chaitanya, Shri P.Narayana Rao, Shri D.Henson Raj, Shri G.Vijayaraghavan, Shri C.Muniyandi from EIRSG, Shri B.S. Ramesh babu, Shri P. Karuppasamy, Shri Mohammed Shijas, Shri M. Praveesh, Shri C. Muthusamy, Shri M. Damodaran, Shri M. Damodaran and Shri Praveen Kumar from ESG, Shri Hemanth Kumar, Shri M. Arul, Shri G. Srinivasan, Dr. Shaju K. Albert, Dr. Arun Kumar Bhadhuri, Dr. S. Murugan, Shri K.A. Gopal, Shri M. Muthu Ganesh, Shri Rajesh Saxena, Shri R. Ramesh , Shri K. Purushothaman, Shri C.N. Venkiteswaran, Shri A. Vijayaraghavan, Shri Ran Vijay Kumar, Shri V. Anandaraj, Smt. M. Padalakshmi, Shri S. Vinod Kumar and Kum. S. Gomathi from MMG, Shri S. Clement Ravichandar, Shri M. Asokkumar and Shri T Rajkumar from RDG, Shri P. Muralidaran, Shri T.V. Prabhu and Shri M. Santhosh from ROMG.

The award is also shared by Shri K K Abdulla, Dr. (Smt.) S.B. Roy, Shri S K Jha, Shri D. Mukherjee, Shri Arbind Kumar, Shri Santanu Das, Shri M T Saify, Shri Raj Kumar, Shri Mukesh Pandit, Shri C K Achankunju, Shri N M Bhoite, Shri Dharmendra Prasad, Shri M.A. Acharekar, Shri Rajendra Prasad, Shri N.D. Sharma, Shri S.K. Sharma and Shri J.R. D'souza from NFG, BARC.

IGCAR Publications during the Year 2103
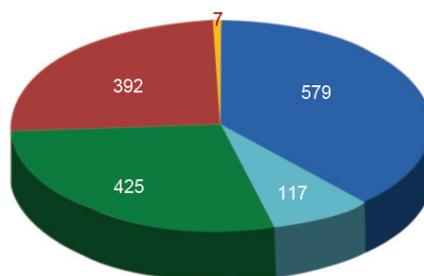
Articles in Journals: 579
Articles in Press: 117
Conference Papers: 425
Internal Reports: 392
Books/Book Chapters: 7

Special Lectures and Colloquia Series

1. "Nuclear Fuel Reprocessing: Past, Present and Future" IIChE Colloquium by Dr. R. Natarajan, Director, RpG, January 22, 2013.

2. "Publicly Funded Research Institutions and the Legacy of Sir Shanti Swarup Bhatnagar" Bhatnagar Memorial Lecture by Dr. S. Sivaram, National Chemical Laboratory, Pune , February 21, 2013.

3. "Caffeine in Radiobiological protection and coffee for Good Health" Curie Memorial Lecture by Prof. P. C. Kesavan, MSSRF, Chennai, March 15, 2013.

4. "International Women's Day" talk on "Laws that Safeguard Women at Workplace: Vishakha Guidelines to Verma Commission Recommendation" by Ms. G. Chamki Raj, Advocate, High Court, Chennai and "Understanding Matter-Antimatter Asymmetry in the Universe through Symmetry Violations" by Dr. K. V. P Lata, Pondicherry University, March 22, 2013.

5. "Matter and materials: Soft and nano, naturally" IGC Colloquium by Dr. Jatinder V. Yakhmi, Chairman, AEES, Mumbai, April 12, 2013.

6. "Evolving Nuclear Fuel Cycle" IGC Colloquium by Dr. Srikumar Banerjee,DAE Homi Bhabha Chair Professor & Former Chairman, AEC, June 3, 2013.

7. "Nuclear Space Power & Propulsion System" IGC Colloquium By Dr. M.Y. S. Prasad, Director, Satish Dhawan Space Centre, Sriharikota, July 22, 2013.

8. "Studies on the synthesis of Glycosidase Inhibitors" P. C. Ray Memorial Lecture by Prof. S. Chandrasekaran, IISC, Bangalore, August 5, 2013.

9. "The Third Industrial Revolution of India" Vikram Sarabhai Memorial Lecture by Dr. R. Chidambaram, Former Chairman, AEC, August 12, 2013.

10. "How to curb the diabetes epidemic?" by AARCO Colloquium Dr. V. Mohan, Mohan Diabetes Centre, Chennai, October 8, 2013.

11. "Materials Science and Engineering - an Interface between Society and Technology" Dr. Placid Rodriguez Memorial Lecture 2013 by Prof. Indranil Manna, Director, IIT, Kanpur, October 5, 2013

12. "What does one do, When the Job is over? " IGC Colloquium by Dr. G. Venkataraman, Director (Retd.) ANURAG, DST &Former VC, Sathya Sai Insititute of Higher Learning, November 11, 2013.

13. "Liquefaction of Helium and the still continuing opening of frontiers in Science & Technology" IGC Colloquium by Dr. Praveen Chaddah, OS, RRCAT, Indore, December 2, 2013.

14. "The Vanishing Art of Lecturing" IGC Colloquium by Prof. K. Ramnarayan, Vice Chancellor, Manipal University, December 23, 2013.

15. "Celebration of Science: Glorious past and challenging Future" IGC Colloquium by Prof. C.N.R. Rao, December 30, 2013.

Seminars, Workshops and Meetings

1. Seminar on "Security Issues for Women" , January 19, 2013

2. Workshop on "Training Need Assessment", February 4, 2013.

3. ATI/DAE Workshop on "Cash and Accounts" during January 28, 2013 to March 2, 2013.

4. Theme Meeting on "Plutonium and Transplutonium Elements (TeMPT)" during April 4-5, 2013.

5. Seminar on "Challenges in Radioactive Waste Management", June 21, 2013.

6. "Security Sensitization Program for Senior Officers of DAE", September 18, 2013.

7. Theme Meeting on "Stainless Steels for Power Sector (SSPS-2013)" during October 20-21, 2013.

8. Seminar on "Electrochemistry & Corrosion Camp (ECC-2013)", November 9, 2013.

9. 9th National Conference on "Recent Advances in Information Technology (READIT -2013)" during December 18-19, 2013.

10. "Fission 75", December 20, 2013.

Nurturing Activities

1. "Science Day", February 28, 2013.

2. "World Environment Day", June 5, 2013.

3. Hindi Workshop for IGCAR officials March 7, May 7, July 23 and December 4, 2013.

4. "Technology Day – 2013" during May 10-11, 2013.

5. "BITS Pilani Practice School" during May 22 – July 13, 2013

6. "Summer Training Program in Physics and Chemistry (STIPAC 2013)" during May 27 – July 5, 2013.

7. "Occupational Health Day", July 10, 2013.

8. Graduation Function of the OCES 2012, 7th Batch of BARC Training School at IGCAR, July 29, 2013.

9. Inauguration Function of the OCES 2013, 8th Batch of BARC Training School at IGCAR, August 8, 2013.

10. "Annual Quality Circle Meet (QCAM 2013)", August 23, 2013.

11. "Hindi Week", September 16-20, 2013.

12. "Prof. Brahm Prakash Memorial Materials Quiz 2013", September 21, 2013.

Inauguration of Integrated Facility for Fusion Reactor Materials
January 28, 2013

Shri S.C. Chetal, the then Director, IGCAR and Prof. D. Bora, Director,
IPR, cutting the ribbon to mark the inauguration of IFFRM building

IGCAR and Institute for Plasma Research (IPR), Gandhinagar have a memorandum of understanding for collaboration towards development of materials, fabrication technologies, NDT techniques and design of components along with setting up of required experimental facilities for the ITER fusion reactor project. The specific responsibilities identified during the initial phase of the collaboration include

(a) development of Indian Reduced Activation Ferritic Martensitic (RAFM) steel for ITER Test Blanket Module (TBM) (b) development of fabrication technologies for RAFM steel and (c) development of non-destructive evaluation methodologies for test blanket module programme.

India is a partner in the international R&D efforts to harness fusion energy through its participation in the ITER project. ITER is the experimental Tokamak nuclear fusion reactor and it is presently under construction at Cadarache in France. The ITER project aims to make the long-awaited transition from experimental studies of plasma physics to full-scale electricity-producing fusion power plant. The project is funded and run by seven member entities, namely, the European Union, India, Japan, China, Russia, South Korea and the United States. ITER has been designed to produce 500 MWe of output power for 50 MWe of input power. The machine is expected to demonstrate the principle of producing more energy from the fusion process than that is used to initiate it, something that has not yet been achieved so far. The first commercial demonstration fusion power plant,

named DEMO, is proposed to follow subsequent to the ITER project, to bring fusion energy to the commercial market.

As part of the international collaboration, different countries will design and fabricate test blanket modules of various designs which would be tested in the ITER, for which specific ports are assigned to each member country. The development of structural materials for test blanket module that faces the high temperature plasma, is considered as one of the main challenges for the realization of fusion power plant. The test blanket module material shall satisfy the requirements of adequate resistance to high energy neutron irradiation, acceptable physical and mechanical properties at high temperatures, low ductile to brittle transition temperature, corrosion resistance to ensure compatibility with the breeding materials, and above all, produce very low levels of induced radioactivity.

Reduced activation ferritic-martensitic steels (RAFM) having 9-12 wt% chromium are presently considered as the main candidate materials for the test blanket modules to be tested in ITER by the different participating countries. Internationally developed RAFM steels have tungsten in the range 1-2 wt% and tantalum in the range 0.02-0.18 wt% and very low levels of residual elements that can transmute to long half-life isotopes. The RAFM steel for Indian test blanket module, and the associated joining technologies are being developed jointly by IGCAR and IPR in collaboration with International

Dr. P. R. Vasudeva Rao, Director, IGCAR, Shri S.C. Chetal, the then Director, IGCAR, Prof. D. Bora, Director, IPR, and other invitees arriving for the inaugural function

Advanced Research Centre for Powder Metallurgy and New Materials (ARCI), Defence Metallurgical Research Laboratory (DMRL), Defence Research & Development Laboratory (DRDL) and Mishra Dhatu Nigam Limited (MIDHANI).

In order to develop an Indian version of RAFM steel for test blanket module applications, by optimising the chemical composition processing steps and qualifying the material in terms of microstructure, mechanical properties and to develop the appropriate fabrication technologies and inspection, a dedicated materials development and testing facility, named as Integrated Facility for Fusion Reactor Materials (IFFRM) is planned at IGCAR, with the support of IPR. IFFRM, when fully commissioned, will have state-of-the-art testing facilities for characterizing microstructures and evaluation of mechanical properties of materials, non-destructive testing and evaluation, and fabrication technologies. The IFFRM building along with a few laboratories was inaugurated on January 28, 2013, by Shri S. C. Chetal, the then Director of IGCAR in the presence of Prof. D. Bora, Director, IPR. Several senior scientists from IPR and many colleagues from IGCAR participated in the function. The IPR team included Shri E. Rajendra Kumar, Head, Test Blanket Module Division, and Dr. Sishir Deshpande, Project Director, ITER India. Dr. P. R. Vasudeva Rao, Director, IGCAR, Shri P. V. Kumar, Project Director, FRFCF, Dr. T. Jayakumar, Director, Metallurgy & Materials Group, Shri Sivathanu Pillai, Associate Director, CEG and many colleagues from Metallurgy & Materials Group as well as Engineering Services Group attended the function. Prof. P.K. Kaw, former Director, IPR, who was instrumental for this fruitful collaboration between IGCAR and IPR, could not attend the function due to prior commitments. His message which was read out by Prof. D. Bora, is reproduced below.

"Shri Chetal and other colleagues from IGCAR and IPR, I convey my greetings to all of you on the occasion of this IGCAR-IPR Collaboration meeting and regret that I am unable to personally participate because of prior engagements with a team from LIGO project, USA. IGCAR- IPR Collaboration on fusion reactor materials has come a long way since its formal inception a few years ago in connection with the TBM and ITER Projects. Director, IGCAR has played a critical role in making this collaboration a great success. I am especially grateful to you, Shri Chetal, for taking a keen and active personal interest in the IPR Projects and ensuring they are completed with high quality and within acceptable cost and schedule. I look forward to continued technical interaction of IPR teams with you, even after you complete your tenure at IGCAR. The inauguration of the IFFRM laboratory buildings marks the reaching of an important milestone in our collaborative programs. Heartiest congratulations to all on this happy occasion.

- P K Kaw"

Speakers at the function sincerely thanked the services rendered by Civil, Air Conditioning and Electrical Divisions of IGCAR for the timely completion of the IFFRM building in spite of several challenges, To mark the occasion, tree saplings were planted on the eastern side of the IFFRM building.

Extensive studies have been done at IGCAR towards developing the Indian RAFM steel and a steel with optimized composition, named as IN-RAFM steel has been developed. Poster presentations were made highlighting the extensive R&D work so far carried out in the development of IN-RAFM steel and the future plans towards development of the associated fabrication and NDT technologies. R&D studies have also been initiated for the development of other fusion reactor materials including oxide dispersion strengthened (ODS)-RAFM steel.

Conference and Meeting Highlights

24th Annual General Meeting of Materials Research Society of India Kalpakkam
February 11-13, 2013

Delegates of the MRSI-AGM-2013 at Kalpakkam

The 24th Annual General Meeting of the Materials Research Society of India (MRSI) was held at the Indira Gandhi Centre for Atomic Research, Kalpakkam, during February 11-13, 2013. Prof. C. N. R. Rao, National Research Professor and Linus Pauling Research Professor, JNCASR, Bangalore addressed the gathering of over three hundred Materials Scientists from all over the Country.

The Annual General Meeting of the Materials Research Society of India, included the following honour lectures: (i) International Materials Science and Technology Award Lecture by Prof. Richard Friend, University of Cambridge; (ii) Distinguished Materials Scientist of the year award Lecture by Dr. T. Ramasami, Secretary, Department of Science and Technology; (iii) Materials Research Society of India Distinguished Lectureship Award Lecture by Dr. Suresh Das, National Institute for Interdisciplinary Science and Technology, Trivandrum and (iv) Prof. C.N.R. Rao Prize lecture in Advanced Materials by Prof. Milan Sanyal, Saha Institute of Nuclear Physics. The MRSI-ICSC Superconductivity and Materials Science Annual Prize lectures were delivered by Dr. R. Muraleedharan, SSPL and Shri M.P. Janawadkar, IGCAR and there were

fourteen Medal lectures of Materials Research Society of India at the Annual General Meeting. About one hundred and fifty contributed poster papers covering the latest research on various aspects of materials science were presented at the meeting. A special session on Exotic Materials under the Asia Pacific Academy of Materials (APAM), was conducted by Prof. O. N. Srivastava, Banaras Hindu University, during the Annual General Meet.

As a part of the Annual General Meeting, a theme symposium on "Advanced Materials for Energy Applications" was conducted, in which lectures were delivered by Dr. S. Banerjee, DAE Homi Bhabha Chair Professor, Mumbai, Dr. Baldev Raj, President-Research, PSG Institutions, Coimbatore, Dr. R. C. Budhani, NPL, New Delhi and Prof. Satish Vitta, Indian Institute of Technology, Mumbai. A special evening talk on " The Development of Solar Energy in India" was delivered by Dr. Anil Kakodkar, DAE Homi Bhabha Chair Professor, Mumbai.

The Annual General Meeting of the Materials Research Society of India, at Kalpakkam, that provided a rich fare of excellent talks on various facets of Materials Science, was widely appreciated.

9th CEA-IGCAR Annual Meeting on Liquid Metal Fast Reactor Safety
March 18-21, 2013

CEA Delegates with Dr. P. R. Vasudeva Rao, Director, IGCAR and senior colleagues of the Centre

Under the continuing Indo-French Collaborative activities, 9th CEA-IGCAR Annual meeting on Fast Reactor Safety was organized by IGCAR during March 18-21, 2013. Thirteen French and thirty seven Indian delegates (from IGCAR, BHAVINI & AERB) participated in the seminar. Dr. P. R. Vasudeva Rao, Director, IGCAR inaugurated the seminar and lucidly presented the overall updates of the CEA-IGCAR collaborations since 2005. Two topical seminars dedicated to safety and materials in support of LMFR safety were held on March 18-19, 2013, respectively. A total of about six presentations were made on the status of FBTR operations, PFBR construction and commissioning status, PHENIX progress report: decommissioning and core flowering test, superphenix decommissioning, ASTRID project overview, design and R&D status of FBR 1&2. A detailed review of the status of collaborative works in the domains of sodium aerosols, electrochemical hydrogen meter on sodium facility, sodium leak detector, code calculations on impingement wastage for 9Cr-1Mo steam generator tubes, mesoscale and microscale atmospheric dispersion, studies on fluid structure interaction, characterization of gas content in sodium, severe accident in sodium-cooled fast reactor, oxide (PHENIX pin) and carbide (FBTR pin) fuels etc. Further, the areas for future collaborative works such as Ferro-boron as shielding material for Fast Reactors, measurement of oxygen activity in sodium, Molten Fuel Coolant Interaction Modeling under severe accident scenario etc. were identified. This was followed by a meeting on review of sodium loop for irradiation of multiple samples at high temperatures towards using in JHR on March 22, 2013. Four French delegates and fourteen Indian delegates participated in the meeting. The introductory remarks were presented by Dr. P. R. Vasudeva Rao, Director, IGCAR and Dr. Giles Bignan, JHR user interface manager. Dr. P. R. Vasudeva Rao, Director, IGCAR highlighted the overall activities of the Centre and construction status of PFBR and Dr. Giles brought out the details, objectives and current status of JHR. There were three technical presentations and the CEA team then visited the test facility, which is in the commissioning stage.

SAFETY PROMOTIONAL ACTIVITIES

In order to fulfill safety, health and environment requirements and promote positive safety culture at the workplace, safety promotional activities such as Fire Service Week and World Environment Day are being organized by Environment and Safety Division of IGCAR every year.

Fire Service Week

April 14, 2013 is observed as Fire Service Day in memory of brave firemen who laid down their lives in fighting the fire that broke out due to a huge explosion from a ship loaded with 1200 tons of explosives, cotton bales and oil drums at Victoria Dockyard, Mumbai. The explosion resulted in huge loss of life and property. Since then April 14-20, has been observed as National Fire Service Week. At IGCAR the same was observed on April 17, 2013. On this occasion, an invited talk on 'Risk Assessment' was delivered by Shri R.M. Kshirsagar, Senior Manager (Fire & Safety), Chennai Petroleum Corporation Limited, Chennai. Live demonstrations of Fire Fighting Equipment was arranged for our employees with the help of M/s. Safex Fire Services Limited, Chennai. To inculcate fire safety culture among employees, competitions such as essay, poster and slogan were conducted. Prizes were distributed to the winners by Shri S.A.V. Satyamurty, Director, EIRSG.

Shri S.A.V. Satyamurty, Director, EIRSG giving away the prize to one of the winners

World Environment Day

World Environment Day (WED) is observed all over the world on 5th of June every year. The same was celebrated at IGCAR on June 5, 2013 at Sarabhai auditorium. Dr. K. K. Satpathy, Head, Environment & Safety Division (EnSD), IGCAR delivered the welcome address. Dr. Prabhat Kumar, Chairman and Managing Director (CMD), BHAVINI, inaugurated the programme and delivered the inaugural address. Dr. R. Natarajan, Director, RpG and ESG (M&E) delivered the presidential address. An invited talk on "Challenges for feeding a billion plus" was delivered by Dr. Ajay Parida, Executive Director, M.S. Swaminathan Research Foundation (MSSRF), Chennai. Dr. Parida highlighted the need for conserving food for future generations with an emphasis on food security of the country and its challenges. Dr. M. V. R. Prasad, Head, Environmental & Occupational Health Section proposed the vote of thanks. About 250 employees participated in the function. About thirty saplings were planted on the new road near FRFCF by the dignitaries.

Dr. K. K. Satpathy, Dr. Ajay Parida, Dr. R. Natarajan, Dr. Prabhat Kumar and Dr. B. Venkatraman during World Environment Day 2013 Celebrations at IGCAR

Technology Day Celebrations 2013
May 11, 2013

Dr. P.R. Vasudeva Rao, Director, IGCAR presided over the function and briefed the gathering about the genesis of the Technology Day Meet 2013

IGCAR organized the "National Technology Day" celebrations on May 11, 2013 at Convention Centre, Anupuram. This trilingual seminar (English, Hindi and Tamil) had participation from non-gazetted staff belonging to the various groups, accounts and administration. The technical meet comprised of oral and poster presentations as well as display of component / product / devices / models developed by the participants. In total, 57 oral presentations, 111 poster presentations and 23 exhibits were presented by the participants show-casing their contribution, capability, knowledge and technical skill.

The programme started with the inaugural session with Dr. P. Sivakumar, Director, CVRDE, DRDO, Chennai as the Chief Guest. Dr. P.R. Vasudeva Rao, Director, IGCAR presided over the function and briefed the gathering about the genesis of the Technology Day Meet 2013. He reiterated that the objective of this event was to recognize and show-case the technical accomplishments of IGCAR personnel that had played a significant role in the success of the FBR programme. On behalf of Shri G. Srinivasan, Chairman, Organising Committee, Shri P.V. Kumar, Project Director, FRFCF highlighted the significance of the National Technology Day and its importance to the gathering. In his inaugural address and technical presentation, Dr. P. Sivakumar brought out the great strides made by the technical

and scientific organizations of our country with specific emphasis on the progress made by the Defence sector. He graphically demonstrated these facts with a very impressive audio visual display highlighting the significant contributions made by the Defence Research and Development Organization (DRDO) of India. He also emphasized the need for the R&D organizations of our country to contribute towards social responsibilities which included but are not limited to providing clean drinking water, energy and better education to the people of our nation at large. Dr. U. Kamachi Mudali, Secretary welcomed the gathering and Dr. K. Ananthasivan, Convenor, proposed the vote of thanks.

Subsequently, four parallel technical sessions comprising oral presentations were conducted at the Convention Centre and SRI Guest House Seminar Hall. Technical posters and exhibits were displayed at the Convention Centre. A total of 202 non-gazetted staff from IGCAR participated with great zeal and enthusiasm and displayed their technical skills and contributions with pride.

In the concluding session, Dr. P.R. Vasudeva Rao, Director, IGCAR appreciated the spirit and enthusiasm shown by the participants in showcasing their excellent contributions that form a significant part of the collective achievements of IGCAR. Participation certificates were given by Director, IGCAR to all the participants.

BITS Practice School
May 22 - July 13, 2013

Dr. P. R. Vasudeva Rao, Director, IGCAR interacting with the students from BITS Practice School

Twenty five students from BITS Pilani, Hyderabad and Goa campuses underwent BITS Practice School at our Centre during May 22 - July 13, 2013. The course aims at exposing the students to industrial and research environments, how the organizations work, to follow and maintain work ethics, study the core subjects and their application in the organization and to participate in some of the assignments given to them in the form of projects.

The students were from various engineering disciplines like Mechanical, Chemical, Electrical, Electronics & Instrumentation, Electronics & Communication Engineering and Computer Science.

Dr. R. Natarajan, Director, Reprocessing Group and ESG(M&E) inaugurated the Practice School at IGCAR on May 22, 2013. Students carried out challenging projects in various groups of the Centre in line with their discipline. During the period of their stay, they visited various facilities at IGCAR, BHAVINI and MAPS. As a part of the curriculum, quiz, project work presentations, group discussions and report writing were conducted. Dr. P. R. Vasudeva Rao, Director, IGCAR interacted with the students on July 4, 2013. Dr. T. Jayakumar, Director, Metallurgy and Materials Group delivered the valedictory address and distributed the certificates to the students during the valedictory function on July 11, 2013.

Dr. R. Natarajan, Director, RpG & ESG(M&E) interacting with the students from BITS Practice School

Dr. T. Jayakumar, Director, MMG delivering valedictory address

Summer Training in Physics and Chemistry (STIPAC - 2013)
May 27 - July 5, 2013

STIPAC students with Dr. P. R. Vasudeva Rao, Director, IGCAR & senior colleagues during the inaugural function

Group photograph taken after the valedictory function

Summer training course in Physics and Chemistry (STIPAC), an annual event of IGCAR was conducted during the period May 27 - July 5, 2013 for the pre-final year M.Sc. students from all over India. The intention of STIPAC is to motivate young students to pursue a scientific research career by providing them the opportunities to take part and become familiar with scientific research through lecture courses and hands-on laboratory experiments in selected areas. A total of forty students attended, twenty each from Physics and Chemistry discipline, respectively.

The theme of this year's summer training in physics (STIP) was on "Structure and Properties of Materials". The lectures addressed the sub-themes of symmetries and crystalline order, XRD and structure determination, optical, transport and thermodynamic properties of solids, electronic structure of materials, cooperative behavior, superconductivity, phase transitions, defects and disorder in solids, soft matter, micro and nano structured materials, surface and interface phenomena, interaction of radiation with matter and basics of quantum & statistical mechanics. There were also introductory lectures on current topics such as graphene, porous solids, multiferroics, topological insulators, quasicrystals, etc. The STIP students were also given individual specific projects under a supervisor.

Summer training in chemistry (STIC) involved lecture courses in the following areas: nuclear chemistry, solid state chemistry, thermochemistry, analytical chemistry, surface chemistry, electrochemistry, quantum chemistry, spectroscopy, coordination chemistry, computational chemistry etc. Areas of laboratory work in the STIC course included thermal analysis, high performance liquid chromatography, super critical fluid extraction, electroanalytical chemistry and infrared spectroscopy.

During the inaugural session, Dr. K. Nagarajan, Associate Director, CG, Dr. C. S. Sundar, Director, MSG and Dr. P. R. Vasudeva Rao, Director, IGCAR emphasized the need for such motivating summer training programmes to enthuse the students into research career. The Chief Guest Prof. Krishan Lal, President, Indian National Science Academy, New Delhi gave a lucid lecture on "A Century of Crystal Structure Determination".

Special evening lectures were given by Prof. E. Prasad, IIT Madras, Ms. Shyleswari M. Rao, Director, Ved Vyas Inner Space, Chennai, Prof. K. S. Viswanathan, IISER, Mohali, Dr. S. Banerjee, DAE Chair Professor and Former Chairman, Atomic Energy Commission of India, Mr. S. Rathakrishnan, Ms. R. M. Nachammai, Dr. K. Hari Krishna, MAPS, Dr. M. Sai Baba, Associate Director, RMG, Dr. C. S. Sundar, Director, MSG, Dr. P. R. Vasudeva Rao, Director, IGCAR, Dr. S. K. Deb, Head, ISUD, RRCAT, Indore, Dr. Saibal Basu, BARC, Dr. A. K. Tyagi, BARC and Dr. M. V. N. Murthy, IMSc, Chennai.

The concluding function on July 5, 2013 had the valedictory address by Dr. Vijayamohanan Pillai, Director, CSIR - Central Electrochemical Research Institute, Karaikudi, a brief session on students response and the lecture by Dr. Pillai entitled "Impact of Molecular Nanotechnology on Materials Research".

Graduation Function of the Seventh Batch of Trainee Scientific Officers of BARC Training School at IGCAR
July 29, 2013

Prof. K. Kasturirangan, Member (Science), Planning Commission, Government of India and former Chairman, Indian Space Research Organization addressing the gathering while Dr. P. R. Vasudeva Rao, Director, IGCAR, Dr. M. Sai Baba, Associate Director, RMG, Shri R. V. Subba Rao, Head, OCES-TS, RMG are seated on the dais during the graduation function

The seventh batch of fifty TSOs from the BARC Training School at IGCAR have successfully completed their training and were graduated in a special ceremony that took place on July 29, 2013 in the Sarabhai Auditorium, Homi Bhabha Building, IGCAR. Prof. K. Kasturirangan, Member (Science), Planning Commission, Government of India and former Chairman, Indian Space Research Organization was the Chief Guest. Dr. M. Sai Baba, Associate Director, RMG welcomed the gathering. Dr. P. R. Vasudeva Rao, Director, IGCAR delivered the presidential address. Prof. Kasturirangan released the souvenir featuring the training school programme in the previous academic year and Dr. P. R. Vasudeva Rao received the first copy. Prof. Kasturirangan gave away the prestigious 'Homi Bhabha Prize' comprising of a medallion and books worth Rs. 5000 to the meritorious toppers in all the disciplines. He also gave away the course completion certificates to all the graduates passing out. A few of the Trainee Scientific Officers passing out shared their experience, gave a feedback on the academic programme and their stay at hostel. Prof. Kasturirangan gave a very inspiring and motivational lecture to the students. Shri R. V. Subba Rao, Head, OCES-TS, RMG proposed the vote of thanks.

Seventh Batch of Graduates of BARC Training School at IGCAR with Prof. K. Kasturirangan, Member (Science), Planning Commission, Government of India and former Chairman, Indian Space Research Organization, Dr. Prabhat Kumar, CMD, BHAVINI, Shri T. J. Kotteeswaran, Station Director, MAPS, Shri Amitava Roy, Facility Director, BARCF, Dr. P. R. Vasudeva Rao, Director, IGCAR, senior colleagues of the Centre and members of RMG

Quality Circle Annual Meet (QCAM) - 2013
August 23, 2013

Dr. K. Narashiman, Director, AU TVS CQM & IQAC, Anna University, Chennai delivering the inaugural address

Quality circle is a small group of employees doing similar or related work who meet regularly to identify, analyze and solve work related problems usually led by a senior team member. After completing their analysis, they present their solutions to management for implementation and to improve the performance of the organization. Thus, implemented correctly, quality circles can help the organization to reduce cost, increase productivity and improve employee morale.

In IGCAR, every year Quality Circle Annual Meet (QCAM) is conducted and the QC case studies are presented by the QC teams. QCAM-2013 was conducted on August 23, 2013 at Sarabhai Auditorium and Raja Ramanna Auditoriums in parallel sessions. Welcome address was given by Shri G. Srinivasan, Director, ROMG. The presidential address was given by Dr. R. Natarajan, Director, RpG & ESG (M&E). Inaugural Address was delivered by Dr. K. Narashiman, Director, AU TVS CQM & IQAC, Anna University, Chennai and vote of thanks by Shri G. Kempulraj, Head, Central Workshop Division.

Totally twenty nine Quality Circles (about 200 members) from IGCAR, schools from Kalpakkam and neighborhood presented QC case studies in a wide spectrum of topics covering Technical, Research & Development, Services and Education. Professional judges from Quality Circle Forum of India, Chennai chapter, adjudged the QC case study presentations. Under the Mechanical and Manufacturing' stream, the Moon QC Team bagged 'Dr. Placid Rodriguez Memorial Trophy', while Rainbow & Excel QC teams won and shared the 'Shri M. K. Ramamurthy Memorial Trophy' in Plant Operation and Services category. Valarpirai Nila QC, Government HSS, Vengappakkam won the Dr. Sarvepalli Radhakrishnan Memorial Trophy' in School category.

During valedictory function, the events were summed up by Shri A. Jyothish Kumar, Associate Director, ESG (M&E). The programme was concluded with the valedictory address and the prizes were distributed to the participants by Shri G. Srinivasan, Director, ROMG, IGCAR. Vote of thanks was proposed by Shri T. V. Maran, Member Secretary, Organising Committee.

Theme Meeting on
Stainless Steels for Power Sector (SSPS 2013)
October 20–21, 2013

Inaugural session of SSPS 2013

The Theme Meeting on "Stainless Steels for Power Sector (SSPS 2013)" was jointly organized by IGCAR, IIM, Kalpakkam Chapter, Society for Failure Analysis and IIW, Chennai Branch.

The objective of the theme meeting was to provide a forum for the designers, practicing engineers, R&D and plant personnel, to interact and discuss the issues, and act as a forum to generate novel ideas and solutions to the application of stainless steels for power sector. The scope of the theme meeting involved manufacturing aspects of conventional stainless steels, high performance stainless steels, design of new alloys, surface engineering and treatment, fabrication and welding including codes and standards, thermo-mechanical processing, advanced welding and testing, coatings and hardfacing; nondestructive evaluation-special NDT techniques, modern testing and advanced protection measures, online corrosion monitoring; New alloys and manufacturing technologies, case studies and recommendations, life prediction and modeling in Thermal and Nuclear Power Plants.

Dr. P. R. Vasudeva Rao, Director, IGCAR welcomed the gathering of the theme meeting and Prof. P. Rama Rao, Chairman, ARCI and Chairman, BRNS, delivered the inaugural address. In his inaugural address Prof. Rama Rao admired the way stainless steels have been developed and utilized for a variety of industrial applications and appreciated the progress made towards the development, fabrication and corrosion control of stainless steels. Dr. T. Jayakumar, Director, MMG outlined the scope and programme of the event and the genesis of the theme meeting. In the first session Shri S.C. Chetal, former Director of our Centre detailed applications of stainless steels for FBR, Dr. Prabhat Kumar, CMD, BHAVINI elaborated the success of stainless steel equipment fabrication for PFBR. Shri M. Narayana Rao, CMD, MIDHANI talked on development and manufacture of stainless steel for nuclear and thermal power plants, and Shri Johan Hernblom from Sandvik, Sweden explained material aspects of advanced ultra super critical boilers for clean energy. In the second session Shri S. Sisodia and Shri Sandeep Maheswari from Salem Steel Plant and JIndal

Stainless Steel respectively described the versatility of stainless steel especially in power plant applications. Dr. Krishnan Balasubramaniam from IIT-M spoke on a specialized topic, NDE of stainless steel components using ultrasonic techniques. In the third session experts from BARC, Shri K.K. Vaze and Dr. V. Kain described the applications of stainless steel in advanced heavy water reactor and corrosion issues for stainless steel in light water reactors, respectively. Shri R. Easwaran detailed the BHEL experience in manufacturing stainless steels for steam generating equipment of power plants.

In the fourth technical session, Shri D. Pramanik of NFC spoke on new manufacturing processes for development of seamless stainless steel tubes for power sector applications, and Dr. P. Chellapandi, Director, RDG of IGCAR presented on stainless steels for FBR-I and FBR-II. Dr. T. Jayakumar Director, MMG covered the developments of advanced stainless steels for sodium cooled fast reactors. In the fifth technical session, in his talk Prof. David J. Smith, Prof. Alan Cocks, Prof. John Bouchard from Universities in UK covered certain aspects in mechanical metallurgy of stainless steels, like effect of repair welds on low temperature fracture, creep deformation, damage development, crack growth, residual stress driven creep etc. Dr. A.K. Bhaduri, AD, MTDG from IGCAR talked on development of 304HCu stainless steel for the Indian advanced ultra super-critical thermal power plants. In the sixth and final session Dr. G. Balachandran explained development of creep resistant stainless steels for power plants and Dr. M.D. Mathew and Dr. U. Kamachi Mudali of IGCAR, talked about evolution of Type 316 SS as a structural material for sodium cooled fast reactors and localized corrosion behaviour of nitrogen alloyed stainless steels, respectively.

About one hundred delegates participated in this theme meeting from different organizations like NFC, AERB, IPR, NPCIL and IGCAR along with institutes and industries like CECRI, IIT-M, Bharat Forge, MIDHANI, Jindal Stainless Steel, SAIL, Salem and Hyderabad, BHEL, Trichy, and Sandvik Asia, Pune. The meeting provided an opportunity for experts and all the stake holders to discuss and share their views.

9th Biennial National Conference on
Recent Advances in Information Technology (READIT)
December 18-19, 2013

Dr. M. Sai Baba, Convener, READIT & AD, RMG, Dr. P.R. Vasudeva Rao, Distinguished Scientist & Director, IGCAR, Dr. J.K. Suresh, Former Vice President, Infosys, Shri S.A.V. Satya Murty, Director, EIRSG and Shri E. Soundararajan, SIRD during the release of souvenir at the inaugural function of READIT-2013

The 9th Biennial National Conference on Recent Advances in Information Technology (READIT) was organized by SIRD, IGCAR in association with the Kalpakkam Chapter of Madras Library Association (MALA) during December 18-19, 2013. The theme of the Conference was "Towards Semantic Digital Library Infrastructure". More than two hundred delegates including information technology professionals, librarians, students and academicians attended the conference.

The conference included invited talks by eminent experts, oral/poster presentations by research scholars/participants. The conference was preceded by a one day tutorial session on the theme "Tools for Creating Content Portals" on December 17, 2013. The conference was inaugurated on December 18, 2013. The function was presided over by Dr. P.R. Vasudeva Rao, Distinguished Scientist & Director, IGCAR. Shri S.A.V. Satya Murty, Director, EIRSG, IGCAR & Chairman, Library and Information Services Committee, who delivered the welcome address. Dr. M. Sai Baba, Convener, READIT, AD, RMG & Head, SIRD briefed about the activities and READIT conference. Dr. P. R. Vasudeva Rao in his presidential address emphasized the importance of libraries in providing access to the semantic information.

Dr. J. K Suresh, former Vice President, Infosys & Consultant, Knowledge Management, Bengaluru delivered the inaugural address. Dr. J. K. Suresh highlighted the methods of creating knowledge in his address. Dr. J. K. Suresh and also released the souvenir and Dr. P. R. Vasudeva Rao inaugurated the exhibition. Shri E. Soundararajan, Organizing Secretary READIT, SIRD proposed the vote of thanks.

Intensive technical discussions on various aspects of virtualized digital library infrastructure, cloud computing techniques, e-books and enabling architecture, semantic metadata creation and retrieval, knowledge dissemination techniques were presented during the conference. There was also a separate poster session for the contributed papers.

An exhibition was organized as a part of the conference in which latest IT gadgets, standards and books were displayed. This conference facilitated good interaction among the young researchers/students, professionals and eminent speakers in the area of semantic technologies. During the valedictory function, Dr. M. Sai Baba, summed up the overall deliberations in the conference.

Dr. P.R. Vasudeva Rao, Distinguished Scientist & Director, IGCAR inaugurating the exhibition of READIT-2013

Eminent Visitors to IGCAR

Delegates from Czech Republic with Dr. P. R. Vasudeva Rao, Director, IGCAR, Dr. Prabhat Kumar, CMD, BHAVINI and senior colleagues of the Centre

His Excellency Mr. Vaclav Bartuska, Ambassador at Large for Energy Security of the Czech Republic, His Excellency Mr. Miloslav Stasek, Ambassador of the Czech Republic to India visited the Centre on January 7, 2013. After a meeting with Director, IGCAR and senior colleagues of the Department, the dignitaries visited the Fast Breeder Test Reactor & KAMINI Reactor, Hot Cells and Non-Destructive Evaluation Division, facilities in Fast Reactor Technology Group and Construction site of Prototype Fast Breeder Reactor.

Dr. S. Sivaram from National Chemical Laboratory, Pune delivering the Bhatnagar Memorial Lecture

Dr. S. Sivaram from National Chemical Laboratory, Pune delivered the Bhatnagar Memorial Lecture on "Publicly Funded Research Institutions and the Legacy of Sir Shanti Swarup Bhatnagar" organized by Society for Advancement of Chemical Sciences and Education during his visit to the Centre on February 21, 2013.

Delegates from ASEAN countries visited the Centre on February 22, 2013. During the meeting with Dr. P. R. Vasudeva Rao, Director, IGCAR and senior colleagues, the delegates were briefed about the R&D activities of IGCAR by Dr. M. Sai Baba, Associate Director, Resources Management Group. After the meeting, the delegation visited the Fast Breeder Test Reactor and Madras Atomic Power Station.

Delegates from ASEAN countries with Dr. P. R. Vasudeva Rao, Director, IGCAR and senior colleagues of the Centre

Dr. Jatinder V. Yakhmi, Chairman, Atomic Energy Education Society, DAE delivering the IGC Colloquium on " Matter and Materials: Soft and Nano, Naturally" during his visit to the Centre

Dr. Jatinder V. Yakhmi, Chairman, Atomic Energy Education Society (DAE), Advisor to the Chairman, AEC and Raja Ramanna Fellow, Homi Bhabha National Institute, Mumbai, delivered the IGC Colloquium on "Matter and Materials: Soft and Nano, Naturally", during his visit to the Centre on April 12, 2013.

Delegation of Editors/Senior Journalists from Nepal visited the Centre on April 25, 2013. During the meeting with Shri R. Natarajan, Director, RpG and ESG (M&E), they were briefed about "Fast Reactors for Energy Security" by Dr. M. Sai Baba, Associate Director, Resources Management Group, followed by presentation on "Plant Overview" by Shri V. G. Mohan Nayar, Training Superintendent, Nuclear Training Centre, NPCIL. After the meeting the delegation visited the Madras Atomic Power Station.

Delegation of Editors/Senior Journalists from Nepal with Shri R. Natarajan, Director, RpG and ESG (M&E) and senior colleagues of the Department

Dr. Srikumar Banerjee, DAE Homi Bhabha Chair Professor & Former Chairman, AEC, delivering the IGC Colloquium during his visit to the Centre

Dr. Srikumar Banerjee, DAE Homi Bhabha Chair Professor & Former Chairman, AEC, during his visit to the Centre on June 3, 2013 delivered the IGC Colloquium on "Evolving Nuclear Fuel Cycle".

Dr. G. Venkataraman, Director (Retd.) ANURAG, DRDO & Former Vice-Chancellor,
Sri Sathya Sai Institute of Higher Learning delivering the IGC Colloquium

IGC Colloquium on "What Does One do, when the Job is Over ?" was delivered by Dr. G. Venkataraman, Director (Retd.) ANURAG, DRDO & Former Vice- Chancellor, Sri Sathya Sai Institute of Higher Learning during his visit to the Centre on November 13, 2013. He also visited various facilities in the centre.

Dr. Praveen Chaddah, Outstanding Scientist, RRCAT, Indore, delivered the IGC Colloquium on "Liquefaction of Helium and the Opening of Frontiers in Science & Technology" during his visit to the Centre on December 02, 2013.

Dr. Praveen Chaddah, Outstanding Scientist, RRCAT, Indore delivering the
IGC Colloquium

Prof. K. Ramnarayan, Vice Chancellor, Manipal University delivering the IGC Colloquium

Prof. K. Ramnarayan, Vice Chancellor, Manipal University during his visit to the Centre on December 23, 2013 delivered the IGC Colloquium on "The Vanishing art of Lecturing".

Visit of Bharat Ratna Prof. C.N.R. Rao to IGCAR
December 28-30, 2013

Prof. C.N.R. Rao with Dr. P.R. Vasudeva Rao, Director, IGCAR, Dr. C.S. Sundar, Director, MSG and Dr. M. Sai Baba, RMG during his visit to the Materials Science Group

Bharat Ratna Prof. C.N.R. Rao, F.R.S., National Research Professor, Honorary President & Linus Pauling Research Professor, Jawaharlal Nehru Centre for Advanced Scientific Research visited IGCAR during December 28-30, 2013. He met the senior colleagues of the Centre and discussed about various programmes in progress. He visited the Magnetocardiography/magnetoencephalography facility at Materials Science Group, spot technique facility for measurement of solidus-liquidus temperature of fuels & sensor laboratory in Chemistry Group, sodium fire and safety related facilities in Reactor Design Group, components testing facilities in Fast Reactor Technology Group and construction site of PFBR at BHAVINI. As a part of his visit, Prof. C.N.R. Rao interacted with Young Officers of the Centre and shared his experiences.

Prof. C.N.R. Rao, delivered the IGC Colloquium on "Celebration of Science" during his visit to the Centre on December 30, 2013. His lecture highlighted the contributions made by the eminent scientists in the field of Chemistry in the past tracing back to history and he also introduced many of them to the audience through his collection of rare historical photographs. Apart from this he highlighted the significance of year 2011 and 2012 especially with reference to Chemistry and their impact on further progress. The year 2011 marked the centenary of discovery of atomic structure by Rutherford, discovery of superconductivity by Kamerlingh Onnes and second Nobel Prize of Marie Curie, and the year 2012 marked the Centenary of the discovery of X-ray Crystallography. It is well known that Prof. Rao is an excellent orator, the lecture was very informative at the same time thought provoking.

Prof C.N.R. Rao delivering the IGC Colloquium

IGC COUNCIL

Chairman

Dr. P. R. Vasudeva Rao

Distinguished Scientist & Director, IGCAR

Dr. P.R. Vasudeva Rao, is currently the Director of Indira Gandhi Centre for Atomic Research (IGCAR) and General Services Organization and also Director of Chemistry Group, IGCAR at Kalpakkam. After graduating from Vivekananda College, Chennai, he joined DAE in the 16th batch of BARC training school. He obtained his Ph.D. Degree from Bombay University in 1979. He shifted to IGCAR in 1978 and was instrumental in setting up of the Radiochemistry Laboratory.   He is a recipient of the Indian Nuclear Society award (2007) for his contributions in the area of nuclear fuel cycle technologies. He has delivered the MRSI medal lecture in 1998 and has been awarded the MRSI-ICSC Superconductivity and Materials Science Senior Award in 2011. He was also selected for the award of the Silver Medal by the Chemical Research Society of India in 2011. He is a senior professor at the Homi Bhabha National Institute (HBNI) and has nearly 250 publications in peer reviewed international journals. His areas of interest include development of technologies for fast reactors and associated fuel cycles, actinide separations and education in the field of chemical sciences.

Members

Shri Sekhar Basu is a renowned nuclear engineer graduated from VJTI, University of Mumbai in mechanical engineering in 1974 and completed post graduate training programme in Nuclear Engineering at Bhabha Atomic Research Centre in 1975. Later he joined Reactor Engineering Division of BARC and completed the development of fuel for Boiling Water Reactors. He was shifted to Kalpakkam in 1988 and was responsible for commissioning of Land Based Nuclear Submarine Propulsion Plant. Subsequently, he was assigned the responsibility of Nuclear Recycle Programme and constructed reprocessing and waste management plants at Tarapur and Kalpakkam. Recently, he has also been involved in Fusion Reactor Programme, ITER. After taking over as Director, Bhabha Atomic Research Centre in 2012, Shri Basu is associated with research in basic and engineering sciences covering physics, chemistry, bio-medical, materials, etc. The work also involves development and application of technology for energy, health, food and agriculture sectors. Shri Basu is a recipient of awards from Indian Nuclear Society and Department of Atomic Energy for his significant contributions to the Atomic Energy Programme. He is a fellow of Indian National Academy of Engineers and has a number of publications to his credit. A degree of Doctor of Literature was conferred honoris causa on Shri Basu at the special convocation function held at Jadavpur University in December 2013. Apart from pursuing programmes of BARC in various strategic areas, he is also working towards major expansion programmes of BARC in food and health sector.

Shri Arun Kumar is a Graduate in Engineering (Metallurgy) and joined Bhabha Atomic Research Centre (BARC), Trombay after completing 16th Batch of Orientation Programme of BARC Training School. He is presently the Director of Nuclear Fuels Group and Head, Radiometallurgy Division in BARC. He had worked initially at Radiometallurgy Division for 14 years. In 1987, he was posted to Advanced Fuel Fabrication Facility (AFFF), BARC, Tarapur which is an Industrial Scale Plant for fabrication of (U-Pu)O$_2$ fuels. In 2004, he returned to Radiometallurgy Division, Trombay and was designated as Head, Radiometallurgy Division. Some of the highlights in his career in which he is deeply involved are development of Pu bearing fuel for thermal and fast reactors, development / fabrication of advanced fuel for fast reactors like mixed carbide fuel, metallic fuel and cermet fuel. He is a member of Project Management Committee of FRFCF, Kalpakkam, Safety Review Committee for Transport of Radioactive materials, Specialist Group, theme number 6, i.e. Fast Reactor Technology for reviewing XIth Plan Projects, AHWR Plant Siting Committee, Committee for review of AHWR Fuel Cycle activities, Task Force for assessment of preparedness of BARC facilities in the light of recent events in Japan, Convenor – Task force on Compact High Temperature Reactor (CHTR) fuel, a member of the NFC Board and the IGC Council and he is also Chairman of many BSC-SF Committees. He is recipient of DAE Special Contribution Award for excellence in Science, Engineering & Technology in 2008 and Group Achievement Award for FBTR fuel fabrication in 2009. He has authored more than 100 technical publications to his credit.

Shri Pradip R. Baviskar is from the Indian Administrative Service of the 1985 Batch, West Bengal Cadre. He is B.Sc. (Chemistry) with Post Graduate Diploma in Marketing Management. Major postings held by him so far include District Magistrate and Collector, Darjeeling District (West Bengal) (1994-1997). Joint Textile Commissioner, Ministry of Textiles, Government of India (1997-2002). Chief Executive Officer, Kolkata Metropolitan Development Authority (KMDA), Kolkata (2004-2009). Chief Vigilance Officer, Mumbai Port Trust (2010-2012). In January 2013 he joined Department of Atomic Energy as Joint Secretary in-charge of R&D wing which deals with units like BARC, IGCAR, RRCAT, VECC and all Aided Institutions under DAE.

Dr. P. Chellapandi is a Distinguished Scientist and Director, Reactor Design Group, IGCAR, Kalpakkam. He is from 22nd batch of BARC training school with first rank and joined IGCAR in 1979. He is responsible for the design and development of fast reactor power plant systems and components including core and shutdown and energy conversion systems. He is one of the key persons, who have been involved in the design and development activities of 500 MWe PFBR. His current activities focus on the development of innovative design features for the future fast breeder reactors beyond PFBR, planned by the Department. He has established two dedicated and unique laboratories at IGCAR: one for structural mechanics studies and another for safety engineering studies for the design validations. He has formulated many national collaborations with various reputed institutes and played a key role for establishing MoUs, particularly with IIT Madras, IIT Kanpur, IIT Kharagpur and IISc Bangaluru. He is the member of many important national and international committees including Project Design Safety Committee for PFBR (PDSC- PFBR), Apex Committee on Nuclear Power and Associated Fuel Cycle (AC-NP&AFC), Advisory Committee for Project Safety Review of Light Water Reactors (ACPSR-LWR-2), Nuclear Fuel Complex Board of Management, Convener, Task Force for Conceptual Design of Future FBRs, Advisory Committee for Nuclear Reactors & Fuel Cycle Committee (NRFCC) of Board of Research in Nuclear Sciences (BRNS), Advisory Committee on Codes, Guides and Associated Manuals for Safety in Design of Nuclear Power Plants (ACCGD)and Safety Research Scientific Committee, DAE, International Atomic Energy Agency (IAEA) Technical Working Group on Fast Reactors (TWG-FR), during the period 2006-2011, the Chairman for the IAEA Technical Co-Operation Expert Mission for Codes and Standards for Sodium Cooled Fast Reactors. (NSR-1), coordinator from India in executing the implementing agreement

under CEA-IGCAR Liquid Metal Fast Reactor Safety projects and an expert consultant for the conceptual design of an in-core sodium loop for high temperature multi sample, high dpa material experiments high flux reactor (JHR), CEA Cadrache. He has an outstanding academic record in Mechanical Engineering and a Gold Medal with perfect grade point average of 10 in his Master's Degree in the field of applied mechanics, from IIT Madras. He has guided more than ~15 PhDs, ~120 M.Tech projects and more than ~300 B.E Projects, all relevant to fast reactor design. He has a very impressive record of publications ~680 to his credit out of which 130 are in journals. He is a Fellow of Indian National Academy of Engineering. He has received the Homi Bhabha Science and Technology Award for the year 1997, Indian Nuclear Society Award and National Design Award in Mechanical Engineering in 2006, Agni Award for Excellence in Self-reliance – DRDO-2007, DAE Group Achievement Awards in 2006, 2007, 2008, 2009, 2010 and 2011 for design, manufacture and erection of PFBR reactor assembly components and Vasvik award 2009. He has been bestowed upon Distinguished Alumnus Award of the IIT Madras in 2010
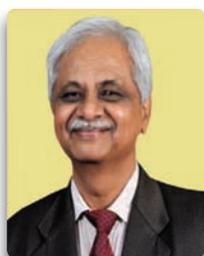
Shri S. G. Ghadge, Mechanical Engineering Graduate from Visvesvaraya National Institute of Technology, Nagpur, and Post Graduation in Nuclear Technology in BARC now known as Homi Bhabha National Institute. He has a distinguished career in the Department of Atomic Energy, Nuclear Power Corporation of India spanning 36 years, which covered multiple fields of Nuclear Reactor Process Design, Commissioning, Operational Improvements, Safety, Thermo Hydraulic Analysis with complex code development. He spearheaded the internal reviews for post Fukushima safety assessment taking into account international thinking and worked out safety enhancement measures arising out of these reviews apart from reviews by AERB. He was member of the Indian delegation to IAEA in the Convention of Nuclear Safety and contributed in generation of design and safety codes and guides for IAEA and AERB. He has several international and national publications to his credit. He is a Distinguished Scientist of the Department of Atomic Energy. Presently his responsibilities encompass design, health & safety, safety and licensing analysis, procurement for 700 MWe PHWR and building up of R&D facility at Tarapur. He is a full time Director on the Board of NPCIL from 1st July 2013.

Dr. P.D. Gupta, Distinguished Scientist is the Director, Raja Ramanna Centre for Advanced Technology, Indore. Dr. Gupta is an internationally known laser-plasma physicist who has made pioneering research contributions in this area. He passed M.Sc. Hons (Physics) from Punjab University in 1972 and joined Bhabha Atomic Research Centre. He is a recipient of four gold medals for securing first rank in various university examinations. He joined BARC in August 1973 after passing out from 16th batch (1972-73) of Training School and was awarded Homi Bhabha Medal and Prize. He received his Ph.D. from Bombay University in 1984 and did his Post-doctoral work at the Department of Electrical Engineering, University of Alberta, Canada during 1984-86. He is recipient of Young Scientist Award of Indian National Science Academy (1984) and Young Associateship of Indian Academy of Sciences (1986-91) and became Fellow of the National Academy of Sciences, India, in 2004. As Director, Dr. Gupta is steering many R&D programmes in frontline areas of accelerators and lasers at RRCAT. These include synchrotron radiation sources and their utilization, development of superconducting radio-frequency cavities for high energy accelerators, proton linac spallation neutron source, cryogenics and magnet technology, ultra-intense laser-plasma interaction, and lasers in research and industry. Dr. Gupta is a Senior Professor of Homi Bhabha National Institute (HBNI), Mumbai, and a member of the Academic Council. He has guided many young researchers for the award of Ph.D / M.Tech / M.Sc degrees. He has made ~ 350 research contributions of which 185 are published in international journals.

Dr. T. Jayakumar, B.Tech. (Metallurgy, REC Warangal), M.S (Metallurgy, IIT Madras), Ph.D (Engineering, University of Saarland, Germany) is currently a Distinguished Scientist and the Director, Metallurgy and Materials Group at IGCAR. Since 1978, he has been engaged in the field of Non-Destructive Evaluation. Over the years he has carried out and steered innovative research and development programmes in the areas of Non-Destructive Evolution, Failure Analysis and structural integrity of nuclear components specifically for the Fast Breeder Reactor. For the last few years he is actively coordinating and guiding research activities related to development of materials and manufacturing technologies for sodium cooled fast reactors, associated fuel cycle and Indian fusion programme. He is a Fellow of the Indian National Academy of Engineering. He has been a recipient of several awards such as National NDT Award from ISNT, Metallurgist of the Year award from IIM, Homi Bhabha Science and Technology Award from DAE, Outstanding Services Award from INS. He has co-authored three books, co-edited four books and has published over 270 papers in international journals. He also has six patents to his credit.

Dr. R. Natarajan, a Chemical Engineer is from the 19th batch of BARC training school and joined the Department of Atomic Energy in 1975. He is presently the Director of Reprocessing Group and Project Director, FRFCF in IGCAR. Under his leadership, the CORAL facility, for establishing the process technology for the reprocessing of fast reactor fuels was designed, erected and commissioned. He led the team which has successfully completed the reprocessing of fast reactor spent fuel, with a burn-up of as high as 155 GWd/t of a plutonium rich fuel, which is an international benchmark. He is also responsible for the R&D activities of fast reactor fuel reprocessing and setting up of demonstration as well as the commercial PFBR fuel reprocessing plants. The Demonstration Plant (DFRP) is in advanced stage of construction while the detailed design of commercial reprocessing plant has been completed. He is also responsible for the construction of the fuel cycle facility (FRFCF) for PFBR which is just about to commence. His specialization is in the design, development of process flow sheets and radiochemical plant design. He has also experience in the design and operation of equipment for thorium-uranium cycles. He has participated in the irradiated thorium fuel reprocessing campaigns at the Reprocessing Development Laboratory and the uranium recovered is used as fuel for the reactor, KAMINI. He has interest in solvent extraction process modeling, extraction equipment design, design of feed clarification systems of high active solutions, acid recovery systems, system designs of radioactive off-gas circuits and ventilation design of radioactive plants. He has over hundred technical presentations and publications to his credit. He has won the prestigious NOCIL Award for Excellence in Design and Development of Process Plant and Equipment for the year 2005 for his contribution in the development of fast reactor fuel reprocessing. He is also the recipient of   the INS award for the year 2006 for his contributions to Nuclear Fuel Cycle technologies. He is a Fellow of the Indian National Academy of Engineering d nd a honorary fellow of Indian Institute of Chemical Engineers.

Shri S. Paramasivam graduated as Mechanical Engineer from Madras Institute of Technology in the year 1981 and joined BARC in the 25th batch of Training School. After successful completion of training, he was posted at Heavy Water Board Head Office, Mumbai and was associated in mechanical project activities for Heavy Water Plant (Manuguru). In the year 1986, he was transferred to HWP (Manuguru), where he was involved in erection and commissioning activities pertaining to exchange units. He was promoted as Deputy Maintenance Manager (Mechanical) in the year 1998 as head of Mechanical Maintenance Section. In the year 2003 he was posted to HWP (Tuticorin) as Maintenance Manager in the year 2005 and promoted as Officer On Special Duty in the year 2008, subsequently as General Manager of Heavy Water Plant, Tuticorin. In July, 2013, he was appointed as Regional Director, MRPU, DPS, Chennai.

Shri C.K. Pithawa is Distinguished Scientist and Director, Electronics & Instrumentation Group, Bhabha Atomic Research Centre, Trombay, Mumbai. He did his Degree in Electrical Engineering from Government Engineering College, Rewa in 1973 and joined Reactor Control Division in August 1974 after completing one year training from 17th batch of BARC training school. He did his M.E. in Automation from I.I.Sc., Bengaluru in 1981 and M.S. in Electronics from University of Southampton, U.K. in 1986. He is a Fellow of National Academy of Engineering. Shri Pithawa has made significant contributions to the computer based control and monitoring systems for Pressurized Heavy Water Reactors, Light Water Reactors, Research Reactors and for particle accelerators. He is spearheading the development of radiation detectors, reactor instrumentation, semiconductor detectors and ASICs, RF instrumentation and ultrasonic instrumentation, PLC for safety systems, HPC and information security. He was deputed for about two years to Raja Ramanna Centre for Advanced Technology, Indore as Incharge, Indus Accelerator Complex to improve operational performance of Indus-2 accelerator. He has been associated with many important and strategic programmes of DAE. He received four DAE Group Achievement Awards in 2006, 2008 and 2012 and Special Contribution Award in 2007.

Dr. Prabhat Kumar, Distinguished Scientist, Chairman and Managing Director, BHAVINI is responsible for construction and commissioning of India's first Prototype Fast Breeder Reactor which has been designed indigenously and launched as a precursor to commercial exploitation of FBRs on a large scale. This advanced technology reactor requires understanding of various disciplines of science, multidisciplinary capability of engineering and management skills to achieve the success. In his career, he has worked on nuclear system and component design, indigenisation of critical nuclear equipment, participated in erection of the equipment and their commissioning. He has headed Quality Assurance Group of Kudankulam project during its formative years, later he worked for coolant channel life management, remote tooling for reactor inspection, maintenance and started the R&D centre for NPCIL. He has steered many programmes of vital importance for Indian nuclear power plants. He believes in inclusive growth and win-win situation for industrial participants, suppliers, contractors, employees and neighbourhood to the nuclear establishments. With a large exposure on Pressurized Heavy Water Reactor and Pressurized Water Reactor technologies, he has been chosen to construct India's prestigious Prototype Fast Breeder Reactor, PFBR. He has lead a multi disciplinary team from NPCIL and IGCAR directed towards ensuring a robust construction of PFBR.Dr. Prabhat Kumar is the recipient of Indian Nuclear Society Award for Excellence in Nuclear Technology. In addition, he has been conferred with "Prof. D.R.G. Achar Memorial Medal Award", "Life Time Achievement Award", "Best Philanthropist Award", "CEO with HR orientation Award", "Vignan Sankethika Puraskar", "IIW Sharp Tools Award", "For the sake of Honour Award" and many more awards & honors by various organizations/societies/university for his outstanding contributions in versatile fields. Under the leadership of Dr. Prabhat Kumar, a new company with small team has got many awards and honors for the BHAVINI such as "Green Site Award", "Safety Award", "Outstanding Concrete Structure Award" "Best in-house magazine Award", "Best HR Practices Award" and "Second Best Engineering Marvel of India Award for self reliance" by various prestigious organizations/Institutes. Dr.Prabhat Kumar has held positions of Chairman and expert member for various technical and management committees throughout the country. He is the alternate Chairman for the Site Selection Committee for construction of Nuclear Power Plants in India. Dr.Prabhat Kumar is the National Vice President of Indian Society of Non Destructive Testing (ISNT). He is also the Chairman of Authorized National Board for Company Certification (ANBCC) of Indian Institute of Welding. Due to his vast technical knowledge and experience, Dr. Prabhat Kumar has been conferred as the fellow of ISNT and fellow of "Indian National Academy of Engineering".

Shri K. K. Rajan is currently an Outstanding Scientist and Director of both Fast Reactor Technology Group and Engineering Services Group. He is from 24th batch of BARC Training School and joined IGCAR in 1981. He graduated in Electrical Engineering from NIT, Calicut. His initial contributions include purification, transportation and charging of sodium required for FBTR, calibration of FBTR sodium flowmeters and other sodium experiments in support of FBTR. He has been steering a multidisciplinary programme in the area of Sodium Technology. He is primarily responsible for design, construction, commissioning, safe operation and maintenance of high temperature experimental sodium facilities and conducting sodium experiments in support of FBR. He has made substantial contributions towards testing of PBFR model steam generator in SGTF and PFBR fuel handling machines at reactor operating conditions in LCTR. He was also involved in the development of permanent magnet flowmeters and special type of heaters required for FBR sodium systems. He has played a key role in the receipt and safe transfer of 1750 tonnes of nuclear grade liquid sodium to PFBR storage tanks.. He has published more than 140 papers in reputed national and international journals. He is a member of Indian Nuclear Society, Instrument Society of India and a fellow of Institution of Engineers (India).

Shri Rajnish Prakash, Chairman and Chief Executive, Heavy Water Board, has graduated in Chemical Engineering from University of Roorkee (presently I.I.T. Roorkee) in 1974. He has done post graduate course DIIT in Chemical Reaction Engineering from I.I.T. Delhi. Shri Prakash has worked in most of the Heavy Water Plants in various capacities. Shri Prakash played an important role in setting up and commissioning of India's first ammonia based Heavy Water Plant at Baroda and later in new generation plants. He also worked in the area of process development of ammonia-water exchange process which included pilot plant studies and development of efficient column internals. He is credited with indigenous development of catalyst for ammonia based Heavy Water Plants. Shri Prakash has been instrumental in process development for production of various stable isotopes like Oxygen 18 and is instrumental in promoting the non nuclear applications of Deuterium in the country through collaboration with academics and industry. Shri Prakash was also involved in design and implementation of various modifications and ENCON schemes at the plants which resulted in substantial saving of energy and reduction in cost of production. Shri Prakash was elevated to the post of Associate Director (Operation) at Heavy Water Board (Corporate Office) in April 2005. Later he was elevated to the post of Director (Technical) in January 2008. He was also working as Technical Advisor to Chief Executive, HWB, looking after Corporate / Strategic Planning, diversification & growth strategies, export of heavy water and alternate applications of heavy water. Shri Prakash coordinated the first export of Heavy Water to South Korea; a proud moment for DAE and the country. Later his efforts led to further export of heavy water to South Korea, China, USA & France. Shri Prakash is a recipient of many awards including Group Achievement Award of DAE for the year 2010 for his excellent contribution in "Indigenous Development of 2nd Stage Cylinder Body of High Pressure Synthesis Gas Compressor at HWP (Baroda)" and Group Achievement Award 2011 for "Development of Deuterated Solvents". Shri Prakash is also conferred with the "Technology Excellence Award" by the Indian Technology Congress. Shri Prakash took over as Chairman & Chief Executive of Heavy Water Board from April 2011.

Shri M. Raju is from Indian Administrative Service of the 2005 Batch, Jammu & Kashmir Cadre. He has done M.Sc. (Microbiology) and M.A. (History). Major postings held by him so far include District Magistrate and Collector, Kargil District (2010-2012), Vice-Chairman, Kargil Renewable Energy Development Agency, Chairman, DSSRB, Additional Secretary, Department of Rural Development, Government of Jammu & Kashmir. In October 2013, he joined Department of Atomic Energy as Internal Financial Adviser, Indira Gandhi Centre for Atomic Research.

Shri N. Saibaba is a Gold medalist from Andhra University. He joined the 19th batch of Training School, Mumbai and is the recipient of Bhabha Award for topping the batch. He developed expertise in the manufacture of seamless tubes in a variety of strategic and exotic materials employing hot and cold deformation processes for meeting critical requirements of Atomic Energy, Space and Defence. He has made several pioneering contributions in the manufacture of critical core components of Power Reactors, some of which were developed for the first time in the country. He was responsible, for the first time in the world, for developing a new manufacturing route for extremely thin walled "Seamless Calandria Tubes". These tubes have been in use in the Nuclear Power Reactors for the past 11 years, offering excellent promise and specially shaped pressure tubes for Advanced Heavy Water Reactors, development of hexagonal channels for Prototype Fast Breeder Reactors and square channels for Boiling Water Reactors through pilger route, development of pressure tubes by heat treated and strengthened route and establishment of process technology for manufacture of double clad tubes with zirconium lining. Shri Saibaba, as a team leader, developed a test loop with components made of high temperature alloy Nb-1Zr-0.1C. It is to his credit that the seamless tubes in 304H (Cu) and Inconel-617 for use in the Advanced Ultra Supercritical Boilers were developed to enhance the thermal efficient of the Thermal Power Plants from 28% to 47%. He is presently engaged as Director on the Boards of UCIL & IREL and IGCAR Council. Presently, he is the Chairman of Indian Institute of Metals (IIM), Hyderabad Chapter and Chairman for Indian Society for Non-Destructive Testing (ISNT), Hyderabad Chapter He is appointed as Chairman for Center of Plant Engineering Services (CoPES). He received Bharat Ratna Sir M. Visvesvaraya Award from the Institution of Engineers (India), DAE Award for Group contribution as Group Leader - 2006, 2009, 2010, 2011 & 2012,INS Award for contributions in the field of Nuclear Fuel Cycle Technologies – 2008, Annual NFC Award for Meritorious contribution – 2005, 2006 & 2007, Outstanding contribution from NFC Management – 1993 & 1998 and Gold Medal from Andhra University for securing First Rank – 1975. He is a Fellow of Andhra Pradesh Akademi of Sciences, Life Member of IIM, ISNT and INS.

Shri S. A. V. Satya Murty did his B.Tech. from Jawaharlal Nehru Technological University in 1977. He was a University Gold Medalist in his B.Tech. Later, he joined one year orientation course in Nuclear Science & Engineering (21st Batch) at BARC. He was awarded Homi Bhabha prize for getting 1st rank. In the initial years, he was working in the Central Data Processing System Section of FBTR. In 1981, he joined Computer Division and played a key role in the establishment of Mainframe Computer System for IGCAR. He is instrumental in establishing internet and E-Mail facilities, Network Security Systems, IGCAR Campus network etc. He also played an important role in the installation and development of High Performance Computing Facility, Intra DAE VSAT Network (Anunet), Grid Computing facility, PFBR Simulator, Advanced Visualization Centre, Wireless Sensor Networks lab etc., He has more than 110 Journal Publications / Conference Papers and edited two International Conference Proceedings Currently he is the Director of EIRSG and is responsible for the development of robust I&C systems for PFBR.

Dr. D.N. Sharma joined BARC in 1971. Since then he has carried out R&D in the area of Radiation Physics, Radiation Protection, and Development of radiation safety systems and Emergency Preparedness & Response. The Aerial Gamma Spectrometer developed by him had international recognition when it was used for around 2 years by IAEA team at Georgia (Russia) to search orphan sources. During his carrier spanning around 43 years he held important positions in BARC. Currently, he is Director of Health Safety & Environment Group, National Emergency Response Director and member of the Crisis Management Committee (CMG) of DAE. He is member of a no of National committees constituted by MHA (Ministry of Home affairs) and NDMA (National Disaster Management Authority). He was also a member RASSC committee of IAEA for nearly 12 years. He has steered the issue of deployment of radiation monitoring systems at all entry and exit ports of the country. These systems developed under his guidance at BARC are now being mass produced and are being deployed at all Seaports, Airports and border crossings of the country for detecting the unauthorized movement of radioactive materials.

Shri G. Srinivasan is a mechanical engineer from the 18th batch of BARC Training School. He joined FBTR project as a designer in 1975, and participated in the design, fabrication and installation of Reactor Assembly Components. He moved over to O&M in 1983. After holding the positions of Senior Engineer (Planning) & Senior Engineer (Technical), he took over as Technical Services Superintendent and later as AD (O&M). He is Director, ROMG since September 2008.

Dr. C. S. Sundar, obtained his Masters degree in Physics from the University of Delhi in 1973, and Ph.D in Physics from the University of Madras in 1983. He heads the Materials Science Group at IGCAR with a comprehensive research programme on basic research in materials science. He is also a Senior Professor at the Homi Bhabha National Institute. Dr. Sundar's research contributions, spanning over three decades, has been on the investigation of structure, defects and phase transitions in novel materials that include high temperature superconductors, fullerenes, strongly correlated systems and colossal magnetoresistive manganites using the techniques of positron annihilation and infrared spectroscopy. He has over 100 journal publications. He is a recipient of the Materials Research Society of India Medal, 1994, the Young Research award, IUMRS, ICA the MRSI-ICSC superconductivity and Materials Research Annual Prize 2007 and the Tamil Nadu Scientist (TANSA) award, 2008. He is a Fellow of the Indian Academy of Sciences, Bengaluru, National Academy of Sciences, Allahabad and has recently been elected as a Fellow of the Indian National Science Academy, New Delhi. Dr. Sundar is a member of the Nano Science Advisory Group of Department of Science and Technology, Research Council of the National Physical laboratory, New Dehi, and UGC-DAE CSR, Indore. He is on the Editorial Board of Solid State Communications and is an Associate Editor, Bulletin of Materials Science.

Shri K. K. Vaze obtained his B.Tech. degree in Mechanical Engineering from IIT, Bombay in 1973 and thereafter joined 17th batch of BARC Training School. After graduation from BARC Training School in 1974, he joined the Nuclear Systems Division of Indira Gandhi Centre for Atomic Research, Kalpakkam where he worked in the area of Structural Analysis and Design of Fast Reactor Components. In 1989, he joined the Reactor Safety Division of Bhabha Atomic Research Centre, Mumbai. His current fields of work include Design & Detailed Engineering of Advanced Heavy Water Reactor, Reactor Safety, Earthquake engineering, Fatigue and Fracture Analysis, Experimental Stress Analysis, Fitness-for-Purpose Evaluation, Residual Life Estimation and Life Extension. At present he holds the post of Director, Reactor Design & Development Group in Bhabha Atomic Research Centre. He is a fellow of Indian National Academy of Engineering (INAE) and recipient of Indian Nuclear Society (INS) Award: Nuclear Reactor Technology, including Reactor Safety in 2007 for his contributions in the area of structural analysis and design related to reactor safety. He has also received DAE Special Contributions Award in the year 2007 and Group Achievement Award 2010.

Shri P. K. Wattal is a Graduate in Chemical Engineering and joined Bhabha Atomic Research Centre (BARC), Trombay after completing 18th Batch of Orientation Programme of BARC Training School. Since then, he has been involved with the R&D activities in the area of backend of nuclear fuel cycle. Presently, as Director, Nuclear Recycle Group, BARC, he is heading the Reprocessing & Waste Management Programmes at the back-end of Nuclear Fuel Cycle at Trombay and holding the responsibility of setting up and operation of Reprocessing and Waste Management Plants. Among the international assignments, Shri Wattal is Chairing a Working Group on Rad-waste of Test Blanket Modulefor ITER Organization, Cadarache, France. He is also leading Indo-French Bilateral Programme on waste management. He is also a Member of Technical Working Group on Nuclear Fuel Cycle Options and Spent Fuel Management (TWGNFCO) of International Atomic Energy Agency (IAEA), Vienna.

Organisation and Activities of Various Groups

Dr. P.R. Vasudeva Rao
Director, IGCAR

Chemistry Group

Dr. P.R. Vasudeva Rao
Director, CG

Dr. K. Nagarajan
AD, CG & Head, FChD

Dr. K.V. Govindan Kutty
Head, LMSCD

Shri G. Ravishankar
Head, CFD

The Chemistry Group is responsible for carrying out R&D to provide inputs with respect to all the chemistry aspects of the fast reactor and its fuel cycle. Besides the R&D activities, the Chemistry Group also provides extensive analytical support using a wide range of analytical techniques to all the programmes at Kalpakkam. The areas of R&D in Chemistry Group include sodium chemistry, chemistry of un-irradiated as well as irradiated fuel materials, development of fuel cycle, high temperature chemistry, analytical chemistry, spectroscopy and boron chemistry. Chemistry Group also has been developing instrumentation and facilities in support of the R&D programme. Development of sensors for PFBR and sensors for environmental applications, development of radionuclide traps for PFBR, development of cleaning and decontamination techniques for fast reactor components, development of technology for production of plutonium rich fuels and minor actinide containing fuels through sol-gel route, development of sodium bonding for metallic fuels and pyroprocessing are some of the R&D programmes on the anvil. Recent achievements include the fabrication of test fuel pins containing microspheres of $(U,Pu)O_2$ for irradiation in FBTR, demonstration of uranium recovery from U-Zr slugs by electrorefining, determination of burn-up of MOX(PFBR) test fuel by HPLC and development of unsymmetrical diglyoclamides as candidate extractants for minor actinide partitioning.

Electronics, Instrumentation and Radiological Safety Group

Shri S.A.V. Satya Murty
Director, EIRSG

Shri N. Murali
AD, ICG & Head, RTSD

Dr. B. Venkatraman
AD, RSEG & Head, RSD

Shri B. Ananthapadmanaban
Head, QAD

Shri K.K. Kuriakose
Head, CD

Dr. K.K. Satpathy
Head, EnSD

Shri D. Thirugnanamurthy
Head, EID

The Electronics, Instrumentation and Radiological Safety Group is actively involved in the development of Instrumentation & Control for the 500 MWe Prototype Fast Breeder Reactor. Towards this the I&C systems are designed with safety and availability of the reactor as the guiding requirements through redundant systems and also keeping in mind the simplicity of design and maintainability. A judicious combination of hardwired and computer based I&C systems, state-of-the-art design, manufacturing processes and testing were employed in the design of I&C systems. The systems developed include safety critical, safety related and non safety I&C systems. The Prototype systems were qualified after rigorous environmental, EMI/EMC and seismic testing. The application software developed was subjected to thorough Verification & Validation procedures. The Group is also developing a full scope replica type Operator Training Simulator for PFBR. An advanced visualization centre was established and various PFBR systems are modeled for visualization in 3D and walkthrough. R&D activities in the areas of innovative instrumentation using pulsating sensors, Wireless Sensor Networks for use in future reactors, computational intelligence, knowledge management etc. are in progress. State-of-theart computational facilities with a total processing power of about 30 tera FLOPS and data communication facilities are being provided. To take care of the security challenges the security electronics systems are constantly deployed and upgraded. The Group is also responsible for providing quality assurance/quality control services for all the major projects being undertaken by IGCAR through the ISO 9001-2008 certified Quality Assurance Division. The Radiological Safety Division of the Group is responsible for R&D activities in the areas of radioactivity transport and improving the radiation detection and measurements through advanced techniques. This Division provides health physics and radiation safety services for the radioactive facilities in IGCAR. Environmental and Industrial Safety Division provides industrial safety services to all the facilities at IGCAR. This Division also carries out R&D in the domain of aquatic and terrestrial biodiversity and sediment characterization. The Group organizes public awareness programs on radiation safety and nuclear energy in addition to training and awareness programs on industrial, radiation and fire safety to occupational workers.

Engineering Services Group

Shri K.K. Rajan
Director, ESG

Shri A. Jyothish Kumar
AD, ESG &Head, ESD

Shri C. Sivathanu Pillai
AD, CEG

Shri C. Chandran
Head, AC&VSD

Shri B. Harikrishnan
Head,CMWD

Shri G. Kempulraj
Head,CWD

Shri C. Sundaramurthy
Head,ASED

The Engineering Services Group (ESG) is responsible for providing quality services and activities pertaining to Civil engineering, Electrical Engineering, Voice Communication Systems, Air-conditioning and Ventilation Systems, Material Handling Equipments and Central Workshop activities. The group also coordinates the BSNL requirements of the Centre. The group has a mandate to establish additional infrastructure requirements so as to meet Design, R&D and operational objectives of IGCAR. The group has expert teams with capability to design, engineer and execute systems under their jurisdiction. Electricity, water, quality-air and other services including services from Central Workshop are being extended to other units of DAE located at Kalpakkam. The nature of work involves interaction with several State Government and Central Government Organisations. AC&VSD is responsible for providing reliable air-conditioning and ventilation services to various radioactive laboratories and R&D facilities of the Centre.

Fast Reactor Technology Group

Shri K.K. Rajan
Director, FRTG

Shri B. Babu
Head, IDSD

Shri B.K. Nashine
Head, DDRSD

Shri G. Padmakumar
Head, SEHD & CTD

Shri V. Prakash
Head, VDD

Fast Reactor Technology Group (FRTG) has the mandate of development and testing of reactor components of FBRs The group was responsible for the engineering development and testing of many components of PFBR in air, water and sodium. Design validation of critical components of FBR is achieved through experiments in sodium and water using full scale/scaled down models. FRTG has acquired expertise in the development of sensors and devices for sodium application, such as - EM flow meters, level probes, leak detectors, plugging indicator, cold trap and electromagnetic pumps. The group is entrusted with the responsibility of engineering development towards scaling up of pyro processing techniques from laboratory to engineering scale. Setting up of engineering scale facilities for demonstration of pyroprocessing is being pursued by the group. Expertise has been developed in sodium handling and in the design, construction, commissioning and operation of high temperature sodium systems. The major sodium test facilities of FRTG include - 5.5 MWt Steam Generator Test Facility (SGTF) for testing the model SG of PFBR, SADHANA loop for experimentally demonstrating natural convection based safety grade decay heat removal system of PFBR, Large Component Test Rig (LCTR) for testing critical full scale PFBR components, In Sodium Test facility (INSOT) for creep and fatigue testing and Sodium Water Reaction Test (SOWART) facility to study self wastage and impingement wastage of SG tubes. Recent achievements of FRTG towards PFBR include- sodium testing of PR&PTM of Inclined Fuel Transfer Machine (IFTM), testing and qualification of under sodium ultrasonic scanner, design, fabrication, qualification and supply of two nos. of Core Flow Monitoring Mechanisms, development of extended spark plug type leak detector, testing of Eddy Current Position Sensor (ECPS) for DSRDM, development of SONAR device for subassembly vibration measurement, commissioning and operation of Ambient temperature Electro refiner and manufacture and sodium calibration of eddy current flow sensors for primary sodium pumps. Major activities currently being pursued in FRTG include - sodium testing of transfer arm for PFBR, integrated testing of IFTM of PFBR, development of RADAR level probes for sodium level measurement, conduct of high temperature tribology and thermal striping experiments for evaluating FBR component materials, design, fabrication and erection of facilities for development of pyroprocessing technology, fabrication of integrated cold trap for in-vessel purification, and development of pressure measurement device and ex-vessel level probe for sodium applications.

Materials Science Group

Dr. C.S. Sundar
Director, MSG

Dr. G. Amarendra
Head, MPD

Shri M.P. Janawadkar
Head, CMPD

Dr. A.K. Tyagi
Head, SND

The Materials Science Group, comprising of three Divisions, has the mandate of pursuing high quality basic research on topical problems in Materials Science, to work towards ion beam and computer simulation of radiation damage and to pursue research on innovative sensors accruing from basic research in superconductivity and nanomaterials. The Condensed Matter Physics Division focuses on the investigation of physical properties of novel materials under temperature, pressure and magnetic fields. Active research programs on Raman spectroscopy studies of vibrational properties, Dynamic light scattering and Confocal Microscopy studies of soft condensed matter, Laser heated diamond anvil cell facility for synthesis and study of materials under high pressure and high temperature and investigation of material properties at low temperatures under high magnetic fields and pressures are being pursued. The indigenously built SQUID sensors and control electronics have been translated into SQUID based measuring systems such as a high field magnetometer, a SQUID based set-up for Non-Destructive Evaluation (NDE), and SQUID based Magnetoencephalography (MEG). The activities of Materials Physics Division pertain to studies on Ion beam simulation of radiation damage using a 1.7 MV tandem accelerator; in depth studies on defects using Positron Annihilation Spectroscopy and Computer simulation of material properties. The Surface and Nanoscience Division focuses on studies on thin films using a variety of techniques such as Secondary Ion Mass Spectrometry and Scanning Probe Microscopy. Studies on controlled growth of nanometric multi-layer films for increased hardness and exploration of nanomaterials micromachined cantilevers and MEMS as sensors are being actively pursued.

Metallurgy and Materials Group

Dr. T. Jayakumar
Director, MMG

Dr. A.K. Bhaduri
AD ,MDTG

Dr. U. Kamachi Mudali
AD, CSTG

Dr. S. Venugopal
AD, GRIP & Head, RIRD

Dr. M. Vijayalakshmi
AD, PMG

Shri Jojo Joseph
Head, PIED

Dr. M.D. Mathew
Head, MMD

Shri E. Mohandas
Head, MSSCD

Dr. B. Purna Chandra Rao
Head, NDED

Dr. Saroja Saibaba
Head, MTPD

Dr. Shaju K. Albert
Head, MTD

The Metallurgy and Materials Group (MMG) of IGCAR has, ever since its genesis pursued a vibrant research and development agenda that is targeted to provide a comprehensive package of knowledge driven solutions to a variety of materials related issues of India's fast reactor and associated fuel cycle programmes. In tune with this philosophy, MMG has made a major contribution towards successful development of three generations of structural materials, such as, austenitics, ferritics and the most recent oxide dispersion strengthened (ODS) steels for withstanding irradiation levels of up to 200 dpa for core components and a life span of about 60 years for structural components of reactor systems. In addition, an extensive array of new materials, like ferroboron for meeting the requirement of cheap and alternate neutron shield material, high temperature ferroseals for sodium pumps, iron based soft magnetic alloy for control rod applications, and corrosion resistant materials and coatings for aqueous and pyrochemical reprocessing applications, have come out of MMG's broad based R&D programmes. Over the years, MMG has also pioneered the design, fabrication and in-pile testing of irradiation capsules, which is supported by the deployment of extensive post irradiation examination facilities. Thus, extremely valuable data on in-pile performance of various fuel and structural materials have been gathered till date. In a related context, MMG has also specialized in developing a spectrum of nuclear sector specific non destructive evaluation (NDE) techniques that are aimed at inspecting difficult to handle as well as to approach large sized and intricate reactor components. The human resource expertise of MMG has been an exquisite blend of experienced and energetic talents, which specialize in almost all branches of theoretical and experimental aspects of materials science and component manufacturing technology. Advanced welding techniques for joining special materials with tight control over process parameters and ensuring component integrity, automated and robotic systems for remote inspection of critical engineering components as well as for post irradiation examination facilities, robust modeling protocols for predicting high temperature phase stability, thermophysical properties, deformation behavior and mechanical properties of materials under various loading conditions etc. have been successfully developed by MMG. In a nutshell, MMG houses a very elaborate and state of the art materials characterization and testing facilities that have also been extensively used for catering to some of the materials developmental issues of fusion reactors and advanced ultrasupercritical power plant programmes. The ready availability of abundant technical expertise combined with a wide range of advanced characterization tools has made it possible to attract many a young brains to pursue their research programs at MMG under the banner of Homi Bhabha National Institute (HBNI).

Reactor Design Group

Dr. P. Chellapandi
Director, RDG

Shri K. Madhusoodanan
AD, PPG & Head, I&CD

Shri P. Puthiyavinayagam
AD, CDG

Shri P. Selvaraj
AD, RAG

Shri V. Balasubramaniyan
Head, RCD

Dr. K. Devan
Head, RND

Shri A. John Arul
Head, RSDD

Shri B.K. Nashine
Head, SED

Shri S. Raghupathy
Head, CH & MD

Shri N. Theivarajan
Head, PPCD

Dr. K. Velusamy
Head, MHD

Reactor Design Group is responsible for analysis of FBR power plant systems and design and development of components including core, shutdown and handling mechanisms and balance of plant. The group is responsible for getting safety clearance from Atomic Energy Regulatory Board (AERB). The group comprises of Core Design Group (CDG), Reactor Analysis Group (RAG), Power Plant Group (PPG), Reactor Components Division (RCD) and Component Handling & Mechanism Division (CHMD). The group also executes R&D in the domain of structural mechanics, thermal hydraulics and safety engineering, involving national and international institutions. It provides design support to the construction and commissioning of 500 MWe Prototype Fast Breeder Reactor (PFBR), which is under construction at Kalpakkam. It also provides analytical support to other groups in the Centre including Fast Breeder Test Reactor (FBTR) as well as for other strategic and high end technologies in the country. The responsibility of group includes developing high quality human resource for the design and analysis of SFRs in the country. It is currently engaged in conceptualizing as well as detailing the innovative reactor components for the reactor assembly of future SFRs. The group has about 145 scientists and engineers, who are relatively younger consisting of three groups and two divisions and two laboratories. These apart, it has a modern design office with many advanced modeling and analysis softwares, Structural Mechanics Laboratory (SML) having state-of-the-art facilities for carrying out tests on large components, high temperature structural integrity and seismic tests with large size shake tables and safety research laboratory (SRL) for carrying out tests in the domain of severe accidents and to study the science & technology of sodium fires and fire extinguishers. This group has high quality expertise in the domain of design of mechanisms operating in sodium, mechanical design and analysis of components as per the American (ASME) and French (RCC-MR) design codes, thermal hydraulics of liquid metal, plant dynamics etc.

The group is periodically providing design supports to other national mission projects, especially in space and other energy sectors.

Reprocessing Group

Dr. R. Natarajan
Director, RpG

| **Shri A. Ravishankar**
AD, ROG | **Shri V. Sundararaman**
AD, PDCG & Head, FRPD | **Shri B. M. Anandarao**
Head, RPDD | **Dr. U. Kamachi Mudali**
Head, RRDD | **Shri V. Vijayakumar**
Head, RPOD |

The success of Indian Fast Breeder Reactor (FBR) programme depends on closing the fuel cycle within a short period so that the inventory of fissile material outside the reactor can be as small as possible. The Reprocessing Group (RpG) of IGCAR is responsible for achieving this objective. Various activities with regard to the fast reactor fuel reprocessing technology such as the design, construction and operation of the reprocessing plants are being undertaken by this group. There are facilities to carry on extensive engineering scale testing of equipment and systems before installation in radioactive hot cells. Chopper, dissolver, feed clarification equipment, centrifugal extractors and different types of pulse columns are a few important equipment that are being developed for deployment in fast reactor fuel reprocessing plants. Apart from equipment development, research is towards understanding and solving various process, chemistry and analytical problems of fast reactor fuel reprocessing such as, process flow sheet studies to improve the plant performance for higher recoveries and reduced waste generation, mathematical modeling of solvent extraction of the complex U-Pu system, solvent management, development of alternate solvent-diluent systems, development of online monitoring of Pu for process control, liquid flow metering in high radioactive fields, development of material handling equipment inside the hot cells etc. In one of the hot cell facilities, uranium was recovered from irradiated thorium rods using THOREX process which is used as fuel in KAMINI reactor and in FBTR (as PFBR test fuel). The other hot cell facility, called CORAL (Compact facility for Reprocessing Advanced fuels in Lead cells) commissioned in 2003, is being deployed as a versatile test bed for validating the process flow sheet and scaling up of equipment designs for fast reactor fuel reprocessing, by processing the FBTR spent fuel. This experimental facility has been used for reprocessing several batches of mixed carbide fuels irradiated in FBTR with 25, 50, 100 and 155 GWd/t burn-ups. This has provided valuable experience to the design of Demonstration Fast Reactor Fuel Reprocessing Plant in which all the types of FBTR fuels, such as the mixed carbide and oxide of different compositions, will be reprocessed on a regular basis. DFRP is also designed to reprocess PFBR fuel subassemblies also for demonstrating the reprocessing of irradiated PFBR oxide fuels.In addition to these activities, RpG is also carrying out the design of the reprocessing plant, for reprocessing spent fuels of PFBR on commercial basis.

Reactor Operations and Maintenance Group

Shri G. Srinivasan
Director, ROMG

Dr. V. Ganesan
Project Manager, DFMF
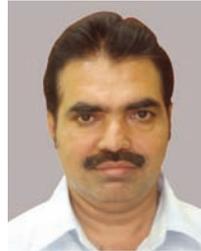
Shri K.V. Suresh Kumar
Head, ROD

Shri A. Babu
Head, RMD

Shri N. Kasinathan
Head, RAD

Dr. R. S. Keshavamurthy
Head, RPD

Ms. S. Usha
Head, TSD

ROMG is responsible for safe operation of Fast Breeder Test Reactor (FBTR) and KAMINI reactor within the limits given in technical specification documents. The group also takes part in the operational safety review of PFBR Project documents. The Training section of the group is also responsible for training the O&M staff of PFBR and future FBR's besides training O&M staff of FBTR and KAMINI,. Progressive modifications in FBTR to increase its availability and for gaining newer experience in operation, utilizing the reactor for irradiation of advanced fuels and materials for fast reactors and conducting safety related experiments form a major part of ROMG's activities.

Fast Reactor Fuel Cycle Facility

Dr. R. Natarajan
Project Director

Fast Reactor Fuel Cycle Facility is entrusted with the work of planning, designing and constructing the Fast Reactor Fuel Cycle Facility to close the fuel cycle of PFBR. FRFCF is a multi unit project involving BARC, IGCAR and NFC. IGCAR is piloting the work on this project. The Group interacts with the participating groups from different units of DAE . Coordination of activities related to design of the facility, obtaining regulatory and statutory approvals for the project, preparation of the detailed project report, processing for obtaining financial sanction and development of infrastructure at the project site, is the mandate of this group.

Resources Management Group

Dr. M. Sai Baba
AD, RMG & Head, SIRD/
SPHRDD

Resources Management Group comprises of the Scientific Information Resource Division, Strategic Planning and Human Resources Development Division and OCES-Training Section. The mandate of the Group is towards planning and management of resources like financial (budget), human and scientific information resources in the Centre. This significant activities of the Group include: Strategic planning and human resource management, Conducting the academic programmes of BARC Training school at IGCAR, Formulating and monitoring Capital projects towards budget planning and management including providing necessary reports and proposals to DAE, Automation and integration of activities pertaining to administration, accounts, stores, budget and procurement on a single platform, Coordinating the visits of important dignitaries and delegations to the Centre, Formulating and facilitating collaborations and MoU, Providing technical coordination with various agencies and conducting public awareness programmes for the benefit of public and media, Providing information resources through conventional library and the library on the desktop by digital networking with special emphasis to cater to the needs of students and young scholars and publishing important documents of the Centre like IGC Newsletter, Annual Report, Benchmarks, preparation of annual reports and plan related documents.

Technical Co-ordination & Quality Control Division

Shri N.Vijayan Varier
Head, TC&QCD

Technical Co-ordination & Quality Control Division is primarily responsible for quality control of several critical equipments for IGCAR in the western region. TC&QCD has also been providing technical co ordination services for various activities of IGCAR including PFBR, FRFCF. TC&QCD also participates in a number of R&D activities which are being carried out at BARC towards meeting the mandate of IGCAR and PFBR. Staff of TC&QCD completed the QA support for manufacture of waste transfer casks and shell shielding units at Baroda and Mumbai, Ferro boron capsules, indigenous development of LRP and SRP. TC&QCD is continuing to participate in the R&D activities for development of high temperature fission chambers, other neutron detectors for PFBR along with various divisions of BARC and ECIL, under sodium ultrasonic scanner, for PFBR including manufacture of scanner, participation in task force for the reactor worthy scanner and spare scanner, ISI vehicle development and manufacture at Pune and sputter ion pump development at BARC and inspection. TC&QCD participated in the inspection activities for the major components of welded grid plate technology development, inner vessel sector model, tri-junction forging, motors for centrifugal extractors for DFRP, safety grade decay heat exchanger and air heat exchanger models, integrated cold traps for purification of Na, sodium to air heat exchanger, and PFBR Neutron Detector Assembly components for development.

Madras Regional Purchase Unit

Shri S.Paramasivam
RD, MRPU

Material Management activities for IGCAR, GSO, BARCF & HWP(T) are taken care of by Madras Regional Purchase Unit (MRPU) which comes under Directorate of Purchase & Stores of Department of Atomic Energy. Procurement and payment to suppliers are carried out at Chennai and inventory and accounting are carried out by Central Stores at Kalpakkam. MRPU was the first DAE unit to introduce e-tendering and more than 70% of files were processed by e-tendering mode. MRPU switched over to the e-tender system of M/s ITI Ltd in June 2013. During the year 2013, MRPU processed 4476 indents with an estimated cost of 611 Crores and released 3052 purchase orders worth 191 Crores.

Administration & Accounts

Shri M. Raju
Internal Financial Adviser

Shri N.G. Krishnan
Chief Administrative Officer

Shri K.R.Sethuraman
AO(R&SR) & Secretary, IGCSC

247

LIST OF IMPORTANT ABBREVIATIONS

AC&VSD	Air Conditioning and Ventilation System Division
AERB	Atomic Energy Regulatory Board
A&SED	Architecture & Structural Engineering Division
BARC	Bhabha Atomic Research Centre
BARCF	Bhabha Atomic Research Centre Facilities
BHAVINI	Bharatiya Nabhikiya Vidyut Nigam Limited
CD	Computer Division
CDG	Core Design Group
CED	Civil Engineering Division
CEG	Civil Engineering Group
CERMON	Continuous Environmental Radiation Monitoring Network
CFD	Chemical Facilities Division
CG	Chemistry Group
CTD	Chemical Technology Division
CH&MD	Components Handling & Mechanism Division
CMPD	Condensed Matter Physics Division
C&MWD	Contracts & Major Works Division
CORAL	Compact facility for Reprocessing Advanced fuels in Lead cell
CSTG	Corrosion Science & Technology Group
CWD	Central Workshop Division
DDRSD	Device Development and Rig Services Division
DFMFF	Demonstration Facility for Metallic Fuel Fabrication
EID	Electronics and Instrumentation Division
EIRSG	Electronics and Instrumentation and Radiological Safety Group
EnSD	Environmental & Safety Division
ESD	Electrical Services Division
ESG	Engineering Services Group
FBR	Fast Breeder Reactor
FBTR	Fast Breeder Test Reactor
FChD	Fuel Chemistry Division
FRFCF	Fast Reactor Fuel Cycle Facility
FRPD	Fuel Reprocessing Process Division
FRTG	Fast Reactor Technology Group
GRIP	Group for Remote Handling, Robotics, Irradiation Experiments and PIE
GSO	General Services Organisation
IAEA	International Atomic Energy Agency
IIT	Indian Institute of Technology
ID&SD	Instrumentation Development & Services Division
IMSc	Institute of Mathematical Sciences
I&CD	Instrumentation & Control Division
ICG	Instrumentation & Control Group
LMFBR	Liquid Metal Cooled Fast Breeder Reactor
MAPS	Madras Atomic Power Station
MCD	Materials Chemistry Division
MDTG	Materials Development and Technology Group
MHD	Mechanics & Hydraulics Division
MMD	Mechanical and Metallurgy Division
MMG	Metallurgy and Materials Group
MPD	Metal Physics Division
MRPU	Madras Regional Purchase Unit
MSG	Materials Science Group
MSSCD	Materials Synthesis & Structural Characterization Division
MTD	Materials Technology Division
MTPD	Microscopy & Thermo-Physical Property Division
NDED	Non-Destructive Evaluation Division
NFC	Nuclear Fuel Complex
NICB	Nuclear Island Connected Building
NPCIL	Nuclear Power Corporation of India Ltd.
PDCG	Process Design & Commissioning Group
PFBR	Prototype Fast Breeder Reactor
PHWR	Pressurized Heavy Water Reactor
PIED	Post Irradiation Examination Division
PMG	Physical Metallurgy Group
PPCD	Power Plant Control Division
PPG	Power Plant Group
PDCG	Process Design & Commissioning Group
QAD	Quality Assurance Division
RAD	Reactor Analysis Division
RAG	Reactor Analysis Group
RCD	Reactor Components Division
RDG	Reactor Design Group
RIRD	Remote Handling, Irradiation Experiments and Robotics Division
RMD	Reactor Maintenance Division
RMG	Resources Management Group
RND	Reactor Neutronics Division
ROD	Reactor Operation Division
ROMG	Reactor Operation and Maintenance Group
RPDD	Reprocessing Plant Design Division
RpG	Reprocessing Group
RPOD	Reprocessing Plant Operations Division
RPOG	Reprocessing Projects & Operation Group
RRDD	Reprocessing Research and Development Division
RSD	Radiological Safety Division
RSDD	Reactor Shielding and Data Division
RSEG	Radiological Safety & Environmental Group
RTSD	Real Time Systems Division
SED	Safety Engineering Division
SE&HD	Sodium Experiments & Hydraulics Division
SGTF	Steam Generator Test Facility
SIRD	Scientific Information and Resource Division
SND	Surface and Nanoscience Division
SOWART	Sodium Water Reaction Test facility
SP&HRDD	Strategic Planning & Human Resource Development Division
TC&QCD	Technical Coordination & Quality Control Division
TSD	Technical Services Division
VDD	Vibration Diagnostics Division

INDIRA GANDHI CENTRE FOR ATOMIC RESEARCH

Dr. P. R. VASUDEVA RAO
DIRECTOR, IGCAR

IGC COUNCIL

IGC SCIENTIFIC COMMITTEE [IGCSC]

DIRECTOR'S ADVISORY COMMITTEE [DAC]

Dr. P. R. VASUDEVA RAO
DIRECTOR
CHEMISTRY GROUP

Dr. C. S. SUNDAR
DIRECTOR
MATERIALS SCIENCE GROUP

Shri S. A. V. SATYA MURTY
DIRECTOR
ELECTRONICS, INSTRUMENTATION AND
RADIOLOGICAL SAFETY GROUP

Dr. T. JAYAKUMAR
DIRECTOR
METALLURGY & MATERIALS GROUP

Dr. R. NATARAJAN
DIRECTOR
REPROCESSING GROUP
Project Director, FAST REACTOR FUEL CYCLE FACILITY

Dr. P. CHELLAPANDI
DIRECTOR
REACTOR DESIGN GROUP

Shri K. K. RAJAN
DIRECTOR
FAST REACTOR TECHNOLOGY GROUP &
ENGINEERING SERVICES GROUP

Shri G. SRINIVASAN
DIRECTOR
REACTOR OPERATIONS & MAINTENANCE GROUP

Dr. M. SAI BABA
ASSOCIATE DIRECTOR
RESOURCES MANAGEMENT GROUP

Shri N. VIJAYAN VARIER
TECHNICAL CO-ORDINATION &
QUALITY CONTROL DIVISION,
(Station at Mumbai)

Shri M. RAJU
INTERNAL FINANCIAL ADVISER

Shri N. G. KRISHNAN
CHIEF ADMINISTRATIVE OFFICER

Groups / Divisions / Heads

Chemistry Group

Dr. P. R. VASUDEVA RAO
DIRECTOR

- Dr. K. NAGARAJAN
  ASSOCIATE DIRECTOR
  CHEMISTRY GROUP

- Dr. K. NAGARAJAN
  FUEL CHEMISTRY DIVISION

- Dr. K. V. GOVINDAN KUTTY
  MATERIALS CHEMISTRY DIVISION

- Shri G. RAVISHANKAR
  CHEMICAL FACILITIES DIVISION

Electronic, Instrumentation and Radiological Safety Group

Shri S.A.V. SATYA MURTY
DIRECTOR

- Shri K. K. KURIAKOSE
  COMPUTER DIVISION

- Shri N. MURALI
  ASSOCIATE DIRECTOR
  INSTRUMENTATION & CONTROL GROUP

- Shri N. MURALI
  REAL TIME SYSTEMS DIVISION

- Shri D. THIRUGNANAMURTHY
  ELECTRONICS & INSTRUMENTATION
  DIVISION

- Dr. B. VENKATARAMAN
  ASSOCIATE DIRECTOR
  RADIOLOGICAL SAFETY & ENVIRONMENTAL GROUP

- Dr. B. VENKATARAMAN
  RADIOLOGICAL SAFETY DIVISION

- Shri B. ANANTHAPADMANABAN
  QUALITY ASSURANCE DIVISION

- Dr. K. K. SATPATHY
  ENVIRONMENTAL & SAFETY DIVISION

Resources Management Group

Dr. M. SAI BABA
ASSOCIATE DIRECTOR

- Dr. M. SAI BABA
  STRATEGIC PLANNING & HUMAN RESOURCE
  DEVELOPMENT DIVISION

- Dr. M. SAI BABA
  SCIENTIFIC INFORMATION RESOURCE DIVISION

Administration

Shri N. G. KRISHNAN
CHIEF ADMINISTRATIVE OFFICER

- Shri K. R. SETHURAMAN
  ADMINISTRATIVE OFFICER (R&SR)

- Shri S. S. BOOPATHY
  ADMINISTRATIVE OFFICER (P)

Accounts

Shri M. RA JU
INTERNAL FINANCIAL ADVISER

- Shri T. M. G. KUTTY
  DEPUTY CONTROLLER OF ACCOUNTS

Groups / Divisions / Heads

Engineering Services Group

Shri K. K. RAJAN
DIRECTOR

Shri A. JYOTHISHKUMAR
ASSOCIATE DIRECTOR
ENGINEERING SERVICES GROUP

Shri SIVATHANU PILLAI
ASSOCIATE DIRECTOR
CIVIL ENGINEERING GROUP

Shri A. JYOTHISHKUMAR
ELECTRICAL SERVICES DIVISION

Shri SIVATHANU PILLAI
CIVIL ENGINEERING DIVISION

Shri G. KEMPULRAJ
CENTRAL WORKSHOP DIVISION

Shri C. SUNDARAMURTHY
ARCHITECTURE & STRUCTURAL
ENGINEERING DIVISION

Shri C. CHANDRAN
AIR-CONDITIONING & VENTILATION
SYSTEM DIVISION

Shri B. HARIKRISHNAN
CONTRACT & MAJOR WORKS DIVISION

Fast Reactor Technology Group

Shri K. K. RAJAN
DIRECTOR

Shri V. PRAKASH
VIBRATION DIAGNOSTICS DIVISION

Shri G. PADMAKUMAR
CHEMICAL TECHNOLOGY DIVISION

Shri B. K. NASHINE
DEVICE DEVELOPMENT & RIG
SERVICES DIVISION

Shri G. PADMAKUMAR
SODIUM EXPERIMENTS & HYDRAULICS
DIVISION

Shri B. BABU
INSTRUMENTATION DEVELOPMENT &
SERVICES DIVISION

Materials Science Group

Dr. C. S. SUNDAR
DIRECTOR

Shri M. P. JANAWADKAR
CONDENSED MATTER PHYSICS DIVISION

Dr. G. AMARENDRA
MATERIALS PHYSICS DIVISION

Dr. A. K. TYAGI
SURFACE & NANOSCIENCE DIVISION

Metallurgy & Materials Group

Dr. T. JAYAKUMAR
DIRECTOR

Dr. S. VENUGOPAL
ASSOCIATE DIRECTOR
GROUP FOR REMOTE HANDLING, ROBOTICS,
IRRADIATION EXPERIMENTS AND PIE

Dr. A. K. BHADURI
ASSOCIATE DIRECTOR
MATERIALS DEVELOPMENT AND
TECHNOLOGY GROUP

Shri JOJO JOSEPH
POST IRRADIATION
EXAMINATION DIVISION

Dr. M. D. MATHEW
MECHANICAL METALLURGY DIVISION

Dr. S. VENUGOPAL
REMOTE HANDLING, IRRADIATION
EXPERIMENTS AND ROBOTICS DIVISION

Dr. SHAJU K. ALBERT
MATERIALS TECHNOLOGY DIVISION

Dr. U. KAMACHI MUDALI
ASSOCIATE DIRECTOR
CORROSION SCIENCE & TECHNOLOGY GROUP

Dr. M. VIJAYALAKSHMI
ASSOCIATE DIRECTOR
PHYSICAL METALLURGY GROUP

Shri E. MOHANDAS
MATERIALS SYNTHESIS & STRUCTURAL
CHARACTERIZATION DIVISION

Dr. B. PURNA CHANDRA RAO
NON-DESTRUCTIVE
EVALUATION DIVISION

Dr. SAROJA SAIBABA
MICROSCOPY & THERMO-PHYSICAL
PROPERTY DIVISION

Groups / Divisions / Heads

Reactor Design Group

Dr. P. CHELLAPANDI
DIRECTOR

Shri P. PUTHIYAVINAYAGAM
ASSOCIATE DIRECTOR
CORE DESIGN GROUP

Dr. K. DEVAN
REACTOR NEUTRONICS DIVISION

Shri A. JOHN ARUL
REACTOR SHIELDING AND DATA DIVISION

Shri V. BALASUBRAMANIYAN
REACTOR COMPONENTS DIVISION

Shri S. RAGHUPATHY
COMPONENTS HANDLING &
MECHANISM DIVISION

Shri K. MADHUSOODANAN
ASSOCIATE DIRECTOR
POWER PLANT GROUP

Shri K. MADHUSOODANAN
INSTRUMENTATION & CONTROL DIVISION

Shri N. THEIVARAJAN
POWER PLANT CONTROL DIVISION

Shri P. SELVARAJ
ASSOCIATE DIRECTOR
REACTOR ANALYSIS GROUP

Dr. K. VELUSAMY
MECHANICS & HYDRAULICS DIVISION

Shri B. K. NASHINE
SAFETY ENGINEERING DIVISION

Reactor Operation and Maintenance Group

Shri G. SRINIVASAN
DIRECTOR

Shri K. V. SURESH KUMAR
REACTOR OPERATION DIVISION

Miss. S. USHA
TECHNICAL SERVICES DIVISION

Dr. R. S. KESHAVAMURTHY
REACTOR PHYSICS DIVISION

Shri A. BABU
REACTOR MAINTENANCE DIVISION

Shri N. KASINATHAN
REACTOR ANALYSIS DIVISION

Dr. V. GANESAN
PROJECT MANAGER, DFMF

Reprocessing Group

Dr. R. NATARAJAN
DIRECTOR

Shri V. SUNDARARAMAN
ASSOCIATE DIRECTOR
PROCESS DESIGN &COMMISSIONING GROUP

Shri. V. SUNDARARAMAN
FUEL REPROCESSING PROCESS DIVISION

Dr. U. KAMACHI MUDALI
REPROCESSING RESEARCH &
DEVELOPMENT DIVISION

Shri A. RAVISHANKAR
ASSOCIATE DIRECTOR
REPROCESSING PROJECTS & OPERATION GROUP

Shri V. VIJAYAKUMAR
REPROCESSING PLANT OPERATIONS
DIVISION

Shri B. M. ANANDARAO
REPROCESSING PLANT DESIGN DIVISION